

Nº d'ordre : 41214

THÈSE

Présentée à l'Université de Lille 1

Sciences et Technologies

pour obtenir le grade de

DOCTEUR

Discipline : Molécules et Matière Condensée

Présentée par

Almaz ALIEV

le 7 Novembre 2013

Nouvelles Topologies structurales d'oxydes et sels de
bismuth ; cristallographie, approche modulaire et
propriétés.

Jury:

Philippe BOULLAY	DR CNRS, CRISMAT Caen	Rapporteur
Patrick ROZIER	MdC, Université Paul Sabatier	Rapporteur
Sergey KRIVOVICHEV	Professor, St.Petersburg State University	Examineur
Olivier MENTRE	DR CNRS, UCCS, Lille	Directeur
Marie COLMONT	MdC, ENSCL, Lille	Co-encadrant

Table of Contents

Table of Contents	1
List of figures	4
List of tables	12
Abstract	15
Résumé	17
Introduction	21
I. Anion-centered tetrahedra concept of BUs, their Design and the description of the thesis	24
I.1 Anion-centered tetrahedra in structural descriptions	24
I.1.1 Why an alternative structural description?	24
I.1.2 Chemistry of anion-centered XA_4 tetrahedra	25
I.1.3 Preferred cations for oxo-centered tetrahedra	25
I.1.4 OBi_4 and $\text{O}(\text{Bi}/\text{M})_4$ as oxo-centered tetrahedra.	26
I.1.5 Lonepair of Bi^{III}	27
I.1.6 The heritage of fluorite type $\delta\text{-Bi}_2\text{O}_3$	28
I.1.7 Available Dimensionalities for edifices built from oxocentered tetrahedra	29
I.2 The case of bismuth oxo-phosphates	35
I.2.1 Empirical structural rules	36
I.2.2 Possible Design of new terms	38
I.2.3 The benefit of HREM	38
I.3 Description of my thesis	40
I.3.1 Design of new materials	40
I.3.2 Shake and bake synthesis	41
I.3.3 Arsenates versus phosphates	42
I.3.4 Separating of building units by chloride ions	42
I.3.5 The incorporation of SeO_3^{2-}	43
I.3.6 Summary	43
II. New bismuth-based oxides and salts - original topologies of oxocentered tetrahedra	50
II.1 1D compounds – ribbons and columns as BUs	50

II.1.1	n = 1 ribbons: $\text{BiCoO}(\text{AsO}_4)$	50
II.1.2	n = 2 ribbons: $\text{BiCu}_2\text{O}_2(\text{AsO}_4)$ and $\text{BiCu}_2\text{O}_2(\text{PO}_4)$	54
II.1.3	n = 2 ribbons: $\text{NaBiO}(\text{MoO}_4)$	61
II.1.4	Potentialities of bismuth containing compounds as luminescent materials	62
II.1.5	n = 3 ribbons and 2x2 column: Labile degree of disorder in Bismuth-oxyphosphate compounds: illustration through three new structural types	64
II.1.6	n = 3 ribbons: $\text{Bi}_4\text{Cu}_3\text{O}_6(\text{AsO}_4)_2$ and $\text{Bi}_4\text{Cu}_3\text{O}_6(\text{VO}_4)_2$	83
II.1.7	n = 3 / n = 4 ribbon intergrowths: $\text{Bi}_{29.4}\text{Cu}_{9.29}\text{O}_{32}(\text{PO}_4)_{16}\text{Cu}_{2.63}$ and $\text{Bi}_{37.2}\text{Cu}_{18.8}\text{O}_{44}(\text{PO}_4)_{24}\text{Cu}_5$	90
II.1.8	n = 4 ribbons: $\text{KBi}_5\text{O}_5(\text{AsO}_4)_2$	98
II.1.9	n = 5 ribbons: $\text{Bi}_6\text{ZnO}_7(\text{AsO}_4)_2$ against $\text{Bi}_6\text{ZnO}_7(\text{PO}_4)_2$	100
II.2	Compounds with 2D-units - Layers	105
II.2.1	Phase homology in new layered mixed Li, M (M = Cu, Cd, Bi...) bismuth oxophosphates and oxoarsenates: $(\text{Bi}_7\text{O}_7)(\text{BiO})_7\text{CdLi}_2(\text{PO}_4)_6$ and $[\text{Bi}_4\text{O}_4][\text{BiO}]_4\text{CuLi}_2(\text{AsO}_4)_4$	105
II.2.2	The new $[\text{PbBi}_2\text{O}_4][\text{Bi}_2\text{O}_2]\text{Cl}_2$ and $[\text{Pb}_m\text{Bi}_{10-m}\text{O}_{13}][\text{Bi}_2\text{O}_2]_m\text{Cl}_{4+m}$ series by association of sizeable subunits; Relationship with the Arppe's compound $\text{Bi}_{24}\text{O}_{31}\text{Cl}_{10}$	109
II.2.3	$\text{Bi}_6\text{O}_{8.5}\text{Cl}$	125
II.2.4	$\text{Bi}_9\text{O}_9\text{Cl}_4(\text{Pb}_{0.2}\text{Mn}_{0.8})\text{O}_3\text{Cl}$	129
II.3	3D-units - frameworks	133
II.3.1	$\text{Bi}_{46}\text{O}_{53}(\text{AsO}_4)_8$ and $\text{Bi}_{14}\text{O}_{15}(\text{AsO}_4)_4$	133
II.3.2	$\text{NaBi}_{13}\text{O}_{14}(\text{AsO}_4)_4$	143
III.	Other specific Bi-based Compounds	148
III.1.1	$\text{Bi}_4\text{Mn}_{3+x}\text{O}_{11.5-y}$ - a new bismuth manganite with 2D-magnetic properties	148
III.2	New Compounds in the system $\text{BOCl-SeO}_2\text{-M}_x\text{O}_y$	171
III.2.1	$\beta\text{-BiSeO}_3\text{Cl}$, $\text{Bi}_6(\text{SeO}_3)_4\text{Cl}_{10}$ and $\text{PbBi}_{10}(\text{SeO}_3)_{12}\text{Cl}_8$	171
III.2.2	$\text{Bi}_2\text{MnO}(\text{SeO}_3)_2\text{Cl}_3$	182
Conclusion		186
Reference		189
Annex		Erreur ! Signet non défini.
S.1	n = 1 ribbons: BiCoAsO_5	205
S.2	n = 3 ribbons: $\text{Bi}_4\text{Cu}_3\text{O}_6(\text{AsO}_4)_2$ and $\text{Bi}_4\text{Cu}_3\text{O}_6(\text{VO}_4)_2$	206
S.3	n = 3 ribbons and 2x2 column: Labile degree of disorder in Bismuth-oxyphosphate compounds: illustration through three new structural types	209
S.4	n = 3 / n = 4 ribbon intergrowths: $\text{Bi}_{29.4}\text{Cu}_{9.29}\text{O}_{32}(\text{PO}_4)_{16}\text{Cu}_{2.63}$ and $\text{Bi}_{37.2}\text{Cu}_{18.8}\text{O}_{44}(\text{PO}_4)_{24}\text{Cu}_5$	217
S.5	n = 4 ribbons: $\text{KBi}_5\text{O}_5(\text{AsO}_4)_2$	221
S.6	n = 5 ribbons: $\text{Bi}_6\text{ZnO}_7(\text{AsO}_4)_2$ versus $\text{Bi}_6\text{ZnO}_7(\text{PO}_4)_2$	224

S.7	Phase homology in new layered mixed Li, M (M = Cu, Cd, Bi...) bismuth oxophosphates and oxoarsenates: $(\text{Bi}_7\text{O}_7)(\text{BiO})_7\text{CdLi}_2(\text{PO}_4)_6$ and $[\text{Bi}_4\text{O}_4][\text{BiO}]_4\text{CuLi}_2(\text{AsO}_4)_4$	226
S.8	The new $[\text{PbBi}_2\text{O}_4][\text{Bi}_2\text{O}_2]\text{Cl}_2$ and $[\text{Pb}_m\text{Bi}_{10-m}\text{O}_{13}][\text{Bi}_2\text{O}_2]_m\text{Cl}_{4+m}$ series by association of sizeable subunits; Relationship with the Arppe's compound $\text{Bi}_{24}\text{O}_{31}\text{Cl}_{10}$	230
S.9	$\text{Bi}_9\text{O}_9\text{Cl}_4(\text{Pb}_{0.2}\text{Mn}_{0.8})\text{O}_3\text{Cl}$	237
S.10	$\text{Bi}_{46}\text{O}_{53}(\text{AsO}_4)_8$ and $\text{Bi}_{14}\text{O}_{15}(\text{AsO}_4)_4$	239
S.11	$\text{Bi}_4\text{Mn}_{3+x}\text{O}_{11.5-y}$ - a new bismuth manganite with 2D-magnetic properties	249
S.12	β' - BiSeO_3Cl , $\text{Bi}_6(\text{SeO}_3)_4\text{Cl}_{10}$ and $\text{PbBi}_{10}(\text{SeO}_3)_{12}\text{Cl}_8$	252
S.13	$\text{Bi}_2\text{MnO}(\text{SeO}_3)_2\text{Cl}_3$	269

List of figures

Figure I.1. a) The crystal structure of dolerophanite. $\text{Cu}_2\text{O}(\text{SO}_4)$, where SO_4 tetrahedra in blue. Os are the oxygen atoms of sulphate groups, O_a are the “additional” oxygen atoms in the center of OCu_4 tetrahedra b) edge- and corner-sharing (OCu_4) tetrahedra in the tetrahedra presentation (green).....	24
Figure I.2. Combination of OBi_4 , OBi_{3+1} and OBi_{2+2} in $(\text{Bi}_2\text{O}_2)(\text{TeO}_3)$	26
Figure I.3. Bi^{5+}O_6 octahedra and distorted $\text{Bi}^{3+}\text{O}_4\text{LP}$ polyhedra in Bi_2O_4	27
Figure I.4. Reorganization of the $[\text{OBi}_2]\text{O}_2$ chains between a) the metastable $\epsilon\text{-Bi}_2\text{O}_3$, with a DFT visualization of LP electronic density b) $\alpha\text{-Bi}_2\text{O}_3$ c) ideal structure of oxygen-deficient fluorite $\delta\text{-Bi}_2\text{O}_3$ and d) $\theta\text{-Bi}_2\text{O}_3$	28
Figure I.5. a) The ideal structure of the oxygen-deficient fluorite type $\delta\text{-Bi}_2\text{O}_3$ projection along the b-axis, b) the cationic grid representation of the same structure in blue (Bi-Bi bonds).	28
Figure I.6. OD units: a) $[\text{O}(\text{Bi}_3\text{K})]$ in $\text{K}[\text{KBi}_3\text{O}](\text{PO}_4)_3$, b) $[\text{Sr}_2\text{Bi}_3\text{O}_2]$ in $[\text{Sr}_2\text{Bi}_3\text{O}_2](\text{VO}_4)_3$, c) protonated $[(\text{O},\text{OH})_8\text{Bi}_6]$ polycationic-clusters	30
Figure I.7. 1D chain-like topology. Projection of corner sharing (OBi_2) chains in a) $(\text{Bi}_2\text{O})_2(\text{AuO}_4)$ and b) $(\text{Bi}_4\text{O}_2)(\text{BiO})_2\text{Bi}(\text{MoO}_4)_2(\text{AsO}_4)_3$	30
Figure I.8. Edge-sharing $\text{O}(\text{Bi},\text{M})_4$ units: a) single-chains in $\text{BiNiO}(\text{PO}_4)$ b) $n = 2$ ribbons in $\text{BiCu}_2\text{O}_2(\text{PO}_4)$	31
Figure I.9. 1D-units as columns with cross-section: a) 2×2 tetrahedra in $(\text{Bi}_{14}\text{Cd}_4\text{O}_{16})(\text{PO}_4)_8\text{Bi}_{1.2}\text{Cd}_{1.2}$ (mixed sites are not shown), b) 3×2 in $[\text{Bi}_6\text{O}_5]\text{O}_2(\text{CrO}_4)_2$, c) 4×3 in $\gamma\text{-Bi}_2\text{MoO}_6$. d) shifted 2×4 cross section in $(\text{Bi}_6\text{O}_7)_2\text{O}_4(\text{SO}_4)_5$. (\otimes denote the infinite character perpendicular to the projected plane) The oxygen atoms of OBi_3 are marked as 3.	31
Figure I.10. Layered 2D units: a) (Bi_2O_2) double-layer in $(\text{Bi}_2\text{O}_2)(\text{UO}_4)$. (Bi_2O_2) simple layer in b) the Aurivillius- Bi_2MoO_6 compound c) in various polytypes described in [55] d) double ribbons of OBi_2Y_2 in $(\text{O}_4\text{YBi}_2)\text{YCu}_2\text{Se}_2$. (\otimes denote the infinite character perpendicular to the projected plane), e) infinite extension of 1D-ribbons with O-Bi excesses in $(\text{Bi}_2\text{O}_2)_{11/6}(\text{BiO})_{1/3}\text{M}_1(\text{PO}_4)_2$	32
Figure I.11. Crenel 2D units (\otimes denote the infinite character perpendicular to the projected plane) a) $m = 5$ of $\text{Bi}_{2m}\text{Mo}_{m-2}\text{O}_{6m-6}$, b) 8×3 crenel junctions by edge-sharing in $\text{Bi}_{18.71}\text{Cr}_{0.27}\text{P}_6\text{O}_{43.22}$. c) $(\text{Bi}_6\text{O}_7)_4\text{O}_3\text{Cl}_{10}$ case with detail of the mixed edge and corner-sharing junctions between $n = 12$ ribbons in the perpendicular plane.	33
Figure I.12. 2D-Crenel ribbons by corner-sharing of $\text{O}(\text{Bi},\text{M})_4$ tetrahedra from a) $n = 2$ Td ribbons in $(\text{Bi}_5\text{O}_4)\text{O}_{0.5}(\text{PO}_4)_2$, b) $n = 3$ Td in $(\text{Cu}_3\text{Bi}_4\text{O}_6)(\text{VO}_4)_2$, c) $n = 4$ Td in $(\text{Bi}_{8.67}\text{O}_8)(\text{SO}_4)_4$. (\otimes denote the infinite character perpendicular to the projected plane).....	33
Figure I.13. $[\text{O}_4\text{Bi}_8]$ stella quadrangulae in $(\text{Bi}_3\text{O}_2)(\text{Ru}_3\text{O}_9)$ and $(\text{Bi}_3\text{O}_2)(\text{GaSb}_2\text{O}_9)$	34
Figure I.14. 3D framework of $\text{O}(\text{Bi},\text{M})_4$ tetrahedra. Triangular networks in a) $(\text{M}_5\text{Cl})(\text{Bi}_8\text{O}_9)_6\text{O}_5\text{Cl}_{30}$ with $\text{M}^+ = \text{Cu}$ or Ag , b) $(\text{Bi}_6\text{O}_6\text{F})\text{OCl}_3$, c) $(\text{Bi}_6\text{O}_7)_2\text{OCl}$, d) connection of infinite ribbons by OLa_4 tetrahedra in $\text{Bi}_8\text{La}_{10}\text{O}_{27}$. e) voids in of $(\text{Bi}_3\text{O}_2)(\text{BiO})(\text{BO}_3)_2$ filled by BO_3	34

Figure I.15. Incorporation of PO_4 groups in Bi_2O_3 oxides: a) conservation of the 3D character based on OBi_4 linkage in $\text{Bi}_{46}\text{O}_{57}(\text{PO}_4)_8$ and b) 2D character in $\text{Bi}_{14}\text{O}_{15}(\text{PO}_4)_4$	35
Figure I.16. Structural organization of BUs in a $n = 4 / n = 6$ phase	36
Figure I.17. Subsequent stages in structure-deduction process using HREM images.	39
Figure I.18. Possible arrangements of 2D-BU's and XO_4 groups in hypothetical structures.....	40
Figure I.19. A scheme to formulate new compounds.....	41
Figure II.1. $\text{BiMO}(\text{XO}_4)$: a) The structure of $\text{BiNiO}(\text{PO}_4)$, where M atoms in trans position, b) the structure of $\text{BiCaO}(\text{VO}_4)$, where M atoms in cis position.....	50
Figure II.2. Crystal structure of a) $\text{BiCoO}(\text{AsO}_4)$ and b) $\text{BiCoO}(\text{PO}_4)$	51
Figure II.3. DTA plot (top graph) and unit-cell parameters evolution of $\text{BiCoO}(\text{AsO}_4)$ as functions of temperature. Red arrows show an anomaly on the unit cell parameters evolution as well as an endothermic peak on the DTA.....	52
Figure II.4. $\chi(T)$ and $\chi^{-1}(T)$ plots of $\text{BiCoO}(\text{AsO}_4)$	53
Figure II.5. The structures of: a) $\text{BiCu}_2\text{O}_2(\text{PO}_4)$ and b) $\text{BiCu}_2\text{O}_2(\text{AsO}_4)$. J_{1-2} , J_3 and J_4 are the spin-exchange paths.	55
Figure II.6. Schematic representation of the Cu^{2+} ion arrangement and the SE/SSE spin-exchange paths in $\text{BiCu}_2\text{O}_2(\text{PO}_4)$. The two crystallographically nonequivalent copper atoms are indicated by blue and cyan circles, and the oxygen atoms by red circles.	55
Figure II.7. Diffraction patterns of solid solutions $\text{BiCu}_2\text{O}_2(\text{As}_x\text{P}_{1-x}\text{O}_4)$, x changing from 0 to 1. The peaks of the phase $\text{BiCu}_2\text{O}_2(\text{AsO}_4)$ denoted by black triangles whereas that of $\text{BiCu}_2\text{O}_2(\text{PO}_4)$ with white squares.	57
Figure II.8 Variation of the lattice parameters versus x in $\text{BiCu}_2\text{O}_2(\text{As}_x\text{P}_{1-x}\text{O}_4)$	57
Figure II.9. Magnetic measurements of $\text{BiCu}_2\text{O}_2(\text{As}_x\text{P}_{1-x}\text{O}_4)$: a) susceptibilities and b) inverse susceptibilities vs. T collected at $H = 0.05$ T for $x = 0$, $H = 0.1$ T for $x = 0.25$ and $H = 0.5$ T for $x = 1$	58
Figure II.10. a) The evidence of a spin gap in $\text{BiCu}_2\text{O}_2(\text{PO}_4)$ and b) the absence of that in $\text{BiCu}_2\text{O}_2(\text{AsO}_4)$ on inelastic neutron scattering.	58
Figure II.11. Profile fitting of $\text{BiCu}_2\text{O}_2(\text{AsO}_4)$ refined taking into account of minor second phase – $\text{Bi}_4\text{Cu}_3\text{O}_6(\text{AsO}_4)_2$. * - denotes some extra peaks the origin of which is nonmagnetic, since they are observed at the temperature above T_N (see inset).	59
Figure II.12. $\text{BiCu}_2\text{O}_2(\text{AsO}_4)$: ZFC/FC plots of M/H versus the temperature at 0.01 Tesla in black. $\chi^{-1}(T)$ is shown in blue and refers to the right-axis.	60
Figure II.13. $\text{BiCu}_2\text{O}_2(\text{AsO}_4)$: $M(H)$ at $T = 1.8$ K (black), 10 K (red) and 30 K (green) in $\mu_B/\text{f.u.}(\text{Oe})$	60
Figure II.14. a) The structure of $\text{NaBiO}(\text{MoO}_4)$, b) Na channel surrounded by MoO_4 tetrahedra and c) the cationic grid representation of the structure	61
Figure II.15 a) $\text{BiMg}_2\text{O}_2(\text{AsO}_4)$ under UV-lamp excited at 254 nm and b) Stokes shift in $\text{BiCd}_2\text{O}_2(\text{PO}_4)$	63
Figure II.16. a) Projection along c-axis of the crystal structure of $[\text{Bi}_2(\text{Bi}_{1.56}\text{K}_{0.44})^{\text{dis}}\text{O}_3]\text{K}_{0.88}^{\text{dis}}(\text{PO}_4)_2$, b) representation of the channels (the yellow continuum along the tunnel is the electron density obtained after Fourier difference of the electron map without K ($14 e^-/\text{\AA}^3$) and c) hypothetic possible K arrangement along c-axis.	67

- Figure II.17. $[\text{Bi}_2(\text{Bi}_{1.56}\text{K}_{0.44})^{\text{dis}}\text{O}_3]\text{K}_{0.88}^{\text{dis}}(\text{PO}_4)_2$: a) calculated precession frame of the 0kl layer from single crystal XRD data, b) ED patterns of the corresponding compound. c) Profile fitting of the corresponding powder (refined unit cell parameters $a = 13.6922(3) \text{ \AA}$, $c = 5.6602(2) \text{ \AA}$, $V = 1061.16(4) \text{ \AA}^3$, $\chi^2 = 2.25$). 69
- Figure II.18. ^{31}P MAS spectra at 18.8 T of a) $[\text{Bi}_2(\text{Bi}_{1.56}\text{K}_{0.44})^{\text{dis}}\text{O}_3]\text{K}_{0.88}^{\text{dis}}(\text{PO}_4)_2$, b) and b) $[\text{Bi}_{18}\text{Zn}_{10}\text{O}_{21}]^{\text{ord}}\text{Zn}_5^{\text{ord}}(\text{PO}_4)_{14}$. In (a), the star * denotes an impurity phase. The spectra were acquired with a total of 32 scans, a short pulse excitation of $0.8 \mu\text{s}$ and a recycling delay of 10 s. 70
- Figure II.19. a) Projection along c-axis of the average crystal structure of $[\text{Bi}_{10}(\text{Bi}_{-0.5}\text{Cd}_{-0.5})_8^{\text{dis}}\text{O}_{16}](\text{Bi}_{0.6}\text{Cd}_{0.8})_2^{\text{ord}}(\text{PO}_4)_8$ and b) the square based columns and PO_4 tunnels along c-axis on the left (the yellow continuum along the tunnel is the electron density obtained after Fourier difference of the electron map without cation ($30 \text{ e}^-/\text{\AA}^3$)). 72
- Figure II.20. $[\text{Bi}_{10}(\text{Bi}_{-0.5}\text{Cd}_{-0.5})_8^{\text{dis}}\text{O}_{16}](\text{Bi}_{0.6}\text{Cd}_{0.8})_2^{\text{ord}}(\text{PO}_4)_8$: a) Calculated precession of (h0l) layer (XRD on single crystal) and b) ED image of (h0l) layer with enhancement of substructure spots ($q \approx 0.4 \text{ c}^*$), c) the comparison between the calculated XRD patterns (average and modulated models) and the experimental one. Green indices are the fundamental and black ones are the modulation peaks. 73
- Figure II.21. a) Fourier difference along (x4, z) in the tunnel (contribution from $x_4=0$ to 1 are summed), b) separation of 2 sites Bi/Cd at different section along x4, c) Bi/Cd repartition in the modulated structure of $[\text{Bi}_{10}(\text{Bi}_{-0.5}\text{Cd}_{-0.5})_8^{\text{dis}}\text{O}_{16}](\text{Bi}_{0.6}\text{Cd}_{0.8})_2^{\text{ord}}(\text{PO}_4)_8$, d) electronic density and occupancy of Bi/Cd sites of the columns e) coordination of Bi and Cd in the tunnel. 74
- Figure II.22. The crystal structure of $[\text{Bi}_{18}\text{Zn}_{10}\text{O}_{21}]^{\text{ord}}\text{Zn}_5^{\text{ord}}(\text{PO}_4)_{14}$ (projection along b-axis) on the left and the ribbon and PO_4 tunnel (projection along c-axis) on the right. 77
- Figure II.23. a) Calculated precession frame from single crystal XRD data of $[\text{Bi}_{18}\text{Zn}_{10}\text{O}_{21}]^{\text{ord}}\text{Zn}_5^{\text{ord}}(\text{PO}_4)_{14}$, b) ED patterns of the 0kl layer of the corresponding powder and c) XRD patterns calculated from the disordered structure of $\text{Bi}_{1.2}\text{Zn}_{1.2}\text{O}_{1.5}\text{PO}_4$ (red), from the ordered single crystal of $[\text{Bi}_{18}\text{Zn}_{10}\text{O}_{21}]^{\text{ord}}\text{Zn}_5^{\text{ord}}(\text{PO}_4)_{14}$ (black) and experimental (blue). Inset - selected 2θ range showing some superstructure peaks - a sign of cation ordering. * - an impurity 80
- Figure II.24. SHG response vs. particle size of $[\text{Bi}_{18}\text{Zn}_{10}\text{O}_{21}]^{\text{ord}}\text{Zn}_5^{\text{ord}}(\text{PO}_4)_{14}$. The line is drawn to guide the eye.... 81
- Figure II.25. Cationic grid representation of the structures of a) $[\text{Bi}_{18}\text{Zn}_{10}\text{O}_{21}]^{\text{ord}}\text{Zn}_5^{\text{ord}}(\text{PO}_4)_{14}$ b) $[\text{Bi}_2(\text{Bi}_{1.56}\text{K}_{0.44})^{\text{dis}}\text{O}_3]\text{K}_{0.88}^{\text{dis}}(\text{PO}_4)_2$, and c) $[\text{Bi}_{10}(\text{Bi}_{-0.5}\text{Cd}_{-0.5})_8^{\text{dis}}\text{O}_{16}](\text{Bi}_{0.6}\text{Cd}_{0.8})_2^{\text{ord}}(\text{PO}_4)_8$. Minus (-) and plus (+) signs indicate x and $x + \frac{1}{2}$ "out-of-plane" respectively, regard to a $\sim 5.5 \text{ \AA}$ parameter. The tunnel cations are shown on both representations and are interstitial cations. In (b) and (c) small open squares show the virtual cationic vacancies. 82
- Figure II.26. The diffraction patterns of $\text{BiCu}_2\text{O}_2(\text{AsO}_4)$ with some impurities. Green lines are the diffraction pattern of $\text{BiCu}_2\text{O}_2(\text{AsO}_4)$, red lines are the peaks of $\text{Bi}_4\text{Cu}_3\text{O}_6(\text{VO}_4)_2$ 84
- Figure II.27. Diffraction pattern of prepared $\text{Bi}_4\text{Cu}_3\text{O}_6(\text{AsO}_4)_2$ (black) and theoretical diffraction pattern of $\text{Bi}_4\text{Cu}_3\text{O}_6(\text{VO}_4)_2$ with As atoms instead of V (in red). 84
- Figure II.28. Crystal structure of: a) $\text{Bi}_4\text{Cu}_3\text{O}_6(\text{AsO}_4)_2$; and b) $\text{Bi}_4\text{Cu}_3\text{O}_6(\text{VO}_4)_2$, c) the cationic network of $\text{Bi}_4\text{Cu}_3\text{O}_6(\text{AsO}_4)_2$. In a) and b) the colored circles show the difference of the orientation of the XO_4

tetrahedra from one cell to another). In a) the unit cell of $\text{Bi}_4\text{Cu}_3\text{O}_6(\text{AsO}_4)_2$ compared to that of $\text{Bi}_4\text{Cu}_3\text{O}_6(\text{VO}_4)_2$ (broken lines).....	85
Figure II.29. Cu_3O_4 chains in a) $\text{Bi}_4\text{Cu}_3\text{O}_6(\text{AsO}_4)_2$ and b) $\text{Bi}_4\text{Cu}_3\text{O}_6(\text{VO}_4)_2$	86
Figure II.30. Cu_3O_4 chain of $\text{Bi}_4\text{Cu}_3\text{O}_6(\text{VO}_4)_2$ with J2 and J4 exchanges.....	87
Figure II.31. $\text{Bi}_4\text{Cu}_3\text{O}_6(\text{AsO}_4)_2$: a) Magnetic susceptibility vs. temperature. Inset: zoom of the temperature range 0-20 K, b) Inverse susceptibility vs. temperature.....	88
Figure II.32. $\text{Bi}_4\text{Cu}_3\text{O}_6(\text{AsO}_4)_2$: Magnetization $M(H)$ vs. magnetic field at 2K. Inset: metamagnetic transition at $\mu_0 H = 0.06\text{T}$	88
Figure II.33. Neutron diffraction structure refinement of $\text{Bi}_4\text{Cu}_3\text{O}_6(\text{AsO}_4)_2$. * denotes some extra peaks the origin of which is nonmagnetic, since they are observed at the temperature above T_N (see inset).	89
Figure II.34 a) hypothetical crystal structure of the $n = 4 / n = 4$ compound and its calculated c unit cell parameter.....	90
Figure II.35. Projections of the crystal structures of (a) $\text{Bi}_{29.4}\text{Cu}_{9.29}\text{O}_{32}(\text{PO}_4)_{16}\text{Cu}_{2.63}$ and (b) $\text{Bi}_{37.2}\text{Cu}_{18.8}\text{O}_{44}(\text{PO}_4)_{24}\text{Cu}_5$ along the b axis. Both structures are built on the association of ribbons $n = 4$ (noted (4)) and $n = 3$ (noted (3)) tetrahedra wide and tunnels (noted (t)). Note the different (4)t(4)t(3)(3) and (3)t(4)t(3)/(4)t(3)(3)t sequences in both compounds. The corresponding 2D-square cationic networks are presented underneath of respective structures as well as the tunnel arrangements as blue inserts.....	93
Figure II.36. Profile fitting of the compound and refined parameters of a) $\text{Bi}_{37.2}\text{Cu}_{18.8}\text{O}_{44}(\text{PO}_4)_{24}\text{Cu}_5$ $a = 11.6121(6)$, $b = 47.584(3)$, $c = 5.2700(3)$, $V = 2911.9(3)$, $\chi^2 = 1.75$ and b) the powder corresponding to $\text{Bi}_{29.4}\text{Cu}_{9.29}\text{O}_{32}(\text{PO}_4)_{16}\text{Cu}_{2.63}$: i) measured, ii) calculated, iii) and compared to the 4/6 intergrowth present as an impurity.....	94
Figure II.37. (0kl), (h0l) and (hk0) layers showing the low quality of crystal 2. Thus, overlaps, streaks and extra spots are observed on the different layers.....	95
Figure II.38. a)[010] ZAP of $\text{Bi}_{29.4}\text{Cu}_{9.29}\text{O}_{32}(\text{PO}_4)_{16}\text{Cu}_{2.63}$ compared to b) the corresponding [100] ZAP of $\text{Bi}_{37.2}\text{Cu}_{18.8}\text{O}_{44}(\text{PO}_4)_{24}\text{Cu}_5$ which exhibits diffuses streaks indicating by white arrows.....	96
Figure II.39. a) transmission image of a crystal of $\text{Bi}_{37.2}\text{Cu}_{18.8}\text{O}_{44}(\text{PO}_4)_{24}\text{Cu}_{5.4}$ b) green: emitting surface ($\lambda_{em} = 420\text{-}440\text{ nm}$, $\lambda_{em} = 860\text{ nm}$)	98
Figure II.40. a) The crystal structure of $\text{KBi}_5\text{O}_5(\text{AsO}_4)_2$ and b) its cationic grid representation.....	99
Figure II.41. Pattern matching of $\text{KBi}_5\text{O}_5(\text{AsO}_4)_2$ with the refined parameters $a = 8.2504(2)\text{\AA}$, $b = 5.5454(1)\text{\AA}$, $c = 28.4068(6)\text{\AA}$, $\beta = 95.8796(8)^\circ$ and $V = 1292.81(4)\text{\AA}^3$ with reliability parameter $\chi^2 = 2.60$	99
Figure II.42. Crystal structure of a) $\text{Bi}_6\text{ZnO}_7(\text{AsO}_4)_2$ and b) $\text{Bi}_6\text{ZnO}_7(\text{PO}_4)_2$, c) AsO_4 and d) PO_4 tetrahedra of selected regions of the respective structures, e) ZnO_4 and AsO_4 , f) ZnO_4 and PO_4 tetrahedra.	102
Figure II.43. a) Crystal structure $\text{Bi}_6\text{ZnO}_7(\text{AsO}_4)_2$ and b) its cationic grid representation.	103
Figure II.44. DTA plot (top graph) and unit-cell parameters evolution of $\text{Bi}_6\text{ZnO}_7(\text{PO}_4)_2$ as functions of temperature.....	103
Figure II.45. SHG response vs. particle size of $\text{Bi}_6\text{ZnO}_7(\text{PO}_4)_2$. The line is drawn to guide the eye.....	104

Figure II.46. Projections of the crystal structures of a) $[\text{Bi}_7\text{O}_7][\text{BiO}]_7\text{Bi}_{0.67}\text{Li}_2(\text{PO}_4)_6$ and b) $(\text{Bi}_7\text{O}_7)(\text{BiO})_7\text{CdLi}_2(\text{PO}_4)_6$ along the <i>b</i> -axis, c) phosphate-lithium tunnels with the incorporated cations along the <i>b</i> axis. The similarities in the structure are given with dashed rectangulars. LiO_4 tetrahedra in the up and down orientation (labeled in red) for $[\text{Bi}_7\text{O}_7][\text{BiO}]_7\text{Bi}_{0.67}\text{Li}_2(\text{PO}_4)_6$	106
Figure II.47. General projection of the crystal structure of $[\text{Bi}_4\text{O}_4][\text{BiO}]_4\text{CuLi}_2(\text{AsO}_4)_4$ along the <i>c</i> axis (right). The structure of $[\text{LiCu}_{0.5}(\text{AsO}_4)_2]^{4-}$ as the AsO_4 - LiO_4 tunnel with the incorporated Cu is shown as projection along the <i>b</i> axis.....	107
Figure II.48. General projection of the crystal structure of $[\text{Bi}_4\text{O}_4][\text{BiO}]_4\text{CuLi}_2(\text{AsO}_4)_4$ along the <i>b</i> axis and its corresponding 2D-square network.	108
Figure II.49 Relationship and ratio (<i>m</i>) of $[\text{Bi}_2\text{O}_2]^{2+}$ and $[\text{BiO}]/(\text{XO}_4)$ stacking sequences in Aurivillius phases and bismuth oxophosphates: a) <i>k</i> = 1 in BiWO_6 , b) <i>k</i> = 1 in $\text{Bi}_6\text{Zn}(\text{PO}_4)\text{F}_2$, c) <i>k</i> = 2 in $\text{Bi}_3\text{TiNbO}_9$, d) <i>k</i> = 2 in $[\text{Bi}_2\text{O}_2][\text{BiO}]_2\text{M}(\text{PO}_4)_2$ (<i>M</i> = Mg, Zn), e) <i>k</i> = 3 in $\text{Bi}_4\text{Ti}_3\text{O}_{12}$ and f) <i>k</i> = 3 in a hypothetical compound.	108
Figure II.50. (a) Structure of Arppe's compound as an assembly of building units: (b) unit 1, (c) unit 2, (d) unit 3.	111
Figure II.51. Evidence of layered modules in the crystal structures of a) BiOCl , b) $\text{Bi}_2\text{LnO}_4\text{Cl}$, c) PbBiO_2Cl and d) $\text{PbBi}_4\text{O}_6\text{Cl}_2$ (this work).....	111
Figure II.52. a) Crystal structure of Arppe's compound. Occupancy of oxygen atoms in the Bi_6 cavities: b) according to ref ^[137] , c) according to our refinement in the subcell. Ordered O/Bi arrangement in the bordering units 3: d) from ref ^[137] , e) according to our refinement in the subcell.	114
Figure II.53. Profile fitting of the compound $[\text{Pb}_2\text{Bi}_8\text{O}_{13}][\text{Bi}_2\text{O}_2]_2\text{Cl}_6$, <i>m</i> = 2 with refined parameters <i>a</i> = 29.6643(8) Å, <i>b</i> = 3.9694(2) Å, <i>c</i> = 12.2489(4) Å, <i>θ</i> = 107.39(2)°.	118
Figure II.54. The structures of the $[\text{Pb}_m\text{Bi}_{10-m}\text{O}_{13}][\text{Bi}_2\text{O}_2]_m\text{Cl}_{4+m}$ members: a) hypothetical $[\text{PbBi}_9\text{O}_{13}][\text{Bi}_2\text{O}_2]\text{Cl}_5$, <i>m</i> = 1, b) $[\text{Pb}_2\text{Bi}_8\text{O}_{13}][\text{Bi}_2\text{O}_2]_2\text{Cl}_6$, <i>m</i> = 2, c) $[\text{Pb}_3\text{Bi}_7\text{O}_{13}][\text{Bi}_2\text{O}_2]_3\text{Cl}_7$, <i>m</i> = 3 and d) $[\text{Pb}_4\text{Bi}_6\text{O}_{13}][\text{Bi}_2\text{O}_2]_4\text{Cl}_8$, <i>m</i> = 4.....	119
Figure II.55. Arrhenius plot of the conductivity of the <i>m</i> = 2 term $[\text{Pb}_2\text{Bi}_8\text{O}_{13}][\text{Bi}_2\text{O}_2]_2\text{Cl}_6$. Inset: Nyquist plot for the measurement at 665°C with indication of the relaxation frequencies for each events.	121
Figure II.56. a) Fluorescent spectra of $\text{PbBi}_4\text{O}_6\text{Cl}_2$ and $[\text{Pb}_2\text{Bi}_8\text{O}_{13}][\text{Bi}_2\text{O}_2]_2\text{Cl}_6$ (<i>m</i> = 2 term) at 10 K, b) comparison between fluorescent spectra of $\text{PbBi}_4\text{O}_6\text{Cl}_2$ and $\text{BaBi}_4\text{O}_6\text{Cl}_2$ at 10 K, c) sketch of charge transfer between Pb^{2+} and Bi^{3+}	123
Figure II.57. The EPMA spectrum of $\text{Bi}_6\text{O}_{8.5}\text{Cl}$ showing the absence of Pb and Mn.	127
Figure II.58. Experimental (black) and calculated (green) XRD patterns of $\text{Bi}_6\text{O}_{8.5}\text{Cl}$	127
Figure II.59. The crystal structure of $\text{Bi}_6\text{O}_{8.5}\text{Cl}$	128
Figure II.60. Distorted octahedral coordination of a) O and b) Bi atoms, c) distorted rectangular pyramidal environment of O atom.....	128
Figure II.61. a) The crystal structure of $\text{Bi}_9(\text{Pb}_{0.2}\text{Mn}_{0.8})\text{O}_{12}\text{Cl}_5$ and b) one of the possible arrangements of $(\text{Pb}_{0.2}\text{Mn}_{0.8})\text{O}_3\text{Cl}$ rectangular pyramids; c) the channel walls are formed by oxocentered OBi_4 tetrahedra (cyan), while the connection of OBi_3M_2 (<i>M</i> = Pb/Mn) rectangular pyramids are highlighted in purple.....	132

Figure II.62. Comparison of the Porous 3D networks of $O(\text{Bi},\text{M})_4$ tetrahedra in cyan (the connection of $O(\text{Bi},\text{M})_5$ rectangular pyramid is highlighted in purple): a) $[\text{Bi}_6\text{O}_6\text{F}]\text{OCl}_3$ where in yellow is the FBi_4 tetrahedra, b) $(\text{Ag}_{4.78}\text{Cl}_{1.5})(\text{Bi}_{48}\text{O}_{58.64}\text{Cl}_{30})$, c) $\text{Bi}_{12}\text{O}_{15}\text{Cl}_6$, d) $\text{Bi}_6\text{NaO}_{7.5}\text{Cl}_4$, e) $\text{Bi}_{17}\text{PbO}_{22}\text{Cl}_9$, f) $\text{Bi}_9(\text{Pb}_{0.2}\text{Mn}_{0.8})\text{O}_{12}\text{Cl}_5$. The same scale is given for all the structures.	133
Figure II.63. The reflections in the $(h0l)$ and $(h1l)$ precession frames in good agreement with the C-Bravais lattice	137
Figure II.64. a) The structure of $\text{Bi}_{46}\text{O}_{53}(\text{AsO}_4)_8$, projection along b-axis and b) the structure of $\beta\text{-Bi}_{46}\text{O}_{53}(\text{VO}_4)_8$, projection along b-axis.	137
Figure II.65. Disordered a) $\text{As}(2)\text{O}_4$ and b) $\text{As}(4)\text{O}_4$ tetrahedra with two tilted positions in black and blue. The occupations of splitted O atoms fixed to 0.5.	138
Figure II.66. a) The structure of $\text{Bi}_{14}\text{O}_{15}(\text{AsO}_4)_4$, and that of b) $\text{Bi}_{14}\text{O}_{15}(\text{AsO}_4)_4$	139
Figure II.67. The pattern matching fit of the $\text{Bi}_{46}\text{O}_{53}(\text{AsO}_4)_8$ phase.	140
Figure II.68. a) Niqyst plots for $\beta\text{-Bi}_{46}\text{O}_{53}(\text{VO}_4)_8$ at 679°C in black from ref ^[167] (platinum electrode) and measured data of $\text{Bi}_{46}\text{O}_{53}(\text{VO}_4)_8$ at 675°C in blue squares and at 694°C in red circles (gold electrode); b) Arrhenius plots of conductivities of $\text{Bi}_{46}\text{O}_{53}(\text{XO}_4)_8$, ($\text{X} = \text{P}, \text{V}$ and As). Inset: Niqyst plot for $\text{X} = \text{As}$ at 618°C	141
Figure II.69. Profile matching fit of the $\text{Bi}_{14}\text{O}_{15}(\text{AsO}_4)_4$ phase.	142
Figure II.70. The crystal structure of $\text{NaBi}_{13}\text{O}_{14}(\text{AsO}_4)_4$	144
Figure III.1. The preparation with two types of crystal: black platelets of $\text{Bi}_4\text{Mn}_{3.03}\text{O}_{11.5}$ and transparent yellow platelets of $\text{Bi}_6\text{O}_{8.5}\text{Cl}$	148
Figure III.2 Comparison of: a-d) experimental XRD and e) calculated patterns after different synthesis stages. In b) and c) the residue from citrate method was decomposed in situ in the diffractometer.	149
Figure III.3. The TDA-TG curves of the residue obtained from citrate method at 300°C	150
Figure III.4. Schema for powder synthesis by modified citrate method.	150
Figure III.5. Experimental XRD patterns of $\text{Bi}_4\text{Mn}_3\text{O}_{11.5}$ (blue) and $\text{Bi}_4\text{Mn}_{2.4}\text{Fe}_{0.6}\text{O}_{11.5}$ (black).	151
Figure III.6. a) View of the $[\text{Bi}_4\text{O}_{4.5-y}][\text{Mn}_{3+x}\text{O}_7]$ intergrowth. b) Details of O-Bi connection at the apex of a void and c) the same part of the structure from PND data with less disorder.	153
Figure III.7 a) the ideal $[\text{Mn}_3\text{O}_7]$ array with the ordering of the $1/7^{\text{th}}$ vacancies, b) the structure of chalcophanite $[\text{ZnMn}_3\text{O}_7 \cdot 3\text{H}_2\text{O}]$, c) maple leaf lattice. ¹⁷² d) honeycomb lattice, e) parent triangular lattice	154
Figure III.8. Rietveld refinement fit from PND data of $\text{Bi}_4\text{Mn}_3\text{O}_{11.5}$ at 300 K.	156
Figure III.9. Rietveld refinement fit from PND data of $\text{Bi}_4\text{Mn}_{2.63}\text{Fe}_{0.4}\text{O}_{11.5}$ at 300 K.	157
Figure III.10. a) systematic $[100]$ and b) particular $[001]$ zone axes of the powder ED pattern, with evidence of primitive spots (rare case) in the later, c) a precession frame calculated from the single crystal XRD	158
Figure III.11. Evidence of a transition below 240 K, as: a) a lattice volume contraction from single crystal XRD; b) an anomaly on the electric 4-probes resistivity measurement on a single crystal.	159
Figure III.12 Rietveld refinement fit from PND data of $\text{Bi}_4\text{Mn}_3\text{O}_{11.5}$ at 180K.	160

Figure III.13. The electric 4-probes resistivity measurement on pressed bars of $\text{Bi}_4\text{Mn}_3\text{O}_{11.5}$ and $\text{Bi}_4\text{Mn}_{2.63}\text{Fe}_{0.4}\text{O}_{11.5}$	162
Figure III.14. The maple leaf lattice of $\text{Bi}_4\text{Mn}_3\text{O}_{11.5}$ created by connecting Mn1 atoms. J1-J5 super exchange paths are shown.	163
Figure III.15. ZFC/FC plots of M/H of $\text{Bi}_4\text{Mn}_3\text{O}_{11.5}$ versus the temperature at 0.1 Tesla in black and red. * show magnetic anomalies. $\chi^{-1}(T)$ is shown in blue and refers to the right-axis. The inset shows a portion of $M(H)$ at $T = 6$ K and 1.8 K in $\mu\text{B}/\text{f.u.}(\text{Oe})$. b) $M(H)$ at $T = 1.8$ K (blue), 6 K (red) in $\mu\text{B}/\text{f.u.}(\text{Oe})$ measured until 70 kOe.	164
Figure III.16. a) ZFC/FC plots of M/H of $\text{Bi}_4\text{Mn}_{2.63}\text{Fe}_{0.4}\text{O}_{11.5}$ versus the temperature at 0.02 Tesla in black and red. $\chi^{-1}(T)$ is shown in blue and refers to the right-axis. b) $M(H)$ at $T = 2$ K (blue), 9 K (green) and 18 K (red) in $\mu\text{B}/\text{f.u.}(\text{Oe})$	165
Figure III.17. a) Evolution of isotopomers fraction with reaction temperature during TPIE experiment over $\text{Bi}_4\text{Mn}_3\text{O}_{11.5}$ b) Evolution of isotopomers fraction with reaction temperature during TPIE experiment over $\text{Bi}_4\text{Mn}_{2.63}\text{Fe}_{0.4}\text{O}_{11.5}$ c) Evolution of the fraction of oxygen from the solid exchanged with the reaction temperature. (●) $\text{Bi}_4\text{Mn}_3\text{O}_{11.5}$ (◆) $\text{Bi}_4\text{Mn}_{2.63}\text{Fe}_{0.4}\text{O}_{11.5}$	167
Figure III.18. Evolution of the rate of exchange with reaction temperature. (●) $\text{Bi}_4\text{Mn}_3\text{O}_{11.5}$ (◆) $\text{Bi}_4\text{Mn}_{2.63}\text{Fe}_{0.4}\text{O}_{11.5}$	167
Figure III.19 a) Evolution of isotopomer concentrations with b) exchange time at 400°C. $\text{Bi}_4\text{Mn}_3\text{O}_{11.5}$ sample exchanged at 400 °C. α_{eq} is the fraction of ^{18}O in the gas phase if all the oxygen from the solid exchanged.....	168
Figure III.20. CVT process in a sealed quartz ampule.	172
Figure III.21. The crystal structure of $\alpha\text{-BiSeO}_3\text{Cl}$: a) projection along b-axis, b) projection along a-axis. The crystal structure of $\gamma\text{-BiSeO}_3\text{Cl}$: c) projection along c-axis, b) projection along b-axis.....	173
Figure III.22. a) $\beta'\text{-BiSeO}_3\text{Cl}$ crystal structure projected along a-axis, BiO_x polyhedra shown in yellow, BiO_xCl_y in green; b) the same projection without interlayer BiO_xCl_y polyhedra. It evidences an alternation of 3 different parallel layers: c) $[\text{Bi}_{12}\text{Cl}_{32}]^{+4}$, d) $[\text{Bi}_8\text{Cl}_{16}]^{+8}$ and e) $[\text{Bi}_{14}(\text{SeO}_3)_{24}]^{-6}$ presented as association of distorted Bi-O polyhedra and SeO_3 by sharing edges and corners.	176
Figure III.23. a) Transmission image of a crystal of $\text{Bi}(\text{SeO}_3)\text{Cl}$, b) color: emitting surface ($\lambda_{\text{em}}=420\text{--}440$ nm, $\lambda_{\text{em}} = 860$ nm).....	178
Figure III.24. Infrared red spectrum of the prepared $\beta'\text{-BiSeO}_3\text{Cl}$ (in blue) compared to the spectrum of $\beta\text{-BiSeO}_3\text{Cl}$ (in black) (from Oppermann et al. ¹⁸⁴).	178
Figure III.25. a) Crystal structure of $\text{Bi}_6(\text{SeO}_3)_4\text{Cl}_{10}$ projection along the b-axis, shows BiO_xCl_y polyhedra (in dark grey) and SeO_3 groups (in blue) sharing edges and corners. b) the same projection without drawing the BiO_xCl_y polyhedra	179
Figure III.26. a) The environment around Bi1a and Se3a atoms, b) a part of the structure of the structure of $\text{Bi}_6(\text{SeO}_3)_4\text{Cl}_{10}$ projection along the c-axis.....	180

Figure III.27. a) crystal structure of $PbBi_{10}(SeO_3)_{12}Cl_8$ projected along a -axis. The structure includes two parallel layers, b) $[Pb_2Bi_{12}(SeO_3)_{24}]^{+4}$ built on association of distorted Bi-O polyhedra (in dark grey) and SeO_3 groups (in blue) and c) $[Bi_{12}Cl_{32}]^{+4}$. Each layer is parallel to (a,c) plane.	181
Figure III.28. a) The structure of $Bi_2MnO(SeO_3)_2Cl_3$, b) MnO_5 chains.....	183

List of tables

Table I.1 s_j values of cations and related distortion of the oxo-centered tetrahedra.....	26
Table I.2. Formulation for the ribbons of different width.....	37
Table II.1. Spin exchange parameters J1–J6 in meV of $\text{BiCu}_2\text{O}_2(\text{PO}_4)$ obtained from the GGA+U calculations ($U = 4$ eV) the numbers in parentheses are the relative values with respect to the strongest exchange parameter.	55
Table II.2. Unit cell parameters of $\text{BiCu}_2\text{O}_2(\text{PO}_4)$ and $\text{BiCu}_2\text{O}_2(\text{AsO}_4)$	56
Table II.3. Crystal data, measurement and structural refinement parameters for $[\text{Bi}_2(\text{Bi}_{1.56}\text{K}_{0.44})^{\text{dis}}\text{O}_3]\text{K}_{0.88}^{\text{dis}}(\text{PO}_4)_2$, $[\text{Bi}_{18}\text{Zn}_{10}\text{O}_{21}]^{\text{ord}}\text{Zn}_5^{\text{ord}}(\text{PO}_4)_{14}$ and $[\text{Bi}_{10}(\text{Bi}_{\sim 0.5}\text{Cd}_{\sim 0.5})_8^{\text{dis}}\text{O}_{16}](\text{Bi}_{0.6}\text{Cd}_{0.8})_2^{\text{ord}}(\text{PO}_4)_8$	66
Table II.4 Interatomic distances (Å) of the atoms on the edges of the ribbons and in the cationic channels of $[\text{Bi}_2(\text{Bi}_{1.56}\text{K}_{0.44})^{\text{dis}}\text{O}_3]\text{K}_{0.88}^{\text{dis}}(\text{PO}_4)_2$	68
Table II.5 Interatomic distances (Å) of the atoms on the edges of the ribbons and in the cationic channels of $[\text{Bi}_{10}(\text{Bi}_{\sim 0.5}\text{Cd}_{\sim 0.5})_8^{\text{dis}}\text{O}_{16}](\text{Bi}_{0.6}\text{Cd}_{0.8})_2^{\text{ord}}(\text{PO}_4)_8$	75
Table II.6. Calculated BVS of selected atoms in $[\text{Bi}_{18}\text{Zn}_{10}\text{O}_{21}]^{\text{ord}}\text{Zn}_5^{\text{ord}}(\text{PO}_4)_{14}$	78
Table II.7 Selected interatomic distances (Å) of $[\text{Bi}_{18}\text{Zn}_{10}\text{O}_{21}]^{\text{ord}}\text{Zn}_5^{\text{ord}}(\text{PO}_4)_{14}$	79
Table II.8. The cell parameters of $\text{Bi}_4\text{Cu}_3\text{O}_6(\text{AsO}_4)_2$ and $\text{Bi}_4\text{Cu}_3\text{O}_6(\text{VO}_4)_2$	85
Table II.9. Crystal data, measurement and structure refinement parameters for $\text{Bi}_{29.4}\text{Cu}_{9.29}\text{O}_{32}(\text{PO}_4)_{16}\text{Cu}_{2.63}$ et $\text{Bi}_{37.2}\text{Cu}_{18.8}\text{O}_{44}(\text{PO}_4)_{24}\text{Cu}_5$	92
Table II.10. Crystal data, measurement and structural refinement parameters of $\text{Bi}_6\text{ZnO}_7(\text{AsO}_4)_2$ and $\text{Bi}_6\text{ZnO}_7(\text{PO}_4)_2$	101
Table II.11 Crystal data, measurement and structural refinement parameters of the studied derivatives of $\text{Bi}_{24}\text{O}_{31}\text{Cl}_{10}$	110
Table II.12. Conditions and results of the attempts to reproduce the compounds in the form of powder (u.p. denote unknown peaks).....	113
Table II.13. BVS of the atoms: Bi6 in the Arppe's compound, Pb7 in $m = 2$, Pb8 in $m = 3$, Pb8 in $m = 4$, Bi1, Bi2 and Pb1 in $\text{PbBi}_4\text{O}_6\text{Cl}_2$ with R and b parameters of Krivovichev ¹⁴¹	116
Table II.14. Optical properties of $\text{PbBi}_4\text{O}_6\text{Cl}_2$, $m = 2$ term $[\text{Pb}_2\text{Bi}_8\text{O}_{13}][\text{Bi}_2\text{O}_2]_2\text{Cl}_6$ and $\text{BaBi}_4\text{O}_6\text{Cl}_2$. Excitation and emission maximum and Stokes shift.	124
Table II.15 BVS calculation of $\text{Bi}_6\text{O}_{8.5}\text{Cl}$	126
Table II.16 Selected distances in $\text{Bi}_6\text{O}_{8.5}\text{Cl}$ ($d_{\text{max}} = 3$ Å).....	129
Table II.17. BVS of the atoms in $\text{Bi}_9\text{O}_9\text{Cl}_4(\text{Pb}_{0.2}\text{Mn}_{0.8})\text{O}_3\text{Cl}$	131
Table II.18. Crystal data, measurement and structural refinement parameters of $\text{Bi}_{46}\text{O}_{53}(\text{AsO}_4)_8$ and $\text{Bi}_{14}\text{O}_{15}(\text{AsO}_4)_4$	135
Table II.19. Published $\text{Bi}_{46}\text{O}_{53}(\text{XO}_4)_8$ structures with their the respective unit cell parameters.....	136
Table III.1. Crystal data, measurement and structural refinement parameters for $\text{Bi}_4\text{Mn}_3\text{O}_{11.5}$ at 100 K and 293 K.	152

Table III.2. Calculation of bond valences of Mn1 and Mn2 in $\text{Bi}_4\text{Mn}_3\text{O}_{11.5}$ at $T = 293\text{K}$. The retained model are in bold. (R values are taken from ref [¹⁴⁰])	155
Table III.3. Mn-O distances (\AA) from single crystal XRD data of $\text{Bi}_4\text{Mn}_3\text{O}_{11.5}$, PND data of $\text{Bi}_4\text{Mn}_3\text{O}_{11.5}$ and PND data of $\text{Bi}_4\text{Mn}_{2.63}\text{Fe}_{0.4}\text{O}_{11.5}$ at 300 K.	157
Table III.4 Selected A1 (cation) to A2 (anion) distances in $\text{Bi}_4\text{Mn}_3\text{O}_{11.5}$ at both sides of the order - disorder transition.....	159
Table III.5. Atomic parameters of $\text{Bi}_4\text{Mn}_3\text{O}_{11.5}$ at 180 K	160
Table III.6. Atomic parameters of $\text{Bi}_4\text{Mn}_3\text{O}_{11.5}$ at 300 K	161
Table III.7. Radii of Mn and Fe ions	165
Table III.8 Oxygen exchange rates and number of exchangeable oxygen atoms in the $\text{Bi}_4\text{Mn}_3\text{O}_{11.5}$ and $\text{Bi}_4\text{Mn}_{2.63}\text{Fe}_{0.4}\text{O}_{11.5}$	167
Table III.9 Crystal data, measurement and structural refinement parameters for $\beta\text{-BiSeO}_3\text{Cl}$, $\text{Bi}_6(\text{SeO}_3)_4\text{Cl}_{10}$ and $\text{PbBi}_{10}(\text{SeO}_3)_{12}\text{Cl}_8$	175
Table III.10. BVS of atoms in $\text{Bi}_2\text{MnO}(\text{SeO}_3)_2\text{Cl}_3$	183

Abstract

One of the primary challenges concerns the discovery of novel inorganic compounds using a rational “design” in order to predict crystal structures and possible structure/properties relationships. In the absence of unified protocol for such a task, it remains a hot topic in the solid state chemistry community. At the UCCS, our group has a long experience and a strong “savoir-faire” related to the elaboration and characterization on new bismuth based compounds. Recently, a strategy to Design novel innovative compounds and/or establish bases for related mega-series of related compounds have been developed for these broad series compounds by our group. Results are such as a large family of compounds with related crystal structures have been understood in terms of building principles leading to the post prediction, preparation and characterization of novel members. In the chemical $\text{Bi}_2\text{O}_3 - \text{MO} - \text{P}_2\text{O}_5$ (M = various divalent metals) systems, at the origin of this work, these predictions have been feasible because versatile building units (BU) can be handled, modified and assembled in various manners. The key-description used for BUs relies on the anion-centered polyhedra theory related to the bismuth atom.

Thus, in the framework of ANR Multi-D InMaDe we have explored the Bi/M/X/O system, where $\text{M} = \text{Cu}, \text{Co}, \text{Mn}$ etc. and $\text{X} = \text{P}, \text{V}, \text{As}, \text{Mo}, \text{Se}$ and Cl . Several new compounds with new topologies have been obtained and their corresponding properties have been measured.

Résumé

Un des enjeux majeurs en chimie du solide concerne la découverte de matériaux inorganiques à propriétés ciblées. En l'absence d'un protocole unique permettant d'y arriver, la situation des laboratoires français de « chimie du solide » en termes de prospection de nouveaux composés reste critique. A l'UCCS, notre groupe a une grande expérience et un savoir-faire reconnu liés à l'élaboration et la caractérisation de nouveaux matériaux à base de bismuth. Récemment, une stratégie de Design de composés innovants a été mise en place et développée pour cette série de composés. Il a ainsi été possible de décrire la majeure partie de nos composés en termes de briques élémentaires structurales permettant, à posteriori de prédire, préparer et caractériser de nouveaux membres. Dans les systèmes ternaires $\text{Bi}_2\text{O}_3 - \text{MO} - \text{P}_2\text{O}_5$ (M = métal de transition) à l'origine de ce travail, ces prédictions ont été rendues possibles parceque chacune de ces unités structurales peut être utilisée, modifiée et assemblée de différentes façons. Le point commun à ces briques élémentaires repose sur la description mettant en œuvre des tétraèdres centrés sur les anions (ici O^{2-}) et entourés par des atomes de bismuth.

Ainsi, dans le cadre de l'ANR jeune chercheur Multi-D InMaDe, nous avons exploré les systèmes Bi/M/X/O avec $\text{M} = \text{Cu}, \text{Co}, \text{Mn} \dots$ et $\text{X} = \text{P}, \text{V}, \text{As}, \text{Mo}, \text{Se}$ et Cl . De nouveaux composés présentant des topologies innovantes ont été obtenus et leurs propriétés mesurées dans certains cas.

Introduction

Introduction

The search for new materials with intrinsic desirable properties has been a driving force of the solid state chemical community. When we take a glance at many recent technological breakthroughs and to their significant impact on our daily life, we appreciate how much they have relied on new materials. Some of these advances include the increase in hard-drive storage capacity because of new magneto-resistive materials, the ever-shrinking cell phone because of new microwave dielectric materials, the enhancement in lithium battery storage capacity because of new intercalation materials, and the improved capacitor because of new ferroelectric materials¹. Nevertheless, the French “solid state chemistry community” is nowadays in a critical position concerning its lowering contribution to the prospection for new inorganic compounds with new atomic architectures and related properties, which has also negative consequences at a multidisciplinary level since chemists, physicians, theoreticians and even industrial partners are impacted.

In this particular context, one of the primary challenges implies the discovery of novel inorganic compounds using a rational “design” in order to predict crystal structures and possible structure/properties relationships. In the absence of unified protocol for such a task, it remains a hot topic in the solid state chemistry community.

At the UCCS, our group has a long experience and a strong “savoir-faire” related to the elaboration and characterization on new bismuth based compounds. Recently, a strategy to design novel innovative compounds and/or establish bases for related large series of related compounds have been developed for these broad series compounds by our group. Results are such as a large family of compounds with related crystal structures have been understood in terms of building/principles leading to the post prediction, preparation and characterization of novel members. In the chemical $\text{Bi}_2\text{O}_3 - \text{MO} - \text{P}_2\text{O}_5$ (M = various divalent metals) systems at the origin of this work, these predictions have been feasible because versatile building units can be handled, modified and assembled in various manners. The key-description used for such units rely on the anion-centered polyhedra theory.

*Chapter I. Anion-centered tetrahedra
concept of BUs, their Design and the
description of the thesis*

I. Anion-centered tetrahedra concept of BUs, their Design and the description of the thesis

I.1 Anion-centered tetrahedra in structural descriptions

I.1.1 Why an alternative structural description?

It is a common procedure in the description and evaluation of the crystal-structures of inorganic compounds to consider them in terms of coordination of cations, i.e. as extended arrays of coordination polyhedral with centres occupied by cations and corners occupied by anions. However, there are cases, when this kind of structure interpretation does not reflect neither basic principles of structural architecture nor relationships between different structures and between crystal structure and their physical properties.

In 1968 for the first time, Bergerhoff and Paeslack² got the idea to focus on oxygen atoms to describe the whole crystal structure. Considering the example of $\text{Cu}_2\text{O}(\text{SO}_4)$, some oxygen atoms are strongly bonded and involved in “acid residues”, here sulfates, (O_s atoms on the Figure I.1a) and the other coordinated by four Cu atoms making OCu_4 tetrahedron (O_a on the Figure I.1a). Moreover those OCu_4 tetrahedra share edges and corners creating 2-dimensional arrangement giving structural subunit $[\text{OCu}_2]^{2+}$ (Figure I.1b). The positive charge of these layers are compensated by sulfate (SO_4)²⁻ groups.

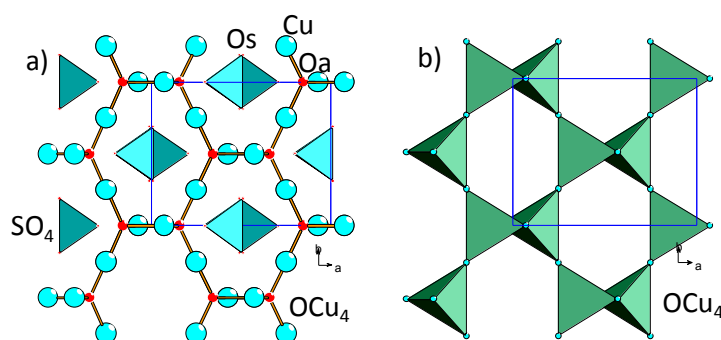


Figure I.1. a) The crystal structure of dolerophanite, $\text{Cu}_2\text{O}(\text{SO}_4)$, where SO_4 tetrahedra are in blue. O_s are the oxygen atoms of sulphate groups, O_a are the “additional” oxygen atoms in the center of OCu_4 tetrahedra b) edge- and corner-sharing (OCu_4) tetrahedra in the tetrahedra presentation (green).

Also the authors have found that the same is true for several structure as $\text{Bi}_2\text{O}_2\text{GeO}_3$ for example (the negative charge of corner shared chains, GeO_3^{2-} , is compensated by the $\text{Bi}_2\text{O}_2^{2+}$ layers constructed from edge-shared OBi_4 tetrahedra)³. Other oxocentred polyhedra OM_x have been shown by Bergerhoff and Paeslack² are: OZn_4 in $\text{Zn}_4\text{O}(\text{BO}_2)_6$ ⁴, OBe_4 in

$\text{Be}_4\text{O}(\text{CH}_3\text{COO})_6$ ⁵, OAl_4 in Al_2OSiO_4 ⁶, OLa_4 in $\text{La}_2\text{O}_2\text{S}$ ⁷, OPb_4 in Pb_2OF_2 ⁸. The anion-centered tetrahedral concept is born, successively used by Magaril and coworkers⁹ (OHg_4 tetrahedra in mercury oxysalts), Schleid et al.^{10,11} (lanthanide compounds describing nitro- and oxo-centered XM_4 tetrahedra (where $\text{X} = \text{O}^{2-}$, N^{3-} and $\text{M} = \text{Ln}$)) and now frequently used. Recent papers testify increasing attention to inorganic compounds consisting of anion-centered polyhedra XA_n , ($\text{X} = \text{O}^{2-}$, N^{3-} , S^{2-} , Cl^- etc), where oxygen-centered and nitrogen-centered tetrahedra being most abundant^{10–16}. We note other ancient related works, using this oxocentered polyhedral for various reasons, disorder, irregular cationic coordination and so on.^{17–19}

I.1.2 Chemistry of anion-centered XA_4 tetrahedra

The explanation of the abundance of the structures with oxygen-centered and nitrogen-centered tetrahedra lies on their electronegativities and hardnesses²⁰. Electronegativity, is a chemical property that describes the tendency of an atom to attract electrons or electron density towards itself²¹. It can be determined as the first derivative of energy with respect to the number of electrons²². To the contrary, the second derivative of the energy relative to the number of electrons gives us the hardness of an atom which reflects its resistivity to transfer electrons. Thus the most electronegative elements are F(3.98), O(3.44), N(3.04) and Cl (3.16)²³. However, out of them the first three elements possess the highest hardnesses: F(7.01), O(6.08) and N(7.23), whereas Cl(4.68) being soft²⁴. Among these four elements O and N suit well to make anion-centered tetrahedra due to the necessary properties as high electronegativity, high hardness as well as higher charge in comparison to F and Cl thereby explaining the abundance of structures with oxo- and nitro-centered tetrahedra in nature.

I.1.3 Preferred cations for oxo-centered tetrahedra

In order to understand what kind of cations can tetrahedrally surround O or N atom, Krivovichev and Filatov²⁵ suggested to use bond valence theory²⁶ and the concept of Lewis Acid(Base) Strength of cations (anions) (LAS and LBS)²⁷. In order to check the ability of X-A pairs to form of anion-centered tetrahedra XA_4 , which has to be close to regular tetrahedra, one has to compare s_{ij} and LBS of X. The LBS values of O^{2-} and N^{3-} anions in the regular tetrahedral coordination are 0.50 and 0.75 v.u. (valence units) respectively. So, in order to have OA_4 or NA_4 tetrahedra in a given structure the s_{ij} values of the O-A and N-A bonds have to be close to the respective LBS values. Krivovichev and Filatov²⁵ reviewed in detail most

common metal cations and their ability to form the O-A bonds with the bond-valence of 0.5 v.u. The typical s_{ij} values of O-A bonds in the structures with “additional” O atoms are given in the Table I.1.

Table I.1 s_{ij} values of cations and related distortion of the oxo-centered tetrahedra

Atom	s_{ij}	Regularity of tetrahedra
Cu^{2+}	0.5	regular
Pb^{2+}	0.51	distorted
Hg^{2+}	0.61	strongly distorted
Bi^{3+}	0.6	strongly distorted
Sb^{3+}	0.7	strongly distorted
Y^{3+}	0.5	regular
La^{3+}	0.5	regular
Nd^{3+}	0.5	regular

I.1.4 OBi_4 and $\text{O}(\text{Bi}/\text{M})_4$ as oxo-centered tetrahedra.

The typical $\text{Bi}^{3+}\text{--O}$ bond valence is 0.596 v.u. which is slightly higher than the 0.5 v.u. needed to form an ideal (OBi_4) tetrahedron with four equal bonding contributions on the central oxygen. As a result of this over bonded character of central oxygen atoms, the (OBi_4) tetrahedra are usually strongly distorted, which often leads to the deterioration of the tetrahedral geometry and formation of the OBi_3 triangles or bent OBi_2 groups. However, the latter two configurations are usually complemented by one or two long ($>3 \text{ \AA}$) O–Bi bonds to balance the oxygen charge. The structure of smirnite, $[\text{Bi}_2\text{O}_2](\text{TeO}_3)$, is a representative example. It is based upon the $[\text{O}_2\text{Bi}_2]^{2+}$ layers parallel to (100) and consisting of three oxo-centered groups with different degrees of distortion (Figure I.2).

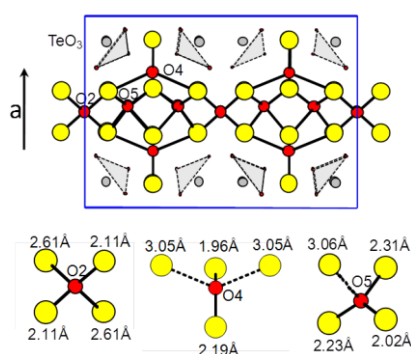


Figure I.2. Combination of OBi_4 , OBi_{3+1} and OBi_{2+2} in $(\text{Bi}_2\text{O}_2)(\text{TeO}_3)$.

The coordination of the oxygen atoms can be considered as distorted tetrahedral: O(2) is located with four neighboring Bi at the distances less than 2.7 Å; the coordination of the atoms O(4) and O(5) can be described as (2+2) and (3+1), respectively.

Also, in the following sections, we will consider several topologies formed by mixed O(Bi,M)₄ tetrahedra in inorganic Bi-based compounds will be considered, where M brings stability to the oxo-centered tetrahedra for the reasons given above.

I.1.5 Lonepair of Bi^{III}

It has been long-established in the laboratory UCCS to study bismuth oxide compounds due to striking properties for ionic properties^{28–30}, dielectrics³¹, optics³² etc. In general they arise from the stereo active lonepair and strong polarizability associated with those 6s²-cations Bi³⁺, Pb²⁺, Tl⁺. About the lonepair (LP) effect, it is generally admitted that this “electronic delocalization occurs due to 6s and 6p mixing. However, this assignment was revised in the last decade and it appears that a mediation of the indirect mixing through O2p levels is most probable³³. The lone pair effect is obvious in the crystal structure of Bi³⁺Bi⁵⁺O₄³⁴ which adopts the β-Sb₂O₄ type, Bi³⁺ occupies one corner of a BiO₄ square pyramid whereas 6s² lacking Bi⁵⁺ ions are at the centre of regular BiO₆ octahedra, Figure I.3.

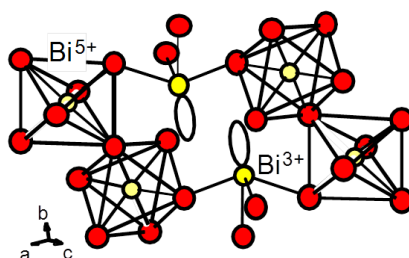


Figure I.3. Bi⁵⁺O₆ octahedra and distorted Bi³⁺O₄LP polyhedra in Bi₂O₄

Whatever the electronic origin of the structural distortion comes from, the present manuscript thesis mainly focuses on new structures built up from the association of OBi₄ tetrahedra in which, in general, the orientations of the LPs of Bi³⁺ are outwards with respect to oxygen centers. The examination of the Bi₂O₃ polymorphs clearly shows that the coordination around Bi³⁺ is highly distorted because of the pronounced LP effect³⁵ which justifies the available description of these compounds using oxo-centered units (OBi₄ and OBi₃). Also, it was shown by DFT calculations using the electron localisation function iso-surface (at 0.64 electrons) for the ε-form of Bi₂O₃ that the 6s² excrescences point outwards the created oxo-centered units (Figure I.4a). Finally, the most convenient way to rationalize the structural changes between the several Bi₂O₃ forms goes through the notion of edge-sharing OBi₄

tetrahedra forming chains (1D subunit), and linked by bordering oxygen atoms with triangular OBi_3 coordinations³⁵ has shown on the Figure I.4a-d

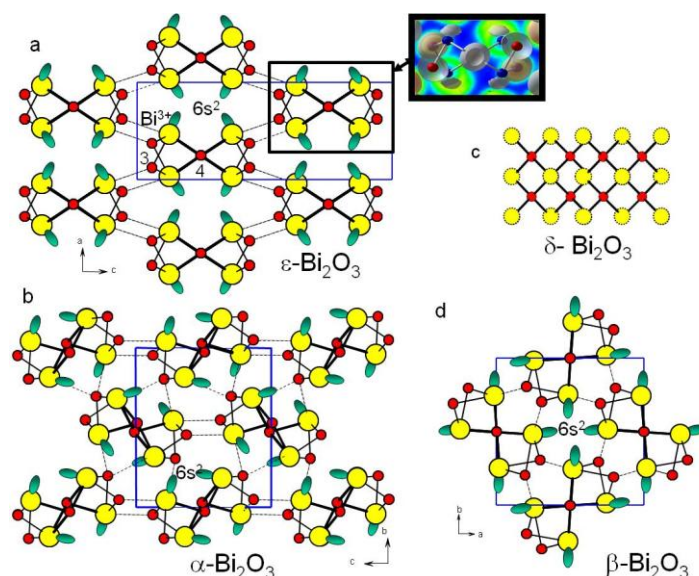


Figure I.4. Reorganization of the $[\text{OBi}_2]\text{O}_2$ chains between a) the metastable $\epsilon\text{-Bi}_2\text{O}_3$, with a DFT visualization of LP electronic density b) $\alpha\text{-Bi}_2\text{O}_3$ c) ideal structure of oxygen-deficient fluorite $\delta\text{-Bi}_2\text{O}_3$ and d) $\beta\text{-Bi}_2\text{O}_3$

I.1.6 The heritage of fluorite type $\delta\text{-Bi}_2\text{O}_3$

The majority of the bismuth oxide compounds obtained in our laboratory can be considered as derivatives of the fluorite-like $\delta\text{-Bi}_2\text{O}_3$ crystal structure (Figure I.5a) in terms of their cationic arrangement (Figure I.5b).^{36–40}

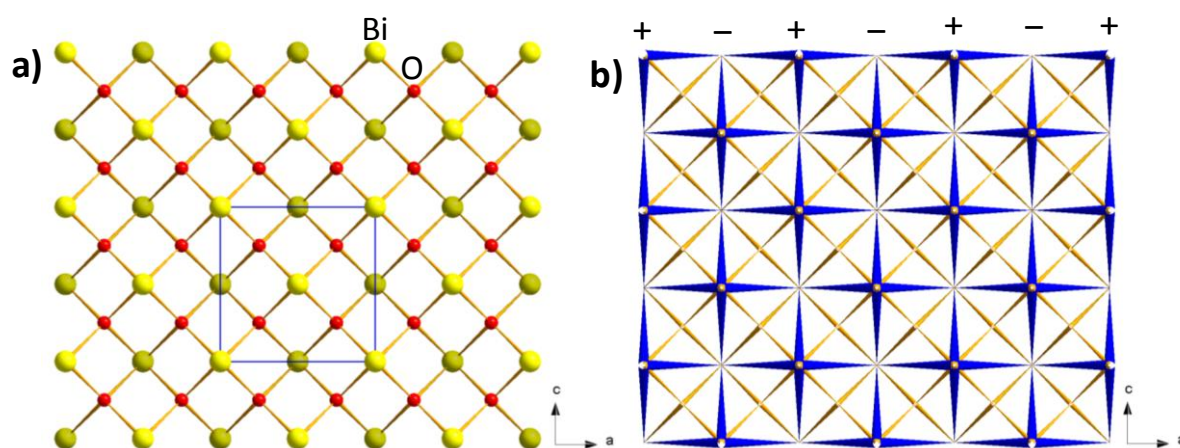


Figure I.5. a) The ideal structure of the oxygen-deficient fluorite type $\delta\text{-Bi}_2\text{O}_3$ projection along the b -axis, b) the cationic grid representation of the same structure in blue (Bi-Bi bonds). Minus (-) and plus (+) signs indicate y and $y + \frac{1}{2}$ "out-of-plane" positions of Bi atoms.

The alien atoms (M = metal atoms) or XO_4 groups (X = As, V and P) substitute the Bi-positions while the resulting network is strongly distorted, for instance due to the incorporation of extra-oxygen atoms with XO_4 groups, which will be discussed later.

This fluorite-heritage is of primary importance, since the notion of the substitution of Bi^{3+} ions by various cations guaranties the conservation of the cationic architecture, at the basis of the possible prediction, formulation and preparation of hypothetical members intensively studied by our group.³⁸⁻⁴¹ The 2D-projection of the lattice perpendicularly to the ~ 5.5 Å axis (or super-cell related lattice parameter) helps to view the distortion due to the incorporation of XO_4 , and allows to distinguish the topology of oxocentered tetrahedra preserved from the parent-fluorite structure. In such sketch, two adjacent cations (Bi^{3+} , Bi^{3+}/M^{n+} , P^{5+}) along horizontal and vertical grid-lines occupy x (in plane) and $x + 1/2$ (out of plane) in regard to the ~ 5.5 Å parameter. Such 2D-cationic projections have been drawn and discussed for non-centrosymmetric compounds with $n = 5, 8, 11$ tetrahedra-wide ribbons⁴⁰ and for compounds with infinite layers.⁴¹

Our results seem to confirm the general idea that in this family of compounds a cationic architecture is conserved where the periodic $O(Bi,M)_4$ units are surrounded by more or less disordered counter ions including the interstitial hosted cations. Slight compositional changes seem to modify the interstitial sublattice while the main oxocentered-sublattice is not sensitively modified.

I.1.7 Available Dimensionalities for edifices built from oxocentered tetrahedra

The oxo-centered polyhedra theory is also pertinent in terms of relationships between various topologies as it will be shown later. Following, the several topologies formed by mixed 0D, 1D, 2D or 3D subunits formed from $O(Bi,M)_4$ exist in the literature and are detailed below.

1) 0D-units: isolated $O(Bi,M)_4$ tetrahedra

Only few structures are built on 0D $O(Bi,M)_4$ tetrahedra. The OBi_4 regular tetrahedra alone would not be stabilized as 0D units, because of the bond valence effect already discussed, moreover the charge would be too high to compensate. On the other hand, heterovalent sites at the corners of tetrahedra would decrease the geometrical symmetry of the finite clusters²⁰ as well as its charge. The Figure I.6a-c shows example of 0D units observed on $K_2Bi_3O(PO_4)_3$ ⁴² (with OBi_3K tetrahedron), $(Sr_2Bi_3O_2)(VO_4)_3$ ⁴³ (linear tetramer formed by

edge-shared $\text{O}(\text{Bi},\text{Sr})_4$, and $[\text{Bi}_6(\text{O},\text{OH})_8]$ (clusters commonly observed in bismuth basic nitrates^{44–46}).

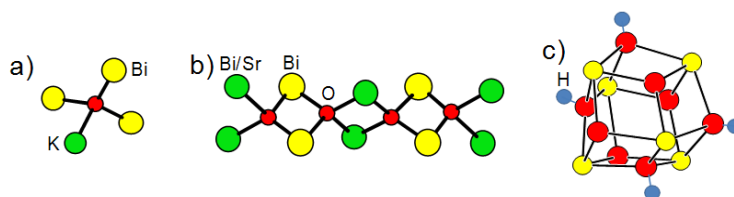


Figure I.6. 0D units: a) $[\text{O}(\text{Bi}_3\text{K})]$ in $\text{K}[\text{KBi}_3\text{O}](\text{PO}_4)_3$, b) $[\text{Sr}_2\text{Bi}_3\text{O}_2]$ in $[\text{Sr}_2\text{Bi}_3\text{O}_2](\text{VO}_4)_3$, c) protonated $[(\text{O},\text{OH})_8 \text{Bi}_6]$ polycationic-clusters

2) 1D-units: chains and ribbons

The elementary 1D entities corresponds to the chains of interconnected OBi_4 or $\text{O}(\text{Bi}/\text{M})_4$ tetrahedra. The $[\text{OBi}_2]^{4+}$ chains exist in $\text{Bi}_2\text{O}(\text{AuO}_4)^{47}$, where the former are growing between stacks of AuO_4 square-planes, Figure I.7a. This kind of chains $[\text{O}_2\text{Bi}_4]^{8+}$ bordered by OBi_3 triangles are found also in the mineral schlegelite $(\text{Bi}_4\text{O}_2)(\text{BiO})_2\text{Bi}(\text{MoO}_4)_2(\text{AsO}_4)_3^{48}$, Figure I.7b.

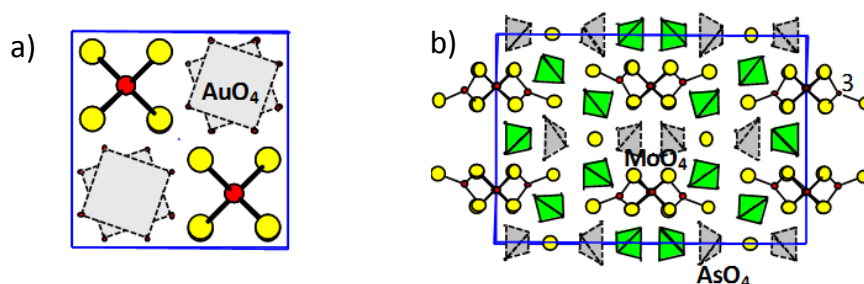


Figure I.7. 1D chain-like topology. Projection of corner sharing (OBi_2) chains in a) $(\text{Bi}_2\text{O})(\text{AuO}_4)$ and b) $(\text{Bi}_4\text{O}_2)(\text{BiO})_2\text{Bi}(\text{MoO}_4)_2(\text{AsO}_4)_3$.

Regarding oxy-phosphates Bi compounds^{37,38,49,50} which are the origin of this work, the most common 1D chains concern the ribbon-like polycations, $[\text{O}(\text{Bi},\text{M})_2]^{n+}$, made from the linkage of edge-sharing tetrahedra OBi_2M_2 . An ordering takes place on the mixed Bi/M sites in the chains of the $\text{BiMO}(\text{XO}_4)$ ($\text{M} = 3\text{d transition metal and } \text{X} = \text{P, V, As}$)⁵¹, where M atoms are in *trans* position with respect to Bi atoms in majority of compounds except BiCaVO_5 and BiCdVO_5 . The width of the chains can vary depending on the number of the condensed tetrahedra in the direction perpendicular to the chain (n tetrahedra wide). The Figure I.8a-b shows examples of compounds built on ribbons $n = 1$ and two tetrahedra wide. Several 1D ribbons with various width are commonly found in a number of bismuth oxo-phosphates, -vanadates, -arsenates and can coexist in the same structure.^{36,49} This will be largely discussed later.

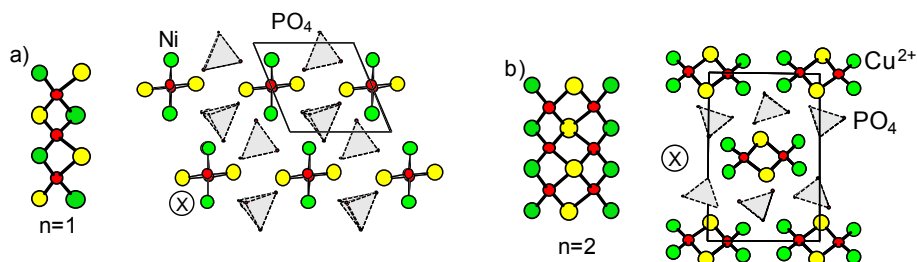


Figure I.8. Edge-sharing $O(\text{Bi},\text{M})_4$ units: a) single-chains in $\text{BiNiO}(\text{PO}_4)$ b) $n = 2$ ribbons in $\text{BiCu}_2\text{O}_2(\text{PO}_4)$

The chains of OBi_4 tetrahedra may be not only wider, making ribbons, but also thicker yielding columnar 1D-units. The most simple case concerns the recent compound $\text{Bi}_{1.2}\text{Cd}_{1.6}(\text{Bi}_{14}\text{Cd}_4\text{O}_{16})(\text{PO}_4)_8$, see the Figure I.9a, in which the section of the columns forms square of 2×2 tetrahedra with mixed Bi/Cd corners with modulated occupancies.³⁹ Different topologies of the columns exist such as 3×3 crosses in $[\text{Bi}_6\text{O}_5]\text{O}_2(\text{CrO}_4)_2$ (Figure I.9b), 4×3 crosses in the high-temperature form $\gamma\text{-Bi}_2\text{MoO}_6 (= (\text{Bi}_8\text{O}_6)\text{O}_2(\text{MoO}_4)_4)^{52}$ (Figure I.9c), or four-tetrahedra wide ribbons with two shifted tetrahedra on each sides in $(\text{O}_6\text{Bi}_7)_2\text{O}_4(\text{SO}_4)_5$.⁵³

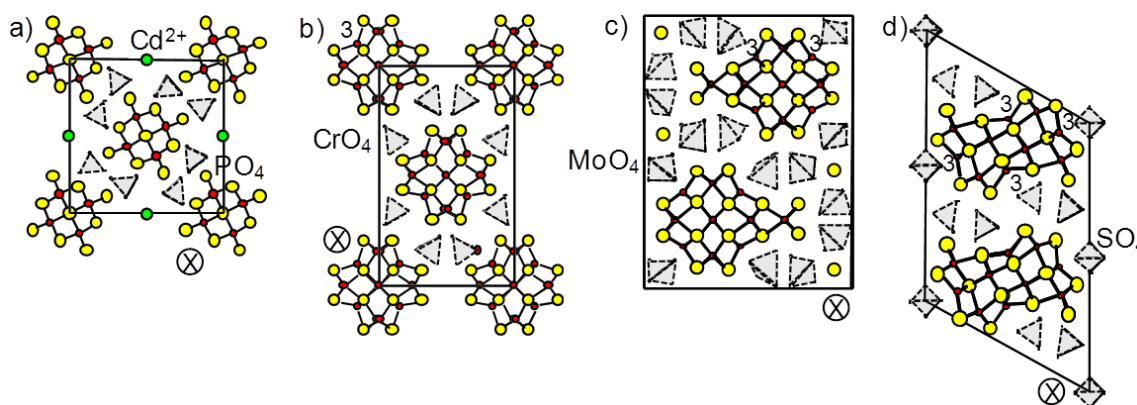


Figure I.9. 1D-units as columns with cross-section: a) 2×2 tetrahedra in $(\text{Bi}_{14}\text{Cd}_4\text{O}_{16})(\text{PO}_4)_8\text{Bi}_{1.2}\text{Cd}_{1.2}$ (mixed sites are not shown), b) 3×2 in $[\text{Bi}_6\text{O}_5]\text{O}_2(\text{CrO}_4)_2$, c) 4×3 in $\gamma\text{-Bi}_2\text{MoO}_6$, d) shifted 2×4 cross section in $(\text{Bi}_6\text{O}_7)_2\text{O}_4(\text{SO}_4)_5$. (\otimes denote the infinite character perpendicular to the projected plane) The oxygen atoms of OBi_3 are marked as 3.

In these kinds of topologies the space at the angles of the crosses are generally completed by oxygen atoms in triangular OBi_3 coordination that appear isolated in the previous formulae.

3) 2D-units: planes and layers

Plenty of structures with the layers of oxo-centered tetrahedra have been reported with more or less exotic topologies depending on the ratio between corner-sharing and edge-sharing connections. For instance, in $(\text{Bi}_2\text{O}_2)(\text{UO}_4)$ the uranyl layers are separated by $[\text{Bi}_2\text{O}_2]^{2+}$ layers formed of two corner-sharing tetrahedra (with up and down apices)

connected by edges as shown on the Figure I.10a.⁵⁴ In fact, the most representative topology of dense bidimensional OBi_4 based units is incontestably the $[\text{O}_2\text{Bi}_2]^{2+}$ layers that correspond to the 2D infinite extension of the 1D ribbons preliminary discussed earlier.

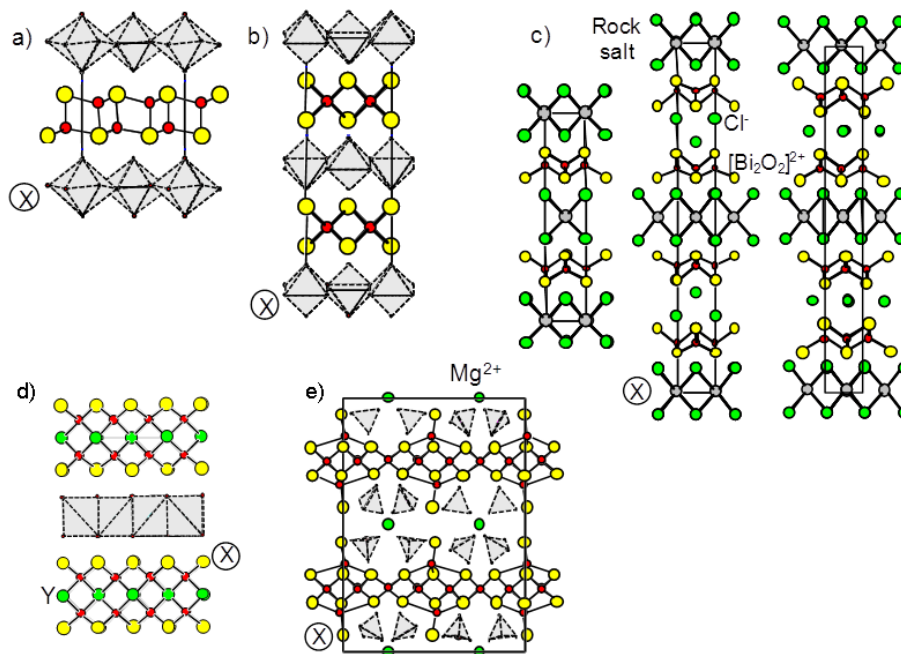


Figure I.10. Layered 2D units: a) (Bi_2O_2) double-layer in $(\text{Bi}_2\text{O}_2)(\text{UO}_4)$. (Bi_2O_2) simple layer in b) the Aurivillius- Bi_2MoO_6 compound c) in various polytypes described in [55] d) double ribbons of OBi_2Y_2 in $(\text{O}_4\text{YBi}_2)\text{YCu}_2\text{Se}_2$ (\otimes denote the infinite character perpendicular to the projected plane), e) infinite extension of 1D-ribbons with O-Bi excrecences in $(\text{Bi}_2\text{O}_2)_{11/6}(\text{BiO})_{1/3}\text{M}_1(\text{PO}_4)_2$.

These infinite layers may be separated by slabs of tetrahedra (Figure I.10b), isolated halides, perovskite blocks of variable thickness (n-octahedra thick) in the Aurivillius series (Figure I.10c). Other metals, for example $\text{M} = \text{Ln}$, Ba, Ca etc., can enter $[\text{Bi}_2\text{O}_2]^{2+}$ layers thus creating $[\text{MBi}_2\text{O}_2]^{n+}$ layers the thickness of which is doubled. The cationic ordering takes place in the (MBi_2O_4) layer wherein central row is occupied by cations such as Ba^{2+} , Y^{3+} or a lanthanide^{57,58}, Figure I.10d. In the field of mixed Bi/M oxophosphates, the infinite extension of the 1D ribbons decorated by Bi-O excrecences have been recently isolated in $\text{Bi}_4\text{MP}_2\text{O}_{12}$ ($= (\text{Bi}_2\text{O}_2)_{11/6}(\text{BiO})_{1/3}\text{M}_1(\text{PO}_4)_2$) (where $\text{M} = \text{Mg}$, Zn). PO_4 groups surround tunnels of M in a similar way as in the case of the structures with finite ribbons, Figure I.10e.³⁹ 1D finite ribbons can also be connected in different ways forming zig-zag or crenel-like 2D layers. In the Bi_2O_3 - MoO_3 system a representative series of oxides with general formula $\text{Bi}_{2m}\text{Mo}_{m-2}\text{O}_{6m-6}$, where m is varying from 5 to 8, illustrates well the crenel-like layers.⁵⁹ In these series T_d denotes the number of tetrahedra, with respect to the width of the elementary ribbons, which share edges laterally to create zig-zag layers, see Figure I.11a.

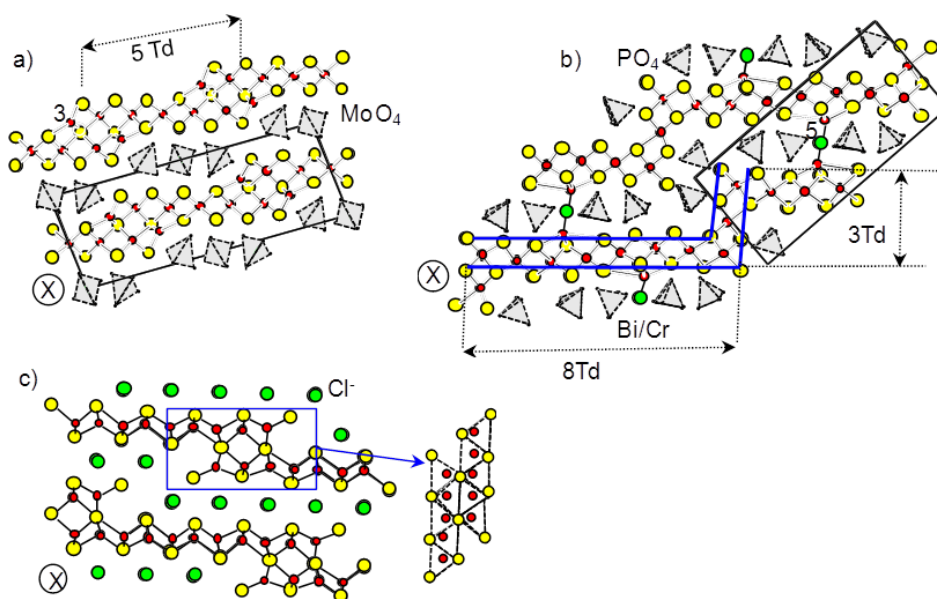


Figure I.11. Crenel 2D units (\otimes denote the infinite character perpendicular to the projected plane
 a) $m = 5$ of $\text{Bi}_{2m}\text{Mo}_{m-2}\text{O}_{6m-6}$, b) 8×3 crenel junctions by edge-sharing in $\text{Bi}_{18.71}\text{Cr}_{0.27}\text{P}_6\text{O}_{43.22}$. c)
 $(\text{Bi}_6\text{O}_7)_4\text{O}_3\text{Cl}_{10}$ case with detail of the mixed edge and corner-sharing junctions between $n = 12$
 ribbons in the perpendicular plane.

Several other examples are reported in the literature, for instance, the $n = 8$ ribbons sharing edges with perpendicular $n = 3$ ribbons in $\text{Bi}_{18.71}\text{Cr}_{0.27}\text{P}_6\text{O}_{43.22}$ ⁶⁰, Figure I.11b. This kind of ribbon “overlapping” into *crenel* can also be found in other kind of layers. Thus, in $(\text{Bi}_6\text{O}_7)_4\text{O}_3\text{Cl}_{10}$, the finite ribbons of $n = 12$ tetrahedra connected by a common $n=3$ tetrahedra wide junction, Figure I.11c.⁶¹ All the crenel-like 2D layers, discussed above, described as the finite ribbons connected via lateral edge sharing connection of certain number of tetrahedra, however the former can also be created by sharing corners of n -wide ribbons. It exists in the literature at least three representative cases corresponding to $n = 2$ in⁶² and⁶³, $n = 3$ in⁶⁴ and $n = 4$ ⁵³ as shown on the Figure I.12a-c.

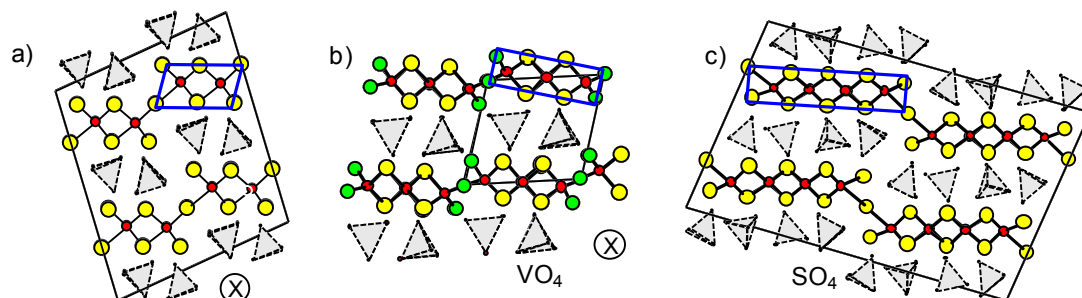


Figure I.12. 2D-Crenel ribbons by corner-sharing of $\text{O}(\text{Bi},\text{M})_4$ tetrahedra from a) $n = 2$ Td ribbons
 in $(\text{Bi}_5\text{O}_4)\text{O}_{0.5}(\text{PO}_4)_2$, b) $n = 3$ Td in $(\text{Cu}_3\text{Bi}_4\text{O}_6)(\text{VO}_4)_2$, c) $n = 4$ Td in $(\text{Bi}_{8.67}\text{O}_8)(\text{SO}_4)_4$ (\otimes denote the
 infinite character perpendicular to the projected plane)

4) 3D-units: frameworks

The robust $[O_4Bi_8]$ *stella quadrangulae* 0D clusters (Figure I.13) formed by strong connection of OBi_4 tetrahedra interconnect to 3D $KSbO_3$ -type framework in the structures $(Bi_3O_2)(GaSb_2O_9)$ and $(Bi_3O_2)(Ru_3O_9)^{65,66}$.

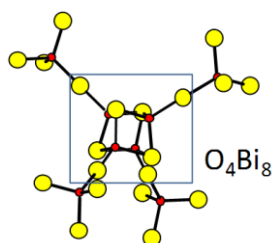


Figure I.13. $[O_4Bi_8]$ *stella quadrangulae* in $(Bi_3O_2)(Ru_3O_9)$ and $(Bi_3O_2)(GaSb_2O_9)$

The structures of oxychlorides such as $(M_5Cl)(Bi_8O_9)_6O_5Cl_{30}$ where $M^+ = Cu$ or Ag^{67} , $(Bi_6O_7)_2OCl_6^{68}$ and $(Bi_6O_6F)OCl_3^{69}$ can be considered as 3D-networks of connected OBi_4 tetrahedra, Figure I.14a-c.

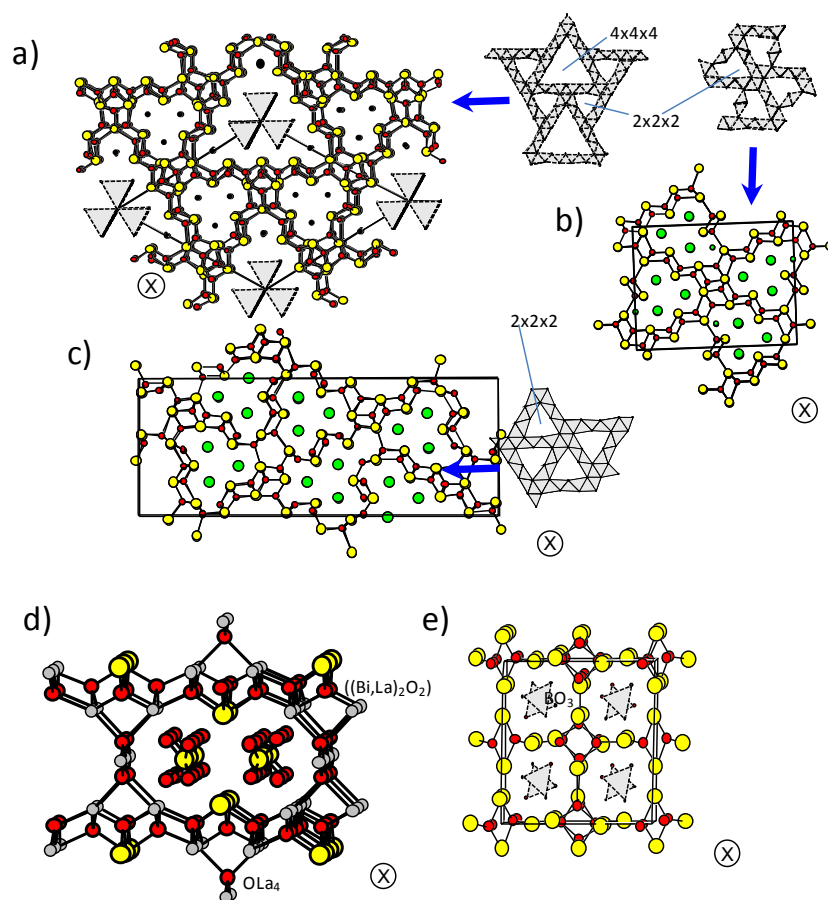


Figure I.14. 3D framework of $O(Bi,M)_4$ tetrahedra. Triangular networks in a) $(M_5Cl)(Bi_8O_9)_6O_5Cl_{30}$ with $M^+ = Cu$ or Ag , b) $(Bi_6O_6F)O, Cl_3$, c) $(Bi_6O_7)_2O, Cl$, d) connection of infinite ribbons by OLa_4 tetrahedra in $Bi_8La_{10}O_{27}$. e) voids in of $(Bi_3O_2)(BiO)(BO_3)_2$ filled by BO_3

The triangular channels of the frameworks are filled by chlorides except for $(M_5Cl)(Bi_8O_9)_6O_5Cl_{30}$ where the channels host M^+ as well. In the structure of $Bi_8La_{10}O_{27}$, the infinite $[(Bi/La)_2O_2]$ planes connected to each other by OLa_4 tetrahedra thereby forming hollow 3D framework, Figure I.14d, filled with disordered Bi_8O_{11} chains.⁷⁰

Voids are also found in $(Bi_3O_2)(BiO)(BO_3)_2$ ⁷¹ the framework of which is created by edge-sharing and corner-sharing tetrahedra, Figure I.14e.

The structural rearrangement of δ - Bi_2O_3 by introduction of XO_4^{3-} groups ($X = P, V$) into its structure, produces 3D-framework of oxo-centered tetrahedra as in $Bi_{46}O_{57}(PO_4)_8$ ⁷², $Bi_{46}O_{57}(VO_4)_8$.⁷² On the other hand, pronounced 2D-character of OBi_4 tetrahedra framework in the structure of $Bi_{14}O_{15}(PO_4)_4$ ⁷³ can be distinguished, Figure I.15a-b.

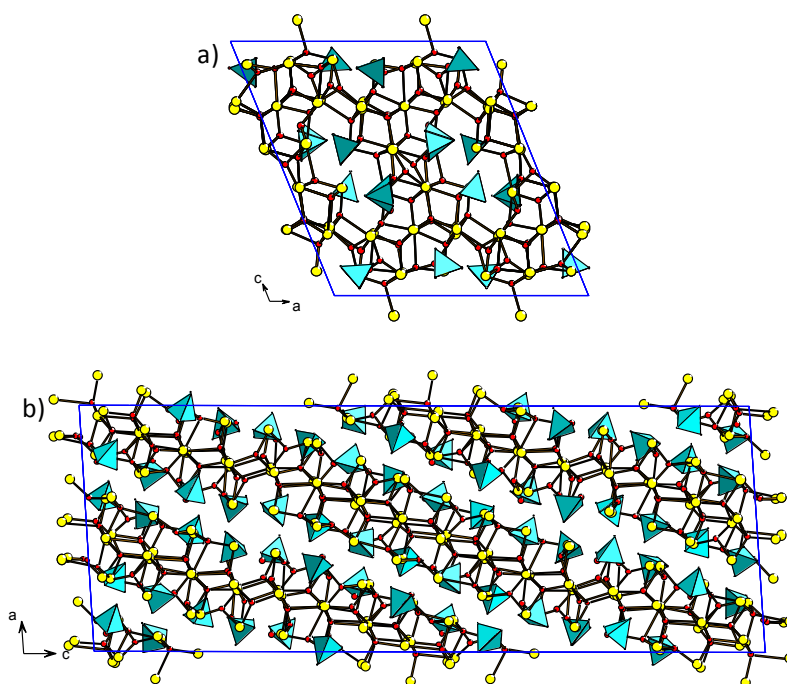


Figure I.15. Incorporation of PO_4 groups in Bi_2O_3 oxides: a) conservation of the 3D character based on OBi_4 linkage in $Bi_{46}O_{57}(PO_4)_8$ and b) 2D character in $Bi_{14}O_{15}(PO_4)_4$

I.2 The case of bismuth oxo-phosphates

The organization of bismuth-based 1D sizeable building-units (BUs) into new $X^V O_4$ containing frameworks ($X = P, As$ and V) has been the scope of the ANR project “Multi-D InMaDe”. In the $Bi_2O_3 - X_2O_5 - MO_x$ ($M =$ various metal cations) ternary diagrams, structural filiations between most of the phases in competition can be generalized with respect to

systematically found sizeable BUs^{38–40,50}. The structures of this family of compounds are built on two kinds of elementary BUs, the isolated XO_4 groups and the $\text{O}(\text{Bi},\text{M})_4$ tetrahedra sharing edges to form ribbons of variable width. These polycationic ribbons are infinite along a crystallographic axis commonly assigned to b and equal to $\sim 5.2 \text{ \AA}$ corresponding to twice the height of two $\text{O}(\text{Bi},\text{M})_4$ tetrahedra sharing edges. These ribbons are, most of the time, parallel to the a axis equal to $\sim 11.5 \text{ \AA}$ because of the arrangement of ribbons and the surrounding XO_4 groups. The third unit cell parameter depends on the width of involved ribbons and their association. Its value can be predicted by counting the number of tetrahedra ($\sim 2.785 \text{ \AA}$) along c axis, taking into account the systematic “overlapping” between two ribbons (Figure I.16). In the particular case of one type of ribbons in the unit cell, c parameter is equal to $(2n-1) \cdot 2.785 \text{ \AA}$ with n the number of linked tetrahedra.

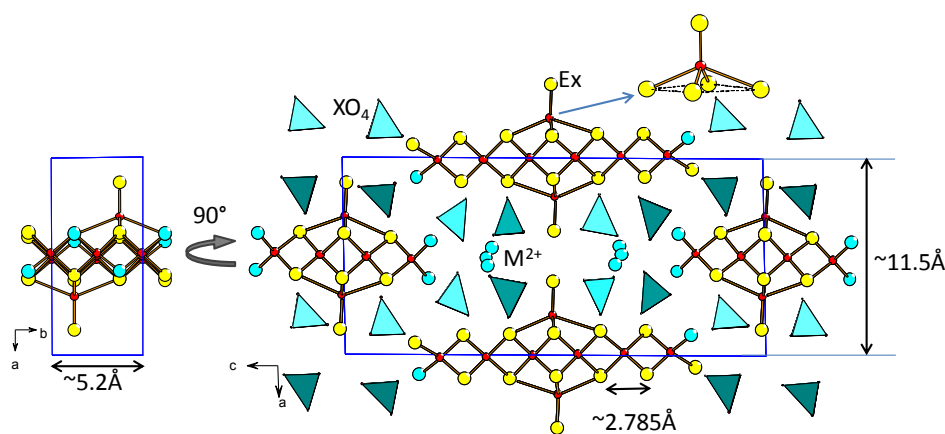


Figure I.16. Structural organization of BUs in a $n = 4 / n = 6$ phase

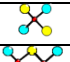
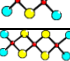
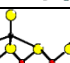
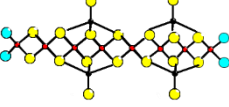
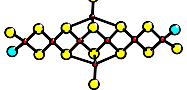
I.2.1 Empirical structural rules

Several compounds with ribbons of variable width have been characterized and from their study, several empirical structural rules have been deduced.

- The width of ribbons is varying from $n = 1$ to ∞ tetrahedra wide. The Figure I.7 already evidenced structure with width $n = 2$ and $n = 3$. But various types of ribbons may coexist in the same crystal structure, for example $n = 4/n = 6$ in the Figure I.16.
- In between 4 isolated PO_4 groups (projected along b) there is a tunnel hosting M^{2+} cations - generally in a disordered manner. To respect reasonable M-M distances, in average, two M^{2+} cations aligned along b in the same tunnel have to be separated by at least $b/2$ ($\sim 2.6 \text{ \AA}$). So a maximum of two M^{2+} cations may take place in the same tunnel.

- In the case of large ribbons ($n > 3$), there is an additional $(\text{O-Bi})^+$ excrescence coming in addition to the ribbons for stabilization with the surrounding XO_4 groups. The additional oxygen atom is quintuply coordinated, as shown on the Figure I.16. In average, the excrescences are decorating the ribbons every three on sites normally dedicated to phosphorus atoms but, because of steric considerations a maximum of two subsequent XO_4 generally surround one ribbon (Figure I.16).
- The ribbons are exclusively formed by OBi_4 tetrahedra in the middle whereas the extremities may host Bi^{3+} , M^{2+} or mixed sites $\text{Bi}^{3+}/\text{M}^{2+}$. It is important to recall that the presence of mixed sites is at the origin of a strong disorder in the inter ribbons space (PO_4 configurations and tunnels occupancy).⁴⁹ Considering the previous points, the size of ribbons is in direct relation with the number of surrounding PO_4 groups and Bi excrescences, and the number of tunnels as recalled on Table I.2
- The nomenclature used to describe the final edifice is based on $(n) - t$ sequences where n is the width of respective tetrahedra and t denote cationic tunnel along c -axis along the rows centered in $x = 0$ and $x = 1/2$ separated by “/”. For instance, for $\text{Bi}_{5.69}\text{Cu}_{2.4}(\text{PO}_4)_3\text{O}_6$, the nomenclature led to $t(4)t/(6)$ (Figure I.16).

Table I.2. Formulation for the ribbons of different width

n	Ribbon	Formula of ribbon	number of PO_4 per ribbon	number of tunnels per ribbon
1		$[\text{O}_2\text{Bi}_2\text{M}_2]^{x+}$	6	No tunnel
$n \leq 3$	$n = 2$ 	$[\text{O}_{2n}\text{Bi}_n^{\text{C}}\text{M}_{2n-2}^{\text{E}}(\text{Bi})_4^{\text{E}}]^{x+}$	$2\text{int}[(n+1)/2]$	$\text{int}[(n+1)/3]-1$
	$n = 3$ 			$n/3$
$n > 3$	$n \neq 3n'$ 	$[\text{O}_{2n+2\text{int}[(n-1)/3]}\text{Bi}_n^{\text{C}}\text{M}_{2n-2\text{int}[(n-1)/3]}^{\text{E}}(\text{Bi})_4^{\text{E}}]^{x+}$	$2[(n-1)-(\text{int}[(n-1)/3])]$	$\text{int}[(n+1)/3]-1$
	$n = 3n' *$ 			$n/3$

* n is divisible by 3

Using these structural rules, one can make an association of various building units in a unit cell, thereby predicting a number of new hypothetical crystal structures.

I.2.2 The possibility of design of new terms

As briefly described above, in the concerned series of materials the arrangement between polycationic BUs, PO_4 and interstitial channels can be fully rationalized, at least in the cases dealing with intergrowths between one single-nature of BUs³⁸. It means that, according to systematic rules, the choice of the n values leads to defined structural model assorted with a typical chemical formula $\text{Bi}_a\text{M}_b(\text{PO}_4)_c\text{O}_d$.⁵⁰ In details Bi_a includes Bi^{3+} in the cores of BUs(= Bi^{core} : 100% Bi sites), at their edges (= Bi^{edge} : mixed Bi/M sites) and the surrounding ones (= Bi^{Ex} , for excrescence). M_b include interstitial M cations (= M^{tunnel}) and mixed Bi/M sites (= M^{edge}). Finally the O_d stoichiometry includes both the $\text{O}(\text{Bi}/\text{M})_4$ tetrahedra and those of the $(\text{O}-\text{Bi}^{\text{Ex}})$ excrescences, one per Bi^{Ex} . For charge electroneutrality, the potentiality of aliovalent $(\text{Bi}^{3+}/\text{M}^{n+})^{\text{edge}}$ sites and aliovalent interstitial M^{tunnel} cations (e.g. $\text{Zn}^{2+}/\text{Li}^+$) allows for chemical degrees of freedom to stabilize the target edifice. Systematic relationships have been intensively studied between structures and chemical formulae. It has been established that long-sized ribbon BUs ($n > 3$) have the general formula $\{(\text{M}/\text{Bi})^{\text{Edge}}_4\text{Bi}^{\text{Core}}_{2n-2}\text{Bi}^{\text{Ex}}_{2\text{Int}[(n-1)/3]}\text{O}_{2n+2\text{Int}[(n-1)/3]}\}^{x+}$ surrounded by $2((n-1)-\text{Int}[(n-1)/3])\text{PO}_4$ per ribbon. $\text{Int}[x]$ denote the integer part of x . For the determination of the number of created interstitial tunnels, two cases should be distinguished depending on the n -size (Table I.2)⁵⁰.

→ $n \neq 3$ n' : there are $\text{Int}[(n+1)/3]-1$ tunnels per ribbon, which leads to the compounds formulated $\{\text{ribbon}\}_1(\text{PO}_4)_{2((n-1)-\text{Int}[(n-1)/3])}\text{M}^{\text{tunnel}}_{\sim 2\{\text{Int}[(n+1)/3]-1\}}$. We have ~ 2 M cations per tunnel in a formula unit.

→ $n = 3n'$: there are $n/3$ tunnels per ribbon, which leads to the compounds formulated $\{\text{ribbon}\}_1(\text{PO}_4)_{2((n-1)-\text{Int}[(n-1)/3])}\text{M}^{\text{tunnel}}_{\sim 2n/3}$.

The knowledge and understanding of BUs (structure and environment) is the first step in the design of new materials. The possibility to predict new terms of the series as already proved its efficiency and several terms of the series ($n = 8$ / $n = 8$, $n = 11$ / $n = 11$ etc.) have been successfully designed.^{38,40}

I.2.3 The benefit of HREM

In the last decade the High Resolution Electron Microscopy (HREM) was very efficient in the study of series of compounds with versatile $\text{O}(\text{Bi},\text{M})_4$ 1D-ribbons.^{74,75} Furthermore, the scale of observation of HREM is particularly well suited for the

identification of single crystallite, eventually in multi-phased samples. New structural intergrowths of building units, which are the ribbons with various lengths, can be evidenced by HREM. Indeed, the HREM contrasts are very strong between the Bi-rich and surrounding PO_4 -rich zones and can be directly interpreted as $\text{O}(\text{Bi},\text{M})_4$ ribbons of all sizes, as well as their arrangements in the projected plane. It is performed using an image code previously deduced from HREM images of parent compounds. Finally, a well-oriented image (in the (a, c) plane, since the growing along b is well known) leads to the direct structural deduction and possible formulation of micro-domains on the basis of empirical laws. The main procedure is summarized in the Figure I.17.

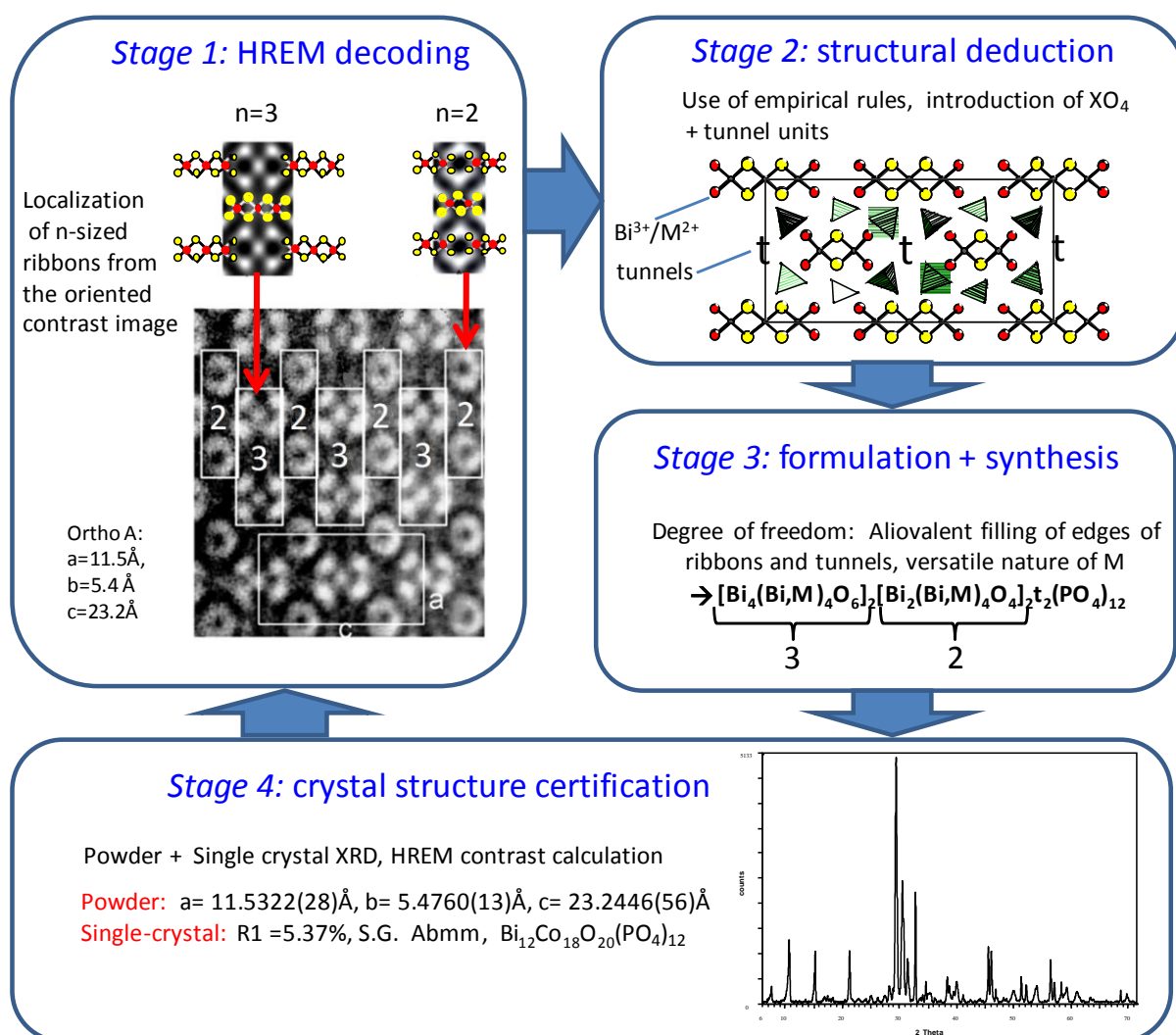


Figure I.17. Subsequent stages in structure-deduction process using HREM images.

I.3 Description of my thesis

A part of my thesis research was conducted in the frame of ANR project Multi-D InMaDe (3D inorganic Material Design, coordinated by Marie Colmont). The aim of this project is the design/prediction, elaboration and characterization of new inorganic oxides according to structural rules. Based on the knowledge learned from previous study in the $\text{Bi}_2\text{O}_3 - \text{X}_2\text{O}_5 - \text{M}_x\text{O}_y$ systems ($\text{X} = \text{P}, \text{V}, \text{As}$ etc. and $\text{M} = \text{Li}, \text{Na}, \text{Cu}, \text{Co}, \text{Ni}$ etc.) the goal of the present work is to go beyond the investigation of classical $\text{Bi}_2\text{O}_3 - \text{P}_2\text{O}_5 - \text{MO}$ ternary systems to reach novel structural archetypes. Thus, the perspectives concern a drastic extension of the targeted chemical systems and structural dimensionalities assorted with versatile physical properties (transport, dielectric, optical, magnetic etc.).

I.3.1 Design of new materials

As already discussed above, the possibility to formulate/predict new compounds appears particularly well suited to Bi-oxophosphates and has successfully achieved for several new polytypes, and therefore, it would be pertinent for the next step, to consider the possibility to modulate the topologies of the BUs and to diversify the structural archetypes and their dimensionality. The Figure I.18 shows several possible arrangements of 2D-BU's and XO_4 groups leading to several hypothetical crystal structures from 1D to 3D.

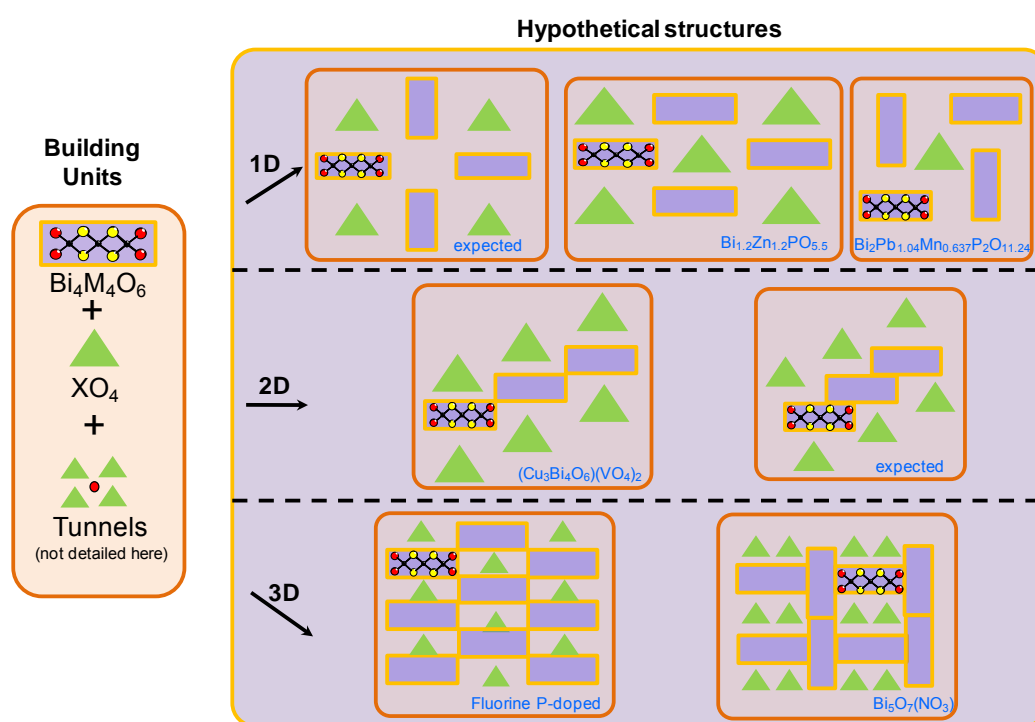


Figure I.18. Possible arrangements of 2D-BU's and XO_4 groups in hypothetical structures

To date, our building units are formed from the association of $O(\text{Bi},\text{M})_4$ tetrahedra by sharing edges to form 1D/2D ribbons (or columns) of variable width depending on the number of n connected tetrahedra along their width. We aim not only to predict new terms of the bismuth oxy-phosphate family (with other n width of ribbons) but also to reach new architectures with building units differently connected to each other (Figure I.18). At this point, the analogies between several crystal structures found in the literature open wide field for investigations in the systems with Ln^{3+} , Pb^{2+} etc.^{10,20,76}, XO_4 ($\text{X} = \text{P}, \text{As}, \text{V}, \text{Mo}, \text{Cr}, \text{Mn}$ etc)^{77–79} and halides^{80,81} as a building units. The rules and numbering of the different sub-units in a standard 1D ribbon scheme mentioned above, are summarized in the Figure I.19 in the case of intergrowth between $n = 2$ and $n = 6$ tetrahedra-wide units. However, in order to reach new edifices, the incorporation of halogen anions might be appropriate in order to modify the dimensionality of the structure since it has a tendency to create 2D building blocks or layers^{56,80,82}, such as Sillen-derivatives.

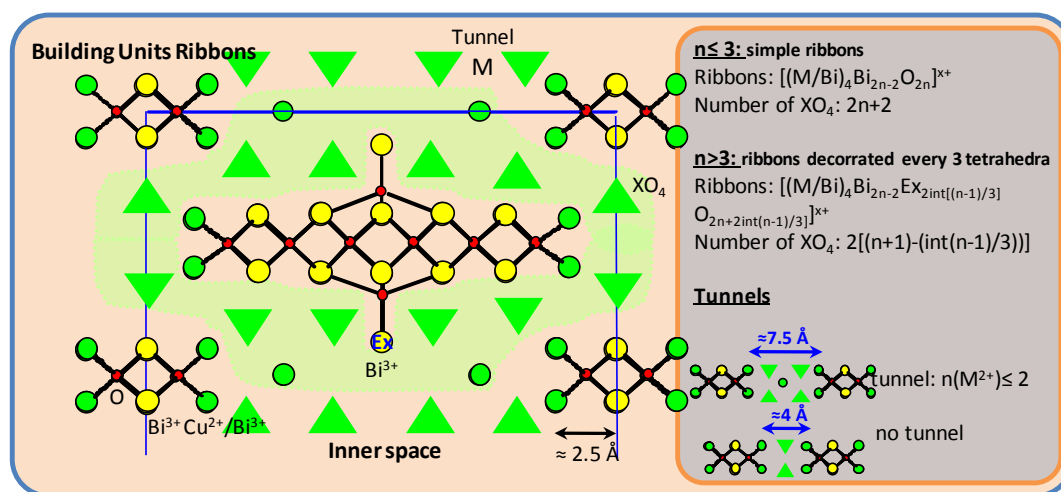


Figure I.19. A scheme to formulate new compounds

I.3.2 Shake and bake synthesis

Despite our predicted models, the achievement to prepare corresponding powder sample is not as simple as it seems, since the associated chemical reaction are ruled out by thermodynamical features related to the phase diagram.⁵⁰ Indeed, the difficulties to reach the optimal experimental conditions for the elaboration of predicted structural architectures should be taken into account. That is why it is inconsiderate to focus only on the accurate stoichiometry matching for targeted new materials. In that sense, it also remains necessary to look for new materials in a blind way, using shake and bake procedure, probing several

promising chemical systems using adapted synthesis routes. One has to recall that the majority of new structures in solid state chemistry have been pointed out “randomly”.

I.3.3 Arsenates versus phosphates

The use of a pertinent anionic group surrounding the building units, ribbons, is very important. To date, we particularly pay attention to the incorporation of phosphates in the inner space. The role played by phosphates is very important because they are serving as junctions between BUs able to create 2D arrangement or to reticulate it. Thus, to achieve new structural archetypes and dimensionalities, an idea would be to modify the nature of the inter-ribbons space. It is noteworthy to point out that PO_4 are easily substituted by VO_4 , AsO_4 , and even WO_4 and MoO_4 (with different charges) etc.⁸³ The substitution of phosphate groups by vanadate ones was not attempted since it is well known that several phases including BiVO_4 , and $\text{Bi}_4\text{V}_2\text{O}_{11}$ are very stable²⁹ and preventing the stabilization of other terms.

We focused on the use of AsO_4^{3-} as anionic groups surrounding ribbons, due to its similar charge and geometry to PO_4^{3-} groups.⁸³ There is scarce data in ICSD database and other data banks about compounds of the systems Bi_2O_3 - As_2O_5 - M_xO_y , therefore offering the possibility to obtain new structures. Thus, the idea is quite simple, the substitution of PO_4 in already-reported structures of the bismuth oxo-phosphate family by arsenic.

I.3.4 Separating of building units by chloride ions

In addition to the structural versatility and adaptability to various topologies such as 2D layers⁸² and 3D frameworks⁶⁷, metal oxyhalides are of general interest since they exhibit several interesting properties including luminescence⁸⁴ and selective oxidation catalysis⁸⁵. Therefore we focus on obtaining new topologies of layered bismuth based oxy-halides compounds. The series of Sillen phases^{86,87} consists of α - PbO (or fluorite) $[\text{M}_2\text{O}_2]^{2+}$ layers intergrown with single $[\text{X}]$, double $[\text{X}_2]$ or triple $[\text{M}'_x\text{X}_3]$ halide layers, where X is halide atom. It produces rather simple structures found for MBiO_2Cl (X1) ($\text{M}^{2+} = \text{Cd}, \text{Ca}, \text{Pb}$ etc)^{82,88,89}, BiOCl (X2)⁹⁰ and $\text{Ca}_{1.25}\text{Bi}_{1.5}\text{O}_2\text{Cl}_3$ (X3)⁹¹. A diversity of ordered intergrown structures have been also reported with sequences giving rise to ideal tetragonal structures with $a \sim 3.9 \text{ \AA}$ (i.e., $\sqrt{2}/2a_{(\text{fluorite})}$) and c varying from 6 to 50 \AA dependent on the structural complexity^{80–82,88,89,91–93}.

I.3.5 The incorporation of SeO_3^{2-}

The thread of this part is more or less driven by the same concept as for the incorporation of arsenates. The reason why we want to use Se^{4+} is that the presence of an extra lone pair (in addition to those of Bi^{3+}) can lead to interesting structural chemistry^{58,94-96}. In virtue of their variable coordination environments, materials with lone pair cations often exhibit certain flexible backbone⁹⁷. In that sense, the transition metal oxyhalides materials enhance a lone pair cation playing a key role of chemical scissor, giving a tendency to build compounds with low dimensional structures such as chains or layers.

Also, the number of noncentrosymmetric structures containing SeO_3 groups is rather high, due to the cooperative orientation of the stereochemical of the lone pair of Se(IV) allowing asymmetric or one-sided coordination of the cation⁹⁵. The subsequent NCS (noncentrosymmetric) materials are very promising for their properties such as non-linear optics, piezoelectricity, and ferroelectricity etc⁹⁷.

The chemistry of selenium is rather hazardous. Especially the melting point of SeO_2 is very low (340°C, in a sealed tube) which implies a re-adaptation of our standard synthesis routes as used in the case of bismuth oxide phosphates. Because of its volatile character and for security reasons related to the use of selenium, syntheses were performed (i) in sealed tubes and (ii) using a chemical vapor phase transport (CVT) method^{98,99} which is, very well adapted to these kinds of compounds. Widening the range of synthesis methods as much as possible was also a guaranty of the success of this part of my thesis.

I.3.6 Summary

With the presented above ideas in mind several exploratory syntheses have been conducted to obtain new bismuth compounds. In the Chapter II, the structures composed of OBi_4 based BUs with various dimensionalities are described and their respective properties have been presented if measured. Whereas, the Chapter III concerns the compounds not containing O(BiM)_4 tetrahedra, where the bismuth centered polyhedra notion was used to describe several structures. And finally, Conclusion of the thesis work is given on the end of the manuscript.

*Chapter II. New bismuth-based
oxides and salts - original topologies
of oxocentered tetrahedra*

II. New bismuth-based oxides and salts - original topologies of oxocentered tetrahedra

Several compounds with various topologies have been obtained and some of their respective properties have been measured and briefly analyzed. Also, the syntheses and corresponding measurements of related known compounds have been conducted for comparison. This chapter is divided to the three subchapters according to the dimensionalities of the BUs built of $O(\text{Bi}/M)_4$ tetrahedra, ranging from 1D to 3D. No compound with 0D BUs (isolated oxocentred units) was obtained in this work.

II.1 1D compounds – ribbons and columns as BUs

Among the new compounds, studied in this work, the majority represent the 1D ones. This subchapter presents the compounds consisting of BUs such as columns and ribbons with various sizes.

II.1.1 $n = 1$ ribbons: $\text{BiCoO}(\text{AsO}_4)$

1) Generalities.

The elementary BU in terms of constituting ribbons is the $n = 1$ terms which have the general formula $\text{BiMO}(\text{XO}_4)$, where $M = \text{Mg}, \text{Ca}, \text{Pb}, \text{Cd}, \text{Mn}, \text{Co}, \text{Ni}$ and $X = \text{P}, \text{As}, \text{V}$. They are all isostructural having $n = 1$ ribbons surrounded by corresponding XO_4 . In general, M atoms are in *trans* position (Figure II.1a) with respect to edges on the tetrahedra in the ribbons except two cases, where M atoms are in *cis* position (Figure II.1b), they are: $\text{BiCaO}(\text{VO}_4)$ and $\text{BiCdO}(\text{VO}_4)$. The new obtained $\text{BiCoO}(\text{AsO}_4)$ belong to the former case.

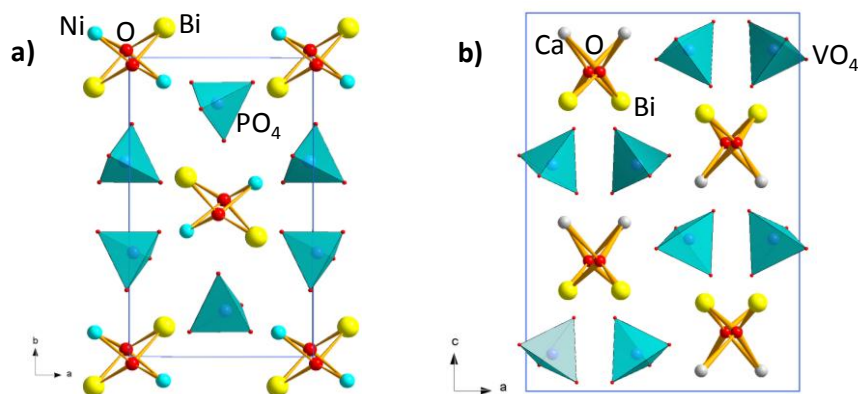


Figure II.1. $\text{BiMO}(\text{XO}_4)$: a) The structure of $\text{BiNiO}(\text{PO}_4)$, with M atoms in *trans* position, b) the structure of $\text{BiCaO}(\text{VO}_4)$, with M atoms in *cis* position.

2) Synthesis of BiCoO(AsO₄).

Single crystal: The single crystals of BiCoO(AsO₄) was found in the synthesis with following protocol: the golden tube with the mixture of Bi₂O₃, CoO and As₂O₅ with the ratio 1:2:1 was heated at 900°C during 12 hours followed by slow cooling down to 700°C at ratio 3°C/hour.

Powder synthesis: In order to obtain the powder the stoichiometric mixture of Bi₂O₃, CoO and As₂O₅ was heated at 800°C in an alumina crucible during 48 hours with intermediate grindings. The XRD pattern of the obtained blue powder showed pure phase of BiCoO(AsO₄)

3) Structural description.

The structure of BiCoO(AsO₄) crystallizes in triclinic system in the space group *P*-*I*, with the unit cell $a = 5.2380(3) \text{ \AA}$, $b = 6.8286(4) \text{ \AA}$, $c = 7.6150(4) \text{ \AA}$, $\alpha = 111.631(2)^\circ$, $\beta = 108.376(2)^\circ$, $\gamma = 108.388(2)^\circ$, and $V = 209.55(2) \text{ \AA}^3$. Crystal data and refinement details are given on the Annex S1.

The structure of BiCoO(AsO₄) contains [O₂Bi₂Co₂]⁶⁺ ribbons which go along the direction parallel to [001] axis, see Figure II.2a. The Co atoms in the ribbons are in the *trans* position with respect to Bi atoms. The ribbons are surrounded by six AsO₄ tetrahedra. The Co atom make CoO₆ octahedron which shares edges with another adjacent one in the same ribbon by forming Co₂O₁₀ dimers (Figure II.2a).

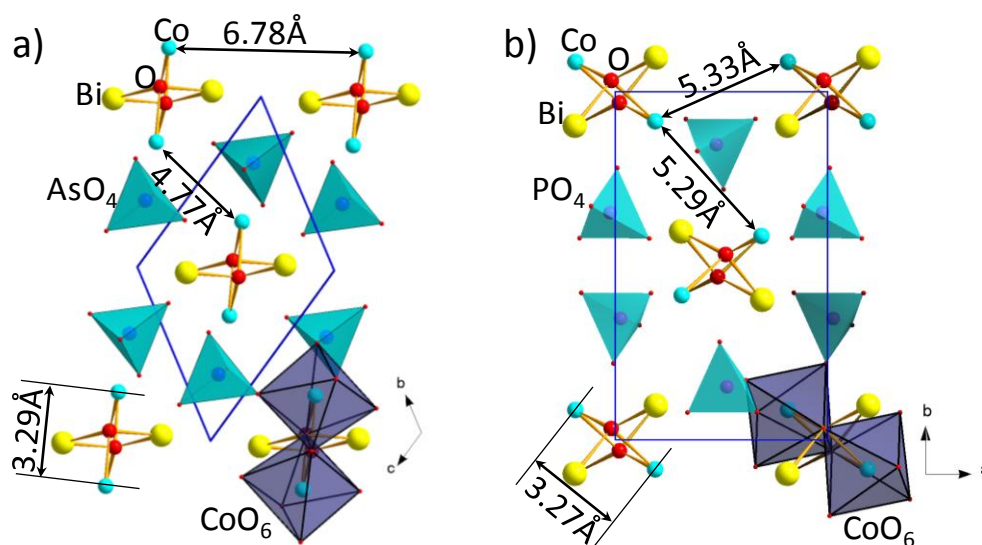


Figure II.2. Crystal structure of a) BiCoO(AsO₄) and b) BiCoO(PO₄)

The obtained BiCoO(AsO₄) is isostructural to existing BiCoO(PO₄) (Figure II.2b), however, the latter crystallizes in monoclinic crystal system, unit cell parameters are: $a = 7.2470(1) \text{ \AA}$,

$b = 11.285\ 1(2)\ \text{\AA}$, $c = 5.2260(1)\ \text{\AA}$, $\beta = 107.843(1)^\circ$ and $V = 406.91\ \text{\AA}^3$, in the space group $P2_1/n$.⁵¹

The orientation of the $[\text{O}_2\text{Bi}_2\text{Co}_2]^{6+}$ ribbons of $\text{BiCoO}(\text{AsO}_4)$ is different than that of $\text{BiCoO}(\text{PO}_4)$ due to steric effects of bigger AsO_4 (Figure II.2). The arrangement of $[\text{O}_2\text{Bi}_2\text{Co}_2]^{6+}$ ribbons affects the spatial inter-orientation of the Co_2O_{10} dimers and consequently the distances between those isolated species. The Co_2O_{10} dimers are the magnetic entities and will be the subject of discussion in the magnetism part below.

4) High Temperature XRD (HTXRD)

HTXRD and DTA measurements were conducted in order to see if there are any structural reorganizations in $\text{BiCoO}(\text{AsO}_4)$. The results are reflected in the Figure II.3. DTA plot showed no phase decomposition until 850°C where melting is taking place. A small endothermic peak is observed around 330°C (red arrow on the Figure II.3) without any

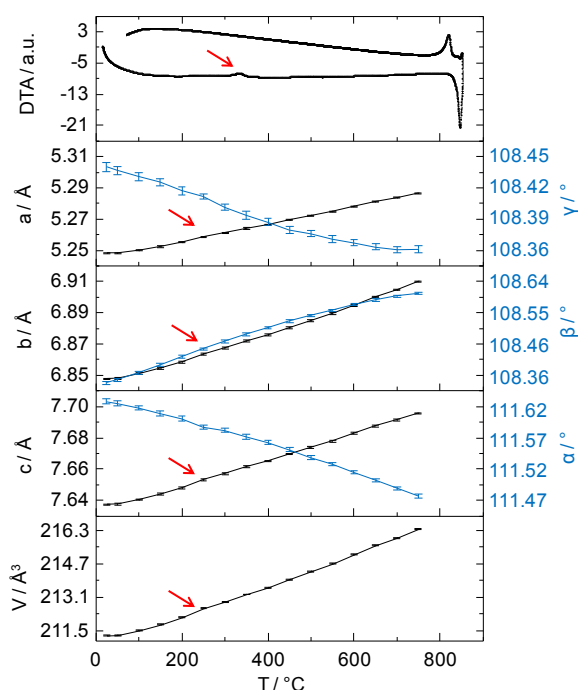


Figure II.3. DTA plot (top graph) and unit-cell parameters evolution of $\text{BiCoO}(\text{AsO}_4)$ as functions of temperature. Red arrows show an anomaly on the unit cell parameters evolution as well as an endothermic peak on the DTA

dependencies with the progression of lattice parameters.

The evolution of unit cell parameters is quite linear however a tiny anomaly occur around 250°C (red arrows on the Figure II.3) in all the lattice constants. The thermal dependencies of the lattice parameters indicate a progressive lattice dilatation with the mean thermal expansion coefficients ($1/L_0(\Delta L/\Delta T)$) along the three crystallographic directions: $\alpha_a = 10.1 \cdot 10^{-6}\ \text{K}^{-1}$, $\alpha_b = 12.6 \cdot 10^{-6}\ \text{K}^{-1}$, $\alpha_c = 10.5 \cdot 10^{-6}\ \text{K}^{-1}$ showing almost isotropic character of the former. The same order of the values of the expansion coefficients shows no particular direction of phosphate reorganization as it is

the case for analogous compounds³⁹ but in opposition with results of the francisite high temperature study¹⁰⁰.

5) Magnetic properties.

The magnetization versus temperature of BiCoO(AsO₄) was collected under an applied field of 0.1 T. At such field we verified that $M(H)$ is linear, such that the magnetic susceptibility $\chi = dM/dH$ is estimated by M/H . $\chi(T)$ and $\chi^{-1}(T)$ plots are shown on the Figure II.4. It evidences a paramagnetic to antiferromagnetic transition at $T_N = 15.4$ K. In the paramagnetic region, the susceptibility data is modeled using a Curie–Weiss law: $\chi = C/(T - \theta_{CW})$ leading to $\theta_{CW} = -75.7$ K and $\mu_{eff} = \sqrt{8C} = 5.17 \mu_B/\text{Co}$. This value is close to that of BiCoO(PO₄) ($5.40 \mu_B/\text{Co}$)^{101,102} and highlights a high spin-orbit coupling by comparison to the spin-only expected value for Co²⁺ ($S = 3/2$, $\mu_{eff} = 3.87 \mu_B$) but lies in the range commonly observed for this cation.

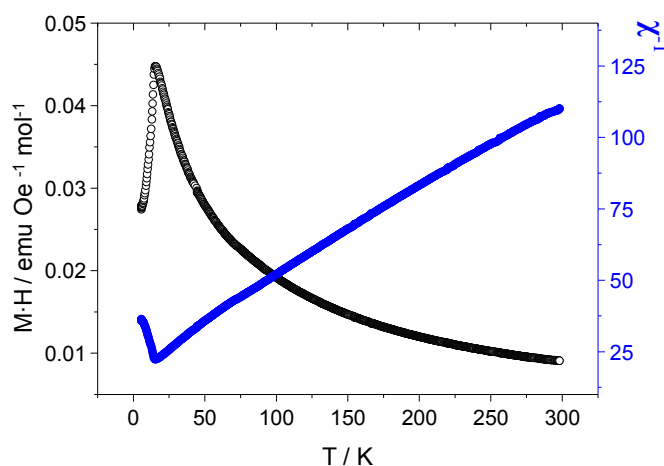


Figure II.4. $\chi(T)$ and $\chi^{-1}(T)$ plots of BiCoO(AsO₄)

The magnetic structure for the monoclinic BiNiO(PO₄) ($T_N = 17.5$ K) and BiCoO(PO₄) ($T_N = 15$ K) was refined using powder neutron diffraction data¹⁰². In both cases the main spin-arrangement is similar, i.e. characterized by the propagation vector $\mathbf{k} = (-1/2, 0, 1/2)$, and ferromagnetic edge-sharing M_2O_{10} dimers antiferromagnetically arranged through the a and c translation, while the spin orientation (M_x , M_y , M_z) is modified by magnetic-symmetry through other crystallographic operators. A similar magnetic structure is expected for the triclinic BiCoO(AsO₄), especially in the edge sharing dimers where the strongest Co-O-Co super-exchange ($\angle \text{Co-O-Co} = 102.2^\circ$, $\text{Co-O} = 2.0\text{--}2.2$ Å, $\text{Co-Co} = 3.3$ Å) are also expected ferromagnetic from Kanamori-Goodenough rules¹⁰³. For BiCoO(AsO₄), the T_N value ($=15.4$ K) is very close to the one of BiCoO(PO₄) ($=15$ K) meaning that in this structural type, the PO₄ and AsO₄ groups have the same magnetic “connector” ability through Co²⁺-O_(XO4)-O_(XO4)-Co²⁺ super super exchanges (SSE) paths that transfer the antiferromagnetic exchanges.

It is in probable relation with the similar electronegativity of P(=2.19) and As(=2.18)²³ that allow a similar Co-3d and O-2p orbitals overlapping. We note that the strengthening of SSE concomitantly with the increasing of T_N could be expected from other XO_4 groups such as VO_4 (electronegativity V = 1.63). For instance, it was observed that $Pb_2(V^{4+}O)(VO_4)_2$ displays AFM magnetic chains with strong AFM $V^{4+}-O_{(VO_4)}-O_{(VO_4)}-V^{4+}$ SSE while $Pb_2(V^{4+}O)(AsO_4)_2$ is paramagnetic due to very weak $V^{4+}-O_{(AsO_4)}-O_{(AsO_4)}-V^{4+}$.¹⁰⁴ Finally, it is striking that the interatomic separation due to the lattice volume plays a minor role compared to the electronegativity since the inverse correlation between coupling constants and the XO_4 steric effect ($VO_4 > AsO_4 > PO_4$) is not respected.

6) Summary

The structure of a new term, $BiCoO(AsO_4)$, in the $BiMO(XO_4)$ series with $n = 1$ ribbons, is described and briefly compared to that of $BiCoO(PO_4)$. No structural change has been observed apart from isotropic expansion during HTXRD studies. Magnetic properties are similar to the isostructural $BiCoO(PO_4)$ due to the close electronegativities of As and P, however, their radii do not seem to play a big role in the magnetic spin interactions of Co atoms.

II.1.2 $n = 2$ ribbons: $BiCu_2O_2(AsO_4)$ and $BiCu_2O_2(PO_4)$

1) Generalities.

As observed for the $BiCoO(XO_4)$ phases, the substitution of PO_4 groups ($r(P^{5+}) = 0.170 \text{ \AA}$) for bigger AsO_4 groups ($r(As^{5+}) = 0.34 \text{ \AA}$) is expected to modify structural features of the expected compounds in the chemical systems we are focused in our work.

A topical case concerns the existing compounds $BiCu_2O_2(XO_4)$, where $X=As, P$, in which double ($n = 2$) OBi_2Cu_2 tetrahedra oxo-centered ribbons $[O_2BiCu_2]^{3+}$ are isolated by XO_4 groups¹⁰⁵ (Figure II.5a). The compound $BiCu_2O_2(PO_4)$ is very interesting from the magnetic properties viewpoint and has been the subject of a number of works^{106–108} devoted to its particular fundamental and excited states. Briefly, it was shown that $BiCu_2O_2(PO_4)$ is a frustrated two-leg spin-ladder compound with a spin gap. The ladders are formed by Cu^{2+} edges of ribbons in a same ribbon (Figure II.5a). The frustration between Cu^{2+} spins along the rungs drives $BiCu_2O_2(PO_4)$ into a gapped quantum singlet ground state with excited magnetic states, showing an incommensurate dispersion. On the Figure II.6 the ladders are defined by J_1 (legs) and J_4 (rungs), the NNN (next nearest neighbor) frustration correspond to J_2 and J_2' .

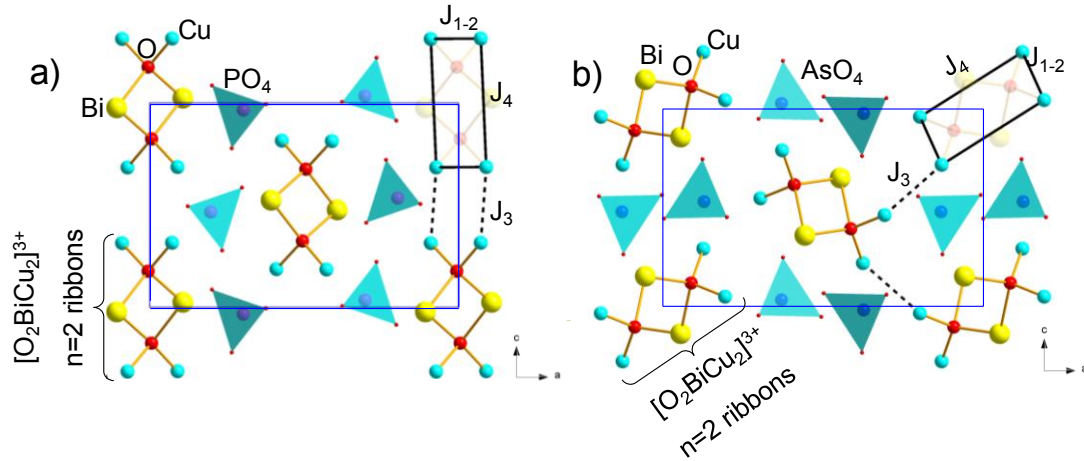


Figure II.5. The structures of: a) $\text{BiCu}_2\text{O}_2(\text{PO}_4)$ and b) $\text{BiCu}_2\text{O}_2(\text{AsO}_4)$. J_{1-2} , J_3 and J_4 are the spin-exchange paths.

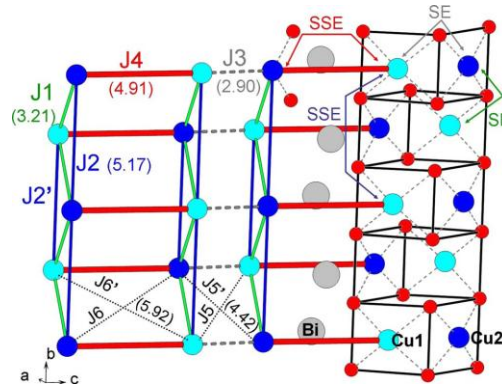


Figure II.6. Schematic representation of the Cu^{2+} ion arrangement and the SE/SSE spin-exchange paths in $\text{BiCu}_2\text{O}_2(\text{PO}_4)$. The two crystallographically nonequivalent copper atoms are indicated by blue and cyan circles, and the oxygen atoms by red circles.

The couplings between the ladders is not neglectable but of weaker importance, see the relative values on the Table II.1.

Table II.1. Spin exchange parameters J_1 – J_6 in meV of $\text{BiCu}_2\text{O}_2(\text{PO}_4)$ obtained from the GGA+ U calculations ($U = 4$ eV) the numbers in parentheses are the relative values with respect to the strongest exchange parameter.

SE	SE values
J1	31.87(0.82)
J2	21.49(0.55)
J3	13.06(0.34)
J4	38.76(1.00)
J5	−0.08(0.00)
J6	3.10 (0.08)

As for the excited states, magnetic field of approximately 20 T closes the gap. This quantum phase transition is accompanied by several other transitions into a complex phase diagram as

a function of magnetic field and temperature (H , T) also due to the frustrated ladders. Measuring of the same properties of the isostructural $\text{BiCu}_2\text{O}_2(\text{AsO}_4)$, could give insights in the magnetic spin interactions in this structural type. To date only the crystal structure has been reported¹⁰⁹, and there is no mention about the possibility to prepare the powder (only single crystals have been prepared by melting/slow cooling). The lattice parameters of both compounds from literature data are given in Table II.2. The cell volume of $\text{BiCu}_2\text{O}_2(\text{AsO}_4)$ is larger than that of $\text{BiCu}_2\text{O}_2(\text{PO}_4)$, on the other hand the c axis is shorter in $\text{BiCu}_2\text{O}_2(\text{AsO}_4)$, 7.577 Å vs. 7.790 Å for $\text{BiCu}_2\text{O}_2(\text{PO}_4)$. The important fact is that the main unit-cell volume shows a strong expansion in the arsenate due to the greater size of AsO_4 groups compared to PO_4 groups ($r_{\text{As}^{5+}} = 0.34$ Å, $r_{\text{P}^{5+}} = 0.17$ Å)¹¹⁰.

Table II.2. Unit cell parameters of $\text{BiCu}_2\text{O}_2(\text{PO}_4)$ and $\text{BiCu}_2\text{O}_2(\text{AsO}_4)$.

Compound	Space Group	a (Å)	b (Å)	c (Å)	Cell volume (Å ³)
$\text{BiCu}_2\text{O}_2(\text{PO}_4)$	$P n m a$ (62)	11,776(1)	5,1730(6)	7,7903(6)	474,56(8)
$\text{BiCu}_2\text{O}_2(\text{AsO}_4)$	$P n m a$ (62)	12,253(1)	5,280(1)	7,577(1)	490.20(12)

Indeed, as it is seen from the Figure II.5b, the replacement of PO_4 by AsO_4 groups strongly modifies the structure, although the main topology of the $[\text{O}_2\text{BiCu}_2]^{3+}$ ribbons remains the same, being tilted differently. This tilting of the ribbons alters the respective spin-exchange J values. In fact, the intra-ladder J_1 , J_2 and J_4 should remain nearly unchanged due to the similar geometry of the $[\text{O}_2\text{BiCu}_2]^{3+}$ ribbons while the inter-ladder J_3 should be strongly different because of the strong reorientation of the ribbons by rotation influencing $d_{\text{Cu-Cu}}$ along J_3 (2.93 Å in the arsenate vs. 2.90 Å in the phosphate). With the hope that J_3 will be strongly reduced to obtain isolated frustrated ladders we have conducted neutron diffraction measurements.

2) Synthesis.

Powder synthesis: Stoichiometric amounts of Bi_2O_3 , CuO and As_2O_5 or/and $(\text{NH}_4)_2\text{HPO}_4$, in the case of the phosphate and solid solutions, were ground together and placed into alumina crucible, first heated at 500°C for 12h then heated at 800°C for 48h with intermediate grindings.

3) Solid solution of $\text{BiCu}_2\text{O}_2(\text{As}_x\text{P}_{1-x}\text{O}_4)$.

A solid solution of $\text{BiCu}_2\text{O}_2(\text{As}_x\text{P}_{1-x}\text{O}_4)$ has been prepared for several x values. Typically two domains of solid solutions exist starting from the two end members: $\text{BiCu}_2\text{O}_2(\text{PO}_4)$ -type

(Figure II.7, white squares) $x = 0$ to $x = 0.5$ and $\text{BiCu}_2\text{O}_2(\text{AsO}_4)$ -type $x = 0.75$ to 1 (Figure II.7, black triangles).

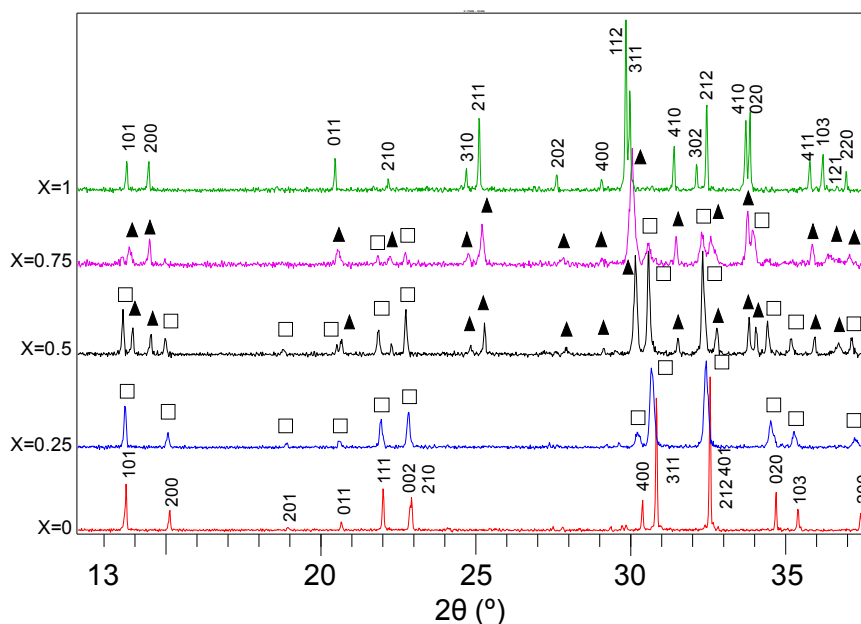


Figure II.7. Diffraction patterns of solid solutions $\text{BiCu}_2\text{O}_2(\text{As}_x\text{P}_{1-x}\text{O}_4)$, x changing from 0 to 1. The peaks of the phase $\text{BiCu}_2\text{O}_2(\text{AsO}_4)$ denoted by black triangles whereas that of $\text{BiCu}_2\text{O}_2(\text{PO}_4)$ with white squares.

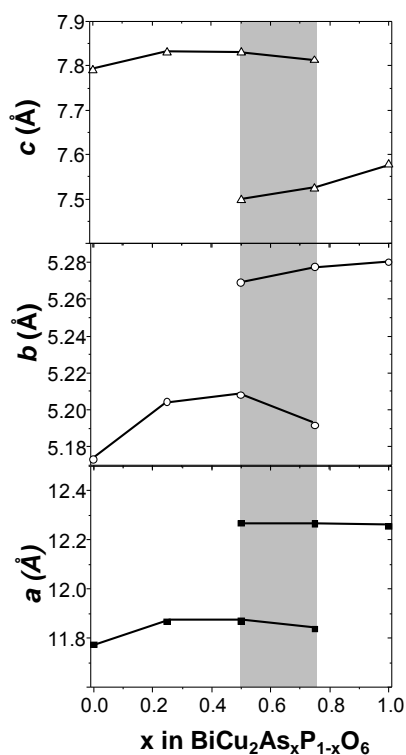


Figure II.8 Variation of the lattice parameters versus x in $\text{BiCu}_2\text{O}_2(\text{As}_x\text{P}_{1-x}\text{O}_4)$

Evaluation of the refined lattice parameters versus the change of x of the solid solutions $\text{BiCu}_2\text{O}_2(\text{As}_x\text{P}_{1-x}\text{O}_4)$ is shown in the Figure II.8. As it is seen in the diagram, in the solid solution domain the a and c cell parameters of phase $\text{BiCu}_2\text{O}_2(\text{PO}_4)$ did not change significantly, whereas the b parameter was changed drastically from 5.175 Å to 5.205 Å in the range $x = 0$ to 0.25. There is bi-phased domain in the range $x = 0.5$ to 0.75. It implies that these two compounds should be considered as different polytypes due to the important re-organization between the sub-units and that the passage from one to another one is not continuous upon increasing the XO_4 size.

4) Magnetism.

The magnetic susceptibilities and inverse susceptibilities versus temperature collected at $H = 0.05$ T for $x = 0$, $H = 0.1$ T for $x = 0.25$ and $H = 0.5$ T for $x = 1$ are shown on the

Figure II.9a and Figure II.9b. In the paramagnetic regimes we find $\mu_{\text{eff}} = 2.11$, 2.04, $2.11\mu_{\text{B}}/\text{Cu}^{2+}$ and $\Theta_{\text{CW}} = -261$, -310 and -358 K for $x = 0$, 0.25 and 1 respectively. It reflects spin-orbit contribution compared to the $1.73 \mu_{\text{B}}/\text{Cu}^{2+}$ expected in a spin-only approximation and increasing AFM exchanges with increasing x . The plot for $x = 0$ is typical of a spin gap even if partially hidden by a strong paramagnetic intrinsic impurity at low temperature. For $x = 0.25$ the same shape but smoother is obtained which suggests a nearly-similar behavior (= frustrated 2-leg-ladders). The maximum of $\chi(T)$ being only slightly shifted same relative J values are expected.

The evidence of the gap in $\text{BiCu}_2\text{O}_2(\text{PO}_4)$ is shown in Figure II.10a by the intense bands observed on inelastic neutron scattering around $Q = 1 \text{ \AA}^{-1}$ and 2 \AA^{-1} for energy transfer $> 2\text{meV}$. This plot will not be detailed (see ref [11]) but is given here for comparison with that of $\text{BiCu}_2\text{O}_2(\text{AsO}_4)$ which pictures the lack of gap (Figure II.10b).

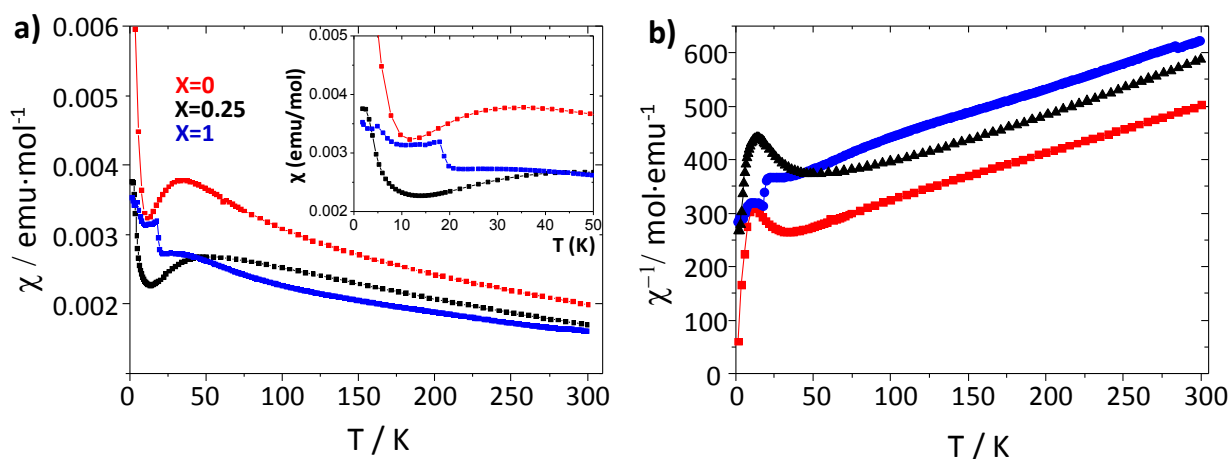


Figure II.9. Magnetic measurements of $\text{BiCu}_2\text{O}_2(\text{As}_x\text{P}_{1-x}\text{O}_4)$: a) susceptibilities and b) inverse susceptibilities vs. T collected at $H = 0.05 \text{ T}$ for $x = 0$, $H = 0.1 \text{ T}$ for $x = 0.25$ and $H = 0.5 \text{ T}$ for $x = 1$.

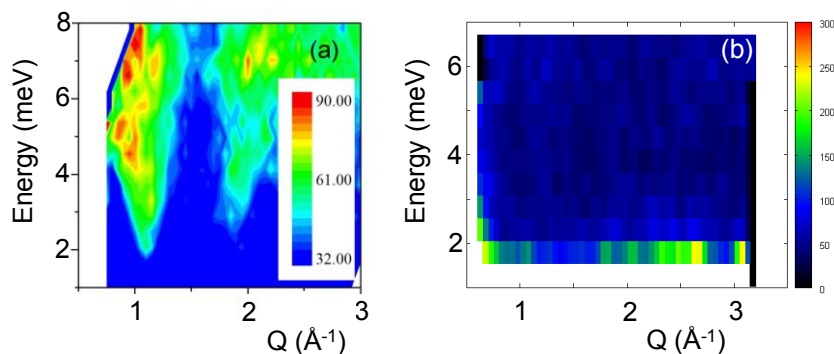


Figure II.10. a) The evidence of a spin gap in $\text{BiCu}_2\text{O}_2(\text{PO}_4)$ and b) the absence of that in $\text{BiCu}_2\text{O}_2(\text{AsO}_4)$ on inelastic neutron scattering.

Indeed, the $\chi(T)$ behavior for BiCu₂AsO₆ differs from that of BiCu₂O₂(PO₄), suggesting an antiferromagnetic 3D ordering below $T_N = 18$ K (Figure II.9). This robust magnetic ordering is such that no inelastic scattering peak is observed (Figure II.10b) (no magnetic absorption) meaning the absence of a spin gap (spectra are collected at 2.7 K at the LLB on the same 4F2 spectrometer).

Using the same principle as for BiCu₂O₂(PO₄) defined above, the calculation of the J values gives $J_1/J_2/J_3/J_4 = 1.0/0.63/0.78/0.61$ respectively, which indicates very strong couplings between the ladders (strong J₃) being in good agreement with a possible 3D ordering. However, as shown on the Figure II.11 our neutron data collected versus temperature do not show any evidence for a magnetic ordering below 18 K.

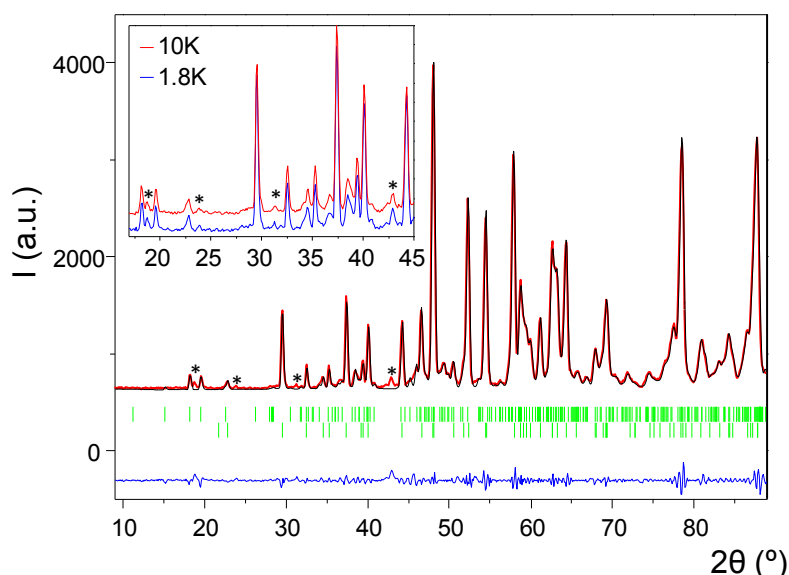


Figure II.11. Profile fitting of BiCu₂O₂(AsO₄) refined taking into account of minor second phase – Bi₄Cu₃O₆(AsO₄)₂. * - denotes some extra peaks the origin of which is nonmagnetic, since they are observed at the temperature above T_N (see inset).

The pattern was satisfactorily refined using the BiCu₂O₂(AsO₄) structural model only in the absence of a magnetic contribution. It means that probably robust AFM units exists but may not be magnetically 3D-ordered below the pseudo- T_N .

In addition, an accurate analysis of $\chi(T)$ shows a ZFC/FC divergence which generally indicates the occurring of a non-compensated net magnetic moment below 18 K (Figure II.12). It could arise from weakly canted spins, which generate a weak magnetization of the sample.

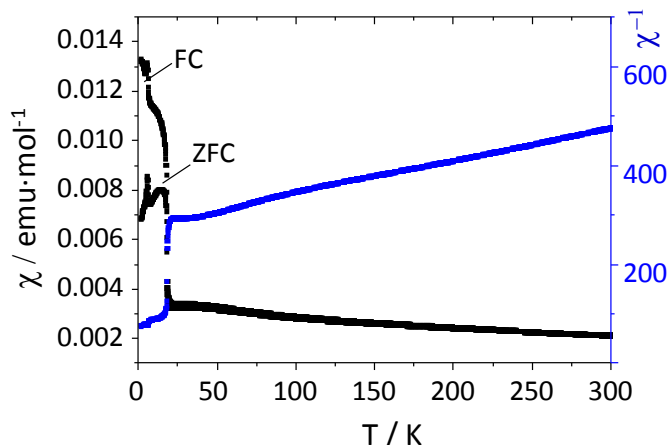


Figure II.12. $\text{BiCu}_2\text{O}_2(\text{AsO}_4)$: ZFC/FC plots of M/H versus the temperature at 0.01 Tesla in black. $\chi^1(T)$ is shown in blue and refers to the right-axis.

The value of such a magnetization can be estimated from our $M(H)$ magnetization plots collected at 2 K., see Figure II.13. The remanent moment is very weak, in fact less than $5 \cdot 10^{-4} \mu_B/\text{f.u.}$

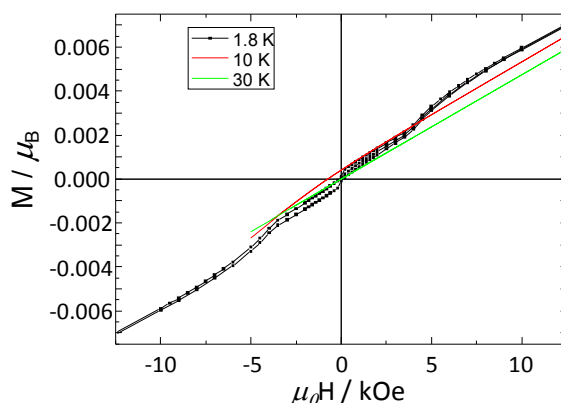


Figure II.13. $\text{BiCu}_2\text{O}_2(\text{AsO}_4)$: $M(H)$ at $T = 1.8 \text{ K}$ (black), 10 K (red) and 30 K (green) in $\mu_B/\text{f.u.}(\text{Oe})$.

At higher field the weak metamagnetic transition at 0.3-0.4 T is to be associated to the peak on $\chi(T)$ observed around 7 K, which probably comes from $\text{Bi}_4\text{Cu}_3\text{O}_6(\text{AsO}_4)_2$, a minor impurity. We note that this impurity was not observed on XRD powder patterns, but the characteristic magnetic events coincide well with those further described in the section II.1.6.

5) Summary

The magnetic properties of $\text{BiCu}_2\text{O}_2(\text{AsO}_4)$ are significantly modified after the $\text{P} \rightarrow \text{As}$ substitution, due to geometrical changes (spin gap vs. gapless). The initial suggestion that the Cu magnetic ladders would be isolated by diminished J_3 spin-exchange pathways in the case

of the arsenate turned out to be wrong. Nevertheless, magnetic structure has not been observed on PND data. Further experiments will be carried out to understand the 3D AFM ordering taking place in BiCu₂O₂(AsO₄).

II.1.3 $n = 2$ ribbons: NaBiO(MoO₄)

The compound NaBiO(MoO₄) was obtained and its structure was solved by a postdoc Dr. Nicolas Renaut. It is presented here to show the possibility of synthesis of new terms of bismuth oxo-molybdates.

1) Synthesis.

Single crystal: The single crystals of NaBiO(MoO₄) were found in the melt of the mixture NaCl + 0.5Bi₂O₃ + 5MoO₃, slow cooled (5°C/h) down to room temperature from 950°C previously kept during 12h.

2) Structural description.

The structure of NaBiO(MoO₄) (Figure II.14a) crystallizes in monoclinic crystal system with space group $P21/n$ (14) with unit cell parameters $a = 5.6097(5)$ Å, $b = 14.6472(15)$ Å, $c = 11.9048(13)$ Å, $\beta = 90.220(4)^\circ$ and $V = 978.17(17)$ Å³. In this case, the $n = 2$ wide [Bi₂NaO₂]³⁺ ribbons and the channels of Na⁺ are separated by MoO₄²⁺ tetrahedral (Figure II.14b) where molybdenum cation is in +6 oxidation state. The *trans* corners of the ribbons are occupied by Na cations, no splitting observed on the corners occupied by Bi.

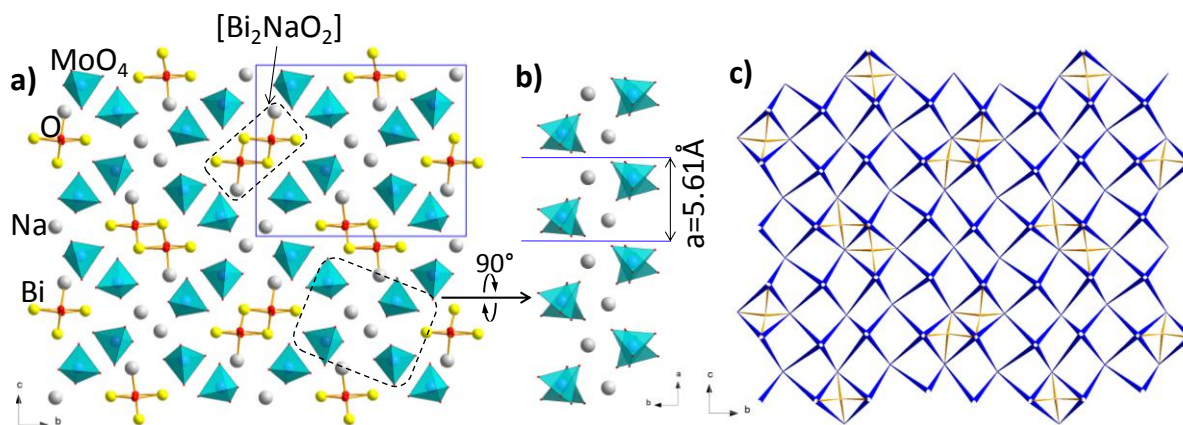


Figure II.14. a) The structure of NaBiO(MoO₄), b) Na channel surrounded by MoO₄ tetrahedra and c) the cationic grid representation of the structure

The structure resembles the one of [Bi₂(Bi_{1.56}K_{0.44})^{dis}O₃][K_{0.88}^{dis}(PO₄)₂] discussed above where ribbon size, however, is $n = 3$ wide. In contrary to “fully disordered”

$[\text{Bi}_2(\text{Bi}_{1.56}\text{K}_{0.44})^{\text{dis}}\text{O}_3]\text{K}_{0.88}^{\text{dis}}(\text{PO}_4)_2$, the edges of the ribbons as well as the cationic channels are completely ordered probably due to the bigger size of MoO_4 ($d(\text{Mo}-\text{O}) \approx 1.8\text{\AA}$), thus, as it is seen in the cationic grid representation, (Figure II.14) Na cations are not interstitial taking particular x and $x + 1/2$ positions, which is quite unexpected for the structures with cationic tunnels.

3) Summary

At the moment we try to reproduce the structure in the polycrystalline form to further studies of its corresponding properties. Moreover, the synthesis of possible new terms of bismuth oxo-molybdates with different n values are under way.

II.1.4 Potentialities of bismuth containing compounds as luminescent materials

We have described several new compounds prepared in the frame of the present PhD work. It is important to notice that in the meantime, I prepared samples of already reported $\text{BiMO}(\text{XO})_4$ and $\text{BiM}_2\text{O}_2(\text{XO}_4)$ ($\text{X} = \text{As}, \text{P}, \text{V}$ etc) compounds for luminescent properties, in collaboration with Prof. Dr. Claudia Wickleder of University of Siegen. The preliminary results were so good, that a thesis (PhD-student Jacob Olchowka) between our two universities have started last year. Here I will present very briefly the main expectations and results of the fascinating properties, of rather simple ordered polytypes.

As first experienced from several terms, the series of $\text{BiM}_2\text{O}_2(\text{XO}_4)$ compounds are very interesting for their optical properties, in fact the samples with $\text{M} = \text{Mg}, \text{Ca}, \text{Zn}$ or Cd and $\text{X} = \text{P}, \text{V}, \text{As}$ emit a yellow/white bright luminescence at room temperature under UV wavelength excitation (example $\text{BiMg}_2\text{O}_2(\text{AsO}_4)$, Figure II.15a). The luminescence of Bi^{3+} , as the other ions with ns^2 electronic configuration comes from the fast and allowed electronic transition $s^2 \rightarrow sp$. The ground state s^2 is the singlet 1S_0 while the excited state sp give rise to a triplet 3P_0 , 3P_1 , 3P_2 and a singlet 1P_1 . The transitions from the ground state to the triplet is spin forbidden but the spin-orbit mixing between 3P_1 and 1P_1 allowed $^1S_0 \rightarrow ^3P_1$ transition (A-band) and the transition from the ground state to the highest energy level $^1S_0 \rightarrow ^1P_1$ (C-band) is an allowed electronic dipole transition. Usually at room temperature we observe the A-band, the C-band is situated in the far UV. Emission and excitation bands are most of the time broad bands for these samples and the Stokes shift difference in energy between the maximum of excitation and emission is high, in fact, in the excited state the asymmetry of Bi is reduced, resulting in a large Stokes shift (see Figure II.15b, example of $\text{BiCd}_2\text{O}_2(\text{PO}_4)$). The transition $s^2 \rightarrow sp$ involved in the outer valence shell of the bismuth expected to have a strong interaction with

the surrounding environment to give access to a large variety in the emission wavelengths in the visible range from UV to red. The $\text{BiM}_2\text{O}_2(\text{XO}_4)$ ($\text{X} = \text{P}$ or As) series are very interesting to study for luminescence properties by having always more or less the same structure with only one bismuth site, and where only the orientation of XO_4^{3-} tetrahedra changes. Hence these compounds allow studying influences of different cations on the second sphere of coordination on the excitation and emission transitions by changing the divalent cation M^{2+} or the nature of tetrahedra XO_4^{3-} or both.

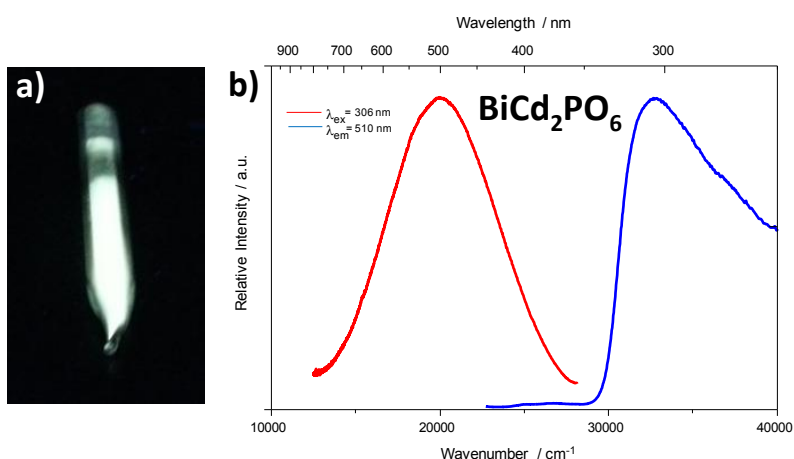


Figure II.15 a) $\text{BiMg}_2\text{O}_2(\text{AsO}_4)$ under UV-lamp excited at 254 nm and b) Stokes shift in $\text{BiCd}_2\text{O}_2(\text{PO}_4)$

The position of the maximum of excitation is strongly influenced by the covalency of Bi-O bonds, the increasing of which causes a shift of excitation band to lower energy (higher wavelength) (*nephelauxetic effect*) whereas the position of emission band in these phases more depends on the structure of the compound and more precisely on the cell parameter a parameter along which the lone-pair has an activity (lone-pair volume effect).

It is more difficult to interpret $\text{BiM}_2\text{O}_2(\text{VO}_4)$ spectra, emission and excitation are still represented by broad bands and the Stokes shift is still high but the luminescence cannot be attributed only to the bismuth. For these series emission and excitation can be interpreted as a charge transfer between the Bi^{3+} and the host lattice (D-band). In this case the excited state 3P_1 of Bi^{3+} is very close from the conduction band of the host lattice and the interaction between ns^2 of the latter and the environment is very strong. The charge transfer is usually demonstrated by measuring lifetime of the emission, for example the decay time for $\text{BiMg}_2\text{O}_2(\text{PO}_4)$ is about 350 ns which is in agreement with a *Laporte* allowed transition while the decay time is about 100 μs for $\text{BiMg}_2\text{O}_2(\text{VO}_4)$.

The $\text{BiM}_2\text{O}_2(\text{XO}_4)$ series is also advantageous because it allowed making solid solution as $\text{BiCd}_x\text{Mg}_{2-x}\text{O}_2(\text{PO}_4)$ which gives us a very large choice in the excitation and emission wavelength. The main drawback with these samples for a possible application, for white LED for example, is that the quantum yield is too low probably due to the high concentration of Bi^{3+} .

II.1.5 $n = 3$ ribbons and 2×2 column: Labile degree of disorder in Bismuth-oxyphosphate compounds: illustration through three new structural types

This section presents three new structural types that cover the full panorama in terms of order-disorder duality: $[\text{Bi}_2(\text{Bi}_{1.56}\text{K}_{0.44})^{\text{dis}}\text{O}_3]\text{K}_{0.88}^{\text{dis}}(\text{PO}_4)_2$; $[\text{Bi}_{10}(\text{Bi}_{\sim 0.5}\text{Cd}_{\sim 0.5})_8^{\text{dis}}\text{O}_{16}](\text{Bi}_{0.6}\text{Cd}_{0.8})_2^{\text{ord}}(\text{PO}_4)_8$; $[\text{Bi}_{18}\text{Zn}_{10}\text{O}_{21}]^{\text{ord}}\text{Zn}_5^{\text{ord}}(\text{PO}_4)_{14}$, where *dis* stands for disordered and *ord* for ordered sub-units of the corresponding structure.

1) Synthesis

1a) $[\text{Bi}_2(\text{Bi}_{1.56}\text{K}_{0.44})^{\text{dis}}\text{O}_3]\text{K}_{0.88}^{\text{dis}}(\text{PO}_4)_2$.

Single crystal: Single crystals of $[\text{Bi}_2(\text{Bi}_{1.56}\text{K}_{0.44})^{\text{dis}}\text{O}_3]\text{K}_{0.88}^{\text{dis}}(\text{PO}_4)_2$ were found in a polyphasic residue obtained as following: the mixture $0.5\text{K}_2\text{CO}_3 + 2.5\text{Bi}_2\text{O}_3 + 2(\text{NH}_4)_2\text{HPO}_4$ was ground and loaded into a gold tube with one end left open which was heated up to 900°C (rate 50°C/h), then left for a 10 hours plateau, cooled down slowly to 600°C (rate 3°C/h) and finally then the furnace was switched off.

Powder synthesis: Polycrystalline sample was prepared at several stoichiometries around the single crystal XRD result, $[\text{Bi}_2(\text{Bi}_{1.56}\text{K}_{0.44})^{\text{dis}}\text{O}_3]\text{K}_{0.88}^{\text{dis}}(\text{PO}_4)_2$, to validate the refined chemical composition. The procedure is following: the stoichiometric amounts of K_2CO_3 , Bi_2O_3 and $(\text{NH}_4)_2\text{HPO}_4$ were ground together and loaded into an alumina crucible, then heated at 400°C for 10h and at 860°C for 48h with intermediate grindings. Several syntheses suggested that the cooling rate is not a decisive parameter.

1b) $[\text{Bi}_{10}(\text{Bi}_{\sim 0.5}\text{Cd}_{\sim 0.5})_8^{\text{dis}}\text{O}_{16}](\text{Bi}_{0.6}\text{Cd}_{0.8})_2^{\text{ord}}(\text{PO}_4)_8$.

Single crystal: Single crystals were isolated in a melted sample of initial composition $\text{Bi}_4\text{CdP}_2\text{O}_{12}$. The mixture $\text{CdO} + 2\text{Bi}_2\text{O}_3 + 2(\text{NH}_4)_2\text{HPO}_4$ was ground and loaded into a gold tube with one end left open which was heated up to 950°C (rate 50°C/h), then left for a 10 hours plateau, cooled down slowly to 600°C (rate 3°C/h) and finally the furnace was switched off.

Powder synthesis: Powder was prepared according the following protocol: stoichiometric amounts of CdO, Bi₂O₃ and (NH₄)₂HPO₄ were ground together and placed into alumina crucible. The crucible heated at 400°C for 10h then at 880°C for 48h with intermediate grindings. Finally, the sample was cooled down to 400°C over 3h after which the furnace was switched off.

1c) [Bi₁₈Zn₁₀O₂₁]^{ord}Zn₅^{ord}(PO₄)₁₄.

Single crystal: Colorless needles of [Bi₁₈Zn₁₀O₂₁]^{ord}Zn₅^{ord}(PO₄)₁₄ were picked out from a polyphasic residue obtained according to the following protocol: the mixture ZnO + 0.5Bi₂O₃ + (NH₄)₂HPO₄ was ground together and loaded into a gold tube with one end left open, heated up to 900°C at a rate 50°C/h, then left over 10h and cooled down to 600°C at a rate 3°C/h, after which the furnace was switched off.

Powder synthesis: A powder sample was prepared by heating the mixture, obtained by grinding together the stoichiometric amounts of ZnO, Bi₂O₃ and (NH₄)₂HPO₄, at 400°C for 10h then at 800°C for 48h with intermediate grindings. Several syntheses also suggested that the cooling rate is not important.

The data collection and pertinent data of the refinements for all single crystals studied in this work are gathered in the Table II.3.

2) Complete Disorder in [Bi₂(Bi_{1.56}K_{0.44})^{dis}O₃]K_{0.88}^{dis}(PO₄)₂.

The compound [Bi₂(Bi_{1.56}K_{0.44})^{dis}O₃]K_{0.88}^{dis}(PO₄)₂ is a pertinent example of “fully disordered” prototype, in the sense that several subunits assembled in the crystal structure all show statistic distribution over mixed sites (edges) or over adjacent positions (PO₄ groups and tunnels) while diffraction patterns show no evidence of any ordering (extra spots) nor pseudo-ordering (diffuse streaks). The crystal structure was solved in the P-4₂c space group ($a = 13.7008(2)$ Å, $c = 5.6633(1)$ Å) with final reliability factors $R_1 = 3.36\%$ $wR_2 = 3.94\%$. The crystal structure is built of triple, $n = 3$, oxo-centered tetrahedra long ribbons, each surrounded by eight PO₄ groups while projected in the (a , b) plane, (see Figure II.16a). The formula of the 1D-ribbons is [Bi_{3.56}K_{0.44}O₃]^{5.12+} in which the site at the edges of the ribbon is mixed and is refined to [Bi_{0.78}K_{0.22}]. For this refinement, due to close Fourier-difference peak, the full occupancy was restrained while K and Bi atomic coordinates were free-refined but restrained to equal thermal parameters.

Table II.3. Crystal data, measurement and structural refinement parameters for $[Bi_2(Bi_{1.56}K_{0.44})^{dis}O_3]K_{0.88}^{dis}(PO_4)_2$, $[Bi_{18}Zn_{10}O_{21}]^{ord}Zn_5^{ord}(PO_4)_{14}$ and $[Bi_{10}(Bi_{0.5}Cd_{0.5})^{dis}O_{16}](Bi_{0.6}Cd_{0.8})_2^{ord}(PO_4)_8$

	$[Bi_2(Bi_{1.56}K_{0.44})^{dis}O_3]K_{0.88}^{dis}(PO_4)_2$	$[Bi_{18}Zn_{10}O_{21}]^{ord}Zn_5^{ord}(PO_4)_{14}$	$[Bi_{10}(Bi_{0.5}Cd_{0.5})^{dis}O_{16}](Bi_{0.6}Cd_{0.8})_2^{ord}(PO_4)_8$
Crystal data			
Crystal symmetry	Tetragonal	Orthorhombic	Tetragonal
space group	P-42 ₁ c	I2mb	I4/m(00γ)s0
a (Å)	13.7008(2)	14.8003(1)	13.7595(6)
b (Å)	13.7008(2)	38.0848(2)	13.7596(6)
c (Å)	5.6633(1)	11.2473(5)	5.6879(3)
V (Å ³)	1063.07(2)	6339.7(3)	1076.85(9)
Z	4	4	1
Dx (g/cm ³)	6.421	6.711	7.423
μ(mm ⁻¹)(0.7107Å)	58.72	55.81	65.14
Appearance	Colorless needle	Colorless needle	Colorless needle
Crystal size (mm)	0.33 × 0.07 × 0.05	0.47 × 0.05 × 0.04	0.09 x 0.04 x 0.04
Data collection			
λ(Mo Kα)(Å)	0.71073	0.71073	0.71073
Scan mode	ω and φ	ω and φ	ω and φ
θ(min–max)(°)	2.1 – 37.6	1.9 – 28.3	1.64 – 27.5
R(int) (%)	5.4	5.6	9.5
Reciprocal space	–22 ≤ h ≤ 23	–19 ≤ h ≤ 19	–17 ≤ h ≤ 17
recording	–21 ≤ k ≤ 22	–50 ≤ k ≤ 50	–17 ≤ k ≤ 17
	–7 ≤ l ≤ 9	–14 ≤ l ≤ 14	–8 ≤ l ≤ 8
			–2 ≤ m ≤ 2
Refinement			
Meas., obs., / indep.all (obs=I>3σ(I))	32075, 2261/2677	63040, 6895/7947	30811, 898/3152
			main obs/all
			1 st sat.obs/all
			2 nd sat.obs/all
No. of Refined parameters	89	391	162
Refinement method	F	F	F
R1(F ²)(obs)/ R1(F ²)(all) (%)	3.36/ 4.42	3.70/4.45	main obs 3.43 1 st sat.obs 8.28 2 nd sat.obs 15.93
wR2(F ²)(obs) /wR2(F ²)(all) (%)	3.94/6.36	4.01/4.53	5.22/6.32 main obs 4.51 1 st sat.obs 7.76 2 nd sat.obs 14.79
GOF(obs) / GOF(all)	2.38/3.52	1.37/1.43	2.36/1.42
Δρ _{max} / Δρ _{min} (e Å ⁻³)	4.10 /–2.77	3.08 /–2.80	15.05/-14.50
Extinction coefficient	0.1860 (40)	0.0155 (5)	0.00057(3)

The initial refined occupancy close to Bi:K = 0.85:0.15 was finally fixed in the last cycles to 0.78:0.22 without significant increasing of R values, in order to reach electroneutrality taking into consideration the occupancy of the interstitial K⁺ channels by PO₄ walls. Fourier difference maps (in absence of cations in the tunnel) show a continuum of electron density shown in yellow in Figure II.16b, for an isoelectronic level of 14 e⁻/Å³.

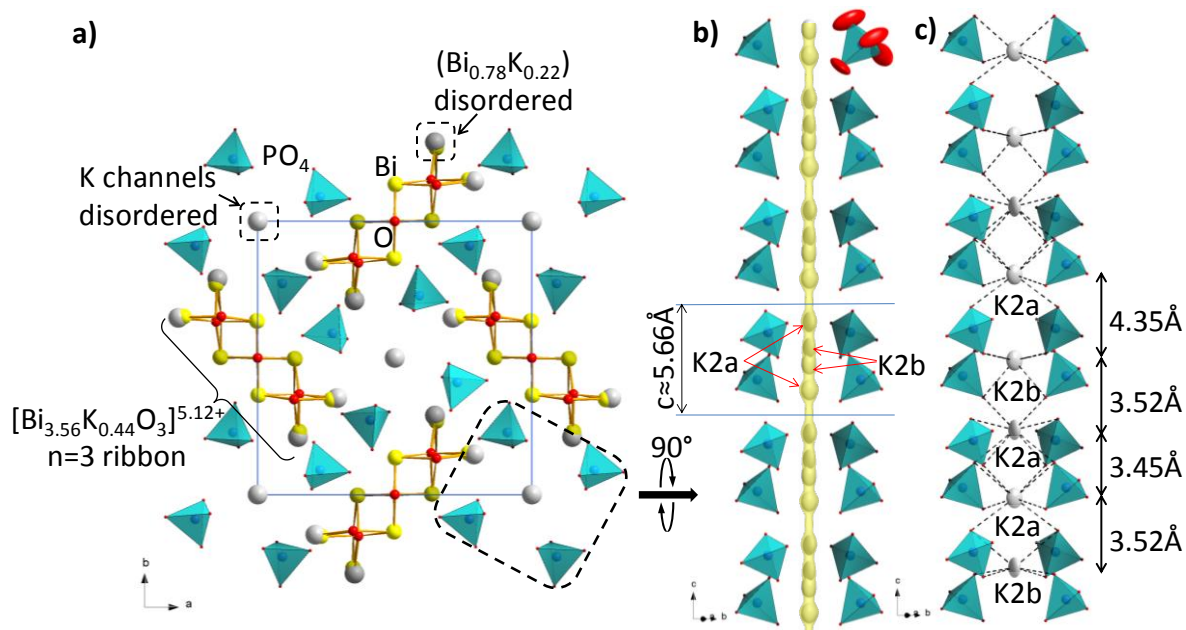


Figure II.16. a) Projection along c -axis of the crystal structure of $[Bi_2(Bi_{1.56}K_{0.44})^{dis}O_3]K_{0.88}^{dis}(PO_4)_2$, b) representation of the channels (the yellow continuum along the tunnel is the electron density obtained after Fourier difference of the electron map without K ($14 e^-/\text{\AA}^3$)) and c) hypothetic possible K arrangement along c -axis.

Two broader positions are highlighted along the c axis, which correspond to two crystallographic sites K2a (44% occupied) and K2b (44% occupied). The total occupancy of the channels ($\sim 88\%$) leads to an average number of cations = 1.76 per tunnel, i.e. along the c -axis (5.66 \AA) with a mean K-K distance of 3.21 \AA ($= 5.66/1.76$) which is a reasonable K-K separation length. The deduced $[Bi_2(Bi_{1.56}K_{0.44})^{dis}O_3]K_{0.88}^{dis}(PO_4)_2$ was confirmed by further syntheses of the polycrystalline sample detailed below. The pertinent distances are listed in the Table II.4. In the Figure II.16c, a hypothetical K2a/K2b sequence along c is shown with respect to the occupancies of K2a and K2b. Of course a diversity of different pseudo-ordered arrangements of this kind is possible and should coexist locally, but without any coherence since no superstructure spots are observed. It is noteworthy that the coordination of the K^+ ions by PO_4 corners leads to reasonable K-O distances. Bond valence sums (BVS) calculations lead to 0.82 and 1.36 for K2a and K2b - slightly underbonded and overbonded respectively - which is reasonable. However, clearly the oxygen atoms involved in K-O bonds (O1, O2, O3, and O4) have large thermal parameters (see Figure II.16b), which probably pictures the existence of slight tilts of the PO_4 groups around the central refined one. It is probable that the exact PO_4 orientation depends on the local neighbors atomic surrounding both at edges of ribbons (K1 versus Bi1) and in the tunnels (K2a versus K2b).

Table II.4 Interatomic distances (Å) of the atoms on the edges of the ribbons and in the cationic channels of $[\text{Bi}_2(\text{Bi}_{1.56}\text{K}_{0.44})^{\text{dis}}\text{O}_3]\text{K}_{0.88}^{\text{dis}}(\text{PO}_4)_2$

Atom 1	Atom 2	d	Atom 1	Atom 2	d
Bi1	1xO5	2.240(16)	K2a	2xO1	2.769(41)
	1xO5	2.280(16)	K2b	2xO4	2.591(40)
	1xO3	2.381(24)		2xO4	2.611(30)
	1xO1	2.472(28)			
	1xO3	2.484(29)			
	1xO4	2.744(28)			
K1	1xO5	2.387(26)			
	1xO1	2.395(36)			
	1xO4	2.487(34)			
	1xO3	2.537(34)			
	1xO3	2.538(36)			
	1xO5	2.554(25)			

Concerning the ribbon edges, using the refined PO_4 position, the calculated BVS for Bi1 and K1, gave respectively i.e. 2.62 and 2.43. The value obtained for Bi1 is close to the expected +3 value, while the K1 coordination is not suitable. Once more, this can be related to the high values of the thermal parameters for the bordering PO_4 due to differently tilted local cationic environment. The possibility to model the diversity of PO_4 satellite positions using a single PO_4 group and high thermal parameters at the corners reinforces the full disordered nature of $[\text{Bi}_2(\text{Bi}_{1.56}\text{K}_{0.44})^{\text{dis}}\text{O}_3]\text{K}_{0.88}^{\text{dis}}(\text{PO}_4)_2$. Indeed, the precession frame (see Figure II.17a), calculated using single crystal XRD data, shows a good crystallinity in absence of any extra spots nor diffuse streaks.

In addition, the ED patterns of the corresponding powder (Figure II.17b) do not show any clue of ordering even at this observation scale which is much lower than for single crystal (a few nanometers compared to few micrometers). Note also that diffractogram of $[\text{Bi}_2(\text{Bi}_{1.56}\text{K}_{0.44})^{\text{dis}}\text{O}_3]\text{K}_{0.88}^{\text{dis}}(\text{PO}_4)_2$ shows the unique expected phase (see Figure II.17c).

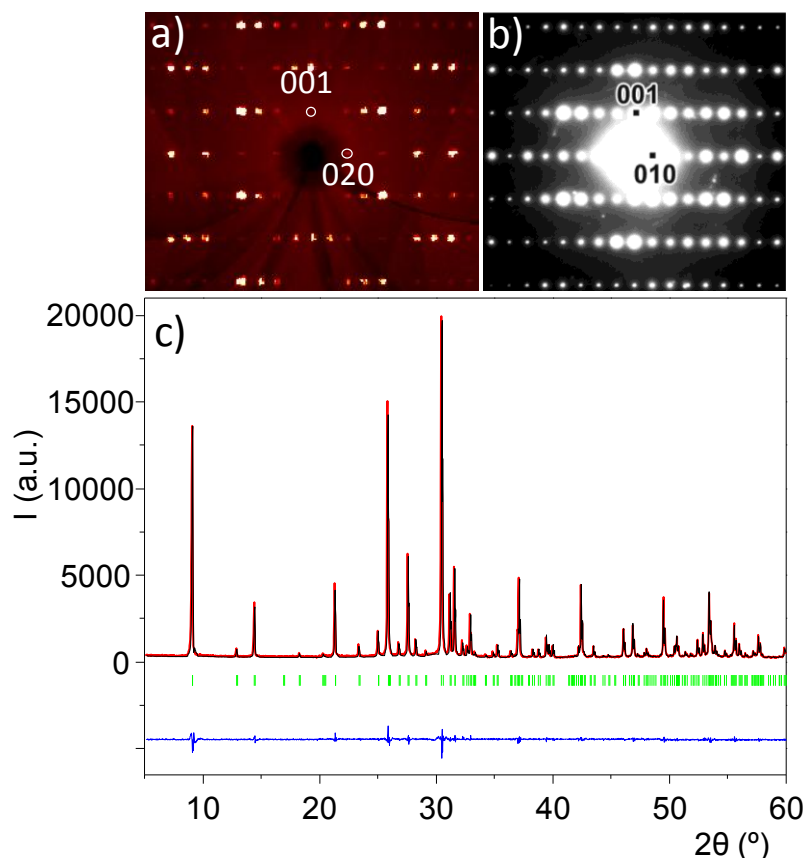


Figure II.17. $[\text{Bi}_2(\text{Bi}_{1.56}\text{K}_{0.44})^{\text{dis}}\text{O}_3]\text{K}_{0.88}^{\text{dis}}(\text{PO}_4)_2$: a) calculated precession frame of the $0kl$ layer from single crystal XRD data, b) ED patterns of the corresponding compound. c) Profile fitting of the corresponding powder (refined unit cell parameters $a = 13.6922(3) \text{ \AA}$, $c = 5.6602(2) \text{ \AA}$, $V = 1061.16(4) \text{ \AA}^3$, $\chi^2 = 2.25$).

2a) ^{31}P NMR experiments.

The disorder around P centers can be characterized by use of solid-state ^{31}P NMR probing the local environment of nuclei. In a general way, under optimum MAS and pulse decoupling conditions, ordered crystal structures are characterized by resonances line widths that do not exceed a few hundred hertz, best fitted with a Lorentzian profile. In disordered compounds, the distribution of geometric parameters around a single site induces chemical shift changes that result in a Gaussian resonance broadening. Figure II.18a shows the ^{31}P MAS NMR spectra of $[\text{Bi}_2(\text{Bi}_{1.56}\text{K}_{0.44})^{\text{dis}}\text{O}_3]\text{K}_{0.88}^{\text{dis}}(\text{PO}_4)_2$. The ^{31}P MAS NMR can be separated into two main groups of resonances, dominated by a gaussian distribution, centered at -2.1 and 0.4 ppm with a ratio of 55:45, together with one of lower intensity around 3 ppm.

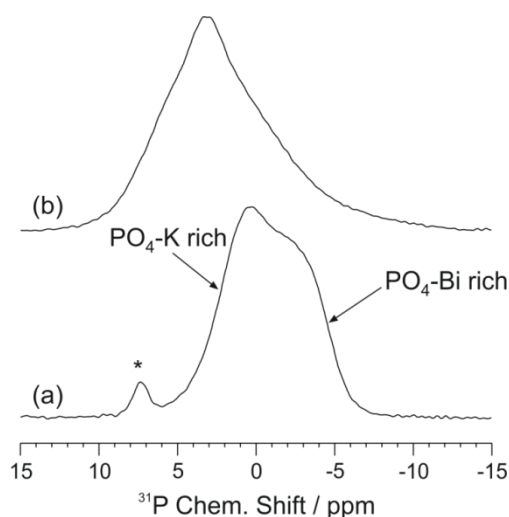


Figure II.18. ^{31}P MAS spectra at 18.8 T of a) $[\text{Bi}_2(\text{Bi}_{1.56}\text{K}_{0.44})^{\text{dis}}\text{O}_3]\text{K}_{0.88}^{\text{dis}}(\text{PO}_4)_2$, b) and b) $[\text{Bi}_{18}\text{Zn}_{10}\text{O}_{21}]^{\text{ord}}\text{Zn}_5^{\text{ord}}(\text{PO}_4)_{14}$. In (a), the star * denotes an impurity phase. The spectra were acquired with a total of 32 scans, a short pulse excitation of 0.8 μs and a recycling delay of 10 s.

This latter is assigned to minor PO_4 containing impurities, and its linewidth of about 900 Hz can be used as a reference that highlights the disordered character of the pertinent phase, especially keeping in mind the unique P crystallographic site. These chemical shift differences are resulting from cationic effects as already reported for the disordered $\text{Bi}_{1.2}\text{Zn}_{1.2}\text{O}_{1.5}(\text{PO}_4)^{112}$ and $\text{BiMg}_{2-x}\text{Cd}_x\text{PO}_6$ solid solutions.¹¹³ Taking into account the first K/Bi disordered cationic sphere ($\text{P-K/Bi} < 5 \text{ \AA}$) four K2/Bi2 sites participate. A statistic K/Bi distribution involves P-Bi₄ (31.2 %), P-Bi₃K₁ (25.6 %), P-Bi₂K₂ (20 %), P-Bi₁K₃ (14.4 %), P-K₄ (8.8 %). In our approach, the K2a/K2b disorder inside the tunnels is considered as an extra degree of resonance broadening.

The ^{31}P NMR chemical shift expected between K and Bi 2nd neighbors can be related to the electronegative effect on P-O bonds through the z/a^2 parameter, where z is the cationic charge and a the mean X-O interatomic (rO+rX).^{113,114} We calculate $z/a^2 = 0.52$ and 0.12 for Bi and K respectively. Therefore, the two main resonances at -2.1 and 0.4 ppm are accounted for Bi-rich and K-rich coordinations, respectively¹¹³ in good agreement between experimental weights and statistic values. The ^{31}P double-quantum MAS NMR spectrum (see Annex IV.23)), with important diagonal and out-of diagonal intensities, highlighting those phosphate groups that are close to each other in absence of segregation, provides further indication on the real disordered structure of $[\text{Bi}_2(\text{Bi}_{1.56}\text{K}_{0.44})^{\text{dis}}\text{O}_3]\text{K}_{0.88}^{\text{dis}}(\text{PO}_4)_2$.

These results clearly indicate a full random statistic distribution over all disordered crystallographic positions, while the rigid/periodic framework is achieved by the oxo-centered ribbon units. It makes sense to consider channel cations and PO_4 groups as counter ions that

make the cohesion between the periodic $O(\text{Bi},\text{K})_4$ based skeleton. Comparing the structure of $[\text{Bi}_2(\text{Bi}_{1.56}\text{K}_{0.44})^{\text{dis}}\text{O}_3]\text{K}_{0.88}^{\text{dis}}(\text{PO}_4)_2$ with that of $\text{Bi}_2\text{PbMnO}_4(\text{PO}_4)_2$ ¹¹⁵, one can note a similar topology of $n = 3$ ribbons. The formula of this compound was later revised into $[\text{Bi}_2(\text{Pb},\text{Mn})_2^{\text{dis}}\text{O}_3](\text{Pb},\text{Mn})_{0.6}^{\text{ord}}(\text{PO}_4)_2$ with both the edges of ribbons and the channels hosting mixed $\text{Pb}^{2+}/\text{Mn}^{2+}$ cations. Contrarily to our compound, the refinement of the structure in $P-42_1c$ ($a = 13.275(3) \text{ \AA}$, $c = 5.500(2) \text{ \AA}$) shows several tetrahedral configurations disordered around the central phosphorus site. In fact this compound displays a modulated structure and was refined, in further stage, in the super space group $\text{Xcc2}(00\gamma)s0s$ ($R_{\text{fund}} = 4.56\%$ and $R_{\text{satellite}} = 12.7\%$).¹¹⁶ It shows disordering of Pb and Mn at edges of ribbons while Pb and Mn were found fully ordered in the cationic channels. It follows that the cationic nature is a key-factor for ordering or not in those compounds. Particularly, the ionicity of M-O bonds could be involved, since ionic $\text{K}^+\text{-O}$ do not involve axial cation orbitals leading to versatile coordinations in the same crystal (e.g. K2a vs. K2b) in the absence of an ordering, comparatively to Mn^{2+} .

3) Partial cationic ordering in the 1D square-columns compound $[\text{Bi}_{10}(\text{Bi}_{\sim 0.5}\text{Cd}_{\sim 0.5})_8^{\text{dis}}\text{O}_{16}](\text{Bi}_{0.6}\text{Cd}_{0.8})_2^{\text{ord}}(\text{PO}_4)_8$.

The study of the compound $[\text{Bi}_{10}(\text{Bi}_{\sim 0.5}\text{Cd}_{\sim 0.5})_8^{\text{dis}}\text{O}_{16}](\text{Bi}_{0.6}\text{Cd}_{0.8})_2^{\text{ord}}(\text{PO}_4)_8$ was initiated by a former PhD student D. Endara.⁵⁰ It was added to this thesis because it has appropriate structure to discuss with other two compounds. In this compound, contrarily to the previous one, we show evidence of an intermediate situation with fully ordered tunnels which generate a structural modulation and disordered mixed Bi/Cd edges at the edges of columnar oxocentered clusters.

A colorless needle was selected for single crystal XRD data collection. The average crystal structure (i.e. without the supplementary superstructure spots) was easily solved in the space group I4/m ($a = 13.7588(7) \text{ \AA}$, $c = 5.6879(3) \text{ \AA}$, $R_{\text{F}}(\text{obs}) = 3.79\%$, $wR_{\text{F}}(\text{obs}) = 4.49\%$, $R_{\text{F}}(\text{all}) = 7.37\%$, $wR_{\text{F}}(\text{all}) = 4.79\%$, with $I_{\text{Obs}} > 3\sigma(I)$), leading to the formula $[\text{Bi}_{10}(\text{Bi}_{\sim 0.5}\text{Cd}_{\sim 0.5})_8^{\text{dis}}\text{O}_{16}](\text{Bi}_{0.6}\text{Cd}_{0.8})_2^{\text{ord}}(\text{PO}_4)_8$. The crystal structure can be described by infinite square based columns (2×2 OBi_4 tetrahedra width) surrounded by eight isolated PO_4 and two tunnels formed by four PO_4 groups.

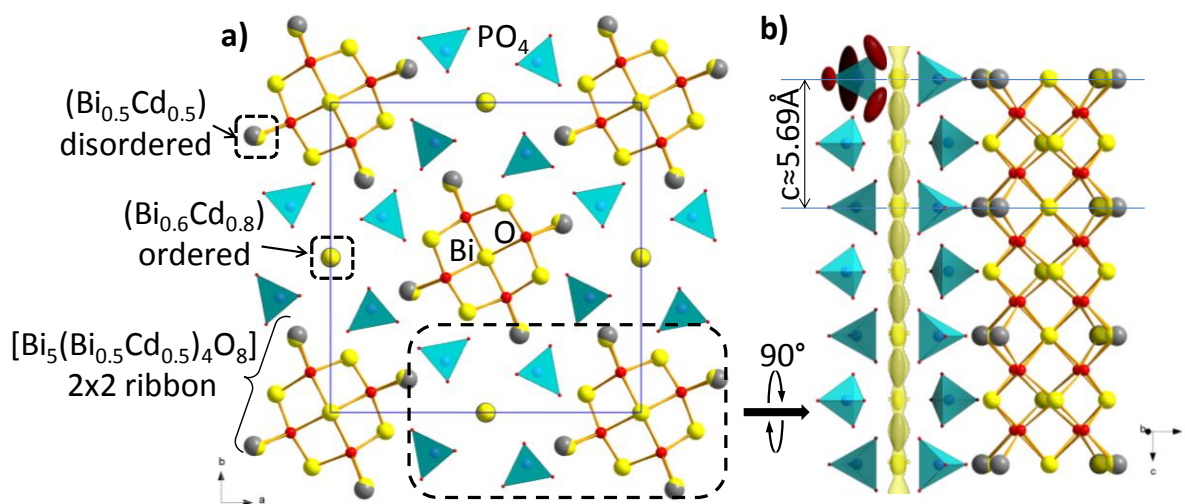


Figure II.19. a) Projection along c -axis of the average crystal structure of $[\text{Bi}_{10}(\text{Bi}_{\sim 0.5}\text{Cd}_{\sim 0.5})_8^{\text{dis}}\text{O}_{16}](\text{Bi}_{0.6}\text{Cd}_{0.8})_2^{\text{ord}}(\text{PO}_4)_8$ and b) the square based columns and PO_4 tunnels along c -axis on the left (the yellow continuum along the tunnel is the electron density obtained after Fourier difference of the electron map without cation ($30 \text{ e}^-/\text{\AA}^3$)).

In its formula, $(\text{Bi}_{\sim 0.5}\text{Cd}_{\sim 0.5})^{\text{dis}}$ stands for mixed sites at the corners of columns whereas $(\text{Bi}_{0.6}\text{Cd}_{0.8})^{\text{ord}}$ is related to the occupancy of tunnels between phosphates as shown in Figure II.19a. The refinement of mixed sites in tunnels is very approximate, two partially occupied sites (one Bi site and one Cd site) being distinct but assorted with very high anisotropic displacement parameters along c -axis (see Figure II.19b). In this average structure, the observation of a continuum of electron density in the tunnel is shown in yellow ($30 \text{ e}^-/\text{\AA}^3$ isosurface) in Figure II.19b, while the located Bi and Cd sites are also drawn.

3a) Modulated structure approach.

In fact, further electron diffraction studies and XRD precession calculations enhance satellite reflections due to an incommensurate structural modulation (Figure II.20). The tetragonal lattice parameters and the modulation vector were refined to $a = b = 13.768(4) \text{ \AA}$, $c = 5.691(2) \text{ \AA}$, $q = 0.000(1)a^*, 0.0003(9)b^*, 0.3984(4)c^*$ from 5046 main reflections and 935 1st and 2nd order satellites using software for refinement NADA.¹¹⁷ Note that for a second batch of single crystals, the modulation vector was refined to $q = 0.000(4)a^*, 0.0005(4)b^*, 0.4086(2)c^*$ which validate the incommensurability ($q \neq 2/5$) and variation from one specimen to another, probably due to minor compositional changes. All reflections were integrated and indexed using the 4D-formalism ($hklm$ spot corresponds to the point $hkl + mq$ of the reciprocal space). The observed satellites spots are limited to small indices ($m_{\text{max}} = 2$) which suggest partial ordering, or smooth atomic displacement along the 4th dimension.

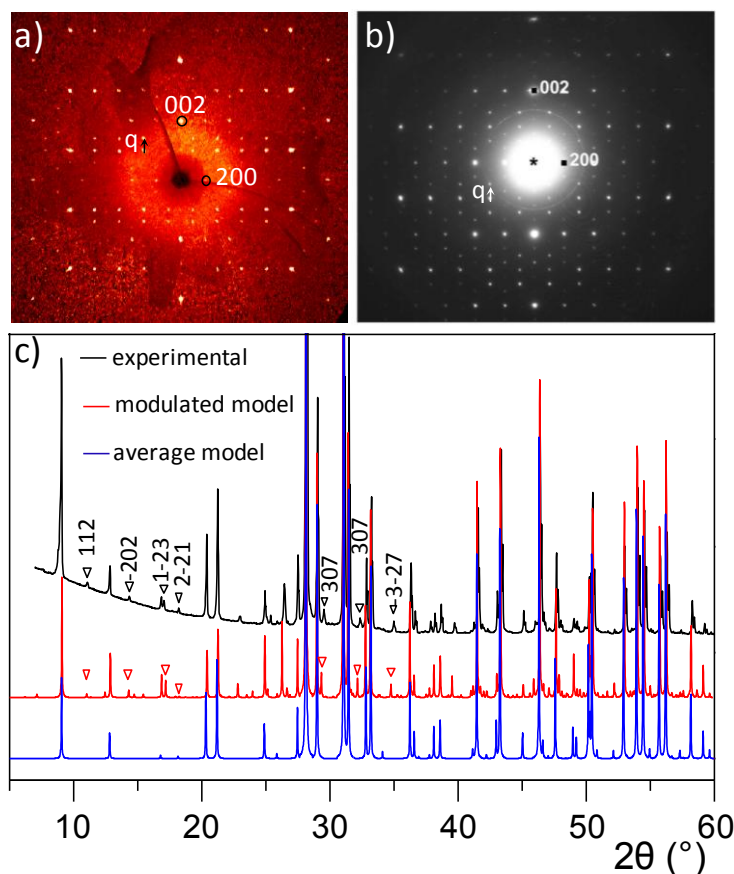


Figure II.20. $[\text{Bi}_{10}(\text{Bi}_{\sim 0.5}\text{Cd}_{\sim 0.5})_8^{\text{dis}}\text{O}_{16}](\text{Bi}_{0.6}\text{Cd}_{0.8})_2^{\text{ord}}(\text{PO}_4)_8$: a) Calculated precession of (h0l) layer (XRD on single crystal) and b) ED image of (h0l) layer with enhancement of substructure spots ($q \approx 0.4 \text{ c}^*$), c) the comparison between the calculated XRD patterns (average and modulated models) and the experimental one. Green indices are the fundamental and black ones are the modulation peaks.

Taking into account the average space group ($I4/m$), the study of the $hklm$ reflections shows the conditions $hklm$: $h + k + l = 2n$, $00lm$: $m = 2n$ leading to only one possible super-space group $I4/m(00-p)s0$. This group is characterized by the translations $(0000; \frac{1}{2} \frac{1}{2} \frac{1}{2} 0)$ and equivalent coordinates: x, y, z, x_4 ; $-x, -y, z, x_4$; $-y, x, z, x_4 + \frac{1}{2}$; $y, -x, z, x_4 + \frac{1}{2}$; $-x, -y, -z, -x_4$; $x, y, -z, -x_4$; $y, -x, -z, x_4 - \frac{1}{2}$; $-y, x, -z, x_4 - \frac{1}{2}$; with x_4 the coordinate along the fourth dimension. The study was performed in this space group using displacement and occupancy modulation waves. In fact, the continuum of density along the channel axis is broken in the 4D-space where for each x_4 value, Fourier peaks correspond to a particular value of z which indicates a segregation of electronic densities in the fourth dimensional space (see Figure II.21a and Figure II.21b).

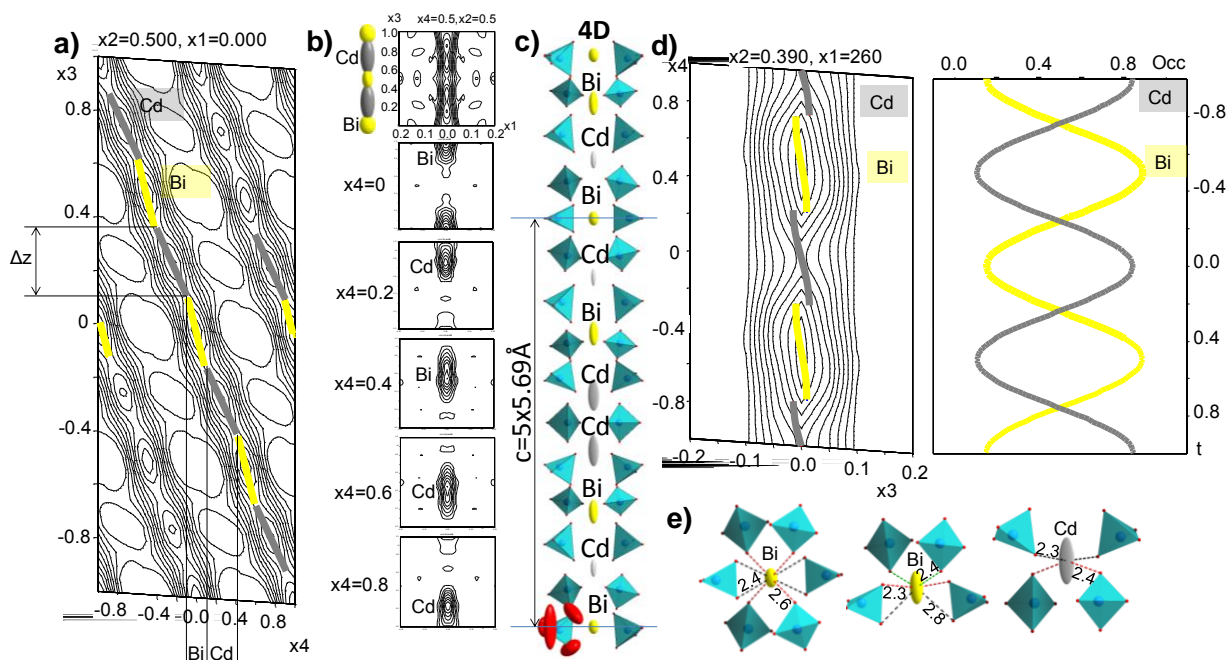


Figure II.21. a) Fourier difference along (x_4, z) in the tunnel (contribution from $x_4=0$ to 1 are summed), b) separation of 2 sites Bi/Cd at different section along x_4 , c) Bi/Cd repartition in the modulated structure of $[\text{Bi}_{10}(\text{Bi}_{\sim 0.5}\text{Cd}_{\sim 0.5})_8^{\text{dis}}\text{O}_{16}](\text{Bi}_{0.6}\text{Cd}_{0.8})_2^{\text{ord}}(\text{PO}_4)_8$, d) electronic density and occupancy of Bi/Cd sites of the columns e) coordination of Bi and Cd in the tunnel.

Several models have been tested but only one converged. The study of the Fourier Difference pertinent section in the (x_4, z) map clearly evidences segments corresponding to Bi or Cd contributions along x_4 . To transfer this information into an atomic distribution, we used saw tooth functions which allow to link a formal occupancy (present or absent) to a small atomic displacement Δz varying with x_4 . These occupancies appear in grey and yellow on Figure II.21a which shows the Fourier difference in the pertinent section of the (x_4, z) plane. At this level, the result of the refinement lead to a total ordering of tunnels as shown on Figure II.21c, showing a Bi/Cd ordering along c with the sequence $-(\text{Bi}-\text{Cd}-\text{Bi}-\text{Cd}-\text{Cd}-\text{Bi}-\text{Cd})_n-$ with distances between cations around 4 \AA . One should mention that strong residual electronic density peaks ($\sim 14e^-/\text{\AA}^3$) and the strong thermal parameters despite the 4D-organization reflect possible satellite position close to the refined ones.

Using an identical process, we tried to distinguish segregation along the fourth dimension of mixed Bi3/Cd3 sites at the corners of columns. Figure II.21d shows the electronic density calculated on Fourier difference maps along x_4 at the concerned position. The more or less condensed density enhances variation of the local electronic density on this particular site. Here we did not succeed in using crenel or saw tooth functions that would point out a formal occupancy of Bi and Cd cations. Only smooth sinusoidal functions (related to a partial occupancy of Bi/Cd sites) were used to improve the refinement. Furthermore, without any

additional constraint, the sinusoidal envelop of each individual Bi and Cd enhances a total occupancy of the crystallographic site with a ratio Bi/Cd~0.52/0.48. This is in good agreement with the model refined in 3D and leading to the stoichiometry (Bi_{~0.5}Cd_{~0.5}) of this site. It indicates a partial disorder Bi/Cd of this site along z. All other atoms have been associated to modulated displacement functions and sometimes to modulated atomic displacement parameters when improving the structure refinement. The created PO₄ are regular but remain associated with strong thermal parameters (even after using modulated thermal parameters) on oxygen corners. At the end of the refinement, we obtain R_{fund.} = 3.4%, R_{sat order 1} = 8.3%, R_{sat order 2} = 15.8%. The final structural model clearly shows partial disorder on O(Bi,M)₄ tetrahedra of columns (probability of presence of Bi/Cd following sinusoidal distributions) and a Bi/Cd well established ordering in tunnels. The refined distances (average, minimum and maximum) are listed in the Table II.5.

Table II.5 Interatomic distances (Å) of the atoms on the edges of the ribbons and in the cationic channels of [Bi₁₀(Bi_{~0.5}Cd_{~0.5})₈^{dis}O₁₆](Bi_{0.6}Cd_{0.8})₂^{ord}(PO₄)₈

Atom 1	Atom 2	d _{average}	d _{min}	d _{max}
O1	2xBi3	2.286(15)	2.176(16)	2.395(16)
	2xCd3	2.24(2)	2.12(2)	2.35(2)
Cdb	4xOp2	2.35(3)	2.27(3)	2.38(3)
Bia	8xOp2	2.47(3)	2.24(3)	2.96(3)
	6xOp2	2.62(3)	2.37(2)	3.06(3)

At least we have shown here that between two mixed sub-units of the crystal structure, namely the cationic channels and the edges of oxo-centered sites, the latter seems more adapted for disorder. Comparatively to results for the M = K case presented in the previous section the M = Cd nature is of probable importance. Bi³⁺ and Cd²⁺ have similar ionic radii (0.95 Å) and due to the participation of stereoactive lone pair in the coordination of the former and 4d orbitals for the latter, both require particular bonding scheme by oxygen. The analysis of the coordination of the channel cations shows difference between Bi and Cd. For Bi the coordination number is either 6 either 8 with Bi-O distances between 2.2 and 2.8 Å, see Figure II.21e. We note for the 8-fold coordination, the lone pair stereoactivity is not apparent in a rough approximation. Cd atoms are in a more or less distorted square plane coordination (Cd-O: 4x2.4 Å). The difference between these coordination polyhedra is the driving force for the full cationic ordering in the channels. Differently at the edges of columns the disordered

Bi/Cd atoms have greater coordination number (from 6 to 8) with longer M-O distances ($M-O > 2.5 \text{ \AA}$). In such environment both Cd and Bi cohabit without ordering.

A perfect ordering of channel cations in PO_4 tunnels was already previously observed, but in a compound with infinite planes instead of ribbons, namely $Bi_4ZnP_2O_{12}$, where the doubling of the b parameters $\sim 2 \times 5.4 \text{ \AA}$ is due to the ordered occupancy of channels by two independent Zn atoms in coordination IV and V respectively.³⁹ However in this latter compound, all sites of the polycationic infinite layers are solely occupied by Bi^{3+} atoms and channels are occupied solely by Zn^{2+} ions. In addition, in the previous TEM investigation of compounds with various-sized ribbons with mixed Bi/M sites at their edges in our laboratory, it is common to evidence some superstructures commensurate or incommensurate. However this information is often lost at the single crystal scale. It follows that their origin remains mysterious, even if one have to keep in mind the case of $Bi_{\sim 6.2}Cu_{\sim 6.2}O_8(PO_4)_5$, where HREM images of modulated zones clearly indicate that ordering phenomena occur in the Cu^{2+} tunnels between double ($n = 2 \text{ O}(\text{Bi},\text{M})_4$ tetrahedra long) and triple ($n = 3 \text{ O}(\text{Bi},\text{M})_4$ tetrahedra long) ribbons.⁴⁹ These features comfort a better suitability for full ordering in tunnels rather than mixed positions belonging to oxocentered sub-units.

4) Full cationic ordering in $[Bi_{18}Zn_{10}O_{21}]^{ord}Zn_5^{ord}(PO_4)_{14}$.

This composition corresponds, in fact, to analogous compounds with $M = \text{Co}$ and Mn originally considered as strongly disordered compounds, in the absence of super-cell spots, leading to the formula $Bi_{\sim 1.2}M_{\sim 1.2}O_{1.5}(PO_4)$.¹¹⁸ It consists of $n = 3$ tetrahedra wide ribbons with mixed Bi/M sites at their edges. A strong disorder over M^{2+} cations was observed in the tunnels while the oxygen coordination of P atoms was also very disordered, due to the superposition of several PO_4 configurations. For $M = \text{Zn}$, XRD powder pattern refinement leads to a similar subcell ($a = 14.809(2) \text{ \AA}$, $b = 11.214(1) \text{ \AA}$, $c = 5.440(1) \text{ \AA}$, S.G. *Ibam*), and identical $Bi_{\sim 1.2}Zn_{\sim 1.2}O_{1.5}(PO_4)$ formula assumption. In the latter, no evidence of supercell ordering was detected on the used single crystals, while ED patterns on $Bi_{\sim 1.2}M_{\sim 1.2}O_{1.5}(PO_4)$ ($M = \text{Zn}$, Mn and Co), show clues for inhomogeneity in the sample with sometimes the presence or not of additional spots (in commensurate or incommensurate positions) or diffuse lines. In the frame of this study we have prepared single crystals of the Zn-compound as detailed in the experimental section.

The single crystal structure was solved in the $I2mb$ space group ($a = 14.8003(1) \text{ \AA}$, $b = 38.0848(2) \text{ \AA}$, $c = 11.2473(5) \text{ \AA}$, $R_1 = 3.7\%$ $wR_2 = 4.0\%$).

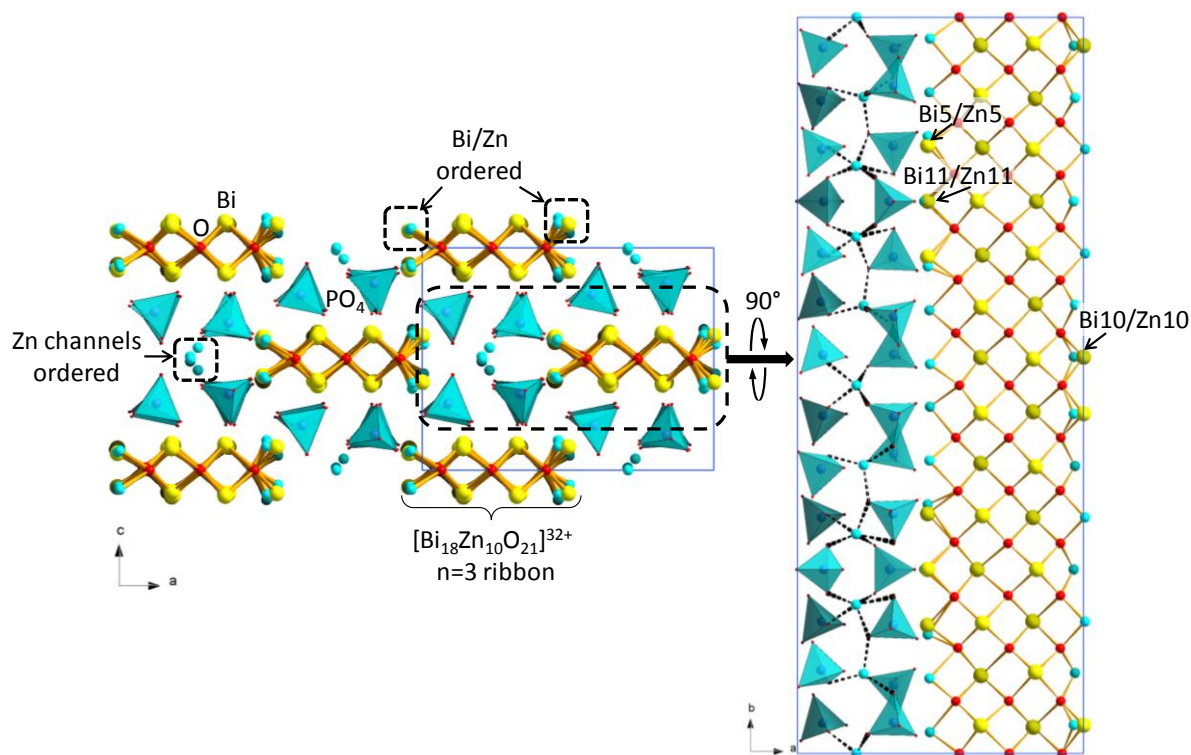


Figure II.22. The crystal structure of $[\text{Bi}_{18}\text{Zn}_{10}\text{O}_{21}]^{\text{ord}}\text{Zn}_5^{\text{ord}}(\text{PO}_4)_{14}$ (projection along b -axis) on the left and the ribbon and PO_4 tunnel (projection along c -axis) on the right.

In fact, as we will see later, this compound shows a nearly perfect ordering of the cations and PO_4 groups in the structure. Indeed, in the tunnels, three fully occupied independent Zn cations are ordered along the $7 \times b$ periodicity as shown on the Figure II.22, with no residual electronic density on Fourier-difference maps.

The coordination of Zn^{2+} is IV or V while the Zn-Zn distances are between 3.62 Å and 4.18 Å. The oxygen of the bordering PO_4 groups has normal thermal parameters which validate the perfect ordering inside the channels. Concerning the ribbons-edges, the situation is less clear, but remains very close to a perfect ordering.

In fact, as shown in Figure II.22, most of the positions are fully occupied by Zn^{2+} while only three mixed sites (out of eight), Bi11(32%)/Zn11(68%) Bi5(90%)/Zn5(10%) and Bi10(94%)/Zn10(6%), contain a significant amount of Bi^{3+} . On the basis of the residual Fourier peaks, these sites are occupied by Bi and Zn at distinct adjacent sites. The refinement of their occupancies lead, without any constraint, to an electroneutral solid of formula $\text{Bi}_{17.95}\text{Zn}_{14.69}\text{O}_{21}(\text{PO}_4)_{14}$. Note also that BVS calculations show that both Zn^{2+} and Bi^{3+} are suitably coordinated by the surrounding PO_4 groups see Table II.6.

Table II.6. Calculated BVS of selected atoms in $[\text{Bi}_{18}\text{Zn}_{10}\text{O}_{21}]^{\text{ord}}\text{Zn}_5^{\text{ord}}(\text{PO}_4)_{14}$

Atom	BVS	Atom	BVS
Bi1	2.91(3)	Zn10	1.71(14)
Bi2	2.94(4)	Bi11	4.27(13)
Bi3	2.99(3)	Zn11	1.78(8)
Bi4	2.88(4)	Zn1	2.02(3)
Bi5	3.13(4)	Zn2	1.92(4)
Zn5	1.68(9)	Zn3	2.04(4)
Bi6	2.98(3)	Zn4	1.97(3)
Bi7	2.85(4)	Zn9	1.94(4)
Bi8	3.05(3)	Zn6	1.98(4)
Bi9	2.91(4)	Zn7	2.04(7)
Bi10	3.02(3)	Zn8	2.09(4)

Only in the mixed Bi11/Zn11 position despite the splitting of the two types of cations, Bi^{3+} seems overbonded (BVS = 4.27), which involves that the mean position is dominated by its major Zn character. It leads to a complex sequence of Bi/Zn and Zn along the ribbon axis as shown on the Figure II.22.

The perfect and almost perfect cationic ordering in the tunnels and inside oxo-centered sites respectively validate what was deduced in the previously presented compound. In this almost fully ordered compound, it is probable that the Zn/Bi ordering is driven by the very different chemical nature of both elements. For Zn^{2+} , the coordination sphere is mediated by its d-orbitals while Bi 6p/6s states create the asymmetric BiO_n coordination. The selected distances are given in Table II.7. The precession image (XRD data) of the single crystal (Figure II.23a) evidences a commensurate 7-fold supercell along the channel axis (0kl layer). At least, the ED patterns of the [001] zone axis on crystals of the powder-sample shows evidence of supercell spots (Figure II.23b), but their intensities are much weaker than found in the single-crystal precession frame.

Table II.7 Selected interatomic distances (Å) of $[Bi_{18}Zn_{10}O_{21}]^{ord}Zn_5^{ord}(PO_4)_{14}$

Atom1	Atom2	d	Atom1	Atom2	D	Atom1	Atom2	d
Bi5	1xO9	2,104(16)	Bi11	1xOp3c	1,941(42)	Zn4	1xOp6d	2,022(16)
	1xO10	2,245(16)		2xO10	2,198(23)		1xO12	2,055(16)
	1xOp5b	2,304(16)		1xOp8a	2,199(32)		1xOp7b	2,061(16)
	1xOp7b	2,367(16)		2xOp5a	2,257(23)		1xOp2a	2,112(14)
Zn5	1xOp4b	2,470(19)	Zn11	1xOp3c	2,067(49)	Zn6	1xOp5b	2,190(16)
	1xO9	1,903(36)		1xOp8a	2,085(41)		1xO9	2,344(16)
	1xOp7b	1,907(41)		2xOp5a	2,132(28)		1xOp7a	1,900(17)
	1xOp5b	2,264(37)		2xO10	2,288(29)		1xOp6c	1,935(16)
Bi10	1xOp4b	2,283(38)	Zn1	1xOp7c	1,967(16)	Zn7	1xOp5c	2,000(16)
	1xO10	2,608(39)		1xOp1b	2,063(16)		1xOp2a	2,042(14)
	1xO5	2,115(15)		1xO7	2,121(15)		1xOp8b	1,895(33)
	1xO6	2,181(90)		1xOp2b	2,143(15)		1xOp3a	1,997(23)
Zn10	1xOp2d	2,409(15)	Zn2	1xOp2b	2,156(16)	Zn8	1xOp4d	2,016(18)
	1xOp1c	2,540(14)		1xO12	2,254(16)		1xOp5c	2,045(16)
	1xOp6d	2,627(16)		2xOp4c	2,018(17)		1xOp5a	2,399(17)
	1xOp1b	2,656(16)		2xO11	2,078(13)		2xOp2c	1,868(16)
Zn10	1xOp6c	2,709(16)	Zn3	1xOp8c	2,116(24)	Zn9	2xOp1c	2,039(15)
	1xO5	1,900(51)		1xOp1d	1,904(16)		1xOp6b	1,949(16)
	1xOp2d	1,954(58)		1xO8	1,985(13)		1xO11	2,027(13)
	1xO6	2,003(50)		1xOp7d	2,105(16)		1xO8	2,066(13)
Zn10	1xOp6d	2,653(51)	Zn3	1xOp4b	2,119(19)	Zn9	1xOp4d	2,116(18)
	1xOp1b	2,719(52)		1xO5	2,121(15)		1xOp3a	2,153(23)

In fact, this contrast is different from one crystallite to the other and suggests that these ordered domains occur only at a nanometric-scale and that the extension of the cation ordering at a greater scale is broken, probably by anti-phase boundaries. Indeed, the XRD pattern shows that supercell lines are lost at the scale of micronic grains (see Figure II.23c). Therefore the studied fully ordered single crystal should be considered as a rare opportunity.

4a) ^{31}P NMR experiments.

We have also performed ^{31}P NMR experiments on the prepared polycrystalline sample (see Figure II.18b). An accurate best-fit simulation into the different types of phosphorus environments is outside the scope of the present work, due to strong overlapping of resonances. However, the overall lineshape follows a lorentzian pattern, confirming the high level of cationic ordering.

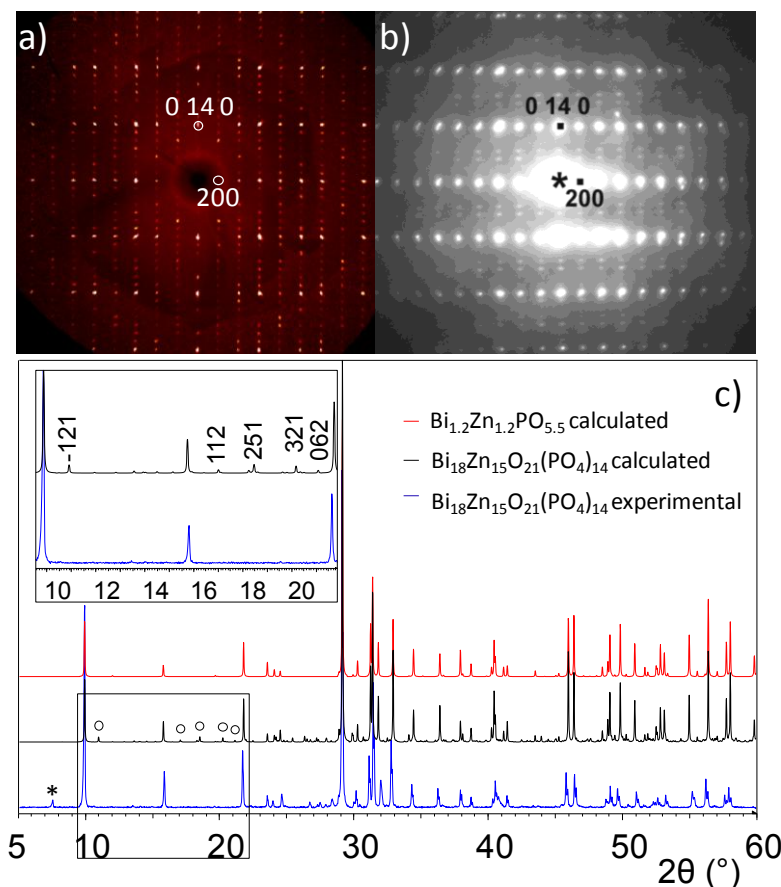


Figure II.23. a) Calculated precession frame from single crystal XRD data of $[\text{Bi}_{18}\text{Zn}_{10}\text{O}_{21}]^{\text{ord}}\text{Zn}_5^{\text{ord}}(\text{PO}_4)_{14}$, b) ED patterns of the 0kl layer of the corresponding powder and c) XRD patterns calculated from the disordered structure of $\text{Bi}_{1.2}\text{Zn}_{1.2}\text{O}_{1.5}\text{PO}_4$ (red), from the ordered single crystal of $[\text{Bi}_{18}\text{Zn}_{10}\text{O}_{21}]^{\text{ord}}\text{Zn}_5^{\text{ord}}(\text{PO}_4)_{14}$ (black) and experimental (blue). Inset - selected 2θ range showing some superstructure peaks - a sign of cation ordering. * - an impurity

4b) SHG measurements.

Powder SHG measurements on $[\text{Bi}_{18}\text{Zn}_{10}\text{O}_{21}]^{\text{ord}}\text{Zn}_5^{\text{ord}}(\text{PO}_4)_{14}$ were performed using 1064nm radiation by professor Shiv Halasyamani in the Department of Chemistry of University of Houston. The experimental description is given in Annex. As it is shown on the Figure II.24, the material has an SHG efficiency of approximately equal to $\alpha\text{-SiO}_2$, confirming the bulk-material conserves its non-centrosymmetric character refined from single crystal XRD data, despite the loss of full-ordering deduced from powder XRD data. In addition, particle size versus SHG efficiency revealed the material is type 1 phase-matchable which means that the fundamental and second-harmonic wavelengths constructively add as the light propagates through the material.

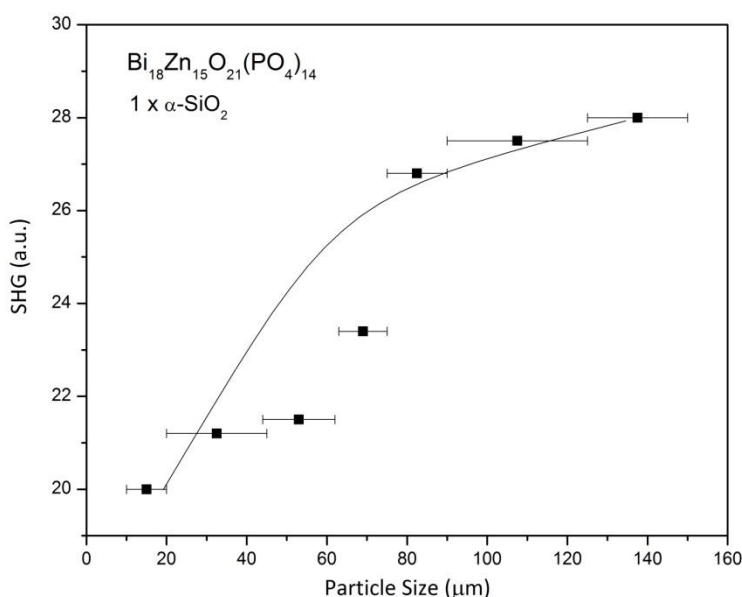


Figure II.24. SHG response vs. particle size of $[\text{Bi}_{18}\text{Zn}_{10}\text{O}_{21}]^{\text{ord}}\text{Zn}_5^{\text{ord}}(\text{PO}_4)_{14}$. The line is drawn to guide the eye showing that the compound is type 1 phase-matchable.

The small residual crystallographic disorder between the Bi^{3+} and Zn^{2+} cations is a likely reason for the relative weak SHG response and may be related to the bad matching between the expected and observed particle-size dependent response.

5) Relation with the fluorite structure: Structural flexibility and gradual ordering.

The obtained bismuth oxo-phosphates can be considered as derivatives of the fluorite-like $\delta\text{-Bi}_2\text{O}_3$ crystal structure in terms of their cationic arrangement. M and P atoms substitute the Bi-positions while the resulting network is strongly distorted, for instance due to the incorporation of extra-oxygen atoms with PO_4 groups. Using this description, the cationic channels can be considered as interstitial sites between PO_4 groups. Thus the same construction for $[\text{Bi}_{18}\text{Zn}_{10}\text{O}_{21}]^{\text{ord}}\text{Zn}_5^{\text{ord}}(\text{PO}_4)_{14}$ is shown on the Figure II.25a where oxocentered units are highlighted in yellow. If one compares it to the ideal square-grid for $\delta\text{-Bi}_2\text{O}_3$, it is clear that the PO_4 -rich area between the ribbons is strongly distorted in agreement with the significant concentration of voluminous phosphate groups. The tunnel cations are considered as interstitial and are not assigned to a particular x coordinate.

A similar construction for $[\text{Bi}_2(\text{Bi}_{1.56}\text{K}_{0.44})^{\text{dis}}\text{O}_3]\text{K}_{0.88}^{\text{dis}}(\text{PO}_4)_2$ is shown in the Figure II.25b. Here, similar $n = 3$ ribbons are arranged according to a four-fold axis, but clearly the distortion of the ideal-square lattice is weakly distorted by PO_4 compared to the previous case. In fact close inspection of the z coordinates indicate that the building of horizontal and vertical lines of the grid involves the creation of cationic vacancies around the tunnels. It is

inherent to the perpendicular disposition of the oxo-centered units, and most probably these “virtual” vacancies allow the relaxation of the structure and are responsible for the regular 2D-lattice. For $[\text{Bi}_{10}(\text{Bi}_{\sim 0.5}\text{Cd}_{\sim 0.5})_8^{\text{dis}}\text{O}_{16}](\text{Bi}_{0.6}\text{Cd}_{0.8})_2^{\text{ord}}(\text{PO}_4)_8$, as shown on the Figure II.25c, once more vacancies relax the structure into a regular lattice.

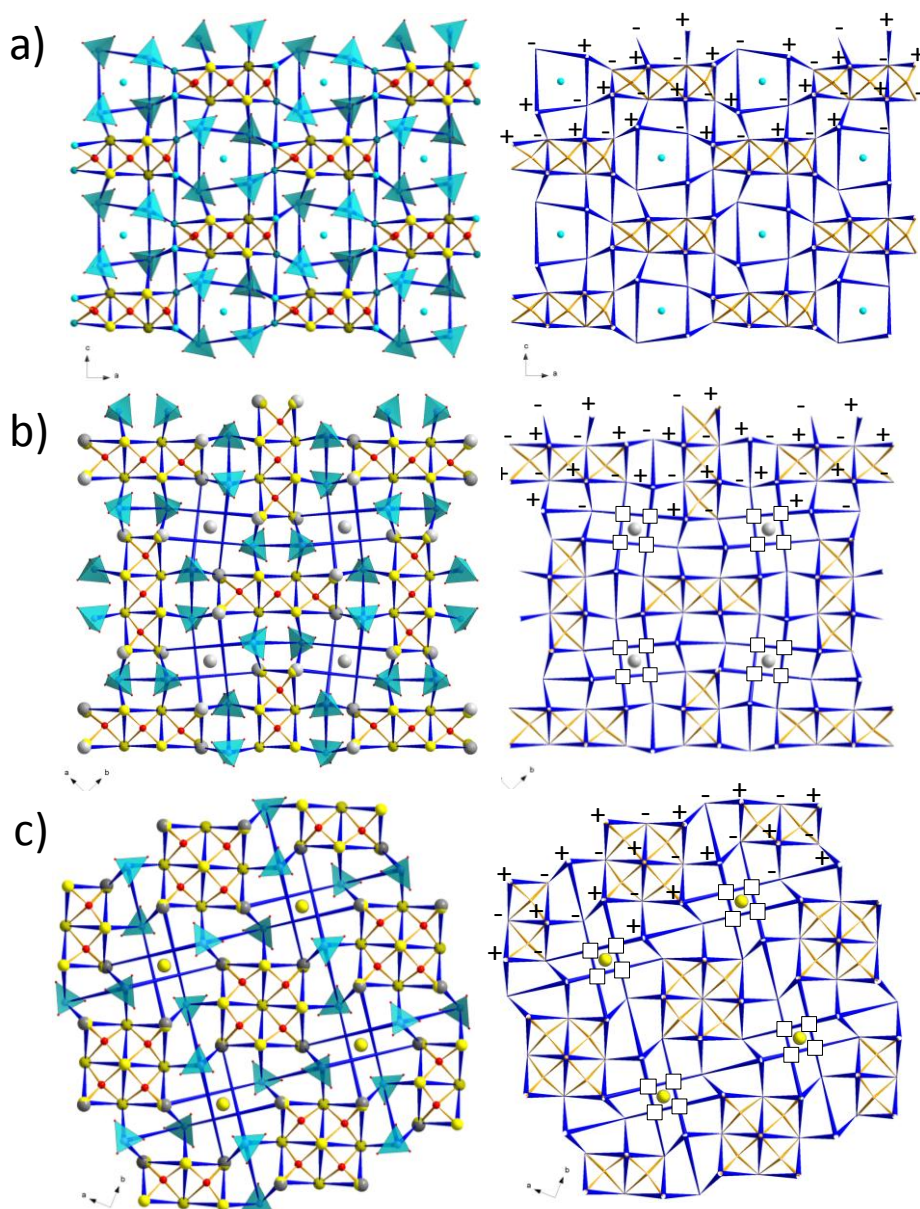


Figure II.25. Cationic grid representation of the structures of a) $[\text{Bi}_{18}\text{Zn}_{10}\text{O}_{21}]^{\text{ord}}\text{Zn}_5^{\text{ord}}(\text{PO}_4)_{14}$ b) $[\text{Bi}_2(\text{Bi}_{1.56}\text{K}_{0.44})^{\text{dis}}\text{O}_3]\text{K}_{0.88}^{\text{dis}}(\text{PO}_4)_2$, and c) $[\text{Bi}_{10}(\text{Bi}_{\sim 0.5}\text{Cd}_{\sim 0.5})_8^{\text{dis}}\text{O}_{16}](\text{Bi}_{0.6}\text{Cd}_{0.8})_2^{\text{ord}}(\text{PO}_4)_8$. Minus (-) and plus (+) signs indicate x and $x + \frac{1}{2}$ “out-of-plane” respectively, with regard to a ~ 5.5 Å parameter. The tunnel cations are shown on both representations and are interstitial cations. In (b) and (c) small open squares show the virtual cationic vacancies.

However, the concentration of oxocentered tetrahedra into square – columns seem to favor a more distorted PO_4 surrounding, compared to $[\text{Bi}_2(\text{Bi}_{1.56}\text{K}_{0.44})^{\text{dis}}\text{O}_3]\text{K}_{0.88}^{\text{dis}}(\text{PO}_4)_2$ despite a smaller ratio of $\text{O}(\text{Bi},\text{M})_4/\text{PO}_4$, i.e. 2 for the former against 3/2 for the latter. According to the

description from this viewpoint we observe a periodic lattice of cations that form the nodes of the cationic-grid, with a cationic disorder in terms of occupancy (external Bi/M sites of oxo-centered units). To understand the “easy” random distribution on the edges of oxo-centered units, one should observe the geometries of the oxo-centered O(Bi,Zn)₄ tetrahedra in [Bi₁₈Zn₁₀O₂₁]^{ord}Zn₅^{ord}(PO₄)₁₄. They undergo various distortions due to the differences between Zn-O (1.90 Å) and Bi-O (2.24 Å) distances which create local constraints and relaxations. At least it seems that the flexibility of oxo-centered poly-units is sufficiently significant to self-adapt Bi/M mixed sites in a fully disordered manner ([Bi₂(Bi_{1.56}K_{0.44})^{dis}O₃]K_{0.88}^{dis}(PO₄)₂ and [Bi₁₀(Bi_{~0.5}Cd_{~0.5})₈^{dis}O₁₆](Bi_{0.6}Cd_{0.8})₂^{ord}(PO₄)₈ or in almost ordered manner as in the case of [Bi₁₈Zn₁₀O₂₁]^{ord}Zn₅^{ord}(PO₄)₁₄.

6) Summary

The structures of the three obtained compounds described as a passage from highly disordered [Bi₂(Bi_{1.56}K_{0.44})^{dis}O₃]K_{0.88}^{dis}(PO₄)₂, via moderately disordered [Bi₁₀(Bi_{~0.5}Cd_{~0.5})₈^{dis}O₁₆](Bi_{0.6}Cd_{0.8})₂^{ord}(PO₄)₈ to most ordered [Bi₁₈Zn₁₀O₂₁]^{ord}Zn₅^{ord}(PO₄)₁₄, both in the cationic channel and the ribbons/columns subunits. The relative stability of ordered versus disordered sites is discussed on the basis of the M nature dealing with alkali (M = K), 3d (M = Zn) and 4d (M = Cd) transition metals, and characterized by use of solid-state ³¹P NMR probing for the first two cases. The SHG measurements confirms the NCS space group of [Bi₁₈Zn₁₀O₂₁]^{ord}Zn₅^{ord}(PO₄)₁₄ at the scale of powder. This family of compounds belong to the δ-Bi₂O₃ heritage having periodic skeleton of O(Bi,M)₄ units holding the crystal structure with the surrounding space is filled by more or less disordered counter ions including interstitial cations.

II.1.6 n = 3 ribbons: Bi₄Cu₃O₆(AsO₄)₂ and Bi₄Cu₃O₆(VO₄)₂

1) Preparation of the new Bi₄Cu₃O₆(AsO₄)₂.

The new phase Bi₄Cu₃O₆(AsO₄)₂ was first evidenced during the attempts to prepare the previous compound BiCu₂O₂(AsO₄), see Figure II.26. The majority of the observed extra peaks, not belonging to BiCu₂O₂(AsO₄), have been identified as very similar to Bi₄Cu₃O₆(VO₄)₂⁶⁴ (*a* = 5.3170Å, *b* = 7.9160Å, *c* = 8.0950Å, *α* = 74.580°, *β* = 89.380° and *γ* = 70.390°, PDF number: 01-082-1157). Therefore, it was concluded that the peaks could belong to a new compound with the formula Bi₄Cu₃O₆(AsO₄)₂.

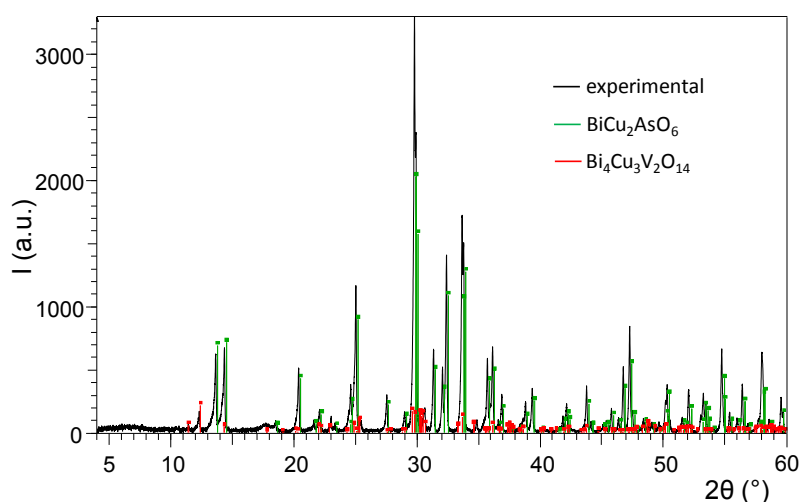


Figure II.26. The diffraction patterns of $\text{BiCu}_2\text{O}_2(\text{AsO}_4)$ with some impurities. Green lines are the diffraction pattern of $\text{BiCu}_2\text{O}_2(\text{AsO}_4)$, red lines are the peaks of $\text{Bi}_4\text{Cu}_3\text{O}_6(\text{VO}_4)_2$.

In the attempts to prepare this compound, the stoichiometric amounts of Bi_2O_3 , CuO and As_2O_5 have been ground together and heated at 800°C . The dark green compound was obtained the diffraction pattern of which is on the Figure II.27.

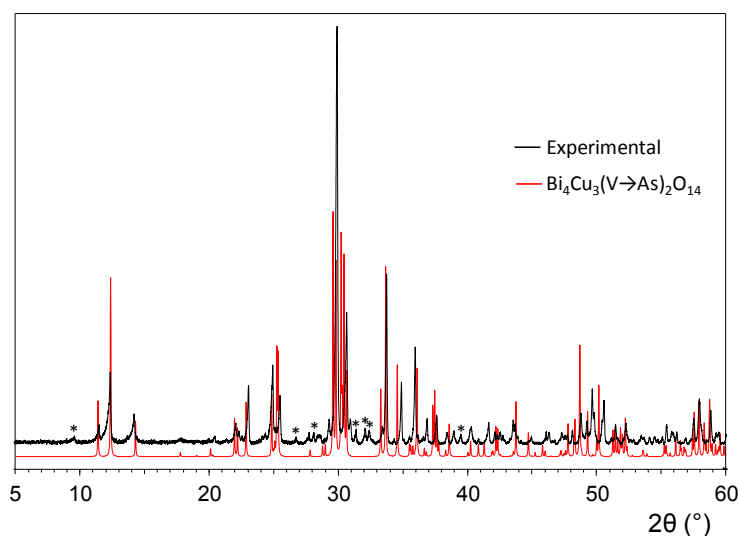


Figure II.27. Diffraction pattern of prepared $\text{Bi}_4\text{Cu}_3\text{O}_6(\text{AsO}_4)_2$ (black) and theoretical diffraction pattern of $\text{Bi}_4\text{Cu}_3\text{O}_6(\text{VO}_4)_2$ with As atoms instead of V (in red).

Several grinding/heating stages were necessary to achieve the completeness of the reaction. To validate our experiment we calculated the theoretical XRD pattern for the arsenate taking the crystal data for the vanadate and changing the nature of V against As using the software PowderCell¹¹⁹ (Figure II.27). An adequate matching between the expected and calculated XRD patterns was obtained. Refinement of cell parameters was performed by measuring the d_{hkl} corresponding to the most significant peaks. The obtained values can be seen in the Table II.8. The cell parameters of $\text{Bi}_4\text{Cu}_3\text{O}_6(\text{AsO}_4)_2$ and $\text{Bi}_4\text{Cu}_3\text{O}_6(\text{VO}_4)_2$ are quite close and in good

agreement with the ionic radii ($r(V^{5+})=0.355 \text{ \AA}$ vs. $r(As)^{5+} = 0.34 \text{ \AA}$). However, there are some extra peaks that could not be indexed as shown on the Figure II.27.

Table II.8. The cell parameters of Bi₄Cu₃O₆(AsO₄)₂ and Bi₄Cu₃O₆(VO₄)₂.

Compound	SG	<i>a</i> , Å	<i>b</i> , Å	<i>c</i> , Å	α , °	β , °	γ , °	<i>V</i> , Å ³
Bi ₄ Cu ₃ O ₆ (AsO ₄) ₂	<i>P</i> -1	5.288(6)	7.916(9)	8.030(7)	73.74(8)	88.61(8)	69.51(7)	301.26(59)
Bi ₄ Cu ₃ O ₆ (VO ₄) ₂	<i>P</i> -1	5.317(2)	7.916(4)	8.095(5)	74.58(5)	89.38(4)	70.39(3)	308.24(29)

Then we decided to try single crystal growth of this mysterious compound. The stoichiometric amounts of Bi₂O₃, CuO and As₂O₅ were ground together, pelletized and loaded into gold boat, followed by heating at 950°C during 12h then slow cooling down to 700°C at the rate of 5°C/min, then the furnace was switched off. A dark green needle-like crystal was selected for single XRD data collection.

2) Structural description of Bi₄Cu₃O₆(AsO₄)₂ and Bi₄Cu₃O₆(VO₄)₂.

As expected, the space group of the crystal structure of Bi₄Cu₃O₆(AsO₄)₂ is *P*-1, however the unit cell parameters are the following: $a = 5.3017(1) \text{ \AA}$, $b = 9.6076(1) \text{ \AA}$, $c = 12.6911(2) \text{ \AA}$, $\alpha = 82.9770(8)^\circ$, $\beta = 79.3990(9)^\circ$, $\gamma = 74.3770(8)^\circ$ and $V = 610.12(2) \text{ \AA}^3$ which shows the doubling of the unit cell (reliability factors $R_1 = 3.33\%$ $wR_2 = 3.47\%$). The refined crystal structure is shown on the Figure II.28a compared to that of the vanadate Bi₄Cu₃O₆(VO₄)₂, Figure II.28b. The projections of both structures along *a* axis give distorted square grids as a resemblance of ideal cationic grid of δ -Bi₂O₃.

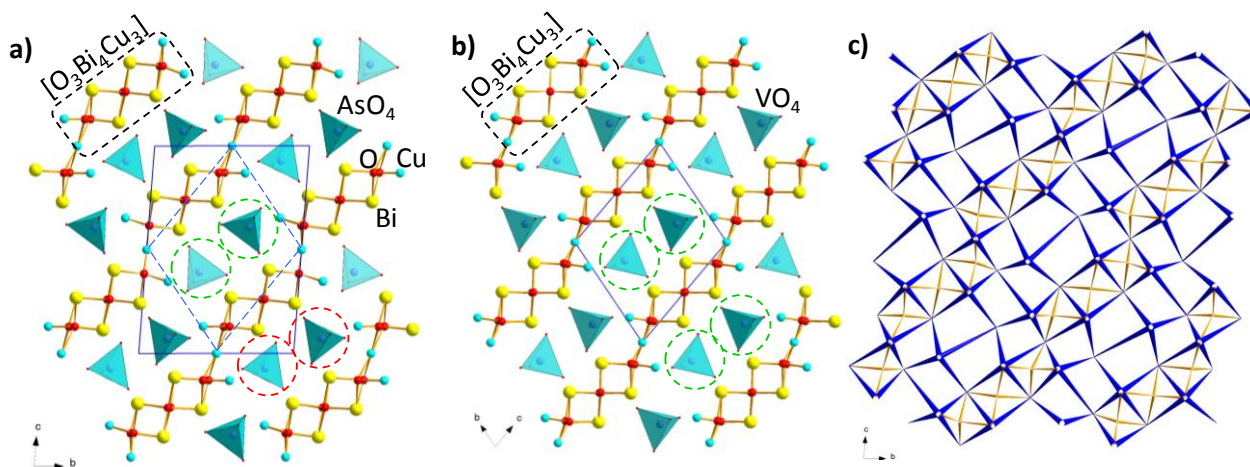


Figure II.28. Crystal structure of: a) Bi₄Cu₃O₆(AsO₄)₂; and b) Bi₄Cu₃O₆(VO₄)₂, c) the cationic network of Bi₄Cu₃O₆(AsO₄)₂. In a) and b) the colored circles show the difference of the orientation of the XO₄ tetrahedra from one cell to another. In a) the unit cell of Bi₄Cu₃O₆(AsO₄)₂ compared to that of Bi₄Cu₃O₆(VO₄)₂ (broken lines).

According to a description based on oxocentered tetrahedra¹²⁰, we observe $n = 3$ ribbons formed of edge-sharing oxygen-centered $O(\text{Bi}/\text{Cu})_4$ tetrahedra. Those trimeric units, $[\text{O}_3\text{Bi}_4\text{Cu}_3]$, consist of central OBi_4 tetrahedron flanked on each part with one OBi_2Cu_2 tetrahedron which shares their Bi–Bi and Bi–Cu edges to form the triple chains. Those ribbons are not completely isolated; they are connected by terminal copper atoms to constitute crenel-like layers of formula $[\text{O}_3\text{Bi}_2\text{Cu}_{1.5}]^{3+}$ which alternate with layers of AsO_4 tetrahedra (Figure II.28a). According to this projection, the doubling of the unit cell seems related only to a slight tilt of half of the AsO_4 groups (compared to the VO_4 groups), see Figure II.28a and Figure II.28b. However a close inspection of the topology formed by the Cu^{2+} environment gives important insights as shown on the Figure II.29a and Figure II.29b. Here we clearly show that on the opposite to the vanadate case (Figure II.29b), where only one kind of chains exist with a zig-zag (Z-like) section with adjacent corner sharing CuO_4 , the arsenate case (Figure II.29a) has additional distinct triple-spin chains with U-like section formed by connection of the diagonal corners of two, up and down, squares of CuO_4 by the adjacent corners of another CuO_4 . In the Z-topology of Cu_3O_4 chains in $\text{Bi}_4\text{Cu}_3\text{O}_6(\text{AsO}_4)_2$ we find Cu–O–Cu angles of 122.4° and 132.4° with a topology very similar to those observed in $\text{Bi}_4\text{Cu}_3\text{O}_6(\text{VO}_4)_2$ despite different angle values, 103.4° and 114.5° . In the second, U-like Cu_3O_4 chains in $\text{Bi}_4\text{Cu}_3\text{O}_6(\text{AsO}_4)_2$, the angles are 108.4° and 101.3° , where the folding generates a U-like section with the separation between opposite Cu^{2+} is 4.59 \AA and d_z^2 orbitals pointing towards each other (Figure II.29a).

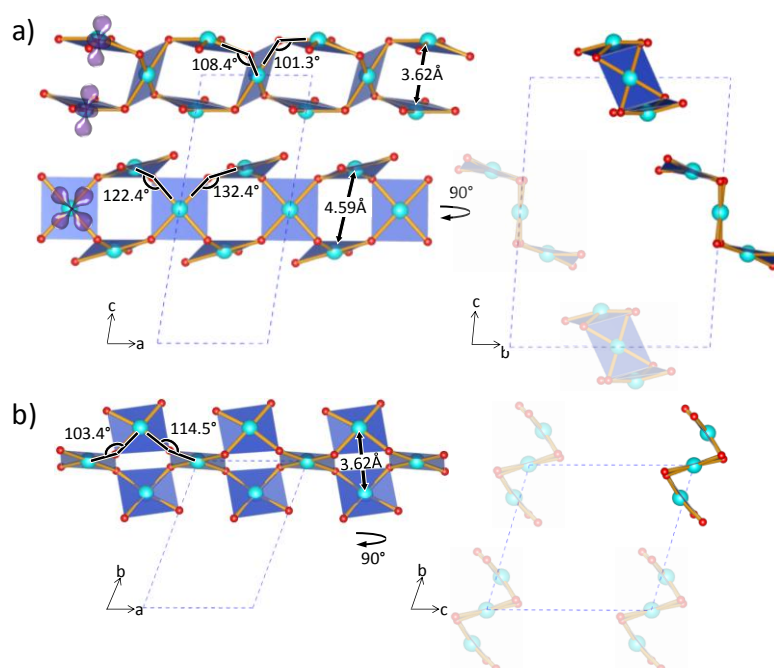


Figure II.29. Cu_3O_4 chains in a) $\text{Bi}_4\text{Cu}_3\text{O}_6(\text{AsO}_4)_2$ and b) $\text{Bi}_4\text{Cu}_3\text{O}_6(\text{VO}_4)_2$.

3) Magnetism.

Several works have been carried out on the magnitude of magnetic exchanges and real nature of the magnetic ground state of the $\text{Bi}_4\text{Cu}_3\text{O}_6(\text{VO}_4)_2$ compound.^{121–123} In summary, the following points can be given:

Firstly, in 2002, it was shown by a combination of NMR, magnetic and specific heat measurements, that the ground state corresponds to an antiferromagnetic ordered state with T_N is determined to be 6 K while the topology of the triple chains was considered as novel.¹²¹

Secondly, in 2008, Koo and Whangbo have evaluated relative exchanges by performing a spin dimer analysis based on tight-binding calculations and a mapping analysis based on first principles density functional theory calculations.¹²² They have shown that the correct spin-lattice is an antiferromagnetic chain made up of antiferromagnetic linear trimers coupled through their midpoints via super-superexchange interaction, which validates previous results ($\text{Bi}_4\text{Cu}_3\text{O}_6(\text{VO}_4)_2$ has an antiferromagnetic spin ground state) and has no spin frustration, both in agreement with experiment. The magnetic topology is drawn on the Figure II.30.

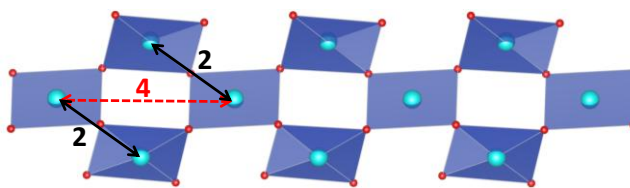


Figure II.30. Cu_3O_4 chain of $\text{Bi}_4\text{Cu}_3\text{O}_6(\text{VO}_4)_2$ with J_2 and J_4 exchanges.

Finally, in 2010, Zhou et al. have successfully grown $\text{Bi}_4\text{Cu}_3\text{O}_6(\text{VO}_4)_2$ crystals by floating-zone technique.¹²³ The magnetic properties reported with $H//a$ show a metamagnetic transition from antiferromagnetism to weak ferromagnetism observed at $H_c = 7.6$ T. The weak ferromagnetism observed for $H_c = 7.6$ T is probably a consequence of a canted antiferromagnetic spin structure with two distinct magnetic sublattices (Cu1 and Cu2) that behave differently at this field maybe from magnetostrictive effects. However, to our knowledge, no neutron diffraction experiment was performed and no one knows about the real spin arrangement.

Necessary measurements on $\text{Bi}_4\text{Cu}_3\text{O}_6(\text{AsO}_4)_2$ could give insights on the magnetic properties of both $\text{Bi}_4\text{Cu}_3\text{O}_6(\text{AsO}_4)_2$ and $\text{Bi}_4\text{Cu}_3\text{O}_6(\text{VO}_4)_2$. The preliminary magnetic measurements performed on $\text{Bi}_4\text{Cu}_3\text{O}_6(\text{AsO}_4)_2$ show that the susceptibility (calculated as M/H) is shown for 3 DC fields (Figure II.31a) for FC ramps.

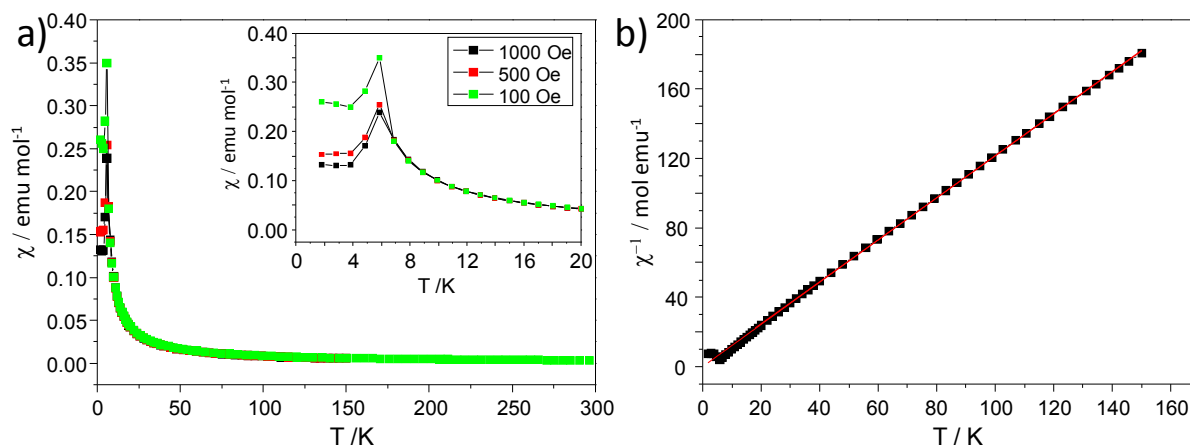


Figure II.31. $\text{Bi}_4\text{Cu}_3\text{O}_6(\text{AsO}_4)_2$: a) Magnetic susceptibility vs. temperature. Inset: zoom of the temperature range 0-20 K, b) Inverse susceptibility vs. temperature.

No divergence is observed between the three plots nor between ZFC/FC data. In the paramagnetic regime we find $\mu_{\text{eff}} = 3.04 \mu_{\text{B}}/\text{F.U.}$ and $\Theta_{\text{CW}} = -39 \text{ K}$ (from our fit between 110 and 300 K (Figure II.31b), below this temperature $\chi^{-1}(T)$ is slightly concave upward, announcing a setting of short range magnetic interactions. At 5.85 K a sharp peak of $\chi(T)$ suggests a Néel AFM 3D-ordering. However, as will be shown below, powder neutron diffraction (PND) data show that there is no evidence of such ordering on the diffraction patterns. $M(H)$ at 2 K show (Figure II.32) the occurrence of a metamagnetic transition at $\mu_0 H = 0.06 \text{ T}$ leading to pronounced jump of $0.3 \mu_{\text{B}}/\text{F.U.}$ ($=0.1 \mu_{\text{B}}/\text{Cu}^{2+}$).

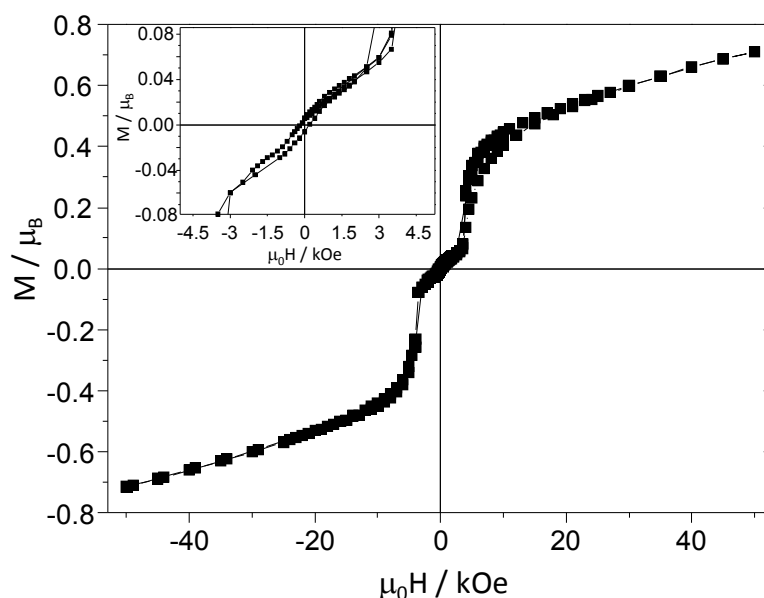


Figure II.32. $\text{Bi}_4\text{Cu}_3\text{O}_6(\text{AsO}_4)_2$: Magnetization $M(H)$ vs. magnetic field at 2K. Inset: metamagnetic transition at $\mu_0 H = 0.06 \text{ T}$

We can propose a scenario that is able to fulfill all the experimental results:

- Half of the Z-like chains of the arsenate behave like that of the vanadate and are potentially ready for a metamagnetic transition at low field, as observed at higher field in the latter. This metamagnetic transition is favored by the absence of robust AFM ordered ground state, which is shown by the weak field, 0.06 T, at which the transition occurs.
- The other half (U-like chains) are mainly paramagnetic, probably due to their particular topology. Indeed they show Cu-O-Cu angles closer to 90° , which are the most unfavorable angles for significant J-exchanges due to the orthogonal overlap.
- Finally, the Néel-like peak at 5.85 K would correspond to the abrupt AFM ordering inside Z-like chains, but not in the full crystallographic lattice. Neutron data collected versus temperature do not show any evidence for a magnetic ordering below 6 K (Figure II.33). The pattern was satisfactorily refined using the $\text{Bi}_4\text{Cu}_3\text{O}_6(\text{AsO}_4)_2$ structural model only.

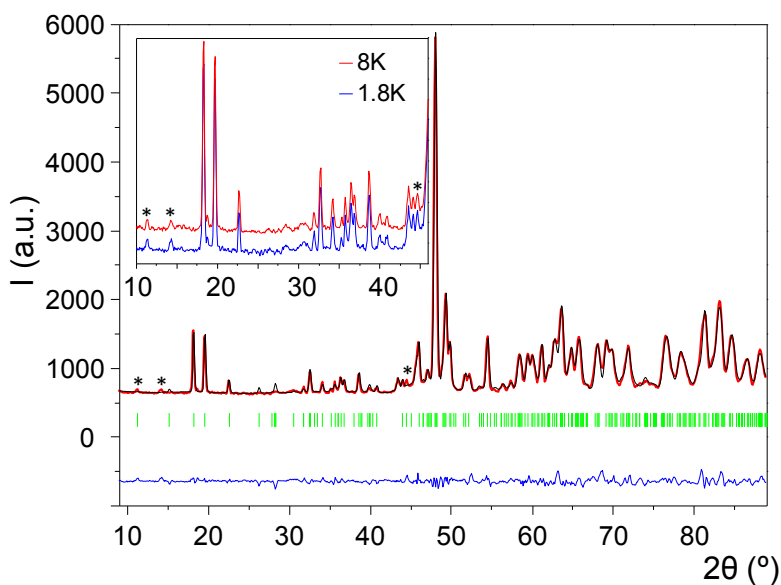


Figure II.33. Neutron diffraction structure refinement of $\text{Bi}_4\text{Cu}_3\text{O}_6(\text{AsO}_4)_2$. * denotes some extra peaks the origin of which is nonmagnetic, since they are observed at the temperature above T_N (see inset).

4) Summary

The structure of new $\text{Bi}_4\text{Cu}_3\text{O}_6(\text{AsO}_4)_2$ compared to existing $\text{Bi}_4\text{Cu}_3\text{O}_6(\text{VO}_4)_2$. Conducted magnetic and neutron diffraction measurements showed contradictory results meaning the 3D AFM ordering showed by former was not observed by latter (magnetic structure). Further investigations have to be done to clarify this issue.

II.1.7 $n = 3$ / $n = 4$ ribbon intergrowths: $\text{Bi}_{29.4}\text{Cu}_{9.29}\text{O}_{32}(\text{PO}_4)_{16}\text{Cu}_{2.63}$ and $\text{Bi}_{37.2}\text{Cu}_{18.8}\text{O}_{44}(\text{PO}_4)_{24}\text{Cu}_5$.

1) Generalities.

Two new phosphates were isolated as “side products” in the $\text{Bi}_2\text{O}_3\text{-CuO-P}_2\text{O}_5$ system by a PhD student Endara D⁵⁰, when an hypothetical $\text{Bi}_6\text{Cu}_4\text{O}_8[\text{BiO}]_2(\text{PO}_4)_4$ compound, with ribbons width $n = 4$, was deduced and attempted to prepare according to systematic rules as summarized in the introduction part. I participated to the study, by solving structure and re-performing the synthesis of crystals and powders. The lattice parameters of those novel intergrowths compounds are as following after refinement:

- $\text{Bi}_{29.4}\text{Cu}_{9.29}\text{O}_{32}(\text{PO}_4)_{16}\text{Cu}_{2.63}$: $a = 33.0549(2)$ Å, $b = 11.6991(4)$ Å and $c = 5.2902(2)$ Å, space group $Pca2_1$, $R_1 = 0.0589$ and $wR_2 = 0.0610$
- $\text{Bi}_{37.2}\text{Cu}_{18.8}\text{O}_{44}(\text{PO}_4)_{24}\text{Cu}_5$: $a = 11.6010(3)$ Å, $b = 47.4384(5)$ Å and $c = 5.267(2)$ Å, space group $Pna2_1$, $R_1 = 0.0940$ and $wR_2 = 0.0981$.

At the origin of this work, the targeted $\text{Bi}_6\text{Cu}_4\text{O}_8[\text{BiO}]_2(\text{PO}_4)_4$ that corresponds to a intergrowth between $n = 4/n = 4$ BUs, was modeled structurally (Figure II.34) and assorted with a general formula $\{(\text{Bi}_6)^{\text{core}}[(\text{M}/\text{Bi})_4^{\text{edge}}(\text{O}_8)(\text{Bi}_2^{\text{ex}}\text{O}_2)](\text{PO}_4)_4$, where M is divalent metal. For this particular n value, no tunnels are anticipated.

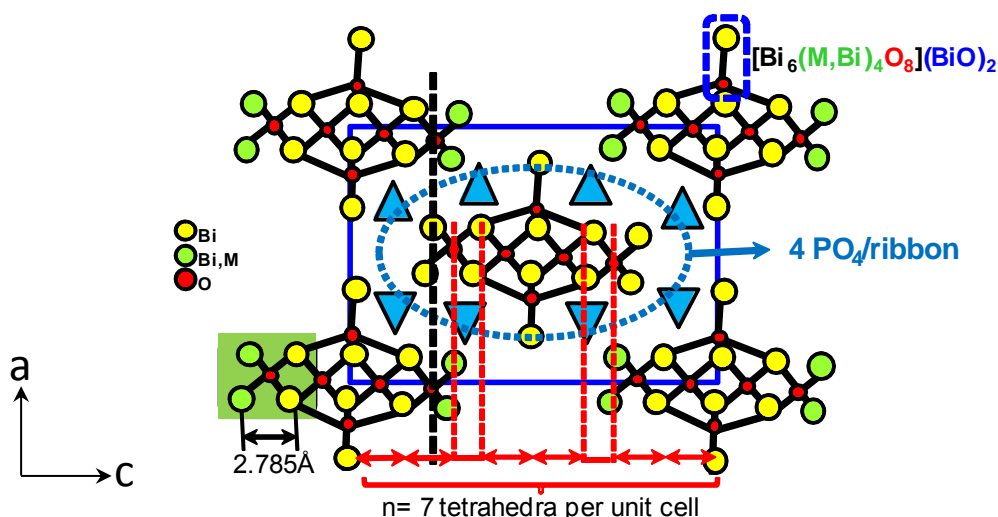


Figure II.34 a) hypothetical crystal structure of the $n = 4$ / $n = 4$ compound and its calculated c unit cell parameter.

The above formula includes Bi^{3+} in the cores of BUs ($=\text{Bi}^{\text{core}}$: 100% Bi sites), mixed Bi/M sites at their edges ($=\text{M}/\text{Bi}^{\text{edge}}$) and the surrounding ones ($=\text{Bi}^{\text{ex}}$, for excrescence). The formula $\text{Bi}_8\text{Cu}_4\text{O}_{10}(\text{PO}_4)_4$ is neutral if the edge-sites are considered as fully occupied by Cu^{2+} .

The expected lattice parameters, if one considers the ideal orthorhombic symmetry, are $a \sim 11.6$, $b \sim 5.4$, $c \sim 19.6\text{\AA}$ (here the order of lattice parameters differs from conventional one), where a and b are quite trivial values in this phosphate structural types, whereas c has to be calculated according to the formula: $(2n-1)*2.8\text{\AA}$. The value of c can be also considered as the total number of $\text{O}(\text{Bi},\text{M})_4$ tetrahedra along c (taking into account the observed overlapping of the heads and tails of BUs along the different rows that cover the unit cell) multiplied by the thickness of $\text{O}(\text{Bi},\text{M})_4$ tetrahedra (2.8\AA) (see Figure II.34). Compared to other compounds previously predicted and synthesized in the lab, the particularity of this case is that the compound expected to be fully ordered (no mixed Bi/M sites and absence of any tunnels between PO_4 groups). In these series of compounds, fully ordered compounds are not predominant but exist, e.g. for $n = 2$ ($\text{BiM}_2\text{O}_2(\text{PO}_4)$ compounds^{105,124–127}) and $n = 1$ ($\text{BiMO}(\text{PO}_4)$ compounds^{51,102}).

Several attempts to prepare the powder of $\text{Bi}_6\text{M}_4\text{O}_8[\text{BiO}]_2(\text{PO}_4)_4$, using different M metal ($M = \text{Cu}, \text{Zn}, \text{Cd}, \text{Mg}, \text{Ni}$ and Co) oxide have been performed in our laboratory⁵⁰. However they all failed systematically; no match between experimental XRD patterns and the expected ones. It could be related to the absence of tunnels in the predicted crystal structure (Figure II.34). Usually, such tunnels as well as the mixed Bi/M occupancy at the edges of the BUs bring a compositional flexibility that could favor the stability of a given structure. Thus the two obtained “as side products” bismuth copper oxophosphates possess cationic tunnels in their structure.

2) $\text{Bi}_{29.4}\text{Cu}_{9.29}\text{O}_{32}(\text{PO}_4)_{16}\text{Cu}_{2.63}$.

A greenish plate-like single crystal of $\text{Bi}_{29.4}\text{Cu}_{9.29}\text{O}_{32}(\text{PO}_4)_{16}\text{Cu}_{2.63}$ was isolated from the inhomogeneous polyphasic melt and mounted on a glass fiber. The observed extinction conditions suggest two possible space groups: $Pcam$ and $Pca2_1$.

Initially, the crystal structure refinement has been performed in the centrosymmetric space group but because of the problems related to the systematic split of atoms, $Pca2_1$ was finally preferred. The z parameter of the Bi1 atom was fixed according to a non-centrosymmetric (NCS) symmetry. Around the four localized P atoms, only two full oxygen tetrahedral configurations have been found from Fourier difference maps. The two others have been idealized using rigid body blocks. Indeed, the compounds of this family usually display significant disorder over several PO_4 orientations around P sites since their oxygen corners are connected to mixed $\text{Bi}^{3+}/\text{M}^{2+}$ crystallographic sites. The strong degree of disorder is

sometimes such, that from ^{31}P and ^{17}O NMR spectroscopy, compounds were announced as in an intermediate glassy/crystalline state among a rigid framework.^{112,113}

At the last cycles of the refinement, anisotropic displacements were considered for every heavy atom of ribbons and for P2 since the residual electron density remaining precisely around this atom. The tunnels are partially occupied by Cu_a atoms. The number of Cu^{2+} cations in tunnels is equal to 1.35 which is less than the maximal 2 cations allowed per b-periodicity ($\sim 5.5\text{\AA}$). A restriction has been set between the occupancies of mixed Bi/Cu sites (Bi/Cu1a and Bi/Cu2a) at the edges of ribbons in order to reach the electroneutrality. At the mixed sites, Bi^{3+} and Cu^{2+} cations have been split in adjacent positions according to the Fourier difference synthesis calculation. Results and refinement are listed in Table II.9.

Table II.9. Crystal data, measurement and structure refinement parameters for $\text{Bi}_{29.4}\text{Cu}_{9.29}\text{O}_{32}(\text{PO}_4)_{16}\text{Cu}_{2.63}$ and $\text{Bi}_{37.2}\text{Cu}_{18.8}\text{O}_{44}(\text{PO}_4)_{24}\text{Cu}_5$

Compound	$\text{Bi}_{29.4}\text{Cu}_{9.29}\text{O}_{32}(\text{PO}_4)_{16}\text{Cu}_{2.63}$	$\text{Bi}_{37.2}\text{Cu}_{18.8}\text{O}_{44}(\text{PO}_4)_{24}\text{Cu}_5$
Crystal Data		
Crystal symmetry	Orthorhombic	Orthorhombic
Space group	$Pca2_1$	$Pna2_1$
a (\AA)	33.0549(2)	11.6010(3)
b (\AA)	11.6991(4)	47.4384(5)
c (\AA)	5.2902(2)	5.267(2)
V (\AA^3)	2045.8(1)	2899(1)
Z	1	1
Mw	8926.6	12285.40
Data collection		
Equipment	Apex DUO (Bruker AXS)	
Radiation wavelength (\AA)	0.71073 (MoK α)	
Absorption corrections	Multiscan (Sadabs)	
Detector distance (mm)	40	55
Recording reciprocal space	$-59 \leq h \leq 53$	$-20 \leq h \leq 20$
	$-20 \leq k \leq 20$	$-76 \leq k \leq 82$
	$-9 \leq l \leq 8$	$-8 \leq l \leq 8$
μ (mm^{-1})	71.07	64.881
D_{calc} (g/cm^3)	7.316	7.041
θ -range (deg.)	3.54-40.23	3.89-39.27
Total Ref.	70469	101687
Unique Ref.	11339	15259
Unique $ I \geq 3\sigma(I)$	7767	11181
Refinement parameters		
Software, refinement type	Jana 2006, L.S. on F	
Refined parameters/restrictions	211/7	229/2
R_{int}	0.064	0.0701
R_1	0.059	0.094
R_1 (all data)	0.094	0.1212
wR_2	0.061	0.0981
Extinction coefficient	90(7)	93(9)

The crystal structure is presented on the Figure II.35a. The refined formula is $\text{Bi}_{29.4}\text{Cu}_{9.29}\text{O}_{32}(\text{PO}_4)_{16}\text{Cu}_{2.63}$. This ratio of the cations is close to the one found by EDS analysis, Bi:Cu:P in ratio 9.6;4;5.4.

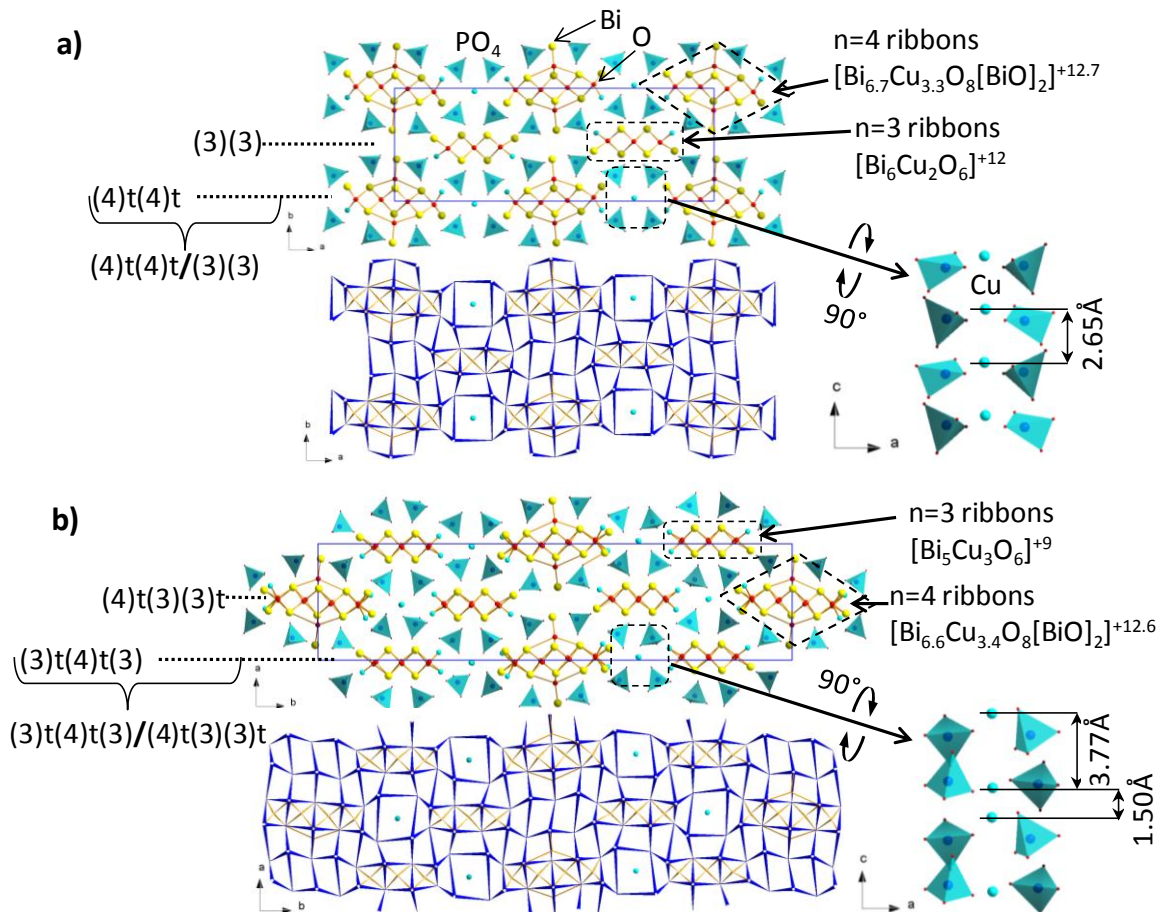


Figure II.35. Projections of the crystal structures of (a) $\text{Bi}_{29.4}\text{Cu}_{9.29}\text{O}_{32}(\text{PO}_4)_{16}\text{Cu}_{2.63}$ and (b) $\text{Bi}_{37.2}\text{Cu}_{18.8}\text{O}_{44}(\text{PO}_4)_{24}\text{Cu}_5$ along the b axis. Both structures are built on the association of ribbons $n = 4$ (noted (4)) and $n = 3$ (noted (3)) tetrahedra wide and tunnels (noted (t)). Note the different (4)t(4)t/(3)(3) and (3)t(4)t(3)/(4)t(3)(3)t sequences in both compounds. The corresponding 2D-square cationic networks are presented underneath of respective structures as well as the tunnel arrangements as blue inserts.

We note a significant residual electron density peak ($20.3 \text{ e}/\text{\AA}^3$) close to one of the Bi position. Such high peaks are rather commonly observed around heavy atoms in so disordered structures. It could also picture the presence of defects or imperfect absorption corrections. Several twin laws have been introduced but did not solve the problem. The ideal crystal structure projected along the b -axis (Figure II.35a) shows ribbons of width $n = 3$ ($[\text{Bi}_6\text{Cu}_2\text{O}_6]^{+12}$) and $n = 4$ ($[\text{Bi}_{6.688}\text{Cu}_{3.312}\text{O}_8[\text{BiO}]_2]^{+12.688}$). Two tunnels take place between two consecutive $n = 4$ ribbons at $x = 0$. Their alternation with tunnels along c axis corresponds to the sequence (4)t(4)t/(3)(3) as shown on Figure II.35a where (4) denote $n = 4$ BUs, (3) denote $n = 3$ BUs, and t denote the interstitial tunnels.

The refined model is relatively inaccurate concerning the Cu^{2+} localization in tunnels and the real orientation of PO_4 (use of a single rigid body per P site, while several PO_4 orientations are expected). It follows that the coordination of Cu^{2+} in tunnels is not well defined. It is shown on the Figure II.35a as refined, and correspond to Cu-Cu minimal separations of 2.65 Å ($=b/2$, but one should keep in mind that Cu_a sites are partially empty) and questionable short Cu-O distances (~ 1.8 Å).

Using the refined chemical composition, we tried to reproduce this compound as the corresponding powder by solid state reaction route. Nevertheless, despite several grindings and thermal conditions, another related phase ((4)tt/(6)) using an identical formalism is always observed in addition to the target compound, see XRD patterns on Figure II.36a.

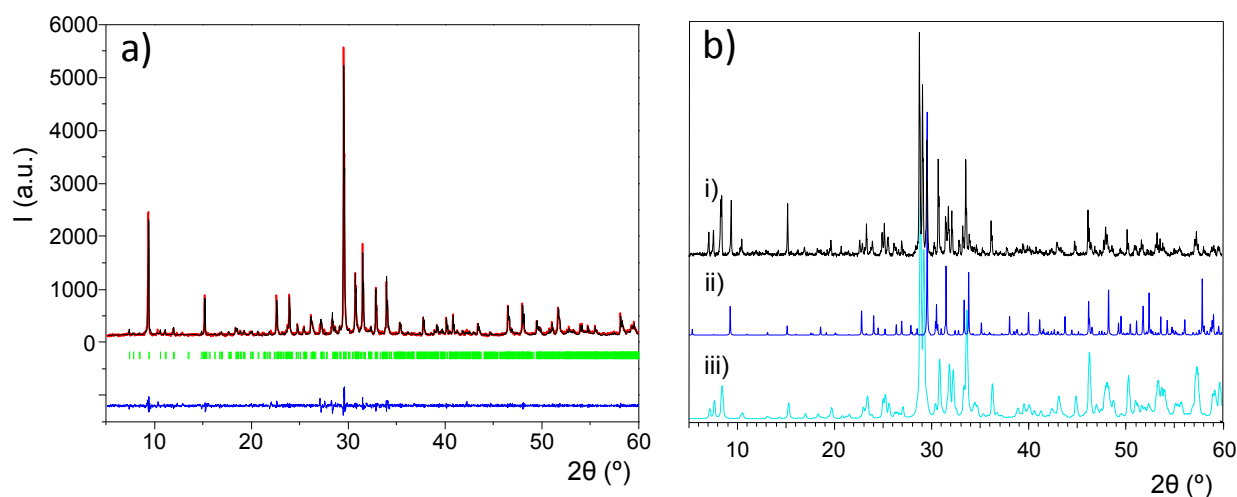


Figure II.36. a) Pattern matching of the compound $\text{Bi}_{37.2}\text{Cu}_{18.8}\text{O}_{44}(\text{PO}_4)_{24}\text{Cu}_5$, the refined parameters are: $a = 11.6121(6)$, $b = 47.584(3)$, $c = 5.2700(3)$, $V = 2911.9(3)$, $\chi^2 = 1.75$ and b) the powder corresponding to $\text{Bi}_{29.4}\text{Cu}_{9.29}\text{O}_{32}(\text{PO}_4)_{16}\text{Cu}_{2.63}$: i) measured, ii) calculated, iii) and compared to the 4/6 intergrowth present as an impurity.

3) $\text{Bi}_{37.2}\text{Cu}_{18.8}\text{O}_{44}(\text{PO}_4)_{24}\text{Cu}_5$.

A green needle single crystal of $\text{Bi}_{37.2}\text{Cu}_{18.8}\text{O}_{44}(\text{PO}_4)_{24}\text{Cu}_5$ was isolated from the same molten preparation as for the previous compound. Apparently the chosen crystal is of rather poor quality since several defects are observed on the calculated precessions $0kl$, $h0l$ and $hk0$ layers (Figure II.37) which most probably result from the local intergrowth between various BUs into defects as recently described for another topology of ribbons. Once more systematic extinctions suggest two possible space groups, either $Pnam$ either the NCS $Pna2_1$.

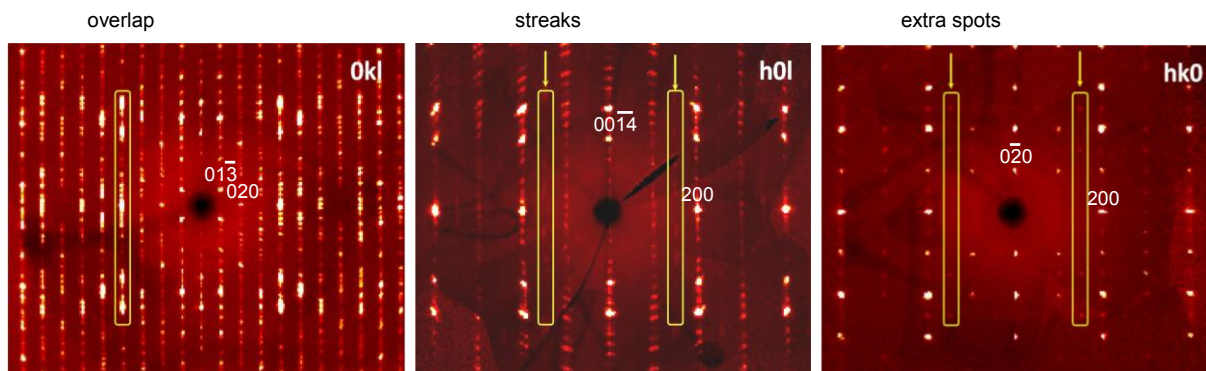


Figure II.37. $(0kl)$, $(h0l)$ and $(hk0)$ layers showing the low quality of crystal 2. Thus, overlaps, streaks and extra spots are observed on the different layers.

The NCS model was preferred since the final R values improved by $\sim 2\%$. The same process as for $\text{Bi}_{29.4}\text{Cu}_{9.29}\text{O}_{32}(\text{PO}_4)_{16}\text{Cu}_{2.63}$ was employed to solve and refine the crystal structure. We note the consideration of two mixed sites, Cu1a/Bi1a (ratio fixed to 0.9/0.1) and Cu2a/Bi2a (ratio fixed to 0.82/0.18) at ribbon edges. Once more, these mixed sites involve a high disorder around the six independent phosphate groups and the introduction of rigid bodies. Two Cu^{2+} cations (Cua and Cub) occupy the unique independent tunnel while their respective occupancies were fixed after preliminary refinement to 0.6 and 0.75. It is noteworthy that, at the last refinement cycle, occupancies of mixed sites and tunnels were locked to conserve the electroneutrality of the crystal structure. The crystal structure is presented on Figure II.35b. The refined formula is $\text{Bi}_{37.2}\text{Cu}_{18.8}\text{O}_{44}(\text{PO}_4)_{24}\text{Cu}_{5.4}$, the cationic ratio of which is quite close to the one found by EDS analysis, Bi:Cu:P (9.7:6.2:6.5).

In the last cycles of the refinement, the reliability factors remain rather high ($R1 = 0.0940$, $Rw = 0.0981$). However, it gives rather accurate picture of the BUs arrangement in the unit cell. The projection of the crystal structure along b is shown on the Figure II.35b. It is based on the association of $(\text{Bi}_{6.56}\text{Cu}_{3.44}\text{O}_8[\text{BiO}]_2)^{+12.56}$ $n = 4$ BUs and $(\text{Bi}_5\text{Cu}_3\text{O}_6)^{+9}$ $n = 3$ BUs, surrounded by PO_4 tetrahedra.

Four tunnels exist in the unit cell, between two consecutive $n = 3$ and $n = 4$ ribbons. By using the same formalism as for the previous compound, we obtain a complex sequence (3)t(4)t(3)/(4)t(3)(3)t as shown in the Figure II.35b. As for the $\text{Bi}_{29.4}\text{Cu}_{9.29}\text{O}_{32}(\text{PO}_4)_{16}\text{Cu}_{2.63}$, in the interleaved space, external Bi^{3+} cations point toward each other but shifted along the b -axis (projection axis for Figure II.35a). Electrostatic interactions between Bi^{3+} cations and lone pairs favor the stabilization. Once more for same reasons than given for $\text{Bi}_{29.4}\text{Cu}_{9.29}\text{O}_{32}(\text{PO}_4)_{16}\text{Cu}_{2.63}$, the environment of Cu^{2+} in the tunnels is rather inaccurately

defined from our refinement. At least, distorted square planar configurations can be deduced from the view of the tunnels, Figure II.35b.

4) Electron microscopy.

It is not rare to observe a high concentration of defects on HREM images showing an alternation of various n -sized BUs ribbons^{39,74}. This is probably the reason why the crystal structure refinement leads to such high reliability factors. Similar defects were evidenced in a previous study with a HREM image enhanced a variety of intergrowths between different ribbons.⁴⁰ Indeed, the crystals ($n = 8$) includes a high concentration of defects and the [010] zone axis patterns and lattice images show the alternation of various n -sized BUs accordingly to multiple local c -periodicities. They are responsible for a high residual electron density peaks. Unfortunately, our crystal of $\text{Bi}_{37.2}\text{Cu}_{18.8}\text{O}_{44}(\text{PO}_4)_{24}\text{Cu}_{5.4}$ is too sensitive to the beam to obtain suitable HR image.

The [100] electron diffraction pattern exhibits diffuse streaks (white arrows in Figure II.38b), like in the h0l layer of Figure II.37 and not observed in the corresponding [010] zone axis pattern of the first compound. These streaks indicate an inherent strong disorder.

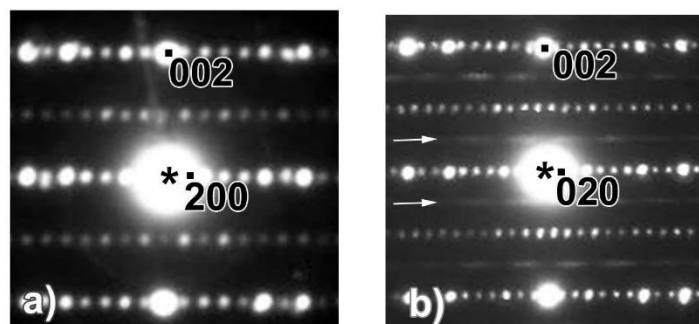


Figure II.38. a)[010] ZAP of $\text{Bi}_{29.4}\text{Cu}_{9.29}\text{O}_{32}(\text{PO}_4)_{16}\text{Cu}_{2.63}$ compared to b) the corresponding [100] ZAP of $\text{Bi}_{37.2}\text{Cu}_{18.8}\text{O}_{44}(\text{PO}_4)_{24}\text{Cu}_5$ which exhibits diffuse streaks indicated by white arrows.

5) Analogy with the fluorite.

These two new compounds can be considered as derivatives from the fluorite-like $\delta\text{-Bi}_2\text{O}_3$ crystal structure in terms of their cationic arrangement. In Figure II.35a and Figure II.35b, this analogy is shown through a representation of the 2D projection of cationic lattice where every lattice node represent a cation Bi^{3+} , mixed $\text{Bi}^{3+}/\text{M}^{2+}$ or a PO_4 barycenter as described in ref.^{39,40} The substitution of Bi-sites by phosphate groups and metal ions led to significant distortions. The oxocentered OBi_4 tetrahedra are marked by crosses enhancing the $n = 3$ and 4 ribbons. Finally the green circles indicate the location of the tunnels which are interstitial in

the fluorite-framework. The interest of this representation is that it shows that the full cationic content is preserved by substitution starting from an ideal square-grid drawn for $\delta\text{-Bi}_2\text{O}_3$, apart from interstitial channels. It is in fact at the origin of the possible formulation of most of the compounds that initialized this work.

6) SHG microscopy.

The experimental description of the SHG microscopy is given in Annex. For both compounds, the use of a NCS space group $Pca2_1/Pna2_1$ rather than $Pcam/Pnam$ leads to a better convergence of the least-squares refinement. However, clearly on the opposite to polar BUs evidenced for peculiar ribbon size $n = 5, 8, 11 \dots (=3n'+2)^{38,40,74}$, the $n = 3$ and $n = 4$ sized BUs are ideally non-polar and only slight atomic shift, PO_4 rotations and occupancies of edges of ribbons break the centrosymmetry of the full model. It follows that this particular space group may not reflect the sample at a macroscopic scale but rather a majority of the domains in the selected single crystal. We have conducted the second harmonic generation measurements on the single crystals of $\text{Bi}_{29.4}\text{Cu}_{9.29}\text{O}_{32}(\text{PO}_4)_{16}\text{Cu}_{2.63}$ and $\text{Bi}_{37.2}\text{Cu}_{18.8}\text{O}_{44}(\text{PO}_4)_{24}\text{Cu}_{5.4}$ after checking the corresponding lattice parameters. We recall that our previous tests on NCS compounds (polycrystalline samples) give rise to intense SHG emission on intense laser pulses, while compounds systematically darken after a short time exposure.^{38,40} The same behavior was verified here using a laser scanning microscope (selected $\lambda = 860$ nm). The Figure II.39 shows the crystal of $\text{Bi}_{37.2}\text{Cu}_{18.8}\text{O}_{44}(\text{PO}_4)_{24}\text{Cu}_{5.4}$ in absence of emission and during emission. The green color at the surface of the single crystals shows an intrinsic homogeneous distribution of the emitted light collected with a band pass filter (420 to 440 nm). However one have to precise that a control-channel set in the red (500-600 nm) also shows an intense emission before the crystal darkens. It means that the SHG might not be a unique process but could be accompanied by an intense fluorescence in a broad spectral range in our experimental conditions.

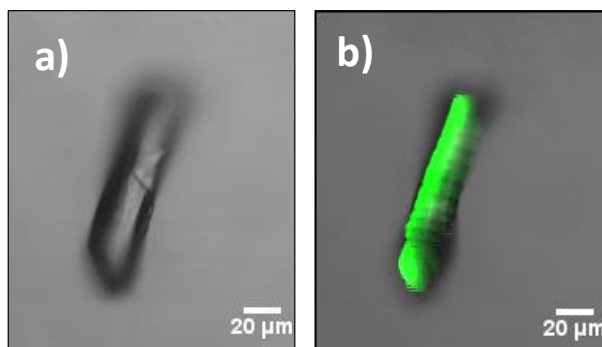


Figure II.39. a) transmission image of a crystal of $\text{Bi}_{37.2}\text{Cu}_{18.8}\text{O}_{44}(\text{PO}_4)_{24}\text{Cu}_{5.4}$ b) green: emitting surface ($\lambda_{em} = 420\text{-}440\text{ nm}$, $\lambda_{em} = 860\text{ nm}$)

Structures $\text{Bi}_{29.4}\text{Cu}_{9.29}\text{O}_{32}(\text{PO}_4)_{16}\text{Cu}_{2.63}$ and $\text{Bi}_{37.2}\text{Cu}_{18.8}\text{O}_{44}(\text{PO}_4)_{24}\text{Cu}_{5.4}$ are similar to the structures of $\text{Bi}_{\sim 3}\text{Cd}_{\sim 3.72}\text{M}_{\sim 1.28}\text{O}_5(\text{PO}_4)_3$ ($M = \text{Co}, \text{Cu}, \text{Zn}$) and $\text{Bi}_{\sim 6.2}\text{Cu}_{\sim 6.2}\text{O}_8(\text{PO}_4)_5$, considering the replacement of $n = 2$ and $n = 3$ in these later by $n = 3$ and $n = 4$ BUs in the title compounds. It leads to the analogue sequence $(4)t(4)t/(3)(3) \rightarrow (3)t(3)t/(2)(2)$ and $(3)t(4)t(3)/(4)t(3)(3)t \rightarrow (2)t(3)t(2)/(3)t(2)(2)t$, once more, opening the door to new possible crystal structures, taking into account the number of reported polymorphs with possible BUs exchanges.

7) Summary

The structures of two new terms in the $\text{Bi}_2\text{O}_3\text{-CuO-P}_2\text{O}_5$ system with $n = 4/ n = 3$ are obtained and their respective structures are described. The conducted SHG microscopy measurements on the corresponding single crystal confirm their NCS space groups.

II.1.8 $n = 4$ ribbons: $\text{KBi}_5\text{O}_5(\text{AsO}_4)_2$

1) Synthesis

Single crystal:

Single crystals of $\text{KBi}_5\text{O}_5(\text{AsO}_4)_2$ were found in the melt obtained by heating of the mixture $2.5\text{Bi}_2\text{O}_3 + 0.5\text{K}_2\text{CO}_3 + \text{As}_2\text{O}_5$ in a gold tube with one end open at 950°C during 12 h then slowly cooling down to 600°C at a rate 3°C/h . Then the furnace was switched off to be cooled down to room temperature.

Powder synthesis:

Polycrystalline single phase sample of $\text{KBi}_5\text{O}_5(\text{AsO}_4)_2$ (Figure II.41) was prepared by heating of co-ground mixture of precursors Bi_2O_3 , K_2CO_3 and As_2O_5 at 600°C during 12h than at 830°C during 48h with intermediate grindings.

2) Structural description.

The structure of $\text{KBi}_5\text{O}_5(\text{AsO}_4)_2$ crystalizes in monoclinic system in space group $P2_1/c$ (14) with unit cell parameters $a = 8.2534(5)\text{ \AA}$, $b = 5.5406(4)\text{ \AA}$, $c = 28.4053(19)\text{ \AA}$, $\beta = 95.936(3)^\circ$ and $V = 1291.97(15)\text{ \AA}^3$. The $[\text{O}_8\text{Bi}_8\text{K}_2]^{10+}$ $n = 4$ ribbons with two $[\text{OBi}]^+$ excrescences are separated by AsO_4^{3-} .

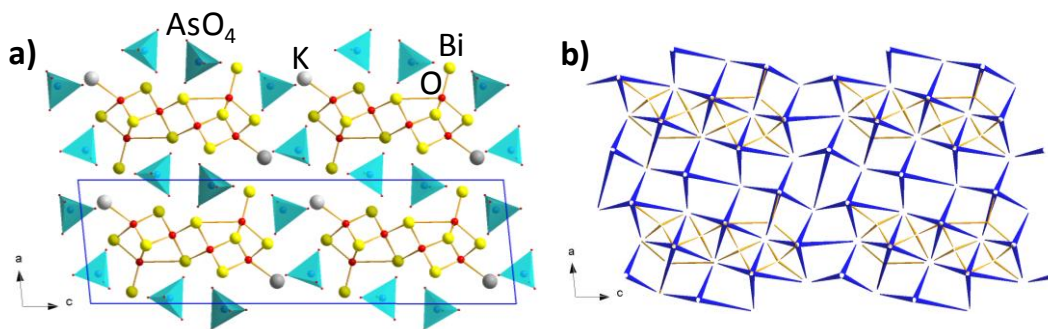


Figure II.40. a) The crystal structure of $\text{KBi}_5\text{O}_5(\text{AsO}_4)_2$ and b) its cationic grid representation

Interestingly in this original topology of ribbons, the two O-Bi excrecences located near to the two extremities at both sides are shifted along the ribbons, which has not been encountered yet. K atoms occupy the edges of the ribbons in *trans* position (Figure II.40a). The cationic grid is shown on Figure II.40b. The lone pair of the excrecences are supposedly participates in the coordination of the K cations.

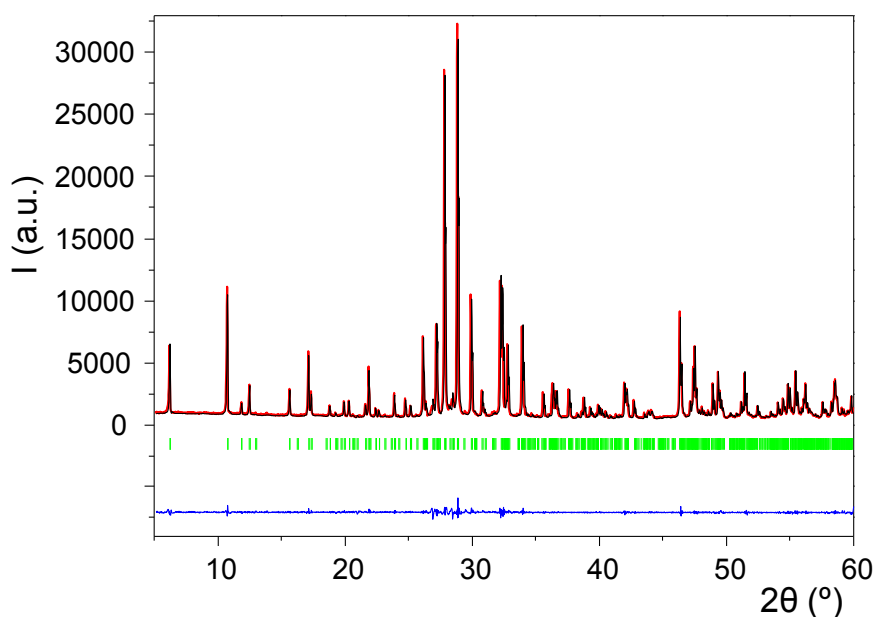


Figure II.41. Pattern matching of $\text{KBi}_5\text{O}_5(\text{AsO}_4)_2$ with the refined parameters $a = 8.2504(2)\text{Å}$, $b = 5.5454(1)\text{Å}$, $c = 28.4068(6)\text{Å}$, $\beta = 95.8796(8)^\circ$ and $V = 1292.81(4)\text{Å}^3$ with reliability parameter $\chi^2 = 2.60$

The Pattern Matching fit performed on XRD data of the polycrystalline sample $\text{KBi}_5\text{O}_5(\text{AsO}_4)_2$ gave the unit cell parameters refined to $a = 8.2504(2)\text{Å}$, $b = 5.5454(1)\text{Å}$, $c = 28.4068(6)\text{Å}$, $\beta = 95.8796(8)^\circ$ and $V = 1292.81(4)\text{Å}^3$ with reliability parameter $\chi^2 = 2.60$.

3) Summary

The structure of new $\text{KBi}_5\text{O}_5(\text{AsO}_4)_2$ is described. Unusual position of the Bi-O excrecences is remarked. The synthesis of possible phosphate analogue is underway.

II.1.9 $n = 5$ ribbons: $\text{Bi}_6\text{ZnO}_7(\text{AsO}_4)_2$ against $\text{Bi}_6\text{ZnO}_7(\text{PO}_4)_2$

1) Generalities.

Another example of different steric effect of AsO_4^{3-} against PO_4^{3-} groups is given by the new compound $\text{Bi}_6\text{ZnO}_7(\text{AsO}_4)_2$ that have been prepared during this work.

Here, we will appreciate how, despite a “main” similar topology of oxocentred BUs, the arrangement between BUs and XO_4 groups is modified between oxo-phosphates and oxo-arsenates, leading to non-centrosymmetric versus centrosymmetric polytypes.

2) Synthesis.

Single crystal:

The transparent colorless needles of $\text{Bi}_6\text{ZnO}_7(\text{AsO}_4)_2$ were found in a polyphasic melt obtained by applying the crystal growth procedure described in the synthesis part to the mixture $0.5\text{Bi}_2\text{O}_3 + \text{ZnO} + 0.5\text{As}_2\text{O}_5$.

Powder synthesis:

The polycrystalline form of $\text{Bi}_6\text{ZnO}_7(\text{PO}_4)_2$ have been prepared according to ref [128]. The same procedure was adapted for the powder synthesis of $\text{Bi}_6\text{ZnO}_7(\text{AsO}_4)_2$.

3) Structural description.

The crystal structure of $\text{Bi}_6\text{ZnO}_7(\text{AsO}_4)_2$ is monoclinic, the unit cell parameters are $a = 34.442(7) \text{ \AA}$, $b = 5.5044(11) \text{ \AA}$, $c = 15.292(3) \text{ \AA}$, $\beta = 100.625(9)$ and $V = 2849.4(10) \text{ \AA}^3$, the space group $C2/c$. Crystal data of this compound is given on the Table II.10 and compared to those of the isostructural $\text{Bi}_6\text{ZnO}_7(\text{PO}_4)_2$.

In the crystal structure of $\text{Bi}_6\text{ZnO}_7(\text{AsO}_4)_2$ the BUs are $[\text{O}_5\text{Bi}_{12}]^{26+}$ $n = 5$ wide tetrahedra are arranged parallelly and isolated by AsO_4 groups (green), Figure II.42a.

Zn atoms play the roles of our so-called excrescences in a fully ordered manner, but here they are represented as ZnO_4 (yellow) tetrahedra which share one corner with that of AsO_4 . Surprisingly, the external edges of the ribbons are not split and fully occupied by Bi^{3+} atoms.

Table II.10. Crystal data, measurement and structural refinement parameters of Bi₆ZnO₇(AsO₄)₂ and Bi₆ZnO₇(PO₄)₂

	Bi ₆ ZnO ₇ (AsO ₄) ₂	Bi ₆ ZnO ₇ (PO ₄) ₂
Crystal data		
Crystal symmetry	Monoclinic	Monoclinic
space group	<i>C2/c</i>	<i>I2</i>
<i>a</i> (Å)	34.442 (7)	19.7271(5)
<i>b</i> (Å)	5.5044 (11)	5.4376(2)
<i>c</i> (Å)	15.292 (3)	16.9730(6)
β (°)	100.625(9)	131.932(1)
<i>V</i> (Å ³)	2849.4 (10)	1354.46(8)
<i>Z</i>	8	4
<i>D_x</i> (g/cm ³)	7.966	7.950
μ (mm ⁻¹)(0.7107Å)	80.18	79.727
Appearance	Colorless needle	Pale green
Crystal size (mm)	0.12 × 0.06 × 0.04	0.006 × 0.029 × 0.144
Data collection		
λ (Mo K α)(Å)	0.71073	0.71073
Scan mode	ω and ϕ	
θ (min–max)(°)	2.7 – 26.5	1 – 27.48
R(int) (%)	5.9	7.4
Reciprocal space recording	–42 ≤ <i>h</i> ≤ 42	–20 ≤ <i>h</i> ≤ 25
	–6 ≤ <i>k</i> ≤ 6	–7 ≤ <i>k</i> ≤ 7
	–19 ≤ <i>l</i> ≤ 19	–21 ≤ <i>l</i> ≤ 21
Refinement		
Meas., obs., / indep.all	30313, 2676/2921	3011/3011
(obs=I>3 σ (I))		
No. of Refined parameters	143	134
Refinement method	F	F ²
R1(F ²)(obs)/	3.18/ 3.48	3.85/3.85
R1(F ²)(all) (%)		
wR2(F ²)(obs) /wR2(F ²)(all) (%)	4.05/4.14	10.23/10.23
GOF(obs) / GOF(all)	1.93/1.88	1.098
$\Delta\rho_{\max}/\Delta\rho_{\min}$ (e Å ⁻³)	3.68/–2.89	5.531/–3.038
Extinction coefficient	0.0191 (15)	0.00022(2)

The structure of the isostructural Bi₆ZnO₇(PO₄)₂¹²⁸, in general, resembles the one of Bi₆ZnO₇(AsO₄)₂, i.e. the [O₅Bi₁₂]²⁶⁺ *n* = 5 ribbons are surrounded by cation-centered tetrahedra, PO₄ and ZnO₄, Figure II.42b. No split positions was reported neither¹²⁸. The interesting aspect of the two structures is that one (arsenates) crystallizes in the centrosymmetric *C2/c* space group while the phosphate crystallizes in the non-centrosymmetric group *I2* (Table II.10), which can trigger NLO properties.

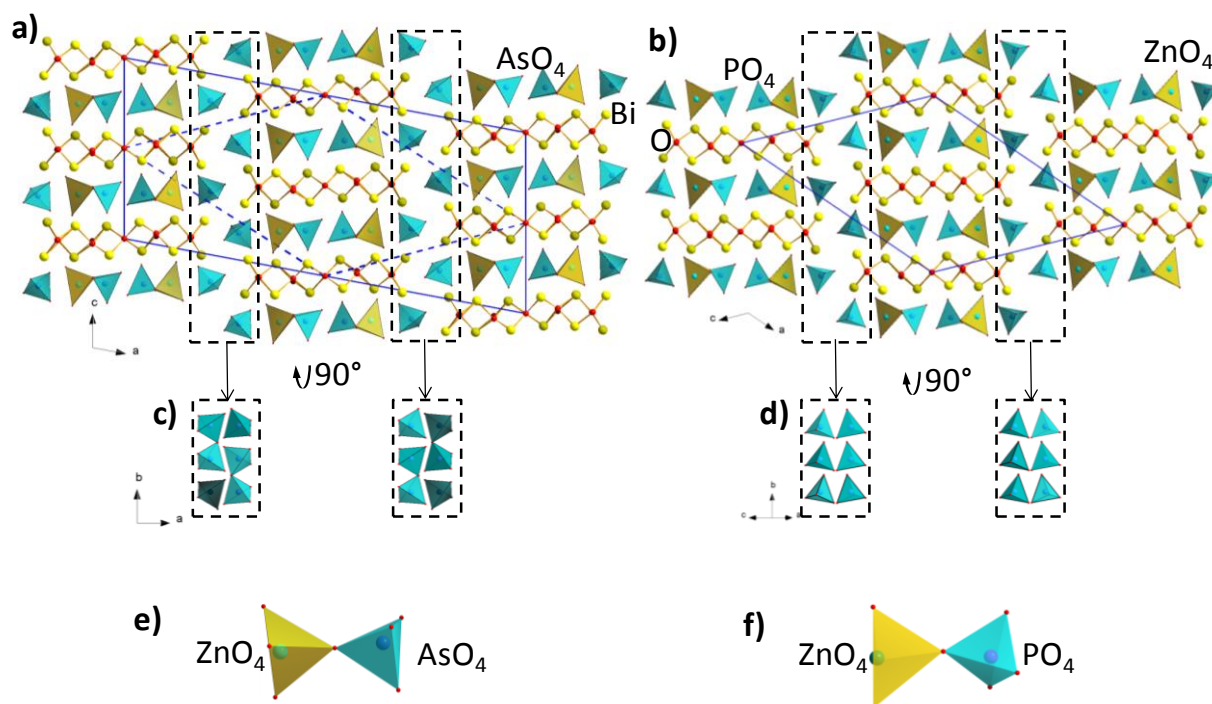


Figure II.42. Crystal structure of a) $\text{Bi}_6\text{ZnO}_7(\text{AsO}_4)_2$ and b) $\text{Bi}_6\text{ZnO}_7(\text{PO}_4)_2$, c) AsO_4 and d) PO_4 tetrahedra of selected regions of the respective structures, e) ZnO_4 and AsO_4 , f) ZnO_4 and PO_4 tetrahedra.

The origin of the absence of the center of inversion is the unilateral arrangement of the PO_4 groups. On the Figure II.42c-d, the rows of XO_4 groups running along the b -2 fold monoclinic axis are compared, and clearly, in the arsenate compound, the AsO_4 are mainly “up” and “down” while a center of inversion related the two individual XO_4 distributions is present (Figure II.42c). This center of symmetry is lost in the phosphate, leading to “up” only tetrahedra (Figure II.42d). The two represented PO_4 areas are related by two-fold axis only.

The local Zn coordinations (Figure II.42e-f) are not really modified by the NCS vs. CS character. The ZnO_4 tetrahedra are rather distorted in the both cases: in the arsenate Zn-O distances are: 1.873 Å, 1.916 Å, 1.952 Å and 2.015 Å and in the phosphate case they are: 1.908 Å, 1.909 Å, 1.943 Å and 2.116 Å. Thus the ZnO_4 tetrahedra in the structure of the arsenate is contracted in comparison to that of the phosphate, which can be explained by the vicinity of bigger AsO_4 in the former case and the neighborhood of smaller PO_4 in the latter case. The next oxygen atom is 3.226 Å away from Zn in the arsenate and 2.714 Å away in the case of phosphate, and belong to XO_4 tetrahedra, that is why the coordination of Zn was chosen to be four.

4) Analogy with the fluorite.

As it is expected, these two isotopic structures, $\text{Bi}_6\text{ZnO}_7(\text{PO}_4)_2$ and $\text{Bi}_6\text{ZnO}_7(\text{AsO}_4)_2$, exhibit a cationic grid close to the ideal fluorite structure of $\delta\text{-Bi}_2\text{O}_3$ due to relatively long sized ($n = 5$) oxo-centered units arranged parallel, as it is shown on Figure II.43a-b on the structure of $\text{Bi}_6\text{ZnO}_7(\text{AsO}_4)_2$.

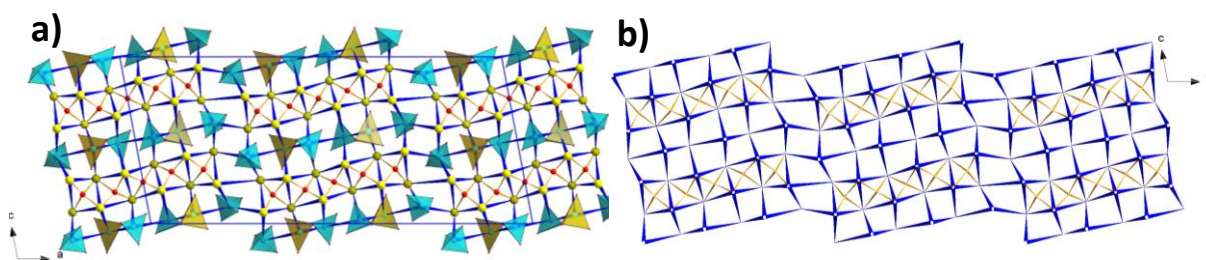


Figure II.43. a) Crystal structure $\text{Bi}_6\text{ZnO}_7(\text{AsO}_4)_2$ and b) its cationic grid representation.

5) NCS \rightarrow CS transition.

It is such that the NCS symmetry of $\text{Bi}_6\text{ZnO}_7(\text{PO}_4)_2$ may appear as fragile, and at least show that the “possible” CS polymorph could exist by tilting of the PO_4 tetrahedra. To travel

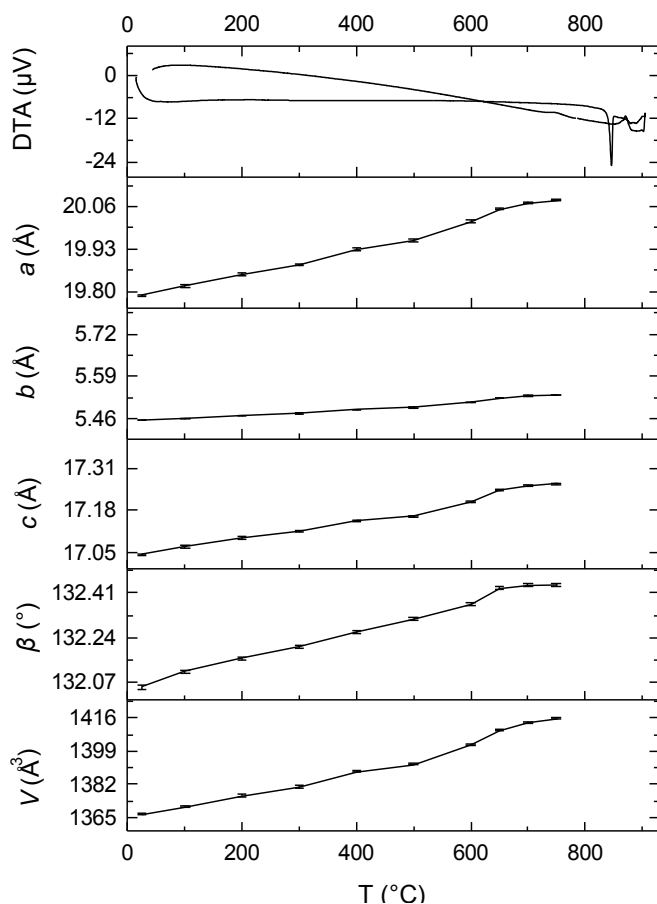


Figure II.44. DTA plot (top graph) and unit-cell parameters evolution of $\text{Bi}_6\text{ZnO}_7(\text{PO}_4)_2$ as functions of temperature

across the possible NCS \rightarrow CS transition on heating two experiments have been performed:

a) A crystal of the CS $\text{Bi}_6\text{ZnO}_7(\text{AsO}_4)_2$ was cooled down to 100K and collected, but no significant structural differences have been observed compared to the RT form (conservation of the $C2/c$ space group)

b) An in-situ HT-XRD analysis was performed to investigate possible symmetrical changes. The DTA analysis shows no particular phenomenon on heating before the melting at 850°C (and recrystallization on cooling), on the top of the Figure II.42. The thermal dependencies of the lattice parameters of $\text{Bi}_6\text{ZnO}_7(\text{PO}_4)_2$ (Figure II.42) indicate a

progressive lattice dilatation with the mean thermal expansion ($1/L_0(\Delta L/\Delta T)$) coefficients along the three crystallographic directions: $\alpha^a = 20.3 \cdot 10^{-6} \text{ }^\circ\text{K}^{-1}$, $\alpha^b = 19.2 \cdot 10^{-6} \text{ }^\circ\text{K}^{-1}$ and $\alpha^c = 16.8 \cdot 10^{-6} \text{ }^\circ\text{K}^{-1}$ showing almost isotropic character of the former. The same order of the values of the expansion coefficients shows no particular direction of potential phosphate reorganization as expected for a progressive tilting. However, an anomaly is detected at 500°C and could be associated to a $\text{NCS} \rightarrow \text{CS}$ displacive transition of the second order (since undetected on DTA). This assumption should be confirmed by extra measurements, but have not been conducted currently because of lack of time.

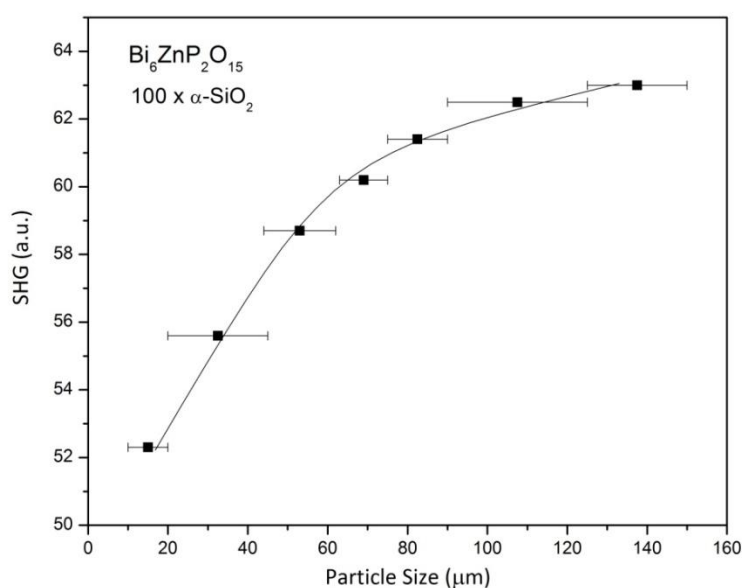


Figure II.45. SHG response vs. particle size of $\text{Bi}_6\text{ZnO}_7(\text{PO}_4)_2$. The line is drawn to guide the eye.

6) SHG measurements on $\text{Bi}_6\text{ZnO}_7(\text{PO}_4)_2$.

Powder SHG measurements were performed using 1064nm radiation by professor Shiv Halasyamani in the Department of Chemistry of University of Houston. The details of the measurements are given in Annex. The SHG results indicate the material is phase-matchable with efficiency of approximately 100 times higher than SiO_2 (Figure II.45). When a material is type 1 phase-matchable it means that the fundamental and second-harmonic wavelengths constructively add as the light propagates through the material. Thus the SHG will increase with particle size and plateau. By observing a SHG signal, we can say that the material is definitely type 1 phase matchable, and thus the refined NCS model is correct.

7) Summary

The structure of new $\text{Bi}_6\text{ZnO}_7(\text{AsO}_4)_2$ is described and compared to that of $\text{Bi}_6\text{ZnO}_7(\text{PO}_4)_2$. The origin of the NCS space group of the latter is discussed. The possibility of CS-NCS transition in the structure of both $\text{Bi}_6\text{ZnO}_7(\text{AsO}_4)_2$ and $\text{Bi}_6\text{ZnO}_7(\text{PO}_4)_2$, have been verified by cooling of the single crystal and powder HT XRD studies, correspondingly.

II.2 Compounds with 2D-units - Layers

II.2.1 Phase homology in new layered mixed Li, M (M = Cu, Cd, Bi...) bismuth oxophosphates and oxoarsenates: $(\text{Bi}_7\text{O}_7)(\text{BiO})_7\text{CdLi}_2(\text{PO}_4)_6$ and $[\text{Bi}_4\text{O}_4][\text{BiO}]_4\text{CuLi}_2(\text{AsO}_4)_4$

1) Synthesis.

1a) $(\text{Bi}_7\text{O}_7)(\text{BiO})_7\text{CdLi}_2(\text{PO}_4)_6$

Powder synthesis: Powder sample of $(\text{Bi}_7\text{O}_7)(\text{BiO})_7\text{CdLi}_2(\text{PO}_4)_6$ was obtained by mixing of Bi_2O_3 , CdO , Li_2CO_3 , $(\text{NH}_4)_2\text{HPO}_4$ in the ratio 7:1:1:6. The produced mixture was loaded into an alumina crucible and heated, first at 300°C then 850°C during 70°C with the subsequent quenching to room temperature. An Energy Dispersive Spectroscopy study confirmed the incorporation of the cations in the expected ratio.

Single crystal: Corresponding single crystals were grown by the melting of appropriate polycrystalline samples in a gold boat at 950°C with the subsequent cooling ($2^\circ\text{C}/\text{hour}$) to room temperature.

1b) $[\text{Bi}_4\text{O}_4][\text{BiO}]_4\text{CuLi}_2(\text{AsO}_4)_4$

Powder synthesis: Powder sample of $[\text{Bi}_4\text{O}_4][\text{BiO}]_4\text{CuLi}_2(\text{AsO}_4)_4$ was obtained by heating of the mixture of stoichiometric amounts of Bi_2O_3 , CuO , Li_2CO_3 , As_2O_5 in alumina crucible at 750°C during 70 hours with the subsequent quenching to room temperature.

Single crystal: Corresponding single crystals were grown by the melting of appropriate polycrystalline samples in a gold boat at 950°C with the subsequent cooling ($2^\circ\text{C}/\text{hour}$) to room temperature.

2) Structural description.

2a) $(\text{Bi}_7\text{O}_7)(\text{BiO})_7\text{CdLi}_2(\text{PO}_4)_6$

The crystal structure of $(\text{Bi}_7\text{O}_7)(\text{BiO})_7\text{CdLi}_2(\text{PO}_4)_6$ is very similar to that of $[\text{Bi}_7\text{O}_7][\text{BiO}]_7\text{Bi}_{0.67}\text{Li}_2(\text{PO}_4)_6$ reported by Muktha et al.¹²⁹ and Arumugam et al.¹²⁸, which are based upon the $[\text{Bi}_2\text{O}_2]^{2+}$ infinite layers with attached $[\text{BiO}]^+$ dimers, as it is shown on the (Figure II.46a-b). Also, note the identical $(-\text{PO}_4-\text{BiO}-\text{PO}_4-\text{BiO}-\text{PO}_4-)$ sequences in the both structures. However, the coordination of lithium cations in the tunnels is different (Figure II.46c).. In the structure of $[\text{Bi}_7\text{O}_7][\text{BiO}]_7\text{Bi}_{0.67}\text{Li}_2(\text{PO}_4)_6$, Li atoms possess a tetrahedral coordination (Li-O distances: 1.86 Å, 1.98 Å, 2.05 Å and 2.13 Å), whereas in $(\text{Bi}_7\text{O}_7)(\text{BiO})_7\text{CdLi}_2(\text{PO}_4)_6$ they are in rectangular pyramid configuration (Li-O distances: 1.82 Å, 2x2.07 Å and 2x2.41 Å).

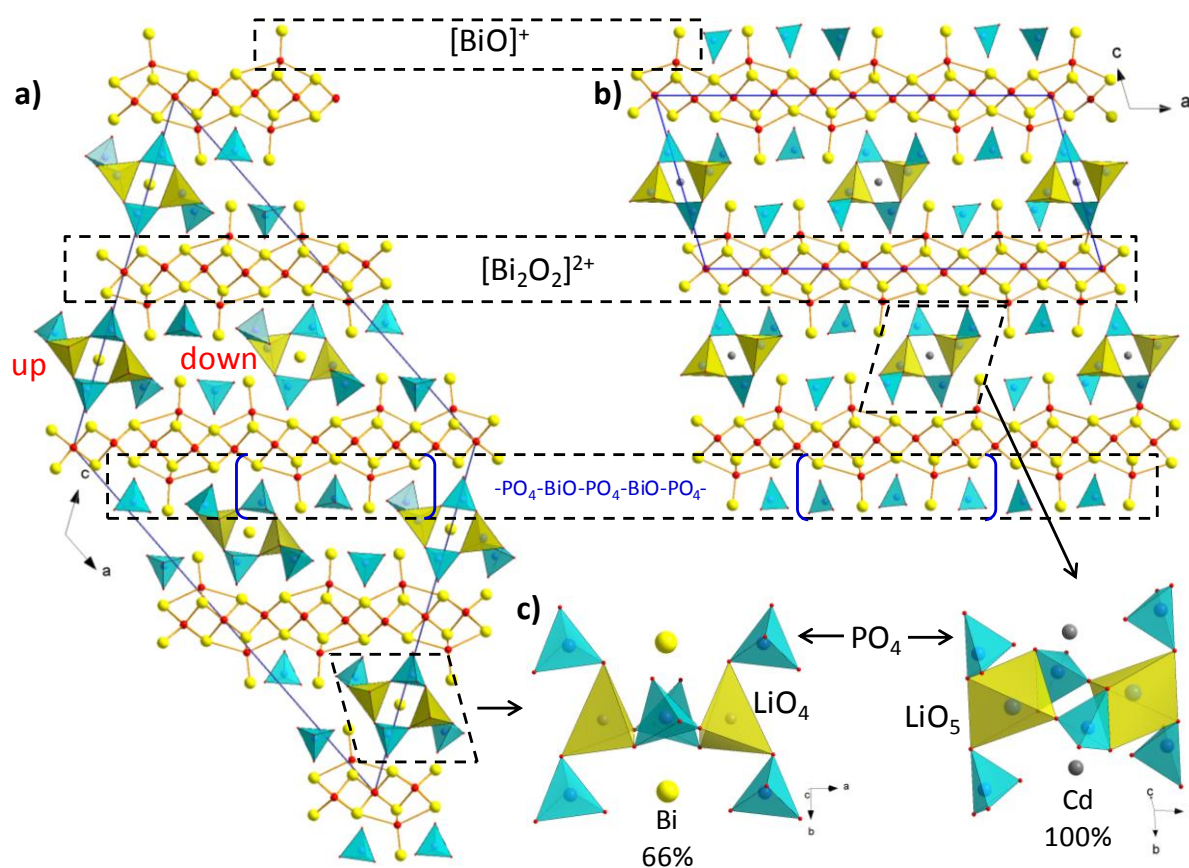


Figure II.46. Projections of the crystal structures of a) $[\text{Bi}_7\text{O}_7][\text{BiO}]_7\text{Bi}_{0.67}\text{Li}_2(\text{PO}_4)_6$ and b) $(\text{Bi}_7\text{O}_7)(\text{BiO})_7\text{CdLi}_2(\text{PO}_4)_6$ along the b-axis, c) phosphate-lithium tunnels with the incorporated cations along the b axis. The similarities in the structure are given with dashed rectangulars. LiO_4 tetrahedra in the up and down orientation (labeled in red) for $[\text{Bi}_7\text{O}_7][\text{BiO}]_7\text{Bi}_{0.67}\text{Li}_2(\text{PO}_4)_6$.

The observed difference is obviously the result of different tiltings of the PO_4 tetrahedra located on the side of the channels. It is worth to note that partially occupied Bi site in

[Bi₇O₇][BiO]₇Bi_{0.67}Li₂(PO₄)₆ is coordinated by eight oxygen atoms with the Bi-O bond lengths equal to 2×2.43 Å, 2×2.38 Å, 2×2.65 Å and 2×2.70 Å. The vacancies present in the Bi sites are probably responsible for the relaxation of the neighboring PO₄ tetrahedra, which had not been discussed earlier by Muktha et al.¹²⁹ and Arumugam et al.¹²⁸. The fully occupied Cd²⁺ site is 6-coordinated with the Cd-O bond lengths equal to 2×2.09 Å and 4×2.47 Å. The doubling of the *a* and *c* parameters in the structure of [Bi₇O₇][BiO]₇Bi_{0.67}Li₂(PO₄)₆ results from the different “up” and “down” orientations of PO₄ tetrahedra relative to the *ac* plane (Figure II.46a). In that structure, all the LiO₄ tetrahedra point toward the same axis direction within the channels. In contrast, the LiO₅ pyramids in the structure of (Bi₇O₇)(BiO)₇CdLi₂(PO₄)₆, do not display any particular orientation (Figure II.46b).

2b) [Bi₄O₄][BiO]₄CuLi₂(AsO₄)₄

The crystal structure of [Bi₄O₄][BiO]₄CuLi₂(AsO₄)₄ is also based on the [Bi₂O₂]²⁺ infinite layers. However, the [BiO]⁺ dimers are attached to the [Bi₂O₂]²⁺ layer with the periodicity of every three OBi₄ tetrahedra (Figure II.47).

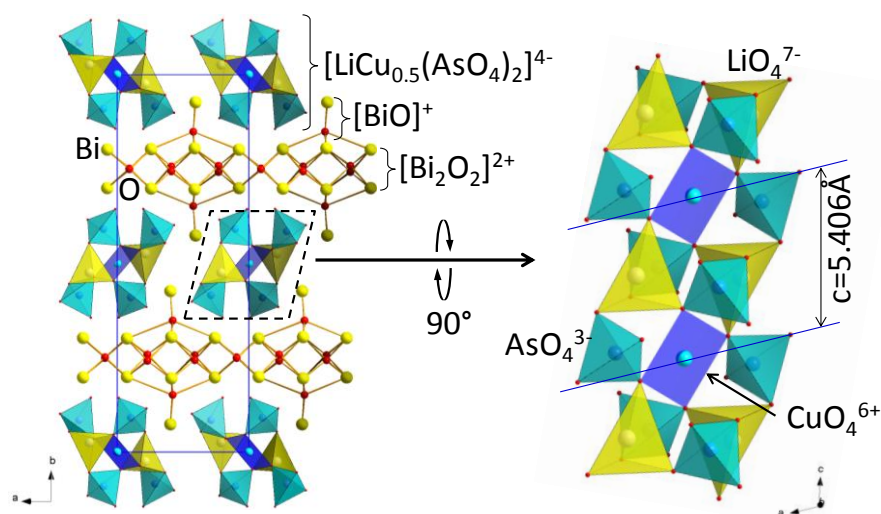


Figure II.47. General projection of the crystal structure of [Bi₄O₄][BiO]₄CuLi₂(AsO₄)₄ along the *c* axis (right). The structure of [LiCu_{0.5}(AsO₄)₂]⁴⁻ as the AsO₄-LiO₄ tunnel with the incorporated Cu is shown as projection along the *b* axis.

The arrangement of the AsO₄ tetrahedra delineates interlayer channels occupied by the Li⁺ and Cu²⁺ cations. As a result, linkage of the LiO₄ tetrahedra, AsO₄ tetrahedra and CuO₄ square planes produces [LiCu_{0.5}(AsO₄)₂]⁴⁻ columns parallel to the *c* axis. It should be noted that the CuO₄ square planes are quite regular with the Cu-O bond lengths of 1.950 (2×) and 1.936 (2×) Å.

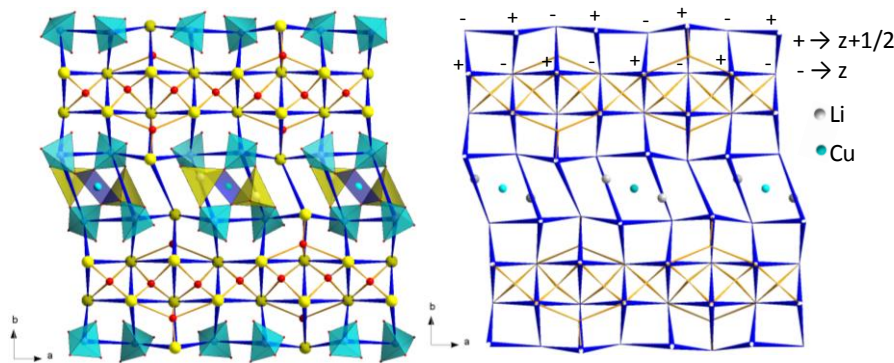


Figure II.48. General projection of the crystal structure of $[\text{Bi}_4\text{O}_4][\text{BiO}]_4\text{CuLi}_2(\text{AsO}_4)_4$ along the b axis and its corresponding 2D-square network.

In the structure of $[\text{Bi}_4\text{O}_4][\text{BiO}]_4\text{CuLi}_2(\text{AsO}_4)_4$, the interlayer block strongly resembles that observed in $[\text{Bi}_2\text{O}_2][\text{BiO}]_2M_2(\text{PO}_4)_2$ ($M = \text{Mg}, \text{Zn}$)³⁹, where one M^{2+} channel cations are

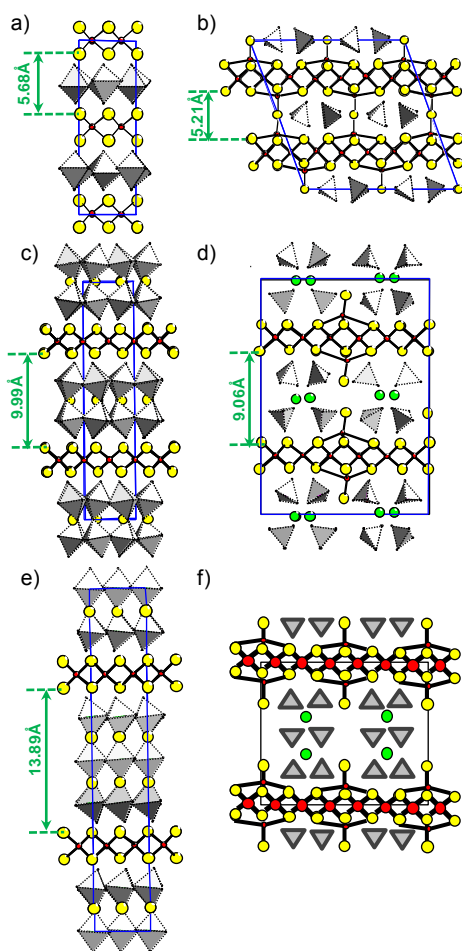


Figure II.49 Relationship and ratio (m) of $[\text{Bi}_2\text{O}_2]^{2+}$ and $[\text{BiO}]/(\text{XO}_4)$ stacking sequences in Aurivillius phases and bismuth oxophosphates: a) $k = 1$ in BiWO_6 , b) $k = 1$ in $\text{Bi}_6\text{Zn}(\text{PO}_4)\text{F}_2$, c) $k = 2$ in $\text{Bi}_3\text{TiNbO}_9$, d) $k = 2$ in $[\text{Bi}_2\text{O}_2][\text{BiO}]_2M(\text{PO}_4)_2$ ($M = \text{Mg}, \text{Zn}$), e) $k = 3$ in $\text{Bi}_4\text{Ti}_3\text{O}_{12}$ and f) $k = 3$ in a hypothetical compound.

replaced by two Li^+ . The AsO_4 tetrahedra are tilted in a different way relative to $y = 0$ and $y = 1/2$, which results in a slight shift of the adjacent $[\text{Bi}_2\text{O}_2]^{2+}$ layers responsible for the doubling of the b -axis in the structure of $[\text{Bi}_4\text{O}_4][\text{BiO}]_4\text{CuLi}_2(\text{AsO}_4)_4$.

The corresponding 2D-square cationic network is shown in Figure II.48. The layers based upon the oxocentered tetrahedra are regular, whereas the interlayer hosting Li^+ and Cu^{2+} is strongly distorted.

3) Relationship with Aurivillius compounds.

There is a strong structural relationship between the $[\text{Bi}_2\text{O}_2](\text{A}_{k-1}\text{B}_k\text{O}_{3k+1})$ ($A = \text{Na}, \text{K}, \text{Ca}, \text{Sr}, \text{Ba}, \text{Bi}, \dots$, $B = \text{Fe}, \text{Cr}, \text{Ti}, \text{Ga}, \text{Nb}, \text{V}, \text{Mo}, \text{W}$) Aurivillius compounds^{130,131} with single perovskite slabs ($k = 1$) sandwiched in between the $[\text{Bi}_2\text{O}_2]^{2+}$ layers and the structures of $\text{Bi}_6\text{TiP}_2\text{O}_{16}$ ¹³² and $\text{Bi}_6(\text{M}, \text{Bi})_1\text{P}_2(\text{O}, \text{F})_{16-x}$ ($M = \text{Cu}, \text{Zn}, \dots$)¹³³ (Figure II.49a,b). In the latter compound, two MO_6 octahedra are replaced by the PO_4 groups, similarly to the reduced form of $\text{Bi}_4\text{V}_2\text{O}_{11}$ ¹⁰⁵, where V^{4+}O_6 polyhedra are surrounded by two V^{5+}O_4 groups each. The typical thickness of the

interlayer between two adjacent $[\text{Bi}_2\text{O}_2]^{2+}$ layers is ~ 5.2 Å in all the compounds mentioned above. The $[\text{BiO}]^+$ dimers and the XO_4 groups can also be considered as substituting octahedral cations of the perovskite slab of Aurivillius phases in the structure $[\text{Bi}_4\text{O}_4][\text{BiO}]_4\text{CuLi}_2(\text{AsO}_4)_4$. However, a doubling of the thickness of the interlayer block is achieved by the incorporation of a second row of cation and anion species so that the distance between the adjacent $[\text{Bi}_2\text{O}_2]^{2+}$ layers is increased to ~ 9.1 Å in $[\text{Bi}_2\text{O}_2][\text{BiO}]_2\text{Mg}(\text{PO}_4)_2$ ³⁹ and to 9.6 Å in the structure of $[\text{Bi}_4\text{O}_4][\text{BiO}]_4\text{CuLi}_2(\text{AsO}_4)_4$. From this point of view, the structure of $[\text{Bi}_2\text{O}_2][\text{BiO}]_2(\text{Mg,Zn})(\text{PO}_4)_2$ as well as that $[\text{Bi}_4\text{O}_4][\text{BiO}]_4\text{CuLi}_2(\text{AsO}_4)_4$ can be considered as derivatives of the Aurivillius phases with $k = 2$ ¹³⁴ (Figure II.49c,d). This observation is relevant and allows to assume that further expansion of the $[\text{BiO}]/(\text{XO}_4)$ ($X = \text{P}, \text{As}$) interlayer is possible. Furthermore, the possibility to replace the atoms incorporating in the tetrahedral channels by the variety of aliovalent cations looks very promising in the sense of the syntheses of novel Aurivillius-phase-related compounds with various interlayer thicknesses ($k = 1, 2, 3 \dots$) (Figure II.49e). The idealized hypothetical $k = 3$ case is shown in Figure II.49f. The general principles and the key parameters for the prediction of new structural archetypes within the studied class of compounds have been formulated recently⁴⁰. Nevertheless, the difficulties to predict the optimal experimental conditions and size of incorporated cations for the elaboration of predicted structural architectures should be taken into account.

4) Summary

The structural description of the new terms, $[\text{Bi}_7\text{O}_7][\text{BiO}]_7\text{Bi}_{0.67}\text{Li}_2(\text{PO}_4)_6$ and $(\text{Bi}_7\text{O}_7)(\text{BiO})_7\text{CdLi}_2(\text{PO}_4)_6$, of so-called “infinite” series is given. Similarities in the structure of the latter to $[\text{Bi}_7\text{O}_7][\text{BiO}]_7\text{Bi}_{0.67}\text{Li}_2(\text{PO}_4)$ highlighted. A structural relationship of the two obtained compounds to the Aurivillius phases $[\text{Bi}_2\text{O}_2](\text{A}_{k-1}\text{B}_k\text{O}_{3k+1})$, $\text{Bi}_6\text{TiP}_2\text{O}_{16}$ and $\text{Bi}_6(\text{M,Bi})_1\text{P}_2(\text{O,F})_{16-x}$, has been shown and a possibility to extend the structural type further on has been suggested briefly.

II.2.2 The new $[\text{PbBi}_2\text{O}_4][\text{Bi}_2\text{O}_2]\text{Cl}_2$ and $[\text{PbmBi}_{10-m}\text{O}_{13}][\text{Bi}_2\text{O}_2]_m\text{Cl}_{4+m}$ series by association of sizeable subunits; Relationship with the Arppe's compound $\text{Bi}_{24}\text{O}_{31}\text{Cl}_{10}$

1) Generalities.

The compound $\text{Bi}_{24}\text{O}_{31}\text{Cl}_{10}$ (also known as the “Arppe's compound”) is a product of the thermal decomposition of BiOCl , which has been known since 1845.¹³⁵ It is formed of rarely observed crenel-like 2D-layers of OBi_4 tetrahedra separated by single Cl^- layers. Its crystal

structure was first resolved by Sillen and Edstrand in 1942⁶¹, while it was revised in doubled unit cell in 2000.¹³⁶ Here we present a novel homologous series related to the original Arppe's compound by modification of the topology of the crenel-layers by incorporation of Pb^{2+} cations with the general formula $[\text{Pb}_m\text{Bi}_{10-m}\text{O}_{13}][\text{Bi}_2\text{O}_2]_m\text{Cl}_{4+m}$ ($m = 1, 2, 3$ and 4) and related compound $[\text{PbBi}_2\text{O}_4][\text{Bi}_2\text{O}_2]\text{Cl}_2$ ($=\text{PbBi}_4\text{O}_6\text{Cl}_2$). The structure of the Arppe's compound, $\text{Bi}_{24}\text{O}_{31}\text{Cl}_{10}$, was first refined in 1942 (space group $A2/m$, $a = 9.99 \text{ \AA}$, $b = 3.97 \text{ \AA}$, $c = 29.44 \text{ \AA}$, $\beta = 88.7^\circ$) and revised one decade ago in the $a, 2b, c$ supercell (space group $P2/c$)^{61,136}, see the Table II.11.

Table II.11 Crystal data, measurement and structural refinement parameters of the studied derivatives of $\text{Bi}_{24}\text{O}_{31}\text{Cl}_{10}$

	$\text{Bi}_{24}\text{O}_{31}\text{Cl}_{10}$ ¹³⁶	$\text{Bi}_{24}\text{O}_{31}\text{Cl}_{10}$	$[\text{Bi}_8\text{Pb}_2\text{O}_{13}][\text{Bi}_2\text{O}_2]_2\text{Cl}_6$ $m = 2$	$[\text{Bi}_7\text{Pb}_3\text{O}_{13}][\text{Bi}_2\text{O}_2]_3\text{Cl}_7$ $m = 3$	$[\text{Bi}_6\text{Pb}_4\text{O}_{13}][\text{Bi}_2\text{O}_2]_4\text{Cl}_8$ $m = 4$	$\text{PbBi}_4\text{O}_6\text{Cl}_2$
Crystal data						
Crys. symmetry	Monoclinic		Monoclinic			Tetragonal
space group	$P2/c$		$C2/m$			$I4/mmm$
a (Å)	10.033(2)	29.486(2)	29.671(2)	29.681(2)	29.783(2)	3.9488(4)
b (Å)	7.9745(16)	3.9683(3)	3.9692(2)	3.9630(2)	3.9639(2)	
c (Å)	29.552(6)	10.0361(8)	12.2477(5)	15.1047(8)	18.3770(9)	31.038 (7)
β (°)	88.742(4)	90.989(4)	107.492(2)	118.387(2)	125.828(2)	
V (Å ³)	2363.8(8)	1174.1(2)	1375.7(2)	1563.0(2)	1759.0(2)	483.98(13)
Z	2	2	2	2	2	2
D_x (g/cm ³)	8.242	8.285	8.233	8.278	8.272	8.303
μ (mm ⁻¹) (for λ K $\alpha=0.7107 \text{ \AA}$)	89.601	90.191	89.819	90.358	90.335	90.355
Appearance	Pale green	Pale green	Pale green	Pale green	Pale green	Pale green
Data collection						
λ (Mo K α) (Å)	0.71073	0.71073	0.71073	0.71073	0.71073	0.71073
Scan mode	ω and φ	ω and φ	ω and φ	ω and φ	ω and φ	ω and φ
θ (min–max)(°)	1.38±28.33	1.4–26.4	1.4–30.5	1.5–25.9	1.4–28.3	2.6–26.4
R(int) (%)	0.1299	0.029	0.045	0.048	0.033	0.047
Recording	$-13 \leq h \leq 13$	$-36 \leq h \leq 36$	$-42 \leq h \leq 42$	$-30 \leq h \leq 35$	$-36 \leq h \leq 38$	$-4 \leq h \leq 4$
reciprocal	$-10 \leq k \leq 0$	$-4 \leq k \leq 4$	$-5 \leq k \leq 5$	$-3 \leq k \leq 4$	$-5 \leq k \leq 4$	$-4 \leq k \leq 4$
space	$0 \leq l \leq 39$	$-12 \leq l \leq 12$	$-17 \leq l \leq 17$	$-17 \leq l \leq 18$	$-24 \leq l \leq 24$	$-37 \leq l \leq 38$
Refinement						
Measured, independent obs.* refl.	5546	10423, 1381, 1236	23978, 2401, 1726	8176, 1404, 1054	15348, 2481, 1836	849, 192, 161
# Ref. param.	218	77	122	102	153	16
Refin. method,	F^2	F^2	F^2	F^2	F^2	F^2
$R1(F^2)$ (obs) / $R1(F^2)$ (all)	0.063	0.0375/ 0.0415	0.0356/ 0.0524	0.0358/ 0.0495	0.0292/ 0.0430	0.059/ 0.0661
$wR2(F^2)$ (obs) / $wR2(F^2)$ (all)	0.146	0.0361/ 0.0375	0.0374/ 0.0459	0.0459/ 0.0483	0.0289/ 0.0348	0.0610/ 0.0639
GOF(obs) / GOF(all)		0.68/0.67	0.66/0.68	1.99/1.79	0.47/0.48	1.75/1.66
$\Delta\rho_{\text{max}} / \Delta\rho_{\text{min}}$ (e Å ⁻³)	5.984/ -6.162	6.83 / -6.14	4.70 / -4.19	2.40 / -2.77	3.69/ -3.26	7.08/ -3.27

Its crystal structure projected along the b -axis is shown on the Figure II.50a. It is formed of crenel-like infinite $[\text{Bi}_{24}\text{O}_{30}]^{10+}$ layers separated by single $[\text{Cl}_{10}]^{10-}$ layers.

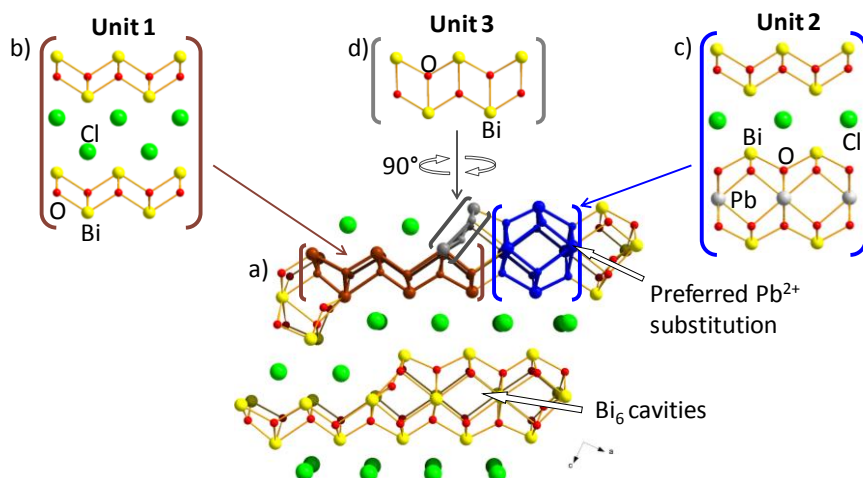


Figure II.50. (a) Structure of Arppe's compound as an assembly of building units: (b) unit 1, (c) unit 2, (d) unit 3.

From the viewpoint of modular chemistry it is convenient to identify and formulate elementary units for the description/design of new compounds. In this frame, the $[\text{Bi}_{24}\text{O}_{30}]^{10+}$ layers can be sliced into three building units:

Units 1: The Bi/O modules which are formed of a linear portion of a fluorite like $[\text{Bi}_2\text{O}_2]^{2+}$ layer, see Figure II.50b. Similar layers are well known and found for instance in the BiOCl crystal structure denoted (X2) due to the double-thickness of the chloride layers⁹⁰, see Figure II.51a.

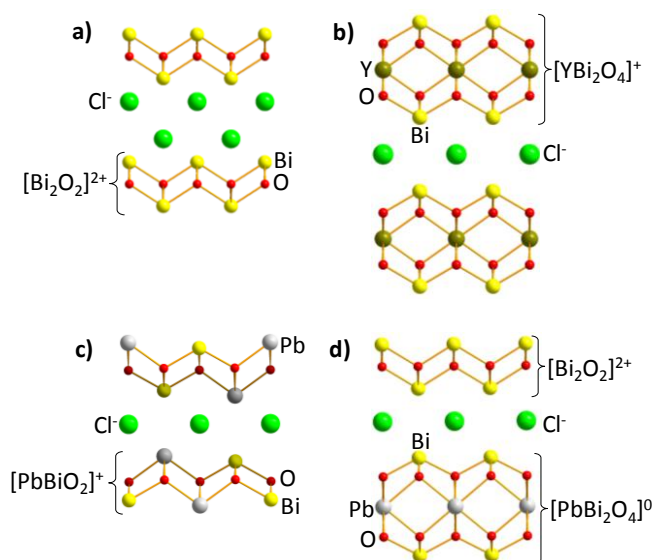


Figure II.51. Evidence of layered modules in the crystal structures of a) BiOCl , b) $\text{Bi}_2\text{LnO}_4\text{Cl}$, c) PbBiO_2Cl and d) $\text{PbBi}_4\text{O}_6\text{Cl}_2$ (this work)

Units 2: Thicker modules play the role of “stairs”, in the 2D-crenel topology of $[\text{Bi}_{24}\text{O}_{30}]^{10+}$ layers, Figure II.50c. They mainly correspond to portions of “3-cations thick” fluorite layers portions similar to $[\text{BaBi}_2\text{O}_4]^0$ found $\text{BaBi}_4\text{O}_6\text{Cl}_2$ ⁵⁶ with Bi^{3+} replacing the central Ba^{2+} cations. Here we will describe the new compound $\text{PbBi}_4\text{O}_6\text{Cl}_2$ with Pb^{2+} in these central sites Figure II.51b. As detailed below, in the Arppe’s compound $\text{Bi}_{24}\text{O}_{31}\text{Cl}_{10}$, central cavities created by Bi_6 octahedra are partially occupied by extra oxygen atoms (O_{octa}). Our reinvestigation of the Arppe’s crystal structure agrees well with that point, but as it is shown later the incorporation of Pb^{2+} into these units systematically removes this interstitial anion. The condensation between **units 1** and **units 2** is performed by edge sharing of OBi_4 tetrahedra and involves a third unit (**unit 3**) bordering the junction.

Units 3: The outer side of the “stair” is formed by a chain of partially filled anion-centered $(\text{O}, \square)\text{Bi}_3$ triangles, Figure II.50d. These kind of bordering OBi_3 -based units are often found in compounds made of finite or infinite topologies of OBi_4 triangles with square angles corners such as columns open tunnels, crenel-planes.^{25,87} For instance, the structure of $\text{Bi}_9\text{A}_2\text{ClO}_{18}$ ($\text{A} = \text{P}, \text{As}$) was recently re-described using similar sub-units.³⁴

2) Syntheses

All the crystals were found in polyphasic residues from the heating of the mixtures of precursors given below case by case. The starting mixtures were loaded into gold tubes, sealed then heated at 900°C during 10 hours and then slowly cooled (1°C/h) down to 600°C. The furnace was then switched off and crystals were handly selected and in the cases where fluxes were used washing with hot water was required to separate crystals from the flux. The following reagents with their respective purities have been used in the syntheses: Bi_2O_3 (Aldrich 99.9%), BiOCl (Alfa Aesar, ultrapure), PbCl_2 (Alfa Aesar, 99.9%), PbO (Aldrich, 99.9%).

The Table II.12 gives a summary of our attempts to prepare polycrystalline compounds of the several phases concerned in this work according to the $[\text{Pb}_m\text{Bi}_{10-m}\text{O}_{13}][\text{Bi}_2\text{O}_2]_m\text{Cl}_{4+m}$ formulation or using slight deviations of the Bi/Pb ratio in various experimental conditions.

2a) $\text{Bi}_{24}\text{O}_{31}\text{Cl}_{10}$ (Arppe’s compound).

The crystals of $\text{Bi}_{24}\text{O}_{31}\text{Cl}_{10}$ were found in the polycrystalline residue from the melt of 10 (wt%) of the $(4\text{BiOCl} + 3\text{KMnO}_4)$ mixture in 90 (wt%) of KCl which was taken as a flux. Note that in the recent literature crystals of this compound were grown from a mixture of BiCl_3 and Bi_2O_3 in 1:3.1 ratio at 450°C K in a sealed quartz ampoule.¹³⁶

Table II.12. Conditions and results of the attempts to reproduce the compounds in the form of powder (u.p. denote unknown peaks)

n	Formulation	Formula	T, °C	Conditions	Phase found
1	$\text{PbmBi}_{10-m}\text{O}_{13}[\text{Bi}_2\text{O}_2]_m\text{Cl}_{4+m}$	$\text{Bi}_9\text{PbO}_{13}[\text{Bi}_2\text{O}_2]\text{Cl}_5$	750	sealed tube	m=2 + weak amount u.p.
		$\text{Bi}_9\text{PbO}_{13}[\text{Bi}_2\text{O}_2]\text{Cl}_5$	730, 750	air	m=1 + $\text{Bi}_{24}\text{O}_{31}\text{Cl}_{10}$ + u.p.
	slight chemical deviation from formulation	$\text{Bi}_{9.5}\text{Pb}_{0.5}\text{O}_{13.25}[\text{Bi}_2\text{O}_2]\text{Cl}_5$	800	sealed tube	m=1 + m=2 + $\text{Bi}_{24}\text{O}_{31}\text{Cl}_{10}$ + u.p.
		$\text{Bi}_{9.66}\text{Pb}_{0.34}\text{O}_{13}[\text{Bi}_2\text{O}_2]\text{Cl}_5$	700, 720	air	m=1 + $\text{Bi}_{24}\text{O}_{31}\text{Cl}_{10}$ + $\text{Bi}_3\text{O}_4\text{Cl}$
2	$\text{PbmBi}_{10-m}\text{O}_{13}[\text{Bi}_2\text{O}_2]_m\text{Cl}_{4+m}$	$\text{Bi}_8\text{Pb}_2\text{O}_{13}[\text{Bi}_2\text{O}_2]_2\text{Cl}_6$	750	sealed tube	m=2 single phase
	slight chemical deviation from formulation	$\text{Bi}_{8.5}\text{Pb}_{1.5}\text{O}_{13.25}[\text{Bi}_2\text{O}_2]_2\text{Cl}_6$	800	sealed tube	m=2+ $\text{Pb}_4\text{Cl}_2\text{O}_4$ + $\text{Pb}_{0.89}\text{Bi}_{12}\text{O}_{19.78}$ + u.p.
		$\text{Bi}_{8.66}\text{Pb}_{1.34}\text{O}_{13}[\text{Bi}_2\text{O}_2]_2\text{Cl}_6$	720	air	m=2 + minor u.p.
		$\text{Bi}_9\text{PbO}_{13}[\text{Bi}_2\text{O}_2]_2\text{Cl}_6$	700	air	m=2 + minor u.p.
3	$\text{PbmBi}_{10-m}\text{O}_{13}[\text{Bi}_2\text{O}_2]_m\text{Cl}_{4+m}$	$\text{Bi}_7\text{Pb}_3\text{O}_{13}[\text{Bi}_2\text{O}_2]_3\text{Cl}_7$	720	air	m=3 + $\text{Bi}_{12}\text{O}_{17}\text{Cl}_2$ + β - Bi_2O_3 + PbBiO_2Cl +u.p.
	slight chemical deviation from formulation	$\text{Bi}_{7.5}\text{Pb}_{2.5}\text{O}_{13.25}[\text{Bi}_2\text{O}_2]_3\text{Cl}_7$	800	sealed tube	m=3 + PbBiO_2Cl + u.p.
		$\text{Bi}_{7.66}\text{Pb}_{2.34}\text{O}_{13}[\text{Bi}_2\text{O}_2]_3\text{Cl}_7$	700, 720	air	m=3 + major u.p.
4	$\text{PbmBi}_{10-m}\text{O}_{13}[\text{Bi}_2\text{O}_2]_m\text{Cl}_{4+m}$	$\text{Bi}_6\text{Pb}_4\text{O}_{13}[\text{Bi}_2\text{O}_2]_4\text{Cl}_8$	720	air	m=4 + PbBiO_2Cl + u.p.
	slight chemical deviation from formulation	$\text{Bi}_{6.5}\text{Pb}_{3.5}\text{O}_{13.25}[\text{Bi}_2\text{O}_2]_4\text{Cl}_8$	800	sealed tube	m=4 + PbBiO_2Cl
		$\text{Bi}_{6.66}\text{Pb}_{3.34}\text{O}_{13}[\text{Bi}_2\text{O}_2]_4\text{Cl}_8$	720	air	m=4 + PbBiO_2Cl + u.p.

2b) $[\text{Pb}_2\text{Bi}_8\text{O}_{13}][\text{Bi}_2\text{O}_2]_2\text{Cl}_6$ (m = 2 term).

The crystals were found in the melt of the mixture $3\text{Bi}_2\text{O}_3 + 6\text{BiOCl} + \text{PbO} + \text{CuO}$. The powder was obtained as a single polycrystalline phase from the stoichiometric mixture of PbCl_2 , Bi_2O_3 and BiOCl heated with several intermediate grindings at 750°C in an evacuated quartz ampoule. It was identified by comparison to the theoretical XRD pattern calculated from the refined crystal structure, Table II.12. The lattice parameters refined from the powder diffraction are $a = 29.6643(8) \text{ \AA}$, $b = 3.9694(2) \text{ \AA}$, $c = 12.2489(4) \text{ \AA}$, $\beta = 107.39(2)^\circ$ which confirms the preparation of the m = 2 term.

2c) $[\text{Bi}_7\text{Pb}_3\text{O}_{13}][\text{Bi}_2\text{O}_2]_3\text{Cl}_7$ (m = 3 term) and $[\text{Bi}_6\text{Pb}_4\text{O}_{13}][\text{Bi}_2\text{O}_2]_4\text{Cl}_8$ (m = 4 term).

The crystals were obtained from the same melt of composition $2\text{PbCl} + 5\text{BiOCl} + 5\text{Bi}_2\text{O}_3$. The attempts to reproduce them in powder as a pure phase were unsuccessful. However the peaks of the theoretical patterns, calculated from the respective single crystal XRD data, were found systematically in preparations which validate the possibility to prepare the phases, Table II.12.

2d) $\text{PbBi}_4\text{O}_6\text{Cl}_2$.

The crystals were found in the molten residue of 5 (wt%) of the $(2\text{PbO} + 3\text{Bi}_2\text{O}_3 + 6\text{MnO}_2)$ mixture in the flux of $(6\text{Bi}_2\text{O}_3 + 6\text{BiOCl})$ 95 (wt%). The corresponding powder was obtained as a single polycrystalline phase from the stoichiometric mixture of PbCl_2 and Bi_2O_3 heated at 750°C in an alumina crucible, after several intermediate grindings. It was obtained as a single phase, see Table II.12. The lattice parameters refined from the powder diffraction pattern lead to $a = 3.9539(8) \text{ \AA}$ and $c = 31.072(2) \text{ \AA}$ in good adequation with the lattice parameters refined from the single crystal data (see Table II.11)

3) Structural description for the related series**3a) Arppe's compound - $\text{Bi}_{24}\text{O}_{31}\text{Cl}_{10}$.**

In the most recent model refined by Eggenweiler et al.¹³⁶ two main crystallographic features are responsible for the b -axis doubling, see Figure II.52a. First, the ordering of the oxygen atoms (O_{octa}) in half of the Bi_6 cavities of the stair-like junctions (**units 2**), Figure II.52b. Second, the fully ordered O/Bi arrangement at the bordering sites of the thick junctions (**units 3**), giving a sequence of OBi_2 and OBi_3 units ordered along the b -axis, see Figure II.52d.

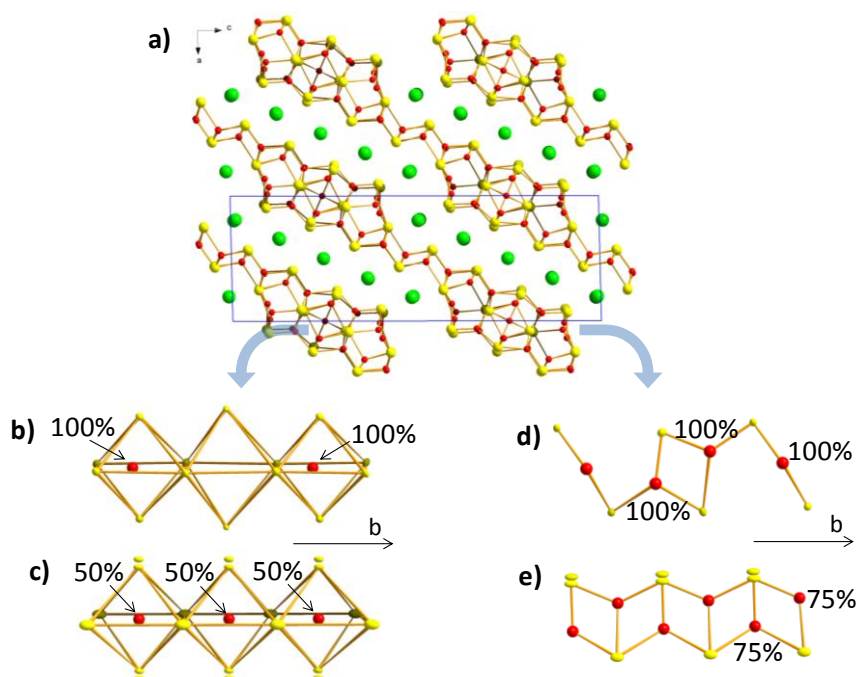


Figure II.52. a) Crystal structure of Arppe's compound. Occupancy of oxygen atoms in the Bi_6 cavities: b) according to ref [¹³⁶], c) according to our refinement in the subcell. Ordered O/Bi arrangement in the bordering units 3: d) from ref [¹³⁶], e) according to our refinement in the subcell.

The oxygen occupancies were constrained to obtain the same stoichiometry as the fully ordered model which involves 50% occupancy of O_{octa} ($=\text{O}_9$), and 75% occupancy of two

oxygen atoms of the **units 3**, (see Annex IV.28)). A similar oxygen distribution will be used for all new compounds related to the Arppe's compound, to be further presented. The expansion or not of the crystal structure in a doubled b supercell most probably pictures an ideal ordering reached in particular equilibrium conditions while our standard synthesis conditions likely generate local ordered domains only. We note that Eggenweiler *et al.* did not succeed refining a supercell model for the isostructural oxobromide $\text{Bi}_{24}\text{O}_{31}\text{Br}_{10}$.¹³⁶

3b) $\text{Bi}^{3+}/\text{Pb}^{2+}$ ordering in the new $\text{PbBi}_4\text{O}_6\text{Cl}_2$.

Taking into account the need for identification of different modules that assemble in the series of new compound described above, the new $\text{PbBi}_4\text{O}_6\text{Cl}_2$ appears as a parent term. It crystallizes in the $I4/mmm$ space group ($a = 3.9488(4)$ Å, $c = 31.038(7)$ Å) with a layered structure which corresponds to the stacking sequence $[\text{Bi}_2\text{O}_2]^{2+} [\text{Cl}]^- [\text{PbBi}_2\text{O}_4]^0 [\text{Cl}]^-$ (Figure II.51d). $[\text{Cl}]^-$ layers are simple contrarily to their double thickness in BiOCl , Figure II.51a. It corresponds to an intergrowth between the $\text{Bi}_2\text{LnO}_4\text{Cl}$ ¹³⁸ and the MBiO_2Cl (*XI*) structures, but with Pb^{2+} instead Ln^{3+} and Bi^{3+} instead M^{2+} in the two distinct metal layers (Figure II.51b). The compound is isostructural with $\text{BaBi}_4\text{O}_6\text{Cl}_2$ where neutral $[\text{BaBi}_2\text{O}_4]^0$ layers also exist.³²

$\text{PbBi}_4\text{O}_6\text{Cl}_2$ is to our knowledge the first example of Pb^{2+} in the central sites of such layers generally hosting large cations without lonepair electrons (Ba^{2+} , Ln^{3+}). It follows that in the $\text{PbBi}_4\text{O}_6\text{Cl}_2$, the lone pair is not stereoactive and Pb^{2+} is at the center of a regular PbO_8 quadratic prism (Pb-O bonds: $8 \times 2.52(3)$ Å). The Bi/Pb segregation into distinct sites is complete and Bi^{3+} occupies a typical BiO_4Cl_4 tetragonal cation-centered prism (Bi-O: $4 \times 2.23(2)$ Å, Bi-Cl: $4 \times 3.437(9)$ Å).

One should note that in $[\text{PbBiO}_2]$ layers of the PbBiO_2Cl - *XI* structure the Pb/Bi ordering is also complete (Bi-O: 4×2.27 Å vs. Pb-O: 4×2.44 Å and Bi-Cl: 4×3.42 Å vs. Pb-Cl 4×3.26 Å) but both cations are located in the same layers and both have a stereoactive lone pair, Figure II.51c. Typically, this disparity in terms of M-O and M-Cl distances can be regarded as a precious tool to distinguish Bi and Pb in complex mixed Bi/Pb compounds as follows. Bond valence calculations using the sums of M-O and M-Cl contributions using bond valence parameters of M-Cl bonds from Brese and O'Keeffe¹³⁹ and more recent ones of M-O bonds revisited by S. Krivovichev¹⁴⁰ lead to BVS values close to the expected ones: $\text{BVS}_{\text{Bi1}} = 2.67$, $\text{BVS}_{\text{Bi2}} = 2.97$, $\text{BVS}_{\text{Pb1}} = 2.25$ (Table II.13).

Table II.13. BVS of the atoms: Bi6 in the Arppe's compound, Pb7 in $m = 2$, Pb8 in $m = 3$, Pb8 in $m = 4$, Bi1, Bi2 and Pb1 in $\text{PbBi}_4\text{O}_6\text{Cl}_2$ with R and b parameters of Krivovichev¹⁴⁰

Arppe's compound				
Atom1	Atom2	d	V _{Bi}	V _{Pb}
Bi6	1xO5	2.317(18)	0.51	0.48
	2xO3	2.431(10)	0.8	0.76
	1xO1	2.606(16)	0.28	0.27
	1xO5	2.613(19)	0.27	0.26
	2xO6	2.619(12)	0.54	0.52
	1xO7	2.736(39)	0.21	0.21
	2xO9	2.7838(8)	0.38	0.37
	BVS(2xO9)		2.99	2.88
BVS(abs.O9)			2.61	2.51
m = 2				
Pb7	1xO6	2.297(18)	0.53	0.5
	2xO7	2.432(8)	0.8	0.76
	1xO2	2.584(15)	0.29	0.28
	1xO6	2.602(19)	0.28	0.27
	2xO5	2.631(9)	0.53	0.51
	1xO8	2.807(35)	0.18	0.18
	BVS		2.6	2.5
m = 3				
Pb8	1xO8	2.268(25)	0.56	0.53
	2xO6	2.427(11)	0.8	0.77
	1xO8	2.559(27)	0.31	0.29
	1xO3	2.564(26)	0.3	0.29
	2xO7	2.626(12)	0.53	0.51
	1xO9	2.774(55)	0.2	0.19
	BVS		2.7	2.59
m = 4				
Pb8	1xO8	2.304(22)	0.52	0.5
	2xO7	2.421(7)	0.81	0.78
	1xO4	2.564(19)	0.3	0.29
	1xO8	2.579(23)	0.29	0.28
	2xO9	2.619(8)	0.54	0.52
	1xO10	2.769(38)	0.2	0.19
	BVS		2.67	2.56
PbBi₄O₆Cl				
Bi1	4xO1	2.323(2)	2	1.91
	4xCl1	3.337(11)	0.67	0.45
	BVS		2.67	2.36
Bi2	4xO2	2.231(24)	2.42	2.3
	4xCl1	3.437(11)	0.54	0.34
	BVS		2.97	2.65
Pb1	8xO2	2.584(29)	2.32	2.24
	BVS		2.32	2.24

3c) The $[\text{Pb}_m\text{Bi}_{10-m}\text{O}_{13}][\text{Bi}_2\text{O}_2]_m\text{Cl}_{4+m}$ compounds ($m = 1$ to 4).

If one considers the condensation of the **units 1** and **units (2+3)** as shown on the Figure II.54, a generic formulation $[\text{Bi}_{10-m}\text{Pb}_m\text{O}_{13}]^{\text{unit}2+3} [\text{Bi}_2\text{O}_2]_m^{\text{unit}1} \text{Cl}_{4+m}$ can be given to the compounds formed by progressive elongation of the linear **unit 1** by addition of extra OBi_4 tetrahedra and by partial substitution of Bi^{3+} for Pb^{2+} in the **unit 2** in order to reach electroneutrality. Here the central oxygen O_{octa} of **units 2** of the parent Arppe's compound was not considered since

it was never observed neither in the single crystals of the novel mixed Bi/Pb $m = 2, 3, 4$ members nor in the similar cavities offered by the crystal structure of $\text{PbBi}_4\text{O}_6\text{Cl}_2$ with similar but infinite $[\text{BiPbO}_4]$ layers. The role of O_{octa} in $\text{Bi}_{24}\text{O}_{31}\text{Cl}_{10}$ is most probably to compensate excess of positive charge created by adjacent Bi^{3+} , and the absence of the former in the Pb-containing compounds is an indicator for the preferred location of Pb^{2+} in the **units 2**. When an extra need for Pb^{2+} cations is required to keep electroneutrality, we have set them in the cationic sites of the **units 3** shown on the Figure II.50a. This aspect will be discussed later concerning the veracity of the Pb/Bi crystallographic discrimination that we applied to further compounds.

3d) Hypothetical $m = 1$ term $[\text{PbBi}_9\text{O}_{13}][\text{Bi}_2\text{O}_2]\text{Cl}_5$.

It would correspond to a slightly modified crystal structure of the Arppe's compound $\text{Bi}_{24}\text{O}_{31}\text{Cl}_{10}$ after doping with Pb^{2+} for removal of O_{octa} for reasons explained above. Here we consider that the Pb^{2+} substitution is efficient in the **units 3** only, preferentially in the sites shown in grey in the Figure II.54a. As briefly announce above, we failed to prepare the single polycrystalline phase from the stoichiometric mixture of PbCl_2 , Bi_2O_3 and BiOCl heated at 750°C in an alumina crucible or evacuated quartz ampoule, after several intermediate grindings. However in some cases, the presence of an isostructural compound was confirmed in the powder XRD pattern, but the presence of other phases avoid to conclude about the real incorporation of mixed $\text{Bi}^{3+}/\text{Pb}^{2+}$ cations in the structure which would yield to the real $m = 1$ compound.

Also, in one of our tests the prepared compound mainly correspond to the $m = 2$ term described below, accompanied by a weak amount of a second unidentified phase. It seems that the incorporation of lead favors the preparation of this phase which appears as the most stable of the $m = 1$ to $m = 4$ series. However the formulation of the $m = 1$ term, even if hypothetical, remains necessary to pave the way from the original Arppe's compound until the further $m = 2, 3$ and 4 compounds.

3e) $m = 2$ term $[\text{Pb}_2\text{Bi}_8\text{O}_{13}][\text{Bi}_2\text{O}_2]_2\text{Cl}_6$.

The full series of compounds $m = 1$ to 4 are shown on the Figure II.54. For $m = 2$, the crystal structure refinement leads to $R = 0.0356$, $wR = 0.0374$ space group $C2/m$ with lattice parameters $a = 29.671(2) \text{ \AA}$, $b = 3.9692(2) \text{ \AA}$, $c = 12.2477(5) \text{ \AA}$, $\beta = 107.492(2)^\circ$. Precession images show no sign for the b -doubling. It corresponds to the formula $[\text{Pb}_2\text{Bi}_8\text{O}_{13}][\text{Bi}_2\text{O}_2]_2\text{Cl}_6$. No oxygen was located in the O_{octa} sites of the **units 2**, which leads us to consider Pb^{2+} cations

in the central sites of these units (=Pb7 site) as shown in grey in the Figure II.54b. Once more, this choice was done by analogy to the structure of $\text{PbBi}_4\text{O}_6\text{Cl}_2$. In addition, the average Bi-O distance concerning the BiO_4 pyramids of the **units 1** is 2.26 Å which is likely for bismuth cations by analogy with the $\text{PbBi}_4\text{O}_6\text{Cl}_2$ and the Arppe's compound. The occupancies of oxygen of the **unit 3** have been fixed to 75 % similarly to our refinement of the disordered Arppe's compound in absence of *b*-doubling. It is noteworthy that two bismuth positions have been split onto satellite positions (Bi4a/Bi4b and Bi6a/Bi6b) in order to minimize local residual electronic density peaks observed on Fourier-difference maps. This could picture a local Pb/Bi mixed occupancy but we preferred for the full series a unified model with Pb^{2+} cations located solely in the **units 2 + 3**. Table II.12 shows the successful preparation of the corresponding powder using the stoichiometric ratio between all elements. The pattern matching is shown on the Figure II.53 ($a = 29.6643(8)$ Å, $b = 3.9694(2)$ Å, $c = 12.2489(4)$ Å, $\beta = 107.39(2)^\circ$ and $V = 1376.35(7)$ Å³ with $\chi^2 = 1.65$).

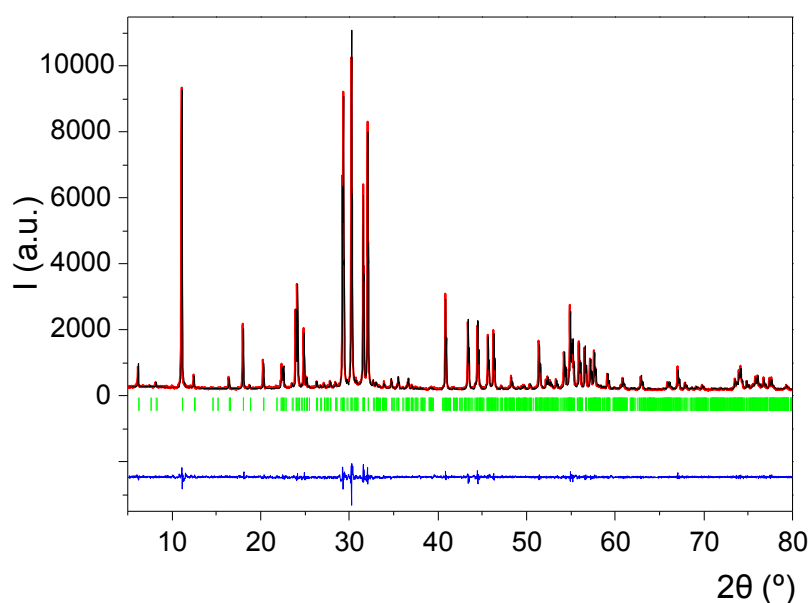


Figure II.53. Pattern matching of the compound $[\text{Pb}_2\text{Bi}_8\text{O}_{13}][\text{Bi}_2\text{O}_2]_2\text{Cl}_6$, $m = 2$ with refined parameters $a = 29.6643(8)$ Å, $b = 3.9694(2)$ Å, $c = 12.2489(4)$ Å, $\beta = 107.39(2)^\circ$.

3f) $m = 3$ term $[\text{Pb}_3\text{Bi}_7\text{O}_{13}][\text{Bi}_2\text{O}_2]_3\text{Cl}_7$.

The projection of the crystal structure is shown on the Figure II.54c. The crystal structure was refined in the space group $C2/m$ leading to $R = 0.0358$, $R_w = 0.0459$, lattice parameters $a = 29.681(2)$ Å, $b = 3.9630(2)$ Å, $c = 15.1047(8)$ Å, $\beta = 118.387(2)^\circ$. Here Pb^{2+} cations have been set in the central sites of the **units 2** (100% Pb8) and in the bordering cationic sites common to **units 2 and 3** (50% Bi7 - 50% Pb7) as shown on the Figure II.54c. The oxygen

atoms of **units 3** are 75% occupied. No cationic atom was found split during the refinement process. Also as for the previous case, no residual electron density was located in the O_{octa} sites which are anion-empty. Once more the presence of Bi^{3+} species only in the **units 1** is supported by the concerned Bi-O distances: the three independent Bi atoms involved in these units have similar BiO_4 coordination with an average Bi-O distance of 2.26-2.27 Å reminiscent of the Bi-oxygen coordination in the $\text{PbBi}_4\text{O}_6\text{Cl}_2$ and the Arppe's compound. This phase was prepared in a polycrystalline state but with some impurities such as $\text{Bi}_{12}\text{O}_{17}\text{Cl}_2$, $\beta\text{-Bi}_2\text{O}_3$ or PbBiO_2Cl , see Table II.12.

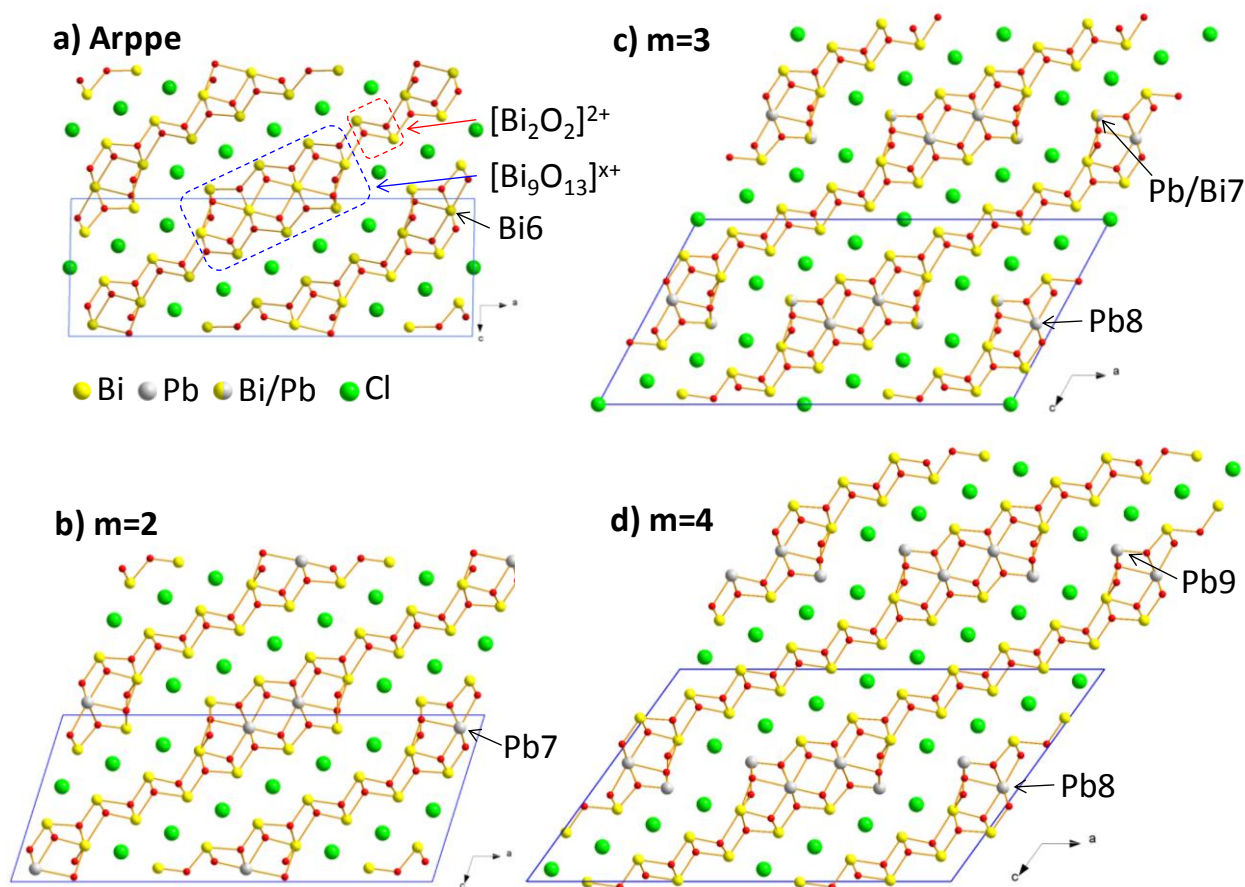


Figure II.54. The structures of the $[\text{PbmBi}_{10-m}\text{O}_{13}][\text{Bi}_2\text{O}_2]_m\text{Cl}_{4+m}$ members: a) hypothetical $[\text{PbBi}_9\text{O}_{13}][\text{Bi}_2\text{O}_2]\text{Cl}_5$, $m = 1$, b) $[\text{Pb}_2\text{Bi}_8\text{O}_{13}][\text{Bi}_2\text{O}_2]_2\text{Cl}_6$, $m = 2$, c) $[\text{Pb}_3\text{Bi}_7\text{O}_{13}][\text{Bi}_2\text{O}_2]_3\text{Cl}_7$, $m = 3$ and d) $[\text{Pb}_4\text{Bi}_6\text{O}_{13}][\text{Bi}_2\text{O}_2]_4\text{Cl}_8$, $m = 4$

3g) $m = 4$ term $[\text{Pb}_4\text{Bi}_6\text{O}_{13}][\text{Bi}_2\text{O}_2]_4\text{Cl}_8$.

The structure of the last term of the series solved in $C2/m$ space group as well in the unit cell parameters: $a = 29.783(2)$ Å, $b = 3.9639(2)$ Å, $c = 18.3770(9)$ Å, $\beta = 125.828(2)^\circ$ with the refinement parameters $R = 0.0292$, $R_w = 0.0289$. In this case Pb^{2+} cations have been set in the central sites of the **units 2** (100%) as well as in the bordering cationic sites common to **units 2 and 3** (100% Pb8 and Pb9) as shown on the Figure II.54d. We note that the site Pb9 was split

into satellite positions Pb9a (66%) and Pb9b (44%) to lower residual electron density. Once again, the occupancies of the oxygen atoms of **units 3** were fixed to 75%. As in the previous $n = 3$ case, no pure polycrystalline sample was obtained for this term, even if the major presence of the compounds was observed in some cases, see Table II.12.

As detailed for each compound the choice for preferential location of Pb^{2+} cations is supported by the Bi-O distances found close to 2.27 Å in the **units 1** which are similar to Bi-O distances in $\text{PbBi}_4\text{O}_6\text{Cl}_2$ and $\text{Bi}_{24}\text{O}_{31}\text{Cl}_{10}$ while Pb-O distances in similar PbO_4 coordinations are closer to 2.44 Å. Therefore we propose that the cationic sites of the **units 1** are filled by 100% Bi. In addition the strict localization of all Pb^{2+} particular subunits enables the setting of the general formula $\text{unit}_{2+3}[\text{Bi}_{10-m}\text{Pb}_m\text{O}_{13}] \text{unit}_1[\text{Bi}_2\text{O}_2]_m\text{Cl}_{4+m}$ that describes the full series from the hypothetical $m = 1$ term (modified Arppe's compound), which is not clearly confirmed on powder, to the refined $m = 2, 3$ and 4 compounds. From the distances listed in the supplementary materials it is clear that inside the **units 2**, the mean Pb/Bi-O distances seem to increase on increasing n which supports the introduction of largest Pb^{2+} in these units. Particularly, in these units taking into account our proposition for Pb/Bi ordering in distinct sites, the Pb-O distances are close to 2.3 Å while Bi-O are closest to 2.2 Å. However several features seem to indicate that this ordering is most probably idealized and that the reality is more contrasted:

i) the split of some atoms in the **units 1** (for instance Bi4a/Bi4b in the $m = 2$ term) could suggest the presence of mixed Bi/Pb sites in these structural fragments.

ii) the bond valence sum calculations on the position preferred for Pb^{2+} (i.e. Bi6 in the Arppe's compound, Pb7 for $m = 2$, Pb8 for $m = 3$, Pb8 for $m = 4$) is given in the Table II.13. For our refinement of the crystal structure of the Arppe's compound with 50% of O_{octa} in the interstices of the **units 2**, bond valence sum was calculated in absence or presence of O_{octa} (=O9) in the Bi and Pb hypotheses. Clearly the presence of O9 stabilizes the presence of Bi^{3+} in this site ($S_{\text{Bi}^{3+}}$ with O9 = 2.99 against $S_{\text{Bi}^{3+}}$ without O9 = 2.61). In the $m = 2, 3$ and 4, where the presence of O_{octa} sites was never observed, the calculations show a under-bonded character in the Bi^{3+} hypothesis ($S_{\text{Bi}^{3+}} = 2.5\text{-}2.7$) and an overbonded character in the Pb^{2+} hypothesis ($S_{\text{Pb}^{2+}} = 2.5\text{-}2.6$) which would play in favor of a mixed distribution rather than the preferential filling of this site by Pb^{2+} only. On the other hand, bond valence sums remain an empirical value which should not be considered *stricto sensu*. At least, the preferred occupancy of this position by Pb^{2+} is reminiscent of the $[\text{PbBi}_2\text{O}_4]$ blocks in the $\text{PbBi}_4\text{O}_6\text{Cl}_2$,

and can be proposed as an ideal scheme, but even in this ordered compound, BVS calculations for Bi1, Bi2 and Pb1 sites also leads to intermediate values, i.e. +2.67 (Bi1), +2.97 (Bi2) and +2.24 (Pb1) in absence of mixed sites.

4) Electric properties of the $m = 2$ term.

Accordingly to the partial disorder that was refined over both cationic and anionic positions for all the compounds of the $[\text{PbmBi}_{10-\text{m}}\text{O}_{13}][\text{Bi}_2\text{O}_2]_m\text{Cl}_{4+\text{m}}$ series, it sounds interesting to evaluate the potentiality for anionic conductivity in such structures. In addition the existence of chloride planes similar to those found in Cl^- conduction rare earth oxychlorides may also favor halides conductivity. The $m = 2$ term was selected as the only compound prepared as a polycrystalline single phase in our study. The conditions of measurements of impedance spectra are briefly given in the experimental section in Annex. Typical semicircles are appearing above 250°C and are better shaped on increasing temperature. For instance at 655°C (see inset of the Figure II.55), we observe two circles between 0.1 Hz and 10 kHz while high frequency points are out of the (Z', Z'') Nyquist diagrams.

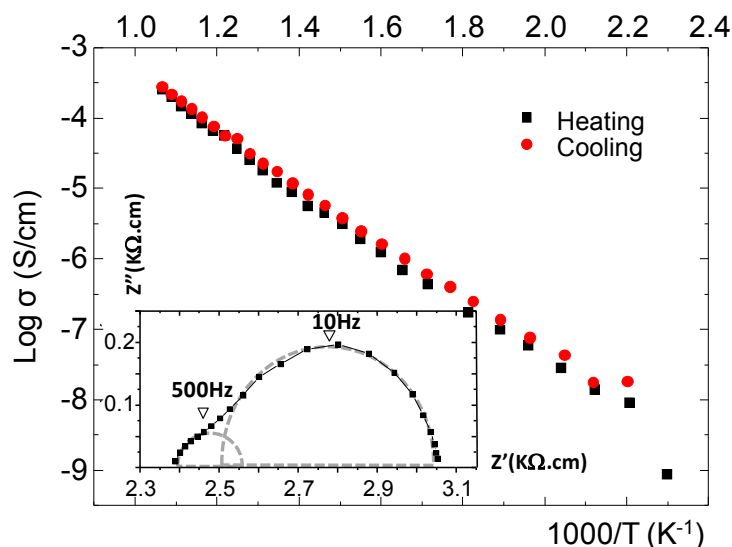


Figure II.55. Arrhenius plot of the conductivity of the $m = 2$ term $[\text{Pb}_2\text{Bi}_8\text{O}_{13}][\text{Bi}_2\text{O}_2]_2\text{Cl}_6$. Inset: Nyquist plot for the measurement at 665°C with indication of the relaxation frequencies for each events.

The intersection of the highest frequency circle with the Z' axis is $2.4 \text{ k}\Omega\cdot\text{cm}$ which indicate a significant resistive contribution in the equivalent electric circuit. Together with the two overlapped circles it would correspond to a pure resistance in series with two RC elements. This shape of impedance diagram is typical for conventional polycrystalline ionic conductors; the high frequency bulk semicircle describes the electrical properties of the grains of the

ceramics, and the low frequency additional contribution is due to the blocking effects of charge carriers at grain boundaries. However the relaxation frequency (f_{\max}) of the low frequency diagram is very low (~ 10 Hz) and coincides better with process associated with the oxygen adsorption–desorption on the gold electrode and surface diffusion of anionic oxygen species.¹⁴¹ Then, this semicircle was assigned to both blocking effects and electrode reaction. It follows that the Arrhenius behavior shown in Figure II.55 was plotted considering the resistive offset and the RC circuit assigned to the bulk effect (with a rather low relaxation frequency ~ 500 Hz at 655°C). It shows a good reproducibility between data taken on heating and cooling, and the calculated activation energy from the Arrhenius law is 0.78eV . For the purpose of identifying the mobile anions (Cl^- vs. O^{2-} vs. mixed of both) species, changing O_2 or Cl_2 gas pressure should be further performed. Despite the well-ordered Cl^- sublattice, at this stage one could imagine a contribution of Cl^- conductivity, since the order of magnitude of the conductivity is comparable to what observed in Ca-doped LaOCl ¹⁴² and taking into account the low frequency associated with the bulk-semicircle compatible with less mobile Cl^- anions.

5) Luminescence properties of the $m = 2$ term and $\text{PbBi}_4\text{O}_6\text{Cl}_2$.

Cations with ns^2 electronic configuration, like Bi^{3+} , Pb^{2+} , Tl^+ and Sb^{3+} , are very promising candidates for applications because they are able to exhibit efficient excitation and extremely bright emission due to parity allowed, fast $s^2 \leftrightarrow sp$ electronic transitions. Spectroscopic properties of Bi^{3+} and Pb^{2+} have been extensively investigated because these ions are effective activators for luminescent materials widely used in scintillation detectors, lamps or X-ray phosphors.^{143–147}

The ground state of the $6s^2$ configuration is 1S_0 while the $6s6p$ excited states give rise to triplet (3P_0 , 3P_1 and 3P_2) and the 1P_1 singlet levels. Transitions between the ground state 1S_0 and 3P_0 , 3P_1 , 3P_2 are spin forbidden; however, the $^1S_0 \rightarrow ^3P_1$ transition (A-band) becomes partly allowed due to coupling of 3P_1 and 1P_1 states. The $^1S_0 \rightarrow ^1P_1$ (C-band) is an allowed electric dipole transition.

In the case of Bi^{3+} ions emission originated by the $^3P_1 \rightarrow ^1S_0$ transition is usually detected at room temperature, but at low temperature the highly forbidden $^3P_0 \rightarrow ^1S_0$ emission is also observed.¹⁴⁸ For Pb^{2+} the situation is slightly different. Commonly, the luminescence is described by $^1S_0 \rightarrow ^3P_{1,2} + ^1P_1$ transitions for excitation and $^3P_1 \rightarrow ^1S_0$ for emission. Another optical transition (D-band) can appear in both cases, which is probably due to an electronic

charge transfer between the metal and the ligand or between two metals.¹⁴⁹ It occurs mostly if there is a significant coupling between the ³P₁ and ³P₀ states and the electronic states of nd¹⁰/nd⁰ ions (for example V⁵⁺ or Ga³⁺).¹⁵⁰ These transitions are quite diverse and depend strongly of the environment conditions of Bi³⁺/Pb²⁺ in a host and also on their crystallographic site.

Here we report preliminary results of the photoluminescence of PbBi₄O₆Cl₂, [Pb₂Bi₈O₁₃][Bi₂O₂]₂Cl₆ as well as BaBi₄O₆Cl₂, details are given in Annex. All compounds show a strong red emission at low temperatures if irradiated with a UV lamp, which is very unusual for s² ions and, thus, extremely remarkable. The respective spectra are depicted in Figure II.56a and Figure II.56b, while the data are collected in Table II.14. The emission is, unfortunately, quenched in all cases at room temperature, which prevents their use for applications.

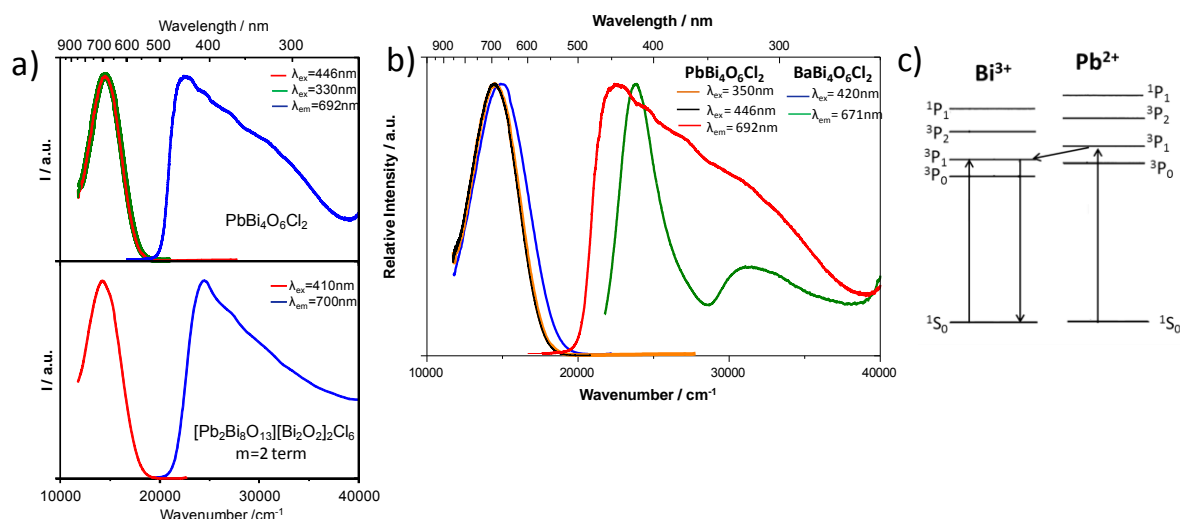


Figure II.56. a) Fluorescent spectra of PbBi₄O₆Cl₂ and [Pb₂Bi₈O₁₃][Bi₂O₂]₂Cl₆ (m = 2 term) at 10 K, b) comparison between fluorescent spectra of PbBi₄O₆Cl₂ and BaBi₄O₆Cl₂ at 10 K, c) sketch of charge transfer between Pb²⁺ and Bi³⁺.

For PbBi₄O₆Cl₂ the emission band is located at 14450 cm⁻¹, while the excitation band starts at about 19000 cm⁻¹ with a maximum at 22420 cm⁻¹ (Figure II.56a, Table II.14). The Stokes shift can therefore be determined to 7970 cm⁻¹. [Pb₂Bi₈O₁₃][Bi₂O₂]₂Cl₆ shows an emission band with a maximum at 14286 cm⁻¹, the excitation band has an onset at about 20500 cm⁻¹ and a maximum at 24390 cm⁻¹. The Stokes shift is 10104 cm⁻¹. Both PbBi₄O₆Cl₂ and [Pb₂Bi₈O₁₃][Bi₂O₂]₂Cl₆ possess two s² cations (Bi³⁺ and Pb²⁺). The energetic position of the excited states and, thus, the location of the emission and excitation bands, are in general at

similar energies.¹⁵¹ Therefore, it is impossible to assign excitation and more particularly emission bands to transition of the respective ions.

[Pb₂Bi₈O₁₃][Bi₂O₂]₂Cl₆ shows an emission band with a maximum at 14286 cm⁻¹, the excitation band has an onset at about 20500 cm⁻¹ and a maximum at 24390 cm⁻¹. The Stokes shift is 10104 cm⁻¹. Both PbBi₄O₆Cl₂ and [Pb₂Bi₈O₁₃][Bi₂O₂]₂Cl₆ possess two s² cations (Bi³⁺ and Pb²⁺). The energetic position of the excited states and, thus, the location of the emission and excitation bands, are in general at similar energies.¹⁵¹ Therefore, it is impossible to assign excitation and more particularly emission bands to transition of the respective ions.

Table II.14. Optical properties of PbBi₄O₆Cl₂, m = 2 term [Pb₂Bi₈O₁₃][Bi₂O₂]₂Cl₆ and BaBi₄O₆Cl₂. Excitation and emission maximum and Stokes shift.

Compound	PbBi ₄ O ₆ Cl ₂	m = 2	BaBi ₄ O ₆ Cl ₂
Excitation / cm ⁻¹ (maximum)	22420	24390	23810
Emission / cm ⁻¹ (maximum)	14450 (red)	14286 (red)	14903(red)
Stokes shift / cm ⁻¹	7970	10104	8907

Due to this reason we synthesized and investigated the luminescence properties of BaBi₄O₆Cl₂, which is isotypic to PbBi₄O₆Cl₂, with very comparable cell parameters and have, thus, the same Bi and Ba/Pb crystallographic site.¹³⁸

The shape and the position ($\lambda_{\max} = 14903 \text{ cm}^{-1}$) of the emission band of PbBi₄O₆Cl₂ is very similar to those of BaBi₄O₆Cl₂ (Figure II.56b) and both can therefore most probably be assigned to ³P₀ → ¹S₀ transition of Bi ions. In contrast, the excitation bands of PbBi₄O₆Cl₂ and BaBi₄O₆Cl₂ are quite different. For BaBi₄O₆Cl₂ two excitation bands located at 23810 and 31000 cm⁻¹ could be detected, which can be assigned to ¹S₀ → ³P₁ and ¹S₀ → ³P₂ transitions of the Bi³⁺ ion. The high energy transition becomes in general allowed at low temperatures but with small intensity. The excitation spectrum of PbBi₄O₆Cl₂ contains some additional transitions (Figure II.56b), which can be assumed to be originated by Pb²⁺ transitions. Because the emission spectrum of PbBi₄O₆Cl₂ show exclusively Bi emission, a complete Pb-Bi energy transfer after Pb excitation can be assumed (Figure II.56c), although some additional investigations, like lifetime measurements, are necessary to overlay this statement. The same behavior can be supposed for [Pb₂Bi₈O₁₃][Bi₂O₂]₂Cl₆, where the shift of the maxima of the excitation and emission bands relative to PbBi₄O₆Cl₂ can be explained by the different structures of both compounds.

As we stated above, the red emission of the compounds presented here, is quite unique. Parke and Webb noticed red emission from Bi³⁺ in calcium phosphor glasses¹⁵², but after recent reinvestigation, Qiu et al.¹⁵³ concluded that this emission is originated by Bi²⁺. More recently, Qiu et al. found a surprising near-to-mid-IR luminescence in Bi₅(AlCl₄)₃, which was attribute to Bi₅³⁺ clusters.¹⁵⁴ Bi₁₂GeO₂₀ is also reported to show an emission band in the red region at low temperature but also an additional band at higher energy was detected.¹⁵¹ To the best of our knowledge the compounds reported here are the first examples for red emission of Bi³⁺ doped in an oxychloride host. In general, red emission in Bi-doped compounds is usually assigned to Bi²⁺.^{155,156}

6) Summary

Here an original description of a novel homologous series of general formula [Pb_mBi_{10-m}O₁₃][Bi₂O₂]_mCl_{4+m} is proposed, which is presented as an assembly of different kinds of well-separated units observed in the new layered PbBi₄O₆Cl₂. The similarities of the new series with the parent well-known Arppe's is unique and lead to an extended family with sizeable crenel-like [Bi/Pb/O] walls isolated by chloride ions. The Bi/Pb segregation in the several building units is discussed and finally, an ideal model with preferred sites for Pb²⁺ proposed which helped to work out the given general formula.

The preparation of the respective powders show the predominant stability of the m = 2 term which was prepared as a single-phase, while other terms have not been obtained in absence of secondary phases. For m = 2, the impedance spectroscopy shows a conductivity value $\sigma \sim 10^{-3}$ S.cm⁻¹ at 650°C and suggests a contribution of Cl⁻ in the diffusion process.

Most remarkable, PbBi₄O₆Cl₂ as well as [Pb₂Bi₈O₁₃][Bi₂O₂]₂Cl₆ show very bright red emission at low temperature, which could be assigned to Bi³⁺ transitions by comparison to BaBi₄O₆Cl₂. Further studies will contribute to the understanding of the structure-luminescence properties relationship of s² ions, which are suitable candidates for the substitution of lanthanide ions in phosphors for saving their scarce resources.

II.2.3 Bi₆O_{8.5}Cl

1) Synthesis.

Single crystal: The colorless transparent crystals of Bi₆O_{8.5}Cl have been found in a melt obtained from cooling down, to 500°C slowly at a rate of 1°C/h, the mixture of 3Bi₂O₃ + 6BiOCl + 1PbO + 1MnO₂ in a sealed gold tube priority heated at 900°C during 12h.

Even though the crystals of $\text{Bi}_6\text{O}_{8.5}\text{Cl}$ were found in the melt containing Pb and Mn, the structure is considered to be free of them. The bond valence calculations (Table II.15) showed adequate values of valences of the corresponding atoms, except Bi12 and O15, which is due to too short distances.

Table II.15 BVS calculation of $\text{Bi}_6\text{O}_{8.5}\text{Cl}$

Atom	BVS	Atom	BVS
Bi1	3.08(10)	O1	2.34(7)
Bi2	3.31(10)	O2	2.24(8)
Bi3	3.0(2)	O3	2.31(7)
Bi4	3.03(13)	O4	2.38(9)
Bi5	2.83(10)	O5	2.21(10)
Bi6	3.04(13)	O6	2.37(13)
Bi7	3.10(19)	O7	2.08(11)
Bi8	2.73(8)	O8	2.34(10)
Bi9	3.1(2)	O9	1.79(7)
Bi10a	2.8(2)	O10	1.74(14)
Bi10b	3.2(3)	O11	1.89(18)
Bi11a	2.69(15)	O12	1.66(15)
Bi11b	2.45(16)	O13	1.92(17)
Bi12	5(2)	O14	1.58(13)
Cl1	0.800(8)	O16	1.54(15)
Cl2	0.821(8)	O15	4(2)

Further analysis of the elemental composition by the Electron Probe Microanalyser technique showed that there are no peaks of Pb nor Mn on the spectrum (Figure II.57).

Powder synthesis: The polycrystalline sample was prepared by heating of the co-ground stoichiometric mixture of Bi_2O_3 and BiOCl at 750°C during 48h with intermediate grindings.

The diffractogram (in black) of the obtained powder is on Figure II.58 and it is compared to that of the calculated one (green). The peak positions match well whereas intensities are quite different, implying strong preferred orientation. Also several peaks at 28° and 39° peaks are broad and overlapping each other, showing some disorder, probably requiring further heat treatment. Heating above 750°C in air can decompose the structure since it can lose chlorine atoms. The next strategy could be heating the powder in the sealed tube at elevated temperatures to obtain the pure polycrystalline phase to study its properties.

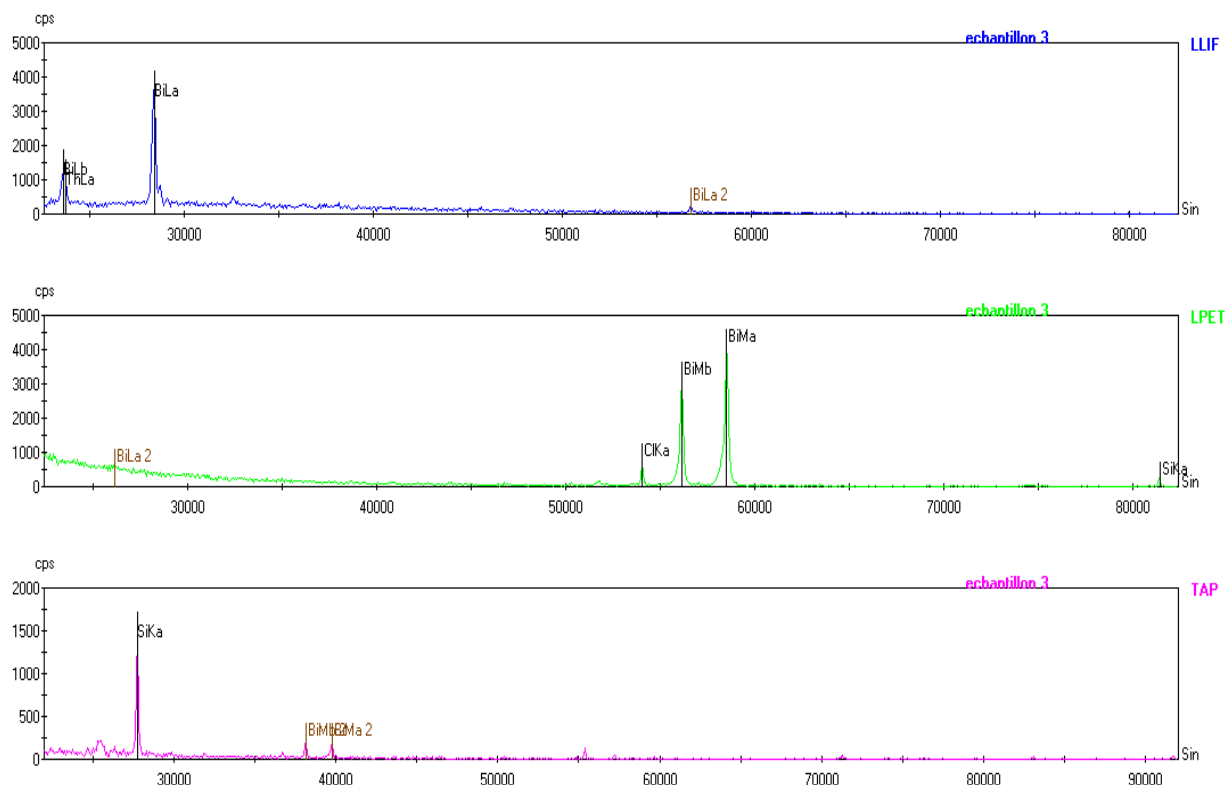


Figure II.57. The EPMA spectrum of Bi₆O_{8.5}Cl showing the absence of Pb and Mn.

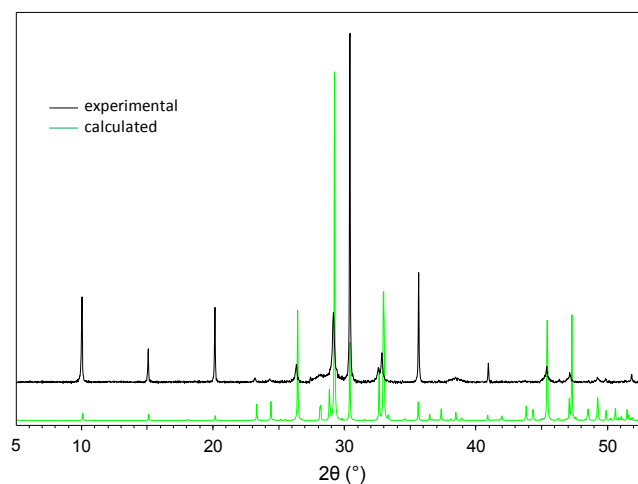


Figure II.58. Experimental (black) and calculated (green) XRD patterns of Bi₆O_{8.5}Cl.

2) Structural description.

The crystal structure of Bi₆O_{8.5}Cl was solved in the space group *Iba2* with the unit cell parameters $a = 21.6954(16)$ Å, $b = 35.271(3)$ Å, $c = 5.4331(5)$ Å and $V = 4157.51(60)$ Å³, however with rather high reliability factors $R1 = 0.0807$, $wR = 0.0740$.

Figure II.59 is the crystal structure of $\text{Bi}_6\text{O}_{8.5}\text{Cl}$. There is a six Bi atom thick $[\text{Bi}_6\text{O}_{8.5}]^+$ layer separated by Cl^- layer in the structure. The $[\text{Bi}_6\text{O}_{8.5}]^+$ layer consists of disordered Bi/O sublayer, $[\text{Bi}_2\text{O}_{4.5}]^{3-}$, which is stacked in between two fluorite like $[\text{Bi}_2\text{O}_2]^{2+}$ layers. The Bi-O distances take quite wide range in the $[\text{Bi}_2\text{O}_2]^{2+}$ layers, they go from 2.16 Å to 2.48 Å, whereas in compound BiOCl which possesses similar layers the Bi-O distance is 2.32 Å.

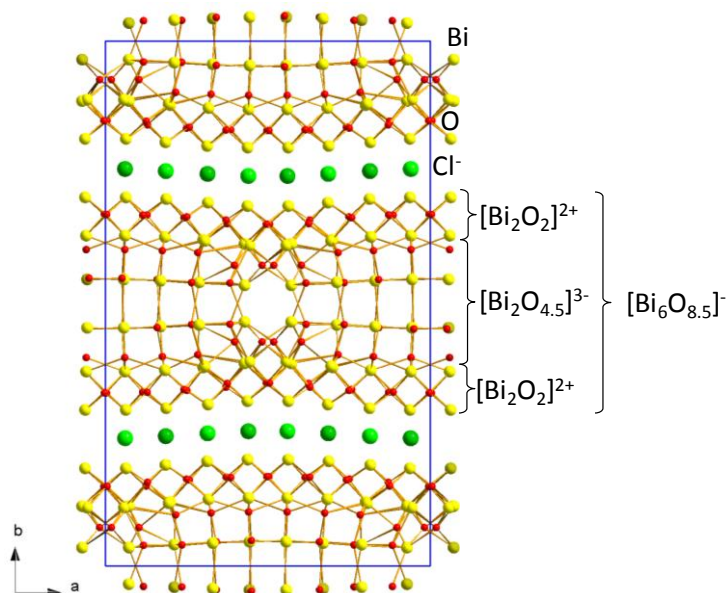


Figure II.59. The crystal structure of $\text{Bi}_6\text{O}_{8.5}\text{Cl}$

The degree of disorder in the center $[\text{Bi}_2\text{O}_{4.5}]^{3-}$ sublayer is quite high due to the presence of split atoms of Bi, abnormal Bi-O distances (Table II.16), high oxygen ADPs and elevated residual electron densities which explains elevated values of reliability factors ($R_1 = 0.0807$, $wR = 0.0740$). The rest of the $[\text{Bi}_2\text{O}_{4.5}]^{3-}$ sublayer resembles the rock-salt like structure, having alternating distorted octahedra of O (Figure II.60a) and Bi (Figure II.60b). The short Bi-O bond of the latter Bi octahedra is an excecence (explained in part of 2D infinite layered structures above, in section II.2.1), the O atom of which makes a distorted rectangular pyramid (Figure II.60c).

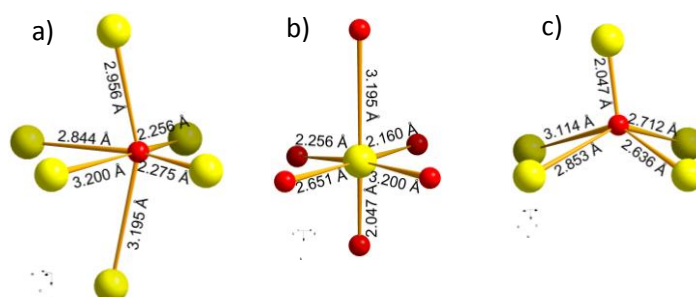


Figure II.60. Distorted octahedral coordination of a) O and b) Bi atoms, c) distorted rectangular pyramidal environment of O atom.

Table II.16 Selected distances in Bi₆O_{8.5}Cl ($d_{max}=3$ Å)

Atom 1	Atom 2	d (Å)	Atom 1	Atom 2	d (Å)	Atom 1	Atom 2	d (Å)
Bi1	O3	2.20(3)	Bi7	O9	2.03(3)	Bi10b	O5	2.19(4)
	O2	2.23(3)		O12	2.12(6)		O17	2.2(1)
	O6	2.25(4)		O14	2.27(5)		O17	2.39(2)
Bi2	O1	2.32(3)	Bi8	O12	2.41(7)		O5	2.5(4)
	O1	2.16(3)		O1	2.28(3)		O7	2.55(5)
	O8	2.22(4)		O8	2.33(4)		O15	2.6(3)
	O8	2.25(4)		O8	2.39(4)		O4	2.62(3)
Bi3	O3	2.25(3)		O3	2.46(3)	Bi11a	O16	2.91(7)
	O10	2.05(4)		O9	2.58(3)		O6	2.27(4)
	O13	2.17(5)		O10	2.71(5)		O4	2.38(3)
	O14	2.28(6)		O9	2.76(3)		O7	2.41(5)
Bi4	O12	2.65(7)	Bi9	O12	2.95(7)		O11	2.42(6)
	O4	2.16(3)		O11	2.04(7)		O2	2.44(3)
	O5	2.20(4)		O13	2.11(6)		O15	2.8(3)
	O7	2.28(5)		O16	2.18(7)		O10	2.85(5)
Bi5	O5	2.36(4)		O14	2.84(5)	Bi11b	O7	2.27(5)
	O2	2.28(3)		O13	2.96(4)		O2	2.43(3)
	O3	2.32(3)	Bi10a	O7	2.22(5)		O6	2.48(4)
	O6	2.40(4)		O5	2.40(4)		O4	2.48(3)
	O11	2.47(5)		O4	2.45(3)		O11	2.59(6)
	O1	2.48(3)		O5	2.52(5)		O15	2.7(3)
	O10	2.63(5)		O17	2.5(1)		O10	2.91(5)
	O9	2.84(3)		O17	2.6(1)	Bi12	O13	2.98(4)
Bi6	O14	2.95(4)		O15	2.6(3)		O15	1.6(3)
	O4	2.16(3)		O16	2.90(8)		O17	2.1(2)
	O6	2.19(4)					O16	2.35(6)
	O2	2.32(3)					O16	2.84(7)
	O7	2.36(5)					O17	2.9(1)

II.2.4 Bi₉O₉Cl₄(Pb_{0.2}Mn_{0.8})O₃Cl

1) Context of the study

Low-dimensional solid-state materials often exhibit unusual anisotropic physical and chemical properties. In this context, research on layered bismuth oxo-halides has been recently intensified owing to luminescence,⁸⁴ selective oxidation catalysts,^{85,157} and multiferroic properties.¹⁵⁸ Most often, these compounds are based on layered intergrowths of bismuth oxide blocks, separated by halide layers. The most famous and simplest phases are known as the Sillén series,^{86,87} i.e. MBiO₂Cl (X_1) ($M^{2+} = \text{Cd, Ca, Pb etc}$)^{82,88,89}, BiOCl (X_2)⁹⁰ etc. As it is discussed in the section II.2.2, in the case of bismuth oxo-halides, the easy substitution of OBi₄ by O(Bi,Pb)₄ enabled the design of the [Pb_mBi_{10-m}O₁₃][Bi₂O₂]_mCl_{4+m} series. More rarely, Cl⁻ occupy 1D channels in porous Bi-based frameworks, such as found in Bi₁₂O₁₅Cl₆.⁶⁸ The potentiality to combine in the same compound 2D-layers and 1D channels of halides was not explored yet but would yield unique structural types. In our group we have successfully reached this goal by the incorporation of alien cations ($M = \text{Na}^+, \text{Pb}^{2+}, \text{Mn}^{2+}$) as

partially substituent for Bi^{3+} , leading to three original multidimensional crystal structures in the chloride rich part of Bi_2O_3 - BiOCl phase diagram. Here one of this compound, $\text{Bi}_9\text{O}_9\text{Cl}_4(\text{Pb}_{0.2}\text{Mn}_{0.8})\text{O}_3\text{Cl}$ will be presented and briefly compared to other two terms.

2) Synthesis.

Single crystal: Single crystals were found in a polyphasic melt obtained as follows: the mixture $6\text{BiOCl} + 6\text{Bi}_2\text{O}_3 + 2\text{PbO} + 6\text{MnO}_2$ was ground together, loaded into a gold tube and placed into a quartz tube and sealed under vacuum, then heated slowly up to 900°C at a rate 50°C/h , then left during 10h and cooled down to 600°C slowly at a rate 3°C/h then the furnace was switched off. The quantitative analysis was conducted on EPMA Cameca SX100. Conditions which operated at a voltage 15kV, with current of the beam being 15 nA. The found ratio of the elements Bi/Pb/Mn/Cl is following 8.2/0.4/0.8/5.0 which is in good agreement with the refined stoichiometry.

Powder synthesis: The corresponding powder was obtained as a main polycrystalline phase from the heating at 600°C of a sealed gold tube with the stoichiometric mixture of BiOCl , Bi_2O_3 and MnO with one intermediate grinding. The sealed gold tube in its turn was sealed into a quartz tube, which was not evacuated. The lattice parameters refined from the powder diffraction are $a = 3.8661(2) \text{ \AA}$, $b = 31.7152(18) \text{ \AA}$, $c = 15.7381(10) \text{ \AA}$.

3) Structural description.

The crystal structure of $\text{Bi}_9\text{O}_9\text{Cl}_4(\text{Pb}_{0.2}\text{Mn}_{0.8})\text{O}_3\text{Cl}$ (Figure II.61a) was solved in the centrosymmetric space group $Cmcm$, with orthorhombic unit cell $a = 3.8695(2) \text{ \AA}$, $b = 31.7369(15) \text{ \AA}$, $c = 15.7602(7) \text{ \AA}$ and $V = 1935.4(2) \text{ \AA}^3$. The structure is almost fully ordered, except the position Pb6/Mn6 the residual electron density about of which suggests a mixed position. The refined ratios are 0.18 for Pb and 0.82 for Mn respectively. It was finally fixed to 0.2/0.8 to obtain the expected charge balance leading to the final formula $\text{Bi}^{\text{III}}_9(\text{Pb}^{\text{II}}_{0.2}\text{Mn}^{\text{II}}_{0.8})\text{O}_{12}\text{Cl}_5$. Concomitantly, in the neighboring of this site inside the channels, a significant splitting of the next Cl4 position into Cl4a and Cl4b with suitable occupancies was observed on Fourier-difference maps. This split is consistent with the presence of two different (in terms of radii) atoms Pb6/Mn6 ($1.19 \text{ \AA} / 0.75 \text{ \AA}$) in the same position leading to 80% Mn-Cl4a ($=2.32 \text{ \AA}$), 20% Pb-Cl4b ($=3.16 \text{ \AA}$). The calculated BVS shown in the Table II.17 validate the predominant Mn^{2+} character of this mixed site, while the concomitant Pb seems overbonded, but its minor occupancy (20%) does not allow to conclude since local shifts of the oxygen neighbors would not be revealed by XRD.

Table II.17. BVS of the atoms in Bi₉O₉Cl₄(Pb_{0.2}Mn_{0.8})O₃Cl

Atom	BVS
Bi1	3.11(8)
Bi2	3.38(10)
Bi3	2.83(8)
Bi4	3.25(8)
Bi5	2.87(7)
Pb6	2.74(4)
Mn6	1.89(5)
Cl1	0.7620(9)
Cl2	0.694(5)
Cl3	0.862(8)
Cl4a	1.29(3)
Cl4b	0.743(9)

It is noteworthy that the choice for Pb in this site rather than Bi is justified by the original coordination of the Pb6/Mn6 site: 4O + 1Cl, which is not common to Bi^{III} compounds. There is no clue for the ordering of the PbO₄Cl and MnO₄Cl polyhedra in single crystal diffraction data. The Figure II.61b, shows the arrangement of the MnO₄Cl/PbO₄Cl rectangular pyramids connected by sharing respective corners along the *a*-axis.

Finally, by applying anisotropic atomic displacement parameters for all Bi/Pb/Cl atoms, the residual factors converged to R1 = 0.047 and wR = 0.067 for 72 refined parameters and 1189 used reflections. The refined atomic positions and anisotropic displacement parameters and the pertinent distances are listed in Annex IV.28).

As it is shown on the Figure II.61a the crystal structure of Bi₉O₉Cl₄(Pb_{0.2}Mn_{0.8})O₃Cl is formed of a fluorite like [(Bi,Pb,Mn)₂O₂]²⁺ layers interconnected by transverse ribbons of OBi₄ tetrahedra into 2x2x2 triangular channels separated with a single chlorine layer (Figure II.61c). The connection between the channel walls is achieved by penta-coordinated O5 atoms (OBi₃(Pb/Mn)₂), shown in magenta in the Figure II.61c, which involves rather long O5-Pb6/Mn6 bond of 3.47 Å. The channels are filled by chlorine ions. The bismuth atoms, surrounding this chlorine channel, are eight coordinated with four Cl and four O atoms, the Bi–O distances range from 2.20 Å to 2.30 Å, giving reliable BVS values, see Table II.17.

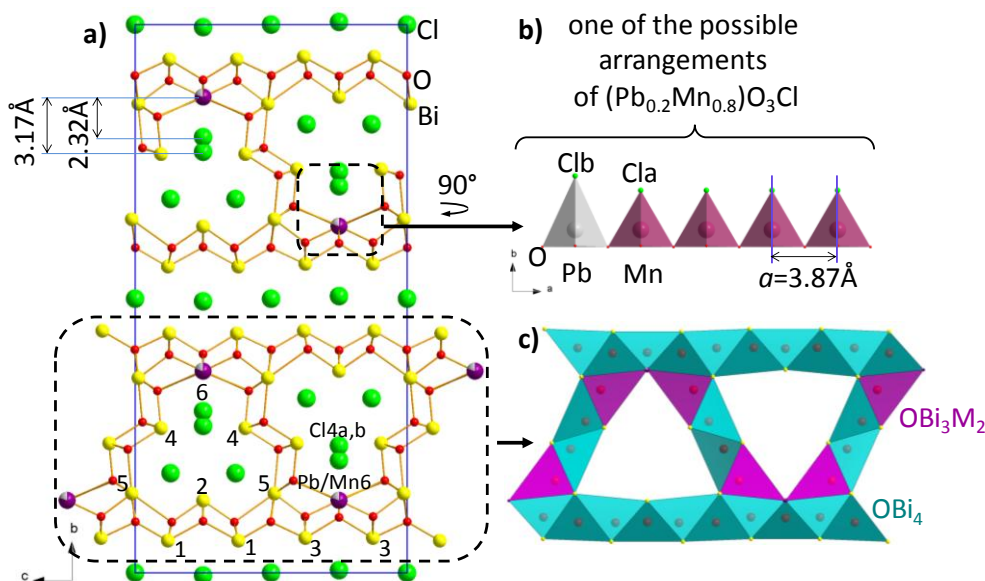


Figure II.61. a) The crystal structure of $\text{Bi}_9(\text{Pb}_{0.2}\text{Mn}_{0.8})\text{O}_{12}\text{Cl}_5$ and b) one of the possible arrangements of $(\text{Pb}_{0.2}\text{Mn}_{0.8})\text{O}_3\text{Cl}$ rectangular pyramids; c) the channel walls are formed by oxocentered OBi_4 tetrahedra (cyan), while the connection of OBi_3M_2 ($\text{M} = \text{Pb}/\text{Mn}$) rectangular pyramids are highlighted in purple.

The framework given on the Figure II.61c resembles that of $[\text{Bi}_6\text{O}_6\text{F}]\text{OCl}_3$ ⁶⁹ (Figure II.62a), $(\text{Ag}_{4.78}\text{Cl}_{1.5})(\text{Bi}_{48}\text{O}_{58.64}\text{Cl}_{30})$ ⁶⁷ (Figure II.62b) and $\text{Bi}_{12}\text{O}_{15}\text{Cl}_6$ ⁶⁸ (Figure II.62c) where the lack of a single halide layer can be noted. In these porous structures the cavities are created by interconnection of the walls of edge shared OBi_4 and $\text{OBi}_4/\text{FBi}_4$ tetrahedra respectively. The numbers of edge shared XBi_4 ($\text{X} = \text{O}, \text{F}$) tetrahedra ($\#Td$) along the width of the inner walls is used in the nomenclature of the sizes of the cavities. Thus for $\text{Bi}_{12}\text{O}_{15}\text{Cl}_6$ it is $4 \times 4 \times 4 Td$ and $2 \times 2 \times 2 Td$, for $[\text{Bi}_6\text{O}_6\text{F}]\text{OCl}_3$ it is $2 \times 2 \times 2 Td$, for $(\text{Ag}_{4.78}\text{Cl}_{1.5})(\text{Bi}_{48}\text{O}_{58.64}\text{Cl}_{30})$ it is $2 \times 2 \times 2 Td$.

Parallely to this study, in our laboratory group, another two new compounds, $\text{Bi}_6\text{NaO}_{7.5}\text{Cl}_4$ (Figure II.62d) and $\text{Bi}_{17}\text{PbO}_{22}\text{Cl}_9$ (Figure II.62e), have been obtained by Dr. Minfeng Lu, the structures of which is very close to that of the present work i.e. $\text{Bi}_9(\text{Pb}_{0.2}\text{Mn}_{0.8})\text{O}_{12}\text{Cl}_5$ (Figure II.62f). The cavity sizes for the last three compounds are: $3 \times 3 \times 3 Td$, $2 \times 2 \times 2 Td$ and $2 \times 2 \times 2 Td$, respectively. The interconnection of the walls is made via $\text{O}(\text{Bi},\text{M})_5$ rectangular pyramids as it is shown in purple on the Figure II.62 in all the structures. However as it is seen in the Figure II.62f, the present compound, $\text{Bi}_9(\text{Pb}_{0.2}\text{Mn}_{0.8})\text{O}_{12}\text{Cl}_5$, is an exception, in a way of the interconnection is made. The difference is that the “short walls” instead of sharing the same $\text{O}(\text{Bi},\text{M})_5$ pyramid in order to be connected onto the “infinite wall”, as it is the case for the rest of the given structures, connected via one pyramid per connection.

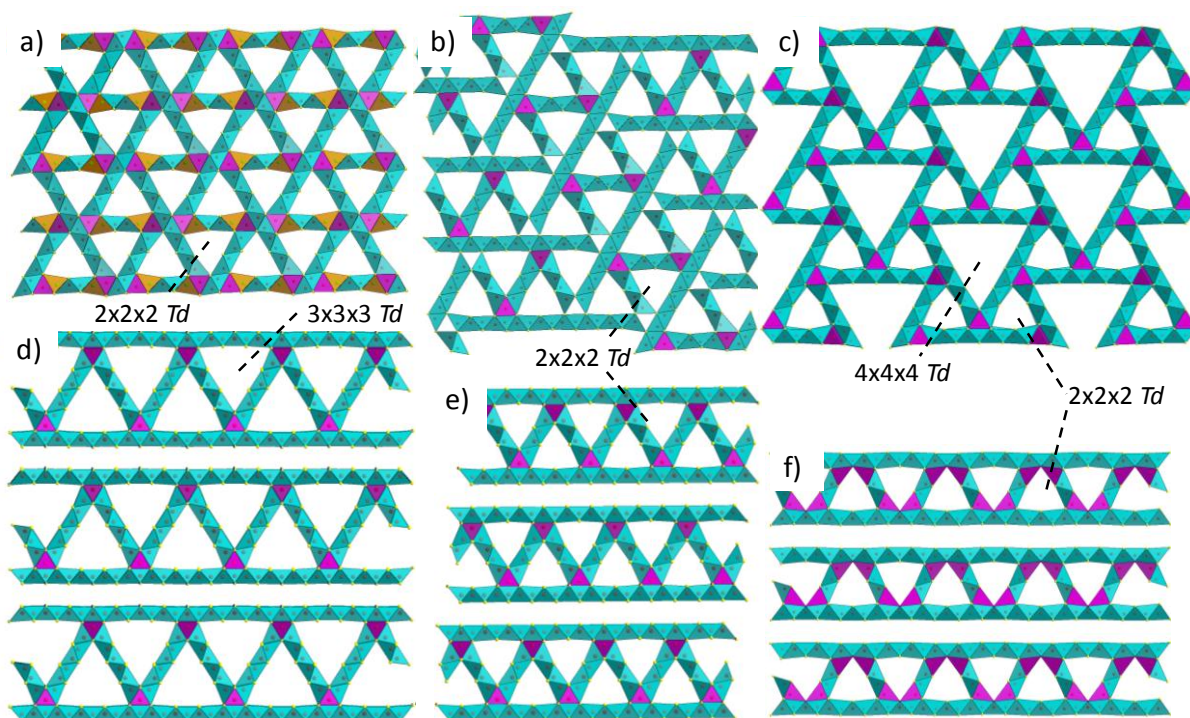


Figure II.62. Comparison of the Porous 3D networks of $O(\text{Bi},\text{M})_4$ tetrahedra in cyan (the connection of $O(\text{Bi},\text{M})_5$ rectangular pyramid is highlighted in purple): a) $[\text{Bi}_6\text{O}_6\text{F}]\text{OCl}_3$ where in yellow is the FBi_4 tetrahedra, b) $(\text{Ag}_{4.78}\text{Cl}_{1.5})(\text{Bi}_{48}\text{O}_{58.64}\text{Cl}_{30})$, c) $\text{Bi}_{12}\text{O}_{15}\text{Cl}_6$, d) $\text{Bi}_6\text{NaO}_{7.5}\text{Cl}_4$, e) $\text{Bi}_{17}\text{PbO}_{22}\text{Cl}_9$, f) $\text{Bi}_9(\text{Pb}_{0.2}\text{Mn}_{0.8})\text{O}_{12}\text{Cl}_5$. The same scale is given for all the structures.

4) Summary

The structure of new $\text{Bi}_9(\text{Pb}_{0.2}\text{Mn}_{0.8})\text{O}_{12}\text{Cl}_5$ is described as a porous interconnected $[\text{O}_2\text{Bi},\text{M}]_2$ network filled with chlorine atoms as related $(\text{Ag}_{4.78}\text{Cl}_{1.5})(\text{Bi}_{48}\text{O}_{58.64}\text{Cl}_{30})$, $\text{Bi}_{12}\text{O}_{15}\text{Cl}_6$ and $[\text{Bi}_6\text{O}_6\text{F}]\text{OCl}_3$. A strong relationship with two other new compounds of the laboratory has been shown which suggest a homology in these series.

II.3 3D-units - frameworks

II.3.1 Bi₄₆O₅₃(AsO₄)₈ and Bi₁₄O₁₅(AsO₄)₄

1) Context of the study

Numerous attempts have been carried out by SOFC community to stabilize fluorite type high temperature $\delta\text{-Bi}_2\text{O}_3$ phase in order to keep its excellent ionic conductivity properties at lower temperature ranges.^{29,30,159,160} It has been shown that in the recognized family of stable BIMEVOX the oxygen mobility is high.^{29,30} Particularly the system $\text{Bi}_2\text{O}_3\text{-M}_2\text{O}_5$ in which M is a pentavalent cation, is attractive, since they have showed satisfactory to good ionic conductivities.^{28,161} Thus, $\text{Bi}_{14}\text{O}_{15}(\text{XO}_4)_4$ ($=\text{Bi}_{14}\text{X}_4\text{O}_{31}$), $\text{Bi}_{46}\text{O}_{53}(\text{XO}_4)_8$ ($=\text{Bi}_{46}\text{X}_8\text{O}_{89}$), and $\text{Bi}_{50}\text{V}_4\text{O}_{85}$ are the three members of a general family type $\text{Bi}_{18-4m}\text{X}_{4m}\text{O}_{27+4m}$ ($\text{X} = \text{V}, \text{P}$), where

m is the ratio of the number of $[\text{Bi}_{14}\text{O}_{15}(\text{XO}_4)_4]$ layers to the total number of layers yielding the definition of the phase.²⁸ This model propose that the structure of $\text{Bi}_{14}\text{O}_{15}(\text{PO}_4)_4$ ($m = 1$) results from the repetition of 16x $\text{Bi}_{14}\text{O}_{15}(\text{PO}_4)_4$ layers parallel to the (001) plane; $\text{Bi}_{46}\text{O}_{53}(\text{XO}_4)_8$ ($\text{X} = \text{V}, \text{P}$ and $m = 2/3$) is formed from the stacking of $[\text{Bi}_{14}\text{O}_{15}(\text{XO}_4)_4, \text{Bi}_{18}\text{O}_{27}, \text{Bi}_{14}\text{O}_{15}(\text{XO}_4)_4]$ successive layers, while $\text{Bi}_{50}\text{V}_4\text{O}_{85}$ ($m = 1/3$) results from $[\text{Bi}_{14}\text{O}_{15}(\text{VO}_4)_4, \text{Bi}_{18}\text{O}_{27}, \text{Bi}_{18}\text{O}_{27}]$ layers. In the compounds described here we have Bi-rich lattice substituted by XO_4 groups (specifically AsO_4) leading to super cell of Bi_2O_3 -fluorites. On the opposite to the compounds described above where the significant amount of XO_4 delimits chains, ribbons or layers, here the substitution is ordered but locally arranged, leading to 3D-frameworks. Of course there are a number of complex supercell of this type obtained in the literature^{72,162–166} by substitution of Bi^{3+} centers by P^{5+} or V^{5+} with different polytypes depending on the Bi/X ratio. Also the electroneutrality can be reached by a complementary substitution of Bi^{3+} by aliovalent A^{n+} cations such as in $(\text{M}, \text{Bi})_{46}\text{V}_8\text{O}_y$ family ($\text{M} = \text{Pb}, \text{Sr}, \text{Ca}, \text{Cd}, \text{Na}_{0.5}\text{Bi}_{0.5}$).¹⁶⁴ However, it turns out that the $\text{XO}_4 = \text{AsO}_4$ case has been less studied, and deserves attention in the frame of this work.

In this work we give crystal structures of two bismuth arsenates $\text{Bi}_{14}\text{O}_{15}(\text{AsO}_4)_4$ and $\text{Bi}_{46}\text{O}_{53}(\text{AsO}_4)_8$ and compare the ionic conductivity of both compounds with known isotypical structures, $\text{Bi}_{46}\text{O}_{53}(\text{XO}_4)_8$ and $\text{Bi}_{14}\text{O}_{15}(\text{XO}_4)_4$ ($\text{X} = \text{P}$ and V).

2) Synthesis.

Single crystal: The single crystals of the two arsenates were found in the preparations obtained in gold tubes by melting of precursor mixtures at 950°C for 5 hours then slowly cooling down to 700°C with the rate of 1°C h⁻¹, then the furnace was switched off. The precursor's mixtures taken for the crystal growth were the following:

for **$\text{Bi}_{46}\text{O}_{53}(\text{AsO}_4)_8$** : $0.5\text{Rb}_2\text{CO}_3 + 2.5\text{Bi}_2\text{O}_3 + \text{As}_2\text{O}_5$

for **$\text{Bi}_{14}\text{O}_{15}(\text{AsO}_4)_4$** : $0.5\text{Li}_2\text{CO}_3 + 2.5\text{Bi}_2\text{O}_3 + \text{As}_2\text{O}_5$.

Powder synthesis:

$\text{Bi}_{46}\text{O}_{53}(\text{XO}_4)_8$: The following reagents with their respective purities have been used in the syntheses: Bi_2O_3 (Aldrich 99.9%), As_2O_5 (Alfa Aesar, 99.6%), $(\text{NH}_4)_2\text{HPO}_4$ (Acros, 99%), V_2O_5 (Aldrich, 99.6%). The polycrystalline samples of all the compounds have been treated in the same way. Namely, the stoichiometric amounts of respective reagents were thoroughly ground in agate mortar followed, first, by heating in alumina crucible at 400°C for 12 hours then after pelletizing heated in alumina crucible at 850°C for 48 hours with several intermediate regrindings.

Bi₁₄O₁₅(AsO₄)₄: The powder of Bi₁₄O₁₅(PO₄)₄ has been treated initially in the same way as Bi₄₆O₅₃(AsO₄)₈ compound, then reheated at 850°C for 48 hours under O₂ flow.

3) Structural description.

3a) Bi₄₆O₅₃(AsO₄)₈

The structure of Bi₄₆O₅₃(AsO₄)₈ has been solved from single crystal X-ray data. The crystal data collection and refinement parameters are gathered in Table II.18. The structure of Bi₄₆O₅₃(AsO₄)₈ is isotypic to Bi₄₆O₅₃(VO₄)₈, mentioned by Kashida et al. in triclinic system¹⁶³ and to the structure of Bi₄₆O₅₃(PO₄)₈, solved by Watanabe et al. in *P2₁/c*.¹⁶² and later by Darriet et al.⁷² in monoclinic *C2/c*. This evidenced difficulties to determine the space groups of corresponding Bi₄₆O₅₃(XO₄)₈ compound. In the Table II.19 different crystal data of listed above Bi₄₆O₅₃(XO₄)₈ structures is given, including our data.

Table II.18. Crystal data, measurement and structural refinement parameters of Bi₄₆O₅₃(AsO₄)₈ and Bi₁₄O₁₅(AsO₄)₄

	Bi ₄₆ O ₅₃ (AsO ₄) ₈	Bi ₁₄ O ₁₅ (AsO ₄) ₄
Crystal data		
Crystal symmetry	Monoclinic	Monoclinic
space group	C2/m	C2/c
a (Å)	20.0213 (5)	19.6944(3)
b (Å)	11.5567 (3)	11.3649(1)
c (Å)	21.1107 (5)	53.3541(7)
β (°)	111.9340 (12)	94.2150(6)
V (Å ³)	4531.0 (2)	11909.7(3)
Z	2	16
Dx (g/cm ³)	8.526	8.299
μ(mm ⁻¹)(for λ Kα=0.7107Å)	91.96	86.93
Appearance	transparent	transparent
Crystal size (mm)	0.13×0.09×0.05	0.22 × 0.11 × 0.05
Data collection		
λ(Mo Kα) (Å)	0.71073	0.71073
Scan mode	ω and φ	ω and φ
θ(min–max) (°)	2.1 – 37.8	1.5 – 26.4
R(int) (%)	0.064	0.073
Recording reciprocal space	–33 ≤ h ≤ 34 –19 ≤ k ≤ 19 –30 ≤ l ≤ 33	–24 ≤ h ≤ 24 –14 ≤ k ≤ 14 –66 ≤ l ≤ 66
Refinement		
Measured, independent obs.* refl.	61767, 11554, 5613	126363, 12244, 9826
No. of Refined parameters	398	568
Refinement method,	F	F
R1(F ²)(obs) / R1(F ²)(all)	0.0494/0.0525	0.0349/0.0485
wR2(F ²)(obs) /wR2(F ²)(all)	0.0525/0.0612	0.0338/0.0470
GOF(obs) / GOF(all)	1.38/1.72	0.28/0.35
Δρ _{max} / Δρ _{min} (e Å ⁻³)	12.49 /–11.82	4.44 /–4.44
Extinction coefficient	0.0098(6)	0.0207(2)

The $\text{Bi}_{46}\text{O}_{53}(\text{AsO}_4)_8$ compound was briefly mentioned in triclinic system with lattice parameters $a = 11.5179$ (5) Å, $b = 11.5226$ (6) Å, $c = 20.6063$ (1) Å, in ref [165] in absence of any structural investigation.

After empirical absorption corrections, the merging in different Laue group symmetries of the significant reflections ($I > 3\sigma(I)$) shows a strong preference for a monoclinic $2/m$ symmetry ($b = 11.5567(3)$ as unique axis), $R_{\text{int}} = 5.21\%$. In his study Darriet et al. proposed for isostructural $\text{Bi}_{46}\text{O}_{53}(\text{VO}_4)_8$ two refinements in two space groups $P2_1/c$ (ordered XO_4 and unique Bi positions) and $C2/m$ (some splitted VO_4 and Bi positions) concluded finally in the former model. In our $X = \text{As}$ case, the observed reflections are coherent with a C centered symmetry. In this case, there is no additional weak intensity as it was the case in Darriet's study (coherent with space group $P2_1/c$) as shown on the calculated precession frames $h0l$ and $h1l$ (Figure II.63).

Table II.19. Published $\text{Bi}_{46}\text{O}_{53}(\text{XO}_4)_8$ structures with their the respective unit cell parameters

	Kashida et al. ¹⁶³ 1996	Watanabe et al. ¹⁶² 1998	Lee et al. ¹⁶⁵ 2005	Darriet et al. ⁷² 2005	Labidi et al. ¹⁶⁴ 2008, $\text{Bi}_{46}\text{V}_8\text{O}_{90}$	Kuang et al. ¹⁶⁶ 2012	Our study
$\text{Bi}_{46}\text{O}_{53}(\text{VO}_4)_8$ S.G. a , Å b , Å c , Å α , ° β , ° γ , °	$P-1$ 20.023(29) 11.668(14) 20.471(27) 90.0(1) 107.13(7) 90.0(1)			$P2_1/c$ 20.0100(3) 11.6445(2) 20.4136(3) 90 107.27(2) 90	$C2/m$ 20.0822(4) 11.6351(2) 21.0878(5) 90 111.678(1) 90	$C2/m$ 20.02938(5) 11.59621(3) 21.12860(6) 90 111.3366(2) 90	
$\text{Bi}_{46}\text{O}_{53}(\text{PO}_4)_8$ S.G. a , Å b , Å c , Å α , ° β , ° γ , °		$P-1$ 11.366(1) 11.369(1) 20.453(3) 77.535(8) 86.214(9) 119.565(7)		$C2/m$ 19.6073(3) 11.4181(2) 21.1119(3) 90 112.14(2) 90			
$\text{Bi}_{46}\text{O}_{53}(\text{AsO}_4)_8$ S.G. a , Å b , Å c , Å α , ° β , ° γ , °			$P-1$ 11.5179 (5) 11.5226 (6) 20.6063 (1) ? ? ?				$C2/m$ 20.0213(5) 11.5567(3) 21.1107(5) 90 111.934(1) 90

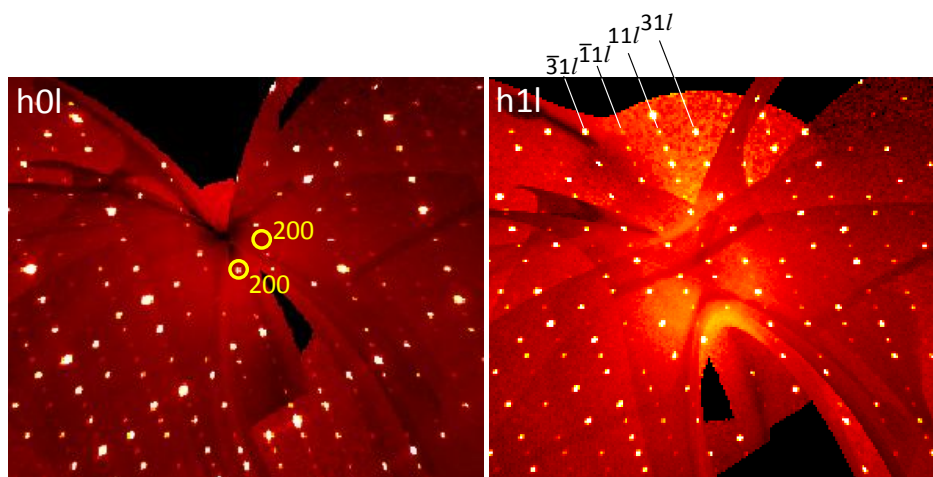


Figure II.63. The reflections in the (*h0l*) and (*h1l*) precession frames in good agreement with the *C*-Bravais lattice ($h+k=2n$)

We have solved it in monoclinic centered lattice with the unit cell parameters $a = 20.0213(5) \text{ \AA}$, $b = 11.5567(3) \text{ \AA}$, $c = 21.1107(5) \text{ \AA}$ and $\beta = 111.9340(12)^\circ$, space group $C2/m$, the R1 value is 4.94.

The structure of Bi₄₆O₅₃(AsO₄)₈ (Figure II.64a) can be considered as a framework [Bi₄₆O₅₇]²⁴⁺, formed by connection of various oxocentered OBi_n polyhedra, incrustated with AsO₄³⁺ tetrahedra and it is compared to the structure of β -Bi₄₆O₅₃(VO₄)₈ (Figure II.64b)

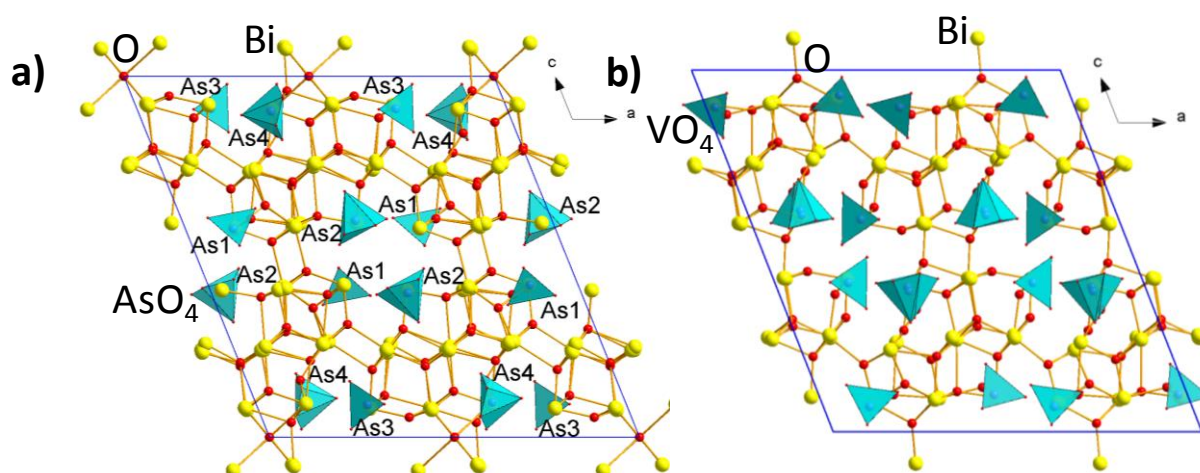


Figure II.64. a) The structure of Bi₄₆O₅₃(AsO₄)₈, projection along *b*-axis and b) the structure of β -Bi₄₆O₅₃(VO₄)₈, projection along *b*-axis.

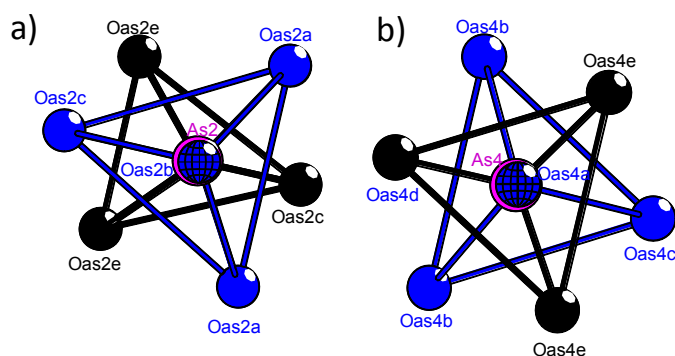


Figure II.65. Disordered a) $\text{As}(2)\text{O}_4$ and b) $\text{As}(4)\text{O}_4$ tetrahedra with two tilted positions in black and blue. The occupations of splitted O atoms fixed to 0.5.

The two arsenate polyhedra created by As2 and As4 atoms, in fact, are quite disordered and the averaged representation of two overlapped tetrahedra (Figure II.65a-b). In the same time, other two arsenates formed by As1 and As3 are well defined tetrahedra however with quite high ADPs of the oxygen atoms (not shown). The residual electronic density remains rather high ($12\text{e}/\text{\AA}^3$) and can be explained by the abundant presence of disorder, which is quite usual to this kind of compounds, for instance $\text{Bi}_{46}\text{O}_{53}(\text{VO}_4)_8$ and $\text{Bi}_{46}\text{O}_{53}(\text{PO}_4)_8$.⁷² The presence of the overlapped tetrahedra assorted with four split bismuth positions is closely related to the choice of the $C2/c$ space group. Indeed, in the structure of $\text{Bi}_{46}\text{O}_{53}(\text{VO}_4)_8$ refined by Darriet et al. in $P2_1/c$ space group, there is no ambiguity with the bismuth positions and the tetrahedra groups are particularly well defined. This polytype, more recently, has been associated to the α -form while a disordered polytype of $\text{Bi}_{46}\text{O}_{53}(\text{VO}_4)_8$ called the β -form ($C2/m$) was also prepared and characterized by HT-powder neutron diffraction. In analogy, one can conclude, that the ordering of AsO_4 groups is partial in our compound, but may be ruled by the thermal conditions for the crystal synthesis. We also note the refinement of the $\text{X} = \text{P}$ case i.e. $\text{Bi}_{46}\text{O}_{53}(\text{PO}_4)_8$ compound by Darriet et al. in $C2/m$ space group, which reinforce the duality between long range and disordered polytypes in the full series.

3b) Structural description of $\text{Bi}_{14}\text{O}_{15}(\text{AsO}_4)_4$

Another new arsenate compound has been isolated as byproduct as it is described in the synthesis part. A colorless crystal has been isolated, mounted on a glass fiber and single crystal XRD data was collected. The final unit cell parameters refined from the data set is $a = 19.6944(3) \text{ \AA}$, $b = 11.3649(1) \text{ \AA}$, $c = 53.3541(7) \text{ \AA}$ and $\beta = 94.2150(6)^\circ$. The observed extinction rules suggested the space group $C2/c$ or Cc . The former space group was chosen as having the lowest agreement factor after using structure solving program Superflip¹⁶⁷. The same program gave the positions of the heavy atoms of the unit cell: 28 positions for Bi and 8

positions for As atoms. The oxygen atom positions were deduced from successive difference Fourier maps. 62 oxygen atoms were localized without any ambiguity. At the end of the refinement, the deduced formula is neutral and Bi₁₄O₁₅(AsO₄)₄. In these last cycles of refinement, anisotropic displacement were considered for every Bi and As atoms yielding final $R_I = 0.0349$ ($R_{\text{all}} = 0.0485$) and $wR_2 = 0.0338$ ($wR_{\text{all}} = 0.0470$). The crystallographic characteristics, conditions of data collection and various refinement parameters are gathered in Table II.18. The atomic coordinates with isotropic and anisotropic thermal parameters and selected bond distances and angles are available on Annex IV.210).

This new bismuth arsenate Bi₁₄O₁₅(AsO₄)₄ is isotypic to Bi₁₄O₁₅(PO₄)₄ which crystallises also in monoclinic crystal system with lattice parameters $a = 19.6944(3) \text{ \AA}$ $b = 11.3649(1) \text{ \AA}$ $c = 53.3541(7) \text{ \AA}$ $\beta = 94.2150(6)^\circ$, space group $C2/c$ and R_1 value is 0.0349⁷³. The structure of Bi₁₄O₁₅(AsO₄)₄ can be described as wave-like [Bi₁₄O₁₅]¹²⁺ layers going vertically (see Figure II.66a) with incorporated AsO₄ tetrahedra as it is the case for its phosphorus analog (see Figure II.66b), however the [Bi₁₄O₁₅]¹²⁺ layers of the latter are plane.

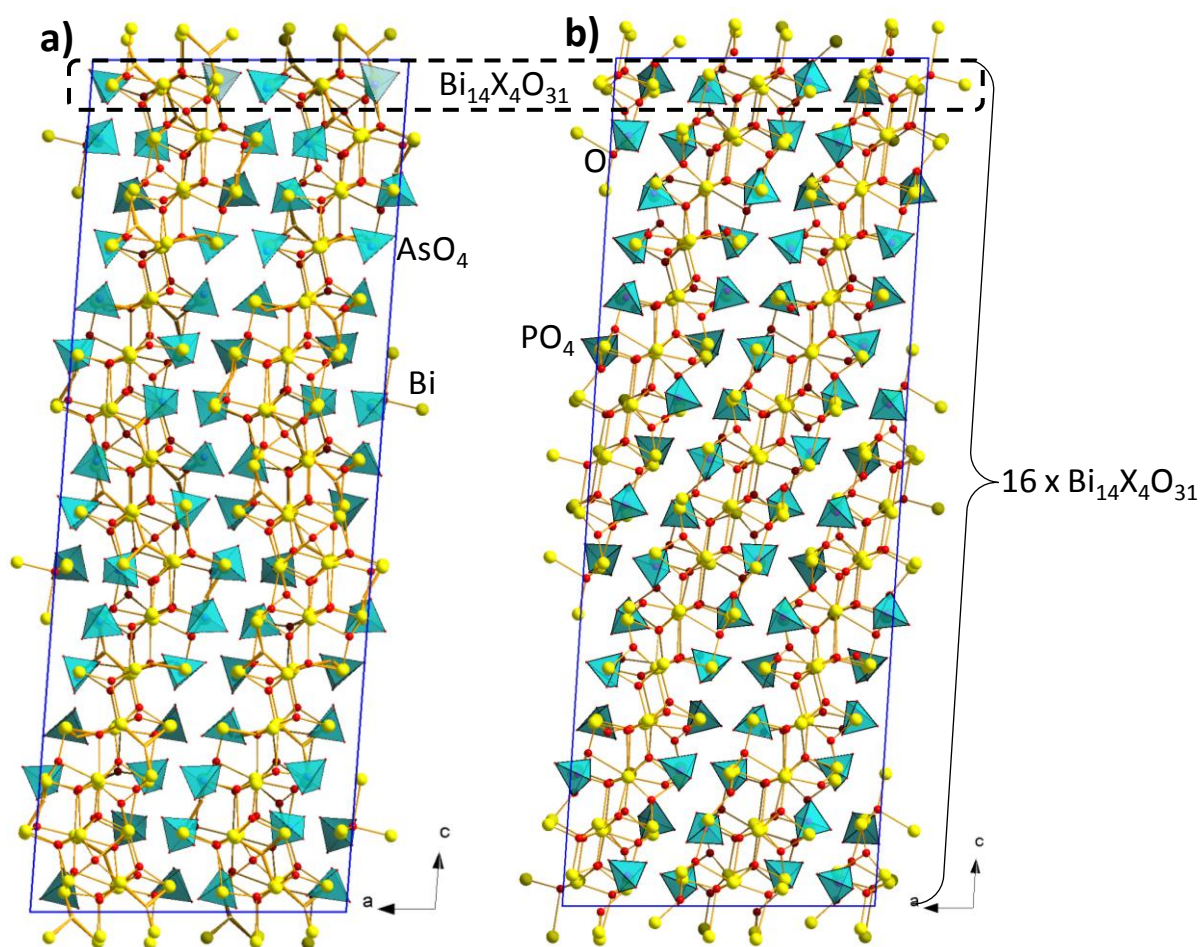


Figure II.66. a) The structure of Bi₁₄O₁₅(AsO₄)₄, and that of b) Bi₁₄O₁₅(AsO₄)₄.

As it is the case for $\text{Bi}_{14}\text{O}_{15}(\text{PO}_4)_4$, the coordination number of Bi^{III} is equal to 3 or 5 due to the stereochemically active lone pair of bismuth. No disorders observed at the bismuth atoms nor at the AsO_4 group. The As-O distances of latter are in between 1.619(2) and 1.717(20) Å, being in acceptable range with respect to corresponding radii.

The $[\text{Bi}_{14}\text{X}_4\text{O}_{31}]$ building block notion was used in the description of the structure of $\text{Bi}_{14}\text{O}_{15}(\text{PO}_4)_4$ and $\text{Bi}_{50}\text{V}_4\text{O}_{85}$ by Mauvy et al.⁷³ Similarly, the structure of $\text{Bi}_{14}\text{O}_{15}(\text{AsO}_4)_4$ can be considered as stacking of $[\text{Bi}_{14}\text{As}_4\text{O}_{31}]$ ($=[\text{Bi}_{14}\text{O}_{15}(\text{AsO}_4)_4]$) layers, parallel to (a, b) plane as it is shown on the Figure II.66a.

4) Conductivity measurements

4a) $\text{Bi}_{46}\text{O}_{53}(\text{AsO}_4)_8$

The powder of $\text{Bi}_{46}\text{O}_{53}(\text{AsO}_4)_8$ was obtained as described in the synthesis part as single phase. the diffraction pattern of which is shown on the Figure II.67. The unit cell parameters were refined to $a = 19.997(2)$ Å, $b = 11.541(2)$ Å, $c = 21.061(2)$ Å, $\beta = 111.863(5)^\circ$ and $V = 4510.8(7)\text{Å}^3$ with reliability parameter $\chi^2 = 2.98$.

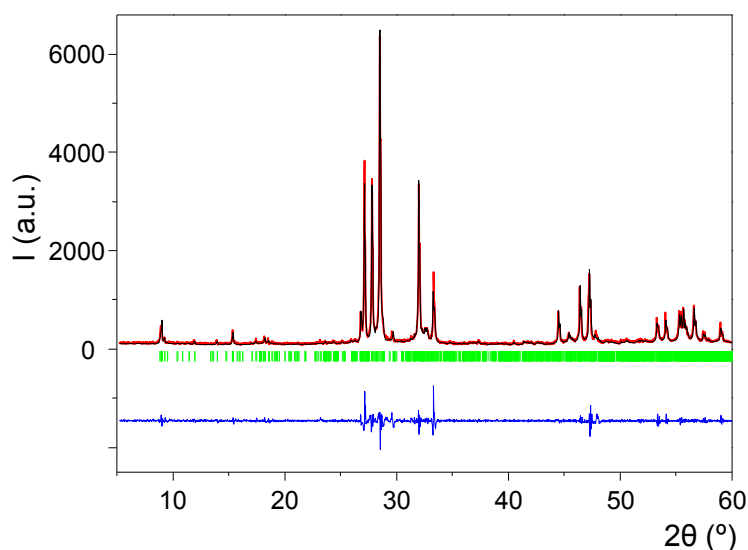


Figure II.67. The pattern matching fit of the $\text{Bi}_{46}\text{O}_{53}(\text{AsO}_4)_8$ phase.

Due to the disorders inherent to the structure we can expect from $\text{Bi}_{46}\text{O}_{53}(\text{AsO}_4)_8$ ionic conductivities comparable to other disordered bismuth oxides. Previously, ionic conductivity was already measured on $\text{Bi}_{46}\text{O}_{53}(\text{PO}_4)_8$ and $\text{Bi}_{46}\text{O}_{53}(\text{VO}_4)_8$ by Wantanabe et al.¹⁶², as well as on $\text{Bi}_{14}\text{O}_{15}(\text{PO}_4)_4$ and $\text{Bi}_{50}\text{V}_4\text{O}_{85}$ by Mauvy et al.⁷³, showing good ionic conductivities for the vanadate ($\sigma_{600} = 10^{-2} \text{ ohm.cm}^{-1}$ for $\text{Bi}_{46}\text{O}_{53}(\text{VO}_4)_8$). More recently $\text{Bi}_{46}\text{O}_{53}(\text{VO}_4)_8$ was reinvestigated for ionics properties using the β -disordered polytype obtained as a powder.¹⁶⁶

The authors found good ionic conductivity previously noted by other groups. Ab-initio molecular dynamics suggest that the ion migration pathways includes vacancy diffusion through the Bi-O lattice as well as the O²⁻ exchange between the Bi-O and the V-O sublattices, facilitated by the disorder. Here we would like to estimate the effect of the AsO₄ introduction on ionic properties transport properties.

For this purpose we have prepared the X = P, V and As compounds as single phase powders and measured the ionic transport properties as detailed in section II.2.2. The Figure II.68a shows the comparison between the Nyquist plots of the X = V vanadate compound between the ref [166] at 679°C and our measurements at 675°C and 694°C. In fact due to the different electrochemical activity of the pasted electrodes (Au in our study versus Pt in ref.[166]) the observed semi-circular contributions of each components are different. However, at 675°C we measure a resistivity of 70 Ω·cm⁻¹ comparable to the 40 Ω·cm⁻¹ measured by the other group at 679°C in terms of decade.

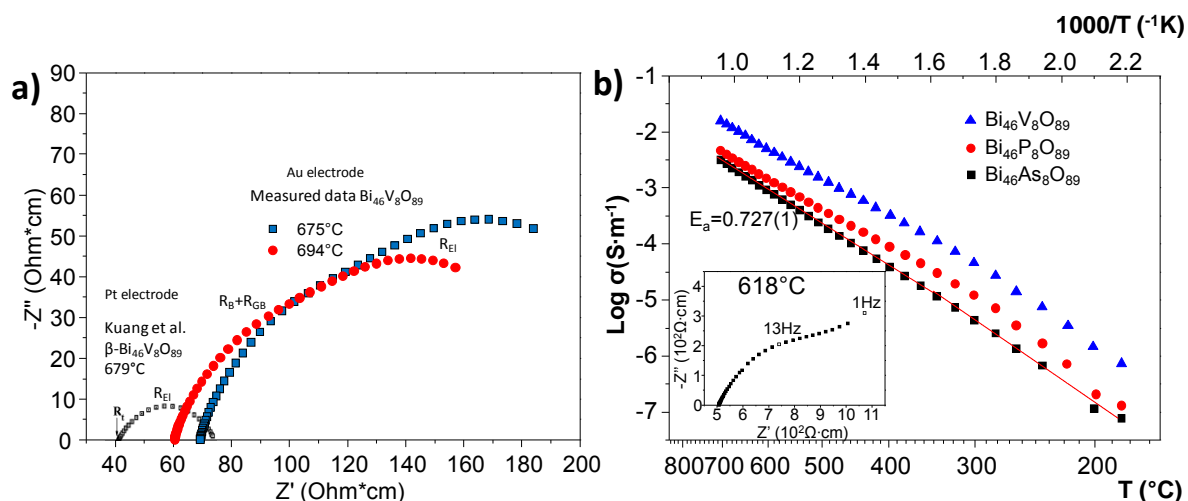


Figure II.68. a) Nyquist plots for β - Bi₄₆O₅₃(VO₄)₈ at 679°C in black from ref [166] (platinum electrode) and measured data of Bi₄₆O₅₃(VO₄)₈ at 675°C in blue squares and at 694°C in red circles (gold electrode); b) Arrhenius plots of conductivities of Bi₄₆O₅₃(XO₄)₈, (X = P, V and As). Inset: Nyquist plot for X = As at 618°C.

It validates our results for the all three compounds (densification of the pellets: 93.3% for Bi₄₆O₅₃(AsO₄)₈, 90.7% for Bi₄₆O₅₃(PO₄)₈ and 95.3% for Bi₄₆O₅₃(VO₄)₈). Indeed, as it is shown in the Figure II.68b, Bi₄₆O₅₃(AsO₄)₈ is effectively an ionic conductor, however, in lesser extent than Bi₄₆O₅₃(VO₄)₈ and Bi₄₆O₅₃(PO₄)₈. It was already checked in ref [162] that the Bi₄₆P_{8-x}V_xO₈₉ solid solution exists and shows the best conductivity for the vanadates are-confirmed here. It is due to the larger cell volume and variability of the vanadium

coordination environments and rotational freedom of the VO_x coordination polyhedral as shown by molecular dynamics.¹⁶⁶

Apart from this V specificity as shown on the Figure II.64b, there is no direct dependency of the conductivities of the compounds on the respective radii of pentavalent cations, since $r(\text{As}^{5+}) = 0.34\text{\AA}$, $r(\text{P}^{5+}) = 0.17\text{\AA}$ and $r(\text{V}^{5+}) = 0.355\text{\AA}$.¹¹⁰ while the arsenate seem a worst conductor than the phosphate despite the same disordered evidenced in our compound and in the phosphate.⁷² Same results are expected on $\text{Bi}_{14}\text{O}_{15}(\text{AsO}_4)_4$, the compound presented in the next section by analogy to the $\text{Bi}_{14}\text{O}_{15}(\text{PO}_4)_4$, but this complementary conductivity study was not achieved in the frame of this work.

4b) $\text{Bi}_{46}\text{O}_{53}(\text{AsO}_4)_8$

Initially, the attempts to prepare this compound in a polyphasic form have been failed showing the mixture of minor $\text{Bi}_{14}\text{O}_{15}(\text{AsO}_4)_4$ and major phase $\text{Bi}_{46}\text{O}_{53}(\text{AsO}_4)_8$. Apparently $\text{Bi}_{46}\text{O}_{53}(\text{AsO}_4)_8$ is more thermodynamically preferred phase in these synthesis conditions, however after treating at 850°C under oxygen flow during 48h shows single phase as it is shown Figure II.69.

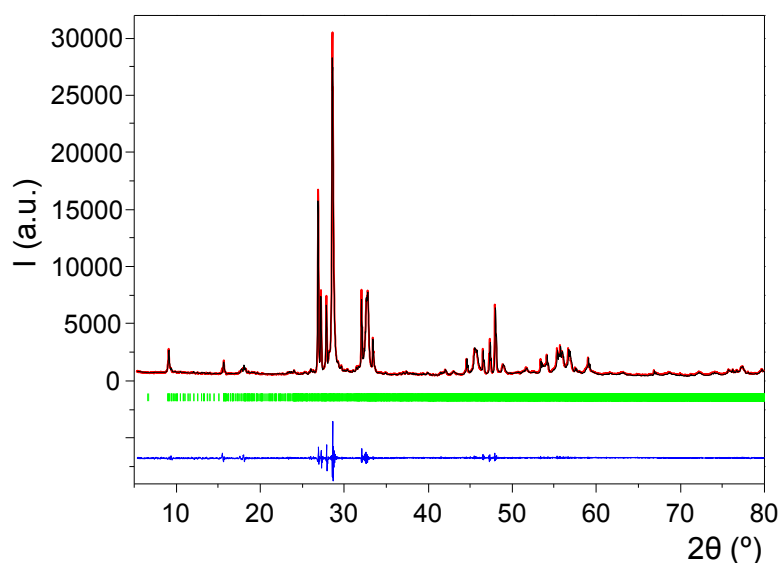


Figure II.69. Profile matching fit of the $\text{Bi}_{14}\text{O}_{15}(\text{AsO}_4)_4$ phase.

The conductivity measurements on $\text{Bi}_{14}\text{O}_{15}(\text{AsO}_4)_4$ has not conducted yet but it is expected that the compound will be a bad conductor due to the absence of disorders in its structure. Indeed the analogous $\text{Bi}_{14}\text{O}_{15}(\text{PO}_4)_4$ showed that this compounds is rather resistive ($\sigma_{600} = 10^{-7} \text{ Ohm}\cdot\text{cm}^{-1}$).

5) Summary

Two bismuth arsenates have been obtained by solid state reactions as single crystal and pure powder. First one, Bi₄₆O₅₃(AsO₄)₈ mentioned by Watanabe in triclinic system, was solved in monoclinic crystal system in the space group *C2/m*, probably showing a new polymorph. The conductivity of the Bi₄₆O₅₃(AsO₄)₈ compound was compared to their homologous vanadate and phosphate showing that the arsenate is the worst of the three Bi₄₆O₅₃(XO₄)₈.

II.3.2 NaBi₁₃O₁₄(AsO₄)₄

1) Synthesis.

Single crystal:

Single crystals of NaBi₁₃O₁₄(AsO₄)₄ were found in the melt obtained by slow (3°C/h) cooling down to 600°C the mixture of 2.5Bi₂O₃ + 0.5Na₂CO₃ + As₂O₅ in a gold tube with one end left open priory heated at 950°C during 12h.

Powder synthesis:

The attempts to reproduce this compound in the polycrystalline form were not successful so far. Probably it requires a treatment under oxygen flows as it was the case for the previous case, Bi₁₄O₁₅(AsO₄)₄.

2) Structural description.

The structure of NaBi₁₃O₁₄(AsO₄)₄ crystalizes in monoclinic system in space group *C2/c* (15) with unit cell parameters $a = 19.8152(2) \text{ \AA}$, $b = 11.4845(2) \text{ \AA}$, $c = 27.7172(5) \text{ \AA}$, $\beta = 110.7910(9)^\circ$ and $V = 5896.8(2) \text{ \AA}^3$.

The structure of NaBi₁₃O₁₄(AsO₄)₄ (Figure II.70) resembles the one of Bi₁₄O₁₅(AsO₄)₄ by having quasi-2D [NaBi₁₃O₁₄]¹²⁺ layers separated double layer of AsO₄. The [NaBi₁₃O₁₄]¹²⁺ layers in this case are parallel along the *c* axis whereas in the case of Bi₁₄O₁₅(AsO₄)₄ the corresponding [Bi₁₄O₁₅]¹²⁺ layers propagated along the *c* axis in zig-zag like manner. No disorders at the AsO₄ tetrahedra nor splitting of bismuth atoms have been observed as it is usually the case with similar structures described in section above (II.3.1).

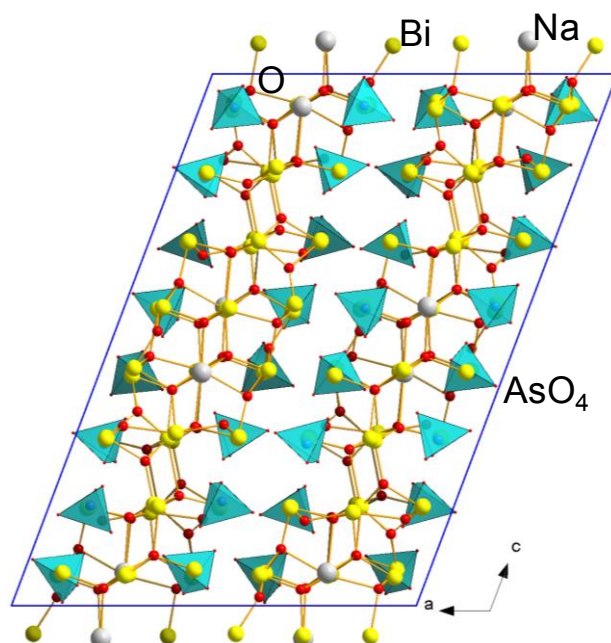


Figure II.70. The crystal structure of $\text{NaBi}_{13}\text{O}_{14}(\text{AsO}_4)_4$

3) Summary

The crystal structure of new $\text{NaBi}_{13}\text{O}_{14}(\text{AsO}_4)_4$ was described the similarities with $\text{Bi}_{14}\text{O}_{15}(\text{AsO}_4)_4$ shown. Synthesis conditions have to be changed to obtain the polycrystalline form to measure ionic conductivity properties.

*Chapter III. Other specific Bi-based
Compounds*

III. Other specific Bi-based Compounds

Owing to the richness of the crystal-chemistry of bismuth compounds, I prepared during my PhD work several other compounds that are gathered in this chapter. Their structural description does not involve the OBi_4 oxocentered groups, the basic units of the BUs described in the previous chapters. Thus, this chapter deals with other compounds in different chemical systems that sound to us sufficiently original for a dedicated thesis chapter.

III.1.1 $\text{Bi}_4\text{Mn}_{3+x}\text{O}_{11.5-y}$ - a new bismuth manganite with 2D-magnetic properties

This part deals with a new mixed $\text{Mn}^{3/4+}$ valence manganite in the system Bi-Mn-O. It possesses number of interesting properties due to its unusual modular structure. Especially, it has a 2D magnetic character owing to the isolated layers of MnO_6 octahedra arranged in a particular manner.

1) Synthesis.

1a) $\text{Bi}_4\text{Mn}_{3+x}\text{O}_{11.5}$

Single crystal: A black triangular-like platelet was selected for single crystal XRD analysis, from the reaction of the mixture $3\text{Bi}_2\text{O}_3 + 6\text{BiOCl} + \text{PbO} + \text{MnO}_2$ in a sealed gold tube during 12 hours at 900°C and slow cooling down to 500°C for 99 hours. The microprobe EPMA elemental analyzes of isolated black plate like crystals indicate the absence of Pb and Cl as constituting elements. The determined Bi/Mn ratio is 8/5.3. In the same preparation (Figure III.1) other type of crystals were found arranged in compact manner with the title compound.

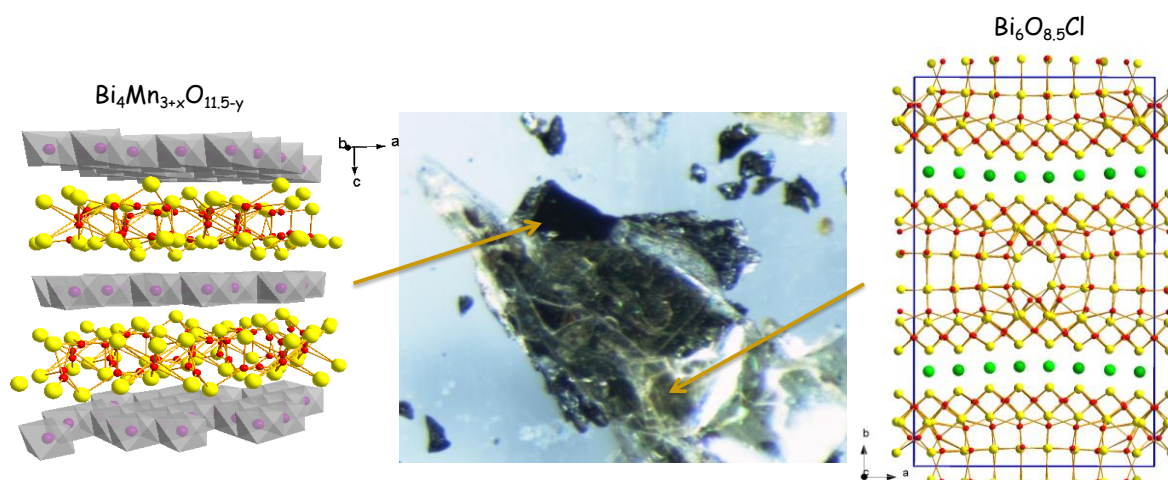


Figure III.1. The preparation with two types of crystal: black platelets of $\text{Bi}_4\text{Mn}_{3.03}\text{O}_{11.5}$ and transparent yellow platelets of $\text{Bi}_6\text{O}_{8.5}\text{Cl}$

That is $\text{Bi}_6\text{O}_{8.5}\text{Cl}$, which is discussed in the section II.2.3. The crystals were handily separated from the alien phase. The crystal structure refinement has given the accurate composition $\text{Bi}_4\text{Mn}_{3.03}\text{O}_{11.5}$ as discussed later on.

Powder synthesis: The powder synthesis deserves a detailed description since it has been quite difficult and time-consuming to obtain the pure target phase on the basis of the refined composition and expected XRD powder pattern.

After a number of different attempts to produce this phase by standard solid state routes (varying the precursors and atmospheres given in), we note the systematic predominance of $\text{Bi}_2\text{Mn}_4\text{O}_{10}$, which seems thermodynamically more stable at the temperature range above 600°C , see Figure III.2a-d.

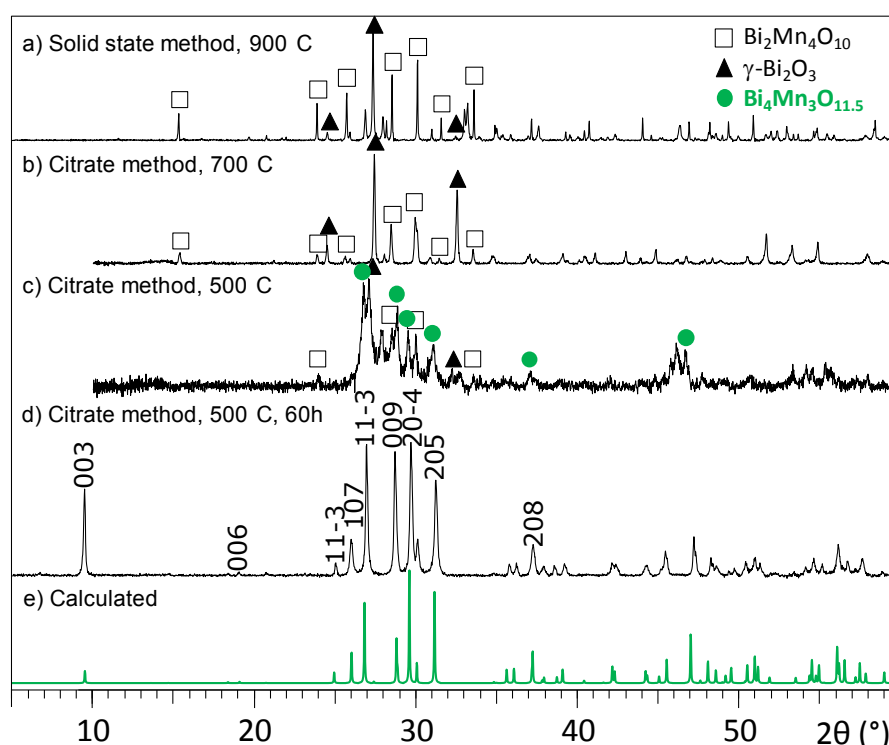


Figure III.2 Comparison of: a-d) experimental XRD and e) calculated patterns after different synthesis stages. In b) and c) the residue from citrate method was decomposed in situ in the diffractometer.

Only the decomposition at intermediate temperature (not more than 500°C) of the product obtained by a *modified*- citrate method¹⁶⁸ (as described below) shows the appearing of the expected phase, see Figure III.2c and also DTA-TG plots of an intermediate (300°C decomposition)-citrate precursor on the Figure III.3. This latter shows a large loss of organic species until 500°C .

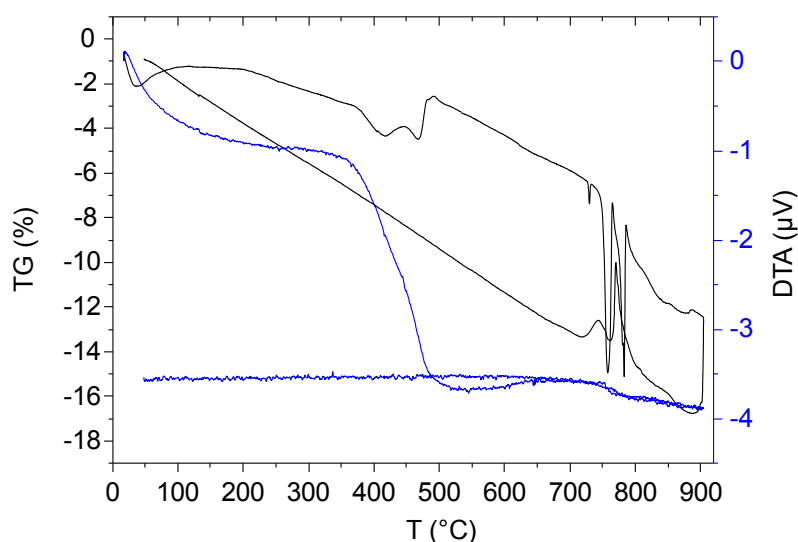


Figure III.3. The TGA-DTA curves of the residue obtained from citrate method at 300°C.

The procedure to obtain the pure phase by “modified” citrate method (Figure III.4) is following: 12.7 mmol of MnO_2 is dissolved with 12.7 mmol of citric acid in a hot DI water (50 ml), and 17.94 mmol of bismuth citrate dissolved separately in a hot DI water (50 ml) with addition of minimum amount of ammonia ($\rightarrow \text{pH} = 8$) to both the two solutions, after a quick evaporation until 20 ml each, the two solutions added together in one beaker and evaporated until very viscose transparent solution. (Note that even if not understood yet the “ammonia stage is necessary”). After removal of a part of the organic species at 300°C, a black powder was obtained which was amorphous, further heating of this black powder at 490°C during 60h gave dark brown powder of $\text{Bi}_4\text{Mn}_3\text{O}_{11.5}$ the XRD pattern of which is on Figure III.2d.

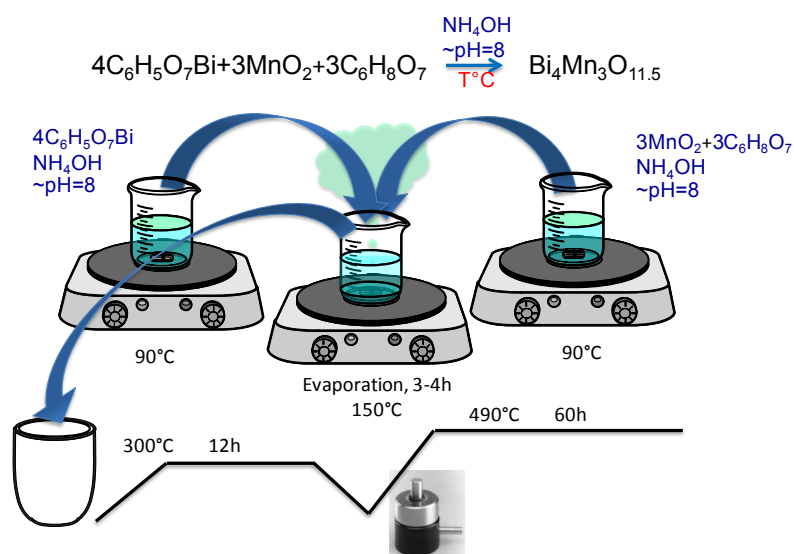


Figure III.4. Schema for powder synthesis by modified citrate method.

1b) Iron-doping $\rightarrow \text{Bi}_4\text{Mn}_{2.4}\text{Fe}_{0.6}\text{O}_{11.5}$

Powder synthesis: Several attempts to dope the structure of the parent $\text{Bi}_4\text{Mn}_3\text{O}_{11.5}$ have been conducted as well with different alien transition metals. At the moment, only Fe doping was successful until a ratio of 20% Fe/Mn. It leads to the possible elaboration of the compound with formula $\text{Bi}_4\text{Mn}_{2.4}\text{Fe}_{0.6}\text{O}_{11.5}$. In fact further PND data will show a slight deviation from this formula in the final compound. The procedure for powder preparation is the same as for $\text{Bi}_4\text{Mn}_3\text{O}_{11.5}$, considering stoichiometric amount of oxalate of iron II, FeC_2O_4 , as a Fe precursor. The diffractogram of the obtained powder of $\text{Bi}_4\text{Mn}_{2.4}\text{Fe}_{0.6}\text{O}_{11.5}$ shown on the figure Figure III.5 in black and it is compared with that of $\text{Bi}_4\text{Mn}_3\text{O}_{11.5}$ (blue). We can remark that there is not significant deviations of the lattice parameters despite Fe-incorporation (refined parameters: $a = 7.7100(7)$, $c = 28.000(3)$) as verified latter from PND data.

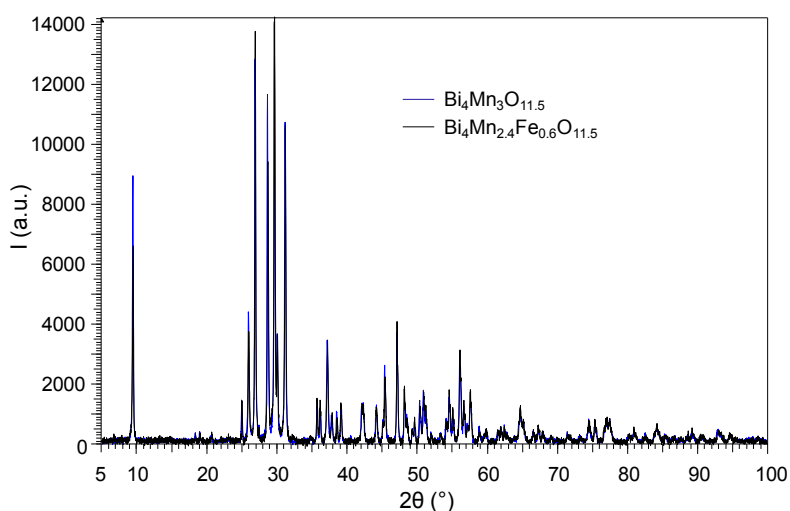


Figure III.5. Experimental XRD patterns of $\text{Bi}_4\text{Mn}_3\text{O}_{11.5}$ (blue) and $\text{Bi}_4\text{Mn}_{2.4}\text{Fe}_{0.6}\text{O}_{11.5}$ (black).

2) Structural description of $\text{Bi}_4\text{Mn}_3\text{O}_{11.5}$.

After structural refinement, the modular single crystal formula is $[\text{Bi}_4\text{O}_{4.5-y}][\text{Mn}_{3+x}\text{O}_7]$ with, $x = 0.03$ and $y = 0.15$. The unit cell parameters are as following: (rhombohedral crystal system, space group $R\bar{3}$, $a = 7.7199(1)$ Å, $c = 27.8588(7)$ Å, $R_F = 1.96\%$, $wR_F = 2.59\%$ for $I > 3\sigma(I)$). Details of the data collection and refined parameters are given in the Table III.1. It corresponds to the intergrowth between two sub-units stacked along the c -axis (Figure III.6a). At least for the single crystal study, besides the ideal framework of formula $\text{Bi}_4\text{Mn}_3\text{O}_{11.5}$, clues for disorder have been located by analyzing the residual electronic density maxima in both the two stacked sub-lattices described hereafter.

Table III.1. Crystal data, measurement and structural refinement parameters for $\text{Bi}_4\text{Mn}_3\text{O}_{11.5}$ at 100 K and 293 K.

Temperature (K)	100	293
Crystal data		
Chemical formula	$\text{Bi}_4\text{Mn}_{3.03}\text{O}_{11.35}$	
Crystal symmetry, space group	Trigonal, R -3 (n° 148)	
Unit cell parameters, a (Å)	7.7090(2)	7.7199(1)
c (Å)	27.8320(15)	27.8588(7)
V (Å ³)	1432.42(9)	1437.86(6)
Crystal size (mm)	$0.06 \times 0.20 \times 0.21$	$0.06 \times 0.20 \times 0.21$
Z	6	6
Dx (g/cm ³)	8.226	8.198
μ (mm ⁻¹) (for $\lambda \text{ K}\alpha=0.7107$ Å)	77.379	77.097
Appearance	Black triangular platelet	Black triangular platelet
Data collection		
Diffractometer	Bruker Duo CCD	Bruker X8 CCD
λ (Mo K α) graphite monochromator (Å)	0.71073	0.71073
Scan mode	ω and ϕ	ω and ϕ
θ (min–max) (°)	2.2 - 37.16	3.13 – 39.4
R(int) (%)	4.62	5.82
Recording reciprocal space	$-11 \leq h \leq 11,$	$-13 \leq h \leq 13,$
	$-12 \leq k \leq 11,$	$-13 \leq k \leq 13,$
	$-41 \leq l \leq 46$	$-49 \leq l \leq 49$
Refinement		
Number of measured independent and observed* reflections	6605, 1307, 1169	24619, 1916, 1718
Number of refined parameters	61	65
Refinement method, software	Least square on F, Jana2006	Least square on F, Jana2006
$R1(F^2)(\text{obs}) / R1(F^2)(\text{all})$ (%)	2.8 / 3.21	3.12 / 3.55
$wR2(F^2)(\text{obs}) / wR2(F^2)(\text{all})$ (%), where $w = 1/\sigma^2(F_o^2)$	3.17 / 3.27	3.75 / 3.83
GOF(obs) / GOF(all)	1.52 / 1.48	1.95 / 2.02
$\Delta\rho_{\text{max}} / \Delta\rho_{\text{min}}$ (e Å ⁻³)	3.80 / -3.08	6.21 / -4.03
Extinction coefficient	0.0131(14)	0.0165(18)

* obs = $[I > 3\sigma(I)]$ **2a) The $[\text{Bi}_4\text{O}_{4.5-y}]$ sublattice.**

It contains three independent oxygen atoms (O1, O2, O6) and two bismuth atoms (Bi1, Bi2) arranged in a complex manner. It follows that both O1 and O2 occupy the centers of OBi_3 triangles, regular around O1 ($3 \times \text{O-Bi} = 2.20$ Å) and distorted around O2 (2.08 Å $<$ O-Bi $<$ 2.51 Å). For O1 this coordination is completed by an apical Bi1 atom, towards the $[\text{Mn}_3\text{O}_7]$ module. O6 is at the centre of a regular OBi_6 octahedron. The latter atom is characterized by

strongly anisotropic thermal parameters, and its refined occupancy converged to $\sim 75\%$. Similarly, due to strong satellite peaks on Fourier-difference maps, Bi1 was split over two close positions (Bi1a ($\sim 75\%$) and Bi1b ($\sim 25\%$)) which denotes the coexistence of $3/4$ of OBi_6 octahedra ($d(\text{O6-Bi1a}) = 2.646(1) \text{ \AA}$) and $1/4$ of $\square\text{Bi}_6$ octahedra ($d(\square\text{-Bi1b}) = 2.727(7) \text{ \AA}$). It yields the formula $[\text{Bi}_4\text{O}_{4.5-y}]$ with $y = 0.15$. The Bi1 split locally affects both O1 and O2 coordinations. Bi2 was also split over two positions aligned along c , due to high residual electronic density, Bi2a(93%) and Bi2b(7%) (Figure III.6b). This disorder is related to an outstanding disorder occurring in the next building units detailed below.

2b) The $[\text{Mn}_{3+x}\text{O}_7]$ sublattice.

It is composed of three oxygen (O3, O4, O5) and two manganese (Mn1, Mn2) independent crystallographic positions. The ideal lattice of formula Mn_3O_7 creates voids among which $\sim 7\%$ are occupied by the interstitial Mn2 (Figure III.6b and Figure III.7a). It follows that, depending on the absence or presence of Mn2 in these cavities, Bi2 occupies either Bi2a or Bi2b within the next sub-units ($7\% d(\text{Mn2-Bi2a}) = 3.082(4) \text{ \AA}$ versus $93\% d(\square\text{-Bi2b}) = 2.415(1) \text{ \AA}$), with respect to strong Bi-Mn electrostatic repulsion. The refined occupancy leads to the formula $[\text{Mn}_{3+x}\text{O}_7]$ with $x = 0.03$.

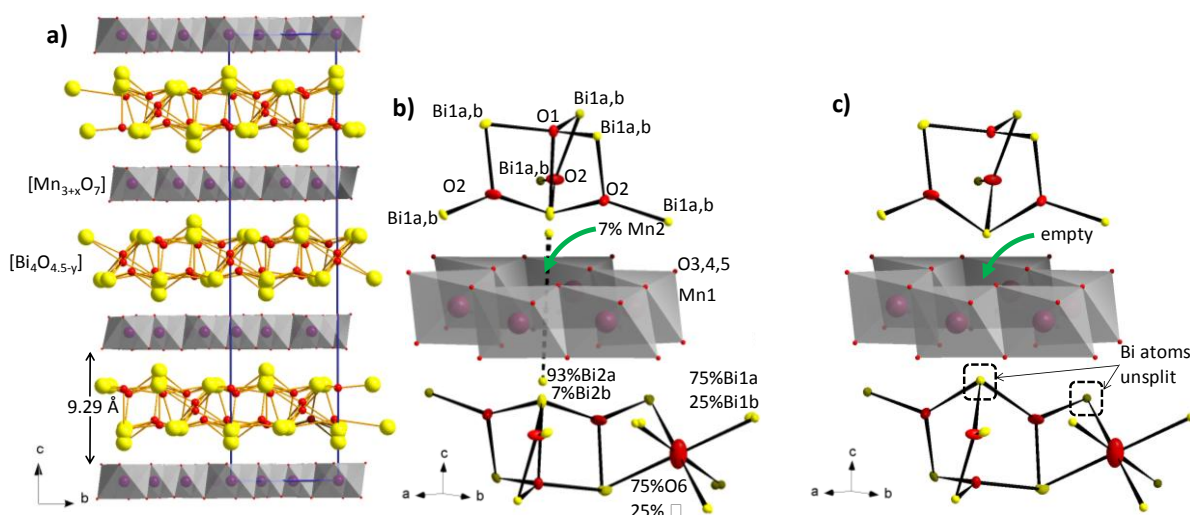


Figure III.6. a) View of the $[\text{Bi}_4\text{O}_{4.5-y}][\text{Mn}_{3+x}\text{O}_7]$ intergrowth. b) Details of O-Bi connection at the apex of a void and c) the same part of the structure from PND data with less disorder.

2c) Topology of the $[\text{Mn}_3\text{O}_7]$ maple leaf lattice.

Layered manganese oxides are often associated to the phyllophanates minerals including lithiophorite, rancieite, takanelite etc.¹⁶⁹ More generally, the structural type birnessite¹⁷⁰ (i.e. layered type triangular MnO_2 , separated by alkali, alkaline earth and water molecules), is

described as the most representative type. In the parent compound, even if the ideal $[\text{Mn}_3\text{O}_7]$ array is related to such network, its main specificity results in the ordering of the $1/7^{\text{th}}$ vacancies (Figure III.7a).

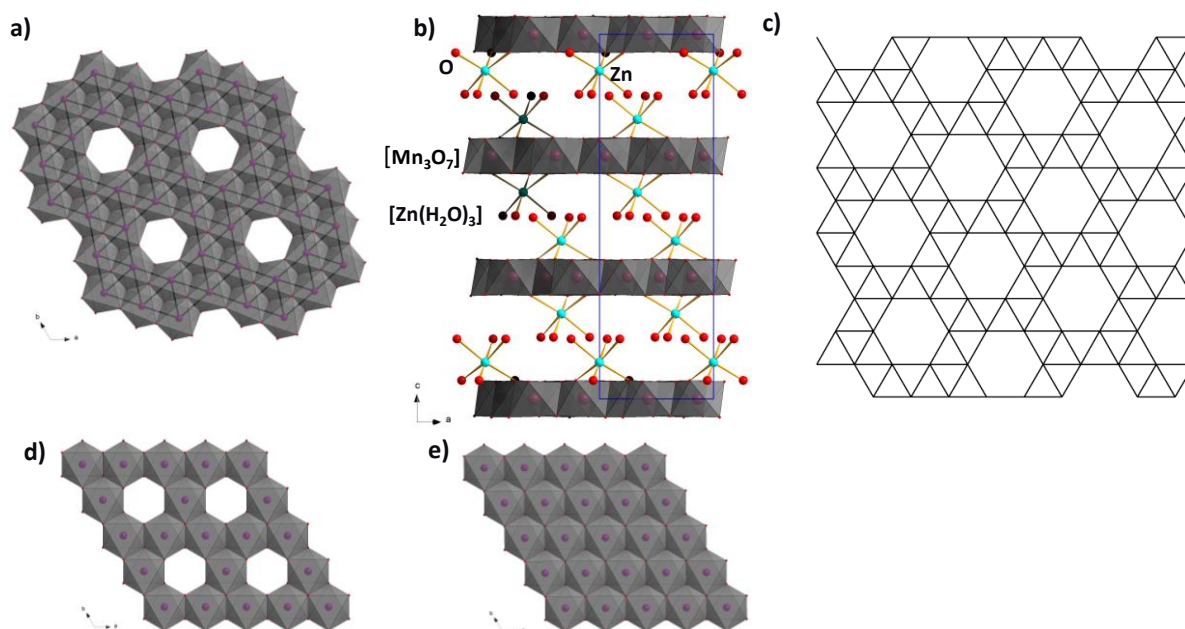


Figure III.7 a) the ideal $[\text{Mn}_3\text{O}_7]$ array with the ordering of the $1/7^{\text{th}}$ vacancies, b) the structure of chalcophanite $[\text{ZnMn}_3\text{O}_7 \cdot 3\text{H}_2\text{O}]$, c) maple leaf lattice.¹⁷¹ d) honeycomb lattice, e) parent triangular lattice

The occurrence of random vacancies in the birnessite was investigated, since some metals such as Zn appears to be located at their vertices by sorption in birnessite minerals found in soils, aquifers, streams, and wetlands.^{172,173} To our knowledge, a regular $1/7$ depleted Mn triangular lattice was only observed in a related mineral, the chalcophanite $[\text{ZnMn}_3\text{O}_7 \cdot 3\text{H}_2\text{O}]$ ¹⁶⁹ (Figure III.7b), which is, to our knowledge, not investigated for its physical properties so far.

This particular topology corresponds to the fourth ($=T_4$) of the eleven Archimedean tiling's, also called the *maple leaf* lattice (Figure III.7c).^{171,174} Topologies T_i ($i = 1$ to 11) represent the prototypes of 2D arrangements of regular polygons, particularly interesting for low dimensional magnetism, where 2D (spin) lattices are obtained by considering spins on each vertices connecting neighboring polygons. More precisely, the T_4 *maple leaf* topology ($1/7$ depleted, M-M connectivity = 5) is rare^{175,176} and corresponds to the intermediate between the well-known *honeycomb* lattice ($1/3$ -depleted, connectivity = 4) (Figure III.7d) and the parent triangular lattice (non-depleted, connectivity = 6) (Figure III.7e).

2d) Mn valence in Bi₄Mn₃O_{11.5}

According to the ideal formula of the structure Bi₄Mn₃O_{11.5}, without taking into account neither the O6 vacancies nor the interstitial Mn₂, the mean Mn valence on the *maple leaf* lattice is Mn^{+3.66}. For interstitial Mn sites, the Mn₂-O bonds are 2.12 Å which suggest a Mn²⁺ valence (see BVS calculation in the Table III.2) while Mn₁ (mean Mn₁-O = 1.96 Å) is consistent mixed Mn^{3/4+} valence.

Table III.2. Calculation of bond valences of Mn₁ and Mn₂ in Bi₄Mn₃O_{11.5} at T = 293K. The retained model are in bold. (R values are taken from ref [139])

Mn ₁								Mn ₂							
hypothesis		Mn ^{II}		Mn ^{III}		Mn ^{IV}				Mn ^{II}		Mn ^{III}		Mn ^{IV}	
Atom	d	R	v	R	v	R	v	Atom	d	R	v	R	v	R	v
O3	1.906	1.79	0.73	1.76	0.67	1.8	0.66	O3	2.119	1.8	0.41	1.76	0.38	1.75	0.37
O4	1.921	1.79	0.7	1.76	0.65	1.8	0.64	O3	2.119	1.8	0.41	1.76	0.38	1.75	0.37
O3	1.937	1.79	0.67	1.76	0.62	1.8	0.61	O3	2.119	1.8	0.41	1.76	0.38	1.75	0.37
O5	1.943	1.79	0.66	1.76	0.61	1.8	0.6	O3	2.119	1.8	0.41	1.76	0.38	1.75	0.37
O4	1.961	1.79	0.63	1.76	0.58	1.8	0.57	O3	2.119	1.8	0.41	1.76	0.38	1.75	0.37
O5	2.059	1.79	0.48	1.76	0.45	1.8	0.44	O3	2.119	1.8	0.41	1.76	0.38	1.75	0.37
		V_{sum}	3.88	V_{sum}	3.6	V_{sum}	3.5			V_{sum}	2.5	V_{sum}	2.27	V_{sum}	2.23

Then, after consideration of the defects, the Bi₄Mn^{+3.54}₃Mn⁺²_{0.03}O_{11.35} formula pictures at best the reduction of octahedral Mn species from Mn^{+3.66} to Mn^{+3.5} by both: i) incorporation of interstitial Mn²⁺ cations and ii) creation of oxygen vacancies. It is noteworthy that the announced defects have been systematically detected in similar proportion on several collected single crystals. This is in good agreement with the mean Mn oxidation state of 3.43(3) titrated by iodometry on the single-phase polycrystalline sample described hereafter.

The striking disproportionation into distinct Mn valences in neighboring crystallographic sites (here, Mn²⁺ interstitial defects versus Mn^{3/4+} network cations) even if rare is not unique. For instance in several hexagonal perovskites such as Ba₇Mn^{3/4+}₃Mn⁵⁺₂Ca₂O₂₀,¹⁷⁷ Mn⁵⁺ occupies tetrahedra separated from Mn^{3/4+} strings of face-sharing octahedra by Ca²⁺ cations. Closer to our compound, a direct connection between ordered Mn²⁺ and Mn⁴⁺ octahedra was pointed out in Pb₃Mn⁴⁺₃Mn²⁺₂V₂O₁₆.¹⁷⁸ In this compound the mean Mn-O distances around both species (d(Mn⁴⁺-O) = 1.93 Å, d(Mn³⁺-O) = 2.15 Å) are very similar to Mn coordinations found in [Bi₄O_{4.5-y}][Mn_{3+x}O₇] which comfort our assignment of oxidation numbers. Even, if only present as minor defects, it could explain the difficulties encountered to prepare single phase materials. In fact, using the stoichiometry deduced from the structure determination,

only the heating at medium temperature ($\sim 500^\circ\text{C}$) of a well dispersed Bi/Mn/O mixture by Pechini method, allows for the preparation of the target sample. At higher temperature $\text{Bi}_2\text{Mn}^{3.5+}_4\text{O}_{10}$ becomes predominant under all tested atmospheres (air, N_2 , Ar, O_2) which could indicate that the stabilization of mixed $\text{Mn}^{2+}\text{-Mn}^{3/4+}$ valence could be essentially governed by the thermal treatment (see the synthesis part). On the opposite the PND analysis shown later will indicate the absence of Mn inclusion in the voids. At this point of our work, more systematic investigations would be needed.

2e) Structural characterization of $\text{Bi}_4\text{Mn}_3\text{O}_{11.5}$ from Powder Neutron Diffraction (PND) data.

The PND data at 300 K, in general, confirms the structure of $\text{Bi}_4\text{Mn}_3\text{O}_{11.5}$, however, at the scale of the crystal cell, the disorders are diminished in the powder. Both the bismuth atoms, Bi1 and Bi2, appear to be unsplit, as well as the voids in the $[\text{Mn}_{3+x}\text{O}_7]$ sublattice turn out to be unoccupied (Figure III.6c). The Rietveld refinement fit is given on Figure III.8, the reliability parameters are: R-factor = 3.64 and Rf-factor = 2.21. These minor differences depending on the microstructure are not essential in the frame of our study for this new compound. The distances are given in the Table III.3

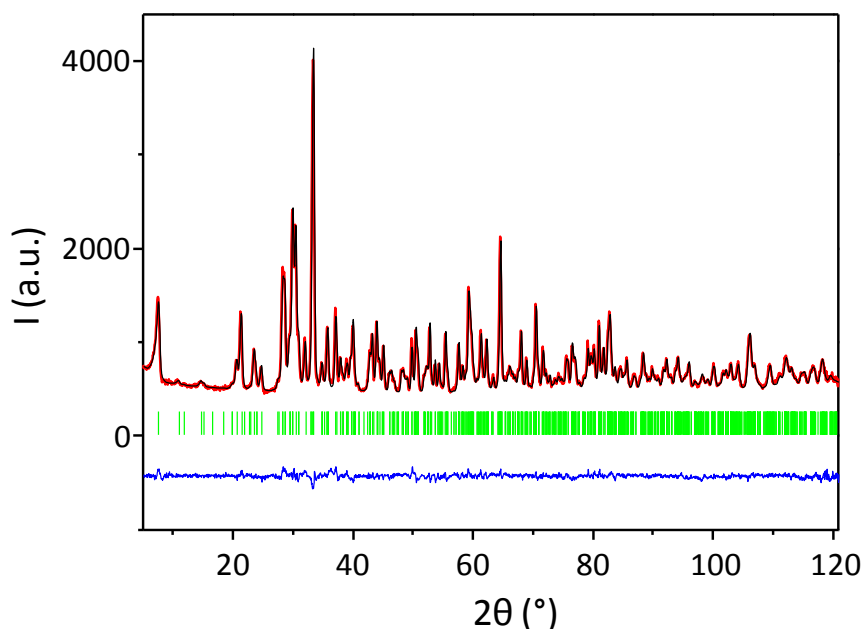


Figure III.8. Rietveld refinement fit from PND data of $\text{Bi}_4\text{Mn}_3\text{O}_{11.5}$ at 300 K.

2f) Structural characterization of $\text{Bi}_4\text{Mn}_{2.4}\text{Fe}_{0.6}\text{O}_{11.5}$ from PND data

On the contrary to the PND data of $\text{Bi}_4\text{Mn}_3\text{O}_{11.5}$ at 300 K, the PND data of the sample prepared with the stoichiometry $\text{Bi}_4\text{Mn}_{2.4}\text{Fe}_{0.6}\text{O}_{11.5}$ at 300 K, is close to the structure of $\text{Bi}_4\text{Mn}_3\text{O}_{11.5}$ from single crystal XRD data in terms of disorders. Namely, Bi2 atoms are split in a ratio 0.88/0.12 and the voids in the $[\text{Mn}_3\text{O}_7]$ layer are occupied 6%. However, the Fe/Mn stoichiometry of the powder synthesis was not conserved and finally the refined Fe/Mn occupations lead to the formula $\text{Bi}_4\text{Mn}_{2.63}\text{Fe}_{0.4}\text{O}_{11.5}$, which will be continued to be named with original (as-prepared) stoichiometry. Rietveld refinement fit of $\text{Bi}_4\text{Mn}_{2.63}\text{Fe}_{0.4}\text{O}_{11.5}$ at 300 K is given on the Figure III.9, the reliability factors are: Bragg R-factor = 4.308 and $R_f = 2.563$. Distances are given in the Table III.3

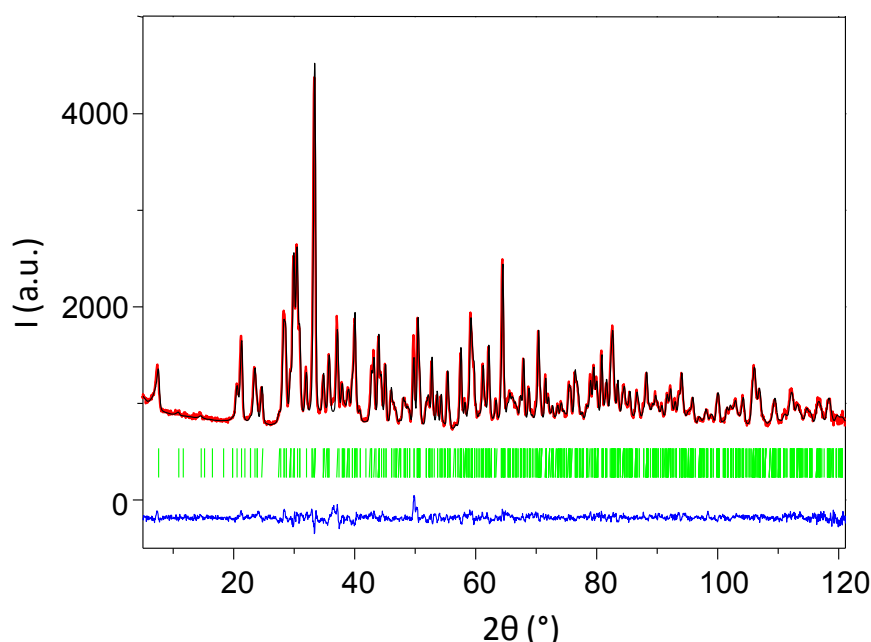


Figure III.9. Rietveld refinement fit from PND data of $\text{Bi}_4\text{Mn}_{2.63}\text{Fe}_{0.4}\text{O}_{11.5}$ at 300 K.

Table III.3. Mn-O distances (Å) from single crystal XRD data of $\text{Bi}_4\text{Mn}_3\text{O}_{11.5}$, PND data of $\text{Bi}_4\text{Mn}_3\text{O}_{11.5}$ and PND data of $\text{Bi}_4\text{Mn}_{2.63}\text{Fe}_{0.4}\text{O}_{11.5}$ at 300 K.

SC XRD $\text{Bi}_4\text{Mn}_3\text{O}_{11.5}$			PND $\text{Bi}_4\text{Mn}_3\text{O}_{11.5}$			PND $\text{Bi}_4\text{Mn}_{2.63}\text{Fe}_{0.4}\text{O}_{11.5}$		
Atom1	Atom2	d	Atom1	Atom2	d	Atom1	Atom2	d
Mn1	O3	1.9062(24)	Mn1	O3	1.8752(57)	Mn1 Fe1	O4	1.913(13)
	O5	1.9210(28)		O5	1.9116(62)		O5	1.926(15)
	O3	1.9368(19)		O3	1.9123(43)		O3	1.939(14)
	O5	1.9428(28)		O5	1.9281(62)		O5	1.946(15)
	O4	1.9616(16)		O4	1.9468(53)		O3	1.961(11)
	O5	2.0584(19)		O5	2.0963(44)		O5	1.994(11)
Mn2	6xO3	2.1193(24)				Mn2	6xO3	2.1260(42)

2g) Electron diffraction/possible ordering

It is striking that selected area electron diffraction patterns (Figure III.10a-b) on powder, most of the time respect the R-lattice conditions ($-h+k+l = 3n$), but sometimes show extra-spots revealed after long-time-acquisition (Figure III.10b). The supercell dataset is indexed in a primitive cell with same lattice parameters, but was only observed on the [001] zone axis patterns. It indicates that the defects mentioned above would (partially) order within (a , b) planes while no correlations are observed between stacked individual modules. Precession frames calculated from the single crystal XRD collection (Figure III.10c) does not show evidence of similar effects, which indicate that it concerns micrometric or smaller domains but is lost at the single crystal scale ($>250\text{ }\mu\text{m}$ in average). It is ambitious to argue about the structural origin of such local orderings. However we can suggest that the weak extra-intensities play in favor of oxygen ordering in the $[\text{Bi}_4\text{O}_{4.5-y}]$ sublattice rather than Mn^{2+} in the $[\text{Mn}_{3+x}\text{O}_7]$ voids, this latter being directly in connection with the Bi2a/Bi2b organization (heavy atoms) on two well-separated positions. In addition we recall the PND data of the polycrystalline sample did not show evidence of a significant presence of Mn^{2+} in the voids.

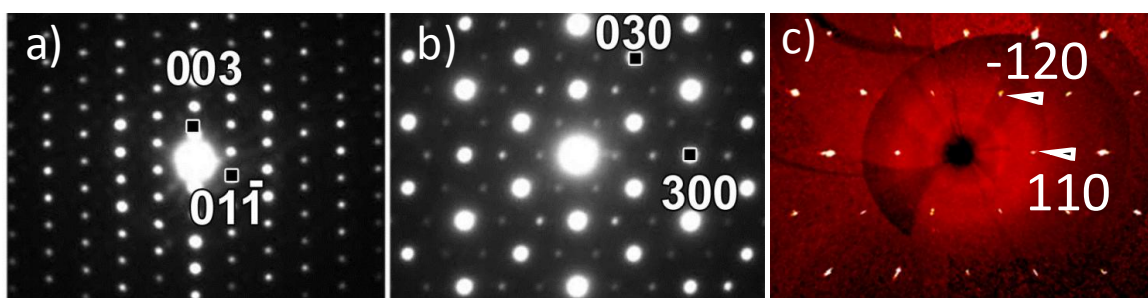


Figure III.10. a) systematic [100] and b) particular [001] zone axes of the powder ED pattern, with evidence of primitive spots (rare case) in the later, c) a precession frame calculated from the single crystal XRD

3) Order-disorder transition around 240 K in $\text{Bi}_4\text{Mn}_3\text{O}_{11.5}$.

Due to the local disorder observed on several sites, single crystals have been *in-situ* cooled down to 100 K. The evolution of the lattice volume upon cooling is given on the Figure III.11a. In addition to the thermal lattice contraction, an abrupt inclination is observed around $T_i = 240\text{ K}$. The crystal structure was then collected and refined at 100 K, the details are given in Table III.1. The crystal structure remains essentially unchanged, while Bi1 does not show any more clues for a split position and O6 is displaced from its central 3(b) site ($1/2, 2/3, 1/6$) into a 6(c) site ($1/3, 2/3, z = 0.176(1)$) but conserves a partial occupancy.

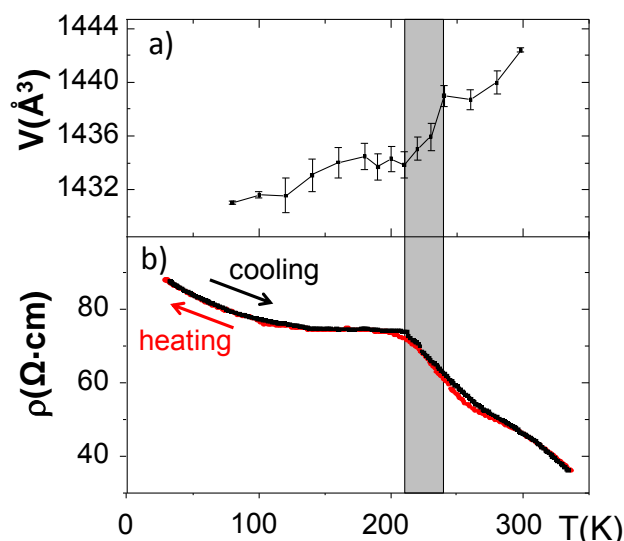


Figure III.11. Evidence of a transition below 240 K, as: a) a lattice volume contraction from single crystal XRD; b) an anomaly on the electric 4-probes resistivity measurement on a single crystal.

Then below 240 K, the corresponding O6Bi1 is characterized by $3 \times \text{O6-Bi1} = 2.545(2) \text{ \AA}$ and $3 \times \text{O6-Bi1} = 2.796(2) \text{ \AA}$ (Table III.4).

Table III.4 Selected A1 (cation) to A2 (anion) distances in $\text{Bi}_4\text{Mn}_3\text{O}_{11.5}$ at both sides of the order - disorder transition.

100K			293K		
Atom 1	Atom 2	d (Å)	Atom 1	Atom 2	d (Å)
Bi1	O1	2.1868(7)	Bi1a / Bi1b	O1	2.146(3)/2.318(3)
	O2	2.115(5)		O2	2.134(4)/2.099(4)
	O2	2.255(5)		O2	2.283(3)/2.247(3)
	O3	2.887(5)		O3	2.886(3)/2.918(4)
	O5	2.532(4)		O5	2.511(3)/2.611(3)
	O6 / O6'	2.80(2)/2.54(2)		O6	2.708(2)/2.522(2)
Bi2a Bi2b	O1	3.355(7)/2.675(9)	Bi2a / Bi2b	O1	3.351(4)/2.685(5)
	O2 x 3	2.518(7)/2.213(8)		O2 x 3	2.489(4)/2.191(5)
	O3 x 3	2.246(5)/2.705(7)		O3 x 3	2.259(3)/2.707(4)
Mn1	O3	1.900(5)	Mn1	O3	1.906(3)
	O3	1.941(5)		O3	1.937(3)
	O4	1.965(3)		O4	1.961(2)
	O5	1.921(5)		O5	1.921(3)
	O5	2.059(4)		O5	2.059(2)
	O5	1.936(6)		O5	1.943(3)
Mn2	O3 x 6	2.107(6)	Mn2	O3 x 6	2.119(3)
Mn1	Mn1 x 2	2.9490(17)	Mn1	Mn1 x 2	2.9540(8)
	Mn1	3.0107(12)		Mn1	3.0166(6)
	Mn1 x 2	2.8732(18)		Mn1 x 2	2.8763(8)
	Mn2	2.8729(8)		Mn2	2.8761(3)

The transition does not affect the Bi2a/Bi2b splitting which comforts its relationship with the partial occupancy of the apical $[\text{Bi}_4\text{O}_{4.5-y}]$ window. However, below T_t the changes in the interatomic distances affect magnetic and transport properties as discussed latter.

3a) Powder Neutron Diffraction of $\text{Bi}_4\text{Mn}_3\text{O}_{11.5}$ at 180 K.

Powder neutron diffraction (PND) measurements were obtained at LLB in collaboration with Gilles André. PND data of $\text{Bi}_4\text{Mn}_3\text{O}_{11.5}$ at 180 K, give essentially the same information as PND data at 300 K i.e. the disorder areas are diminished in the structure of the crystallites compared to the structure from single crystal XRD data. Namely both the bismuth atoms appear to be unsplit, as well as the voids in the $[\text{Mn}_{3+x}\text{O}_7]$ sublattice turns out to be unoccupied. The Rietveld refinement fit is given on the Figure III.12, the reliability parameters are: Bragg R-factor = 3.12 and Rf-factor = 1.73.

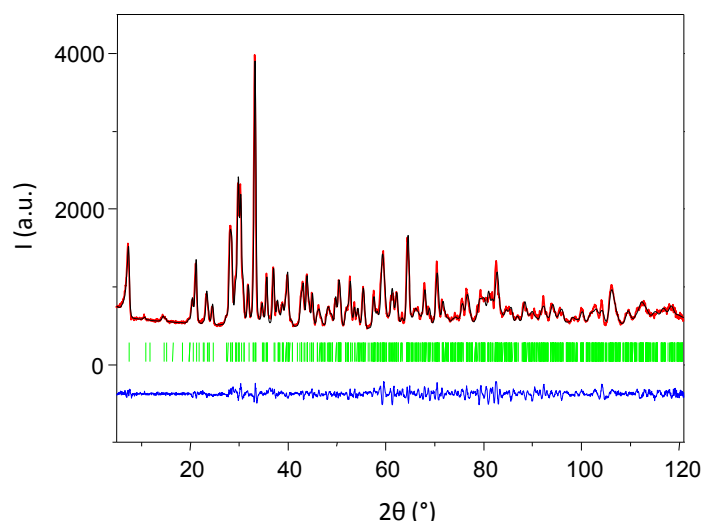


Figure III.12 Rietveld refinement fit from PND data of $\text{Bi}_4\text{Mn}_3\text{O}_{11.5}$ at 180 K.

Here we must note that the final refinement at 180 K is not perfect in terms of the matching between calculated/experimental pattern, but that all the atoms are assigned to smallest thermal parameters at 180 K that at 300 K (Table III.5 and Table III.6)

Table III.5. Atomic parameters of $\text{Bi}_4\text{Mn}_3\text{O}_{11.5}$ at 180 K from NPD

Atom	Wyck.	S.O.F.	x/a	y/b	z/c	U [\AA^2]
Bi1a	18f		0.5315(5)	0.0071(5)	0.11995(12)	0.0082(5)
Bi2a	6c		0	0	0.0889(2)	0.0103(10)
Mn1	18f		0.4188(10)	0.2749(10)	-0.0009(3)	0.0057(10)
O1	6c		2/3	1/3	0.1236(3)	0.0113(16)
O2	18f		0.2469(8)	-0.0295(8)	0.13676(20)	0.0107(9)
O3	18f		0.2183(7)	0.2591(8)	0.03857(18)	0.0146(12)
O4	6c		2/3	1/3	-0.0346(3)	0.0003(17)
O5	18f		0.4634(8)	0.0882(9)	0.03600(17)	0.0090(11)

O6	6c	0.5	1/3	-1/3	0.1750(6)	0.013(4)
-----------	----	-----	-----	------	-----------	----------

 Table III.6. Atomic parameters of $\text{Bi}_4\text{Mn}_3\text{O}_{11.5}$ at 300 K from NPD

Atom	Wyck.	S.O.F.	x/a	y/b	z/c	U [\AA^2]
Bi1a	18f		0.5302(3)	0.0056(3)	0.12034(7)	0.0113(3)
Bi2a	6c		0	0	0.08908(11)	0.0111(5)
Mn1	18f		0.4208(6)	0.2762(5)	-0.00130(17)	0.0075(5)
O1	6c		2/3	1/3	0.12340(15)	0.0122(8)
O2	18f		0.2462(5)	-0.0286(4)	0.13596(11)	0.0149(5)
O3	18f		0.2159(4)	0.2581(4)	0.03827(10)	0.0142(6)
O4	6c		2/3	1/3	-0.03415(17)	0.0098(10)
O5	18f		0.4628(4)	0.0884(5)	0.03565(9)	0.0101(5)
O6	6c	0.5	1/3	-1/3	0.1740(4)	0.023(2)

4) 2D Transport and Magnetic properties.

4a) Conductivity of the single crystal of $\text{Bi}_4\text{Mn}_3\text{O}_{11.5}$.

The resistivity versus temperature was measured on a single crystal using the four probes method, see Figure III.11b. Due to the small size of available crystals, contacts were placed such that both $\rho(a, b)$ and $\rho(c)$ contribute to our experimental data. However, in such 2D crystal structure, the electronic transport is favored *in-plane*, following mixed valence Mn paths. The lattice contraction observed below $T_t = 240$ K is accompanied by a change of $\rho(T)$ such that the resistivity is less temperature dependent below T_t .

Efforts to grow largest well-shaped single-crystals are currently underway, in order to have a more clear picture of the anisotropy of the transport properties.

4b) Conductivity of polycrystalline samples of $\text{Bi}_4\text{Mn}_3\text{O}_{11.5}$ and $\text{Bi}_4\text{Mn}_{2.63}\text{Fe}_{0.4}\text{O}_{11.5}$

The four probes method has been used as well in measuring the resistivity versus temperature of the bars of $\text{Bi}_4\text{Mn}_3\text{O}_{11.5}$ and $\text{Bi}_4\text{Mn}_{2.63}\text{Fe}_{0.4}\text{O}_{11.5}$.

The bars have been prepared by densification of the powder forms in an isostatic press at 200 MPa. The achieved densities of the bars are 63% and 70% respectively. Because of such low densities of the samples their resistivities turned out to be too high to see the transition taking place at 240 K (Figure III.13) compared to single crystal data.

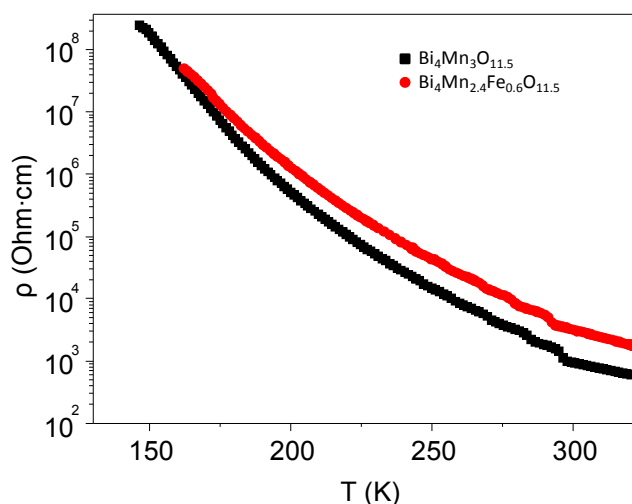


Figure III.13. The electric 4-probes resistivity measurement on pressed bars of $\text{Bi}_4\text{Mn}_3\text{O}_{11.5}$ and $\text{Bi}_4\text{Mn}_{2.63}\text{Fe}_{0.4}\text{O}_{11.5}$

4c) Magnetic properties of $\text{Bi}_4\text{Mn}_3\text{O}_{11.5}$.

Concerning the magnetic properties of the parent compound, our compound is the first synthetic oxide which realizes a true synthetic 2D-1/7 depleted triangular lattice. Its mixed Mn^{3+} (d^4 , $S = 2$) and Mn^{4+} (d^3 , $S = 3/2$) valence is of high importance at both the experimental and theoretical level. To our knowledge, in addition to the chalcophanite¹⁶⁹ mineral, only two magnetic systems built on *maple leaf* lattice were reported, if one only considers the arrangement between magnetic cations:

- i) the organometallic $\text{M}_x[\text{Fe}(\text{O}_2\text{CCH}_2)_2\text{NCH}_2\text{PO}_3]_6 \cdot n\text{H}_2\text{O}$,¹⁷⁶ in which the iron cations approximate this topology but are distant and lead to a paramagnetic behavior at all temperature.
- ii) the mineral spangolite $\text{Cu}_6\text{Al}(\text{SO}_4)(\text{OH})_{12}\text{Cl} \cdot 3\text{H}_2\text{O}$, in which Cu^{2+} cations form a *maple leaf* lattice, but extended antiferromagnetic (AFM) exchanges are dominated by dimerization,¹⁷⁵ out of the theoretical prediction intensively calculated and discussed for $S = 1/2$ Heisenberg antiferromagnet (HAFM) on a 1/7-depleted triangular lattice. Indeed, a well-established 2D magnetic long-range ordering (LRO)¹⁷⁹ is expected to survive strong quantum fluctuations present in such frustrated layer, however strongly weakened.^[17]

The understanding of our mixed valence Mn system deserves theoretical modeling, but predictions for HAFM are informative for preliminary interpretations. The thermal evolution of the susceptibility (approximated as M/H) and its inverse are presented in the Figure III.15. Above 210 K it follows a Curie-Weiss law $\chi = C/(T-\theta)$ leading to $\theta = -184.6\text{K}$ and $\mu_{\text{eff}} =$

$7.78\mu_B/\text{f.u.}$. This value is in excellent agreement with $\mu_{\text{eff}} = 7.65\mu_B/\text{f.u.}$ calculated for $1.5 \text{ Mn}^{3+}(S = 2)$ and $1.5 \text{ Mn}^{4+}(S = 3/2)$ in a spin only approximation, according to the charge distribution discussed above. Strong predominant AFM couplings, pictured by the high negative θ value are responsible for the concave upward evolution of $\chi^{-1}(T)$ below the transition. This behavior, according to the important separation ($> 9 \text{ \AA}$) between the magnetic subunits, most certainly shows the setting of important 2D-AFM correlations, resulting in extended frustrated domains, as described for $S = 1/2$ HAFM 2D *maple leaf* layers.¹⁷⁴ It appears obvious that the structural contraction evidenced below 240 K plays an important role on both the electric conductivity and the magnetic interactions. The magnetic possible paths (J1 to J5) between $\text{Mn}^{3/4+}$ centers are shown in the Figure III.14.

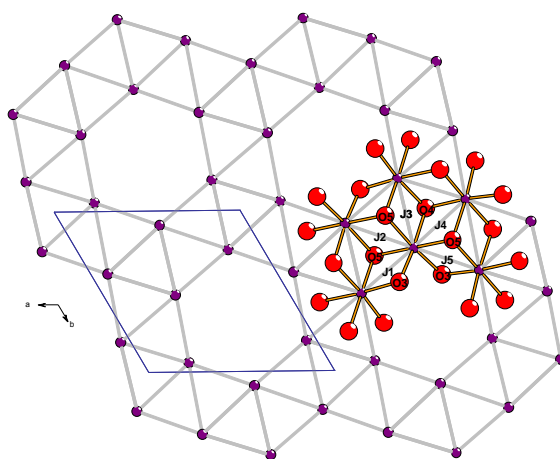


Figure III.14. The maple leaf lattice of $\text{Bi}_4\text{Mn}_3\text{O}_{11.5}$ created by connecting Mn1 atoms. J1-J5 super exchange paths are shown.

They involve interatomic separation in the range $2.87 \text{ \AA} < d_{(\text{Mn-Mn})} < 3.01 \text{ \AA}$ associated with Mn-O-Mn angles of $\sim 97^\circ$ (see Annex IV.211)). According to Goodenough-Kanamori rules, super exchanges between isovalent Mn^{3+} or Mn^{4+} species are expected AFM, while ferromagnetic $\text{Mn}^{3+}\text{-O-Mn}^{4+}$ double-exchanges and super-exchanges do not seem predominant in this compound. No obvious clues for a magnetic ordering were detected on further cooling down to 2 K. However, a weak anomaly was detected at 50 K that could sign a minor structural reorganization. The ZFC/FC divergence observed on $\chi(T)$ at 6 K is not yet clearly understood. It is not typical of 3D Néel ordering, but is reminiscent of what was observed on the birnessite-type layered- MnO_{2-x} structure below 9.2 K.¹⁸⁰ As suggested for this structurally related compound, it could correspond to very weak spin canting or uncompensated spin structure, in our case likely associated to the interstitial Mn^{2+} defects. We note that at 1.8 K, $M(H)$ shows a weak hysteresis opening (Figure III.15a, inset), not observed

at 6 K (remanent moment = $7.10^{-3} \mu_B/\text{f.u.}$). Increasing the applied field, it is striking that $M(H)$ linearly but reversibly increases up to $0.6 \mu_B/\text{f.u.}$ at 7 T, see Figure III.15b. This relatively high value, in the context of predominant AFM exchanges and frustrated spin arrangement denotes a progressive spin reversal under increasing external field which agrees with the 2D-character which breaks a robust 3D-AFM ordering.

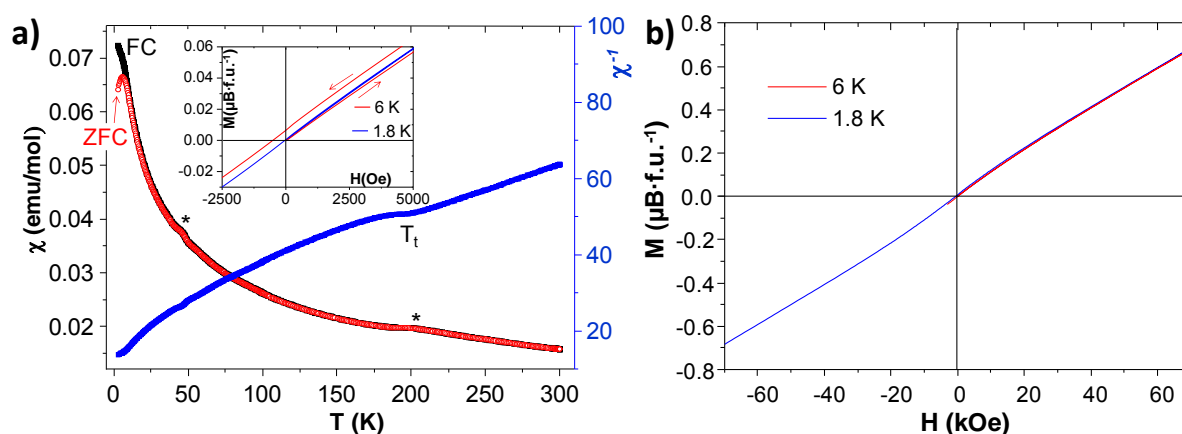


Figure III.15. ZFC/FC plots of M/H of $\text{Bi}_4\text{Mn}_3\text{O}_{11.5}$ versus the temperature at 0.1 Tesla in black and red. * show magnetic anomalies. $\chi^{-1}(T)$ is shown in blue and refers to the right-axis. The inset shows a portion of $M(H)$ at $T = 6$ K and 1.8 K in $\mu_B/\text{f.u.}(Oe)$. b) $M(H)$ at $T = 1.8$ K (blue), 6 K (red) in $\mu_B/\text{f.u.}(Oe)$ measured until 70 kOe.

4d) Magnetic properties of $\text{Bi}_4\text{Mn}_{2.63}\text{Fe}_{0.4}\text{O}_{11.5}$

To contrary of $\text{Bi}_4\text{Mn}_3\text{O}_{11.5}$ no anomaly was observed on the ZFC/FC plots of $\text{Bi}_4\text{Mn}_{2.63}\text{Fe}_{0.4}\text{O}_{11.5}$ (Figure III.16a). From the paramagnetic range of the inverse χ curve the deduced parameters of Curie-Weiss law are following: $C = 5.98 \text{ emu} \cdot \text{K} \cdot \text{Oe}^{-1} \cdot \text{mol}^{-1}$, $\Theta = -167.68$ K and $\mu_{\text{eff}} = 6.92 \mu_B/\text{f.u.}$ In the spin only approximation the calculated value of effective moment $\mu_{\text{eff}} = 7.64 \mu_B/\text{f.u.}$ taking into account $0.6 \text{ Mn}^{3+}(S = 2)$, $2 \text{ Mn}^{4+}(S = 3/2)$ and $0.4 \text{ Fe}^{3+} \text{ HS}(S = 5/2)$ which is in worst agreement compared to the good matching observed for the pristine Mn compound, but remains correct. We recall that after PND analysis we consider the formula $\text{Bi}_4\text{Mn}^{\text{III}}_{0.6}\text{Mn}^{\text{IV}}_2\text{Fe}^{\text{III}}_{0.4}\text{O}_{11.5}$. Thus it appears that the effective moment is mainly reduced from $7.78 \mu_B/\text{f.u.}$ to $6.92 \mu_B/\text{f.u.}$ after Fe incorporation. This could be explained by a low spin state for Fe^{3+} ($S = 1/2$) leading to the expected $\mu_{\text{eff}} = 6.75 \mu_B/\text{f.u.}$ value, in better agreement. However even after confinement in the Mn-Maple leaf lattice, this LS state is unexpected.

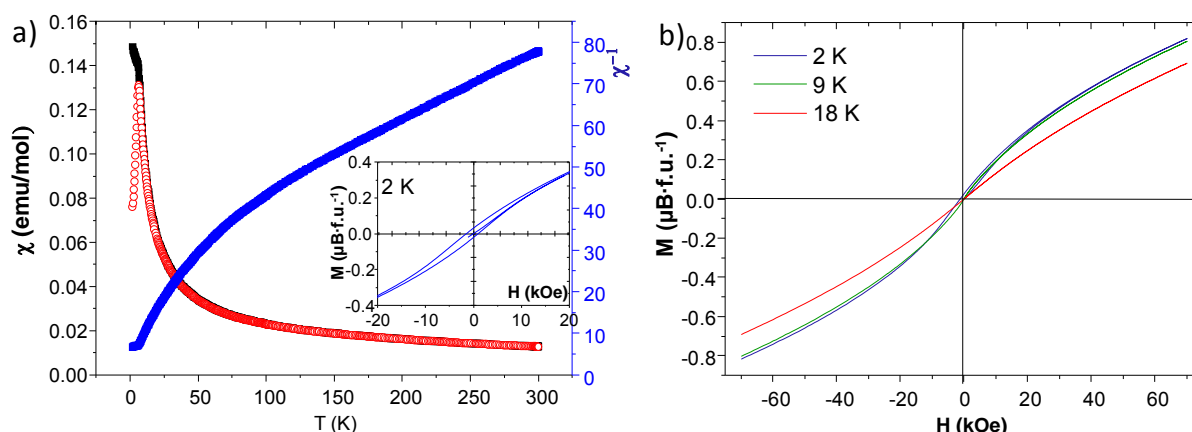


Figure III.16. a) ZFC/FC plots of M/H of $\text{Bi}_4\text{Mn}_{2.63}\text{Fe}_{0.4}\text{O}_{11.5}$ versus the temperature at 0.02 Tesla in black and red. $\chi^{-1}(T)$ is shown in blue and refers to the right-axis. b) $M(H)$ at $T = 2$ K (blue), 9 K (green) and 18 K (red) in $\mu_B/\text{f.u.}(\text{Oe})$

The measured average Mn/Fe-O distance is 1.94 Å (doped) compared to Mn-O = 1.94 Å (undoped). This unchanged value most likely suggests LS- Fe^{III} but it is difficult to conclude since there is ambiguities and multiple possibilities considering the ionic radii (Table III.7). Also we should note that HS- Fe^{3+} (d^5) being a $L=0$ cation, no spin orbit coupling is expected reduce the effective moment compared to LS-Mn species.

Table III.7. Radii of Mn and Fe ions

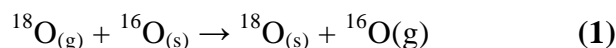
Ion	Elec. Config.	Coord. Number	Spin State	Ionic Radius, Å
Fe^{+3}	3d 5	6	LS	0.55
Fe^{+3}	3d 5	6	HS	0.645
Fe^{+4}	3d 4	6		0.585
Mn^{+3}	3d 4	6	LS	0.58
Mn^{+3}	3d 4	6	HS	0.645
Mn^{+4}	3d 3	6		0.53

5) Oxygen Isotopic Exchange $^{16}\text{O}/^{18}\text{O}$ (OIE) over $[\text{Bi}_4\text{O}_{4.5-y}][\text{Mn}_{3+x}\text{O}_7]$

5a) General considerations.

The potential mixed ionic/electronic conduction in well separated subunits appears promising, taking into account the well-known efficient O^{2-} transport of Bi-based oxides.^{29,30} However, up to now, a limited number of the possible compounds were found to present an interesting activity for gas-phase oxidation reactions.¹⁸¹

Oxygen isotopic exchange technique was used to evaluate oxygen mobility. This work was performed in collaboration with Sebastien Royer from the LACCO (Poitiers). Theory and data treatment can be found in references [^{181,182}]. The exchange reaction is summarized in Eq. (1):



where (s) and (g) refer to the solid and the gas phase oxygen species, respectively.

5b) Temperature Programmed Isotopic Exchange (TPIE)

TPIE experiments were carried out in a closed-recycle reactor coupled to a mass spectrometer (PFEIFFER Vacuum). A recycle pump ensured the gas circulation, in order to avoid any diffusional limitation in the gas phase during the experiment. 50 mg of the sample was loaded in a U-shaped reactor between two quartz wool plugs. The sample was heated under pure O_2 flow (350 °C for 1 h) and temperature was cooled down to 200 °C. The sample was then treated under dynamic vacuum for 30 min. Thereafter, 56 mbar of pure $^{18}\text{O}_2$ was introduced in the system. The MS signals for $^{16}\text{O}_2$ (mass 32), $^{16}\text{O}^{18}\text{O}$ (mass 34), $^{18}\text{O}_2$ (mass 36), C^{16}O_2 (mass 44), $\text{C}^{16}\text{O}^{18}\text{O}$ (mass 46), and C^{18}O_2 (mass 48) were recorded during experiment (60 min). N_2 signal (mass 28) was also recorded to detect any possible leak. Concentration of the isotopomers allows calculating the ^{18}O fraction in the gas phase at each reaction time (α_g^t). In the isothermal tests, $^{18}\text{O}_2$ is added in the recirculation volume when the temperature is stabilized. The initial rate of exchange (V_{ex}) is calculated from the initial slopes (first 30 seconds) of $^{18}\text{O}_2$ (dP_{36}/dt) and $^{16}\text{O}^{18}\text{O}$ (dP_{34}/dt) concentration evolution. In the case of the equilibration reaction, an equimolar volume of $^{18}\text{O}_2$ and $^{16}\text{O}_2$, is introduced in the reactor, and reaction is performed under isothermal conditions.

5c) Results of Oxygen Isotopic Exchange $^{16}\text{O}/^{18}\text{O}$ (OIE).

The evolutions of the partial pressure of the different isotopomers are monitored versus temperature (Figure III.17a for TPIE experiment) or versus reaction time (for isothermal exchange experiment) to extract the number of exchangeable oxygen atoms from the solids, as well as the exchange rates.

The results are gathered in Table III.8 and give a significant oxygen exchange as soon as the temperature reaches 400°C fastly increasing before the temperature of destruction of the phase (~550°C expected). The maximum temperatures are 450°C and 487°C at the maximal exchange rate 1.86 and 1.87 of $\text{Bi}_4\text{Mn}_3\text{O}_{11.5}$ and $\text{Bi}_4\text{Mn}_{2.63}\text{Fe}_{0.4}\text{O}_{11.5}$, respectively (Table III.8 and Figure III.17).

Table III.8 Oxygen exchange rates and number of exchangeable oxygen atoms in the $\text{Bi}_4\text{Mn}_3\text{O}_{11.5}$ and $\text{Bi}_4\text{Mn}_{2.63}\text{Fe}_{0.4}\text{O}_{11.5}$

Materials	TPIE experiments		Isothermal conditions		
	$R_{\text{ex}}^{\text{max}} / 10^{+18} \text{at g}^{-1} \text{s}^{-1} (T_{\text{ex}}^{\text{max}})$	$\alpha_{\text{ex}} / \alpha_{\text{t}} \%$	$R_{\text{ex}}^{\text{a}} / 10^{+18} \text{atom g}^{-1} \text{s}^{-1}$		
			400 °C	450 °C	500 °C
$\text{Bi}_4\text{Mn}_3\text{O}_{11.5}$	1.86 (450°C)	44	0.13	2.67	4.11
$\text{Bi}_4\text{Mn}_{2.63}\text{Fe}_{0.4}\text{O}_{11.5}$	1.87 (487°C)	42	0.14	4.5	6.5

^a initial rate of exchange measured in isothermal conditions; $R_{\text{ex}}^{\text{max}}$ is the maximal rate of exchange measured in TPIE experiment; $T_{\text{ex}}^{\text{max}}$ is the temperature at which the $R_{\text{ex}}^{\text{max}}$ is measured; α_{ex} is the fraction of oxygen in the $\text{Bi}_4(\text{Mn/Fe})_3\text{O}_{11.5}$ that exchanged at the end of the test (700°C)

5d) Temperature-programmed exchange reaction (TPIE)

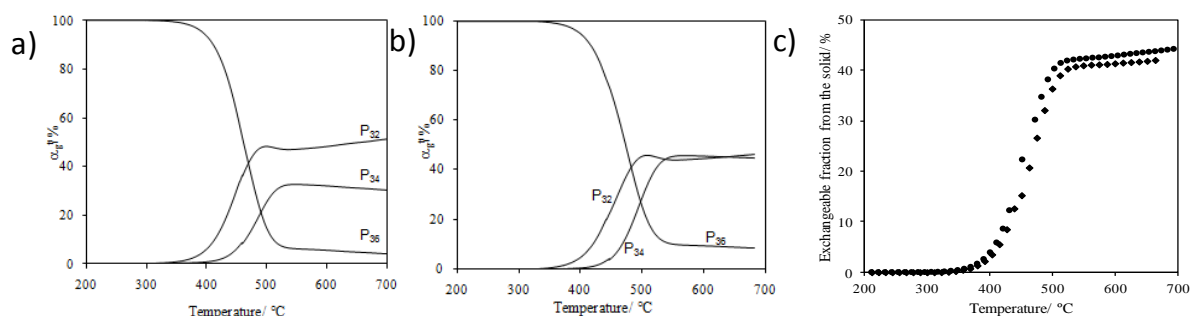


Figure III.17. a) Evolution of isotopomers fraction with reaction temperature during TPIE experiment over $\text{Bi}_4\text{Mn}_3\text{O}_{11.5}$ b) Evolution of isotopomers fraction with reaction temperature during TPIE experiment over $\text{Bi}_4\text{Mn}_{2.63}\text{Fe}_{0.4}\text{O}_{11.5}$ c) Evolution of the fraction of oxygen from the solid exchanged with the reaction temperature. (●) $\text{Bi}_4\text{Mn}_3\text{O}_{11.5}$ (◆) $\text{Bi}_4\text{Mn}_{2.63}\text{Fe}_{0.4}\text{O}_{11.5}$

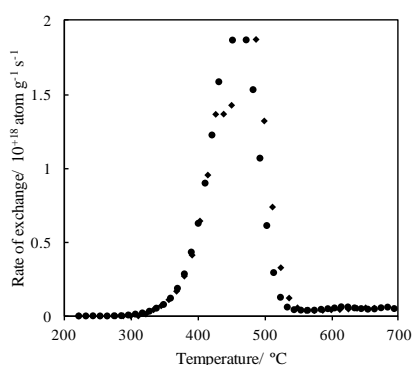


Figure III.18. Evolution of the rate of exchange with reaction temperature. (●) $\text{Bi}_4\text{Mn}_3\text{O}_{11.5}$ (◆) $\text{Bi}_4\text{Mn}_{2.63}\text{Fe}_{0.4}\text{O}_{11.5}$

5e) Isothermal oxygen exchange reaction: bulk properties versus temperature

The evolution of the isotopomers P_{32} ($= {}^{16}\text{O}_2$), P_{34} ($= {}^{16}\text{O}^{18}\text{O}$), P_{36} ($= {}^{18}\text{O}_2$) versus time at different temperatures are plotted on the six next figure for the undoped and iron-doped compounds. Results are briefly discussed below by showing clearly a good exchange ratio (almost 100% at 450°C after 90 minutes) for both compounds.

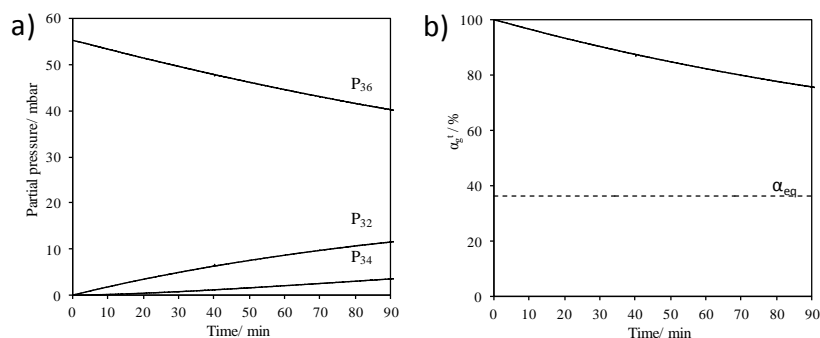


Figure III.19 a) Evolution of isotopomer concentrations with b) exchange time at 400°C. $\text{Bi}_4\text{Mn}_3\text{O}_{11.5}$ sample exchanged at 400 °C. α_{eq} is the fraction of ^{18}O in the gas phase if all the oxygen from the solid exchanged.

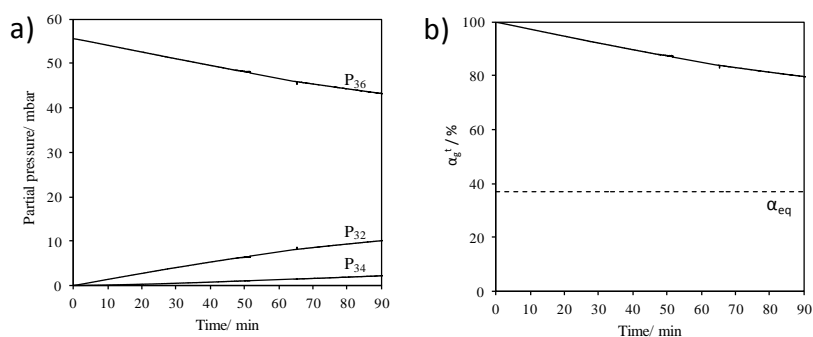


Figure III.19 a) Evolution of isotopomer concentrations with b) exchange time at 400°C. $\text{Bi}_4\text{Mn}_{2.63}\text{Fe}_{0.4}\text{O}_{11.5}$ sample exchanged at 400°C. α_{eq} is the fraction of ^{18}O in the gas phase if all the oxygen from the solid exchanged.

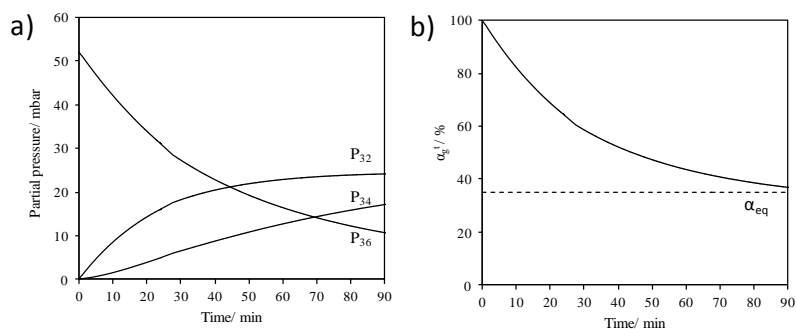


Figure III.20 a) Evolution of isotopomer concentrations with b) exchange time at 450°C. $\text{Bi}_4\text{Mn}_3\text{O}_{11.5}$ sample exchanged at 450°C.

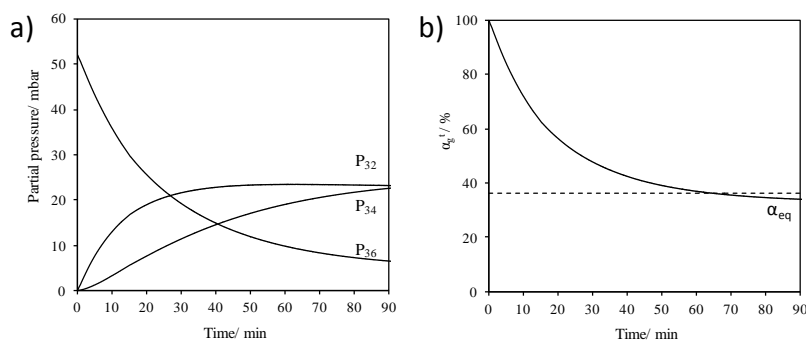


Figure III.21 a) Evolution of isotopomer concentrations with b) exchange time at 450°C. $\text{Bi}_4\text{Mn}_{2.63}\text{Fe}_{0.4}\text{O}_{11.5}$ sample exchanged at 450°C.

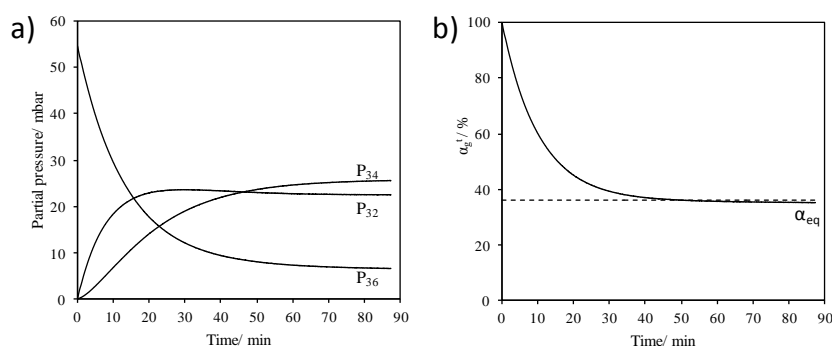


Figure III.22 a) Evolution of isotopomer concentrations with b) exchange time. $\text{Bi}_4\text{Mn}_3\text{O}_{11.5}$ sample exchanged at 500°C.

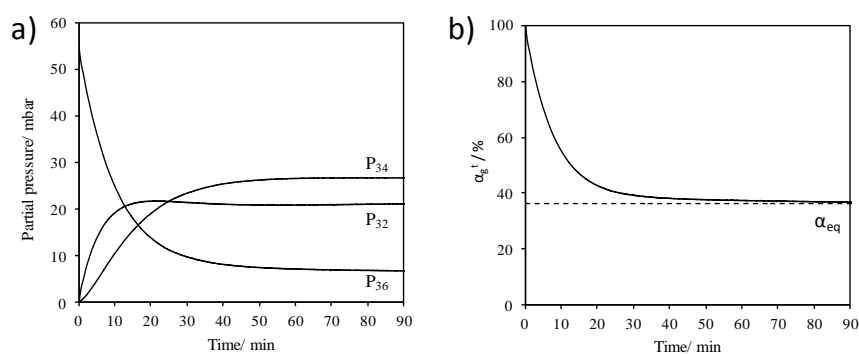


Figure III.23 a) Evolution of isotopomer concentrations with b) exchange time. $\text{Bi}_4\text{Mn}_{2.63}\text{Fe}_{0.4}\text{O}_{11.5}$ sample exchanged at 500°C.

- The principal scheme of oxygen exchange can be deduced from the variation of the partial pressure of the different isotopomers. It can be observed, in both oxides, that the P_{32} increases faster than the P_{34} at the beginning of the exchange reaction, indicating a predominant multiple **heteroexchange mechanism**.
- Exchange capacity :

- At low temperature, eg 400°C: the oxygen mobility in the structure is limited, and it is not possible to exchange all the oxygen from the solid during the time of the test. Indeed, the fraction of the ^{18}O in the gas phase remains far from the equilibrium calculated, assuming that all the oxygen's of the solid are not exchangeable.
- At high temperature, that is $> 450^\circ\text{C}$: oxygen atoms from the lattice are **almost completely exchanged**. The fraction of the ^{18}O in the gas phase reached **the equilibrium value**. It has to be noted that the oxygen exchange rate increase with the exchange temperature. In addition, an increase in oxygen mobility (as characterized by the initial exchange rate, Table III.8) is observed with the iron incorporation in the structure.

5f) Summary of Oxygen isotopic exchange study.

As expected the results of OIE experiments showed high mobility of O^{2-} in $\text{Bi}_4\text{Mn}_3\text{O}_{11.5}$ and $\text{Bi}_4\text{Mn}_{2.63}\text{Fe}_{0.4}\text{O}_{11.5}$. The Fe doping of the parent compound increases not only the exchange rates but also the temperature at which the maximal exchange occurs.

However, it remains unclear the oxygen sorption-desorption mechanism whether it originates from bulk or surface, therefore, further studies have to be conducted.

III.2 New Compounds in the system BOCl-SeO₂-M_xO_y

In the following sections the results obtained from the BiOCl – SeO₂ – M_xO_y ternary systems are presented. Once more it is important to recall that the reason why we tried to introduce Se⁴⁺ is related to the presence of an extra lone pair (in addition to those of Bi³⁺). This might be responsible for innovative structural architectures. In addition, the combined use of selenium and transition metal oxyhalides has a big tendency to form compounds with low dimensional structures built on chains or layers. These particular features increase the probability in obtaining of NCS materials with related properties such as non-linear optics, piezoelectricity and ferroelectricity as already discussed previously.

Four new crystal structures were evidenced and their crystal structure and respective properties are given here if measured. In general, all the oxo-selenites obtained during this work do not have “additional” oxygen atoms to form OX₄ tetrahedra which oblige us to describe the structures by bismuth-centered polyhedra approach.

III.2.1 β -BiSeO₃Cl, Bi₆(SeO₃)₄Cl₁₀ and PbBi₁₀(SeO₃)₁₂Cl₈

1) Generalities

The bismuth selenite halides (Cl, Br or I) systems remain insufficiently explored^{99,183} offering an interesting quest for crystallochemists. Thus, this study led to the discovery of three new architectures built on the cations having lonepairs (that are Bi³⁺, Se⁴⁺ and/or Pb²⁺) with asymmetric coordination environments. Moreover, as expected, the incorporation of Cl⁻ ions (see our results in section II.2.2) allowed us to obtain two layered structures described below, one of them being SHG active. However, these compounds have been obtained only in small amounts, as the scale of several single crystals, due to the used chemical vapour transport (CVT) synthesis method. Up to now, our attempts to get the corresponding powders systematically failed for all compounds. This is a common feature regarding the studies done on several selenites and remains a problem if the measurement of physical properties is considered. Probably this is why the area of selenites is not widely explored whereas such compounds are of fundamental interest in solid-state chemistry and material science especially if the presence of a transition metal in the structure is considered.

2) Crystal growth by CVT.

The crystals of all the three compounds were obtained by chemical vapour transport method,¹⁸⁴ see details of CVT method on the Figure III.20. The precursors ABC, including a transport agent T were ground together and loaded into a quartz tube (ca. 20cm). Then the evacuated and sealed ampoules were placed into tubular furnace with precursors' side of the ampoules being in the center and other side being close to the edge of the furnace. The furnace was heated at 450°C (center) during 14 days. The temperature difference between the hot and cold sides of the ampoule was about 50°C.

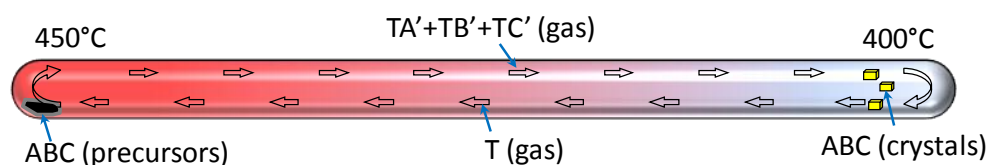


Figure III.20. CVT process in a sealed quartz ampoule.

2a) β' -BiSeO₃Cl

Single crystal: Transparent, colorless, square platelet crystals of β' -BiSeO₃Cl were found on the walls of the cold side of the quartz ampoule with the precursor mixture 1BiOCl+1SeO₂+1MnO₂ and a drop of concentrated solution of HCl. The latter was taken as transport agent in the CVT process.

2b) Bi₆(SeO₃)₄Cl₁₀

Single crystal: And finally, transparent colorless needles of Bi₆(SeO₃)₄Cl₁₀ found on the walls of the cold side of the quartz ampoule with the mixture of 1MnO₂+1BiCl₃+1SeO₂ but in this case without HCl. SeO₂ is considered as a transport agent in this case.

2c) PbBi₁₀(SeO₃)₁₂Cl₈

Single crystal: The crystals of PbBi₁₀(SeO₃)₁₂Cl₈ are the transparent colorless platelets which picked out from the walls of the cold side of the quartz ampoule with the mixture of 1PbO+1BiOCl+1SeO₂ and drop of concentrated solution of HCl as well.

2d) Powder synthesis

So far, the synthesis of the corresponding pure powders always failed, probably because of the rather low temperature at which the precursor SeO₂ becomes volatile (close to 350°C). It could probably also plays the role of a transport agent.

3) BiSeO₃Cl phase diagram

BiSeO₃Cl is already referenced in the literature under 3 different polymorphs: α , β and γ . The γ -form was prepared in evacuated (10^{-2} Pa) silica tubes from 1 : 1 or 3 : 2 mixtures of BiOCl and SeO₂ by Ibragimov et al.⁹⁸ The mixtures were placed in the tubes in a dry chamber under a nitrogen atmosphere. The phase composition of the reaction products was determined by XRD. Solid-state reactions were run at 200°C, 250°C, 300°C, and 350 °C for 240 h, followed by furnace-cooling or quenching in ice water. Single crystals of the α -BiSeO₃Cl was obtained by Berdonosov et al.¹⁸⁵, by heating at 300°C of the evacuated quartz tube with BiOCl and SeO₂ in 2:1 ratio during 240 h. If the starting mixture was enriched in BiOCl, the reaction products occasionally contained yellow BiOCl platelets and colorless γ -BiSeO₃Cl crystals in the shape of parallelepipeds.

The crystal structure of the α -form (Figure III.21a) (lattice parameters $a = 6.353(2)$ Å, $b = 7.978(3)$ Å, $c = 8.651(4)$ Å, space group $P2_12_12_1$ (19)) is detailed in ref [185]. The structure of γ -form (Figure III.21b) is detailed in ref [98] (lattice parameters $a = 11.707(2)$ Å, $b = 7.047(1)$ Å, $c = 5.315(1)$ Å, space group $Pna21$ (33)). Due to the NCS space group of the α -form, its optical properties have been largely studied as well as the dielectric properties.

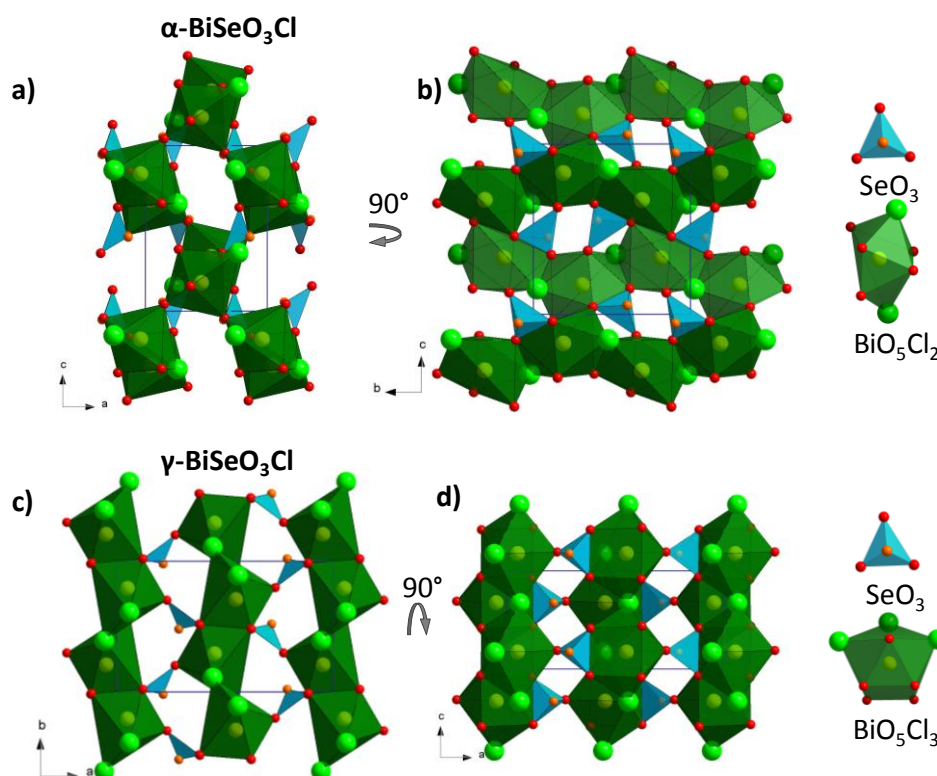


Figure III.21. The crystal structure of α -BiSeO₃Cl: a) projection along b-axis, b) projection along a-axis. The crystal structure of γ -BiSeO₃Cl: c) projection along c-axis, b) projection along b-axis

The β -BiSeO₃Cl polymorph was announced as stable in a very short thermal domain from the heating of α -BiSeO₃Cl between 400°C and 410°C.¹⁸³ However, the crystal structure of former was not solved. From the literature we have only short clues (powder pattern and IR spectra of this β -form, as published in ref [¹⁸³]). Therefore, the formal identification is rather difficult. Here we proposed to solve the structure of a new polymorph β' -BiSeO₃Cl obtained by CVT method (see the synthesis section (2a) above). It may correspond to the announced β -form but further experiments are necessary for full confirmation. At this point of our study, we prefer to call it the β' -polymorph.

4) Crystal structure of β' -BiSeO₃Cl.

Colorless platelet single crystals have been isolated from the CVT products (see 2-a above). An energy dispersive spectroscopy analysis performed on single crystals shows evidence of Bi, Se, and Cl with a stoichiometry which roughly confirms the announced formula. The majority of the tested crystals correspond to identical crystals with lattice parameters, $a = 22.7052(3)$ Å, $b = 76.785(4)$ Å, $c = 16.0550(3)$ Å and $\beta = 135.000(2)^\circ$ (C-centered monoclinic lattice) (Table III.9).

The assorted large volume cell is striking and involves a very complex structure. The crystal structure was solved using the Superflip¹⁶⁷ method. The position of 48 bismuth, selenium and chlorine atoms, were localized easily unlike the environment of selenium was a little tricky. Thus, oxygen atoms were pointed out using several Fourier-Difference around each selenium independently. Because of the high number of parameters to refine, only the atomic displacement parameters of bismuth and selenium atoms were refined in an anisotropic way. The final cycles of least-squares refinement including atomic coordinates and anisotropic thermal parameters for all cations and isotropic thermal parameters of anions converged at $R1 = 0.0612$, $wR2 = 0.0645$. The atomic parameters and selected distances are given in Annex IV.212).

The crystal structures of the α and γ -BiSeO₃Cl structures are shown on the Figure III.21a-d. The BiO₅Cl₂ polyhedra in the former and BiO₅Cl₃ in the latter are interconnected with SeO₃ triangular pyramid by sharing respective edges and corners in a complex manner. All Bi³⁺ can be considered as interstitials in an anionic [Cl⁻/SeO₃²⁻] lattice such that the crystal structures could be considered as mainly 3D.

Table III.9 Crystal data, measurement and structural refinement parameters for β -BiSeO₃Cl, Bi₆(SeO₃)₄Cl₁₀ and PbBi₁₀(SeO₃)₁₂Cl₈

	β -BiSeO ₃ Cl	Bi ₆ (SeO ₃) ₄ Cl ₁₀	PbBi ₁₀ (SeO ₃) ₁₂ Cl ₈
Crystal data			
Crystal symmetry	Monoclinic	Monoclinic	Orthorhombic
space group	Cc	P21/c	Ccca
a (Å)	22.7052(3)	21.460(2)	15.819(6)
b (Å)	76.785(4)	8.4012(9)	17.871(7)
c (Å)	16.0550(3)	15.3370(18)	15.857(6)
β (°)	135.000(2)	110.639(5)	
V (Å ³)	19792(2)	2587.7 (5)	4483 (3)
Z	192	4	4
Dx (g/cm ³)	5.470	5.432	6.079
μ (mm ⁻¹)(for λ)	52.04	47.37	53.17
K α =0.7107Å			
Appearance	Colorless platelet	Colorless needle	Colorles platelet
Crysral size (mm)	0.13×0.09×0.05	0.81×0.37×0.13	0.16×0.15×0.06
Data collection			
λ (Mo K α) (Å)	0.71073	0.71073	0.71073
Scan mode	ω and ϕ	ω and ϕ	ω and ϕ
θ (min–max) (°)	1.1 – 26.5	2.0 – 30.5	2.2 – 26.4
R(int) (%)	0.096	0.045	0.050
Recording reciprocal space	–28 ≤ h ≤ 28 –96 ≤ k ≤ 96 –20 ≤ l ≤ 20	–30 ≤ h ≤ 30 –11 ≤ k ≤ 7 –20 ≤ l ≤ 21	–15 ≤ h ≤ 19 –22 ≤ k ≤ 21 –19 ≤ l ≤ 19
Refinement			
Measured, independent obs. * refl.	242854, 35097, 20337	34697, 7843, 6363	10469, 2253, 1504
No. of Refined parameters	1637	298	115
Refinement method,	F ²	F ²	F ²
R1(F ²)(obs) / R1(F ²)(all)	0.0612/0.1124	0.0299/0.0427	0.0667/0.1057
wR2(F ²)(obs) /wR2(F ²)(all)	0.0645/0.0694	0.0330/0.0442	0.0639/0.0859
GOF(obs) / GOF(all)	1.32/1.63	1.46/1.76	0.84/0.92
$\Delta\rho_{\max}/\Delta\rho_{\min}$ (e Å ⁻³)	5.39 /-4.51	3.42 /-2.97	5.38 /-7.01
Extinction coefficient	-	0.0070(13)	0.0022(13)

*obs=[I>3σ(I)]

It follows that the β' -BiSeO₃Cl crystal structure appearing as layered (Figure III.22a-b) is rather original in this phase diagram. It is built of two original bismuth chloride blocks: [Bi₈Cl₁₆]⁺⁸ (Figure III.22c) and [Bi₁₂Cl₃₂]⁺⁴ (Figure III.22d) which are regularly sandwiched by similar [Bi₁₄(SeO₃)₂₄]⁻⁶. As it is shown on the Figure III.22a, BiO_xCl_y polyhedra (in green) can be drawn, however for the sake of clarity [Bi₈Cl₁₆]⁺⁸ and [Bi₁₂Cl₃₂]⁺⁴ layers represented as an arrangement of Bi (yellow) and Cl (green) atoms (Figure III.22b).

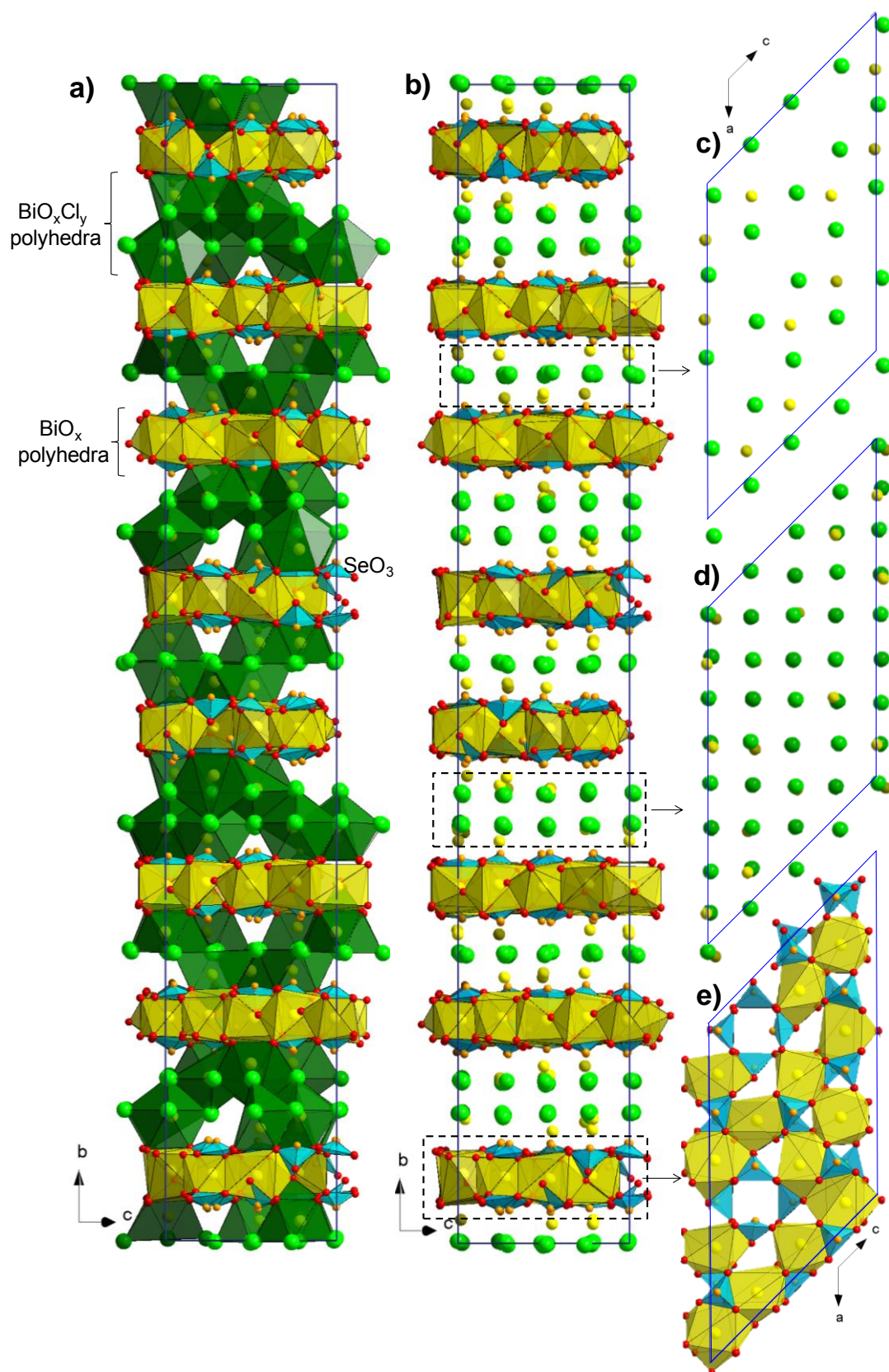


Figure III.22. a) β' - BiSeO_3Cl crystal structure projected along a -axis, BiO_x polyhedra shown in yellow, BiO_xCl_y in green; b) the same projection without interlayer BiO_xCl_y polyhedra. It evidences an alternation of 3 different parallel layers: c) $[\text{Bi}_{12}\text{Cl}_{32}]^{+4}$, d) $[\text{Bi}_8\text{Cl}_{16}]^{+8}$ and e) $[\text{Bi}_{14}(\text{SeO}_3)_{24}]^6$ presented as association of distorted Bi-O polyhedra and SeO_3 by sharing edges and corners.

Similar halide layers as the $[\text{Bi}_{12}\text{Cl}_{32}]^{+4}$ bismuth chloride layers has already been observed in the structure $\text{Bi}_8(\text{SeO}_3)_3\text{Br}_6$ ⁹⁹ and also have been found in $\text{PbBi}_{10}(\text{SeO}_3)_{12}\text{Cl}_8$ described in section (6) below. The layer $[\text{Bi}_{14}(\text{SeO}_3)_{24}]^{-6}$ is built from the association of bismuth oxide SeO_3 triangles and interstitial Bi^{3+} , leading to complex BiO_x polyhedra (in yellow Figure III.22), where x being between 8 and 10. SeO_3 triangular pyramid share faces/edges/corners with BiO_x in a complex manner. Being on the edges of $[\text{Bi}_{14}(\text{SeO}_3)_{24}]^{-6}$ layer SeO_3 pyramids hold the BiO_x polyhedra together, confining them from each side. All the Bi-centered polyhedra are distorted which is typical in the bismuth coordination due to its stereoactive lone pair. The Se^{4+} cations also exhibit an asymmetric coordination environment in SeO_3 triangular pyramid due to its lone pairs as well, the latter being in the apical position. The Se–O bond lengths and the O–Se–O bond angles are in the range from 1.65 to 1.75 Å and from 92.8° to 106.4, respectively (see Annex IV.212)).

The large size of the b-axis is due to a number of different modules stacked along the b-axis for charge balance. In other words the intervening of $[\text{Bi}_{12}\text{Cl}_{32}]^{4+}$ and $[\text{Bi}_8\text{Cl}_{16}]^{8+}$ between similar Bi/ SeO_3 layers is the key factor for this “giant cell”. So, the crystal structure is complicated, due to the great number of local environment around Bi atoms. Briefly, a general idea on Bi-environments is that it is only surrounded by O atoms and the number of surrounded anions is varying from five to ten neighbors.

The drastic differences in the structures of β' -form from the 3D-structures of α and γ -forms is an argument against the correspondence between the former and the reported β -form announced stable by transition ($\alpha \rightarrow \beta$ and $\beta \rightarrow \gamma$) in a 10°C range. Most probably our compound corresponds to a fourth original form.

4a) SHG microscopy of β' -BiSeO₃Cl

We used a laser scanning microscope LSM 710 NLO Zeiss (Iena, Germany) implemented at the Plateforme d'Imagerie Cellulaire et Tissulaire, Reims, France. Excitation was provided by a CHAMELEON femtosecond Titanium-Sapphire laser (Coherent, Santa Clara, USA) set at 860 nm, tuning the power until SHG was detected (\rightarrow 16% maximal power, ~0.55mW) on selected single crystal of β' -BiSeO₃Cl deposited on a glass plate. Samples were imaged with a 20x, 0.8 NA objective lens. Emitted signal of SHG was collected with a bandpass filter (420 to 440 nm).

The Figure III.23a shows the crystal of β' -BiSeO₃Cl in absence of emission and during emission. The color at the surface of the single crystals shows an intrinsic homogeneous distribution of the emitted light collected with a band pass filter (420 to 440 nm).

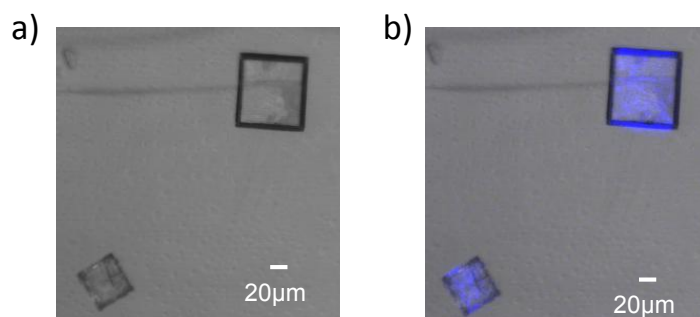


Figure III.23. a) Transmission image of a crystal of $\text{Bi}(\text{SeO}_3)\text{Cl}$, b) color: emitting surface ($\lambda_{em}=420\text{--}440\text{ nm}$, $\lambda_{em} = 860\text{ nm}$).

4b) Infrared Spectroscopy of β -BiSeO₃Cl,

Infrared spectra of several single crystals of β' -BiSeO₃Cl were measured between 4000 and 400 cm^{-1} with a Perkin–Elmer Spectrum Two™ spectrometer equipped with a diamond attenuated total reflectance (ATR) accessory. As it is seen from the Figure III.24, at the first glance, the infrared spectra of our β' -BiSeO₃Cl matches quite well with that of not-solved β -BiSeO₃Cl of Oppermann et al.¹⁸³ However, it is rather difficult to conclude whether the β and β' forms are the same polymorphs, since basically the vibrational spectra for all these polymorphs include Se—O, Bi—O and Bi—Cl bands that are not expected to be drastically shifted (cf. strong similarities between the IR spectra of α , β and γ forms¹⁸³)

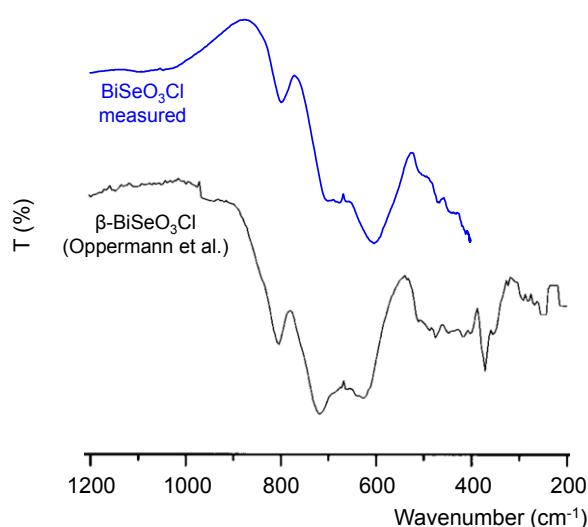


Figure III.24. Infrared red spectrum of the prepared β' -BiSeO₃Cl (in blue) compared to the spectrum of β -BiSeO₃Cl (in black) (from Oppermann et al.¹⁸³).

5) Crystal structure of Bi₆(SeO₃)₄Cl₁₀.

Colorless needle like single crystals have been isolated after the CVT synthesis. The crystallographic data are: $a = 21.460(2)$ Å, $b = 8.4012(9)$ Å, $c = 15.337(2)$ Å and $\beta = 110.64(1)^\circ$, space group $P2_1/c$ and $R_1 = 0.0303$ and $wR_2 = 0.0333$. The details of pertinent XRD data collection and structural refinement are summarized in the Table III.9. The heavy atoms (10 bismuth and 4 selenium atoms) were localized using the Superflip¹⁶⁷ method whereas the remaining atoms (10 chlorine and 12 oxygen atoms) were deduced from successive Fourier difference maps. The structure refinement rapidly converged to a low reliability factors, $R_1 = 3.38$ and $wR_2 = 3.65$, after having applied the ADP parameters for all atoms. The crystal structure is presented on the Figure III.25a.

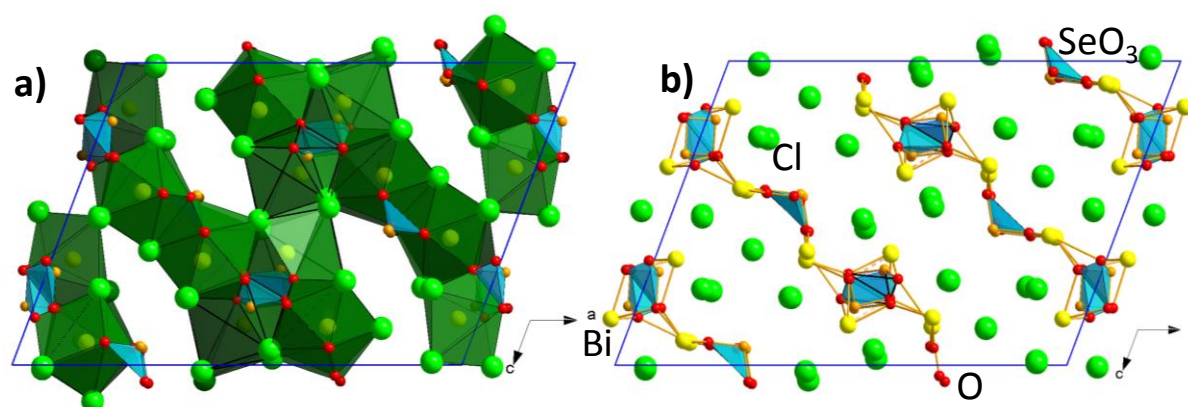


Figure III.25. a) Crystal structure of Bi₆(SeO₃)₄Cl₁₀ projection along the b-axis, shows BiO_xCl_y polyhedra (in dark grey) and SeO₃ groups (in blue) sharing edges and corners. b) the same projection without drawing the BiO_xCl_y polyhedra

The structure is built on association of 6 distorted bismuth oxochloride polyhedra: Bi(1)O₅Cl₄, Bi(2)O₃Cl₅, Bi(3)O₃Cl₄, Bi(4)O₅Cl₄, Bi(5)O₄Cl₄ and Bi(6)O₄Cl₄, connected by four SeO₃ triangular pyramids forming a 3D network. Those polyhedra share edges and corners to build Bi₆(SeO₃)₄Cl₁₀ blocks, which are further interconnected, creating cavities, parallel to b axis. The size of these holes (bordered by anions) is around 9.7 Å long and 3.8 Å wide. The presence of such tunnels with n MR (member rings) was already observed in other selenites and especially bismuth selenites with Bi₂(V^VO₂)₂(SeO₃)₄ (8-MR).¹⁸⁶ If we do not draw the bismuth centered polyhedra we can see the 2D character of the structure as well (Figure III.25b).

The close inspection of once more calculated Fourier-difference map, showed a high residual electronic density ($8.71 \text{ e}/\text{\AA}^3$) 0.86 Å away from Se3 atom indicating its splitting. The refinement of the occupations of Se3/Se3' gave 0.95/0.07. While the Se-O distances for Se3

are in the acceptable range ($1.71 \text{ \AA} - 1.74 \text{ \AA}$) those of Se3' are too long ($2.09 \text{ \AA} - 2.41 \text{ \AA}$) for SeO_3 . Since, the neighboring Bi1 shows similar geometry with the same range of bond distances as Se3' it was suggested that the latter is a Bi atom instead. Indeed the Fourier difference map showed some residual electron density around Bi1 atom, which was attributed to Se3b as it is shown on the Figure III.26a. The final occupations Bi1a/Bi1b and Se3a/Se3b was refined to 0.96/0.04. Thus, a chain of disorder ($-\text{BiO}_3-\text{SeO}_3-$) is observed along the b -axis (Figure III.26b).

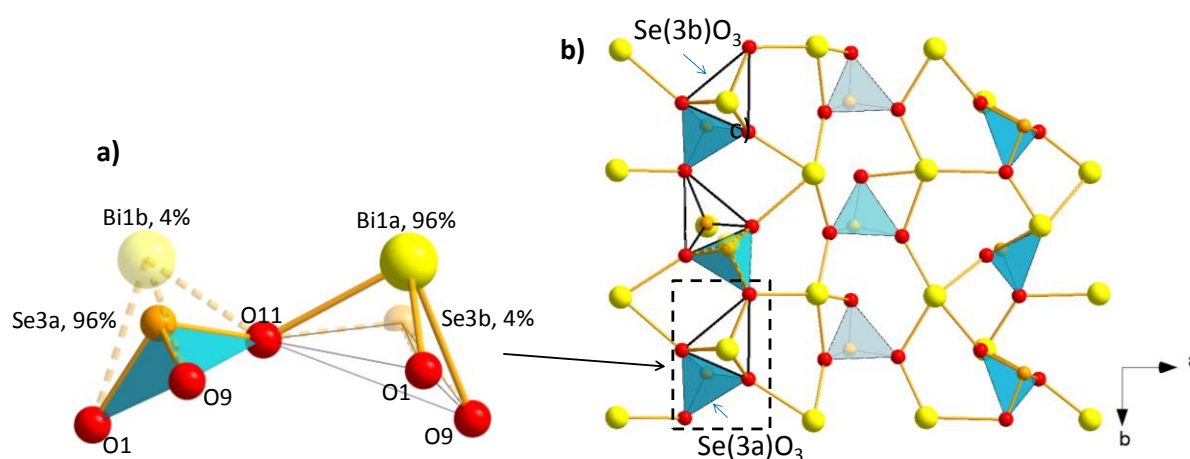


Figure III.26. a) The environment around Bi1a and Se3a atoms, b) a part of the structure of the structure of $\text{Bi}_6(\text{SeO}_3)_4\text{Cl}_{10}$ projection along the c -axis

Atomic parameters and selected Bi-O, Bi-Cl and Se-O distances are given in Annex IV.212).

6) Crystal structure of $\text{PbBi}_{10}(\text{SeO}_3)_{12}\text{Cl}_8$

Colorless platelet crystals of $\text{PbBi}_{10}(\text{SeO}_3)_{12}\text{Cl}_8$ were mounted on a glass fiber for XRD data collection. The measured reflections showed systematic absences consistent with space group $Ccca$. The structure was solved using the Superflip¹⁶⁷ method which localized the 7 bismuth and 4 selenium independent atoms with remarkably different coordination environment. The following 10 chlorine and 12 oxygen atoms were easily observed from consecutive different Fourier maps. At this stage, however, the final formula was not neutral. Because of the presence of lead during the synthesis and since it is not possible to make distinction between lead and bismuth using X-Rays, a complementary study had to be done to reveal the Bi/Pb ratio. The presence of lead was evidenced by a EPMA microprobe analysis, and ratio Pb/Bi was found to be 1:10. So lead cations were introduced in bismuth sites in ratio 1/9 (and fixed to this value) in order to reach the final electroneutrality. Apart from oxygen atoms, all displacement parameters were refined as anisotropic. Technical details of the data acquisition

as well as some refinement results for the concerned compound are summarized in the Table III.8. The crystal structure of PbBi₁₀(SeO₃)₁₂Cl₈ is shown on the Figure III.27.

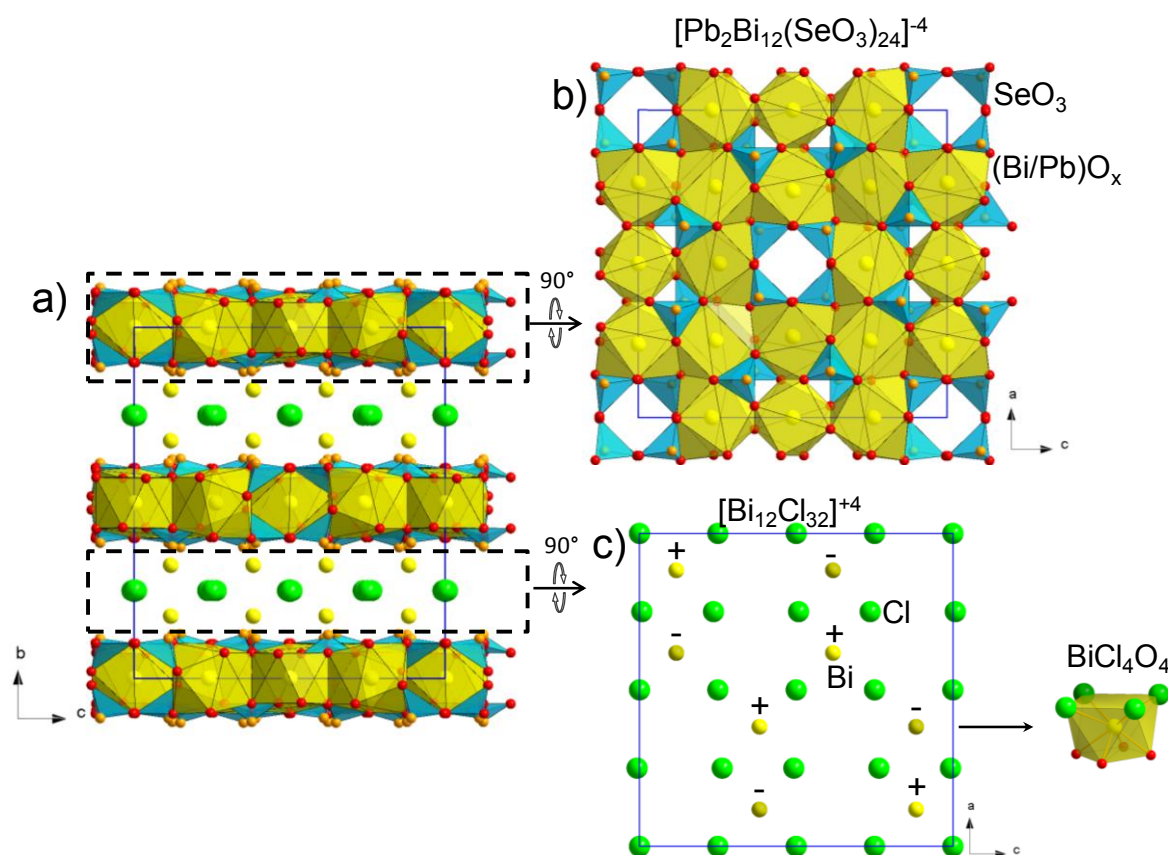


Figure III.27. a) crystal structure of PbBi₁₀(SeO₃)₁₂Cl₈ projected along *a*-axis. The structure includes two parallel layers, b) [Pb₂Bi₁₂(SeO₃)₂₄]⁴⁻ built on association of distorted Bi-O polyhedra (in dark grey) and SeO₃ groups (in blue) and c) [Bi₁₂Cl₃₂]⁴⁺. Each layer is parallel to (*a*, *c*) plane.

Several distorted polyhedra can be observed: Bi(1)O₈, Bi(2)O₁₀, Bi(3)O₁₀, Bi(4)O₁₀ and Bi(5)O₄Cl₄, where Bi-O bond distances vary from 2.37 to 2.75 Å and Bi-Cl bonds are in the range of 2.96 - 3.1 Å (atomic coordinates and precise distances are given in Annex IV.212)). The whole drawing of the compound evidence a 2D network with two independent layers: [Bi₁₂Cl₃₂]⁴⁺ (Figure III.27b) and [Pb₂Bi₁₂(SeO₃)₂₄]⁴⁻ (Figure III.27c) which are parallel to (*a*, *c*) plane. To our knowledge PbBi₁₀(SeO₃)₁₂Cl₈ is a rare example of structure containing three atoms with lonepair. Unfortunately despite of this fact, it has a CS space group and does not exhibit desired optical properties.

7) Summary

The structure of possibly new polymorph of BiSeO₃Cl was solved in NCS space group with very large lattice constants. The NCS space group was confirmed by SHG measurements. The structures of Bi₆(SeO₃)₄Cl₁₀ and PbBi₁₀(SeO₃)₁₂Cl₈ was solved as well, however they

crystallize in CS space groups. The crystal structures of these new selenites have been described by bismuth-centered polyhedra approach, where the SeO_3 triangular pyramids play role of connectors of $\text{Bi}(\text{O}/\text{Cl})_x$ polyhedra. The key-role of the crystal structure is achieved by large Cl^- anions which “template” the crystal structures into various dimensionalities

III.2.2 $\text{Bi}_2\text{MnO}(\text{SeO}_3)_2\text{Cl}_3$

1) Synthesis.

Single crystal: Brown needle-like fragile single crystals of $\text{Bi}_2\text{MnO}(\text{SeO}_3)_2\text{Cl}_3$ was found on the cold side of a quartz tube after CVT experiment with the duration of four weeks. The stoichiometric mixture was following: $\text{MnO}_2 + \text{BiOCl} + \text{SeO}_2$, and as the transport agent 1 ml of 32% solution of HCl was taken.

Powder synthesis: attempts to prepare the corresponding powder systematically failed. The following procedures were accomplished:

- *Hydrothermal synthesis:* 0.5g of stoichiometric amounts of Mn_2O_3 , BiOCl and SeO_2 were ground together and put into Teflon sealed 30ml bombs 1/3 of which was filled with DI water, with the addition of 1ml of 32% solution of HCl, followed by heating at 200°C during two weeks.
- *Solid states synthesis:* stoichiometric amounts of Mn_2O_3 , BiOCl and SeO_2 were ground together and sealed into quartz tube with 1ml of 32% solution of HCl, then heated during two week at 400°C .

2) Structural description.

The structure of $\text{Bi}_2\text{MnO}(\text{SeO}_3)_2\text{Cl}_3$ (Figure III.28) crystallizes in monoclinic crystal system with the space-group $\text{P}2_1/\text{m}$ (11). The unit cell parameters $a = 8.5875(6) \text{ \AA}$, $b = 7.1448(5) \text{ \AA}$, $c = 8.6194(6) \text{ \AA}$, $\beta = 107.015(4)^\circ$ and $V = 505.70(6) \text{ \AA}^3$.

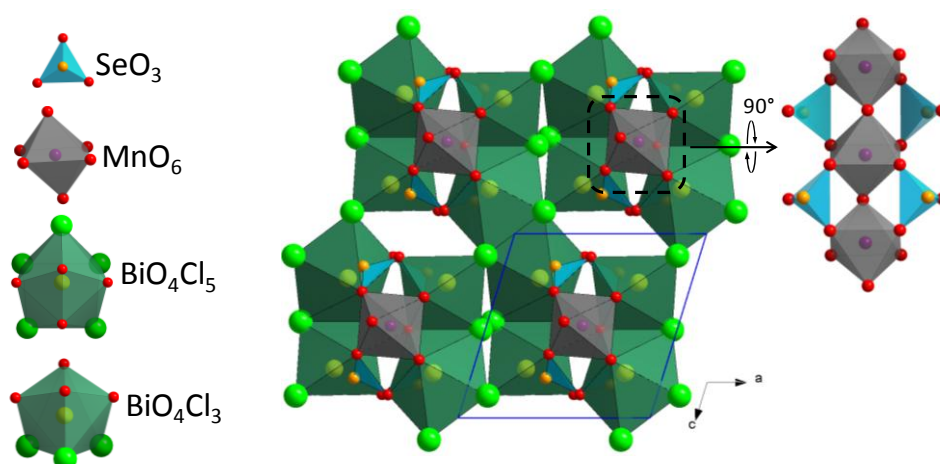


Figure III.28. a) The structure of $\text{Bi}_2\text{MnO}(\text{SeO}_3)_2\text{Cl}_3$, b) MnO_5 chains

OBi_4 tetrahedra are not formed, since there are no “additional” oxygen atoms in the vicinity of bismuth atoms in the structure of $\text{Bi}_2\text{MnO}(\text{SeO}_3)_2\text{Cl}_3$. The individual O atom within the $\text{Bi}_2\text{MnO}(\text{SeO}_3)_2\text{Cl}_3$ formula correspond to the Mn-O-Mn bridges, far to have an oxo-centred role. So the bismuth centered polyhedra BiO_4Cl_5 and BiO_4Cl_3 were drawn to describe the structure (Figure III.28). The bismuth polyhedra are connected by sharing their edges forming layers parallel to the c axis. Also the SeO_3 triangular pyramids bridge two subsequent MnO_6 octahedra. The chains of corner shared MnO_6 octahedra go parallel to b -axis as shown on the Figure III.28b. It leads to $-\text{Mn}^{3+}-\text{O}-\text{Mn}^{3+}-\text{O}-$ zig zag chains with Mn-Mn distances of 3.57 Å, with two apical Mn-O bonds of 1.979 Å, and Mn-O-Mn angles of 129°. The chains are separated at 8.61 Å from each other by Bi polyhedra in c and a direction. The formula $\text{Bi}_2\text{MnO}(\text{SeO}_3)_2\text{Cl}_3$ is neutral if Mn atoms are in the +3 oxidation state which is also confirmed by calculated BVS values (Table III.10).

The preparation of a larger amount of crystals is under way for magnetic characterizations of these low-D units.

Table III.10. BVS of atoms in $\text{Bi}_2\text{MnO}(\text{SeO}_3)_2\text{Cl}_3$

Atom	BVS
Bi1	3.012(11)
Bi2	3.080(7)
Se1	3.92(2)
Se2	3.912(18)
Mn1	3.032(8)
Cl1	1.095(3)
Cl2	0.7665(17)

3) Summary

The structure of $\text{Bi}_2\text{MnO}(\text{SeO}_3)_2\text{Cl}_3$ is described by interconnection of bismuth centred polyhedra. Well separated chains of corner shared MnO_6 octahedra can be distinguished.

Further attempts have to be conducted to prepare the polycrystalline sample for full characterization.

Conclusion

Conclusion

The exploration of the $\text{Bi}_k\text{M}_m\text{X}_n\text{O}_y$ compounds, where $\text{M} = \text{Li, Na, K, Mg, Cd, Zn, Cu, Co, Mn, Fe, Pb}$ and $\text{X} = \text{P, V, As, Mo, Se and Cl}$, reported in this thesis and elsewhere leads to the suggestion that the crystal chemistry of the isolated materials may be “infinitely” adaptive. Particularly a huge number of topologically unique frameworks built on OBi_4 tetrahedra are highlighted in this manuscript. The various topologies evidenced have been either designed using a Lego-like assembly of complex Bi^{3+} building units or obtained from shake-and-bake processing working in selected ternary systems.

- The achievement of new architectures without ulterior-motive remains a gold mine to evidence new crystal structures. Indeed, in the ternary system $\text{Bi}_2\text{O}_3\text{-P}_2\text{O}_5\text{-CuO}$, two new intergrowths with ribbons width $n = 4$ and $n = 3$ were identified after melting of the powder sample. We also pointed out by chance other novel architectures built on $\text{O}(\text{Bi},\text{M})_4$ building units. A new compound with a square based column was also pointed out as well as 3D opened frameworks.
- We didn't focus on the design aspect, since, for the moment, the elaborated empirical rules work only for phosphates as it is evidenced in this and previous works, therefore requiring more results to systematize and work out new empirical rules for further design of new bismuth compounds.

Beyond the novel architectures pointed out, the disorder inherent to these phases was deeply studied for the first time. The possibility to obtain crystallographic data of good quality allowed studying different order and disorder degrees related to the tunnels and edges of ribbons. To do so, complementary methods were combined and the disorder was also studied depending of the scale of observation. Our results confirm the general idea that in this family of compounds a periodic skeleton of $\text{O}(\text{Bi},\text{M})_4$ units is holding the crystal structure while the surrounding space is filled by more or less disordered counter ions including interstitial hosts. Slight compositional changes seem to modify the interstitial sublattice while the main oxocentered sublattice is not sensitively modified. The nature of the cation introduced in the crystal structure next to Bi^{3+} is of huge importance because of the ionic radii effect as well as the coordination sphere impact.

This thesis is one of the first dedicated to this series of compounds in which the physical properties were deeply measured. This is an aim we were able to reach because of several interesting materials:

- BiCoAsO_5 : Magnetic properties are similar to the isostructural BiCoPO_5 due to the close electronegativities of As and P, however, their radii do not seem to play a big role in the magnetic spin interactions of Co atoms.
- $\text{BiCu}_2(\text{As/P})\text{O}_6$: The magnetic properties of BiCu_2XO_6 are significantly modified after the $\text{P} \rightarrow \text{As}$ substitution. The initial suggestion that the Cu magnetic ladders would be isolated by diminished J3 spin-exchange pathways in the case of the arsenate turned out to be wrong. Nevertheless, magnetic structure has not been observed on PND data. Further experiments are needed to understand fully the 3D AFM ordering the As-rich zone.
- $\text{Bi}_4\text{Cu}_3(\text{As/V})\text{O}_{13}$: Conducted magnetic and neutron diffraction measurements showed contradictory results meaning the 3D AFM ordering showed by former was not observed by latter. Further investigations have to be done to clarify this issue.
- The optical properties such as second harmonic generation and luminescent properties measured for several compounds showing good results. Especially the latter results for $\text{BiM}_2\text{O}_2(\text{XO}_4)$ are very promising and are currently largely studied by Jacob Olchowka, another PhD student.
- Several terms of new exciting chloride series have been obtained which show 2D and mixed 1D and 2D character in their structures, possibly having good luminescent properties
- $\text{Bi}_4\text{Mn}_3\text{O}_{11.5}$: it is (to our knowledge) the fourth example of 2D-maple leaf lattice but it is the first synthetic realization in an oxide compound that shows confined 2D-magnetism. In addition, it might have catalytic oxidation properties due the very mobile oxygen atoms as it was shown by OIE measurements.

To finish it is important to emphasize the preliminary/promising results obtained during the diversification of the chemical systems: for example, the introduction of selenium. The crystal structures of the new selenites have been described by bismuth-centered polyhedra approach, where the SeO_3 triangular pyramids play role of connectors of $\text{Bi}(\text{O/Cl})_x$ polyhedra. The introduction of chlorine is also of big interest because of the possibility to obtain multi-dimensional frameworks assorted to the presence of pores, of layers etc. The key-role of the

crystal structure is achieved by large Cl^- anions which “template” the crystal structures into various dimensionalities. Thus introducing this kind of new elements is of big interest since they create new topologies. Indeed, the possibility to get non-centrosymmetric compounds is interesting in itself because of the related possible applications. This subject is just beginning and is clearly promising. The chemical diversification is in process, further using other cations such as Ln^{3+} , Pb^{2+} etc. and XO_y ($\text{X} = \text{Cr}, \text{Mn}, \text{Mo}$ etc.) will be carried out because structural analogies were found in the literature with their use. To do so, the necessity to diversify the synthesis routes is more than ever worth. Indeed, the synthesis methods as CVT method appears particularly well suited to obtain new architectures, however having disadvantages in terms of producing large quantities. Thus further use for new synthesis routes as well as diversification of M and X elements in Bi/M/X/O system will be carried out.

Reference.

- (1) Bugaris, D. E.; zur Loye, H.-C. *Angewandte Chemie International Edition* **2012**, *51*, 3780–3811.
- (2) Bergerhoff, G.; Paeslack, J. *Zeitschrift für Kristallographie* **1968**, *126*, 112–123.
- (3) Aurivillius, B.; Lindblom, C.-I.; Sténson, P.; Seip, H. M. *Acta Chemica Scandinavica* **1964**, *18*, 1555–1557.
- (4) Smith, P.; Garcia-Blanco, S.; Rivoir, L. *Zeitschrift für Kristallographie* **1964**, *119*, 375–383.
- (5) Tulinsky, A.; Worthington, C. R.; Pignataro, F. *Acta Crystallographica* **1959**, *12*, 623–626.
- (6) Burnham, C. W. *Zeitschrift für Kristallographie* **1963**, *118*, 337–360.
- (7) Zachariasen, W. H. *Acta Crystallographica* **1949**, *2*, 60–62.
- (8) Aurivillius, B. *Chemica Scripta* **1976**, 156–158.
- (9) Magarill, S. A.; Romanenko, G. V.; Pervukhina, N. V.; Borisov, S. V.; Palchik, N. A. *J Struct Chem* **2000**, *41*, 96–105.
- (10) Schleid, T. *European journal of solid state and inorganic chemistry* **1996**, *33*, 227.
- (11) Schleid, T.; Lissner, F. *Journal of Alloys and Compounds* **2008**, *451*, 610–616.
- (12) Schnick, W.; Lücke, J. *Angewandte Chemie* **1992**, *104*, 208–209.
- (13) Stock, N.; Irran, E.; Schnick, W. *Chemistry – A European Journal* **1998**, *4*, 1822–1828.
- (14) Qi, R.-Y.; Corbett, J. D. *Inorg. Chem.* **1997**, *36*, 6039–6044.
- (15) Uma, S.; Corbett, J. D. *Inorg. Chem.* **1999**, *38*, 3831–3835.
- (16) Krebs, B. Z. *Naturforsch.* **1970**, *25b*, 223.
- (17) Caro, P. E. *Journal of the Less Common Metals* **1968**, *16*, 367–377.
- (18) O’Keeffe, M.; Hyde, B. G. In *Cation Ordering and Electron Transfer*; Springer Berlin Heidelberg: Berlin, Heidelberg; Vol. 61, pp. 77–144.
- (19) Schleid, T. *Materials Science Forum* **1999**, *315-317*, 163–168.
- (20) Krivovichev, S. V.; Mentre, O.; Siidra, O. I.; Colmont, M.; Filatov, S. K. *Chemical Reviews* **2013**.
- (21) In *IUPAC Compendium of Chemical Terminology*; Nič, M.; Jirát, J.; Košata, B.; Jenkins, A.; McNaught, A., Eds.; IUPAC: Research Triangle Park, NC.
- (22) Parr, R. G.; Pearson, R. G. *J. Am. Chem. Soc.* **1983**, *105*, 7512–7516.
- (23) Pauling, L. *J. Am. Chem. Soc.* **1932**, *54*, 3570–3582.
- (24) Pearson, R. G. *Inorg. Chem.* **1988**, *27*, 734–740.
- (25) Krivovichev, S. V.; Filatov, S. K. *Crystal chemistry of minerals and inorganic compounds with complexes of anion-centered tetrahedra*; St. Petersburg University Press: St. Petersburg, 2001.
- (26) Brown, I. D. *Chem Rev* **2009**, *109*, 6858–6919.
- (27) Brown, I. D.; Skowron, A. *J. Am. Chem. Soc.* **1990**, *112*, 3401–3403.
- (28) Drache, M.; Roussel, P.; Wignacourt, J.-P. *Chem. Rev.* **2007**, *107*, 80–96.
- (29) Abraham, F.; Boivin, J. C.; Mairesse, G.; Nowogrocki, G. *Solid State Ionics* **1990**, *40-41, Part 2*, 934–937.
- (30) Patoux, S.; Vannier, R.-N.; Mairesse, G.; Nowogrocki, G.; Tarascon, J.-M. *Chem. Mater.* **2001**, *13*, 500–507.
- (31) Li, J.-B.; Huang, Y. P.; Rao, G. H.; Liu, G. Y.; Luo, J.; Chen, J. R.; Liang, J. K. *Applied Physics Letters* **2010**, *96*, 222903–222903–3.
- (32) Lee, E. P.; Song, S. Y.; Lee, D. W.; Ok, K. M. *Inorg Chem* **2013**, *52*, 4097–4103.

-
- (33) Payne, D. J.; Egdell, R. G.; Walsh, A.; Watson, G. W.; Guo, J.; Glans, P.-A.; Learmonth, T.; Smith, K. E. *Phys. Rev. Lett.* **2006**, *96*, 157403.
- (34) Kumada, N.; Kinomura, N.; Woodward, P. M.; Sleight, A. W. *Journal of Solid State Chemistry* **1995**, *116*, 281–285.
- (35) Cornei, N.; Tancrét, N.; Abraham, F.; Mentré, O. *Inorganic Chemistry* **2006**, *45*, 4886–4888.
- (36) Colmont, M.; Huvé, M.; Ketatni, E. M.; Abraham, F.; Mentré, O. *Journal of Solid State Chemistry* **2003**, *176*, 221–233.
- (37) Colmont, M.; Endara, D.; Huvé, M.; Krivovichev, S. v.; Mentré, O. *MRS Online Proceedings Library* **2011**, *1309*, null–null.
- (38) Huvé, M.; Colmont, M.; Lejay, J.; Aschehoug, P.; Mentré, O. *Chem. Mater.* **2009**, *21*, 4019–4029.
- (39) Endara, D.; Colmont, M.; Huvé, M.; Tricot, G.; Carpentier, L.; Mentré, O. *Inorg. Chem.* **2012**, *51*, 4438–4447.
- (40) Endara, D.; Colmont, M.; Huvé, M.; Capet, F.; Lejay, J.; Aschehoug, P.; Mentré, O. *Inorg. Chem.* **2012**, *51*, 9557–9562.
- (41) Colmont, M.; Endara, D.; Aliev, A.; Terryn, C.; Huvé, M.; Mentré, O. *Journal of Solid State Chemistry*.
- (42) Debreuille-Gresse, M. F.; Drache, M.; Abraham, F. *Journal of Solid State Chemistry* **1986**, *62*, 351–359.
- (43) Boje, J.; Müller-Buschbaum, H. *Zeitschrift für anorganische und allgemeine Chemie* **1992**, *618*, 39–42.
- (44) Henry, N.; Evain, M.; Deniard, P.; Jobic, S.; Mentré, O.; Abraham, F. *Journal of Solid State Chemistry* **2003**, *176*, 127–136.
- (45) Mehring, M.; Mansfeld, D.; Paalasmaa, S.; Schürmann, M. *Chemistry – A European Journal* **2006**, *12*, 1767–1781.
- (46) Miersch, L.; Rüffer, T.; Schlesinger, M.; Lang, H.; Mehring, M. *Inorg. Chem.* **2012**, *51*, 9376–9384.
- (47) Geb, J.; Jansen, M. *Journal of Solid State Chemistry* **1996**, *122*, 364–370.
- (48) Krause, W.; Bernhardt, H.-J.; Effenberger, H. *European Journal of Mineralogy* **2006**, *18*, 803–811.
- (49) Ketatni, E. M.; Huvé, M.; Abraham, F.; Mentré, O. *Journal of Solid State Chemistry* **2003**, *172*, 327–338.
- (50) Endara, D. «Design» et approche prédictive de nouveaux oxyphosphates de bismuth, UNIVERSITE LILLE 1, 2012.
- (51) Ketatni M.; Abraham F.; Mentré O. *Solid State Sciences* **1999**, *1*, 449–460.
- (52) Begue P.; Enjalbert R.; Galy J.; Castro A. *Solid State Sciences* **2000**, *2*, 637–653.
- (53) Aurivillius, B. *Acta chemica scandinavica. Series A. Physical and inorganic chemistry* **1987**, *41*, 415.
- (54) Koster, A. S.; Renaud, J. P. P.; Rieck, G. D. *Acta Crystallographica Section B* **1975**, *31*, 127–131.
- (55) Charkin, D. O.; Berdonosov, P. S.; Moisejev, A. M.; Shagiakhmetov, R. R.; Dolgikh, V. A.; Lightfoot, P. *Journal of Solid State Chemistry* **1999**, *147*, 527–535.
- (56) Aurivillius, B. *Chemica Scripta* **1987**, *27*, 397–402.
- (57) Kumada, N.; Takahashi, N.; Kinomura, N.; Sleight, A. W. *Journal of Solid State Chemistry* **1998**, *139*, 321–325.
- (58) Evans, J. S. O.; Brogden, E. B.; Thompson, A. L.; Cordiner, R. L. *Chemical Communications* **2002**, 912–913.
- (59) Landa-Cánovas, Á. R.; Vila, E.; Hernández-Velasco, J.; Galy, J.; Castro, A. *Acta Crystallographica Section B* **2009**, *65*, 458–466.
-

- (60) Arumugam, N.; Lynch, V.; Steinfink, H. *Journal of Solid State Chemistry* **2008**, *181*, 2313–2317.
- (61) Sillen, L. G.; Edstrand, M. Z. *Kristall*. **1942**, *104*, 178–196.
- (62) Muktha, B.; Row, T. N. G. *Inorganic Chemistry* **2006**, *45*, 4706–4711.
- (63) Effenberger, H.; Miletich, R. *Zeitschrift für Kristallographie* **1995**, *210*, 421–426.
- (64) Deacon, G. B.; Gatehouse, B. M.; Ward, G. N. *Acta Crystallographica Section C* **1994**, *50*, 1178–1180.
- (65) Ismunandar; Kennedy B.J.; Hunter B.A. *Journal of Solid State Chemistry* **1996**, *127*, 178–185.
- (66) Abraham, F.; Thomas, D. *Bulletin de la Societe Francaise de Mineralogie et de Cristallographie* **1975**, 25–29.
- (67) Aurivillius, B.; Albertsson, J.; Svensson, G.; Eberson, L.; Krogsgaard-Larsen, P.; Maartmann-Moe, K.; Wold, S. *Acta Chemica Scandinavica* **1990**, *44*, 111–122.
- (68) Hopfgarten, F. *Acta Crystallographica Section B Structural Crystallography and Crystal Chemistry* **1976**, *32*, 2570–2573.
- (69) Hopfgarten, F. *Acta Crystallographica Section B* **1975**, *31*, 1087–1092.
- (70) Michel, C.; Caignaert, V.; Raveau, B. *Journal of Solid State Chemistry* **1991**, *90*, 296–301.
- (71) Hyman, A.; Perloff, A. *Acta Crystallographica Section B* **1972**, *28*, 2007–2011.
- (72) Darriet, J.; Launay, J. C.; Zúñiga, F. J. *Journal of Solid State Chemistry* **2005**, *178*, 1753–1764.
- (73) Mauvy, F.; Launay, J. C.; Darriet, J. *Journal of Solid State Chemistry* **2005**, *178*, 2015–2023.
- (74) Huvé, M.; Colmont, M.; Mentré, O. *Chem. Mater.* **2004**, *16*, 2628–2638.
- (75) Huvé, M.; Colmont, M.; Mentré, O. *Inorg. Chem.* **2006**, *45*, 6604–6611.
- (76) Belokoneva, E. L.; Dimitrova, O. V. *Crystallography Reports* **2010**, *55*, 24–27.
- (77) Long, Y. W.; Yang, L. X.; You, S. J.; Yu, Y.; Yu, R. C.; Jin, C. Q.; Liu, J. *J. Phys.: Condens. Matter* **2006**, *18*, 2421.
- (78) Wolfsberg, M.; Helmholz, L. *The Journal of Chemical Physics* **1952**, *20*, 837–843.
- (79) Yang, H.; Sano, J. L.; Eichler, C.; Downs, R. T.; Costin, G. *Acta Crystallogr C* **2007**, *63*, i122–124.
- (80) Ketterer, J.; Krämer, V. *Materials Research Bulletin* **1985**, *20*, 1031–1036.
- (81) Kennard, M. A.; Darriet, J.; Grannec, J.; Tressaud, A. *Journal of Solid State Chemistry* **1995**, *117*, 201–205.
- (82) Fray, S. M.; Milne, C. J.; Lightfoot, P. *Journal of Solid State Chemistry* **1997**, *128*, 115–120.
- (83) Holleman, A. F.; Wibler, E.; Wiberg, N. *Inorganic Chemistry*; Academic Press, 2001.
- (84) Blasse, G.; Sytsma, J.; Brixner, L. H. *Chemical Physics Letters* **1989**, *155*, 64–68.
- (85) Wu, S.; Wang, C.; Cui, Y.; Wang, T.; Huang, B.; Zhang, X.; Qin, X.; Brault, P. *Materials Letters* **2010**, *64*, 115–118.
- (86) Sillén, L. G. *Zeitschrift für anorganische und allgemeine Chemie* **1939**, *242*, 41–46.
- (87) Sillén, L. G. *Naturwissenschaften* **1942**, *30*, 318–324.
- (88) Gilberg, M. *Ark. Kemi Mineral. Geol.* **1960**, *B2*, 565.
- (89) Kirik, S. D.; Yakovleva, E. G.; Shimanskii, A. F.; Kovalev, Y. G. *Acta Crystallographica Section C Crystal Structure Communications* **2001**, *57*, 1367–1368.
- (90) Keramidias, K. G.; Voutsas, G. P.; Rentzeperis, P. I. *Zeitschrift für Kristallographie* **1993**, *205*, 35–40.
- (91) Lopatin S. S. *Žurnal neorganičeskoj himii* **1987**, *32*, 1694–1697.
- (92) Dolgikh, V. A.; Kholodkovskaya, L. N. *Russ. J. Inorg. Chem.* **1992**, *37*, 488.

-
- (93) Deschanvres, A.; Gallay, J.; Hunout, J.-M.; Thiault, M.-T.; Victor, C. *C. R. Acad. Sci. Paris* **1970**, 270, 696.
- (94) Xie, Y. *ChemInform* **38**.
- (95) Mao, J.-G.; Jiang, H.-L.; Kong, F. *Inorg Chem* **2008**, 47, 8498–8510.
- (96) Ling, J. *Hydrothermal Syntheses, Structures, and Properties of New Iodate and Selenite Compounds of Transition Metals, Lanthanides, and Actinides*; ProQuest, 2007.
- (97) Ok, K. M.; Chi, E. O.; Halasyamani, P. S. *Chem Soc Rev* **2006**, 35, 710–717.
- (98) Ibragimov, S. A.; Berdonosov, P. S.; Dolgikh, V. A.; Huong, D. Q.; Oppermann, H. *Inorganic Materials* **2002**, 38, 1291–1296.
- (99) Ruck, M.; Schmidt, P. *Zeitschrift für anorganische und allgemeine Chemie* **2003**, 629, 2133–2143.
- (100) Nazarchuk, E. V.; Krivovichev, S. V.; Pankratova, O. Y.; Filatov, S. K. *Phys Chem Min* **2000**, 27, 440–444.
- (101) Nadir S.; Swinnea J.S.; Steinfink H. *Journal of Solid State Chemistry* **1999**, 148, 295–301.
- (102) Mentre, O.; Bouree, F.; Rodriguez-Carvajal, J.; El Jazouli, A.; El Khayati, N.; Ketatni, E. M. *Journal of Physics: Condensed Matter* **2008**, 20, 415211.
- (103) Goodenough, J. B. *Magnetism and the chemical bond*; R. E. Krieger Pub. Co: Huntington, N.Y., 1976.
- (104) Mentré, O.; Koo, H.-J.; Whangbo, M.-H. *Chem. Mater.* **2008**, 20, 6929–6938.
- (105) Abraham, F.; Ketatni, E. M.; Mairesse, G.; Mernari, B. *European Journal of Solid State and Inorganic Chemistry* **1994**, 31, 313–323.
- (106) Mentré, O.; Ketatni, E. M.; Colmont, M.; Huvé, M.; Abraham, F.; Petricek, V. *J. Am. Chem. Soc.* **2006**, 128, 10857–10867.
- (107) Koteswararao, B.; Mahajan, A. V.; Alexander, L. K.; Bobroff, J. J. *J. Phys.: Condens. Matter* **2010**, 22, 035601.
- (108) Choi, K.-Y.; Hwang, J. W.; Lemmens, P.; Wulferding, D.; Shu, G. J.; Chou, F. C. *Physical Review Letters* **2013**, 110.
- (109) Radosavljevic, I.; Evans, J. S. O.; Sleight, A. W. *ChemInform* **1999**, 30, no–no.
- (110) Shannon, R. D. *Acta Crystallographica Section A* **1976**, 32, 751–767.
- (111) Mentré, O.; Janod, E.; Rabu, P.; Hennion, M.; Leclercq-Hugeux, F.; Kang, J.; Lee, C.; Whangbo, M.-H.; Petit, S. *Phys. Rev. B* **2009**, 80, 180413.
- (112) Colmont, M.; Delevoye, L.; Mentré, O. *New J. Chem.* **2009**, 33, 19–22.
- (113) Colmont, M.; Delevoye, L.; Ketatni, E. M.; Montagne, L.; Mentré, O. *Journal of Solid State Chemistry* **2006**, 179, 2111–2119.
- (114) Sanderson, R. T. *Polar Covalence*; Academic Press, 1983.
- (115) Cousin, O.; Huve, M.; Roussel, P.; Perez, O.; Steinfink, H. *Journal of Solid State Chemistry* **2002**, 165, 324–333.
- (116) Mentre, O.; Roussel, P.; Petricek, V. *Private Communications*.
- (117) Schönleber, A.; Meyer, M.; Chapuis, G. *Journal of Applied Crystallography* **2001**, 34, 777–779.
- (118) Abraham, F.; Cousin, O.; Mentre, O.; Ketatni, E. M. *Journal of Solid State Chemistry* **2002**, 167, 168–181.
- (119) Kraus, W.; Nolze, G. *PowderCell*; Federal Institute for Materials Research and Testing: Berlin, 2000.
- (120) Krivovichev, S. V.; Mentré, O.; Siidra, O. I.; Colmont, M.; Filatov, S. K. *Chem. Rev.* **2013**.
- (121) Sakurai, H.; Yoshimura, K.; Kosuge, K.; Tsujii, N.; Abe, H.; Kitazawa, H.; Kido, G.; Michor, H.; Hilscher, G. *Journal of the Physical Society of Japan* **2002**, 71, 1161–1165.
-

-
- (122) Koo, H.-J.; Whangbo, M.-H. *Inorg Chem* **2008**, *47*, 4779–4784.
- (123) Zhou, H. D.; Choi, E. S.; Jo, Y. J.; Balicas, L.; Lu, J.; Lumata, L. L.; Urbano, R. R.; Kuhns, P. L.; Reyes, A. P.; Brooks, J. S.; Stillwell, R.; Tozer, S. W.; Wiebe, C. R.; Whalen, J.; Siegrist, T. *Phys. Rev. B* **2010**, *82*, 054435.
- (124) Xun, X.; Uma, S.; Yokochi, A.; Sleight, A. W. *Journal of Solid State Chemistry* **2002**, *167*, 245–248.
- (125) Ketatni, E. mostafa; Mernari, B.; Abraham, F.; Mentre, O. *Journal of Solid State Chemistry* **2000**, *153*, 48–54.
- (126) Huang, J.; Gu, Q.; Sleight, A. W. *Journal of Solid State Chemistry* **1993**, *105*, 599–606.
- (127) Giraud, S.; Mizrahi, A.; Drache, M.; Conflant, P.; Wignacourt, J. P.; Steinfink, H. *Solid State Sciences* **2001**, *3*, 593–602.
- (128) Arumugam, N.; Lynch, V.; Steinfink, H. *Journal of Solid State Chemistry* **2007**, *180*, 1504–1511.
- (129) Muktha, B.; Darriet, J.; Guru Row, T. N. *Materials Research Bulletin* **2008**, *43*, 3017–3025.
- (130) Charkin, D. O.; Grischenko, R. O.; Sadybekov, A. A.; Goff, R. J.; Lightfoot, P. *Inorganic Chemistry* **2008**, *47*, 3065–3071.
- (131) AURIVILLIUS, B. *ARKIV FOR KEMI* **1950**, *1*, 499–512.
- (132) Steinfink, H.; Lynch, V. *Journal of Solid State Chemistry* **2004**, *177*, 1412–1415.
- (133) Colmont, M.; Huvé, M.; Ketatni, E. M.; Mentré, O. *Solid State Sciences* **2008**, *10*, 533–543.
- (134) Knight, S. *Mineralogical Magazine* **1992**, *56*, 399–409.
- (135) Arppe, A. E. *Ann. Phys. Chem.* **1845**, *140*, 237–251.
- (136) Eggenweiler, U.; Keller, E.; Krämer, V. *Acta Crystallographica Section B Structural Science* **2000**, *56*, 431–437.
- (137) Kozin, M. S.; Aliev, A.; Colmont, M.; Mentré, O.; Siidra, O. I.; Krivovichev, S. V. *Journal of Solid State Chemistry* **2013**, *199*, 56–61.
- (138) Schmidt, M.; Oppermann, H.; Hennig, C.; Henn, R. W.; Gmelin, E.; Söger, N.; Binnewies, M. *Zeitschrift für anorganische und allgemeine Chemie* **2000**, *626*, 125–135.
- (139) Brese, N. E.; O’Keeffe, M. *Acta Crystallographica Section B Structural Science* **1991**, *47*, 192–197.
- (140) Krivovichev, S. V. *Zeitschrift für Kristallographie - Crystalline Materials* **2012**, *227*, 575–579.
- (141) Rolle, A.; Preux, N.; Ehora, G.; Mentré, O.; Daviero-Minaud, S. *Solid State Ionics* **2011**, *184*, 31–34.
- (142) Okamoto, K.; Imanaka, N.; Adachi, G. *Solid State Ionics* **2002**, *154–155*, 577–580.
- (143) Folkerts, H. F.; Zuidema, J.; Blasse, G. *Chemical Physics Letters* **1996**, *249*, 59–63.
- (144) Manavbasi, A.; LaCombe, J. C. *Journal of Luminescence* **2008**, *128*, 129–134.
- (145) Van de Craats, A. M.; Dirksen, G. J.; Blasse, G. *Journal of Solid State Chemistry* **1995**, *118*, 337–340.
- (146) Blasse, G. *Progress in Solid State Chemistry* **1988**, *18*, 79–171.
- (147) Duffy, J. A.; Ingram, M. D. *The Journal of Chemical Physics* **1970**, *52*, 3752–3754.
- (148) Boulon, G.; Moine, B.; Bourcet, J. C.; Reisefeld, R.; Kalisky, Y. *Journal of Luminescence* **1979**, *18–19, Part 2*, 924–928.
- (149) Sidike, A.; Wang, X.-M.; Sawuti, A.; Zhu, H.-J.; Kusachi, I.; Yamashita, N. *Phys Chem Minerals* **2006**, *33*, 559–566.
- (150) Srivastava, A. M.; Beers, W. W. *Journal of Luminescence* **1999**, *81*, 293–300.
- (151) Timmermans, C. W. M.; Blasse, G. *Journal of Solid State Chemistry* **1984**, *52*, 222–232.
-

-
- (152) Parke, S.; Webb, R. S. *Journal of Physics and Chemistry of Solids* **1973**, *34*, 85–95.
- (153) Xu, W.; Peng, M.; Ma, Z.; Dong, G.; Qiu, J. *Opt. Express* **2012**, *20*, 15692–15702.
- (154) Cao, R.; Peng, M.; Wondraczek, L.; Qiu, J. *Opt Express* **2012**, *20*, 2562–2571.
- (155) Hamstra, M. A.; Folkerts, H. F.; Blasse, G. *J. Mater. Chem.* **1994**, *4*, 1349–1350.
- (156) Peng, M.; Wondraczek, L. *Journal of the American Ceramic Society* **2010**, *93*, 1437–1442.
- (157) Burch, R.; Chalker, S.; Loader, P.; Thomas, J. M.; Ueda, W. *Applied Catalysis A: General* **1992**, *82*, 77–90.
- (158) Liu, S.; Miiller, W.; Liu, Y.; Avdeev, M.; Ling, C. D. *Chem. Mater.* **2012**, *24*, 3932–3942.
- (159) Roussel, P.; Giraud, S.; Suard, E.; Wignacourt, J. P.; Steinfink, H. *Solid State Sciences* **2002**, *4*, 1143–1152.
- (160) Yaremchenko, A. ; Kharton, V. ; Naumovich, E. ; Tonoyan, A. . *Materials Research Bulletin* **2000**, *35*, 515–520.
- (161) Watanabe, A. Bismuth Multiple Oxide and Its Production. JPH10251024 (A), September 22, 1998.
- (162) Watanabe, A.; Kitami, Y. *Solid State Ionics* **1998**, *113–115*, 601–606.
- (163) Kashida, S.; Hori, T. *Journal of Solid State Chemistry* **1996**, *122*, 358–363.
- (164) Labidi, O.; Drache, M.; Roussel, P.; Wignacourt, J.-P. *Solid State Sciences - SOLID STATE SCI* **2008**, *10*, 1074–1082.
- (165) Lee, S. L.; Lee, C. K.; Sinclair, D. C.; Chong, F. K.; Halim, S. A.; Yap, T. *Malaysian Journal of Chemistry* **2005**, *7*, 1–10.
- (166) Kuang, X.; Payne, J. L.; Farrell, J. D.; Johnson, M. R.; Evans, I. R. *Chem. Mater.* **2012**, *24*, 2162–2167.
- (167) Palatinus, L.; Chapuis, G. *Journal of Applied Crystallography* **2007**, *40*, 786–790.
- (168) Guillemet-Fritsch, S.; Alphonse, P.; Calmet, C.; Coradin, H.; Tailhades, P.; Rousset, A. *Comptes Rendus Chimie* **2005**, *8*, 219–227.
- (169) Post, J.; Appleman, D. *Am. Miner.* **1988**, *73*, 1401–1404.
- (170) Gailliot, A.-C.; Drits, V. A.; Manceau, A.; Lanson, B. *Microporous and Mesoporous Materials* **2007**, *98*, 267–282.
- (171) Richter, J.; Schulenburg, J.; Honecker, A. In *Quantum Magnetism*; Schollwöck, U.; Richter, J.; Farnell, D.; Bishop, R., Eds.; Lecture Notes in Physics; Springer Berlin / Heidelberg, 2004; Vol. 645, pp. 85–153.
- (172) Toner, B.; Manceau, A.; Webb, S. M.; Sposito, G. *Geochimica et Cosmochimica Acta* **2006**, *70*, 27–43.
- (173) Kwon, K. D.; Refson, K.; Sposito, G. *Geochimica et Cosmochimica Acta* **2009**, *73*, 1273–1284.
- (174) Schmalfuß, D.; Tomczak, P.; Schulenburg, J.; Richter, J. *Phys. Rev. B* **2002**, *65*, 224405.
- (175) Fennell, T.; Piatek, J. O.; Stephenson, R. A.; Nilsen, G. J.; Rønnow, H. M. *Journal of Physics: Condensed Matter* **2011**, *23*, 164201.
- (176) Cave, D.; Coomer, F. C.; Molinos, E.; Klauss, H.; Wood, P. T. *Angewandte Chemie* **2005**, *118*, 817–820.
- (177) Floros, N.; Michel, C.; Hervieu, M.; Raveau, B. *J. Solid State Chem.* **2002**, *168*, 11–17.
- (178) Henry, N.; Burylo-Dhuime, L.; Abraham, F.; Mentre, O. *Solid State Sci.* **2002**, *4*, 1023–1029.
- (179) Capriotti, L.; Trumper, A. E.; Sorella, S. *Phys. Rev. Lett.* **1999**, *82*, 3899–3902.
- (180) Zhu, H. T.; Luo, J.; Yang, H. X.; Liang, J. K.; Rao, G. H.; Li, J. B.; Du, Z. M. *J. Phys. Chem. C* **2008**, *112*, 17089–17094.
- (181) Royer, S.; Duprez, D.; Kaliaguine, S. *Journal of Catalysis* **2005**, *234*, 364–375.
-

-
- (182) D, M.; D, D. *J. Phys. Chem.* **1996**, *100*, 9429–9438.
- (183) Oppermann, H.; Huong, D. Q.; Zhang, M.; Schmidt, P.; Popovkin, B. A.; Ibragimov, S. A.; Berdonosov, P. S.; Dolgikh, V. A. *Zeitschrift für anorganische und allgemeine Chemie* **2001**, *627*, 1347–1356.
- (184) Binnewies, M.; Glaum, R.; Schmidt, M.; Schmidt, P. *Zeitschrift für anorganische und allgemeine Chemie* **2013**, *639*, 219–229.
- (185) Berdonosov, P. S.; Stefanovitch, S. Y.; Dolgikh, V. A. *Journal of Solid State Chemistry* **2000**, *149*, 236–241.
- (186) Li, P.-X.; Kong, F.; Hu, C.-L.; Zhao, N.; Mao, J.-G. *Inorg. Chem.* **2010**, *49*, 5943–5952.

Annex

IV. Annex

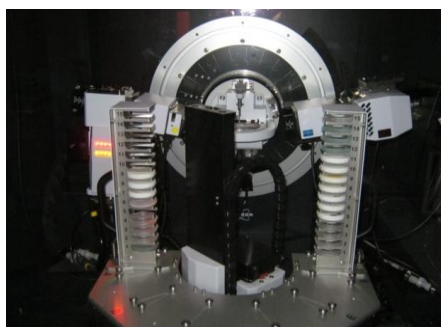
IV.1 Experimental techniques

IV.1.1 Structural characterization

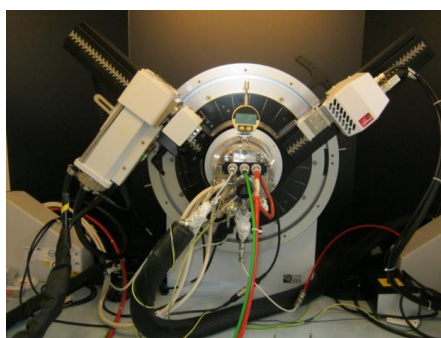
1) Powder RX diffraction.

To obtain XRD powder patterns different diffractometers were used:

D8 Advance (Bruker-AXS) equipped with a rapid Lynxeye detector and an auto sampler with 90 positions working in transmission as well as in reflection geometry, using $\text{CuK}\alpha 1$ and $\text{CuK}\alpha 2$ radiation ($\lambda_1 = 1.54056\text{\AA}$ and $\lambda_2 = 1.54439\text{\AA}$ and $\lambda_1/\lambda_2 = 0.5$). It enables a quick switch between the para-focusing Bragg-Brentano geometry to parallel beam geometry without realignment of the system.



D8 Advance - XRK900 (Bruker-AXS): Diffractometer dedicated to the study of polycrystalline samples at high temperature (1000°C) and under gas flow (vacuum, various gases). It is equipped with a Lynxeye rapid sensor type and an Anton Paar XRK900 reactive room.



SMARTLAB (Rigaku) with rotating anode, for the study of massif polycrystalline samples and thin layers. It is equipped with a $\theta - \theta$ goniometer and Euler circle. The detector can

come out of the vertical plane and thus enable a complete structural characterization of thin films (*in-plane and out-plane*), at R.T. and H.T. (1100°C).



The samples were recorded between 5 and 90°, depending on the sample for a simple identification and refinement of the cell parameters

1a) Cell parameters refinement (pattern matching)

The cell parameters refinement was carried out using Fullprof program which is based on mathematical calculation of the peak positions using cell parameters, space group, the reflections read out from the input file where background points given manually. To match the experimental and theoretical profiles, the least squares method is used. The cell parameters, the 2θ zeropoint and the shape of the peaks are refined. In order to describe the angular dependence of the peak full-width at half-maximum (H), the formula of Caglioti was used: $H^2 = U \tan^2\theta + V \tan\theta + W$, where U, V and W were parameters refined in the process.

1b) Structure refinement (Rietveld)

The Rietveld method uses a least squares approach to refine a theoretical profile taking into account unit cell parameters, atomic positions and thermal parameters until it matches the measured profile. In the structural refinement the same input file is used as in the case of the pattern matching. In the case of mixed site occupation or in the case of oxygen occupation, the refinement of the corresponding occupancies is required. For a Rietveld refinement, a diffractogram with wide range of 2θ (for example, 4 – 120°) is required.

2) Neutrons diffraction

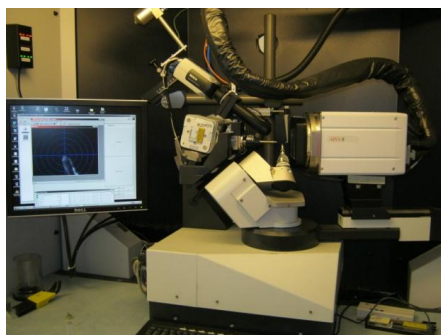
The transitional metals used in this work (Fe, Mn, Co, for example) are non-distinguishable by X rays (close Z) in terms of their positions in a lattice. For this reason, neutrons diffraction investigations were required. For neutron diffraction measurements diffractograms with angular 2θ range 4° – 120° were collected using “thermal neutrons” 2 axis (20 detectors) high

resolution powder diffractometer (R.T. 3T2) with $\lambda = 1.225\text{\AA}$ incident wavelength, at the Laboratoire Léon Brillouin (LLB – France).

Furthermore, for the 3D magnetic ordering in the structures the low temperature neutrons diffraction was necessary. Low temperature neutron diffractograms were collected using the LLB “cold neutrons” 2 axis (multidetector 800 cells) high flux powder diffractometer (G4.1) to obtain magnetic structure. The diffractograms were recorded from 4 to 90° in 2 theta, from 1.5K to R.T. using the $\lambda = 2.4226\text{\AA}$ wavelength at the same Laboratoire Léon Brillouin (LLB – France).

3) Single crystals RX diffraction

The singles crystals samples were analyzed using a X8 (Bruker-AXS) single crystal diffractometer ($\lambda = 0.71073\text{\AA}$ and a $\text{MoK}\alpha$ radiation selected by a graphite monochromator) with 4 circles and equipped with a bi - dimensional CDD 4K detector allowing the resolution of the crystalline structures at R.T. and at low temperatures (to reduce the atoms vibration and observe the eventual structure transformation) by the usage of a N_2 cooling system. The temperature can reach down to 100K.



“Well shaped” single crystals have to be selected from the synthesis mixture priority washed from the small crystals stuck on the surface using a special grease. The crystal is then mounted on a glass fiber and aligned (centered) on the diffractometer. The first step is to conduct test measurements to check the quality of the crystal and find out respective cell parameters and symmetry. If the crystal is suitable, the next step is the collecting of the respective reflections of the complete reciprocal space with suitable intensities. After the collection has finished, the intensities from all the photos are harvested, integrated corrected from absorption. The structure solution can be done with several methods: direct method, Patterson method, Superflip etc. For refinement of the structures several softwares are available as well like Jana, ShelX etc.

4) Solid-State NMR

The phosphorus environments were analyzed by Solid-State NMR under magic angle spinning (MAS) at 20 kHz (3.2 mm probehead) on an 18.8 T Bruker spectrometer operating at 323.87 MHz for ^{31}P nucleus.

5) Transmission electron microscopy.

Electron Diffraction Patterns (EDP) have been obtained on a FEI Technai G220 transmission electron microscope equipped with a precession system. The material was crushed and dispersed on a holey carbon film deposited on a Cu grid.

6) Scanning electron microscopy and energy dispersive X-ray spectroscopy (EDS)

A scanning electron microscope (SEM) is a type of electron microscope that give images of a sample by scanning it with a high-energy beam of electrons in a raster scan pattern. The electrons interact with the atoms that make up the sample producing signals that contain information about the sample's surface topography and composition.

7) Electron microprobe (EMP)

An electron microprobe (EMP), also known as an electron probe microanalyzer (EPMA) or electron micro probe analyzer (EMPA), is an analytical tool used to non-destructively determine the chemical composition of small volumes of solid materials. It works similarly as a scanning electron microscope: the sample is bombarded with an electron beam, emitting x-rays at wavelengths characteristic to the elements being analyzed. This enables the abundances of elements present within small sample volumes (typically 10-30 cubic micrometers or less) to be determined.

IV.1.2 Characterizations of physical properties

1) Second harmonic generation

Second harmonic generation (SHG) is a nonlinear optical process, in which photons interacting with a nonlinear material are effectively "combined" to form new photons with twice the energy, and therefore twice the frequency and half the wavelength of the initial photons. The effect of second harmonic generation is used for SHG microscopy. Because of the non-zero second harmonic coefficient, only non-centrosymmetric structures are capable of emitting SHG light. Using a short-pulse laser such as a femtosecond laser and a set of appropriate filters the excitation light can be easily separated from the emitted, frequency-doubled SHG signal. This allows for very high axial and lateral resolution comparable to that of confocal microscopy without having to use pinholes.

The SHG microscopy measurements on single crystals have been carried out with the collaboration with Dr. Christine TERRY at Plateforme Imagerie Cellulaire et Tissulaire, Université de Reims. A laser scanning microscope LSM 710 NLO Zeiss (Jena, Germany) have been used for measurement with the excitation provided by a CHAMELEON femtosecond Titanium-Sapphire laser (Coherent, Santa Clara, USA) set at 860 nm, tuning the power until SHG was detected (\rightarrow 16% maximal power, ~ 0.55 mW) on selected single crystal samples deposited on a glass plate. Samples were imaged with a 20x, 0.8 NA objective lens. Emitted signal of SHG was collected with a bandpass filter (420 to 440 nm).

The Powder SHG measurements were performed in collaboration with Dr. Shiv Halasyamani at University of Houston, on a modified Kurtz –NLO system using a pulsed Nd:YAG laser with a wavelength of 1064 nm. As the powder SHG efficiency has been shown to depend strongly on particle size, the reported materials were ground and sieved into distinct particle size ranges (<20 , 20–45, 45–63, 63–75, 75–90, >90 μm). Comparisons with known SHG materials were made by grinding and sieving crystalline α -SiO₂ and LiNbO₃ into the same particle size ranges. No index matching fluid was used in any of the experiments.

2) Impedance spectroscopy

Electrical measurements were performed on the samples by impedance spectroscopy between room-temperature and 700°C using a Solartron 1260 impedance analyzer with a 500 mV amplitude signal over the 0.1 Hz to 10 MHz frequency range. Gold electrodes were deposited by evaporation at both sides of a sintered pellet. Three heating/cooling cycles were applied to the sample, while only the third one are presented, for which extra-densification effects are

negligible. All impedance diagrams were normalized using the *thickness/surface* geometrical factor. Fitting of impedance spectra was performed using local software to extract characteristic of typical RC circles.

3) Photoluminescence

Photoluminescence measurements have been carried out in collaboration with Dr. Claudia Wickleder at the University of Siegen. Excitation and emission spectra were collected on a FluoroMax HORIBA fluorescence spectrometer within the spectral range of 250 nm – 800nm using excitation and emission slit widths of 2 nm at 10K. Each excitation spectrum was taken while observing emission at the predetermined emission wavelength maxima, and likewise, the emission spectra was taken while exciting at the sample's excitation wavelength maxima.



4) Magnetism

Magnetic measurements have been carried out in collaboration with Dr. Silviu Colis at Institut de Physique et Chimie des Matériaux de Strasbourg (IPCMS), on a MPMS SQUID-VSM (Quantum Design) magnetometer between 1.8 and 300K at 0 to 7T. The susceptibility versus temperature was carried out under 0.1 Tesla after the sample was cooled in a field of 0.1T (FC) or in zero field (ZFC). Previously powders were magnetically “aligned” at 7T in a polymeric gel that freezes the particle orientation below ~303K.

5) Isotopic exchange experiments (OIE)

Oxygen mobility studies have been carried out in collaboration with Dr. Sébastien ROYER at Institut de Chimie des Milieux et Matériaux de Poitiers (IC2MP) Université de Poitiers. The experiments were carried out in a recycling U-shaped microreactor to eliminate kinetic limitation due to gas-phase diffusion. The recirculation volume was coupled to a quadrupolar mass spectrometer (MQG Blazers). The gas sampling was regulated by a thermo-valve adjusted to maintain a constant pressure of 1×10^{-6} mbar in the ionization chamber. At this pressure, the vacuum sampling leak creates a negligible decrease in the pressure in the

microreactor. 20 mg of the sample was weighed and inserted in a microreactor between two quartz wool plugs. Then the sample was fired at its calcination temperature under O₂ (ramp = 10 K/ min–DO₂ = 20 mL/ min). Thereafter, the sample was cooled to room temperature under O₂ and then heated again under dynamic vacuum until the temperature of the test was reached (ramp = 10 K/min). For the exchange experiments, pure ¹⁸O₂ at a pressure of about 70.0 mbar was introduced into the nonheated zone of the recirculation volume. This allowed to maintain a constant number of oxygen atoms in the gas phase. This volume of gas was then expended in the heated zone, yielding a pressure of ¹⁸O₂ in the total recirculation volume around 52.0 ± 1.5 mbar, depending on the temperature of the test. In the case of the equilibration reaction, an equimolar volume of ¹⁸O₂ and ¹⁶O₂, instead of pure ¹⁸O₂, was introduced. The partial pressure evolution of ¹⁸O₂ (mass 36), ¹⁶O₂ (mass 32), and ¹⁶O¹⁸O (mass 34) was followed on the mass spectrometer for an experiment time of 90 min. N₂ (mass 28) was also recorded to detect any possible leak. Taking into account the error in the volume of gas introduced into the non-heated zone of the recirculation volume and the error in the temperature, a maximum relative error of 1.0% can be estimated in the values of the initial rates of exchange. For rate values calculated at nonzero times, a third source of error (the decrease in pressure due to the vacuum sampling leak) of 2%/h is added.

IV.2 Supplementary data of the obtained structures

1) $n = 1$ ribbons: BiCoAsO_5

Table S 1. Crystal data, measurement and structural refinement parameters of BiCoAsO_5

<i>Crystal data</i>	
BiCoAsO_5	$\gamma = 108.388 (2)^\circ$
$M_r = 422.8$	$V = 209.55 (2) \text{ \AA}^3$
Triclinic, $P1$	$Z = 2$
Hall symbol: $-P 1$	$F(000) = 366$
$a = 5.2380 (3) \text{ \AA}$	$D_x = 6.699 \text{ Mg m}^{-3}$
$b = 6.8286 (4) \text{ \AA}$	Mo $K\alpha$ radiation, $\lambda = 0.71073 \text{ \AA}$
$c = 7.6150 (4) \text{ \AA}$	$\mu = 53.63 \text{ mm}^{-1}$
$\alpha = 111.631 (2)^\circ$	$T = 293 \text{ K}$
$\beta = 108.376 (2)^\circ$	$\times \times \text{ mm}$
<i>Data collection</i>	
Radiation source: X-ray tube	$\theta_{\max} = 32.8^\circ$, $\theta_{\min} = 3.3^\circ$
6889 measured reflections	$h = -7 \rightarrow 7$
1537 independent reflections	$k = -10 \rightarrow 10$
1512 reflections with $I > 3\sigma(I)$	$l = -11 \rightarrow 11$
$R_{\text{int}} = 0.042$	
<i>Refinement</i>	
Refinement on F	0 constraints
$R[F^2 > 2\sigma(F^2)] = 0.022$	Weighting scheme based on measured s.u.'s $w = 1/(\sigma^2(F) + 0.0001F^2)$
$wR(F^2) = 0.034$	$(\Delta/\sigma)_{\max} = 0.014$
$S = 1.78$	$\Delta\rho_{\max} = 2.17 \text{ e \AA}^{-3}$
1537 reflections	$\Delta\rho_{\min} = -2.41 \text{ e \AA}^{-3}$
39 parameters	Extinction correction: B-C type 1 Gaussian isotropic (Becker & Coppens, 1974)
0 restraints	Extinction coefficient: 316 (16)

Table S 2. Fractional atomic coordinates and isotropic or equivalent isotropic displacement parameters (\AA^2) of BiCoAsO_5

	x	y	z	$U_{\text{iso}}^*/U_{\text{eq}}$		
Bi1	0.32716 (3)	0.26673 (3)	0.23955 (2)	0.00558 (10)		
As1	0.47132 (10)	0.20231 (9)	−0.18365 (8)	0.00416 (11)*		
Co1	0.96338 (15)	0.36023 (12)	0.63371 (11)	0.00586 (13)*		
O1	0.1230 (9)	0.1787 (7)	−0.2432 (6)	0.0113 (7)*		
O2	0.6912 (8)	0.4041 (6)	−0.2245 (6)	0.0068 (6)*		
O3	1.2357 (8)	0.4564 (6)	0.5042 (6)	0.0054 (6)*		
O4	0.6593 (8)	0.2875 (7)	0.0814 (6)	0.0082 (6)*		
O5	0.4270 (8)	−0.0678 (7)	−0.3440 (6)	0.0078 (6)*		
	U^{11}	U^{22}	U^{33}	U^{12}	U^{13}	U^{23}
Bi1	0.00448 (11)	0.00427 (11)	0.00323 (11)	0.00118 (7)	0.00035 (7)	−0.00021 (7)

2) n = 3 ribbons: $\text{Bi}_4\text{Cu}_3\text{O}_6(\text{AsO}_4)_2$ and $\text{Bi}_4\text{Cu}_3\text{O}_6(\text{VO}_4)_2$ *Table S 3. Crystal data, measurement and structural refinement parameters of $\text{Bi}_4\text{Cu}_3\text{O}_6(\text{AsO}_4)_2$.*

$\text{Bi}_4\text{Cu}_3\text{O}_6(\text{AsO}_4)_2$	
Crystal data	
Crystal symmetry	Triclinic
space group	P-1
a (Å)	5.3017(1)
b (Å)	9.6076(1)
c (Å)	12.6911(2)
α (°)	82.9770(8)
β (°)	79.3990(9)
γ (°)	74.3770(8)
V (Å ³)	610.12(2)
Z	2
Dx (g/cm ³)	7.62
$\mu(\text{mm}^{-1})$ (for λ	68.06
$K\alpha=0.7107\text{Å}$)	
Appearance	green needle
Crystal size (mm)	0.10×0.05×0.04
Data collection	
$\lambda(\text{Mo K}\alpha)$ (Å)	0.71073
Scan mode	ω and ϕ
$\theta(\text{min-max})$ (°)	1.6 – 38.2
R(int) (%)	0.063
	$-8 \leq h \leq 9$
Recording reciprocal space	$-15 \leq k \leq 14$
	$-22 \leq l \leq 21$
Refinement	
Measured, independent	23697, 5824,
obs.* refl.	4266
No. of Refined parameters	212
Refinement method,	F
$R1(F^2)(\text{obs}) / R1(F^2)(\text{all})$	0.0333/0.0516
$wR2(F^2)(\text{obs}) / wR2(F^2)(\text{all})$	0.0347/0.0395
GOF(obs) / GOF(all)	1.12/1.15
$\Delta\rho_{\text{max}} / \Delta\rho_{\text{min}}$ (e Å ⁻³)	3.82 / -3.52
Extinction coefficient	0.0198(9)

Table S 4. Fractional atomic coordinates and isotropic or equivalent isotropic displacement parameters (\AA^2) of $\text{Bi}_4\text{Cu}_3\text{O}_6(\text{AsO}_4)_2$

	<i>x</i>	<i>y</i>	<i>z</i>	$U_{\text{iso}}^*/U_{\text{eq}}$
Bi1	0.35605 (5)	0.70072 (3)	0.098057 (19)	0.00741 (7)
Bi2	−0.11580 (5)	0.51736 (3)	0.258442 (19)	0.00737 (7)
Bi3	0.21999 (5)	0.74343 (3)	0.385285 (19)	0.00878 (7)
Bi4	0.68612 (5)	0.93191 (3)	0.23076 (2)	0.00934 (8)
As1	1.14423 (14)	0.14984 (8)	0.10828 (5)	0.0071 (2)
As2	0.32753 (13)	1.32447 (8)	0.42823 (5)	0.00580 (19)
Cu1	0.53302 (17)	0.34663 (10)	0.15320 (7)	0.0072 (2)
Cu2	−0.00255 (17)	1.09830 (10)	0.36917 (7)	0.0088 (2)
Cu3	1	0.5	0	0.0066 (3)
Cu4	0.5	1	0.5	0.0075 (3)
O1	0.0453 (9)	0.7153 (5)	0.2387 (4)	0.0077 (14)
O2	0.5368 (9)	0.7299 (5)	0.2404 (4)	0.0073 (14)
O3	0.5961 (9)	1.1784 (6)	0.4252 (4)	0.0097 (15)
O4	0.8668 (10)	0.2171 (6)	0.1982 (4)	0.0150 (17)
O5	0.3513 (10)	0.9635 (6)	0.3712 (4)	0.0091 (15)
O6	0.7013 (9)	0.5046 (5)	0.1160 (4)	0.0067 (14)
O7	0.2551 (12)	1.3794 (7)	0.5518 (4)	0.020 (2)
O8	1.1904 (12)	−0.0305 (6)	0.1215 (5)	0.0185 (19)
O9	−0.1208 (10)	0.9281 (6)	0.3706 (4)	0.0107 (15)
O10	0.3861 (11)	1.4503 (6)	0.3290 (4)	0.0136 (17)
O11	1.4044 (10)	0.1790 (6)	0.1554 (5)	0.0155 (18)
O12	0.0632 (10)	1.2718 (6)	0.4046 (4)	0.0128 (16)
O13	0.7896 (9)	0.5122 (6)	−0.1150 (4)	0.0079 (14)
O14	1.1245 (11)	0.2276 (6)	−0.0158 (4)	0.0162 (18)

Table S 5. Atomic displacement parameters (\AA^2) of $\text{Bi}_4\text{Cu}_3\text{O}_6(\text{AsO}_4)_2$

	U^{11}	U^{22}	U^{33}	U^{12}	U^{13}	U^{23}
Bi1	0.00811(11)	0.00832(12)	0.00545(10)	−0.00167 (9)	−0.00062 (8)	−0.00080 (8)
Bi2	0.00824(11)	0.00712(12)	0.00674(10)	−0.00177 (9)	−0.00150 (8)	−0.00041 (8)
Bi3	0.00876(12)	0.00968(13)	0.00650(10)	−0.00001 (9)	−0.00056 (8)	−0.00152 (8)
Bi4	0.01081(12)	0.00754(12)	0.01015(11)	−0.00283 (9)	−0.00255 (9)	−0.00001 (8)
As1	0.0081 (3)	0.0055 (3)	0.0078 (3)	−0.0019 (2)	−0.0015 (2)	0.0003 (2)
As2	0.0075 (3)	0.0050 (3)	0.0048 (3)	−0.0015 (2)	−0.0008 (2)	−0.0005 (2)
Cu1	0.0064 (4)	0.0060 (4)	0.0095 (3)	−0.0016 (3)	−0.0019 (3)	−0.0007 (3)
Cu2	0.0077 (4)	0.0065 (4)	0.0127 (4)	−0.0018 (3)	−0.0012 (3)	−0.0035 (3)
Cu3	0.0048 (5)	0.0100 (6)	0.0049 (4)	−0.0015 (4)	−0.0002 (4)	−0.0017 (4)
Cu4	0.0095 (5)	0.0059 (5)	0.0069 (5)	−0.0017 (4)	−0.0018 (4)	−0.0002 (4)
O1	0.007 (2)	0.007 (2)	0.0063 (19)	0.0009 (18)	0.0032 (16)	−0.0025 (16)
O2	0.009 (2)	0.004 (2)	0.008 (2)	0.0012 (18)	−0.0030 (17)	−0.0039 (16)
O3	0.007 (2)	0.007 (2)	0.012 (2)	0.0018 (18)	0.0021 (17)	−0.0006 (17)
O4	0.007 (2)	0.019 (3)	0.014 (2)	0.003 (2)	−0.0006 (19)	−0.001 (2)
O5	0.010 (2)	0.008 (2)	0.009 (2)	−0.0011 (19)	−0.0004 (17)	−0.0035 (17)
O6	0.009 (2)	0.007 (2)	0.0060 (19)	−0.0036 (18)	−0.0019 (16)	−0.0016 (16)
O7	0.028 (3)	0.024 (3)	0.010 (2)	−0.005 (3)	−0.001 (2)	−0.010 (2)
O8	0.024 (3)	0.006 (3)	0.026 (3)	−0.007 (2)	−0.002 (2)	−0.001 (2)
O9	0.012 (2)	0.005 (2)	0.016 (2)	−0.0007 (19)	−0.0053 (19)	−0.0055 (18)
O10	0.016 (3)	0.013 (3)	0.011 (2)	−0.004 (2)	−0.0019 (19)	0.0040 (19)
O11	0.009 (2)	0.012 (3)	0.027 (3)	−0.006 (2)	−0.009 (2)	0.006 (2)
O12	0.009 (2)	0.005 (2)	0.025 (3)	−0.0020 (19)	−0.004 (2)	−0.004 (2)
O13	0.007 (2)	0.010 (2)	0.0061 (19)	−0.0002 (18)	−0.0029 (16)	−0.0011 (17)
O14	0.026 (3)	0.013 (3)	0.008 (2)	−0.004 (2)	−0.004 (2)	0.0032 (19)

Table S 6. Selected distances in $\text{Bi}_4\text{Cu}_3\text{O}_6(\text{AsO}_4)_2$ (max. $d=3\text{\AA}$)

Atom1	Atom2	d, Å	Atom1	Atom2	d, Å
Bi1	O1	2.1851(45)	Cu1	O11	1.9061(64)
	O6	2.2679(41)		O6	1.9291(53)
	O2	2.2728(56)		O13	1.9736(46)
	O13	2.3472(61)		O4	2.0046(50)
	O8	2.5295(56)	Cu2	O9	1.8995(64)
	O14	2.8130(59)		O12	1.9121(64)
	O14	2.9894(60)		O5	1.9744(48)
	O6	2.2330(55)		O3	2.0786(44)
Bi2	O1	2.2558(53)	Cu3	O6	1.9487(45)
	O13	2.2559(44)		O6	1.9487(45)
	O2	2.3727(41)		O13	1.9685(55)
	O7	2.6199(54)		O13	1.9685(55)
	O10	2.8453(60)	Cu4	O3	1.9983(56)
	O10	2.8478(59)		O3	1.9983(56)
	O12	2.8773(50)		O5	2.0444(59)
	O9	2.1825(48)		O5	2.0444(59)
Bi3	O2	2.2413(45)	As1	O14	1.6672(50)
	O1	2.2985(56)		O8	1.6750(58)
	O5	2.3752(62)		O11	1.7004(64)
	O12	2.8171(47)		O4	1.7129(46)
	O10	2.8534(56)	As2	O7	1.6604(54)
	O7	2.9314(61)		O10	1.6822(53)
	O3	2.9997(58)		O12	1.6981(62)
	O9	2.1980(57)		O3	1.7074(46)
Bi4	O5	2.2578(46)			
	O2	2.2677(53)			
	O1	2.4191(41)			
	O11	2.6157(51)			
	O8	2.8696(62)			

3) $n = 3$ ribbons and 2x2 column: Labile degree of disorder in Bismuth-oxyphosphate compounds: illustration through three new structural types

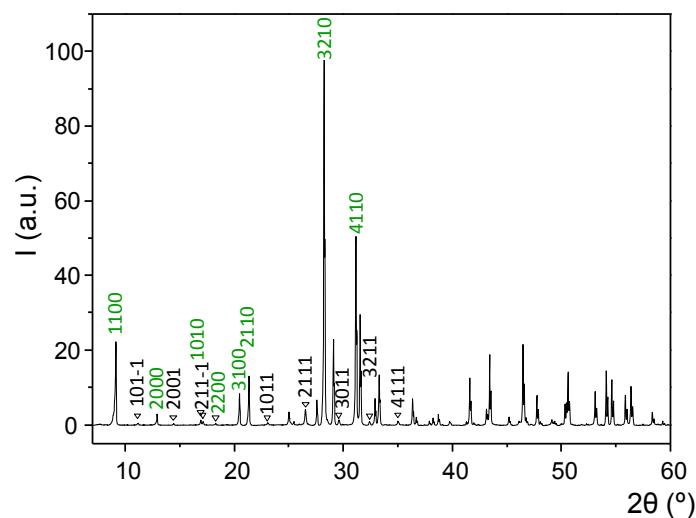


Figure S 1. Experimental XRD pattern of $[\text{Bi}_{10}(\text{Bi}_{0.5}\text{Cd}_{0.5})_8^{\text{dis}}\text{O}_{16}](\text{Bi}_{0.6}\text{Cd}_{0.8})_2^{\text{ord}}(\text{PO}_4)_8$. Green indices are the fundamental and black ones are the modulation peaks.

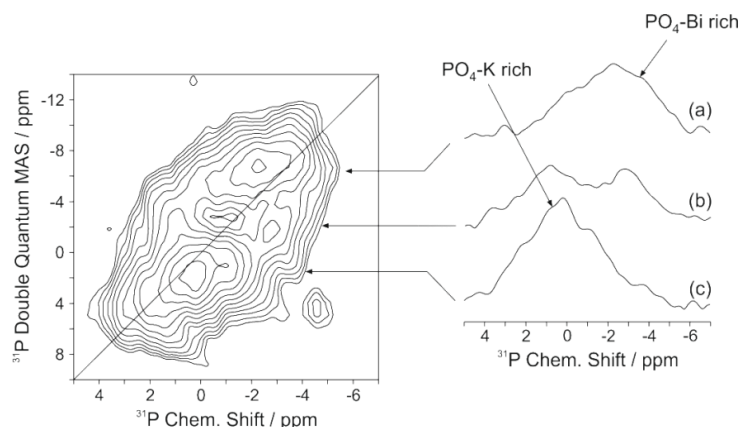


Figure S 2. ^{31}P Double Quantum MAS spectrum of $[\text{Bi}_2(\text{Bi}_{1.56}\text{K}_{0.44})^{\text{dis}}\text{O}_3]\text{K}_{0.88}^{\text{dis}}(\text{PO}_4)_2$ at 18.8 T. The sample spinning frequency was 20 kHz, the excitation and reconversion periods were set to a total of 500 μs each and the repetition time was 90 s. A total of 16 scans were used and 40 t_1 increments were collected for a total . The ^{31}P chemical shift was referenced externally at 0 ppm to a 85% H_3PO_4 solution.

Off-diagonal resonances (slice b in Figure S2) extracted from ^{31}P Double-quantum MAS spectrum of $[\text{Bi}_2(\text{Bi}_{1.56}\text{K}_{0.44})^{\text{dis}}\text{O}_3]\text{K}_{0.88}^{\text{dis}}(\text{PO}_4)_2$ is due to proximity of Bi-rich phosphate groups with those in the K-rich channels. On-diagonal resonance around -2.1 ppm shows the proximity of Bi-rich phosphate groups with themselves (slice a). The same conclusion can be drawn for on-diagonal resonance around 0.4 ppm (phosphate groups close to the K-rich channel). Note that the on-diagonal signal is slightly shifted from the true diagonal, due to substitution effect in the Bi-rich mixed site or to the K arrangement in the K channel.

Table S 7. Fractional atomic coordinates and isotropic or equivalent isotropic displacement parameters (\AA^2) of $[\text{Bi}_2(\text{Bi}_{1.56}\text{K}_{0.44})^{\text{dis}}\text{O}_3]\text{K}_{0.88}^{\text{dis}}(\text{PO}_4)_2$

	x	y	z	$U_{\text{iso}}^*/U_{\text{eq}}$	Occ. (<1)
Bi1	0.34845 (6)	−0.26957 (5)	0.20447 (18)	0.01670 (16)	0.78
K1	0.3537 (16)	−0.2922 (13)	0.221 (4)	0.01670 (16)	0.22
Bi2	0.36447 (4)	−0.00279 (4)	0.21968 (10)	0.01769 (12)	
K2a	0.5	0.5	0.191 (5)	0.053 (6)	0.4414
K2b	0.5	0.5	0.47 (3)	0.21 (5)	0.4381
P1	0.4102 (3)	0.2724 (3)	0.2877 (8)	0.0168 (8)	
O1	0.479 (2)	0.304 (3)	0.098 (4)	0.083 (11)	
O2	0.419 (2)	0.1645 (13)	0.354 (4)	0.074 (10)	
O3	0.3083 (13)	0.294 (2)	0.202 (5)	0.084 (11)	
O4	0.433 (3)	0.3262 (19)	0.509 (5)	0.097 (14)	
O5	0.3485 (12)	−0.1328 (11)	−0.025 (3)	0.031 (4)	
O6	0.5	0	0.027 (3)	0.020 (4)	

Table S 8. Atomic displacement parameters (\AA^2) of $[\text{Bi}_2(\text{Bi}_{1.56}\text{K}_{0.44})^{\text{dis}}\text{O}_3]\text{K}_{0.88}^{\text{dis}}(\text{PO}_4)_2$

	U^{11}	U^{22}	U^{33}	U^{12}	U^{13}	U^{23}
Bi1	0.0163 (3)	0.0146 (3)	0.0193 (3)	−0.0014 (3)	0.0022 (2)	0.0012 (3)
K1	0.0163 (3)	0.0146 (3)	0.0193 (3)	−0.0014 (3)	0.0022 (2)	0.0012 (3)
Bi2	0.0158 (2)	0.0185 (2)	0.0188 (2)	−0.00201 (17)	0.00474 (17)	−0.0015 (2)
K2a	0.062 (12)	0.021 (6)	0.077 (14)	−0.007 (7)	0	0
K2b	0.10 (3)	0.024 (11)	0.52 (13)	0.043 (16)	0	0
P1	0.0139 (13)	0.0176 (14)	0.0188 (15)	0.0012 (11)	0.0012 (13)	0.0021 (14)
O1	0.065 (16)	0.14 (3)	0.039 (11)	−0.028 (17)	0.017 (10)	0.033 (15)
O2	0.15 (2)	0.020 (7)	0.057 (13)	0.004 (11)	−0.053 (15)	0.002 (8)
O3	0.022 (7)	0.15 (3)	0.079 (16)	0.023 (11)	−0.009 (10)	0.059 (19)
O4	0.18 (4)	0.043 (13)	0.065 (17)	0.005 (18)	−0.05 (2)	−0.018 (12)
O5	0.038 (8)	0.029 (7)	0.027 (6)	−0.008 (6)	0.000 (6)	−0.007 (5)
O6	0.012 (6)	0.030 (8)	0.018 (6)	−0.002 (5)	0	0

Table S 9. Selected interatomic distances (\AA) of $[\text{Bi}_2(\text{Bi}_{1.56}\text{K}_{0.44})^{\text{dis}}\text{O}_3]\text{K}_{0.88}^{\text{dis}}(\text{PO}_4)_2$

Atom 1	Atom 2	d	Atom 1	Atom 2	d
Bi1	1xO5	2.240(16)	K2a	2xO1	2.769(41)
	1xO5	2.280(16)		2xO4	2.591(40)
	1xO3	2.381(24)		2xO4	2.611(30)
	1xO1	2.472(28)	P1	1xO4	1.488(29)
	1xO3	2.484(29)		1xO1	1.502(27)
	1xO4	2.744(28)		1xO3	1.504(22)
K1	1xO5	2.387(26)	K2b	1xO2	1.533(19)
	1xO1	2.395(36)			
	1xO4	2.487(34)			
	1xO3	2.537(34)			
	1xO3	2.538(36)			
Bi2	1xO5	2.554(25)			
	1xO6	2.157(9)			
	1xO5	2.267(16)			
	1xO2	2.402(23)			
	1xO5	2.501(16)			

1xO2	2.524(22)
1xO6	2.542(12)

Table S 10. Fractional atomic coordinates and isotropic or equivalent isotropic displacement parameters (\AA^2) of $[\text{Bi}_{10}(\text{Bi}_{\sim 0.5}\text{Cd}_{\sim 0.5})_8^{\text{dis}}\text{O}_{16}](\text{Bi}_{0.6}\text{Cd}_{0.8})_2^{\text{ord}}(\text{PO}_4)_8$

Atom	Occ./Wave	x	y	z	U_{eq}
Bi1	0.5	0.05987(4)	0.17608(3)	0	0.02144(17)
	s,1	0	0	0.00463(15)	
	c,1	0.00090(7)	0.00013(5)	0	
Bi2	0.5	0	0	-0.5	0.0284(2)
	s,1	0	0	0	
	c,1	0	0	0	
Bi3	0.261(2)	0.2620(6)	0.3862(9)	0	0.0194(11)
	s,1	0	0	0.0106(7)	
	c,1	0.0096(5)	-0.0062(8)	0	
Cd3	0.239(2)	0.2569(13)	0.3953(19)	0	0.0194(11)
	s,1	0	0	-0.0143(17)	
	c,1	0.0117(11)	-0.0067(14)	0	
Bia*	1	0	0.5	0	0.407(19)
	px,py,pz	0.0019	0.0009	-0.122	
	X40,delta	0	0.272(5)		
Cdb*	1	0	0.5	0.25	0.407(19)
	px,py,pz	0.001	0.001	-0.1201	
	X40,delta	0.75	0.401(10)		
O1	1	0.1275(4)	0.0639(4)	0.2324(9)	0.028(2)
	s,1	0.0071(6)	0.0016(7)	0.0110(17)	
	c,1	-0.0058(8)	-0.0039(7)	-0.0077(15)	
P	0.5	0.1658(4)	0.6307(4)	0	0.054(2)
	s,1	0	0	0.0451(14)	
	c,1	0.0116(6)	0.0021(6)	0	
Op1	0.5	0.2431(10)	0.5599(11)	0	0.109(8)
	s,1	0	0	0.015(3)	
	c,1	-0.0013(15)	-0.0076(15)	0	
Op2	1	0.1032(10)	0.6276(13)	-0.199(3)	0.161(9)
	s,1	-0.0098(14)	0.0133(16)	0.047(4)	
	c,1	-0.0082(13)	0.0053(15)	0.065(3)	
Op3	0.5	0.2071(18)	0.7216(15)	0	0.30(3)
	s,1	0	0	0.108(9)	
	c,1	0.009(3)	-0.010(2)	0	

*Special Crenel functions

Table S 11. Atomic displacement parameters (\AA^2) of $[\text{Bi}_{10}(\text{Bi}_{\sim 0.5}\text{Cd}_{\sim 0.5})_8^{\text{dis}}\text{O}_{16}](\text{Bi}_{0.6}\text{Cd}_{0.8})_2^{\text{ord}}(\text{PO}_4)_8$

Atom		U11	U22	U33	U12	U13	U23
Bi1		0.0286(3)	0.0159(3)	0.0199(3)	-0.00393(19)	0	0
	s,1	0	0	0	0	0.0013(4)	-0.0005(3)
	c,1	0.0036(5)	-0.0017(5)	0.0002(5)	0.0000(4)	0	0
Bi2		0.0290(4)	0.0290(4)	0.0272(5)	0	0	0
	s,1	0	0	0	0	0	0
	c,1	-0.0038(9)	0.0038(9)	0	-0.0049(9)	0	0
Bi3		0.0188(14)	0.023(2)	0.0169(14)	-0.0068(12)	0	0
	s,1	0	0	0	0	-0.0066(12)	0.0069(12)
	c,1	-0.011(3)	0.001(3)	-0.003(3)	-0.001(2)	0	0
Cd3		0.0188(14)	0.023(2)	0.0169(14)	-0.0068(12)	0	0
	s,1	0	0	0	0	-0.002(3)	0.007(3)
	c,1	0.029(6)	0.007(5)	0.006(5)	-0.001(4)	0	0
Bia		0.062(19)	0.068(19)	1.09(5)	-0.0005(17)	0	0
	s,1	0	0	0	0	0	0
	c,1	-0.01(2)	-0.03(2)	-0.99(5)	-0.008(3)	0	0
Cdb		0.062(19)	0.068(19)	1.09(5)	-0.0005(17)	0	0
	s,1	0.05(2)	0.05(2)	0.98(6)	0	0	0
	c,1	0.028(7)	-0.028(7)	0	-0.022(7)	0	0
O1		0.025(4)	0.029(4)	0.029(4)	0.005(3)	0.007(3)	-0.001(3)
	s,1	0.003(6)	-0.007(6)	0.009(6)	0.003(5)	-0.007(5)	0.012(5)
	c,1	0.013(7)	0.000(7)	-0.004(7)	0.001(5)	0.004(5)	0.011(5)
P		0.060(4)	0.050(3)	0.052(4)	0.032(3)	0	0
	s,1	0	0	0	0	-0.015(4)	-0.001(4)
	c,1	-0.007(6)	-0.019(5)	0.017(6)	-0.021(5)	0	0
Op1		0.073(12)	0.120(14)	0.135(15)	0.057(10)	0	0
	s,1	0	0	0	0	-0.032(13)	-0.094(14)
	c,1	0.031(18)	0.03(2)	0.09(2)	0.019(15)	0	0
Op2		0.132(14)	0.197(17)	0.155(18)	-0.044(12)	-0.063(11)	0.051(12)
	s,1	-0.081(19)	-0.11(2)	-0.01(2)	0.025(15)	0.019(15)	0.031(16)
	c,1	0.027(18)	0.04(2)	0.09(2)	-0.047(15)	-0.051(14)	0.093(15)
Op3		0.20(3)	0.074(17)	0.62(7)	0.020(16)	0	0
	s,1	0	0	0	0	-0.27(4)	-0.04(3)
	c,1	-0.11(4)	0.01(3)	0.46(9)	0.01(2)	0	0

Table S 12. Selected interatomic distances (Å) of $[Bi_{10}(Bi_{\sim 0.5}Cd_{\sim 0.5})_8]^{dis}O_{16} (Bi_{0.6}Cd_{0.8})_2^{ord}(PO_4)_8$

Atom 1	Atom 2	d _{average}	d _{min}	d _{max}
P1	1xOp1	1.45(2)	1.41(3)	1.50(3)
	2xOp2	1.46(2)	1.42(2)	1.52(2)
	1xOp3	1.40(3)	1.22(4)	1.54(4)
O1	2xBi1	2.235(11)	2.184(11)	2.287(11)
	2xBi1	2.260(11)	2.194(11)	2.329(11)
	2xBi3	2.286(15)	2.176(16)	2.395(16)
	2xCd3	2.24(2)	2.12(2)	2.35(2)
Cdb	4xOp2	2.35(3)	2.27(3)	2.38(3)
Bia	8xOp2	2.47(3)	2.24(3)	2.96(3)
	6xOp2	2.62(3)	2.37(2)	3.06(3)

Table S 13. Fractional atomic coordinates and isotropic or equivalent isotropic displacement parameters (Å²) of $[Bi_{18}Zn_{10}O_{21}]^{ord}Zn_5^{ord}(PO_4)_{14}$

	x	y	z	U_{iso}^*/U_{eq}	Occ. (<1)
Bi1	0.14052 (11)	0.53793 (2)	0.09739 (7)	0.00863 (19)	
Bi2	0.12812 (13)	0.25	0.09874 (12)	0.0163 (4)	
Bi3	0.14101 (12)	0.60594 (2)	-0.11974 (7)	0.0096 (2)	
Bi4	0.14620 (12)	0.67712 (2)	0.11187 (7)	0.0108 (2)	
Bi5	-0.04510 (13)	0.67426 (3)	-0.07572 (9)	0.0112 (3)	0.902 (7)
Zn5	-0.045 (2)	0.6616 (10)	-0.081 (3)	0.0112 (3)	0.098 (7)
Bi6	0.32418 (11)	0.535768 (19)	-0.11676 (7)	0.0090 (2)	
Bi7	0.33579 (13)	0.75	0.10382 (11)	0.0124 (3)	
Bi8	0.33160 (11)	0.61048 (2)	0.10547 (7)	0.0091 (2)	
Bi9	0.32314 (11)	0.67949 (2)	-0.11111 (7)	0.0084 (2)	
Bi10	0.50011 (13)	0.53848 (2)	0.10460 (8)	0.0088 (3)	0.940 (7)
Zn10	0.466 (4)	0.5387 (13)	0.108 (4)	0.0088 (3)	0.060 (7)
Bi11	0.9552 (14)	0.75	0.098 (2)	0.020 (2)	0.32 (2)
Zn11	0.943 (2)	0.75	0.092 (3)	0.020 (2)	0.68 (2)
Zn1	0.9628 (2)	0.02898 (6)	0.0872 (2)	0.0091 (6)	
Zn2	0.4657 (3)	0.25	0.1336 (3)	0.0143 (9)	
Zn3	0.4704 (2)	0.10945 (6)	0.1255 (2)	0.0115 (6)	
Zn4	0.9609 (2)	0.60203 (7)	0.0750 (2)	0.0094 (6)	
Zn9	0.5053 (2)	0.67927 (6)	0.0663 (2)	0.0132 (7)	
Zn6	0.7307 (2)	0.60822 (7)	0.0507 (2)	0.0130 (6)	
Zn7	0.7043 (2)	0.70197 (8)	0.0107 (3)	0.0234 (8)	
Zn8	0.7060 (3)	0	0	0.0176 (10)	
P1	0.5882 (4)	0.45858 (13)	0.2006 (4)	0.0093 (12)	
Op1a	0.6709 (11)	0.4614 (4)	0.2811 (14)	0.017 (3)*	
Op1b	0.5114 (10)	0.4827 (4)	0.2455 (14)	0.016 (3)*	
Op1c	0.6059 (9)	0.4698 (4)	0.0710 (12)	0.008 (3)*	

Op1d	0.5549 (10)	0.4201 (4)	0.2048 (14)	0.014 (3)*
P2	0.8358 (4)	0.54243 (13)	0.1606 (4)	0.0083 (12)
Op2a	0.8347 (9)	0.5819 (3)	0.1300 (12)	0.010 (3)*
Op2b	0.9144 (10)	0.5244 (4)	0.0917 (13)	0.014 (3)*
Op2c	0.7453 (11)	0.5257 (4)	0.1317 (14)	0.017 (3)*
Op2d	0.8558 (10)	0.5378 (4)	0.2964 (13)	0.013 (3)*
P3	0.5912 (6)	0.75	0.1926 (7)	0.015 (2)
Op3a	0.6043 (15)	0.7821 (6)	0.117 (2)	0.039 (5)*
Op3b	0.658 (2)	0.75	0.298 (3)	0.038 (7)*
Op3c	0.496 (3)	0.75	0.238 (3)	0.052 (8)*
P4	0.5844 (4)	0.32058 (13)	0.2021 (4)	0.0094 (12)
Op4a	0.6637 (13)	0.3246 (5)	0.2834 (17)	0.029 (4)*
Op4b	0.5167 (12)	0.3494 (5)	0.2367 (16)	0.025 (4)*
Op4c	0.5378 (11)	0.2854 (4)	0.2275 (15)	0.020 (3)*
Op4d	0.6034 (12)	0.3244 (4)	0.0700 (15)	0.020 (3)*
P5	0.8343 (4)	0.67453 (13)	0.1628 (5)	0.0107 (13)
Op5b	0.9182 (10)	0.6559 (4)	0.1134 (14)	0.015 (3)*
Op5c	0.7487 (11)	0.6583 (4)	0.0988 (15)	0.019 (3)*
Op5a	0.8374 (11)	0.7133 (4)	0.1263 (15)	0.021 (3)*
Op5d	0.3265 (11)	0.6701 (4)	0.2031 (14)	0.018 (3)*
P6	0.5819 (4)	0.61342 (13)	0.2114 (4)	0.0099 (12)
Op6a	0.6621 (12)	0.6119 (4)	0.3012 (15)	0.021 (3)*
Op6b	0.5525 (10)	0.6515 (4)	0.1979 (14)	0.014 (3)*
Op6c	0.6081 (10)	0.5958 (4)	0.0931 (13)	0.012 (3)*
Op6d	0.5032 (11)	0.5903 (4)	0.2587 (14)	0.018 (3)*
P7	0.8361 (4)	0.59328 (12)	-0.1585 (4)	0.0088 (12)
Op7a	0.7433 (12)	0.6031 (4)	-0.1165 (15)	0.020 (3)*
Op7b	0.9096 (11)	0.6148 (4)	-0.0898 (14)	0.017 (3)*
Op7c	0.8543 (10)	0.5543 (4)	-0.1407 (13)	0.014 (3)*
Op7d	0.8439 (10)	0.6016 (4)	-0.2931 (14)	0.015 (3)*
P8	0.8217 (7)	0.25	0.1506 (9)	0.036 (3)
Op8a	0.9094 (18)	0.25	0.088 (2)	0.026 (5)*
Op8b	0.770 (2)	0.2175 (9)	0.124 (3)	0.079 (9)*
Op8c	0.8368 (16)	0.25	0.285 (2)	0.019 (5)*
O1	0.2386 (10)	0.5713 (4)	-0.0056 (12)	0.006 (2)*
O2	0.2405 (9)	0.6430 (3)	-0.0030 (11)	0.004 (2)*
O3	0.2362 (10)	0.7146 (4)	-0.0027 (13)	0.010 (3)*
O4	0.2402 (15)	0.5	0	0.011 (4)*
O5	0.4204 (9)	0.5711 (4)	-0.0056 (12)	0.008 (3)*
O6	0.4253 (11)	0.5	0	0.002 (3)*
O7	1.0657 (13)	0	0	0.006 (3)*
O8	0.4188 (9)	0.1428 (3)	0.0081 (12)	0.006 (2)*
O9	0.0604 (10)	0.6435 (4)	-0.0060 (14)	0.014 (3)*
O10	1.0482 (10)	0.7872 (4)	0.0122 (14)	0.014 (3)*
O11	0.4192 (9)	0.7145 (3)	-0.0073 (11)	0.005 (2)*
O12	1.0534 (10)	0.5710 (4)	-0.0118 (13)	0.011 (3)*

Table S 14. Atomic displacement parameters (\AA^2) of $[\text{Bi}_{18}\text{Zn}_{10}\text{O}_{21}]^{\text{ord}}\text{Zn}_5^{\text{ord}}(\text{PO}_4)_{14}$

	U^{11}	U^{22}	U^{33}	U^{12}	U^{13}	U^{23}
Bi1	0.0089 (3)	0.0105 (4)	0.0064 (3)	−0.0012 (3)	0.0008 (3)	−0.0010 (3)
Bi2	0.0203 (7)	0.0135 (5)	0.0150 (5)	0	0.0056 (5)	0
Bi3	0.0093 (4)	0.0104 (3)	0.0092 (4)	0.0001 (3)	−0.0019 (3)	0.0002 (3)
Bi4	0.0125 (4)	0.0123 (4)	0.0075 (4)	−0.0006 (3)	0.0027 (3)	−0.0008 (2)
Bi5	0.0090 (4)	0.0126 (6)	0.0121 (4)	0.0014 (4)	−0.0014 (3)	0.0005 (4)
Zn5	0.0090 (4)	0.0126 (6)	0.0121 (4)	0.0014 (4)	−0.0014 (3)	0.0005 (4)
Bi6	0.0082 (4)	0.0108 (3)	0.0079 (4)	−0.0002 (3)	0.0011 (3)	0.0001 (2)
Bi7	0.0164 (6)	0.0100 (5)	0.0109 (5)	0	0.0032 (4)	0
Bi8	0.0094 (4)	0.0108 (3)	0.0071 (3)	0.0002 (3)	−0.0011 (3)	0.0011 (3)
Bi9	0.0084 (4)	0.0099 (3)	0.0070 (3)	−0.0004 (3)	0.0014 (3)	0.0003 (3)
Bi10	0.0089 (6)	0.0083 (4)	0.0091 (4)	0.0009 (4)	−0.0047 (4)	−0.0002 (3)
Zn10	0.0089 (6)	0.0083 (4)	0.0091 (4)	0.0009 (4)	−0.0047 (4)	−0.0002 (3)
Bi11	0.022 (6)	0.0206 (13)	0.017 (3)	0	0.001 (3)	0
Zn11	0.022 (6)	0.0206 (13)	0.017 (3)	0	0.001 (3)	0
Zn1	0.0081 (11)	0.0135 (11)	0.0057 (10)	0.0006 (9)	0.0009 (9)	−0.0014 (8)
Zn2	0.0169 (17)	0.0092 (15)	0.0167 (17)	0	−0.0079 (15)	0
Zn3	0.0162 (12)	0.0088 (10)	0.0095 (11)	−0.0008 (9)	−0.0065 (9)	0.0023 (8)
Zn4	0.0073 (10)	0.0149 (10)	0.0059 (10)	0.0004 (9)	−0.0017 (8)	0.0024 (8)
Zn9	0.0134 (12)	0.0095 (11)	0.0168 (12)	0.0009 (9)	−0.0092 (11)	0.0012 (9)
Zn6	0.0074 (10)	0.0191 (12)	0.0124 (11)	−0.0002 (9)	0.0012 (9)	−0.0008 (9)
Zn7	0.0151 (11)	0.0345 (16)	0.0204 (13)	0.0011 (11)	0.0002 (10)	0.0053 (12)
Zn8	0.0139 (15)	0.0195 (17)	0.0195 (17)	0	0	0.0043 (15)
P1	0.011 (2)	0.012 (2)	0.005 (2)	0.0009 (18)	−0.0047 (18)	0.0001 (17)
P2	0.009 (2)	0.012 (2)	0.004 (2)	0.0024 (18)	0.0002 (17)	−0.0014 (17)
P3	0.015 (4)	0.014 (3)	0.015 (4)	0	−0.006 (3)	0
P4	0.011 (2)	0.011 (2)	0.006 (2)	0.0018 (18)	−0.0025 (17)	0.0000 (17)
P5	0.014 (3)	0.012 (2)	0.006 (2)	0.0009 (19)	−0.0010 (19)	0.0024 (17)
P6	0.011 (2)	0.013 (2)	0.006 (2)	−0.0030 (18)	−0.0007 (17)	0.0019 (18)
P7	0.015 (2)	0.0055 (19)	0.006 (2)	−0.0013 (18)	0.0000 (18)	−0.0003 (17)
P8	0.015 (4)	0.083 (9)	0.009 (4)	0	0.008 (3)	0

Table S 15. Selected interatomic distances (Å) in $[\text{Bi}_{18}\text{Zn}_{10}\text{O}_{21}]^{\text{ord}}\text{Zn}_5^{\text{ord}}(\text{PO}_4)_{14}$

A 1	A 2	d	A 1	A 2	d	A 1	A 2	d	A 1	A 2	d
Bi1	1xO7	2,124(11)	Bi7	2xO11	2,217(13)	Zn1	1xOp7c	1,967(16)	P1	1xOp1a	1,526(17)
	1xO12	2,181(15)		2xO3	2,329(15)		1xOp1b	2,063(16)		1xOp1c	1,541(15)
	1xO1	2,250(15)		1xOp3c	2,811(42)		1xO7	2,121(15)		1xOp1b	1,546(16)
	1xO4	2,337(15)		1xOp3b	2,854(31)		1xOp2b	2,143(15)		1xOp1d	1,547(16)
Bi2	2xO10	2,228(16)	Bi8	1xO8	2,194(13)		1xOp2b	2,156(16)	P2	1xOp2c	1,519(18)
	2xO3	2,354(15)		1xO2	2,200(13)		1xO12	2,254(16)		1xOp2a	1,542(13)
	2xOp4c	2,725(17)		1xO5	2,353(15)	Zn2	2xOp4c	2,018(17)		1xOp2b	1,557(16)
Bi3	1xO12	2,219(15)		1xO1	2,384(15)		2xO11	2,078(13)		1xOp2d	1,566(16)
	1xO9	2,260(16)		1xOp5d	2,523(16)		1xOp8c	2,116(24)	P3	1xOp3c	1,499(45)
	1xO1	2,340(15)		1xOp6a	2,720(18)	Zn3	1xOp1d	1,904(16)		2xOp3a	1,502(24)
	1xO2	2,426(13)	Bi9	1xO2	2,215(13)		1xO8	1,985(13)		1xOp3b	1,544(34)
	1xOp1d	2,550(16)		1xO3	2,221(15)		1xOp7d	2,105(16)	P4	1xOp4a	1,496(20)
	1xOp1a	2,831(16)		1xO11	2,272(13)		1xOp4b	2,119(19)		1xOp4d	1,519(18)
	1xOp4a	2,881(20)		1xO8	2,302(13)		1xO5	2,121(15)		1xOp4c	1,534(17)
Bi4	1xO9	2,238(16)		1xOp4a	2,646(20)	Zn4	1xOp6d	2,022(16)		1xOp4b	1,536(20)
	1xO10	2,282(16)	Bi10	1xO5	2,115(15)		1xO12	2,055(16)	P5	1xOp5d	1,522(17)
	1xO2	2,303(13)		1xO6	2,181(90)		1xOp7b	2,061(16)		1xOp5a	1,533(17)
	1xO3	2,339(15)		1xOp2d	2,409(15)		1xOp2a	2,112(14)		1xOp5b	1,534(17)
	1xOp6a	2,680(16)		1xOp1c	2,540(14)		1xOp5b	2,190(16)		1xOp5c	1,583(18)
	1xOp6b	2,730(16)		1xOp6d	2,627(16)		1xO9	2,344(16)	P6	1xOp6b	1,522(16)
	1xOp5d	2,871(17)		1xOp1b	2,656(16)	Zn9	1xOp6b	1,949(16)		1xOp6c	1,540(16)
Bi5	1xO9	2,104(16)		1xOp6c	2,709(16)		1xO11	2,027(13)		1xOp6d	1,554(17)
	1xO10	2,245(16)	Zn10	1xO5	1,900(51)		1xO8	2,066(13)		1xOp6a	1,560(19)
	1xOp5b	2,304(16)		1xOp2d	1,954(58)		1xOp4d	2,116(18)	P7	1xOp7a	1,500(19)
	1xOp7b	2,367(16)		1xO6	2,003(50)		1xOp3a	2,153(23)		1xOp7c	1,522(16)
	1xOp4b	2,470(19)		1xOp6d	2,653(51)	Zn6	1xOp7a	1,900(17)		1xOp7d	1,551(17)
Zn5	1xO9	1,903(36)		1xOp1b	2,719(52)		1xOp6c	1,935(16)		1xOp7b	1,566(17)
	1xOp7b	1,907(41)	Bi11	1xOp3c	1,941(42)		1xOp5c	2,000(16)	P8	1xOp8a	1,477(28)
	1xOp5b	2,264(37)		2xO10	2,198(23)		1xOp2a	2,042(14)		2xOp8b	1,486(34)
	1xOp4b	2,283(38)		1xOp8a	2,199(32)	Zn7	1xOp8b	1,895(33)		1xOp8c	1,528(25)
	1xO10	2,608(39)		2xOp5a	2,257(23)		1xOp3a	1,997(23)			
Bi6	1xO1	2,236(15)	Zn11	1xOp3c	2,067(49)		1xOp4d	2,016(18)			
	1xO4	2,264(13)		1xOp8a	2,085(41)		1xOp5c	2,045(16)			
	1xO5	2,324(15)		2xOp5a	2,132(28)		1xOp5a	2,399(17)			
	1xO6	2,413(11)		2xO10	2,288(29)	Zn8	2xOp2c	1,868(16)			
	1xOp1a	2,545(17)					2xOp1c	2,039(15)			
	1xOp7d	2,720(16)									
	1xOp7c	2,853(15)									

4) $n = 3$ / $n = 4$ ribbon intergrowths: $\text{Bi}_{29.4}\text{Cu}_{9.29}\text{O}_{32}(\text{PO}_4)_{16}\text{Cu}_{2.63}$ and $\text{Bi}_{37.2}\text{Cu}_{18.8}\text{O}_{44}(\text{PO}_4)_{24}\text{Cu}_5$.

Table S 16. Crystal data, measurement and structure refinement parameters for $\text{Bi}_{29.4}\text{Cu}_{9.29}\text{O}_{32}(\text{PO}_4)_{16}\text{Cu}_{2.63}$ and $\text{Bi}_{37.2}\text{Cu}_{18.8}\text{O}_{44}(\text{PO}_4)_{24}\text{Cu}_5$

Crystal Data		
Compound	$\text{Bi}_{29.4}\text{Cu}_{9.29}\text{O}_{32}(\text{PO}_4)_{16}\text{Cu}_{2.63}$	$\text{Bi}_{37.2}\text{Cu}_{18.8}\text{O}_{44}(\text{PO}_4)_{24}\text{Cu}_5$
Crystal symmetry	Orthorhombic	Orthorhombic
Space group	$Pca2_1$	$Pna2_1$
a (Å)	33.0549(2)	11.6010(3)
b (Å)	11.6991(4)	47.4384(5)
c (Å)	5.2902(2)	5.267(2)
V (Å ³)	2045.8(1)	2899(1)
Z	1	1
Mw	8926.6	12285.4
Data collection		
Equipment	Apex DUO (Bruker AXS)	
Radiation wavelength (Å)	0.71073 (MoK α)	
Absorption corrections	Multiscan (Sadabs)	
Detector distance (mm)	40	55
Recording reciprocal space	$-59 \leq h \leq 53$ $-20 \leq k \leq 20$ $-9 \leq l \leq 8$	$-20 \leq h \leq 20$ $-76 \leq k \leq 82$ $-8 \leq l \leq 8$
μ (mm ⁻¹)	71.07	64.881
D_{calc} (g/cm ³)	7.316	7.041
θ -range (deg.)	3.54-40.23	3.89-39.27
Total Ref.	70469	101687
Unique Ref.	11339	15259
Unique $ I \geq 3\sigma(I)$	7767	11181
Refinement parameters		
Software, refinement type	Jana 2006, L.S. on F	
Refined parameters / restrictions	211/7	229/2
R_{int}	0.064	0.0701
R_1	0.059	0.094
R_1 (all data)	0.094	0.1212
wR_2	0.061	0.0981
Weight	Unit	Unit
Extinction coefficient	90(7)	93(9)

Table S 17. Atomic coordinates and displacement parameters (\AA^2) for $\text{Bi}_{29.4}\text{Cu}_{9.29}\text{O}_{32}(\text{PO}_4)_{16}\text{Cu}_{2.63}$.

Atom	x	y	z	U_{eq}	Occ.
Bi1	0.20979(2)	0.58303(5)	0.000105	0.0120(1)	
Bi2	0.29057(2)	0.36128(5)	0.0005(3)	0.0116(1)	
Bi3	0.37641(2)	0.55562(6)	-0.0013(5)	0.018(2)	
Cu3	0.63122(8)	0.6038(2)	0.010(1)	0.0167(6)	
Bi4	0.42243(2)	0.87778(5)	-0.0028(3)	0.0144(1)	
Bi5	0.00650(2)	0.36998(5)	0.0013(5)	0.0196(2)	
Bi6	0.00188(2)	0.11288(6)	-0.5097(5)	0.0188(2)	
Bi7	0.58415(2)	0.90881(5)	-0.0041(3)	0.0141(2)	
Cu1a	0.16055(8)	0.8975(2)	0.002(1)	0.0099(4)	0.855(6)
Bi1a	0.1479(2)	0.8714(5)	-0.010(3)	0.023(2)	0.145(6)
Cu2a	0.3521(1)	0.0811(3)	-0.006(2)	0.0205(6)	0.801(5)
Bi2a	0.3379(1)	0.0557(3)	-0.001(2)	0.015(1)	0.199(5)
Cua	0.2507(3)	-0.027(1)	0.093(2)	0.025(2)	0.3367
O1	0.2511(6)	0.4728(9)	0.760(4)	0.007(2)	
O2	0.6674(5)	0.533(2)	0.241(3)	0.009(2)	
O3	-0.1688(6)	0.521(2)	0.244(3)	0.013(3)	
O4	0.3785(4)	-0.014(1)	0.247(3)	0.006(2)	
O5	0.3766(6)	0.967(2)	0.750(4)	0.014(3)	
O6	0.5420(7)	0.013(2)	0.749(4)	0.017(3)	
O7	-0.0412(5)	0.005(1)	0.750(3)	0.0042	
Oex	0.0012(6)	0.196(2)	0.029(5)	0.029(4)	
P1	-0.0670(1)	0.3459(4)	-0.502 (2)	0.0136(7)	
Op1a	-0.1098(4)	0.394(1)	0.467(3)	0.016(3)	
Op1b	-0.0447(7)	0.405(2)	0.271(4)	0.023(4)	
Op1c	0.5466(7)	0.383(2)	0.246(4)	0.020(3)	
Op1d	-0.0682(5)	0.217(2)	-0.509(7)	0.028(3)	
P2	0.4242(2)	0.3112(4)	0.015(2)	0.024(2)	
Op2a	0.4131(8)	0.346(3)	0.269(3)	0.042(6)	
Op2b	0.4694(5)	0.342(2)	-0.030(5)	0.030(4)	
Op2c	0.4174(5)	0.182(2)	-0.014(6)	0.021(3)	
Op2d	0.3979(9)	0.380(3)	0.844(6)	0.040(6)	
P3	0.3095(2)	0.7773(4)	-0.017(2)	0.0168(8)	
O3a	0.353(1)	0.738(3)	0.060(7)	0.052(8)	
O3b	0.2804(6)	0.679(1)	-0.012(7)	0.029(3)	
O3c	0.295(1)	0.876(2)	0.121(8)	0.08(1)	
O3d	0.335(1)	0.759(4)	-0.237(5)	0.06(1)	
P4	0.1920(2)	0.1709(5)	0.001(2)	0.0195(8)	
O4a	0.2218(5)	0.267(1)	-0.012(6)	0.023(3)	
O4b	0.2080(8)	0.058(1)	0.057(5)	0.040(6)	
O4c	0.159(1)	0.192(3)	0.203(7)	0.048(7)	
O4d	0.178(2)	0.177(5)	-0.259(4)	0.09(2)	

Table S 18. Displacement parameters (\AA^2) for $\text{Bi}_{29.4}\text{Cu}_{9.29}\text{O}_{32}(\text{PO}_4)_{16}\text{Cu}_{2.63}$.

Atom	U11	U22	U33	U12	U13	U23
Bi1	0.0104(2)	0.0120(2)	0.0136(2)	0.0037(2)	0.0003(4)	-0.0007(4)
Bi2	0.0094(2)	0.0099(2)	0.0156(2)	0.0019(2)	-0.0008(4)	0.0080(4)
Bi3	0.0113(2)	0.0124(2)	0.0303(3)	-0.0023(2)	0.0004(5)	0.0001(5)
Cu3	0.0168(8)	0.020(1)	0.013(1)	0.0045(7)	-0.002(1)	0.005(1)
Bi4	0.0188(2)	0.0137(2)	0.0108(2)	-0.006(2)	0.0020(4)	0.0055(4)
Bi5	0.0112(2)	0.0104(2)	0.0371(4)	-0.0011(2)	-0.0050(5)	-0.0007(5)
Bi6	0.0073(2)	0.0130(2)	0.0360(4)	0.0002(2)	-0.0013(5)	-0.0058(5)
Bi7	0.0172(2)	0.0144(2)	0.0105(2)	0.0051(2)	0.0014(4)	-0.0026(4)
P2	0.009(2)	0.011(2)	0.053(4)	0.006(1)	-0.004(4)	0.005(4)

Table S 19. Atomic coordinates and displacement parameters (\AA^2) for $\text{Bi}_{37.2}\text{Cu}_{18.8}\text{O}_{44}(\text{PO}_4)_{24}\text{Cu}_5$.

Atom	X	Y	Z	Ueq	Occ.
Bi1	0.13608(7)	0.85115(2)	0.44992	0.0139(2)	
Bi2	0.12881(7)	0.99429(2)	0.9481(5)	0.0143(2)	
Bi3	-0.05678(8)	0.91193(2)	0.4446(5)	0.0215(3)	
Bi4	-0.37427(7)	0.94743(2)	0.4534(4)	0.0141(2)	
Bi5	0.41057(7)	0.93997(2)	0.9527(4)	0.0131(2)	
Bi6	0.13541(7)	0.7946(2)	0.9531(5)	0.0137(2)	
Bi7	0.61320(7)	0.00166(2)	0.9698(5)	0.0142(2)	
Bi8	-0.08686(7)	0.85192(2)	-0.0437(5)	0.0147(2)	
Bi9	-0.08631(8)	0.79443(2)	0.4501(5)	0.0161(2)	
Cu1a	0.4408(3)	0.88871(7)	0.449(1)	0.0101(5)	0.9
Bi1a	0.4240(7)	0.8953(2)	0.424(2)	0.0101(5)	0.1
Cu2	0.1009(3)	0.74136(9)	0.442(1)	0.0213(8)	
Cu3	-0.0665(4)	0.74500(9)	0.949(1)	0.028(1)	
Cu2a	0.6390(4)	0.89961(8)	0.941(2)	0.0182(5)	0.82
Bi2a	0.6016(5)	0.8864(1)	0.981(1)	0.0182(5)	0.18
Cu5	0.1058(3)	0.90647(7)	-0.050(1)	0.0203(8)	
Cua	0.5259(9)	0.825(2)	0.424(5)	0.064(5)	0.60(1)
Cub	0.5225(7)	0.823(2)	0.139 (2)	0.032(1)	0.75
O1	0.014(2)	0.8248(5)	0.213(4)	0.012(3)	
O2	0.302(2)	0.9996(4)	0.921(4)	0.013(3)	
O3	0.017(2)	0.8780(5)	-0.304(5)	0.017(4)	
O4	0.034(2)	0.8827(4)	0.200(3)	0.005(2)	
O5	-0.482(2)	0.9733(4)	0.711(4)	0.010(3)	
O6	0.535(2)	0.9149(3)	0.193(3)	0.002(2)	
O7	0.014(2)	0.7652(4)	0.703(4)	0.010(3)	
O8	-0.494(1)	0.9698(3)	0.205(3)	0.0001	
O9	0.516(2)	0.9154(5)	0.699(5)	0.016(4)	
O10	0.031(1)	0.8229(3)	0.703(3)	0.002(2)	
O11	0.033(2)	0.7681(5)	0.202(5)	0.015(4)	

P1	0.1912(7)	0.9455(2)	0.419(2)	0.0212(5)
Op1a	0.318(1)	0.9412(4)	0.458(5)	0.023(2)
Op1b	0.162(2)	0.9757(5)	0.467(6)	0.047(3)
Op1c	0.156(3)	0.9391(6)	0.146(5)	0.052(4)
Op1d	0.121(3)	0.9282(7)	0.623(5)	0.058(5)
P2	0.3307(7)	0.7835(2)	0.485(2)	0.0212(5)
Op2a	0.231(1)	0.8033(5)	0.447(5)	0.023(2)
Op2b	0.438(2)	0.7971(5)	0.389(6)	0.047(3)
Op2c	0.350(3)	0.7771(6)	0.766(5)	0.052(4)
Op2d	0.314(3)	0.7562(6)	0.317(5)	0.058(5)
P3	0.2247(6)	0.6319(2)	0.456(2)	0.0212(5)
Op3a	0.313(2)	0.6549(4)	0.451(5)	0.023(2)
Op3b	0.250(2)	0.6124(6)	0.672(5)	0.047(3)
Op3c	0.104(2)	0.6437(6)	0.498(6)	0.052(4)
Op3d	0.235(3)	0.6131(6)	0.208(6)	0.058(5)
P4	0.1482(6)	0.0455(2)	0.454(2)	0.0212(5)
Op4a	0.103(2)	0.0302(4)	0.683(5)	0.023(2)
Op4b	0.103(3)	0.0750(5)	0.455(6)	0.047(3)
Op4c	0.280(2)	0.0476(7)	0.459(6)	0.052(4)
Op4d	0.100(2)	0.0316(7)	0.203(6)	0.058(5)
P5	0.1715(7)	0.3644(2)	0.416(2)	0.0212(5)
Op5a	0.27(1)	0.3439(4)	0.430(5)	0.023(2)
Op5b	0.062(2)	0.3492(5)	0.471(6)	0.047(3)
Op5c	0.184(3)	0.3876(6)	0.616(5)	0.052(4)
Op5d	0.159(3)	0.3761(7)	0.136(5)	0.058(5)
P6	0.3089(6)	0.2055(2)	0.431(2)	0.0212(5)
Op6a	0.1837(16)	0.1985(5)	0.463(5)	0.023(2)
Op6b	0.3204(19)	0.2298(6)	0.253(6)	0.047(3)
Op6c	0.363(3)	0.2145(6)	0.683(5)	0.052(4)
Op6d	0.374(3)	0.1802(6)	0.299(6)	0.058(5)

Table S 20. Displacement parameters (\AA^2) for $\text{Bi}_{37.2}\text{Cu}_{18.8}\text{O}_{44}(\text{PO}_4)_{24}\text{Cu}_5$.

Atom	U11	U22	U33	U12	U13	U23
Bi1	0.0090(3)	0.0118(3)	0.0208(4)	-0.0018(2)	-0.0036(5)	-0.0012(5)
Bi2	0.0069(2)	0.0126(3)	0.0233(4)	-0.0019(2)	-0.0026(4)	0.0015(5)
Bi3	0.0134(3)	0.0115(3)	0.0396(6)	0.0020(2)	-0.0146(6)	-0.0032(6)
Bi4	0.0095(3)	0.0213(3)	0.0113(3)	0.0082(2)	-0.0046(4)	-0.0051(5)
Bi5	0.0110(3)	0.0148(3)	0.0132(3)	-0.0036(2)	-0.0062(4)	0.0025(5)
Bi6	0.0090(3)	0.0140(3)	0.0181(4)	0.0034(2)	0.0055(5)	0.0053(5)
Bi7	0.0051(2)	0.0087(3)	0.0288(6)	0.0005(2)	0.0026(4)	-0.0014(4)
Bi8	0.0111(3)	0.0144(3)	0.0187(4)	0.0034(2)	-0.0069(5)	0.0048(5)
Bi9	0.0150(3)	0.0150(3)	0.0184(4)	-0.0047(2)	0.0070(5)	-0.0003(5)
Cu2	0.019 (1)	0.032(2)	0.012(1)	-0.003(1)	-0.002(2)	-0.003(2)
Cu3	0.031(2)	0.033(2)	0.021(2)	-0.026(2)	0.005(2)	-0.011(2)
Cu5	0.034(2)	0.016(1)	0.012(1)	-0.004(1)	0.008(2)	-0.005(2)
Cua	0.049(5)	0.010(2)	0.13(1)	-0.015(3)	0.043(9)	-0.006(7)

5) n = 4 ribbons: $\text{KBi}_5\text{O}_5(\text{AsO}_4)_2$

Table S 21. Crystal data, measurement and structural refinement parameters for $\text{KBi}_5\text{O}_5(\text{AsO}_4)_2$

$\text{KBi}_5\text{O}_5(\text{AsO}_4)_2$	
Crystal data	
Crystal symmetry	Monoclinic
space group	$P2_1/c$
a (Å)	8.2534 (5)
b (Å)	5.5406 (4)
c (Å)	28.405 (2)
β (°)	95.936 (3)
V (Å ³)	1292.0 (1)
Z	4
Dx (g/cm ³)	7.41
$\mu(\text{mm}^{-1})(0.7107\text{Å})$	73.35
Appearance	Colorless needle
Crystal size (mm)	$0.21 \times 0.07 \times 0.02$
Data collection	
$\lambda(\text{Mo K}\alpha)(\text{Å})$	0.71073
Scan mode	ω and ϕ
$\theta(\text{min-max})(^\circ)$	1.4 – 30.8
R(int) (%)	5.5
Reciprocal space recording	$-11 \leq h \leq 11$
	$-7 \leq k \leq 7$
	$-40 \leq l \leq 40$
Refinement	
Meas., obs., / indep.all	40750,
(obs= $I > 3\sigma(I)$)	2792 / 4020
No. of Refined parameters	191
Refinement method	F
R1(F ²)(obs)/	2.39/ 4.27
R1(F ²)(all) (%)	
wR2(F ²)(obs)	2.51/2.83
/wR2(F ²)(all) (%)	
GOF(obs) / GOF(all)	1.20/1.12
$\Delta\rho_{\text{max}} / \Delta\rho_{\text{min}}$ (e Å ⁻³)	2.39/−1.92
Extinction coefficient	0.0386 (8)

Table S 22. Fractional atomic coordinates and isotropic or equivalent isotropic displacement parameters (\AA^2) of $\text{KBi}_5\text{O}_5(\text{AsO}_4)_2$

	<i>x</i>	<i>y</i>	<i>z</i>	$U_{\text{iso}}^*/U_{\text{eq}}$
Bi1	0.24383 (3)	0.73592 (5)	0.18275 (1)	0.01088 (7)
Bi2	0.01469 (3)	0.75201 (5)	0.069959 (9)	0.01071 (7)
Bi3	0.15578 (3)	1.22992 (5)	0.267340 (9)	0.01110 (7)
Bi4	0.59501 (3)	−0.23975 (5)	0.099488 (9)	0.01085 (7)
Bi5	−0.02843 (3)	1.24113 (5)	0.143865 (9)	0.01162 (7)
As1	0.54566 (8)	0.2469 (1)	0.18744 (3)	0.0091 (2)
As2	0.74125 (9)	0.2738 (1)	0.02520 (3)	0.0115 (2)
K1	0.3188 (2)	0.2525 (3)	0.05658 (6)	0.0202 (5)
O1	0.7316 (6)	0.2452 (8)	−0.0340 (2)	0.016 (2)
O2	0.9355 (7)	0.246 (1)	0.0493 (2)	0.031 (2)
O3	0.8366 (6)	−0.2313 (9)	0.1251 (2)	0.020 (2)
O4	0.5557 (6)	−0.0515 (8)	0.1747 (2)	0.021 (2)
O5	0.1465 (6)	0.9912 (8)	0.1188 (2)	0.010 (2)
O6	0.6763 (7)	0.5534 (9)	0.0363 (2)	0.027 (2)
O7	0.6233 (7)	0.070 (1)	0.0474 (2)	0.031 (2)
O8	0.1424 (6)	0.5087 (8)	0.1198 (2)	0.012 (2)
O9	0.3713 (6)	0.312 (1)	0.2104 (2)	0.025 (2)
O10	0.7135 (6)	0.3184 (9)	0.2245 (2)	0.023 (2)
O11	0.5504 (7)	0.400 (1)	0.1362 (2)	0.029 (2)
O12	0.0536 (6)	0.5017 (8)	0.2085 (2)	0.010 (1)
O13	0.0626 (6)	1.0086 (8)	0.2067 (2)	0.010 (1)

Table S 23. Atomic displacement parameters (\AA^2) of $\text{KBi}_5\text{O}_5(\text{AsO}_4)_2$

	U^{11}	U^{22}	U^{33}	U^{12}	U^{13}	U^{23}
Bi1	0.0094 (1)	0.0120 (1)	0.0116 (1)	−0.0007 (1)	0.00270 (9)	0.0003 (1)
Bi2	0.0116 (1)	0.0119 (1)	0.0087 (1)	−0.0003 (1)	0.00131 (9)	0.0000 (1)
Bi3	0.0119 (1)	0.0111 (1)	0.0100 (1)	−0.0013 (1)	−0.00024 (9)	−0.0006 (1)
Bi4	0.0097 (1)	0.0130 (1)	0.0100 (1)	−0.0007 (1)	0.00173 (9)	0.0004 (1)
Bi5	0.0112 (1)	0.0121 (1)	0.0115 (1)	0.0004 (1)	0.00118 (9)	0.0012 (1)
As1	0.0089 (3)	0.0100 (3)	0.0086 (3)	−0.0011 (3)	0.0013 (2)	−0.0008 (3)
As2	0.0147 (3)	0.0116 (3)	0.0081 (3)	0.0007 (3)	0.0012 (3)	−0.0011 (3)
K1	0.0222 (8)	0.0151 (7)	0.0229 (9)	−0.0015 (7)	0.0012 (7)	0.0044 (7)
O1	0.018 (3)	0.024 (3)	0.008 (3)	0.003 (2)	0.003 (2)	−0.002 (2)
O2	0.024 (3)	0.047 (4)	0.022 (3)	0.006 (3)	−0.002 (3)	−0.004 (3)
O3	0.009 (2)	0.033 (3)	0.018 (3)	0.007 (2)	0.000 (2)	−0.003 (3)
O4	0.026 (3)	0.013 (3)	0.023 (3)	−0.006 (2)	0.008 (3)	−0.007 (2)
O5	0.010 (3)	0.010 (2)	0.011 (3)	−0.003 (2)	0.002 (2)	0.001 (2)
O6	0.044 (4)	0.019 (3)	0.018 (3)	0.013 (3)	0.004 (3)	−0.006 (2)
O7	0.036 (4)	0.029 (3)	0.029 (4)	−0.010 (3)	0.009 (3)	0.010 (3)
O8	0.020 (3)	0.006 (2)	0.010 (3)	−0.001 (2)	0.001 (2)	0.000 (2)
O9	0.012 (3)	0.033 (3)	0.032 (4)	0.009 (2)	0.010 (2)	0.000 (3)
O10	0.023 (3)	0.023 (3)	0.021 (3)	−0.006 (2)	−0.008 (2)	−0.001 (2)
O11	0.045 (4)	0.028 (3)	0.013 (3)	−0.011 (3)	0.002 (3)	0.011 (3)
O12	0.013 (2)	0.007 (2)	0.009 (3)	0.001 (2)	0.001 (2)	−0.003 (2)
O13	0.010 (2)	0.009 (2)	0.010 (3)	0.003 (2)	0.000 (2)	−0.003 (2)

Table S 24. Selected interatomic distances ($d_{\max}=3\text{\AA}$)

Atom 1	Atom 2	d (Å)	Atom 1	Atom 2	d (Å)
Bi1	O12	2.2185(51)	As1	O9	1.6794(54)
	O8	2.2745(51)		O11	1.6886(57)
	O13	2.2788(50)		O4	1.6963(45)
	O5	2.3756(51)		O10	1.6978(50)
	O9	2.6589(54)	As2	O7	1.6575(58)
	O10	2.6612(56)		O6	1.6798(52)
	O4	2.8612(50)		O1	1.6827(57)
Bi2	O5	2.1336(49)	K1	O2	1.6839(56)
	O8	2.1503(49)		O7	2.7463(61)
	O3	2.2580(56)		O5	2.7860(56)
	O1	2.4229(54)		O8	2.8107(56)
	O2	2.8607(55)		O1	2.8519(48)
	O2	2.9244(55)		O6	2.8532(59)
Bi3	O13	2.1882(51)		O1	2.8766(48)
	O12	2.3025(51)		O11	2.9227(57)
	O12	2.3411(50)			
	O10	2.5228(50)			
	O13	2.5399(50)			
	O9	2.5655(56)			
Bi4	O3	2.0512(49)			
	O6	2.2878(57)			
	O7	2.2936(57)			
	O11	2.2992(56)			
	O4	2.4291(55)			
Bi5	O5	2.1729(50)			
	O8	2.2028(50)			
	O13	2.2655(51)			
	O12	2.3783(51)			
	O2	2.6719(57)			
	O3	2.8729(50)			

6) n = 5 ribbons: $\text{Bi}_6\text{ZnO}_7(\text{AsO}_4)_2$ versus $\text{Bi}_6\text{ZnO}_7(\text{PO}_4)_2$
Table S 25. Crystal data, measurement and structural refinement parameters of $\text{Bi}_6\text{ZnO}_7(\text{AsO}_4)_2$ and $\text{Bi}_6\text{ZnO}_7(\text{PO}_4)_2$

	Bi₆ZnO₇(AsO₄)	Bi₆ZnO₇(PO₄)₂
	2	
Crystal data		
Crystal symmetry	Monoclinic	Monoclinic
space group	<i>C2/c</i>	<i>I2</i>
a (Å)	34.442 (7)	19.7271(5)
b (Å)	5.5044 (11)	5.4376(2)
c (Å)	15.292 (3)	16.9730(6)
β (°)	100.625(9)	131.932(1)
V (Å ³)	2849.4 (10)	1354.46(8)
Z	8	4
Dx (g/cm ³)	7.966	7.950
μ(mm ⁻¹)(0.7107Å)	80.18	79.727
Appearance	Colorless needle	Pale green
Crystal size (mm)	0.12 × 0.06 × 0.04	0.006 × 0.029 × 0.144
Data collection		
λ(Mo Kα)(Å)	0.71073	0.71073
Scan mode	ω and φ	
θ(min–max)(°)	2.7 – 26.5	1 – 27.48
R(int) (%)	5.9	7.4
Reciprocal space recording	–42 ≤ h ≤ 42 –6 ≤ k ≤ 6 –19 ≤ l ≤ 19	–20 ≤ h ≤ 25 –7 ≤ k ≤ 7 –21 ≤ l ≤ 21
Refinement		
Meas., obs., / indep.all (obs=I>3σ(I))	30313, 2676/2921	3011/3011
No. of Refined parameters	143	134
Refinement method	F	F ²
R1(F ²)(obs)/ R1(F ²)(all) (%)	3.18/ 3.48	3.85/3.85
wR2(F ²)(obs) /wR2(F ²)(all) (%)	4.05/4.14	10.23/10.23
GOF(obs) / GOF(all)	1.93/1.88	1.098
Δρ _{max} / Δρ _{min} (e Å ⁻³)	3.68/–2.89	5.531/-3.038
Extinction coefficient	0.0191 (15)	0.00022(2)

Table S 26. Fractional atomic coordinates and isotropic or equivalent isotropic displacement parameters (\AA^2) $\text{Bi}_6\text{ZnO}_7(\text{AsO}_4)_2$

	x	y	z	$U_{\text{iso}}^*/U_{\text{eq}}$
Bi1	0.699626 (12)	0.26678 (7)	0.43129 (3)	0.00614 (14)
Bi2	0.544080 (12)	−0.22065 (7)	0.20022 (3)	0.00679 (14)
Bi3	0.691856 (12)	0.78560 (7)	0.23876 (3)	0.00702 (14)
Bi4	0.537430 (12)	0.27779 (7)	0.35607 (3)	0.00716 (14)
Bi5	0.621934 (12)	0.31527 (7)	0.23033 (3)	0.00703 (14)
Bi6	0.625160 (12)	−0.18368 (7)	0.40483 (3)	0.00640 (14)
As1	0.78513 (3)	−0.24888 (17)	0.39879 (8)	0.0060 (3)
Oas11	0.7671 (3)	−0.5059 (14)	0.4300 (6)	0.025 (2)*
Oas12	0.7492 (2)	−0.0676 (14)	0.3462 (5)	0.0207 (19)*
Oas13	0.8155 (2)	−0.3301 (12)	0.3281 (5)	0.0171 (18)*
Oas14	0.8138 (2)	−0.1004 (13)	0.4843 (5)	0.0185 (18)*
As2	0.54851 (4)	0.74776 (17)	0.51925 (7)	0.0052 (3)
Oas21	0.5428 (3)	0.7334 (12)	0.6238 (6)	0.0184 (19)*
Oas22	0.5778 (2)	0.5144 (13)	0.4957 (5)	0.0175 (18)*
Oas23	0.5766 (2)	0.9922 (13)	0.5049 (5)	0.0197 (18)*
Oas24	0.5080 (3)	0.7489 (13)	0.4408 (7)	0.027 (2)*
Zn1	0.61410 (4)	0.2631 (2)	0.55152 (9)	0.0083 (4)
O1	0.5793 (2)	0.0119 (12)	0.3111 (5)	0.0082 (15)*
O2	0.6295 (2)	0.3143 (13)	0.6741 (5)	0.0147 (17)*
O3	0.5794 (2)	0.5068 (12)	0.2965 (4)	0.0078 (15)*
O4	0.5	−0.4526 (16)	0.25	0.007 (2)*
O5	0.5	0.0258 (16)	0.25	0.008 (2)*
O6	0.6669 (2)	0.4944 (12)	0.3268 (5)	0.0130 (17)*
O7	0.6645 (2)	−0.0051 (12)	0.3249 (5)	0.0082 (15)*
O8	0.6457 (2)	0.1567 (12)	0.4679 (5)	0.0117 (16)*

Table S 27. Atomic displacement parameters (\AA^2) of $\text{Bi}_6\text{ZnO}_7(\text{AsO}_4)_2$

	U^{11}	U^{22}	U^{33}	U^{12}	U^{13}	U^{23}
Bi1	0.0007 (2)	0.0101 (2)	0.0071 (2)	−0.00026 (14)	−0.00083 (18)	0.00136 (14)
Bi2	0.0020 (2)	0.0114 (2)	0.0070 (2)	−0.00034 (14)	0.00120 (18)	0.00034 (14)
Bi3	0.0034 (2)	0.0110 (2)	0.0072 (2)	0.00156 (14)	0.00211 (18)	−0.00115 (14)
Bi4	0.0035 (3)	0.0118 (2)	0.0058 (2)	−0.00085 (14)	−0.00024 (19)	−0.00014 (14)
Bi5	0.0035 (2)	0.0107 (2)	0.0064 (2)	0.00049 (14)	−0.00037 (18)	−0.00120 (14)
Bi6	0.0021 (2)	0.0097 (2)	0.0071 (2)	−0.00101 (14)	0.00005 (17)	0.00057 (14)
As1	0.0014 (6)	0.0108 (5)	0.0055 (6)	−0.0013 (4)	−0.0005 (5)	−0.0016 (4)
As2	0.0005 (6)	0.0103 (5)	0.0045 (6)	−0.0010 (4)	−0.0005 (5)	0.0001 (4)
Zn1	0.0087 (7)	0.0113 (6)	0.0050 (7)	0.0018 (5)	0.0014 (6)	−0.0020 (5)

7) Phase homology in new layered mixed Li, M (M = Cu, Cd, Bi...) bismuth oxophosphates and oxoarsenates: $(\text{Bi}_7\text{O}_7)(\text{BiO})_7\text{CdLi}_2(\text{PO}_4)_6$ and $[\text{Bi}_4\text{O}_4][\text{BiO}]_4\text{CuLi}_2(\text{AsO}_4)_4$

Table S 28. Crystallographic data and refinement parameters for $[\text{Bi}_7\text{O}_7][\text{BiO}]_7\text{CdLi}_2(\text{PO}_4)_6$ and $[\text{Bi}_4\text{O}_4][\text{BiO}]_4\text{CuLi}_2(\text{AsO}_4)_4$.

Crystal Data		
Compound	$[\text{Bi}_7\text{O}_7][\text{BiO}]_7\text{CdLi}_2(\text{PO}_4)_6$	$[\text{Bi}_4\text{O}_4][\text{BiO}]_4\text{CuLi}_2(\text{AsO}_4)_4$
Space group	$C2/m$	$P2_1/c$
Unit cell (\AA)	a= 26.923 (2) b= 5.2926(5) c= 12.3024(10) β = 106.45(5) $^\circ$	a= 8.8133 (4) b= 24.3456(10) c= 5.4056(2) β = 106.93(2) $^\circ$
Volume (\AA^3)	1681.30 (27)	1109.58 (11)
Z	2	4
Mw, calculated density (g/cm^3)	3845.9	1216.5
F(000)	3219	2046
Data collection		
Equipment		Bruker X8
λ (MoK α) (Angstrom)		0.71069
Scan mode		ω/ρ -scan
θ min-max ($^\circ$)	1.58/33.40	2.42/39.5
Recording reciprocal space	$-41 \leq h \leq 41$ $-8 \leq k \leq 8$ $-19 \leq l \leq 19$	$-14 \leq h \leq 15$ $-40 \leq k \leq 42$ $-8 \leq l \leq 9$
Number of measured reflections	26764	36759
Number of independent reflections	3564	6161
μ (cm^{-1})	79.00	74.49
Absorption correction		Multiscan (Sadabs)
Transmission Tmin/Tmax	0.393	0.369
R merging factor (%)	9.09	4.13
Refinement parameters		
Software, refinement type		Jana 2006, L.S. on F
Number of refined parameters	124	147
$R_1(F)(\%)$, $[I > 3\sigma(I)]$	4.56 / 6.59	3.14 / 4.97
$wR_2(F^2)(\%)$, $[I > 3\sigma(I)]$	7.91 / 9.65	3.52 / 6.07
Goodness of fit	0.87	1.69
Max/Min $\Delta\rho$ e/ (\AA^3)	3.75/-3.01	2.86/-2.54

Table S 29. Atomic coordinates and displacement parameters (\AA^2) for $[\text{Bi}_7\text{O}_7][\text{BiO}]_7\text{CdLi}_2(\text{PO}_4)_6$

Atom	Site	x	y	z	U_{eq}
Bi(1)	4i	0.06691(2)	0	0.10142(6)	0.0124(2)
Bi(2)	4i	0.02988(3)	$\frac{1}{2}$	-0.11796(6)	0.0109(2)
Bi(3)	4i	0.13667(3)	0	-0.12385(6)	0.0109(2)
Bi(4)	4i	0.16106(3)	$-\frac{1}{2}$	0.08944(6)	0.00926(19)
Bi(5)	4i	0.23980(3)	$-\frac{1}{2}$	-0.11383(6)	0.0128(2)
Bi(6)	4i	0.39092(3)	-1	0.63873(7)	0.0262(3)
Bi(7)	4i	0.28220(3)	$-\frac{1}{2}$	0.36926(7)	0.0297(3)
O(1)	4g	0	0.256(3)	0	0.012(2)
O(2)	4i	-0.9222(10)	$\frac{1}{2}$	-0.811(2)	0.094(11)
O(3)	8j	0.5982(3)	-0.7485(19)	-0.0231(8)	0.012(2)
O(4)	8j	0.6975(3)	0.2545(19)	-0.0140(8)	0.012(3)
O(5)	4i	0.2667(9)	$-\frac{1}{2}$	0.195(2)	0.094(11)
Cd(1t)	2d	$\frac{1}{2}$	0	0.5	0.0132(5)
Li(1)	4i	0.0804(12)	0	0.555(3)	0.010(6)
P(1)	4i	0.3722(2)	0	0.3407(5)	0.0195(16)
O(p1a)	8j	0.3572(7)	0.234(4)	0.3811(16)	0.072(5)
O(p1b)	4i	0.3733(16)	0	0.230(4)	0.119(14)
O(p1c)	4i	0.428(2)	0	0.420(6)	0.23(3)
P(2)	4i	0.8113(2)	0	-0.3162(5)	0.0249(18)
O(p2a)	4i	0.8583(9)	0	-0.359(3)	0.107(12)
O(p2b)	8j	0.7786(4)	-0.22673(9)	-0.3617(17)	0.54(6)
O(p2c)	4i	0.6729(6)	$-\frac{1}{2}$	0.1840(13)	0.017(3)
P(3)	4i	0.0099(2)	0	0.3300(5)	0.0177(15)
O(p3a)	8j	0.0366(7)	0.234(4)	0.3824(15)	0.068(5)
O(p3b)	4i	-0.0371(14)	0	0.372(5)	0.19(2)
O(p3c)	4i	-0.0095(9)	0	0.203(2)	0.052(6)

Table S 30. Displacement parameters (\AA^2) for $[\text{Bi}_7\text{O}_7][\text{BiO}]_7\text{CdLi}_2(\text{PO}_4)_6$

Atom	U_{11}	U_{22}	U_{33}	U_{12}	U_{13}	U_{23}
Bi(1)	0.0056(3)	0.0229(4)	0.0086(3)	0	0.0019(2)	0
Bi(2)	0.0137(3)	0.0126(3)	0.0067(3)	0	0.0036(2)	0
Bi(3)	0.0110(3)	0.0137(3)	0.0068(3)	0	0.0009(2)	0
Bi(4)	0.0095(3)	0.0114(3)	0.0082(3)	0	0.0046(2)	0
Bi(5)	0.0062(3)	0.0251(4)	0.0076(3)	0	0.0027(2)	0
Bi(6)	0.0156(4)	0.0574(6)	0.0051(3)	0	0.0020(3)	0
Bi(7)	0.0168(4)	0.0652(7)	0.0056(4)	0	0.0007(3)	0
O(1)	0.005(3)	0.019(4)	0.011(4)	0	0.000(3)	0
O(2)	0.036(9)	0.23(3)	0.023(9)	0	0.012(7)	0
O(3)	0.005(3)	0.019(4)	0.011(4)	0	0.000(3)	0
O(4)	0.004(3)	0.018(5)	0.013(4)	0.004(3)	-0.002(3)	0.007(3)
O(5)	0.036(9)	0.23(3)	0.023(9)	0	0.012(7)	0
Cd(1t)	0.0146(8)	0.0210(9)	0.0063(8)	0	0.0065(6)	0
P(1)	0.023(3)	0.021(2)	0.010(2)	0	-0.0029(19)	0
P(2)	0.016(2)	0.054(4)	0.005(2)	0	0.0035(18)	0
P(3)	0.021(2)	0.021(2)	0.011(2)	0	0.0039(19)	0

Table S 31. Selected bond distances (\AA) in $[\text{Bi}_7\text{O}_7][\text{BiO}]_7\text{CdLi}_2(\text{PO}_4)_6$

Bi(1)-O(1)	$2.318(8) \times 2$	Li-O(p3b)	$1.66(7)$
Bi(1)-O(2)	$2.349(10) \times 2$	Li-O(p1a)	$2.162(2) \times 2$
Bi(2)-O(1)	$2.253(8) \times 2$	Li-O(p3a)	$2.45(6) \times 2$
Bi(2)-O(3)	$2.303(9) \times 2$	Li-O(p1c)	$2.68(3) \times 2$
Bi(3)-O(3)	$2.250(10) \times 2$		
Bi(3)-O(4)	$2.224(8) \times 2$	P(1)-O(p1b)	$1.37(5)$
Bi(4)-O(3)	$2.285(9) \times 2$	P(1)-O(p1a)	$1.43(2) \times 2$
Bi(4)-O(4)	$2.260(10) \times 2$	P(1)-O(p1c)	$1.54(6)$
Bi(5)-O(4)	$2.326(10) \times 2$		
Bi(5)-O(4)	$2.346(8) \times 2$	P(2)-O(p2a)	$1.50(3)$
Bi(6)-O(2)	$2.05(2)$	P(2)-O(p2b)	$1.500(7) \times 2$
Bi(7)-O(5)	$2.07(2)$	P(2)-O(p2c)	$1.5060(17)$
Cd(1)-O(p1c)	$1.91(6) \times 2$	P(3)-O(p3a)	$1.485(19) \times 2$
Cd(1)-O(p3a)	$2.41(6) \times 4$	P(3)-O(p3b)	$1.50(5)$
		P(3)-O(p3c)	$1.50(3)$

Table S 32. Atomic coordinates and displacement parameters (\AA^2) for $[\text{Bi}_4\text{O}_4][\text{BiO}]_4\text{Cu}_1\text{Li}_2(\text{AsO}_4)_4$

Atom	Site	x	y	z	U_{eq}
Bi(1)	4e	0.58848(5)	0.195489(16)	0.00244(8)	0.00742(9)
Bi(2)	4e	0.59534(5)	0.073591(16)	-0.51411(8)	0.00814(9)
Bi(3)	4e	0.25785(5)	0.197776(16)	0.29787(8)	0.00800(9)
Bi(4)	4e	0.92503(5)	0.300926(16)	0.13221(8)	0.00818(9)
As(1)	4e	0.28791(13)	0.08464(5)	-0.1383(2)	0.0068(2)
As(2)	4e	0.89642(13)	0.09062(5)	0.1165(2)	0.0077(3)
Cu(1)	2a	0	0	-1/4	0.0128(5)
O(1)	4e	0.4110(10)	0.2433(4)	0.1100(19)	0.011(2)
O(2)	4e	0.0924(10)	0.2489(3)	0.0119(17)	0.0085(19)
O(3)	4e	0.5781(16)	0.1515(4)	-0.648(2)	0.019(3)
O(4)	4e	0.7701(9)	0.2416(4)	0.2836(16)	0.0082(18)
O(a1a)	4e	0.4325(14)	0.1013(5)	-0.270(3)	0.022(3)
O(a1b)	4e	0.3636(12)	0.0541(4)	0.1514(19)	0.015(2)
O(a1c)	4e	0.1752(12)	0.0364(4)	-0.3356(19)	0.013(2)
O(a1d)	4e	0.1989(13)	0.1442(4)	-0.1111(18)	0.014(2)
O(a2a)	4e	0.7878(14)	0.0542(5)	0.271(3)	0.021(3)
O(a2b)	4e	0.7772(13)	0.1155(5)	-0.165(3)	0.022(3)
O(a2c)	4e	0.0260(11)	0.0470(4)	0.049(2)	0.013(2)
O(a2c)	4e	0.9867(13)	0.1435(5)	0.285(2)	0.018(3)
Li(1)	4e	0.212(2)	0.0250(10)	0.328(4)	0.007(5)

Table S 33. Displacement parameters (\AA^2) for $[\text{Bi}_4\text{O}_4][\text{BiO}]_4\text{Cu}_7\text{Li}_2(\text{AsO}_4)_4$

Atom	U_{11}	U_{22}	U_{33}	U_{12}	U_{13}	U_{23}
Bi(1)	0.00599(13)	0.00750(14)	0.00863(14)	0.00047(10)	0.00191(11)	-0.00056(11)
Bi(2)	0.00854(14)	0.00640(14)	0.00935(15)	0.00008(10)	0.00240(11)	0.00090(11)
Bi(3)	0.00799(14)	0.00770(14)	0.00758(14)	-0.00035(10)	0.00112(11)	0.00136(11)
Bi(4)	0.00869(14)	0.00761(14)	0.00938(15)	0.00016(11)	0.00444(11)	-0.00095(11)
As(1)	0.0065(4)	0.0058(4)	0.0085(4)	-0.0011(3)	0.0028(3)	-0.0020(3)
As(2)	0.0068(4)	0.0057(4)	0.0114(4)	-0.0006(3)	0.0039(3)	-0.0013(3)
Cu(1)	0.0111(8)	0.0116(8)	0.0180(9)	-0.0058(6)	0.0078(7)	-0.0089(7)
O(a1a)	0.017(4)	0.029(6)	0.028(6)	-0.008(4)	0.018(4)	-0.011(5)
O(a1b)	0.014(3)	0.014(3)	0.012(2)	-0.006(2)	0.003(2)	-0.001(2)
O(a1c)	0.014(3)	0.014(3)	0.012(2)	-0.006(2)	0.003(2)	-0.001(2)
O(a1d)	0.022(4)	0.011(3)	0.010(3)	0.008(3)	0.003(3)	-0.001(3)
O(a2a)	0.023(5)	0.017(4)	0.034(6)	-0.003(4)	0.025(5)	0.002(4)
O(a2b)	0.015(4)	0.016(4)	0.030(6)	0.005(3)	-0.002(4)	0.010(4)
O(a2c)	0.009(3)	0.014(4)	0.018(4)	0.001(3)	0.008(3)	-0.005(3)
O(a2d)	0.014(4)	0.018(4)	0.024(5)	0.000(3)	0.008(4)	-0.006(4)

Table S 34. Selected bond distances (\AA) in $(\text{Bi}_4\text{O}_4)(\text{BiO})_4\text{Cu}_7\text{Li}_2(\text{AsO}_4)_4$

Bi(1)-O(1)	2.160(10)	As(2)-O(a2a)	1.692(15)
Bi(1)-O(1)	2.690(9)	As(2)-O(a2b)	1.687(12)
Bi(1)-O(3)	2.195(11)	As(2)-O(a2c)	1.678(11)
Bi(1)-O(4)	2.173(8)	As(2)-O(a2d)	1.644(11)
Bi(1)-O(4)	2.721(10)		
Bi(2)-O(3)	2.021(10)	Cu(1)-O(a2c)	1.641(11)
Bi(3)-O(1)	2.209(10)	Cu(1)-O(a2c)	1.933(11)
Bi(3)-O(1)	2.324(9)	Cu(1)-O(a1c)	1.951(11)
Bi(3)-O(2)	2.179(9)	Cu(1)-O(a2a)	2.318(11)
Bi(3)-O(9)	2.477(11)	Cu(1)-O(a1c)	2.487(11)
Bi(4)-O(2)	2.183(11)		
Bi(4)-O(2)	2.467(9)	Li(1)-O(a1b)	1.99(3)
Bi(4)-O(4)	2.236(8)	Li(1)-O(a1c)	1.96(3)
Bi(4)-O(4)	2.293(9)	Li(1)-O(a2a)	2.00(2)
		Li(1)-O(a2c)	1.95(2)
As(1)-O(a1a)	1.679(14)		
As(1)-O(a1b)	1.687(10)		
As(1)-O(a1c)	1.698(9)		
As(1)-O(a1d)	1.674(11)		

8) The new $[\text{PbBi}_2\text{O}_4][\text{Bi}_2\text{O}_2]\text{Cl}_2$ and $[\text{Pb}_m\text{Bi}_{10-m}\text{O}_{13}][\text{Bi}_2\text{O}_2]_m\text{Cl}_{4+m}$ series by association of sizeable subunits; Relationship with the Arppe's compound $\text{Bi}_{24}\text{O}_{31}\text{Cl}_{10}$

Table S 35. Fractional atomic coordinates and isotropic or equivalent isotropic displacement parameters (\AA^2) of $\text{Bi}_{24}\text{O}_{31}\text{Cl}_{10}$. CSD-number 425737

	<i>X</i>	<i>y</i>	<i>z</i>	$U_{\text{iso}}^*/U_{\text{eq}}$	Occ. (<1)
Bi1	0.20394 (2)	0	0.43412 (7)	0.0092 (2)	
Bi2	0.08556 (3)	0	0.59897 (8)	0.0113 (2)	
Bi3	0.17663 (3)	0.5	0.75147 (9)	0.0203 (3)	
Bi4a	−0.0342 (7)	0	0.7522 (10)	0.0156 (13)	0.5
Bi4b	−0.0346 (7)	0	0.7813 (10)	0.0156 (13)	0.5
Bi5a	−0.1516 (4)	0	0.9017 (9)	0.0205 (13)	0.487 (15)
Bi5b	−0.1568 (4)	0	0.9317 (10)	0.0205 (13)	0.513 (15)
Bi6	0.05899 (4)	0.5	0.91454 (10)	0.0341 (3)	
Cl1	0.5	0	0.5	0.022 (2)	
Cl2	0.61866 (18)	0	0.3420 (6)	0.0211 (16)	
Cl3	0.7388 (2)	0	0.1927 (7)	0.0279 (19)	
O1	0.1041 (5)	0.5	0.6935 (15)	0.014 (3)*	
O2	0.2776 (5)	0	0.4747 (14)	0.012 (3)*	
O3	0.0455 (5)	0	0.7796 (16)	0.018 (3)*	
O4	0.1624 (5)	0	0.6161 (15)	0.015 (3)*	
O5	−0.0175 (6)	0.5	0.8575 (19)	0.030 (4)*	
O6	−0.0828 (6)	0	0.9289 (17)	0.022 (4)*	
O7	−0.1493 (13)	0.5	1.018 (4)	0.061 (10)*	0.75
O8	−0.1527 (13)	0	1.134 (4)	0.064 (10)*	0.75
O9	0	0	1	0.034 (13)*	0.5

Table S 36. Atomic displacement parameters (\AA^2) of $\text{Bi}_{24}\text{O}_{31}\text{Cl}_{10}$

	U^{11}	U^{22}	U^{33}	U^{12}	U^{13}	U^{23}
Bi1	0.0072 (4)	0.0088 (4)	0.0115 (4)	0	−0.0017 (3)	0
Bi2	0.0108 (4)	0.0114 (4)	0.0115 (4)	0	0.0005 (3)	0
Bi3	0.0080 (4)	0.0365 (6)	0.0163 (4)	0	−0.0003 (3)	0
Bi4a	0.0129 (5)	0.0207 (5)	0.013 (4)	0	0.005 (3)	0
Bi4b	0.0129 (5)	0.0207 (5)	0.013 (4)	0	0.005 (3)	0
Bi5a	0.012 (2)	0.0372 (6)	0.012 (3)	0	−0.0025 (19)	0
Bi5b	0.012 (2)	0.0372 (6)	0.012 (3)	0	−0.0025 (19)	0
Bi6	0.0284 (5)	0.0485 (7)	0.0251 (5)	0	−0.0081 (4)	0

Table S 37. Bond lengths (Å) in $\text{Bi}_{24}\text{O}_{31}\text{Cl}_{10}$

Atom 1	Atom 2	d	Atom 1	Atom 2	d
Bi1 (Unit1)	1xO2	2.203(15)	Bi4b (Unit2)	1xO6	2.071(24)
	1xO4	2.217(16)		2xO5	2.182(10)
	2xO2	2.248(7)		1xO3	2.362(26)
	2xC13	3.309(6)		1xO9	2.404(13)
Bi2	2xC12	3.322(5)	Bi5a (Unit3)	2xC12	3.392(16)
	1xO3	2.181(16)		2xC11	3.612(10)
	2xO1	2.262(8)		1xO6	2.042(22)
	1xO4	2.269(15)		2xO7	2.302(21)
Bi3 (Unit3)	2xC11	3.3469(7)	Bi5b (Unit3)	1xO8	2.332(42)
	2xC12	3.410(5)		2xC12	3.308(9)
	1xO1	2.207(15)		2xC13	3.371(11)
	2xO8	2.405(23)		1xO8	2.032(42)
Bi4a (Unit2)	2xO4	2.437(9)	Bi6 (Unit2)	2xO7	2.175(17)
	1xO7	2.463(41)		1xO6	2.183(22)
	1xO2	2.661(15)		2xC13	3.352(11)
	2xC13	3.228(5)		2xC12	3.585(10)
Bi4a (Unit2)	2xO5	2.297(12)	Bi6 (Unit2)	1xO5	2.317(18)
	1xO6	2.299(24)		2xO3	2.431(10)
	1xO3	2.361(26)		1xO1	2.606(16)
	1xO9	2.667(12)		1xO5	2.613(19)
Bi4a (Unit2)	2xC12	3.309(17)	Bi6 (Unit2)	2xO6	2.619(12)
	2xC11	3.384(10)		1xO7	2.736(39)
				2xO9	2.7838(8)

Table S 38. Fractional atomic coordinates and isotropic or equivalent isotropic displacement parameters (\AA^2) of $[\text{Bi}_3\text{Pb}_2\text{O}_{13}][\text{Bi}_2\text{O}_2]_2\text{Cl}_6$ $m=2$. CSD-number 425738

	x	y	z	$U_{\text{iso}}^*/U_{\text{eq}}$	Occ. (<1)
Bi1	0.45636 (2)	0	0.34693 (5)	0.01061 (17)	
Bi2	0.35618 (2)	0	0.49121 (5)	0.01138 (17)	
Bi3	0.24923 (2)	0.5	0.37219 (5)	0.01091 (17)	
Bi4a	0.56033 (9)	0	0.20589 (16)	0.0137 (5)	0.7813
Bi4b	0.5531 (3)	0	0.1761 (5)	0.0164 (17)	0.2187
Bi5	0.35048 (2)	0.5	0.21520 (6)	0.0208 (2)	
Bi6a	0.66027 (17)	0	0.0813 (3)	0.0107 (8)	0.4126
Bi6b	0.66284 (14)	0	0.0554 (3)	0.0260 (7)	0.5874
Pb7	0.45087 (3)	0.5	0.07559 (7)	0.0289 (3)	
Cl1	0.26008 (18)	0	0.1782 (5)	0.0269 (15)	
Cl2	0.15415 (16)	0	0.2915 (4)	0.0216 (14)	
Cl3	0.05099 (17)	0	0.4295 (4)	0.0232 (14)	
O1	0.3787 (5)	0	0.3354 (13)	0.022 (3)*	
O2	0.4287 (4)	0.5	0.2641 (11)	0.013 (2)*	
O3	0.3255 (5)	0.5	0.4121 (11)	0.015 (2)*	
O4	0.2731 (4)	0	0.4625 (11)	0.012 (2)*	
O5	0.5899 (5)	0	0.0591 (13)	0.024 (3)*	
O6	0.5318 (6)	0.5	0.1204 (14)	0.028 (3)*	
O7	0.4783 (5)	0	0.1913 (13)	0.022 (3)*	
O8	0.6480 (12)	0.5	−0.022 (3)	0.055 (8)*	0.75
O9	0.6373 (11)	1	−0.120 (3)	0.053 (8)*	0.75

Table S 39. Atomic displacement parameters (\AA^2) of $[\text{Bi}_8\text{Pb}_2\text{O}_{13}][\text{Bi}_2\text{O}_2]_2\text{Cl}_6$ $m=2$

	U^{11}	U^{22}	U^{33}	U^{12}	U^{13}	U^{23}
Bi1	0.0116 (3)	0.0106 (3)	0.0107 (3)	0	0.0050 (2)	0
Bi2	0.0121 (3)	0.0111 (3)	0.0115 (3)	0	0.0045 (2)	0
Bi3	0.0097 (3)	0.0113 (3)	0.0128 (3)	0	0.0051 (2)	0
Bi4a	0.0124 (8)	0.0156 (5)	0.0115 (9)	0	0.0015 (7)	0
Bi4b	0.005 (2)	0.034 (2)	0.008 (3)	0	-0.001 (2)	0
Bi5	0.0093 (3)	0.0323 (4)	0.0212 (3)	0	0.0053 (2)	0
Bi6a	0.0105 (9)	0.0111 (9)	0.0118 (15)	0	0.0051 (10)	0
Bi6b	0.0126 (8)	0.0488 (13)	0.0174 (14)	0	0.0056 (9)	0
Pb7	0.0212 (4)	0.0371 (5)	0.0243 (4)	0	0.0006 (3)	0
Cl1	0.020 (2)	0.030 (3)	0.030 (2)	0	0.0071 (19)	0
Cl2	0.0163 (19)	0.025 (2)	0.024 (2)	0	0.0073 (17)	0
Cl3	0.020 (2)	0.030 (3)	0.020 (2)	0	0.0059 (17)	0

Table S 40. Bond lengths (\AA) of $[\text{Bi}_8\text{Pb}_2\text{O}_{13}][\text{Bi}_2\text{O}_2]_2\text{Cl}_6$ $m=2$

Atom 1	Atom 2	d	Atom 1	Atom 2	d
Bi1	1xO7	2.192(18)	Bi5	1xO2	2.216(12)
	1xO1	2.266(16)		1xO8	2.380(39)
	2xO2	2.267(6)		2xO9	2.384(22)
	2xCl3	3.337(4)		2xO1	2.463(9)
	2xCl3	3.441(5)		1xO3	2.728(16)
Bi2 (Unit2)	1xO1	2.203(18)	Bi6a (Unit3)	2xCl1	3.257(5)
	2xO3	2.275(6)		1xO5	2.023(16)
	1xO4	2.383(12)		2xO8	2.323(19)
	2xCl3	3.296(4)		1xO9	2.352(36)
	2xCl2	3.407(5)		2xCl2	3.299(6)
Bi3 (Unit1)	1xO3	2.167(15)	Bi6b (Unit3)	2xCl1	3.465(6)
	2xO4	2.279(6)		1xO9	2.052(35)
	1xO4	2.312(15)		1xO5	2.178(17)
	2xCl1	3.186(6)		2xO8	2.186(14)
	2xCl2	3.346(4)		2xCl1	3.452(5)
Bi4a (Unit2)	1xO5	2.225(18)	Pb7 (Unit2)	2xCl2	3.580(6)
	2xO6	2.285(8)		1xO6	2.297(18)
	1xO7	2.386(16)		2xO7	2.432(8)
	2xCl2	3.322(5)		1xO2	2.584(15)
	2xCl3	3.460(5)		1xO6	2.602(19)
Bi4b (Unit2)	1xO5	2.046(20)		2xO5	2.631(9)
	2xO6	2.132(6)		1xO8	2.807(35)
	1xO7	2.282(19)			
	2xCl2	3.518(8)			
	2xCl3	3.700(8)			

Table S 41. Fractional atomic coordinates and isotropic or equivalent isotropic displacement parameters (\AA^2) of $[\text{Bi}_7\text{Pb}_3\text{O}_{13}][\text{Bi}_2\text{O}_2]_3\text{Cl}_7$ $m=3$. CSD-number 425739

	<i>x</i>	<i>y</i>	<i>z</i>	$U_{\text{iso}}^*/U_{\text{eq}}$	Occ. (<1)
Bi1	0.60014 (4)	0	0.06978 (8)	0.0072 (4)	
Bi2	0.51320 (4)	0	0.19680 (8)	0.0077 (4)	
Bi3	0.71698 (4)	0.5	0.17155 (8)	0.0079 (4)	
Bi4	0.31017 (4)	0	0.05619 (8)	0.0104 (5)	
Bi5	0.42307 (5)	0	0.32117 (9)	0.0146 (5)	
Bi6	0.63107 (4)	0.5	0.31271 (9)	0.0172 (5)	
Pb7	0.33245 (5)	0	0.43895 (11)	0.0268 (6)	0.5
Bi7	0.33245 (5)	0	0.43895 (11)	0.0268 (6)	0.5
Pb8	0.54322 (5)	0.5	0.43538 (9)	0.0209 (5)	
Cl1	0.7247 (3)	0	0.3445 (6)	0.023 (3)	
Cl2	0.8186 (3)	0	0.2391 (6)	0.016 (3)	
Cl3	0	0	0	0.022 (5)	
Cl4	0.9120 (3)	0	0.1257 (6)	0.017 (3)	
O1	0.5910 (8)	0	0.2038 (16)	0.016 (5)*	
O2	0.6367 (7)	0.5	0.1367 (14)	0.007 (4)*	
O3	0.5504 (7)	0.5	0.2728 (15)	0.009 (4)*	
O4	0.3175 (8)	0	−0.0920 (15)	0.010 (4)*	
O5	0.7276 (8)	0.5	0.0309 (15)	0.011 (4)*	
O6	0.5044 (8)	0	0.3350 (16)	0.018 (5)*	
O7	0.4048 (8)	0	0.4457 (16)	0.014 (5)*	
O8	0.4596 (8)	0.5	0.3979 (16)	0.018 (5)*	
O9	0.3547 (18)	0.5	0.520 (4)	0.063 (13)*	0.75
O10	0.3724 (14)	0	0.600 (3)	0.036 (9)*	0.75

Table S 42. Atomic displacement parameters (\AA^2) of $[\text{Bi}_7\text{Pb}_3\text{O}_{13}][\text{Bi}_2\text{O}_2]_3\text{Cl}_7$ $m=3$

	U^{11}	U^{22}	U^{33}	U^{12}	U^{13}	U^{23}
Bi1	0.0078 (6)	0.0086 (6)	0.0023 (6)	0	0.0001 (5)	0
Bi2	0.0101 (6)	0.0081 (6)	0.0025 (6)	0	0.0011 (5)	0
Bi3	0.0082 (6)	0.0085 (6)	0.0041 (6)	0	0.0006 (5)	0
Bi4	0.0129 (6)	0.0109 (6)	0.0082 (6)	0	0.0056 (5)	0
Bi5	0.0140 (6)	0.0163 (6)	0.0134 (6)	0	0.0065 (5)	0
Bi6	0.0077 (6)	0.0303 (8)	0.0118 (6)	0	0.0031 (5)	0
Pb7	0.0096 (6)	0.0270 (8)	0.0331 (8)	0	0.0015 (6)	0
Bi7	0.0096 (6)	0.0270 (8)	0.0331 (8)	0	0.0015 (6)	0
Pb8	0.0165 (7)	0.0246 (7)	0.0136 (7)	0	0.0005 (6)	0
Cl1	0.023 (4)	0.026 (5)	0.018 (4)	0	0.007 (4)	0
Cl2	0.012 (4)	0.017 (4)	0.020 (4)	0	0.007 (4)	0
Cl3	0.017 (6)	0.030 (7)	0.020 (6)	0	0.009 (5)	0
Cl4	0.017 (4)	0.016 (4)	0.021 (4)	0	0.011 (4)	0

Table S 43. Bond lengths (Å) of $[\text{Bi}_7\text{Pb}_3\text{O}_{13}][\text{Bi}_2\text{O}_2]_3\text{Cl}_7$ $m=3$

Atom 1	Atom 2	d	Atom 1	Atom 2	d
Bi1	1xO1	2.167(28)	Bi5	1xO7	2.191(29)
(Unit1)	2xO2	2.255(8)	(Unit2)	2xO8	2.291(9)
	1xO4	2.304(25)		1xO6	2.322(26)
	2xCl3	3.3004(9)		2xCl2	3.380(7)
	2xCl4	3.430(8)		2xCl4	3.439(8)
Bi2	1xO6	2.224(28)	Bi6	1xO3	2.173(21)
	1xO1	2.261(26)	(Unit3)	1xO9	2.356(63)
	2xO3	2.293(8)		2xO10	2.409(29)
	2xCl4	3.322(7)		2xO1	2.487(12)
	2xCl3	3.436(2)		1xO2	2.742(24)
Bi3	1xO2	2.182(22)		2xCl1	3.257(8)
(Unit1)	2xO4	2.291(9)	Pb7/Bi7	1xO7	2.101(26)
	1xO5	2.291(27)	(Unit3)	1xO10	2.140(40)
	2xCl1	3.199(8)		2xO9	2.257(25)
	2xCl2	3.337(7)		2xCl1	3.443(7)
Bi4	1xO5	2.294(25)		2xCl2	3.468(8)
(Unit1)	2xO5	2.348(10)	Pb8	1xO8	2.268(25)
	1xO4	2.350(27)	(Unit2)	2xO6	2.427(11)
	2xCl2	3.311(8)		1xO8	2.559(27)
	2xCl4	3.339(7)		1xO3	2.564(26)
				2xO7	2.626(12)
				1xO9	2.774(55)

Table S 44. Fractional atomic coordinates and isotropic or equivalent isotropic displacement parameters (Å²) of $[\text{Bi}_6\text{Pb}_4\text{O}_{13}][\text{Bi}_2\text{O}_2]_4\text{Cl}_8$ $m=4$. CSD-number 425740

	x	y	z	$U_{\text{iso}}^*/U_{\text{eq}}$	Occ. (<1)
Bi1	0.27372 (3)	0	0.10223 (5)	0.0138 (3)	
Bi2	-0.01042 (3)	0.5	0.22992 (4)	0.0116 (3)	
Bi3	0.06647 (3)	0.5	0.11802 (4)	0.0107 (3)	
Bi4	-0.09138 (3)	0.5	0.33977 (5)	0.0183 (3)	
Bi5	0.19106 (3)	0	0.20783 (4)	0.0119 (3)	
Bi6	0.35465 (3)	0	-0.00476 (5)	0.0131 (3)	
Bi7	0.11657 (3)	1	0.33451 (5)	0.0211 (3)	
Pb8	0.03784 (3)	1	0.44218 (5)	0.0243 (3)	
Pb9a	-0.17264 (17)	0.5	0.4388 (10)	0.0190 (15)	0.66 (6)
Pb9b	-0.1715 (4)	0.5	0.4565 (11)	0.034 (4)	0.34 (6)
Cl1	0.7982 (2)	0	0.2670 (3)	0.023 (2)	
Cl2	0.8801 (2)	0	0.1624 (3)	0.023 (2)	
Cl3	0.9616 (2)	0	0.0568 (3)	0.022 (2)	
Cl4	0.7126 (2)	0	0.3621 (4)	0.030 (3)	
O1	0.1876 (6)	0	0.0791 (9)	0.020 (3)*	
O2	0.1509 (5)	0.5	0.1372 (8)	0.013 (2)*	
O3	0.2707 (6)	0	-0.0271 (9)	0.020 (3)*	
O4	0.0314 (5)	1	0.2968 (9)	0.016 (3)*	
O5	0.1087 (5)	0	0.1788 (8)	0.012 (2)*	
O6	0.0697 (5)	0.5	0.2402 (9)	0.017 (3)*	
O7	-0.0085 (6)	0.5	0.3534 (10)	0.027 (3)*	
O8	-0.0503 (7)	1	0.4066 (11)	0.028 (3)*	
O9	-0.0985 (6)	0.5	0.4520 (10)	0.025 (3)*	
O10	-0.1440 (12)	1	0.514 (2)	0.052 (7)*	0.75
O11	-0.1194 (13)	0.5	0.591 (2)	0.058 (8)*	0.75

Table S 45. Atomic displacement parameters (\AA^2) of $[\text{Bi}_6\text{Pb}_4\text{O}_{13}][\text{Bi}_2\text{O}_2]_4\text{Cl}_8$ $m=4$

	U^{11}	U^{22}	U^{33}	U^{12}	U^{13}	U^{23}
Bi1	0.0171 (3)	0.0119 (3)	0.0175 (3)	0	0.0131 (3)	0
Bi2	0.0139 (3)	0.0102 (3)	0.0124 (3)	0	0.0087 (2)	0
Bi3	0.0119 (3)	0.0099 (3)	0.0111 (3)	0	0.0072 (2)	0
Bi4	0.0193 (3)	0.0171 (3)	0.0230 (4)	0	0.0148 (3)	0
Bi5	0.0115 (3)	0.0117 (3)	0.0145 (3)	0	0.0088 (2)	0
Bi6	0.0162 (3)	0.0110 (3)	0.0171 (3)	0	0.0125 (3)	0
Bi7	0.0131 (3)	0.0310 (4)	0.0224 (4)	0	0.0122 (3)	0
Pb8	0.0190 (3)	0.0262 (4)	0.0237 (4)	0	0.0104 (3)	0
Pb9a	0.0141 (8)	0.0156 (17)	0.026 (2)	0	0.0113 (10)	0
Pb9b	0.0144 (16)	0.074 (10)	0.014 (3)	0	0.0090 (16)	0
Cl1	0.022 (2)	0.023 (2)	0.028 (2)	0	0.018 (2)	0
Cl2	0.021 (2)	0.028 (3)	0.023 (2)	0	0.0155 (19)	0
Cl3	0.024 (2)	0.025 (2)	0.021 (2)	0	0.0152 (19)	0
Cl4	0.029 (3)	0.033 (3)	0.033 (3)	0	0.020 (2)	0

Table S 46. Bond lengths (\AA) of $[\text{Bi}_6\text{Pb}_4\text{O}_{13}][\text{Bi}_2\text{O}_2]_4\text{Cl}_8$ $m=4$

Atom 1	Atom 2	d	Atom 1	Atom 2	d
Bi1	1xO3	2.325(20)	Bi6	1xO3	2.284(20)
(Unit1)	2xO3	2.334(6)	(Unit1)	2xO1	2.316(6)
	1xO1	2.342(20)		1xO2	2.341(17)
	2xCl1	3.323(5)		2xCl3	3.337(5)
	2xCl2	3.33(5)		2xCl2	3.349(5)
Bi2	1xO7	2.236(21)	Bi7	1xO4	2.204(16)
	2xO4	2.28(5)	(Unit3)	2xO11	2.382(24)
	1xO6	2.281(18)		1xO10	2.399(38)
	2xCl2	3.371(5)		2xO6	2.459(7)
	2xCl3	3.412(5)		1xO5	2.731(17)
Bi3	1xO6	2.19(19)		2xCl4	3.266(6)
(Unit1)	2xO5	2.261(5)	Pb8	1xO8	2.304(22)
	1xO2	2.326(17)	(Unit2)	2xO7	2.421(7)
	2xCl3	3.292(5)		1xO4	2.564(19)
	2xCl3	3.436(5)		1xO8	2.579(23)
Bi4	1xO9	2.193(22)		2xO9	2.619(8)
(Unit2)	2xO8	2.275(7)		1xO10	2.769(38)
	1xO7	2.331(21)	Pb9a	1xO9	2.076(23)
	2xCl1	3.374(5)	(Unit3)	1xO11	2.268(34)
	2xCl2	3.469(5)		2xO10	2.277(16)
Bi5	1xO5	2.184(16)		2xCl1	3.382(16)
(Unit1)	2xO2	2.286(5)		2xCl4	3.458(7)
	1xO1	2.307(20)	Pb9b	1xO11	2.007(33)
	2xCl4	3.201(6)	(Unit3)	2xO10	2.169(12)
	2xCl1	3.351(5)		1xO9	2.224(28)
				2xCl4	3.441(10)
				2xCl1	3.632(18)

Table S 47. Fractional atomic coordinates and isotropic or equivalent isotropic displacement parameters (\AA^2) of $\text{PbBi}_4\text{O}_6\text{Cl}_2$. CSD-number 425741

	<i>x</i>	<i>y</i>	<i>z</i>	$U_{\text{iso}}^*/U_{\text{eq}}$
Bi1	0.5	0.5	0.21050 (8)	0.0124 (7)
Bi2	0	0	0.41291 (10)	0.0365 (9)
Pb1	0	0	0	0.0362 (13)
Cl1	0	0	0.1519 (6)	0.025 (4)
O1	0.5	1	0.25	0.014 (9)*
O2	0	0.5	0.4494 (15)	0.066 (15)*

Table S 48. Atomic displacement parameters (\AA^2) of $\text{PbBi}_4\text{O}_6\text{Cl}_2$

	U^{11}	U^{22}	U^{33}	U^{12}	U^{13}	U^{23}
Bi1	0.0079 (10)	0.0079 (10)	0.0214 (14)	0	0	0
Bi2	0.0431 (15)	0.0431 (15)	0.0232 (16)	0	0	0
Pb1	0.0258 (17)	0.0258 (17)	0.057 (3)	0	0	0
Cl1	0.024 (6)	0.024 (6)	0.027 (8)	0	0	0

Table S 49. Bond lengths (\AA) of $\text{PbBi}_4\text{O}_6\text{Cl}_2$

Atom 1	Atom 2	d
Bi1	4xO1	2.324(2)
(Unit1)	4xCl1	3.332(11)
Bi2	4xO2	2.276(24)
(Unit2)	4xCl1	3.441(11)
Pb1	8xO2	2.523(29)
(Unit2)		

9) $\text{Bi}_9\text{O}_9\text{Cl}_4(\text{Pb}_{0.2}\text{Mn}_{0.8})\text{O}_3\text{Cl}$ **Table S 50. Crystal data, measurement and structural refinement parameters for $\text{Bi}_9\text{O}_9\text{Cl}_4(\text{Pb}_{0.2}\text{Mn}_{0.8})\text{O}_3\text{Cl}$**

<i>Crystal data</i>	
$\text{Bi}_9\text{O}_9\text{Cl}_4(\text{Pb}_{0.2}\text{Mn}_{0.8})\text{O}_3\text{Cl}$	$Z = 4$
$M_r = 2332.3$	$F(000) = 3853$
Orthorhombic, $Cmcm$	$D_x = 8.001 \text{ Mg m}^{-3}$
Hall symbol: $-C -2x; -2y; -2z$	Mo $K\alpha$ radiation, $\lambda = 0.71073 \text{ \AA}$
$a = 3.8695 (2) \text{ \AA}$	$\mu = 84.31 \text{ mm}^{-1}$
$b = 31.7369 (15) \text{ \AA}$	$T = 293 \text{ K}$
$c = 15.7602 (7) \text{ \AA}$	Transparent, colorless
$V = 1935.45 (16) \text{ \AA}^3$	$0.26 \times 0.05 \times 0.02 \text{ mm}$
<i>Data collection</i>	
Radiation source: X-ray tube	$R_{\text{int}} = 0.036$
Absorption correction: multi-scan	$\theta_{\text{max}} = 28.2^\circ$, $\theta_{\text{min}} = 1.3^\circ$
Bruker	$h = -4 \rightarrow 5$
$T_{\text{min}} = 0.296$, $T_{\text{max}} = 0.747$	$k = -25 \rightarrow 42$
5015 measured reflections	$l = -18 \rightarrow 18$
1189 independent reflections	
1039 reflections with $I > 3\sigma(I)$	
<i>Refinement</i>	
Refinement on F	9 constraints
$R[F^2 > 2\sigma(F^2)] = 0.047$	Unit
$wR(F^2) = 0.067$	$(\Delta/\sigma)_{\text{max}} = 0.044$
$S = 1.03$	$\Delta\rho_{\text{max}} = 4.77 \text{ e \AA}^{-3}$
1189 reflections	$\Delta\rho_{\text{min}} = -4.76 \text{ e \AA}^{-3}$
72 parameters	Extinction correction: B-C type 1 Gaussian
0 restraints	isotropic (Becker & Coppens, 1974)
	Extinction coefficient: 58 (10)

Table S 51. Atomic displacement parameters (\AA^2)

	U^{11}	U^{22}	U^{33}	U^{12}	U^{13}	U^{23}
Bi1	0.0071 (7)	0.0116 (7)	0.0090 (7)	0	0	0.0001 (5)
Bi2	0.0069 (9)	0.0146 (10)	0.0074 (10)	0	0	0
Bi3	0.0087 (7)	0.0174 (7)	0.0095 (7)	0	0	0.0006 (6)
Bi4	0.0079 (7)	0.0169 (7)	0.0095 (7)	0	0	-0.0026 (5)
Bi5	0.0262 (9)	0.0223 (8)	0.0092 (8)	0	0	0.0038 (6)
Pb6	0.011 (3)	0.031 (3)	0.018 (3)	0	0	0
Mn6	0.011 (3)	0.031 (3)	0.018 (3)	0	0	0
Cl1	0.017 (7)	0.004 (5)	0.024 (7)	0	0	0.001 (5)
Cl2	0.009 (6)	0.016 (6)	0.023 (7)	0	0	0
Cl3	0.014 (5)	0.019 (4)	0.015 (5)	0	0	0.002 (4)
Cl4a	0.027 (9)	0.021 (8)	0.015 (8)	0	0	0
Cl4b	0.027 (9)	0.021 (8)	0.015 (8)	0	0	0

Table S 52. Selected distances (Å) of $\text{Bi}_9\text{O}_9\text{Cl}_4(\text{Pb}_{0.2}\text{Mn}_{0.8})\text{O}_3\text{Cl}$

Atom 1	Atom 2	d
Bi1	1xO7	2.176(32)
	2xO4	2.225(15)
	1xO1	2.330(16)
	2xCl1	3.2877(11)
	2xCl2	3.4586(75)
Bi2	2xO4	2.201(31)
	2xO1	2.278(17)
	4xCl3	3.1300(83)
Bi3	1xO7	2.207(32)
	1xO2	2.292(17)
	2xO6	2.298(16)
	2xCl2	3.3229(72)
	2xCl1	3.4248(12)
Bi4	1xO5	2.171(26)
	2xO3	2.239(16)
	1xO3	2.280(30)
	2xCl4b	3.1192(42)
	2xCl4a	3.2679(59)
	2xCl3	3.2930(79)
Bi5	1xO6	2.227(31)
	2xO5	2.347(17)
	2xO7	2.545(21)
	1xO3	2.566(26)
	2xCl3	3.1886(86)
Mn6 Pb6	2xO2	2.173(15)
	2xO6	2.184(32)
	1xCl4a	2.317(21)
	1xCl4b	3.167(96)
	4xO5	3.472(26)

Table S 53. Fractional atomic coordinates and isotropic or equivalent isotropic displacement parameters (Å²)

	x	y	z	$U_{\text{iso}}^*/U_{\text{eq}}$	Occ. (<1)
Bi1	0.5	0.44138 (4)	0.12047 (9)	0.0092 (4)	
Bi2	0	0.36813 (7)	0.25	0.0096 (5)	
Bi3	0	0.06346 (5)	0.12579 (9)	0.0119 (4)	
Bi4	0	0.23620 (5)	0.09499 (9)	0.0114 (4)	
Bi5	0.5	0.14468 (5)	0.01208 (10)	0.0192 (5)	
Pb6	0.5	0.1322 (2)	0.25	0.0204 (18)	0.179
Mn6	0.5	0.1322 (2)	0.25	0.0204 (18)	0.821
Cl1	0	0.5	0.5	0.015 (4)	
Cl2	0	0.4952 (4)	0.75	0.016 (4)	
Cl3	0	0.1817 (3)	0.6304 (7)	0.016 (3)	
Cl4a	0.5	0.2053 (6)	0.25	0.021 (5)	0.821
Cl4b	0.5	0.233 (3)	0.25	0.021 (5)	0.179
O1	0.5	0.4063 (12)	0.25	0.013 (8)*	
O2	1	0.1006 (12)	0.25	0.013 (8)*	
O3	-0.5	0.2252 (8)	0.0266 (18)	0.013 (6)*	
O4	0	0.4075 (9)	0.3651 (19)	0.018 (6)*	
O5	0	0.1681 (8)	0.0821 (18)	0.013 (6)*	
O6	0.5	0.1025 (9)	0.1252 (19)	0.015 (6)*	
O7	0	0.0931 (10)	-0.001 (2)	0.020 (6)*	

10) $\text{Bi}_{46}\text{O}_{53}(\text{AsO}_4)_8$ and $\text{Bi}_{14}\text{O}_{15}(\text{AsO}_4)_4$ **Table S 54. Crystal data, measurement and structural refinement parameters of $\text{Bi}_{46}\text{O}_{53}(\text{AsO}_4)_8$ and $\text{Bi}_{14}\text{O}_{15}(\text{AsO}_4)_4$**

	$\text{Bi}_{46}\text{O}_{53}(\text{AsO}_4)_8$	$\text{Bi}_{14}\text{O}_{15}(\text{AsO}_4)_4$
Crystal data		
Crystal symmetry	Monoclinic	Monoclinic
space group	C2/m	C2/c
a (Å)	20.0213 (5)	19.6944(3)
b (Å)	11.5567 (3)	11.3649(1)
c (Å)	21.1107 (5)	53.3541(7)
β (°)	111.9340 (12)	94.2150(6)
V (Å ³)	4531.0 (2)	11909.7(3)
Z	2	16
Dx (g/cm ³)	8.526	8.299
μ (mm ⁻¹)(for λ K α =0.7107Å)	91.96	86.93
Appearance	transparent	transparent
Crystal size (mm)	0.13×0.09×0.05	0.22 × 0.11 × 0.05
Data collection		
λ (Mo K α) (Å)	0.71073	0.71073
Scan mode	ω and ϕ	ω and ϕ
θ (min–max) (°)	2.1 – 37.8	1.5 – 26.4
R(int) (%)	0.064	0.073
Recording reciprocal space	$-33 \leq h \leq 34$ $-19 \leq k \leq 19$ $-30 \leq l \leq 33$	$-24 \leq h \leq 24$ $-14 \leq k \leq 14$ $-66 \leq l \leq 66$
Refinement		
Measured, independent obs.* refl.	61767, 11554, 5613	126363, 12244, 9826
No. of Refined parameters	398	568
Refinement method,	F	F
R1(F ²)(obs) / R1(F ²)(all)	0.0494/0.0525	0.0349/0.0485
wR2(F ²)(obs) /wR2(F ²)(all)	0.0525/0.0612	0.0338/0.0470
GOF(obs) / GOF(all)	1.38/1.72	0.28/0.35
$\Delta\rho_{\text{max}}/\Delta\rho_{\text{min}}$ (e Å ⁻³)	12.49 /-11.82	4.44 /-4.44
Extinction coefficient	0.0098(6)	0.0207(2)

Table S 55. Fractional atomic coordinates and isotropic or equivalent isotropic displacement parameters (\AA^2) of $\text{Bi}_{46}\text{O}_{53}(\text{AsO}_4)_8$

	<i>x</i>	<i>y</i>	<i>z</i>	$U_{\text{iso}}^*/U_{\text{eq}}$	Occ. (<1)
Bi1	0.46835 (2)	0.17481 (3)	0.07603 (2)	0.01544 (14)	
Bi2	0.41193 (2)	0.17035 (3)	0.24191 (2)	0.01534 (14)	
Bi3	0.53112 (2)	0.33614 (4)	0.40702 (2)	0.01670 (14)	
Bi4	0.30293 (2)	0.33871 (4)	0.07959 (2)	0.01733 (14)	
Bi5	0.63434 (2)	0.34203 (4)	0.09221 (2)	0.02339 (16)	
Bi6	0.86613 (2)	0.66179 (4)	0.42111 (2)	0.01690 (14)	
Bi7a	0.6846 (2)	0.5	0.40785 (10)	0.0235 (5)	0.702 (9)
Bi7b	0.7063 (3)	0.5	0.4125 (2)	0.0235 (5)	0.298 (9)
Bi8	0.74530 (4)	0.5	0.25714 (4)	0.0290 (3)	
Bi9a	0.42873 (19)	0.5	0.25828 (18)	0.0218 (5)	0.329 (4)
Bi9b	0.41072 (9)	0.5	0.23465 (10)	0.0218 (5)	0.671 (4)
Bi10a	0.5731 (3)	0.3284 (7)	0.2412 (4)	0.0245 (9)	0.453 (10)
Bi10b	0.5864 (3)	0.3169 (6)	0.2504 (3)	0.0245 (9)	0.547 (10)
Bi11a	0.7640 (6)	0.1772 (11)	0.2648 (6)	0.0263 (9)	0.31 (4)
Bi11b	0.7516 (6)	0.1689 (6)	0.2617 (3)	0.0263 (9)	0.69 (4)
Bi12	0.46589 (3)	0.5	0.08098 (3)	0.0241 (2)	
Bi13	0.70143 (3)	0.17013 (4)	0.41688 (2)	0.02291 (16)	
Bi14	0.58030 (3)	0	0.24183 (4)	0.0254 (2)	
As1	0.87002 (9)	0	0.42224 (9)	0.0217 (6)	
Oas1a	0.7890 (9)	0	0.3665 (13)	0.149 (13)	
Oas1b	0.8715 (11)	−0.109 (2)	0.4690 (12)	0.248 (18)	
Oas1c	0.9271 (11)	0	0.3923 (12)	0.25 (2)	
As2	0.53131 (8)	0	0.39956 (8)	0.0143 (5)	
Oas2a	0.5759 (7)	−0.1166 (12)	0.4375 (7)	0.015 (3)*	0.5
Oas2b	0.5282 (11)	0	0.3186 (9)	0.119 (12)	
Oas2c	0.4455 (10)	0	0.3952 (10)	0.016 (4)*	0.5
Oas2d	0.6007 (16)	0	0.467 (2)	0.10 (2)	0.5
Oas2e	0.482 (4)	0.091 (6)	0.413 (4)	0.42 (5)*	0.5
As3	0.30033 (8)	0	0.08984 (8)	0.0129 (5)	
Oas3a	0.3465 (5)	−0.1197 (9)	0.0918 (7)	0.081 (7)	
Oas3b	0.5509 (9)	0.5	0.3750 (7)	0.063 (8)	
Oas3c	0.2777 (15)	0	0.1548 (11)	0.19 (2)	
Oas3d	0.2295 (9)	0	0.0220 (8)	0.104 (8)	
As4	0.64002 (9)	0	0.09672 (10)	0.0193 (6)	
Oas4a	0.7234 (11)	0	0.1075 (12)	0.145 (15)	
Oas4b	0.5930 (9)	−0.1179 (15)	0.0574 (10)	0.047 (8)	0.5
Oas4c	0.641 (2)	0	0.176 (2)	0.13 (3)	0.5
Oas4d	0.595 (2)	0	0.022 (2)	0.09 (2)	0.5
Oas4e	0.642 (3)	0.111 (2)	0.1364 (18)	0.31 (4)	0.5
O1	0.6299 (4)	0.3105 (7)	0.3880 (4)	0.026 (3)	
O2	0.6657 (5)	0.5	0.3038 (5)	0.019 (4)	
O3	0.4787 (4)	0.3098 (7)	0.2993 (4)	0.036 (3)	
O4	0.3515 (4)	0.3112 (7)	0.1871 (4)	0.034 (3)	
O5	0.6588 (6)	0.1500 (10)	0.2922 (6)	0.067 (6)	
O6	0.8120 (5)	0.5	0.3949 (5)	0.021 (4)	
O7	0.5022 (6)	0.5	0.2065 (6)	0.040 (5)	
O8	0.3563 (6)	0.5	0.1154 (5)	0.027 (4)	
O9	0.3993 (4)	0.3199 (6)	0.0550 (4)	0.022 (3)	
O10	0.6939 (5)	0.3175 (8)	0.2119 (5)	0.048 (4)	
O11	0.5749 (7)	0.5	0.0409 (9)	0.065 (8)	
O12	0.4985 (6)	0.1754 (11)	0.1973 (6)	0.086 (7)	
O13	0.8336 (7)	0.3014 (10)	0.3122 (6)	0.100 (7)	
O14	0.5	0.2565 (19)	0	0.26 (3)	
O15	0.5474 (4)	0.3161 (8)	0.1273 (5)	0.044 (4)	
O16	0.7801 (5)	0.6954 (11)	0.4585 (8)	0.097 (8)	
O17	0.6451 (9)	0.5	0.1576 (9)	0.015 (6)	0.5
O18	0.7589 (7)	0.7401 (14)	0.3580 (9)	0.032 (7)	0.5

Table S 56. Atomic displacement parameters (\AA^2) of $\text{Bi}_{46}\text{O}_{53}(\text{AsO}_4)_8$

	U^{11}	U^{22}	U^{33}	U^{12}	U^{13}	U^{23}
Bi1	0.0216 (2)	0.0112 (2)	0.0141 (2)	0.00043 (16)	0.00738(15)	0.00070 (14)
Bi2	0.01643(19)	0.0121 (2)	0.0183 (2)	-0.00176(16)	0.00745(15)	0.00044 (15)
Bi3	0.0216 (2)	0.0133 (2)	0.0173 (2)	0.00022 (16)	0.00963(16)	0.00311 (14)
Bi4	0.01711(19)	0.0191 (2)	0.0128 (2)	-0.00513(17)	0.00219(14)	-0.00272(15)
Bi5	0.0292 (2)	0.0238 (3)	0.0189 (2)	0.0064 (2)	0.01103(18)	0.00166 (18)
Bi6	0.0166 (2)	0.0159 (2)	0.0164 (2)	-0.00188(16)	0.00411(15)	-0.00171(14)
Bi7a	0.0168 (11)	0.0346 (5)	0.0141 (4)	0	0.0001 (7)	0
Bi7b	0.0168 (11)	0.0346 (5)	0.0141 (4)	0	0.0001 (7)	0
Bi8	0.0276 (3)	0.0307 (4)	0.0362 (4)	0	0.0204 (3)	0
Bi9a	0.0131 (7)	0.0355 (5)	0.0168 (8)	0	0.0057 (5)	0
Bi9b	0.0131 (7)	0.0355 (5)	0.0168 (8)	0	0.0057 (5)	0
Bi10a	0.0250 (16)	0.0236(11)	0.0154(13)	-0.0003 (10)	-0.0033(10)	0.0084 (7)
Bi10b	0.0250 (16)	0.0236(11)	0.0154(13)	-0.0003 (10)	-0.0033(10)	0.0084 (7)
Bi11a	0.027 (2)	0.0234 (8)	0.0322 (6)	-0.0027 (11)	0.0152 (11)	-0.0013 (5)
Bi11b	0.027 (2)	0.0234 (8)	0.0322 (6)	-0.0027 (11)	0.0152 (11)	-0.0013 (5)
Bi12	0.0236 (3)	0.0211 (3)	0.0191 (3)	0	-0.0021 (2)	0
Bi13	0.0288 (2)	0.0167 (2)	0.0218 (2)	0.00879 (18)	0.00784(18)	0.00776 (17)
Bi14	0.0208 (3)	0.0180 (3)	0.0354 (4)	0	0.0082 (3)	0
As1	0.0246 (9)	0.0166 (9)	0.0291(10)	0	0.0159 (7)	0
Oas1a	0.043 (11)	0.091 (18)	0.23 (3)	0	-0.042 (13)	0
Oas1b	0.23 (2)	0.26 (3)	0.24 (3)	-0.061 (19)	0.07 (2)	0.12 (2)
Oas1c	0.075 (15)	0.60 (7)	0.09 (2)	0	0.058 (15)	0
As2	0.0144 (7)	0.0116 (8)	0.0170 (8)	0	0.0062 (6)	0
Oas2b	0.148 (18)	0.15 (2)	0.053 (14)	0	0.033 (13)	0
Oas2d	0.05 (2)	0.15 (4)	0.14 (4)	0	0.06 (2)	0
As3	0.0133 (7)	0.0128 (8)	0.0091 (7)	0	0.0003 (5)	0
Oas3a	0.053 (7)	0.021 (6)	0.179 (14)	0.017 (5)	0.055 (8)	0.025 (7)
Oas3b	0.150 (15)	0.018 (7)	0.050 (10)	0	0.070 (10)	0
Oas3c	0.28 (3)	0.28 (4)	0.060 (17)	0	0.11 (2)	0
Oas3d	0.112 (14)	0.042 (10)	0.068 (12)	0	-0.071 (10)	0
As4	0.0198 (8)	0.0102 (8)	0.0310(10)	0	0.0130 (7)	0
Oas4a	0.094 (16)	0.22 (3)	0.11 (2)	0	0.032 (14)	0
Oas4b	0.041 (11)	0.030 (11)	0.054 (13)	-0.024 (9)	-0.001 (9)	-0.020 (9)
Oas4c	0.09 (3)	0.19 (6)	0.16 (5)	0	0.10 (3)	0
Oas4d	0.13 (3)	0.025 (19)	0.16 (4)	0	0.11 (3)	0
Oas4e	0.59 (9)	0.033 (19)	0.10 (3)	0.10 (3)	-0.11 (4)	-0.034 (18)
O1	0.030 (4)	0.029 (5)	0.025 (5)	0.014 (4)	0.015 (3)	0.008 (3)
O2	0.015 (5)	0.024 (6)	0.020 (6)	0	0.009 (4)	0
O3	0.039 (5)	0.029 (5)	0.021 (5)	-0.013 (4)	-0.012 (4)	-0.001 (3)
O4	0.052 (5)	0.030 (5)	0.012 (4)	0.015 (4)	0.002 (4)	0.007 (3)
O5	0.072 (7)	0.064 (8)	0.076 (9)	0.043 (6)	0.041 (7)	0.024 (6)
O6	0.033 (6)	0.009 (5)	0.020 (6)	0	0.008 (5)	0
O7	0.030 (7)	0.062 (10)	0.027 (7)	0	0.010 (5)	0
O8	0.043 (7)	0.013 (6)	0.013 (6)	0	-0.003 (5)	0
O9	0.025 (4)	0.004 (4)	0.040 (5)	0.003 (3)	0.016 (4)	-0.003 (3)
O10	0.056 (6)	0.053 (7)	0.030 (6)	-0.013 (5)	0.011 (5)	0.003 (4)
O11	0.040 (8)	0.019 (7)	0.165 (17)	0	0.072 (10)	0
O12	0.100 (10)	0.095 (11)	0.065 (9)	-0.051 (8)	0.034 (7)	-0.039 (7)
O13	0.143 (12)	0.057 (8)	0.047 (8)	-0.002 (8)	-0.025 (7)	-0.025 (6)
O14	0.51 (5)	0.061 (16)	0.46 (5)	0	0.47 (5)	0
O15	0.025 (5)	0.054 (7)	0.060 (7)	-0.014 (4)	0.022 (5)	-0.012 (5)
O16	0.037 (6)	0.082 (10)	0.194 (16)	0.021 (6)	0.070 (9)	0.011 (9)
O17	0.015 (9)	0.008 (10)	0.010 (10)	0	-0.010 (7)	0
O18	0.018 (8)	0.029 (10)	0.053 (12)	-0.004 (7)	0.019 (8)	0.008 (8)

Table S 57. Selected distances in $\text{Bi}_{46}\text{O}_{53}(\text{AsO}_4)_8$ (max. $d=3\text{\AA}$)

Atom1	Atom2	d, Å	Atom1	Atom2	d, Å	Atom1	Atom2	d, Å
Bi1	O9	2.1122(72)	Bi7a	O2	2.0839(11)	Bi10a	O15	2.2677(14)
	O14	2.1540(11)		O1	2.4142(81)		O12	2.2800(14)
	O15	2.2501(82)		O1	2.4142(81)		O7	2.3891(94)
	O12	2.4008(13)		Oas3b	2.5020(18)		O3	2.6181(13)
	Oas3a	2.6599(13)		O6	2.6644(12)		O5	2.6408(14)
	Oas4b	2.6925(20)		O16	2.8898(11)		O2	2.6993(89)
	Oas4b	2.7513(21)		O16	2.8898(11)		O10	2.7140(14)
	Oas4d	2.8305(25)		O2	2.1291(11)		O1	2.8822(12)
Bi2	O4	2.0991(75)	Bi7b	O6	2.2812(13)	Bi10b	O12	2.3599(13)
	O3	2.1546(74)		O1	2.6100(85)		O5	2.3758(13)
	O12	2.2613(15)		O1	2.6100(85)		O15	2.4181(12)
	O13	2.5514(16)		O16	2.6707(12)		O10	2.5690(14)
	Oas3a	2.9999(14)		O16	2.6707(12)		O2	2.6329(80)
Bi3	Oas3b	2.0976(81)	Bi8	Oas3b	2.9098(19)	Bi11a	O7	2.6479(89)
	O3	2.1407(76)		O2	2.1640(12)		O1	2.7041(11)
	O1	2.1803(91)		O17	2.3002(15)		O3	2.7175(12)
	Oas2a	2.6834(12)		O10	2.3844(90)		O13	1.9887(16)
	Oas1b	2.6946(18)		O10	2.3844(90)		O10	2.1639(14)
	Oas1c	2.7456(15)		Oas3c	2.4764(32)		O18	2.2252(23)
Bi4	O4	2.1328(77)	Bi9a	O6	2.7092(95)	Bi11b	O5	2.4038(20)
	O8	2.1411(48)		O13	2.8689(12)		O4	2.8151(18)
	O9	2.1881(92)		O13	2.8689(12)		Oas1a	2.8636(19)
	Oas3a	2.6581(11)		O7	2.1362(16)		Oas4e	2.9966(40)
	Oas4a	2.6669(17)		O3	2.4363(79)		O10	2.1170(12)
	Oas3d	2.7304(12)		O3	2.4363(79)		O5	2.1927(19)
Bi5	O15	2.1521(11)	Bi9b	Oas3b	2.7481(14)	Bi12	O13	2.2034(15)
	O11	2.2270(74)		O4	2.7701(78)		O18	2.2452(20)
	O17	2.2500(12)		O4	2.7701(78)		Oas4e	2.8203(39)
	O10	2.3740(94)		O8	2.8169(11)		Oas1a	2.8261(16)
	Oas4b	2.7352(23)		Oas1c	2.8354(23)		O4	2.9811(15)
	Oas4e	2.8108(26)		O7	2.1269(14)		Oas4c	2.9989(26)
	O14	2.8421(80)		O8	2.3409(97)		O11	2.3911(19)
	O9	2.9348(84)		O4	2.5072(78)		O9	2.4216(70)
Bi6	O6	2.1281(42)		O4	2.5072(78)		O9	2.4216(70)
	O16	2.1801(15)		O3	2.6753(77)		O7	2.4720(13)
	O13	2.1855(13)		O3	2.6753(77)		O8	2.5560(14)
	O18	2.2504(13)					O11	2.619(18)
	Oas2e	2.5253(87)					O15	2.6352(85)
	Oas2c	2.6351(17)					O15	2.6352(85)
	Oas2a	2.8171(14)						
	Oas1b	2.824(23)						
	Oas2d	2.8891(32)						

Table S 58. Continued

Atom 1	Atom 2	d, Å
Bi13	O1	2.0981(78)
	O16	2.1560(11)
	O18	2.2397(19)
	O5	2.456(12)
	O16	2.5325(17)
	Oas2a	2.7750(16)
Bi14	Oas4c	2.1610(49)
	Oas2b	2.2340(23)
	O5	2.3146(11)
	O5	2.3146(11)
	O12	2.5507(12)
	O12	2.5507(12)
As1	Oas1c	1.5010(24)
	Oas1b	1.5960(23)
	Oas1b	1.5960(23)
	Oas1a	1.6131(16)
As2	Oas2e	1.5396(83)
	Oas2e	1.5396(83)
	Oas2d	1.5779(33)
	Oas2a	1.6531(12)
	Oas2a	1.6531(12)
	Oas2b	1.6855(21)
	Oas2c	1.6944(22)
As3	Oas3d	1.5952(14)
	Oas3c	1.5973(32)
	Oas3a	1.6557(11)
	Oas3a	1.6557(11)
As4	Oas4d	1.4958(36)
	Oas4e	1.5202(32)
	Oas4e	1.5202(32)
	Oas4a	1.5878(21)
	Oas4c	1.6668(45)
	Oas4b	1.6908(21)
	Oas4b	1.6908(21)

Table S 59. Fractional atomic coordinates and isotropic or equivalent isotropic displacement parameters (\AA^2) of $\text{Bi}_{14}\text{O}_{15}(\text{AsO}_4)_4$

	<i>x</i>	<i>y</i>	<i>z</i>	$U_{\text{iso}}^*/U_{\text{eq}}$
Bi1	0.13044 (4)	0.30436 (6)	0.412884 (15)	0.0106 (2)
Bi2	0.14116 (4)	−0.03052 (6)	0.409170 (15)	0.0087 (2)
Bi3	0.40110 (4)	0.46773 (7)	0.281374 (14)	0.00773 (19)
Bi4	0.35121 (4)	−0.02274 (7)	0.340185 (15)	0.0087 (2)
Bi5	0.06992 (4)	0.79761 (7)	0.283620 (15)	0.0109 (2)
Bi6	0.18043 (4)	0.15736 (6)	0.343358 (14)	0.00754 (19)
Bi7	−0.22173 (4)	0.46233 (6)	0.465043 (15)	0.0093 (2)
Bi8	0.46524 (4)	−0.03382 (6)	0.407491 (14)	0.0086 (2)
Bi9	0.01967 (4)	−0.01109 (7)	0.346859 (15)	0.0103 (2)
Bi10	0.34208 (4)	−0.35587 (7)	0.347426 (14)	0.00820 (19)
Bi11	0.24305 (4)	0.95034 (7)	0.279326 (17)	0.0136 (2)
Bi12	0.10306 (4)	0.49368 (6)	0.476823 (14)	0.00755 (19)
Bi13	0.18484 (4)	0.50542 (7)	0.349995 (15)	0.0096 (2)
Bi14	0.12361 (4)	0.63131 (7)	0.410440 (15)	0.0125 (2)
Bi15	0.26679 (4)	0.79194 (7)	0.219603 (15)	0.0103 (2)
Bi16	0.43399 (4)	0.96002 (6)	0.215312 (14)	0.00805 (19)
Bi17	0.18826 (4)	0.83478 (7)	0.346598 (15)	0.0128 (2)
Bi18	0.43351 (4)	0.48095 (7)	0.469231 (15)	0.0124 (2)
Bi19	−0.03363 (4)	0.81121 (7)	0.404406 (16)	0.0114 (2)
Bi20	0.39559 (4)	0.79326 (7)	0.282311 (15)	0.0092 (2)
Bi21	−0.06531 (4)	0.30787 (6)	0.470161 (14)	0.00743 (19)
Bi22	0.26536 (4)	0.32234 (6)	0.469929 (15)	0.0099 (2)
Bi23	0.22456 (4)	0.61902 (7)	0.285243 (15)	0.0136 (2)
Bi24	0.11340 (4)	0.82300 (7)	0.463725 (15)	0.0105 (2)
Bi25	0.28642 (4)	0.45974 (7)	0.407948 (17)	0.0141 (2)
Bi26	0.01643 (4)	0.67926 (7)	0.344146 (16)	0.0125 (2)
Bi27	0.29231 (4)	0.77713 (8)	0.404483 (17)	0.0169 (2)
Bi28	−0.27310 (4)	0.35668 (8)	0.528416 (17)	0.0166 (2)
As1	0.29961 (10)	0.12662 (18)	0.40135 (4)	0.0079 (5)
Oas1a	0.3466 (10)	0.2302 (19)	0.4141 (4)	0.032 (4)*
Oas1b	0.3455 (9)	0.0188 (16)	0.3880 (3)	0.021 (4)*
Oas1c	0.2356 (9)	0.1828 (17)	0.3814 (3)	0.025 (4)*
Oas1d	0.2535 (9)	0.0573 (16)	0.4230 (3)	0.024 (4)*
As2	0.48393 (10)	0.15902 (17)	0.65435 (4)	0.0071 (5)
Oas2a	0.4312 (9)	0.0810 (16)	0.6725 (3)	0.022 (4)*
Oas2b	0.4428 (10)	0.2738 (17)	0.6418 (4)	0.028 (4)*
Oas2c	0.5045 (11)	0.061 (2)	0.6324 (4)	0.036 (5)*
Oas2d	0.5576 (9)	0.1925 (16)	0.6706 (3)	0.023 (4)*
As3	0.07614 (11)	0.12247 (18)	0.28068 (4)	0.0097 (6)
Oas3a	0.0883 (13)	0.248 (2)	0.2667 (5)	0.048 (6)*
Oas3b	0.0027 (15)	0.112 (3)	0.2932 (5)	0.062 (7)*
Oas3c	0.0944 (10)	0.0109 (18)	0.2610 (4)	0.028 (4)*
Oas3d	0.1423 (15)	0.120 (3)	0.3025 (6)	0.062 (7)*
As4	0.44364 (10)	0.15129 (17)	0.46628 (4)	0.0069 (5)
Oas4a	0.4443 (9)	0.0280 (16)	0.4487 (3)	0.021 (4)*
Oas4b	0.3718 (9)	0.1562 (17)	0.4807 (3)	0.025 (4)*
Oas4c	0.4614 (8)	0.2747 (15)	0.4507 (3)	0.018 (3)*
Oas4d	0.5091 (9)	0.1277 (16)	0.4879 (3)	0.023 (4)*
As5	0.96142 (10)	0.12828 (17)	0.40773 (4)	0.0074 (5)
Oas5a	0.9269 (10)	0.0466 (18)	0.4300 (4)	0.031 (4)*
Oas5b	1.0083 (8)	0.0356 (14)	0.3915 (3)	0.016 (3)*
Oas5c	0.8957 (10)	0.1794 (18)	0.3888 (4)	0.029 (4)*
Oas5d	1.0030 (8)	0.2414 (15)	0.4212 (3)	0.019 (3)*
As6	0.15167 (10)	0.17435 (18)	0.65905 (4)	0.0091 (5)
Oas6a	0.1132 (11)	0.289 (2)	0.6451 (4)	0.038 (5)*
Oas6b	0.2280 (11)	0.208 (2)	0.6742 (4)	0.039 (5)*

Oas6c	0.1007 (9)	0.1096 (16)	0.6793 (3)	0.023 (4)*
Oas6d	0.1666 (14)	0.070 (3)	0.6387 (5)	0.057 (7)*
As7	0.10397 (11)	0.13759 (18)	0.47117 (4)	0.0101 (4)
Oas7a	0.0294 (13)	0.141 (2)	0.4846 (5)	0.053 (6)*
Oas7b	0.1517 (13)	0.090 (2)	0.4954 (5)	0.053 (6)*
Oas7c	0.0927 (10)	0.0313 (17)	0.4489 (4)	0.028 (4)*
Oas7d	0.1255 (9)	0.2638 (16)	0.4583 (3)	0.022 (4)*
As8	0.40491 (11)	0.12448 (18)	0.27522 (4)	0.0101 (4)
Oas8a	0.455 (3)	0.102 (5)	0.3003 (11)	0.146 (19)*
Oas8b	0.3386 (19)	0.120 (3)	0.2935 (7)	0.089 (11)*
Oas8c	0.414 (3)	0.248 (5)	0.2621 (10)	0.135 (18)*
Oas8d	0.4108 (14)	0.004 (2)	0.2567 (5)	0.055 (7)*
O1	0.0758 (7)	0.4575 (12)	0.4218 (3)	0.007 (3)*
O2	0.2224 (8)	0.3588 (14)	0.4323 (3)	0.015 (3)*
O3	0.1250 (7)	0.0019 (13)	0.3557 (3)	0.008 (3)*
O4	0.5011 (7)	0.1341 (13)	0.3995 (3)	0.009 (3)*
O5	0.3311 (8)	0.4483 (14)	0.4567 (3)	0.014 (3)*
O6	0.3906 (8)	0.6438 (15)	0.4806 (3)	0.018 (3)*
O7	0.0180 (8)	-0.1700 (14)	0.3684 (3)	0.014 (3)*
O8	0.2125 (7)	0.4713 (13)	0.4817 (3)	0.011 (3)*
O9	0.3238 (8)	0.8808 (14)	0.3051 (3)	0.015 (3)*
O10	0.0710 (7)	0.8248 (13)	0.4204 (3)	0.011 (3)*
O11	0.2445 (8)	0.0137 (14)	0.3350 (3)	0.014 (3)*
O12	-0.1341 (8)	0.3893 (14)	0.4934 (3)	0.012 (3)*
O13	0.1928 (7)	0.8358 (13)	0.3873 (3)	0.009 (3)*
O14	0.1931 (8)	-0.1318 (15)	0.4391 (3)	0.017 (3)*
O15	0.2627 (8)	-0.3841 (15)	0.3724 (3)	0.018 (3)*
O16	0.2032 (8)	0.9327 (15)	0.2285 (3)	0.018 (3)*
O17	0.3073 (7)	-0.1801 (13)	0.3557 (3)	0.011 (3)*
O18	0.3944 (9)	1.1271 (16)	0.2053 (3)	0.022 (4)*
O19	0.1807 (8)	0.4423 (14)	0.3901 (3)	0.013 (3)*
O20	0.2511 (7)	0.6244 (12)	0.4235 (2)	0.005 (3)*
O21	0.2441 (7)	0.6267 (13)	0.3236 (3)	0.011 (3)*
O22	0.0540 (7)	0.8330 (13)	0.3233 (3)	0.009 (3)*
O23	-0.1652 (8)	0.3249 (14)	0.4467 (3)	0.013 (3)*
O24	0.2971 (7)	0.8144 (12)	0.2600 (3)	0.008 (3)*
O25	0.3544 (8)	0.6277 (14)	0.2918 (3)	0.013 (3)*
O26	0.1206 (8)	0.6482 (14)	0.3579 (3)	0.012 (3)*
O27	0.1780 (7)	0.8185 (13)	0.2918 (3)	0.011 (3)*
O28	0.3274 (7)	0.9365 (13)	0.2084 (3)	0.010 (3)*
O29	0.1296 (7)	0.6411 (13)	0.4525 (3)	0.009 (3)*
O30	-0.2829 (8)	0.3340 (14)	0.4858 (3)	0.013 (3)*

Table S 60. Atomic displacement parameters (\AA^2) of $\text{Bi}_{14}\text{O}_{15}(\text{AsO}_4)_4$

	U^{11}	U^{22}	U^{33}	U^{12}	U^{13}	U^{23}
Bi1	0.0114 (4)	0.0017 (3)	0.0183 (4)	−0.0004 (3)	−0.0012 (3)	−0.0019 (3)
Bi2	0.0076 (3)	0.0035 (3)	0.0148 (4)	0.0017 (3)	0.0001 (3)	−0.0001 (3)
Bi3	0.0049 (3)	0.0060 (3)	0.0124 (3)	0.0004 (3)	0.0011 (3)	0.0000 (3)
Bi4	0.0049 (3)	0.0045 (3)	0.0166 (4)	−0.0017 (3)	0.0005 (3)	−0.0006 (3)
Bi5	0.0106 (3)	0.0080 (3)	0.0137 (4)	0.0034 (3)	−0.0019 (3)	−0.0024 (3)
Bi6	0.0061 (3)	0.0038 (3)	0.0127 (3)	0.0005 (3)	0.0006 (3)	0.0018 (3)
Bi7	0.0085 (3)	0.0029 (3)	0.0165 (4)	−0.0010 (3)	0.0008 (3)	0.0008 (3)
Bi8	0.0084 (3)	0.0043 (3)	0.0129 (4)	−0.0026 (3)	0.0003 (3)	−0.0003 (3)
Bi9	0.0064 (3)	0.0064 (3)	0.0177 (4)	0.0005 (3)	−0.0016 (3)	0.0034 (3)
Bi10	0.0042 (3)	0.0057 (3)	0.0147 (4)	0.0005 (3)	0.0013 (3)	−0.0015 (3)
Bi11	0.0086 (3)	0.0036 (3)	0.0291 (4)	0.0000 (3)	0.0048 (3)	0.0049 (3)
Bi12	0.0055 (3)	0.0038 (3)	0.0133 (4)	−0.0021 (3)	0.0012 (3)	−0.0021 (3)
Bi13	0.0084 (3)	0.0036 (3)	0.0171 (4)	−0.0011 (3)	0.0030 (3)	−0.0002 (3)
Bi14	0.0128 (4)	0.0107 (4)	0.0140 (4)	−0.0022 (3)	0.0017 (3)	0.0001 (3)
Bi15	0.0124 (4)	0.0037 (3)	0.0151 (4)	−0.0012 (3)	0.0028 (3)	−0.0015 (3)
Bi16	0.0052 (3)	0.0045 (3)	0.0143 (4)	0.0015 (3)	−0.0002 (3)	0.0011 (3)
Bi17	0.0118 (4)	0.0129 (4)	0.0138 (4)	0.0009 (3)	0.0013 (3)	−0.0027 (3)
Bi18	0.0164 (4)	0.0057 (3)	0.0145 (4)	0.0015 (3)	−0.0041 (3)	−0.0011 (3)
Bi19	0.0100 (3)	0.0050 (3)	0.0195 (4)	0.0042 (3)	0.0022 (3)	0.0006 (3)
Bi20	0.0049 (3)	0.0065 (3)	0.0165 (4)	−0.0009 (3)	0.0022 (3)	0.0015 (3)
Bi21	0.0064 (3)	0.0038 (3)	0.0124 (3)	−0.0009 (3)	0.0031 (3)	−0.0007 (3)
Bi22	0.0093 (3)	0.0021 (3)	0.0186 (4)	0.0006 (3)	0.0032 (3)	0.0030 (3)
Bi23	0.0200 (4)	0.0111 (4)	0.0093 (4)	−0.0062 (3)	−0.0018 (3)	0.0013 (3)
Bi24	0.0117 (4)	0.0039 (3)	0.0165 (4)	−0.0003 (3)	0.0041 (3)	−0.0012 (3)
Bi25	0.0056 (3)	0.0102 (4)	0.0267 (4)	0.0000 (3)	0.0035 (3)	−0.0073 (3)
Bi26	0.0065 (3)	0.0051 (3)	0.0254 (4)	−0.0013 (3)	−0.0018 (3)	−0.0035 (3)
Bi27	0.0074 (4)	0.0175 (4)	0.0255 (4)	0.0024 (3)	−0.0001 (3)	0.0063 (3)
Bi28	0.0137 (4)	0.0128 (4)	0.0229 (4)	−0.0058 (3)	−0.0007 (3)	0.0019 (3)
As1	0.0086 (9)	0.0045 (9)	0.0107 (9)	0.0043 (7)	0.0006 (7)	0.0028 (7)
As2	0.0046 (9)	0.0038 (9)	0.0129 (10)	−0.0008 (7)	0.0006 (7)	0.0015 (7)
As3	0.0094 (9)	0.0056 (9)	0.0143 (10)	0.0004 (7)	0.0025 (8)	−0.0004 (8)
As4	0.0071 (9)	0.0007 (8)	0.0133 (10)	−0.0001 (7)	0.0041 (7)	−0.0003 (7)
As5	0.0053 (9)	0.0042 (9)	0.0126 (10)	−0.0001 (7)	−0.0013 (7)	−0.0016 (7)
As6	0.0075 (9)	0.0041 (9)	0.0159 (10)	0.0007 (7)	0.0026 (8)	−0.0013 (8)
As7	0.0123 (7)	0.0045 (6)	0.0131 (7)	−0.0020 (5)	−0.0015 (5)	0.0013 (5)
As8	0.0123 (7)	0.0045 (6)	0.0131 (7)	−0.0020 (5)	−0.0015 (5)	0.0013 (5)

Table S 61. Selected distances in $\text{Bi}_{14}\text{O}_{15}(\text{AsO}_4)_4$ (max. $d=3\text{\AA}$)

Atom1	Atom2	d, Å	Atom1	Atom2	d, Å	Atom1	Atom2	d, Å
Bi1	O2	2.113(15)	Bi7	O23	2.189(15)	Bi13	O26	2.117(14)
	O1	2.123(13)		O30	2.236(15)		O15	2.256(15)
	O19	2.254(15)		O14	2.353(15)		O19	2.265(16)
	Oas7d	2.475(17)		O12	2.362(15)		O21	2.344(15)
	Oas5d	2.679(17)		Oas1d	2.503(18)		Oas2a	2.688(18)
Bi2	O14	2.165(15)	Bi8	O8	2.934(16)	Bi14	O29	2.241(16)
	O13	2.207(14)		Oas4b	2.951(21)		O1	2.284(13)
	O10	2.255(13)		O4	2.200(13)		O4	2.441(14)
	Oas7c	2.485(22)		O1	2.256(14)		O10	2.507(13)
	Oas1d	2.488(19)		Oas2c	2.276(22)		O20	2.557(14)
Bi3	Oas5b	2.819(16)	Bi9	Oas4a	2.373(17)	Bi15	O19	2.693(14)
	O3	2.871(16)		Oas1b	2.577(18)		O26	2.806(16)
	O16	2.120(16)		Oas5d	2.749(22)		O16	2.110(14)
	O25	2.133(13)		O3	2.099(14)		O28	2.137(13)
	Oas6c	2.280(18)		O7	2.142(13)		O24	2.208(16)
Bi4	Oas3c	2.322(22)	Bi10	O22	2.303(14)	Bi16	Oas6b	2.486(21)
	Oas3b	2.632(27)		Oas5b	2.467(16)		Oas8b	2.904(37)
	Oas8c	2.722(57)		Oas2b	2.846(23)		Oas3a	2.942(20)
	O11	2.141(16)		Oas6c	2.889(18)		Oas3d	2.958(30)
	O17	2.176(13)		O15	2.151(17)		O18	2.106(22)
Bi5	O9	2.201(15)	Bi11	O17	2.169(12)	Bi17	O28	2.122(14)
	Oas1b	2.606(17)		O21	2.240(14)		Oas2a	2.328(17)
	Oas2d	2.722(21)		Oas5c	2.411(21)		Oas8d	2.341(27)
	Oas6a	2.844(23)		Oas6d	2.554(34)		Oas3a	2.641(24)
	Oas8b	2.967(37)		Oas2d	2.929(20)		Oas8a	2.883(59)
Bi6	O18	2.131(22)	Bi12	O27	2.115(14)		O13	2.167(16)
	O27	2.154(14)		O9	2.172(15)		O3	2.343(13)
	O22	2.200(16)		O24	2.182(14)		O17	2.365(14)
	Oas8c	2.541(55)		Oas8b	2.766(37)		O11	2.421(13)
	Oas3c	2.765(23)		O16	2.774(16)		O26	2.601(14)
Bi6	O11	2.128(14)		O12	2.129(15)		O22	2.838(14)
	O3	2.202(13)		O8	2.167(14)		O21	2.914(13)
	Oas1c	2.250(16)		O29	2.205(14)		O27	2.922(16)
	Oas3d	2.294(31)		Oas4d	2.503(20)			
	Oas6b	2.592(22)		Oas7d	2.837(22)			
	Oas2b	2.725(21)		Oas4b	2.848(19)			
				O1	2.973(16)			

Table S 62. Continued

Atom 1	Atom 2	d, Å	Atom 1	Atom 2	d, Å	Atom 1	Atom 2	d, Å
Bi18	O5	2.111(16)	Bi24	O14	2.181(17)	As1	Oas1a	1.619(22)
	O6	2.143(22)		O29	2.183(12)		Oas1b	1.707(21)
	Oas5a	2.218(22)		O30	2.285(16)		Oas1c	1.713(18)
	Oas4c	2.615(13)		O10	2.400(16)	As2	Oas1d	1.714(19)
	Oas7a	2.70(22)		Oas7c	2.516(23)		Oas2b	1.651(22)
	Oas7b	2.741(25)	Bi25	O20	2.178(12)		Oas2d	1.678(18)
	Oas7a	2.875(26)		O2	2.198(16)		Oas2c	1.684(23)
Bi19	O4	2.149(12)		O19	2.234(16)	As3	Oas2a	1.717(20)
	O10	2.177(14)	Bi26	O15	2.615(14)		Oas3a	1.634(24)
	O7	2.249(17)		O5	2.687(16)		Oas3b	1.635(23)
	Oas4c	2.513(16)		Oas6d	2.736(27)		Oas3d	1.679(25)
	Oas1a	2.612(21)		Oas1a	2.879(23)		Oas3c	1.699(23)
	Oas5b	2.787(13)		O7	2.146(14)	As4	Oas4b	1.660(18)
Bi20	O25	2.122(13)		O26	2.157(16)		Oas4c	1.683(14)
	O9	2.174(16)	Bi27	O22	2.227(14)	As5	Oas4a	1.687(21)
	O24	2.213(14)		Oas6a	2.678(21)		Oas4d	1.687(17)
	Oas2d	2.617(16)		Oas8a	2.714(54)		Oas5d	1.656(21)
	Oas3a	2.708(27)		O20	2.200(12)		Oas5c	1.679(21)
	Oas8d	2.785(24)		O13	2.206(14)		Oas5b	1.680(15)
	Oas3b	2.979(28)		O23	2.407(16)	As6	Oas5a	1.686(22)
	O12	2.114(16)		Oas5c	2.523(21)		Oas6d	1.650(31)
	O6	2.146(22)	Bi28	O15	2.545(14)		Oas6a	1.659(22)
Bi21	O23	2.261(16)		O17	2.685(16)	As7	Oas6c	1.694(19)
	Oas4d	2.530(17)		O14	2.971(16)		Oas6b	1.697(20)
	Oas7a	2.726(22)		O30	2.283(16)		Oas7b	1.636(24)
	Oas4a	2.764(22)		O6	2.329(16)		Oas7d	1.661(22)
	O5	2.085(15)		O8	2.376(13)	As8	Oas7a	1.689(23)
Bi22	O8	2.104(13)	Bi27	O30	2.571(14)		Oas7c	1.700(23)
	O2	2.161(16)		O20	2.579(11)		Oas8c	1.587(57)
	Oas7b	2.573(23)		O5	2.645(14)		Oas8a	1.611(54)
	Oas4b	2.850(20)		O23	2.782(14)		Oas8b	1.681(40)
	Oas7d	2.857(18)		O29	2.933(14)		Oas8d	1.698(25)
Bi23	O21	2.057(16)						
	O28	2.354(13)						
	O18	2.434(18)						
	O27	2.475(12)						
	O25	2.557(16)						
	O16	2.680(14)						

11) Bi₄Mn_{3+x}O_{11.5-y} - a new bismuth manganite with 2D-magnetic properties

Table S 63. Refined parameters of SC XRD data of Bi₄Mn₃O_{11.5} at T = 100K. CSD-number 424652

Atom	Wyck.	Occ.	x/a	y/b	z/c	U [Å ²]
Bi1	18f		0.53858(3)	0.00959(3)	0.118783(7)	0.00845(10)
Bi2a	6c	0.9298(12)	0	0	0.086551(14)	0.00554(11)
Bi2b	6c	0.0702(12)	0	0	0.1110(2)	0.00554(11)
Mn1	18f		0.42342(12)	0.27807(12)	-0.00086(3)	0.0042(3)
Mn2	3a	0.0702(12)	0	0	0	0.0042(3)
O1	6c		0.6667	0.3333	0.1262(2)	0.0084(16)
O2	18f		0.2532(7)	-0.0334(8)	0.13684(16)	0.0204(19)
O3	18f		0.2112(6)	0.2528(6)	0.03876(15)	0.0108(15)
O4	6c		0.6667	0.3333	-0.0361(2)	0.0079(16)
O5	18f		0.4676(6)	0.0922(6)	0.03563(14)	0.0093(15)
O6	6c	0.360(18)	0.3333	-0.3333	0.1757(14)	0.031(13)

Table S 64. Anisotropic displacement parameters (Å²) of SC XRD data of Bi₄Mn₃O_{11.5} at T = 100K.

Atom	U ₁₁	U ₂₂	U ₃₃	U ₁₂	U ₁₃	U ₂₃
Bi1	0.01331(13)	0.01360(13)	0.00284(12)	0.01003(9)	-0.00096(6)	-0.00252(6)
Bi2a	0.00710(13)	0.00710(13)	0.0024(2)	0.00355(7)	0	0
Bi2b	0.00710(13)	0.00710(13)	0.0024(2)	0.00355(7)	0	0
Mn1	0.0064(4)	0.0057(4)	0.0012(3)	0.0034(3)	0.0003(3)	0.0004(3)
Mn2	0.0064(4)	0.0057(4)	0.0012(3)	0.0034(3)	0.0003(3)	0.0004(3)
O1	0.0085(19)	0.0085(19)	0.008(3)	0.0042(10)	0	0
O2	0.013(2)	0.034(3)	0.006(2)	0.005(2)	0.0017(16)	-0.0012(18)
O3	0.0079(19)	0.013(2)	0.0094(19)	0.0038(16)	0.0037(14)	-0.0024(15)
O4	0.011(2)	0.011(2)	0.001(3)	0.0057(10)	0	0
O5	0.018(2)	0.0066(18)	0.0029(17)	0.0056(16)	-0.0059(14)	-0.0010(14)
O6	0.028(8)	0.028(8)	0.04(3)	0.014(4)	0	0

Table S 65. Refined parameters of SC XRD data of Bi₄Mn₃O_{11.5} at T = 293K CSD-number 42653.

Atom	Wyck.	Occ.	x/a	y/b	z/c	U [Å ²]
Bi1a	18f	0.728(13)	0.5407(2)	0.0162(4)	0.11835(4)	0.01084(17)
Bi1b	18f	0.272(13)	0.5272(3)	-0.0106(4)	0.12067(8)	0.01084(17)
Bi2a	6c	0.9489(6)	0	0	0.086882(6)	0.00942(4)
Bi2b	6c	0.0511(6)	0	0	0.11079(12)	0.00942(4)
Mn1	18f		0.42331(5)	0.27793(5)	-0.000759(13)	0.00624(10)
Mn2	3a	0.0511(6)	0	0	0	0.004(3)
O1	6c		0.6667	0.3333	0.12615(15)	0.0136(7)
O2	18f		0.2516(4)	-0.0309(5)	0.13635(9)	0.0226(9)
O3	18f		0.2114(3)	0.2545(3)	0.03890(8)	0.0135(6)
O4	6c		0.6667	0.3333	-0.03554(11)	0.0078(6)
O5	18f		0.4681(4)	0.0925(3)	0.03561(7)	0.0130(6)
O6	3b	0.71(4)	0.3333	-0.3333	0.1667	0.058(7)

Table S 66. Anisotropic displacement parameters (\AA^2) of SC XRD data of $\text{Bi}_4\text{Mn}_3\text{O}_{11.5}$ at $T = 293\text{K}$.

Atom	U ₁₁	U ₂₂	U ₃₃	U ₁₂	U ₁₃	U ₂₃
Bi1a	0.01498(13)	0.0114(3)	0.00962(9)	0.00924(19)	0.00082(8)	-0.00026(13)
Bi1b	0.01498(13)	0.0114(3)	0.00962(9)	0.00924(19)	0.00082(8)	-0.00026(13)
Bi2a	0.00896(5)	0.00896(5)	0.01033(7)	0.00448(2)	0	0
Bi2b	0.00896(5)	0.00896(5)	0.01033(7)	0.00448(2)	0	0
Mn1	0.00647(12)	0.00544(12)	0.00736(12)	0.00338(10)	0.00051(9)	0.00055(9)
Mn2	0.005(3)	0.005(3)	0.003(5)	0.0025(16)	0	0
O1	0.0104(8)	0.0104(8)	0.0200(16)	0.0052(4)	0	0
O2	0.0118(9)	0.0376(15)	0.0131(9)	0.0085(9)	0.0023(7)	0.0025(9)
O3	0.0093(7)	0.0125(8)	0.0147(8)	0.0025(6)	0.0054(6)	-0.0013(6)
O4	0.0083(7)	0.0083(7)	0.0069(10)	0.0041(3)	0	0
O5	0.0212(9)	0.0084(7)	0.0090(7)	0.0071(7)	-0.0075(6)	-0.0020(5)
O6	0.029(5)	0.029(5)	0.117(18)	0.015(2)	0	0

Table S 67. Calculation of bond valences of Bi atoms of SC XRD data of $\text{Bi}_4\text{Mn}_3\text{O}_{11.5}$ at $T = 293\text{K}$.

Bi1a				Bi1b				Bi2a				Bi2b			
Atom	d	R	v	Atom	d	R	v	Atom	d	R	v	Atom	d	R	v
O2	2.134	2.09	0.89	O2	2.100	2.09	0.97	O3	2.259	2.09	0.63	O2	2.191	2.09	0.76
O1	2.146	2.09	0.86	O2	2.247	2.09	0.65	O3	2.259	2.09	0.63	O2	2.191	2.09	0.76
O2	2.283	2.09	0.59	O1	2.318	2.09	0.54	O3	2.259	2.09	0.63	O2	2.191	2.09	0.76
O5	2.511	2.09	0.32	O6	2.522	2.09	0.31	O2	2.488	2.09	0.34	O1	2.685	2.09	0.20
O6	2.709	2.09	0.19	O5	2.611	2.09	0.24	O2	2.488	2.09	0.34	O3	2.707	2.09	0.19
O3	2.887	2.09	0.12	O3	2.918	2.09	0.11	O2	2.488	2.09	0.34	O3	2.707	2.09	0.19
O2	3.035	2.09	0.08	O2	2.923	2.09	0.11	O1	3.352	2.09	0.03	O3	2.707	2.09	0.19
Vsum			3.04	Vsum			2.93	Vsum			2.95	Vsum			3.05

Table S 68. Calculation of bond valences of Mn1 and Mn2 in $\text{Bi}_4\text{Mn}_3\text{O}_{11.5}$ at $T = 293\text{K}$. The retained model are in bold.

Mn1								Mn2							
hypothesis		Mn ^{II}		Mn ^{III}		Mn ^{IV}		Mn ^{II}		Mn ^{III}		Mn ^{IV}			
Atom	d	R	v	R	v	R	v	Atom	d	R	v	R	v	R	v
O3	1.906	1.79	0.73	1.76	0.67	1.75	0.66	O3	2.119	1.79	0.41	1.76	0.38	1.75	0.37
O4	1.921	1.79	0.70	1.76	0.65	1.75	0.64	O3	2.119	1.79	0.41	1.76	0.38	1.75	0.37
O3	1.937	1.79	0.67	1.76	0.62	1.75	0.61	O3	2.119	1.79	0.41	1.76	0.38	1.75	0.37
O5	1.943	1.79	0.66	1.76	0.61	1.75	0.60	O3	2.119	1.79	0.41	1.76	0.38	1.75	0.37
O4	1.961	1.79	0.63	1.76	0.58	1.75	0.57	O3	2.119	1.79	0.41	1.76	0.38	1.75	0.37
O5	2.059	1.79	0.48	1.76	0.45	1.75	0.44	O3	2.119	1.79	0.41	1.76	0.38	1.75	0.37
V _{sum}		3.88	3.88	V _{sum}	3.58	V _{sum}	3.51	V _{sum}		2.47	2.47	V _{sum}	2.27	V _{sum}	2.23

Table S 69. Possible superexchange (SE) paths in $\text{Bi}_4\text{Mn}_3\text{O}_{11.5}$

J	d (Å), Mn-Mn	SE	angle (deg)
1	2.8763(7)	Mn1-O3-Mn1	96.82(19)
		Mn1-O5-Mn1	96.3(2)
2	3.0166(4)	Mn1-O5-Mn1	97.8(2)
		Mn1-O5-Mn1	97.8(2)
3	2.9540(8)	Mn1-O5-Mn1	95.56(16)
		Mn1-O4-Mn1	97.3(2)
4	2.9540(8)	Mn1-O4-Mn1	97.3(2)
		Mn1-O5-Mn1	95.56(16)
5	2.8763(7)	Mn1-O5-Mn1	96.3(2)
		Mn1-O3-Mn1	96.82(19)

Table S 70. Precursors, experimental conditions and identified products. The last line show the successful method. It was applied after observation of the target-phase in a mixture at 500°C during the in-situ thermal decomposition of a Pechini-prepared precursor in the XRD diffractometer.

#	Precursors	Conditions	Obtained products
1	$3\text{Bi}_2\text{O}_3 + 6\text{BiOCl} + \text{PbO} + \text{MnO}_2$	Sealed golden tube, heated at 1173K, then slow cooling down	$\text{Bi}_4\text{Mn}_3\text{O}_{11.5}$, $\text{Bi}_6\text{O}_8\text{Cl}$
2	$2\text{PbO} + 3\text{Bi}_2\text{O}_3 + 6\text{MnO}_2$	973K in alumina crucible	$\text{Bi}_{24}\text{Mn}_2\text{O}_{40}$, $\text{Bi}_2\text{Mn}_4\text{O}_{10}$, $\text{Pb}_6\text{Mn}_6\text{O}_{17}$ and Pb_2MnO_4 .
3	$2\text{PbO} + 3\text{Bi}_2\text{O}_3 + 6\text{MnO}_3$	1173K in alumina crucible	$\text{Bi}_2\text{Mn}_4\text{O}_{10}$, $\text{Bi}_8\text{Pb}_5\text{O}_{17}$ and Mn_2O_3 .
4	$2\text{PbO} + 6\text{BiOCl} + 6\text{MnO}_2$	973K in alumina crucible, under O_2 flow	$\text{Bi}_2\text{Mn}_4\text{O}_{10}$, Mn_2O_3 and $\text{PbO}_{1.57}$
5	$2\text{Pb}(\text{acetate}) + 6\text{Bi}(\text{citrate}) + 6\text{Mn}(\text{acetate})$	Pechini method, HTXRD under N_2 flow	$\text{Bi}_2\text{Mn}_4\text{O}_{10}$ and gamma- Bi_2O_3
6	$8\text{Bi}(\text{citrate}) + 6\text{Mn}(\text{acetate})$	Pechini method, HTXRD under N_2 flow	$\text{Bi}_2\text{Mn}_4\text{O}_{10}$ and gamma- Bi_2O_3
7	$4\text{Bi}_2\text{O}_3 + 6\text{MnO}_2$	1173K in golden boat, under Ar	$\text{Bi}_2\text{Mn}_4\text{O}_{10}$ and beta- Bi_2O_3
8	$4\text{Bi}_2\text{O}_3 + \text{Mn}_2\text{O}_3 + 4\text{MnO}_2$	973K in alumina crucible, under Ar flow	$\text{Bi}_{24}\text{Mn}_2\text{O}_{40}$ and Mn_3O_4
9	$\text{Bi}_2\text{O}_3 + \text{MnO}_2$ (2%)	1173K in golden boat	beta- Bi_2O_3
10	$\text{Bi}_2\text{O}_3 + \text{MnO}_2$ (10%)	1103K in alumina crucible, under Ar flow	$\text{Bi}_{24}\text{Mn}_2\text{O}_{40}$ and $\text{Bi}_2\text{O}_{2.5}$
11	$\text{BiOCl} + \text{Bi}_2\text{O}_3 + 2\% \text{MnO}_2$	1073K in alumina crucible	$\text{Bi}_3\text{O}_4\text{Cl}$, $\text{Bi}_{12}\text{O}_{17}\text{Cl}_2$, $\text{Bi}_{12}\text{MnO}_{20}$ and Mn_2O_3 .
12	$6\text{KMnO}_4 + 8\text{BiOCl}$	1073K in alumina crucible	$\text{Bi}_2\text{Mn}_4\text{O}_{10}$ and alpha- Bi_2O_3
13	$50\% (6\text{KMnO}_4 + 8\text{BiOCl}) + 50\% \text{KCl}$	1073K in alumina crucible	$\text{Bi}_2\text{Mn}_4\text{O}_{10}$ and $\text{Bi}_3\text{O}_4\text{Cl}$
14	$20\% \text{KMnO}_4 + 80\% \text{BiOCl}$	1073K in alumina crucible	$\text{Bi}_{24}\text{O}_{31}\text{Cl}_{10}$, $\text{Bi}_3\text{O}_4\text{Cl}$ and $\text{Bi}_2\text{Mn}_4\text{O}_{10}$
15	$8 \text{Bi}(\text{citrate}) + 6\text{Mn}(\text{acetate})$	Pechini method, 773 K, 60 hours	$\text{Bi}_4\text{Mn}_3\text{O}_{11.5}$

12) β' -BiSeO₃Cl, Bi₆(SeO₃)₄Cl₁₀ and PbBi₁₀(SeO₃)₁₂Cl₈Table S 71. Crystal data, measurement and structural refinement parameters for β -BiSeO₃Cl, Bi₆(SeO₃)₄Cl₁₀ and PbBi₁₀(SeO₃)₁₂Cl₈

	β -BiSeO ₃ Cl	Bi ₆ (SeO ₃) ₄ Cl ₁₀	PbBi ₁₀ (SeO ₃) ₁₂ Cl ₈
Crystal data			
Crystal symmetry	Monoclinic	Monoclinic	Orthorhombic
space group	Cc	P21/c	Cc
a (Å)	22.6893(12)	21.460(2)	15.819(6)
b (Å)	76.775(4)	8.4012(9)	17.871(7)
c (Å)	16.0478(14)	15.3370(18)	15.857(6)
β (°)	134.954(2)	110.639(5)	
V (Å ³)	19783(2)	2587.7 (5)	4483 (3)
Z	192	4	4
Dx (g/cm ³)	5.470	5.432	6.079
μ (mm ⁻¹)(for λ)	52.04	47.37	53.17
Appearance	Colorless platelet	Colorless needle	Colorless platelet
Crystal size (mm)	0.13×0.09×0.05	0.81×0.37×0.13	0.16×0.15×0.06
Data collection			
λ (Mo K α) (Å)	0.71073	0.71073	0.71073
Scan mode	ω and ϕ	ω and ϕ	ω and ϕ
θ (min–max) (°)	1.1 – 26.5	2.0 – 30.5	2.2 – 26.4
R(int) (%)	0.096	0.045	0.050
Recording reciprocal space	–28 ≤ h ≤ 28 –96 ≤ k ≤ 96 –20 ≤ l ≤ 20	–30 ≤ h ≤ 30 –11 ≤ k ≤ 7 –20 ≤ l ≤ 21	–15 ≤ h ≤ 19 –22 ≤ k ≤ 21 –19 ≤ l ≤ 19
Refinement			
Measured, independent	243977, 35097,	34697, 7843, 6363	10469, 2253,
obs. refl.	24284		1504
No. of Refined parameters	1637	298	115
Refinement method,	F ²	F ²	F ²
R1(F ²)(obs) / R1(F ²)(all)	0.0647/0.1041	0.0303/0.0431	0.0667/0.1057
wR2(F ²)(obs) / wR2(F ²)(all)	0.1482/0.1632	0.0333/0.0445	0.0639/0.0859
GOF(obs) / GOF(all)	1.043/1.043	1.48/1.77	0.84/0.92
$\Delta\rho_{\max}/\Delta\rho_{\min}$ (e Å ⁻³)	6.09 /–4.26	3.41 /–3.07	5.38 /–7.01
Extinction coefficient	0.00000000	0.0059(13)	0.0022(13)

*obs=[I>3 σ (I)]

Table S 72. Fractional atomic coordinates and isotropic or equivalent isotropic displacement parameters (\AA^2) of $\beta\text{-BiSeO}_3\text{Cl}$

	<i>x</i>	<i>y</i>	<i>z</i>	$U_{\text{iso}}^*/U_{\text{eq}}$
Bi1	0.83058 (11)	0.94300 (3)	0.73001 (15)	0.0177 (4)
Bi2	1.07566 (13)	0.94440 (3)	0.46808 (18)	0.0264 (5)
Bi3	0.70037 (11)	0.97961 (3)	0.20999 (16)	0.0220 (4)
Bi4	1.06773 (11)	0.64526 (3)	−0.03419 (15)	0.0228 (4)
Bi5	1.33606 (11)	0.64057 (2)	0.24423 (15)	0.0212 (4)
Bi6	0.20161 (11)	0.97967 (3)	0.98544 (15)	0.0225 (4)
Bi7	1.07824 (11)	0.93894 (3)	0.97991 (15)	0.0193 (4)
Bi8	1.46187 (12)	0.69444 (2)	0.24901 (16)	0.0203 (4)
Bi9	0.81348 (12)	0.94041 (2)	0.97290 (16)	0.0195 (4)
Bi10	1.32491 (11)	0.72959 (3)	0.23065 (16)	0.0230 (4)
Bi11	0.56859 (11)	0.94315 (3)	0.70624 (16)	0.0226 (5)
Bi12	0.60026 (12)	0.72966 (3)	0.00583 (16)	0.0227 (4)
Bi13	1.71596 (11)	0.69307 (3)	0.49162 (16)	0.0189 (4)
Bi14	0.57719 (11)	0.93881 (3)	0.96639 (15)	0.0182 (4)
Bi15	0.46336 (12)	0.69460 (2)	−0.25002 (17)	0.0205 (4)
Bi16	0.71410 (11)	0.89270 (2)	0.96130 (15)	0.0214 (4)
Bi17	0.19496 (12)	0.89061 (2)	0.96828 (16)	0.0227 (4)
Bi18	0.93629 (11)	0.98330 (2)	0.21303 (15)	0.0208 (4)
Bi19	0.57328 (14)	0.94379 (3)	0.47180 (18)	0.0284 (5)
Bi20	0.33122 (11)	0.94270 (3)	0.72515 (15)	0.0175 (4)
Bi21	0.59311 (11)	0.64301 (3)	0.00160 (16)	0.0228 (4)
Bi22	0.47572 (12)	0.69188 (2)	−0.48591 (16)	0.0200 (4)
Bi23	1.44964 (12)	0.69202 (2)	−0.01131 (16)	0.0202 (4)
Bi24	0.94820 (12)	0.69029 (2)	0.24077 (16)	0.0205 (4)
Bi25	1.43687 (11)	0.98320 (2)	0.45218 (15)	0.0216 (4)
Bi26	0.56673 (11)	0.94148 (2)	0.22464 (16)	0.0194 (4)
Bi27	1.06752 (11)	0.94354 (2)	0.22051 (16)	0.0209 (4)
Bi28	0.31955 (12)	0.94413 (3)	0.96752 (17)	0.0217 (4)
Bi29	0.06782 (11)	0.94169 (3)	0.70155 (16)	0.0192 (4)
Bi30	1.20987 (12)	0.69290 (3)	0.48564 (16)	0.0198 (5)
Bi31	0.86148 (11)	0.64257 (2)	0.25664 (15)	0.0216 (4)
Bi32	0.81983 (12)	0.94446 (3)	0.46690 (17)	0.0223 (4)
Bi33	0.59420 (12)	0.65299 (2)	−0.23989 (16)	0.0236 (4)
Bi34	1.21683 (11)	0.89518 (3)	0.25882 (16)	0.0233 (4)
Bi35	0.71694 (13)	0.69409 (3)	−0.24904 (18)	0.0272 (5)
Bi36	1.31605 (12)	0.94072 (3)	0.44967 (17)	0.0220 (4)
Bi37	0.83292 (11)	0.73328 (2)	0.00286 (15)	0.0213 (4)
Bi38	0.97632 (12)	0.69085 (2)	−0.23281 (16)	0.0215 (4)
Bi39	0.95534 (13)	0.69348 (2)	−0.00543 (16)	0.0220 (4)
Bi40	1.33195 (11)	0.65284 (2)	0.00054 (15)	0.0230 (4)
Bi41	1.97117 (13)	0.69324 (3)	0.50905 (17)	0.0234 (5)
Bi42	0.43823 (11)	0.90224 (2)	1.21751 (15)	0.0244 (4)
Bi43	0.94066 (11)	0.90340 (2)	0.44939 (15)	0.0210 (4)
Bi44	1.71996 (11)	0.68922 (3)	0.24888 (16)	0.0206 (4)
Bi45	0.09225 (11)	0.73326 (2)	−0.23850 (15)	0.0208 (4)
Bi46	0.69651 (11)	0.89252 (2)	0.21257 (15)	0.0226 (4)
Bi47	0.20934 (13)	0.69421 (3)	−0.25626 (18)	0.0279 (5)
Bi48	1.20802 (11)	0.68897 (3)	0.23673 (15)	0.0208 (5)
Se1	0.6006 (3)	0.71982 (6)	−0.2450 (4)	0.0175 (9)
Se2	1.4514 (3)	0.96971 (6)	0.2349 (4)	0.0178 (10)
Se3	0.3584 (3)	0.72290 (6)	−0.2470 (4)	0.0178 (10)
Se4	0.3243 (3)	0.71976 (6)	−0.0211 (4)	0.0159 (9)
Se5	0.6831 (3)	0.97129 (6)	0.7010 (4)	0.0178 (10)
Se6	1.5675 (3)	0.72283 (6)	0.4630 (4)	0.0162 (10)
Se7	1.4418 (3)	0.91766 (6)	0.4442 (4)	0.0152 (9)
Se8	1.1859 (3)	0.97145 (6)	0.4595 (4)	0.0162 (10)

Se9	0.6850 (3)	0.91496 (6)	0.4568 (4)	0.0179 (10)
Se10	1.5892 (3)	0.66495 (6)	0.5095 (4)	0.0162 (9)
Se11	0.1035 (3)	0.71812 (6)	-0.0159 (3)	0.0164 (9)
Se12	0.8577 (3)	0.66381 (6)	-0.2466 (4)	0.0154 (9)
Se13	0.1849 (3)	0.91498 (6)	0.7046 (4)	0.0160 (9)
Se14	0.7102 (3)	0.91368 (6)	0.7519 (4)	0.0193 (10)
Se15	0.0905 (3)	0.72137 (6)	-0.4878 (3)	0.0145 (9)
Se16	0.2123 (3)	0.97271 (6)	0.7549 (4)	0.0161 (10)
Se17	1.0629 (3)	0.72135 (6)	0.2128 (4)	0.0155 (9)
Se18	1.2106 (3)	0.91382 (6)	0.4604 (4)	0.0158 (9)
Se19	0.9402 (3)	0.91799 (6)	0.2301 (4)	0.0188 (9)
Se20	0.9522 (3)	0.96977 (6)	0.4615 (4)	0.0194 (10)
Se21	1.0679 (3)	0.66369 (6)	0.4640 (4)	0.0182 (10)
Se22	1.3324 (3)	0.72079 (6)	0.4516 (4)	0.0182 (10)
Se23	0.7109 (3)	0.97280 (6)	0.4615 (4)	0.0160 (10)
Se24	0.4860 (2)	0.97070 (6)	1.0009 (3)	0.0128 (9)
Se25	1.2252 (3)	0.96822 (6)	0.2314 (3)	0.0164 (9)
Se26	0.8337 (3)	0.72145 (6)	-0.2452 (4)	0.0138 (9)
Se27	0.3371 (3)	0.66498 (6)	-0.2430 (4)	0.0161 (10)
Se28	0.9573 (3)	0.97157 (6)	1.0029 (3)	0.0169 (10)
Se29	1.5631 (3)	0.66412 (6)	0.2150 (4)	0.0156 (9)
Se30	1.0847 (3)	0.66319 (6)	0.2089 (4)	0.0154 (9)
Se31	0.1068 (3)	0.66777 (5)	-0.2272 (4)	0.0166 (9)
Se32	0.4823 (3)	0.91309 (6)	0.7490 (4)	0.0169 (10)
Se33	0.8188 (3)	0.66766 (6)	-0.0164 (4)	0.0224 (11)
Se34	1.8634 (3)	0.72154 (6)	0.5122 (3)	0.0150 (9)
Se35	0.9542 (3)	0.91420 (6)	0.7006 (4)	0.0163 (9)
Se36	0.8230 (3)	0.71815 (6)	0.2031 (4)	0.0178 (10)
Se37	1.5939 (3)	0.72089 (6)	0.2138 (4)	0.0184 (10)
Se38	0.3624 (3)	0.66400 (6)	-0.4850 (4)	0.0152 (9)
Se39	0.4572 (3)	0.97135 (6)	0.7028 (4)	0.0190 (10)
Se40	0.7812 (2)	0.93444 (5)	0.2323 (3)	0.0150 (8)
Se41	1.8414 (3)	0.66332 (6)	0.4651 (4)	0.0172 (9)
Se42	0.7250 (3)	0.96818 (6)	0.0116 (4)	0.0175 (10)
Se43	0.9863 (3)	0.97088 (6)	0.7640 (3)	0.0150 (9)
Se44	0.4531 (3)	0.91378 (6)	0.9988 (4)	0.0182 (10)
Se45	0.2812 (3)	0.93386 (6)	1.1231 (4)	0.0199 (9)
Se46	0.6584 (3)	0.68454 (5)	-0.0166 (3)	0.0179 (9)
Se47	0.9832 (3)	0.91322 (6)	1.0068 (4)	0.0171 (10)
Se48	1.2675 (3)	0.68405 (6)	0.0926 (3)	0.0181 (9)
Cl1	1.2203 (7)	0.63687 (15)	-0.0152 (9)	0.022 (2)*
Cl2	1.2218 (8)	0.74843 (17)	0.2307 (11)	0.035 (3)*
Cl3	0.3422 (7)	0.88815 (15)	0.9989 (10)	0.022 (3)*
Cl4	0.9444 (8)	0.75008 (16)	0.2008 (11)	0.035 (3)*
Cl5	0.8350 (8)	0.88790 (16)	0.9798 (11)	0.028 (3)*
Cl6	0.2023 (8)	0.75092 (17)	-0.0340 (11)	0.034 (3)*
Cl7	0.0885 (8)	0.88932 (17)	0.7398 (11)	0.033 (3)*
Cl8	0.9708 (8)	0.63797 (16)	-0.2603 (10)	0.027 (3)*
Cl9	0.5978 (7)	0.88771 (13)	0.7417 (9)	0.019 (2)*
Cl10	-0.0219 (8)	0.74981 (17)	-0.2656 (11)	0.034 (3)*
Cl11	0.7055 (9)	0.74831 (18)	0.2136 (12)	0.039 (3)*
Cl12	0.7230 (8)	0.75087 (16)	-0.0132 (10)	0.031 (3)*
Cl13	0.4782 (7)	0.63944 (14)	-0.2578 (9)	0.020 (2)*
Cl14	1.4385 (8)	0.74860 (16)	0.4523 (11)	0.035 (3)*
Cl15	0.7021 (7)	0.63785 (16)	-0.0263 (10)	0.026 (3)*
Cl16	0.9658 (7)	0.63849 (15)	-0.0243 (10)	0.027 (2)*
Cl17	0.7048 (7)	0.85959 (16)	0.2259 (10)	0.026 (3)*
Cl18	0.4714 (8)	0.63940 (17)	-0.0122 (11)	0.032 (3)*
Cl19	0.3378 (6)	0.88694 (13)	1.2263 (8)	0.016 (2)*
Cl20	0.9616 (9)	0.63774 (18)	0.2365 (12)	0.038 (3)*

CI21	0.0855 (7)	0.88734 (15)	0.9730 (10)	0.024 (2)*
CI22	0.4835 (8)	0.74876 (16)	-0.0040 (10)	0.032 (3)*
CI23	0.2040 (8)	0.85810 (17)	0.9732 (11)	0.030 (3)*
CI24	1.3371 (8)	0.60863 (17)	0.2333 (11)	0.029 (3)*
CI25	0.8356 (7)	0.61035 (16)	0.2289 (10)	0.026 (3)*
CI26	0.7153 (8)	0.85961 (19)	0.9856 (12)	0.038 (3)*
CI27	0.5891 (7)	0.88808 (16)	-0.0097 (10)	0.025 (3)*
CI28	1.4476 (7)	0.63901 (15)	0.2133 (9)	0.022 (2)*
CI29	0.7059 (8)	0.63807 (18)	0.2208 (11)	0.035 (3)*
CI30	0.5973 (8)	0.99811 (17)	0.0039 (11)	0.034 (3)*
CI31	0.5946 (8)	0.49836 (15)	0.7640 (10)	0.030 (3)*
CI32	1.4547 (7)	0.63925 (15)	0.4691 (10)	0.027 (2)*
CI33	1.2171 (7)	0.63797 (15)	0.2297 (10)	0.025 (2)*
CI34	1.2091 (7)	0.86071 (16)	0.2284 (10)	0.025 (3)*
CI35	1.3300 (7)	0.88723 (14)	0.4703 (10)	0.023 (2)*
CI36	0.5847 (7)	0.61036 (15)	-0.0220 (9)	0.022 (2)*
CI37	0.5921 (8)	0.99879 (17)	0.2158 (11)	0.039 (3)*
CI38	0.8420 (6)	0.88698 (14)	0.2402 (9)	0.018 (2)*
CI39	0.8435 (9)	1.00126 (19)	0.2294 (12)	0.040 (3)*
CI40	0.9596 (8)	0.63859 (16)	0.4735 (10)	0.029 (3)*
CI41	1.3414 (9)	1.00095 (19)	0.2497 (12)	0.041 (3)*
CI42	0.8491 (7)	1.00016 (15)	0.0147 (10)	0.030 (3)*
CI43	0.8391 (7)	0.88829 (14)	0.4706 (9)	0.023 (2)*
CI44	0.5927 (7)	0.89013 (14)	0.2269 (9)	0.023 (2)*
CI45	1.0885 (6)	0.61103 (14)	-0.0217 (9)	0.018 (2)*
CI46	1.3521 (8)	1.00044 (17)	0.4807 (11)	0.038 (3)*
CI47	1.0932 (6)	0.88796 (13)	0.2324 (8)	0.016 (2)*
CI48	0.1005 (9)	0.9987 (2)	0.9883 (12)	0.043 (4)*
O1	1.3423 (16)	0.6703 (3)	0.118 (2)	0.012 (6)*
O2	0.0907 (19)	0.7161 (4)	-0.137 (3)	0.030 (8)*
O3	0.589 (2)	0.6707 (4)	-0.137 (3)	0.027 (8)*
O4	1.8401 (18)	0.6696 (4)	0.364 (3)	0.024 (7)*
O5	0.8377 (18)	0.7166 (4)	0.110 (3)	0.027 (7)*
O6	1.3358 (18)	0.7141 (4)	0.350 (3)	0.024 (7)*
O7	0.2172 (16)	0.7164 (3)	-0.137 (2)	0.016 (6)*
O8	0.7183 (16)	0.7136 (3)	0.116 (2)	0.012 (6)*
O9	0.837 (2)	0.6764 (4)	-0.352 (3)	0.030 (8)*
O10	1.0826 (18)	0.9196 (4)	1.099 (2)	0.022 (6)*
O11	0.0791 (19)	0.9221 (4)	0.599 (3)	0.023 (7)*
O12	0.7136 (19)	0.6708 (4)	-0.133 (3)	0.025 (7)*
O13	0.5801 (16)	0.9218 (3)	0.347 (2)	0.015 (6)*
O14	0.8359 (18)	0.9220 (4)	0.106 (2)	0.022 (7)*
O15	0.4597 (17)	0.7164 (4)	-0.148 (2)	0.019 (6)*
O16	0.4585 (18)	0.9566 (4)	0.896 (2)	0.024 (6)*
O17	0.9566 (17)	0.7156 (3)	0.101 (2)	0.015 (6)*
O18	1.6735 (15)	0.7079 (3)	0.322 (2)	0.010 (5)*
O19	0.9599 (18)	0.9591 (4)	0.652 (2)	0.026 (7)*
O20	0.5825 (18)	0.9195 (4)	0.853 (2)	0.019 (7)*
O21	1.0950 (18)	0.6692 (4)	0.117 (3)	0.026 (7)*
O22	1.0897 (15)	0.7081 (3)	0.156 (2)	0.009 (5)*
O23	0.7102 (16)	0.9586 (4)	0.643 (2)	0.019 (6)*
O24	0.5401 (18)	0.9252 (4)	1.054 (2)	0.023 (6)*
O25	0.9571 (17)	0.9259 (3)	0.896 (2)	0.016 (6)*
O26	0.3346 (16)	0.7098 (3)	-0.356 (2)	0.014 (6)*
O27	1.5960 (18)	0.7100 (4)	0.408 (3)	0.017 (7)*
O28	0.827 (2)	0.9203 (5)	0.348 (3)	0.033 (9)*
O29	1.0407 (17)	0.9586 (3)	1.059 (2)	0.014 (6)*
O30	1.090 (2)	0.9634 (5)	0.863 (3)	0.039 (9)*
O31	1.3469 (17)	0.6947 (3)	0.227 (2)	0.015 (6)*
O32	0.7032 (18)	0.7170 (4)	-0.154 (3)	0.022 (7)*

O33	0.9194 (15)	0.7096 (3)	-0.184 (2)	0.009 (5)*
O34	1.2119 (17)	0.9197 (4)	0.359 (2)	0.012 (6)*
O35	1.4608 (19)	0.6713 (4)	0.105 (3)	0.021 (6)*
O36	1.4620 (17)	0.7158 (3)	0.356 (2)	0.020 (6)*
O37	0.3322 (17)	0.6751 (4)	-0.600 (2)	0.020 (6)*
O38	0.073 (2)	0.6961 (4)	-0.023 (3)	0.037 (8)*
O39	0.6279 (16)	0.9263 (3)	0.643 (2)	0.016 (6)*
O40	0.9538 (17)	0.9214 (4)	0.350 (2)	0.018 (6)*
O41	0.3408 (18)	0.7178 (4)	0.098 (3)	0.025 (7)*
O42	0.7195 (17)	0.9665 (4)	0.369 (2)	0.019 (7)*
O43	1.5947 (18)	0.7135 (4)	0.111 (3)	0.025 (7)*
O44	1.5043 (18)	0.6777 (4)	0.400 (2)	0.019 (6)*
O45	0.2150 (17)	0.9275 (4)	0.817 (2)	0.022 (6)*
O46	1.2095 (19)	0.9592 (4)	0.400 (3)	0.025 (7)*
O47	0.963 (2)	0.6699 (4)	0.357 (3)	0.030 (8)*
O48	0.3262 (18)	0.9204 (4)	1.091 (2)	0.022 (7)*
O49	1.4524 (19)	0.9207 (4)	0.350 (3)	0.018 (7)*
O50	0.2935 (17)	0.9599 (3)	0.808 (2)	0.013 (6)*
O51	0.6835 (19)	0.6709 (4)	0.084 (3)	0.020 (7)*
O52	0.5749 (17)	0.6986 (4)	-0.294 (2)	0.020 (6)*
O53	1.0927 (15)	0.6767 (3)	0.402 (2)	0.011 (5)*
O54	0.2042 (15)	0.7144 (3)	0.100 (2)	0.008 (5)*
O55	0.9637 (15)	0.9212 (3)	0.609 (2)	0.008 (5)*
O56	0.4623 (18)	0.9211 (3)	1.112 (3)	0.023 (6)*
O57	0.7089 (17)	0.9212 (4)	0.129 (2)	0.018 (6)*
O58	0.4648 (16)	0.6717 (3)	-0.390 (2)	0.010 (5)*
O59	0.5909 (18)	0.7176 (4)	-0.157 (2)	0.026 (7)*
O60	1.1684 (18)	0.6750 (4)	0.317 (3)	0.025 (7)*
O61	0.9642 (17)	0.9667 (3)	0.370 (2)	0.018 (6)*
O62	1.9244 (17)	0.6742 (4)	0.577 (2)	0.021 (6)*
O63	0.9523 (17)	0.9248 (3)	1.060 (2)	0.020 (6)*
O64	1.0818 (17)	0.9647 (4)	0.354 (2)	0.019 (6)*
O65	1.9659 (17)	0.7155 (3)	0.612 (2)	0.016 (6)*
O66	0.5792 (17)	0.9639 (4)	0.592 (2)	0.018 (6)*
O67	0.712 (2)	0.9593 (4)	0.816 (3)	0.024 (8)*
O68	0.4602 (18)	0.9655 (4)	0.602 (3)	0.023 (7)*
O69	1.2096 (16)	0.9588 (3)	0.568 (2)	0.017 (6)*
O70	0.7275 (18)	0.9457 (4)	0.255 (2)	0.018 (7)*
O71	1.2015 (19)	0.9471 (4)	0.240 (3)	0.025 (7)*
O72	1.4633 (17)	0.9657 (4)	0.355 (2)	0.021 (6)*
O73	0.6267 (18)	0.9610 (4)	0.402 (2)	0.023 (7)*
O74	0.8617 (17)	0.6971 (3)	0.265 (2)	0.014 (6)*
O75	0.7949 (16)	0.9263 (3)	0.813 (2)	0.012 (6)*
O76	0.8719 (16)	0.9596 (3)	0.891 (2)	0.015 (6)*
O77	1.5868 (17)	0.6724 (3)	0.609 (2)	0.018 (6)*
O78	0.005 (2)	0.7092 (4)	-0.600 (3)	0.043 (8)*
O79	0.2553 (18)	0.6766 (4)	-0.351 (2)	0.022 (7)*
O80	0.4542 (16)	0.9255 (3)	0.806 (2)	0.013 (6)*
O81	0.2157 (18)	0.9654 (4)	0.864 (3)	0.026 (7)*
O82	0.2018 (16)	0.9207 (3)	1.078 (2)	0.014 (6)*
O83	1.349 (2)	0.9676 (4)	0.114 (3)	0.033 (8)*
O84	1.4797 (19)	0.9487 (4)	0.238 (3)	0.029 (7)*
O85	1.5113 (17)	0.7096 (4)	0.159 (2)	0.022 (6)*
O86	1.5934 (16)	0.7112 (3)	0.573 (2)	0.016 (6)*
O87	0.7086 (16)	0.9270 (3)	0.563 (2)	0.015 (6)*
O88	0.8356 (17)	0.6755 (4)	-0.183 (2)	0.017 (6)*
O89	0.0932 (17)	0.6717 (4)	-0.141 (2)	0.020 (6)*
O90	0.0921 (15)	0.6761 (3)	-0.425 (2)	0.010 (5)*
O91	0.7062 (16)	0.9641 (4)	0.098 (2)	0.015 (6)*
O92	1.336 (2)	0.9202 (4)	0.352 (3)	0.023 (7)*

O93	0.5385 (17)	0.9583 (3)	0.810 (2)	0.012 (6)*
O94	0.1773 (17)	0.7097 (4)	-0.427 (2)	0.021 (6)*
O95	1.2923 (17)	0.9254 (3)	0.562 (2)	0.018 (6)*
O96	0.7923 (17)	0.9602 (3)	0.565 (2)	0.017 (6)*
O97	0.2104 (19)	0.6709 (4)	-0.136 (3)	0.026 (7)*
O98	0.4562 (17)	0.9592 (3)	1.057 (2)	0.016 (6)*
O99	1.8351 (15)	0.7087 (3)	0.402 (2)	0.009 (5)*
O100	1.0408 (16)	0.9252 (3)	0.817 (2)	0.012 (6)*
O101	1.5912 (16)	0.6771 (3)	0.325 (2)	0.014 (6)*
O102	0.4555 (19)	0.9252 (4)	0.638 (3)	0.019 (7)*
O103	1.1288 (15)	0.9264 (3)	0.405 (2)	0.007 (5)*
O104	1.4187 (16)	0.7102 (3)	0.568 (2)	0.015 (6)*
O105	1.6697 (16)	0.6772 (3)	0.566 (2)	0.014 (6)*
O106	0.2114 (15)	0.9275 (3)	0.649 (2)	0.011 (6)*
O107	0.7100 (15)	0.9275 (3)	0.396 (2)	0.012 (6)*
O108	1.2102 (16)	0.9633 (4)	0.114 (2)	0.014 (6)*
O109	0.9627 (19)	0.9651 (4)	1.113 (3)	0.021 (6)*
O110	1.5970 (18)	0.6751 (4)	0.162 (3)	0.021 (7)*
O111	0.0828 (18)	0.6889 (4)	-0.289 (2)	0.021 (7)*
O112	0.8480 (16)	0.6887 (3)	-0.020 (2)	0.011 (6)*
O113	1.8368 (18)	0.7101 (4)	0.570 (2)	0.025 (7)*
O114	0.3729 (14)	0.9270 (3)	0.8940 (18)	0.001 (5)*
O115	0.7536 (16)	0.7094 (3)	-0.353 (2)	0.017 (6)*
O116	0.7094 (17)	0.9199 (4)	0.860 (2)	0.021 (6)*
O117	1.0032 (19)	0.6745 (4)	0.158 (3)	0.030 (8)*
O118	0.8382 (17)	0.7143 (4)	-0.139 (2)	0.016 (6)*
O119	0.699 (2)	0.9476 (4)	-0.053 (3)	0.021 (8)*
O120	0.8750 (17)	0.9266 (3)	0.648 (2)	0.018 (6)*
O121	1.2356 (16)	0.6709 (3)	0.136 (2)	0.010 (5)*
O122	0.9617 (17)	0.6697 (3)	-0.145 (2)	0.016 (6)*
O123	0.0931 (15)	0.7146 (3)	-0.385 (2)	0.009 (5)*
O124	0.9804 (18)	0.9383 (4)	0.240 (3)	0.024 (7)*
O125	1.2492 (15)	0.7075 (3)	0.397 (2)	0.008 (5)*
O126	0.8390 (17)	0.6711 (4)	0.104 (2)	0.018 (6)*
O127	0.9749 (15)	0.9487 (3)	0.510 (2)	0.007 (5)*
O128	0.3414 (16)	0.6719 (3)	-0.136 (2)	0.013 (6)*
O129	1.0905 (15)	0.7101 (3)	0.323 (2)	0.015 (6)*
O130	1.7569 (15)	0.6756 (3)	0.409 (2)	0.012 (5)*
O131	0.4248 (15)	0.6773 (3)	-0.181 (2)	0.008 (5)*
O132	0.9588 (18)	0.9583 (4)	0.820 (2)	0.021 (6)*
O133	0.3424 (17)	0.6765 (3)	-0.422 (2)	0.020 (6)*
O134	0.8502 (18)	0.9674 (4)	0.371 (2)	0.020 (6)*
O135	0.1282 (16)	0.9608 (3)	0.644 (2)	0.016 (6)*
O136	0.832 (2)	0.9660 (5)	0.100 (3)	0.036 (9)*
O137	0.3342 (17)	0.7110 (3)	-0.186 (2)	0.020 (6)*
O138	1.3313 (18)	0.9657 (4)	0.348 (2)	0.022 (7)*
O139	0.3482 (17)	0.6976 (4)	-0.023 (2)	0.020 (6)*
O140	1.4721 (17)	0.9383 (3)	0.495 (2)	0.016 (6)*
O141	0.3758 (16)	0.9591 (3)	0.646 (2)	0.017 (6)*
O142	0.585 (2)	0.6946 (4)	-0.036 (3)	0.032 (8)*
O143	0.5877 (18)	0.9629 (4)	1.104 (2)	0.024 (7)*
O144	0.2230 (18)	0.9445 (4)	0.990 (2)	0.022 (7)*

Table S 73. Atomic displacement parameters (\AA^2) of $\beta\text{-BiSeO}_3\text{Cl}$

	U^{11}	U^{22}	U^{33}	U^{12}	U^{13}	U^{23}
Bi1	0.0089 (9)	0.0283 (12)	0.0123 (10)	0.0010 (8)	0.0062 (9)	0.0014 (8)
Bi2	0.0247 (12)	0.0304 (13)	0.0290 (12)	-0.0001 (9)	0.0207 (11)	-0.0009 (9)
Bi3	0.0124 (9)	0.0321 (11)	0.0163 (9)	-0.0045 (8)	0.0082 (8)	-0.0034 (8)
Bi4	0.0140 (9)	0.0317 (12)	0.0202 (9)	-0.0020 (8)	0.0112 (8)	-0.0020 (8)
Bi5	0.0179 (10)	0.0263 (11)	0.0185 (9)	0.0022 (8)	0.0125 (9)	0.0014 (8)
Bi6	0.0136 (9)	0.0325 (12)	0.0203 (9)	-0.0023 (8)	0.0116 (9)	-0.0007 (8)
Bi7	0.0141 (10)	0.0264 (11)	0.0178 (10)	-0.0006 (7)	0.0114 (9)	-0.0003 (7)
Bi8	0.0178 (10)	0.0246 (10)	0.0171 (10)	-0.0014 (8)	0.0118 (9)	-0.0006 (8)
Bi9	0.0114 (10)	0.0255 (10)	0.0170 (10)	0.0002 (7)	0.0084 (9)	0.0000 (7)
Bi10	0.0179 (10)	0.0324 (12)	0.0226 (10)	-0.0016 (8)	0.0157 (9)	0.0014 (8)
Bi11	0.0135 (10)	0.0303 (12)	0.0207 (11)	-0.0039 (8)	0.0109 (10)	-0.0050 (8)
Bi12	0.0191 (10)	0.0277 (11)	0.0181 (9)	0.0028 (8)	0.0120 (9)	0.0039 (8)
Bi13	0.0157 (11)	0.0237 (11)	0.0176 (11)	0.0001 (7)	0.0118 (10)	0.0002 (7)
Bi14	0.0172 (10)	0.0233 (11)	0.0150 (9)	-0.0005 (7)	0.0117 (9)	0.0001 (7)
Bi15	0.0192 (10)	0.0247 (10)	0.0194 (10)	0.0017 (8)	0.0142 (10)	0.0022 (8)
Bi16	0.0182 (10)	0.0298 (11)	0.0187 (9)	-0.0009 (8)	0.0139 (9)	-0.0003 (7)
Bi17	0.0181 (10)	0.0239 (11)	0.0206 (10)	-0.0009 (8)	0.0117 (9)	-0.0020 (8)
Bi18	0.0188 (10)	0.0266 (10)	0.0197 (9)	-0.0006 (8)	0.0146 (9)	-0.0020 (7)
Bi19	0.0287 (12)	0.0275 (13)	0.0259 (12)	0.0029 (9)	0.0182 (11)	0.0021 (8)
Bi20	0.0109 (10)	0.0292 (12)	0.0119 (10)	-0.0003 (8)	0.0078 (9)	-0.0015 (7)
Bi21	0.0182 (10)	0.0262 (11)	0.0238 (9)	-0.0022 (8)	0.0148 (9)	-0.0001 (8)
Bi22	0.0185 (11)	0.0261 (11)	0.0157 (10)	0.0003 (8)	0.0122 (10)	-0.0015 (8)
Bi23	0.0177 (10)	0.0262 (10)	0.0171 (10)	-0.0003 (8)	0.0124 (9)	-0.0011 (7)
Bi24	0.0191 (11)	0.0264 (11)	0.0182 (10)	0.0020 (8)	0.0140 (10)	0.0008 (7)
Bi25	0.0157 (10)	0.0261 (10)	0.0218 (10)	0.0001 (8)	0.0128 (9)	0.0003 (8)
Bi26	0.0112 (10)	0.0298 (11)	0.0173 (9)	0.0001 (7)	0.0101 (9)	0.0014 (7)
Bi27	0.0136 (10)	0.0270 (11)	0.0186 (10)	-0.0023 (8)	0.0102 (9)	0.0007 (8)
Bi28	0.0145 (10)	0.0315 (11)	0.0184 (10)	-0.0023 (8)	0.0113 (9)	-0.0009 (8)
Bi29	0.0126 (10)	0.0269 (11)	0.0155 (10)	-0.0003 (7)	0.0089 (9)	-0.0021 (8)
Bi30	0.0178 (11)	0.0221 (12)	0.0207 (11)	0.0001 (8)	0.0141 (10)	-0.0011 (7)
Bi31	0.0134 (9)	0.0298 (11)	0.0196 (9)	0.0001 (8)	0.0109 (9)	0.0002 (7)
Bi32	0.0142 (10)	0.0329 (12)	0.0193 (10)	-0.0014 (9)	0.0117 (9)	-0.0031 (9)
Bi33	0.0209 (10)	0.0293 (11)	0.0208 (10)	-0.0008 (8)	0.0148 (9)	-0.0005 (8)
Bi34	0.0195 (10)	0.0296 (11)	0.0233 (9)	-0.0011 (8)	0.0160 (9)	-0.0010 (8)
Bi35	0.0240 (12)	0.0234 (12)	0.0284 (12)	-0.0002 (8)	0.0164 (11)	-0.0021 (8)
Bi36	0.0136 (10)	0.0280 (11)	0.0213 (10)	0.0015 (8)	0.0112 (9)	0.0018 (8)
Bi37	0.0206 (10)	0.0243 (10)	0.0212 (9)	0.0002 (8)	0.0155 (9)	0.0010 (7)
Bi38	0.0173 (11)	0.0282 (11)	0.0175 (10)	-0.0021 (8)	0.0117 (10)	-0.0022 (8)
Bi39	0.0235 (11)	0.0245 (11)	0.0177 (10)	-0.0019 (8)	0.0144 (10)	-0.0020 (7)
Bi40	0.0211 (10)	0.0262 (11)	0.0224 (10)	0.0000 (8)	0.0156 (9)	-0.0016 (8)
Bi41	0.0250 (12)	0.0247 (11)	0.0259 (11)	0.0028 (8)	0.0199 (11)	0.0028 (8)
Bi42	0.0149 (10)	0.0346 (11)	0.0200 (9)	-0.0002 (8)	0.0110 (9)	0.0007 (8)
Bi43	0.0133 (9)	0.0303 (11)	0.0152 (9)	0.0011 (8)	0.0085 (8)	0.0010 (7)
Bi44	0.0133 (10)	0.0276 (12)	0.0168 (10)	0.0002 (8)	0.0092 (9)	-0.0004 (8)
Bi45	0.0192 (10)	0.0248 (10)	0.0222 (9)	0.0013 (8)	0.0160 (9)	0.0016 (7)
Bi46	0.0196 (10)	0.0247 (11)	0.0196 (9)	-0.0006 (8)	0.0124 (9)	0.0024 (8)
Bi47	0.0262 (12)	0.0218 (12)	0.0265 (12)	-0.0007 (8)	0.0154 (11)	-0.0034 (8)
Bi48	0.0148 (10)	0.0291 (12)	0.0183 (10)	0.0010 (8)	0.0116 (10)	0.0006 (7)
Se1	0.015 (2)	0.018 (2)	0.019 (2)	0.0055 (19)	0.012 (2)	0.0058 (19)
Se2	0.015 (2)	0.028 (3)	0.010 (2)	-0.002 (2)	0.009 (2)	-0.0045 (19)
Se3	0.016 (3)	0.020 (3)	0.014 (2)	0.000 (2)	0.009 (2)	0.0012 (18)
Se4	0.010 (2)	0.020 (2)	0.013 (2)	0.0002 (19)	0.006 (2)	0.0015 (18)
Se5	0.014 (3)	0.025 (3)	0.020 (2)	-0.002 (2)	0.014 (2)	-0.002 (2)
Se6	0.011 (2)	0.018 (3)	0.018 (2)	-0.0006 (19)	0.010 (2)	0.0013 (19)
Se7	0.012 (2)	0.024 (2)	0.014 (2)	-0.0016 (18)	0.011 (2)	0.0009 (18)
Se8	0.015 (2)	0.022 (3)	0.014 (2)	-0.0028 (19)	0.011 (2)	-0.0036 (18)
Se9	0.009 (2)	0.027 (3)	0.008 (2)	0.0023 (19)	0.003 (2)	0.0015 (18)

Se10	0.013 (2)	0.016 (2)	0.017 (2)	-0.0013 (18)	0.010 (2)	-0.0023 (18)
Se11	0.010 (2)	0.023 (3)	0.009 (2)	0.0055 (18)	0.005 (2)	0.0021 (17)
Se12	0.012 (2)	0.024 (3)	0.016 (2)	0.0013 (19)	0.012 (2)	0.0004 (18)
Se13	0.011 (2)	0.024 (3)	0.013 (2)	0.0041 (19)	0.009 (2)	0.0025 (18)
Se14	0.017 (3)	0.015 (3)	0.023 (3)	0.0015 (19)	0.014 (2)	-0.001 (2)
Se15	0.011 (2)	0.025 (3)	0.009 (2)	-0.0004 (18)	0.008 (2)	-0.0001 (18)
Se16	0.011 (2)	0.025 (3)	0.006 (2)	0.0009 (19)	0.004 (2)	-0.0014 (18)
Se17	0.006 (2)	0.029 (3)	0.017 (2)	0.0026 (18)	0.010 (2)	0.0035 (19)
Se18	0.017 (2)	0.022 (3)	0.012 (2)	0.0003 (19)	0.012 (2)	0.0018 (18)
Se19	0.012 (2)	0.020 (2)	0.013 (2)	0.0016 (18)	0.005 (2)	0.0017 (18)
Se20	0.012 (2)	0.023 (3)	0.025 (3)	0.000 (2)	0.014 (2)	-0.001 (2)
Se21	0.020 (3)	0.015 (3)	0.014 (2)	0.003 (2)	0.010 (2)	0.0024 (18)
Se22	0.016 (3)	0.019 (2)	0.017 (2)	0.0013 (19)	0.011 (2)	-0.0009 (18)
Se23	0.009 (2)	0.021 (3)	0.018 (2)	-0.0021 (18)	0.009 (2)	-0.0038 (19)
Se24	0.002 (2)	0.022 (2)	0.007 (2)	0.0018 (17)	0.0004 (19)	0.0026 (17)
Se25	0.005 (2)	0.030 (3)	0.007 (2)	0.0027 (18)	0.002 (2)	-0.0002 (18)
Se26	0.007 (2)	0.024 (3)	0.014 (2)	0.0004 (18)	0.009 (2)	0.0006 (18)
Se27	0.012 (2)	0.020 (3)	0.015 (2)	-0.0010 (18)	0.009 (2)	0.0011 (18)
Se28	0.009 (2)	0.034 (3)	0.0015 (19)	0.000 (2)	0.0015 (19)	-0.0013 (18)
Se29	0.017 (2)	0.016 (2)	0.015 (2)	0.0001 (19)	0.012 (2)	-0.0005 (17)
Se30	0.014 (2)	0.021 (2)	0.014 (2)	0.0017 (18)	0.011 (2)	0.0019 (17)
Se31	0.020 (3)	0.014 (2)	0.023 (2)	0.0003 (18)	0.017 (2)	0.0026 (18)
Se32	0.014 (2)	0.019 (2)	0.020 (2)	0.0000 (18)	0.013 (2)	-0.0009 (18)
Se33	0.022 (3)	0.021 (3)	0.014 (2)	-0.001 (2)	0.009 (2)	-0.0004 (18)
Se34	0.010 (2)	0.022 (2)	0.007 (2)	0.0003 (19)	0.005 (2)	0.0013 (17)
Se35	0.014 (2)	0.028 (3)	0.015 (2)	-0.0008 (19)	0.013 (2)	0.0019 (18)
Se36	0.009 (2)	0.027 (3)	0.016 (2)	-0.0010 (19)	0.009 (2)	-0.0026 (19)
Se37	0.021 (3)	0.018 (2)	0.020 (2)	0.0027 (19)	0.016 (2)	-0.0004 (18)
Se38	0.010 (2)	0.022 (2)	0.017 (2)	-0.0001 (18)	0.010 (2)	0.0000 (19)
Se39	0.016 (2)	0.028 (3)	0.020 (2)	0.001 (2)	0.015 (2)	-0.001 (2)
Se40	0.004 (2)	0.024 (2)	0.012 (2)	0.0027 (17)	0.0039 (19)	-0.0003 (17)
Se41	0.018 (2)	0.016 (2)	0.019 (2)	0.0010 (18)	0.013 (2)	0.0008 (18)
Se42	0.013 (2)	0.026 (3)	0.011 (2)	0.0029 (19)	0.007 (2)	0.0010 (18)
Se43	0.010 (2)	0.022 (2)	0.009 (2)	0.0014 (18)	0.006 (2)	0.0006 (17)
Se44	0.015 (2)	0.023 (3)	0.016 (2)	-0.001 (2)	0.011 (2)	-0.0011 (19)
Se45	0.015 (2)	0.029 (3)	0.019 (2)	0.0016 (19)	0.013 (2)	0.0002 (18)
Se46	0.014 (2)	0.026 (2)	0.011 (2)	0.0014 (19)	0.008 (2)	-0.0002 (17)
Se47	0.009 (2)	0.024 (3)	0.019 (2)	-0.0023 (18)	0.010 (2)	-0.0025 (19)
Se48	0.012 (2)	0.028 (3)	0.016 (2)	0.0032 (18)	0.010 (2)	0.0019 (18)

Table S 74. Selected Bi-O distances (Å) in β -BiSeO₃Cl ($d_{\max}=3\text{\AA}$)

Atom1	Atom2	d, Å	Atom1	Atom2	d, Å	Atom1	Atom2	d, Å
Bi1	O23	2.336(33)	Bi9	O14	2.299(44)	Bi15	O131	2.264(39)
	O75	2.366(40)		O116	2.301(35)		O15	2.383(21)
	O76	2.399(32)		O67	2.356(27)		O26	2.402(45)
	O87	2.423(21)		O119	2.387(33)		O142	2.453(40)
	O132	2.448(36)		O75	2.531(44)		O133	2.525(38)
	O120	2.492(42)		O136	2.643(24)		O104	2.609(32)
	O25	2.501(22)		O63	2.663(28)		O3	2.734(25)
	O96	2.502(33)		O76	2.849(36)		O59	2.760(38)
Bi2	O103	2.472(39)	Bi10	O6	2.115(28)	Bi16	O58	2.871(28)
	O69	2.479(31)		O54	2.268(29)		O116	2.602(38)
	O64	2.482(39)		O36	2.450(53)		O20	2.973(38)
	O61	2.486(28)		O41	2.562(37)		O82	2.842(29)
	O135	2.494(31)		O31	2.733(47)		O136	2.142(30)
	O40	2.636(30)		O102	2.390(35)		O61	2.473(21)
	O106	2.639(20)		O140	2.436(41)		O109	2.500(33)
	O124	2.666(40)		O68	2.445(49)		O64	2.739(34)
Bi3	O11	2.668(48)	Bi11	O93	2.490(23)	Bi19	O66	2.399(35)
	O127	2.822(43)		O39	2.539(29)		O72	2.441(36)
	O143	2.220(31)		O66	2.565(55)		O39	2.465(10)
	O91	2.236(40)		O67	2.670(25)		O73	2.528(15)
	O42	2.480(39)		O119	2.765(21)		O23	2.536(22)
	O134	2.588(28)		O20	2.809(40)		O140	2.607(35)
	O70	2.655(31)		O116	2.888(25)		O87	2.623(14)
	O122	2.535(13)		O43	2.169(31)		O49	2.629(20)
Bi4	O21	2.743(20)	Bi12	O8	2.265(42)	Bi20	O13	2.706(14)
	O89	2.965(25)		O15	2.485(41)		O84	2.733(30)
	O121	2.836(12)		O59	2.636(40)		O106	2.356(34)
Bi5	O30	2.192(14)	Bi13	O142	2.736(39)	Bi22	O69	2.381(35)
	O108	2.303(44)		O115	2.347(32)		O16	2.410(53)
	O81	2.446(14)		O27	2.395(38)		O50	2.419(13)
Bi6	O83	2.559(20)	Bi14	O9	2.396(28)	Bi21	O141	2.457(23)
	O144	2.735(11)		O105	2.404(50)		O114	2.463(29)
	O25	2.267(24)		O18	2.435(27)		O80	2.469(38)
	O100	2.352(33)		O113	2.436(26)		O95	2.476(29)
	O10	2.366(38)		O101	2.443(41)		O51	2.590(30)
	O82	2.462(54)		O130	2.482(32)		O52	2.241(45)
	O29	2.478(36)		O80	2.304(14)		O58	2.317(23)
	O132	2.512(32)		O24	2.334(32)		O77	2.342(46)
Bi7	O30	2.797(23)	Bi8	O20	2.415(37)	Bi22	O104	2.446(32)
	O108	2.826(12)		O16	2.469(28)		O44	2.576(44)
	O44	2.270(34)		O93	2.489(41)		O86	2.580(36)
	O31	2.372(34)		O57	2.559(32)		O37	2.682(41)
	O36	2.373(39)		O143	2.759(37)		O6	2.848(31)
	O27	2.495(29)		O91	2.840(21)		O36	2.965(21)
	O101	2.610(40)						
	O85	2.644(25)						
Bi8	O1	2.675(51)						
	O41	2.689(28)						
	O35	2.902(34)						

Table S 75. Continued

Atom1	Atom2	d, Å	Atom1	Atom2	d, Å	Atom1	Atom2	d, Å
Bi23	O139	2.215(24)	Bi29	O127	2.242(42)	Bi36	O34	2.334(24)
	O35	2.326(41)		O55	2.303(55)		O46	2.402(41)
	O128	2.340(41)		O11	2.373(31)		O71	2.441(51)
	O85	2.418(30)		O19	2.380(21)		O92	2.479(50)
	O137	2.543(32)		O135	2.583(36)		O95	2.509(33)
	O131	2.616(33)		O100	2.649(37)		O102	2.656(23)
	O110	2.732(13)		O45	2.651(29)		O138	2.694(18)
	O43	2.877(12)		O30	2.811(27)		O141	2.779(12)
Bi24	O47	2.271(32)	Bi30	O53	2.318(54)	Bi37	O68	2.999(37)
	O74	2.314(22)		O94	2.375(40)		O5	2.084(11)
	O126	2.333(21)		O79	2.384(24)		O17	2.440(37)
	O78	2.376(23)		O125	2.423(30)		O32	2.468(16)
	O53	2.558(36)		O129	2.430(48)		O118	2.776(13)
	O117	2.671(29)		O26	2.447(36)	Bi38	O122	2.322(36)
	O5	2.708(40)		O60	2.550(37)		O33	2.405(27)
	O129	2.576(44)		O133	2.555(35)		O89	2.417(47)
Bi25	O138	2.163(34)	Bi31	O47	2.657(38)		O38	2.424(31)
	O72	2.433(33)		O4	2.948(44)		O9	2.518(37)
	O68	2.472(28)	Bi32	O107	2.279(27)		O2	2.687(20)
	O66	2.724(44)		O42	2.337(24)		O62	2.694(41)
Bi26	O84	2.202(46)		O96	2.391(26)	Bi39	O113	2.840(47)
	O56	2.297(23)		O70	2.428(50)		O112	2.306(21)
	O13	2.321(31)		O120	2.599(39)		O17	2.394(33)
	O98	2.417(21)		O19	2.617(40)		O22	2.471(25)
	O107	2.579(36)		O134	2.728(40)		O117	2.481(42)
	O73	2.593(27)		O28	2.747(33)		O118	2.483(31)
	O24	2.662(33)		O55	2.920(24)		O88	2.543(43)
	O143	2.825(46)	Bi33	O3	2.206(30)		O33	2.666(32)
Bi27	O124	2.245(46)		O12	2.363(42)		O38	2.883(51)
	O109	2.361(26)		O58	2.548(34)		O21	2.929(41)
	O63	2.454(40)		O77	2.749(40)		O122	2.971(26)
	O29	2.489(22)	Bi34	O34	2.529(20)	Bi40	O1	2.186(39)
	O64	2.520(56)		O92	2.743(21)		O97	2.406(31)
	O103	2.572(29)		O10	2.886(45)		O35	2.538(48)
	O46	2.647(30)	Bi35	O32	2.488(33)		O128	2.766(31)
	O71	2.841(42)		O118	2.496(13)	Bi41	O111	2.330(27)
	O10	2.871(48)		O88	2.525(13)		O65	2.438(12)
Bi28	O34	2.955(21)		O86	2.535(26)		O62	2.467(20)
	O45	2.235(15)		O115	2.611(32)		O90	2.505(40)
	O81	2.334(29)		O12	2.621(30)	Bi42	O99	2.529(36)
	O144	2.459(56)		O112	2.661(30)		O123	2.567(38)
	O50	2.496(26)		O105	2.673(41)		O78	2.655(33)
	O114	2.570(34)		O77	2.679(26)		O4	2.788(37)
	O98	2.593(21)		O52	2.782(31)		O74	2.802(36)
	O48	2.617(21)					O47	2.926(34)
	O83	2.646(32)					O48	2.288(34)
	O56	2.895(38)					O49	2.381(24)
							O56	2.563(42)
							O13	2.736(34)

Table S 76. Continued

Atom1	Atom2	d, Å
Bi43	O28	2.248(21)
	O40	2.284(43)
	O55	2.610(27)
	O11	2.652(24)
Bi44	O130	2.314(34)
	O110	2.325(58)
	O4	2.449(35)
	O99	2.455(29)
	O18	2.509(35)
	O51	2.563(10)
	O43	2.750(18)
	O8	2.818(38)
Bi45	O2	2.115(21)
	O7	2.417(35)
	O65	2.473(42)
	O123	2.765(32)
Bi46	O57	2.694(29)
	O28	2.991(26)
Bi47	O123	2.444(56)
	O7	2.473(29)
	O90	2.483(26)
	O137	2.539(28)
	O111	2.560(48)
	O94	2.576(50)
	O97	2.620(16)
	O139	2.709(13)
	O128	2.732(27)
	O79	2.733(37)
Bi48	O60	2.292(40)
	O37	2.346(35)
	O21	2.368(29)
	O125	2.473(11)
	O22	2.476(19)
	O121	2.522(33)
	O6	2.826(37)
	O54	2.892(31)
	O99	2.455(21)
	O18	2.509(38)
	O51	2.563(46)
	O43	2.750(29)
	O8	2.818(35)

Table S 77. Selected Bi-Cl distances (\AA) in $\beta\text{-BiSeO}_3\text{Cl}$ ($d_{\text{max}}=4\text{\AA}$)

Atom1	Atom2	d, \AA	Atom1	Atom2	d, \AA	Atom1	Atom2	d, \AA
Bi1	Cl24	3.966(14)	Bi25	Cl46	2.628(21)	Bi48	Cl33	3.927(12)
Bi3	Cl30	2.738(13)		Cl41	2.676(15)			
	Cl37	2.922(21)		Cl37	3.341(12)			
	Cl39	3.461(23)		Cl30	3.425(20)			
	Cl42	3.794(12)	Bi26	Cl44	3.983(12)			
Bi4	Cl16	2.483(20)	Bi31	Cl40	2.493(13)			
	Cl45	2.652(12)		Cl25	2.509(13)			
	Cl8	2.653(14)		Cl20	2.538(26)			
	Cl33	3.075(11)		Cl29	3.169(22)			
	Cl1	3.317(19)		Cl15	3.259(11)			
Bi5	Cl24	2.460(14)	Bi33	Cl13	2.650(18)			
	Cl33	2.548(20)		Cl15	2.690(12)			
	Cl32	2.560(11)		Cl34	3.168(20)			
	Cl28	2.905(20)		Cl47	3.173(11)			
	Cl1	2.977(12)		Cl32	3.472(12)			
Bi6	Cl48	2.747(23)	Bi34	Cl35	2.484(11)			
	Cl31	2.897(12)		Cl47	2.584(16)			
	Cl41	3.422(14)		Cl34	2.674(13)			
	Cl46	3.790(22)		Cl19	3.199(17)			
Bi7	Cl21	3.970(12)		Cl21	3.312(13)			
Bi10	Cl2	2.751(21)	Bi37	Cl4	2.607(12)			
	Cl14	2.910(13)		Cl12	2.684(20)			
	Cl6	3.430(14)		Cl14	3.329(22)			
	Cl10	3.780(21)		Cl2	3.442(15)			
Bi12	Cl11	2.760(14)	Bi40	Cl28	2.648(10)			
	Cl22	2.933(20)		Cl1	2.661(18)			
	Cl12	3.421(21)		Cl43	3.215(12)			
	Cl4	3.798(13)		Cl17	3.270(13)			
Bi13	Cl23	3.935(14)		Cl18	3.469(22)			
Bi14	Cl27	3.904(13)	Bi42	Cl19	2.655(16)			
Bi16	Cl9	2.528(10)		Cl3	2.725(13)			
	Cl26	2.568(15)		Cl8	3.136(13)			
	Cl5	2.569(22)		Cl45	3.165(10)			
	Cl27	3.202(21)		Cl44	3.525(19)			
	Cl38	3.208(12)	Bi43	Cl38	2.693(11)			
Bi17	Cl23	2.501(14)		Cl43	2.807(19)			
	Cl21	2.550(20)		Cl36	3.144(18)			
	Cl7	2.603(14)		Cl18	3.325(14)			
	Cl19	2.961(90)		Cl7	3.471(13)			
	Cl3	3.020(19)	Bi44	Cl29	3.940(14)			
Bi18	Cl42	2.612(13)	Bi45	Cl10	2.631(20)			
	Cl39	2.680(23)		Cl6	2.695(13)			
	Cl31	3.377(19)		Cl22	3.360(14)			
	Cl48	3.471(13)		Cl11	3.462(25)			
Bi21	Cl29	2.519(13)	Bi46	Cl44	2.530(20)			
	Cl36	2.522(12)		Cl17	2.533(13)			
	Cl18	2.624(22)		Cl27	2.549(12)			
	Cl15	2.835(21)		Cl43	2.965(10)			
	Cl13	2.977(12)		Cl38	3.034(17)			

Table S 78. Selected Se-O distances (Å) in β -BiSeO₃Cl

Atom1	Atom2	d, Å	Atom1	Atom2	d, Å	Atom1	Atom2	d, Å
Se1	O59	1.585(46)	Se17	O129	1.643(32)	Se33	O126	1.662(39)
	O32	1.672(33)		O22	1.737(39)		O12	1.716(28)
	O52	1.722(31)		O17	1.765(27)		O112	1.762(28)
Se2	O83	1.679(28)	Se18	O95	1.617(23)	Se34	O113	1.670(44)
	O84	1.724(35)		O103	1.684(30)		O99	1.705(31)
	O72	1.774(41)		O34	1.709(43)		O65	1.710(29)
Se3	O137	1.689(42)	Se19	O14	1.733(25)	Se35	O120	1.645(33)
	O15	1.702(29)		O40	1.740(41)		O100	1.696(21)
	O26	1.740(33)		O124	1.756(36)		O55	1.716(41)
Se4	O41	1.675(54)	Se20	O134	1.658(33)	Se36	O8	1.740(31)
	O7	1.745(24)		O61	1.688(45)		O5	1.750(59)
	O139	1.793(33)		O127	1.709(24)		O74	1.771(23)
Se5	O67	1.724(46)	Se21	O90	1.732(33)	Se37	O85	1.646(36)
	O23	1.733(42)		O47	1.751(32)		O18	1.685(21)
	O66	1.764(27)		O53	1.759(39)		O43	1.757(55)
Se6	O86	1.671(33)	Se22	O104	1.678(21)	Se38	O133	1.673(41)
	O27	1.725(52)		O125	1.742(30)		O37	1.678(35)
	O36	1.778(27)		O6	1.762(56)		O58	1.751(28)
Se7	O140	1.690(24)	Se23	O96	1.665(23)	Se39	O141	1.658(31)
	O49	1.706(59)		O73	1.675(36)		O93	1.698(22)
	O92	1.724(37)		O42	1.699(44)		O68	1.726(56)
Se8	O46	1.675(53)	Se24	O98	1.705(42)	Se40	O57	1.622(25)
	O69	1.715(33)		O16	1.706(34)		O28	1.726(41)
	O64	1.750(28)		O143	1.740(29)		O70	1.730(45)
Se9	O87	1.660(33)	Se25	O108	1.704(39)	Se41	O62	1.640(24)
	O107	1.727(39)		O138	1.723(27)		O4	1.673(55)
	O13	1.766(25)		O71	1.744(36)		O130	1.714(31)
Se10	O105	1.644(31)	Se26	O115	1.646(21)	Se42	O91	1.743(44)
	O44	1.724(26)		O33	1.696(30)		O119	1.748(34)
	O77	1.733(42)		O118	1.724(42)		O136	1.752(39)
Se11	O54	1.660(22)	Se27	O79	1.643(25)	Se43	O19	1.699(36)
	O2	1.757(55)		O128	1.733(40)		O132	1.709(44)
	O38	1.800(35)		O131	1.745(30)		O30	1.763(35)
Se12	O88	1.680(43)	Se28	O76	1.705(21)	Se44	O114	1.687(20)
	O9	1.701(47)		O29	1.725(33)		O24	1.726(38)
	O122	1.730(28)		O109	1.754(55)		O56	1.767(53)
Se13	O106	1.685(39)	Se29	O101	1.710(32)	Se45	O82	1.717(33)
	O45	1.704(34)		O110	1.718(54)		O144	1.729(28)
	O11	1.785(31)		O35	1.737(29)		O48	1.766(44)
Se14	O39	1.694(21)	Se30	O117	1.645(41)	Se46	O51	1.652(44)
	O75	1.712(31)		O60	1.668(27)		O142	1.654(50)
	O116	1.812(43)		O21	1.712(57)		O3	1.744(30)
Se15	O123	1.691(39)	Se31	O89	1.644(45)	Se47	O10	1.673(32)
	O94	1.708(35)		O97	1.692(35)		O63	1.690(42)
	O78	1.715(28)		O111	1.774(31)		O25	1.724(33)
Se16	O135	1.687(21)	Se32	O20	1.684(29)	Se48	O121	1.656(39)
	O50	1.694(33)		O102	1.696(46)		O31	1.754(21)
	O81	1.788(55)		O80	1.725(40)		O1	1.784(36)

Table S 79. Fractional atomic coordinates and isotropic or equivalent isotropic displacement parameters (\AA^2) of $\text{Bi}_6(\text{SeO}_3)_4\text{Cl}_{10}$

	<i>x</i>	<i>y</i>	<i>z</i>	$U_{\text{iso}}^*/U_{\text{eq}}$	Occ. (<1)
Bi1a	0.48273 (2)	0.34082 (5)	0.36920 (3)	0.01344 (12)	0.960 (2)
Bi1b	0.5189 (5)	0.4141 (18)	0.1366 (8)	0.025 (4)	0.040 (2)
Se3a	0.51770 (5)	0.43441 (13)	0.19264 (8)	0.01236 (19)*	0.9604
Se3b	0.4825 (11)	0.331 (3)	0.3145 (16)	0.005 (4)*	0.0396
Bi2	0.853973 (19)	1.11560 (5)	0.57426 (3)	0.01572 (12)	
Bi3	0.95274 (2)	0.83971 (5)	0.84829 (3)	0.01647 (12)	
Bi4	0.66931 (2)	0.61536 (6)	0.37377 (3)	0.02098 (13)	
Bi5	0.86877 (2)	0.62396 (5)	0.58018 (3)	0.01797 (12)	
Bi6	0.66324 (2)	1.12862 (5)	0.34402 (3)	0.01840 (12)	
Se1	0.73099 (5)	1.34197 (12)	0.56176 (7)	0.0113 (3)	
Se2	1.01931 (5)	0.93685 (12)	0.69363 (7)	0.0109 (3)	
Se4	0.72380 (5)	0.84150 (12)	0.55349 (7)	0.0124 (3)	
Cl1	0.84786 (13)	0.6432 (3)	0.74343 (18)	0.0175 (7)	
Cl2	1.06902 (13)	0.8894 (4)	1.00701 (18)	0.0180 (7)	
Cl3	0.55971 (17)	0.6180 (4)	0.4501 (2)	0.0263 (10)	
Cl4	0.86972 (16)	1.1267 (4)	0.75028 (19)	0.0233 (9)	
Cl5	0.92933 (14)	0.6500 (3)	0.98585 (18)	0.0186 (8)	
Cl6	0.79082 (14)	0.6136 (4)	0.38048 (19)	0.0221 (8)	
Cl7	0.79039 (13)	1.1190 (4)	0.37837 (19)	0.0211 (8)	
Cl8	0.57275 (15)	0.1470 (4)	0.4788 (2)	0.0259 (9)	
Cl9	0.66974 (17)	0.3475 (5)	0.2228 (2)	0.0324 (11)	
Cl10	0.66601 (15)	0.8907 (5)	0.2209 (2)	0.0313 (11)	
O1	0.5591 (4)	0.3434 (10)	0.2993 (6)	0.017 (2)	
O2	0.7435 (4)	1.1414 (9)	0.5547 (6)	0.016 (3)	
O3	0.8129 (4)	1.3825 (9)	0.5756 (6)	0.017 (2)	
O4	0.7267 (5)	0.6416 (10)	0.5358 (6)	0.020 (3)	
O5	0.8063 (4)	0.8702 (9)	0.5658 (6)	0.016 (2)	
O6	1.0442 (4)	0.9601 (10)	0.8133 (5)	0.015 (2)	
O7	0.9458 (4)	0.8439 (10)	0.6870 (5)	0.016 (2)	
O8	0.6905 (4)	0.3686 (9)	0.4441 (5)	0.014 (2)	
O9	0.4469 (4)	0.4603 (12)	0.2189 (6)	0.021 (3)	
O10	0.9888 (4)	1.1233 (10)	0.6566 (5)	0.015 (2)	
O11	0.4453 (4)	0.1178 (10)	0.2828 (6)	0.020 (2)	
O12	0.6821 (4)	0.8812 (11)	0.4383 (6)	0.018 (2)	

Table S 80. Atomic displacement parameters (\AA^2) of $\text{Bi}_6(\text{SeO}_3)_4\text{Cl}_{10}$

	U^{11}	U^{22}	U^{33}	U^{12}	U^{13}	U^{23}
Bi1a	0.01377 (18)	0.01563 (19)	0.01177 (19)	−0.00004 (13)	0.00556 (13)	−0.00031 (13)
Bi1b	0.004 (4)	0.047 (8)	0.025 (6)	0.006 (4)	0.005 (4)	0.003 (5)
Bi2	0.01209 (16)	0.01578 (18)	0.01791 (18)	−0.00019 (13)	0.00359 (13)	−0.00043 (14)
Bi3	0.01887 (18)	0.01502 (18)	0.01827 (18)	0.00109 (14)	0.00996 (14)	−0.00113 (14)
Bi4	0.01430 (18)	0.0215 (2)	0.0221 (2)	−0.00059 (15)	0.00018 (15)	0.00140 (16)
Bi5	0.02051 (19)	0.01522 (18)	0.01863 (18)	0.00105 (15)	0.00744 (15)	0.00117 (14)
Bi6	0.01736 (18)	0.01718 (19)	0.01796 (18)	−0.00022 (14)	0.00287 (14)	0.00045 (15)
Se1	0.0126 (4)	0.0113 (4)	0.0120 (4)	−0.0002 (3)	0.0069 (3)	−0.0006 (3)
Se2	0.0122 (4)	0.0127 (4)	0.0082 (4)	−0.0001 (3)	0.0041 (3)	0.0006 (3)
Se4	0.0139 (4)	0.0118 (4)	0.0123 (4)	0.0012 (3)	0.0058 (3)	−0.0004 (3)
Cl1	0.0170 (11)	0.0231 (12)	0.0134 (10)	−0.0039 (9)	0.0064 (9)	−0.0034 (9)
Cl2	0.0158 (11)	0.0257 (13)	0.0116 (10)	−0.0023 (10)	0.0036 (8)	0.0000 (9)
Cl3	0.0315 (15)	0.0270 (15)	0.0253 (14)	−0.0046 (12)	0.0162 (12)	−0.0074 (11)
Cl4	0.0295 (14)	0.0265 (14)	0.0145 (11)	0.0063 (11)	0.0086 (10)	0.0026 (10)
Cl5	0.0221 (12)	0.0229 (13)	0.0148 (11)	0.0014 (10)	0.0116 (9)	0.0031 (9)
Cl6	0.0156 (11)	0.0343 (15)	0.0168 (11)	−0.0004 (11)	0.0063 (9)	0.0013 (11)
Cl7	0.0140 (11)	0.0334 (15)	0.0157 (11)	0.0009 (10)	0.0049 (9)	−0.0010 (10)

Cl8	0.0228 (13)	0.0334 (16)	0.0182 (12)	0.0072 (12)	0.0032 (10)	0.0061 (11)
Cl9	0.0288 (15)	0.048 (2)	0.0249 (14)	0.0100 (14)	0.0148 (12)	0.0150 (14)
Cl10	0.0196 (13)	0.048 (2)	0.0287 (15)	−0.0069 (13)	0.0113 (11)	−0.0183 (14)
O1	0.013 (3)	0.018 (4)	0.020 (4)	0.005 (3)	0.005 (3)	0.007 (3)
O2	0.015 (3)	0.007 (3)	0.032 (4)	0.002 (3)	0.014 (3)	0.001 (3)
O3	0.008 (3)	0.010 (3)	0.026 (4)	0.000 (3)	0.000 (3)	0.001 (3)
O4	0.032 (5)	0.008 (3)	0.022 (4)	−0.002 (3)	0.013 (3)	−0.004 (3)
O5	0.010 (3)	0.009 (3)	0.025 (4)	−0.001 (3)	0.001 (3)	−0.001 (3)
O6	0.018 (4)	0.017 (4)	0.011 (3)	−0.009 (3)	0.008 (3)	0.000 (3)
O7	0.015 (3)	0.019 (4)	0.016 (3)	−0.006 (3)	0.006 (3)	−0.001 (3)
O8	0.018 (3)	0.013 (3)	0.012 (3)	0.002 (3)	0.006 (3)	−0.006 (3)
O9	0.014 (4)	0.035 (5)	0.017 (4)	0.004 (3)	0.007 (3)	0.011 (3)
O10	0.012 (3)	0.014 (3)	0.015 (3)	−0.003 (3)	0.001 (3)	−0.001 (3)
O11	0.013 (3)	0.015 (4)	0.021 (4)	0.000 (3)	−0.007 (3)	−0.004 (3)
O12	0.013 (3)	0.022 (4)	0.016 (4)	−0.002 (3)	0.001 (3)	−0.001 (3)

Table S 81. Selected interatomic distances (Å) in $\text{Bi}_6(\text{SeO}_3)_4\text{Cl}_{10}$

atom1	atom2	d, Å	atom1	atom2	d, Å
Bi1a	O1	2.2609(89)	Bi3	Cl1	2.7965(23)
	O11	2.2646(70)		Cl5	2.8249(29)
	O9	2.3769(73)		Cl2	2.8372(21)
Bi2	O5	2.2821(60)	Bi4	Cl4	3.0602(25)
	O2	2.2942(67)		Cl2	3.3248(28)
	O3	2.4182(61)		Cl6	3.6969(29)
Bi3	O10	2.7141(59)	Bi5	Cl6	2.5742(28)
	O10	2.2280(69)		Cl3	2.9752(35)
	O7	2.4266(79)		Cl9	3.2382(33)
Bi4	O6	2.4297(75)	Bi6	Cl10	3.2768(33)
	O8	2.3042(68)		Cl1	2.7006(31)
	O4	2.3528(68)		Cl6	2.9281(26)
Bi5	O12	2.4172(68)	Se1	Cl2	2.9506(28)
	O11	2.7751(64)		Cl5	2.9548(29)
	O3	2.3472(62)		Cl7	2.5934(26)
Bi6	O6	2.4315(60)	Se2	Cl9	2.6494(34)
	O5	2.4457(61)		Cl10	2.7642(33)
	O7	2.6416(62)		Cl8	3.3001(35)
Bi1	O4	2.8847(84)	Se3a	O2	1.7118(60)
	O8	2.4721(69)		O3	1.7225(67)
	O12	2.4833(69)		O8	1.7253(69)
Bi2	O9	2.6416(64)	Se4	O10	1.7182(66)
	O1	2.7607(64)		O7	1.7220(69)
	Cl8	2.6322(24)		O6	1.7309(74)
Bi3	Cl3	2.8738(25)	Se4	O9	1.7093(77)
	Cl10	3.0243(26)		O11	1.7097(66)
	Cl3	3.2240(35)		O1	1.7380(77)
Bi4	Cl4	2.5999(30)		O12	1.7067(68)
	Cl7	2.8238(27)		O4	1.7166(69)
	Cl5	3.3140(29)		O5	1.7198(68)
Bi5	Cl2	3.3211(28)			

Table S 82. Fractional atomic coordinates and isotropic or equivalent isotropic displacement parameters (\AA^2) in $\text{PbBi}_{10}(\text{SeO}_3)_{12}\text{Cl}_8$

	<i>x</i>	<i>y</i>	<i>z</i>	$U_{\text{iso}}^*/U_{\text{eq}}$	Occ. (<1)
Bi1	0.5	0	0	0.0157 (10)	
Bi2	0.25	0	0.25	0.0390 (10)	0.9
Pb2	0.25	0	0.25	0.0390 (10)	0.1
Bi3	0.5	0	0.26397 (19)	0.0359 (11)	0.9
Pb3	0.5	0	0.26397 (19)	0.0359 (11)	0.1
Bi4	0.2407 (2)	0	0	0.0279 (9)	0.9
Pb4	0.2407 (2)	0	0	0.0279 (9)	0.1
Bi5	0.61813 (12)	−0.17735 (7)	0.38264 (13)	0.0278 (5)	0.9
Pb5	0.61813 (12)	−0.17735 (7)	0.38264 (13)	0.0278 (5)	0.1
Se1	0.3767 (2)	0.12635 (19)	0.1494 (2)	0.0090 (9)	
Se2	0.6504 (3)	0.1232 (2)	0.1218 (2)	0.0197 (11)	
Se3	0.3905 (3)	−0.11306 (18)	0.3900 (2)	0.0184 (11)	
Cl1	0.5	−0.2528 (7)	0.5	0.041 (6)	
Cl2	0.75	0.25	0.2359 (9)	0.046 (7)	
Cl3	0	0.25	0.25	0.072 (11)	
Cl4	0.75	0.25	0.0086 (11)	0.044 (7)	
O1	0.7551 (18)	0.0913 (16)	0.1223 (17)	0.017 (5)*	
O2	0.2930 (17)	0.0761 (14)	0.1235 (16)	0.013 (5)*	
O3	0.4605 (19)	0.0742 (17)	0.1230 (18)	0.021 (6)*	
O4	0.6216 (17)	0.0715 (16)	0.2073 (17)	0.016 (6)*	
O5	0.371 (2)	−0.098 (2)	0.4956 (19)	0.026 (9)*	
O6	0.6236 (17)	0.0679 (15)	0.0364 (17)	0.014 (5)*	
O7	0.4953 (16)	−0.099 (2)	0.3767 (18)	0.013 (6)*	
O8	0.3779 (17)	0.1014 (16)	0.2539 (19)	0.021 (6)*	
O9	0.3631 (18)	−0.0214 (12)	0.3627 (18)	0.018 (5)*	

Table S 83. Atomic displacement parameters (\AA^2) in $\text{PbBi}_{10}(\text{SeO}_3)_{12}\text{Cl}_8$

	U^{11}	U^{22}	U^{33}	U^{12}	U^{13}	U^{23}
Bi1	0.025 (2)	0.0130 (10)	0.0091 (16)	0	0	0
Bi2	0.065 (2)	0.0204 (9)	0.0315 (15)	0.0145 (12)	0.0253 (11)	0.0127 (10)
Pb2	0.065 (2)	0.0204 (9)	0.0315 (15)	0.0145 (12)	0.0253 (11)	0.0127 (10)
Bi3	0.057 (2)	0.0246 (15)	0.0259 (16)	−0.0132 (12)	0	0
Pb3	0.057 (2)	0.0246 (15)	0.0259 (16)	−0.0132 (12)	0	0
Bi4	0.0326 (19)	0.0227 (14)	0.0283 (13)	0	0	−0.0011 (9)
Pb4	0.0326 (19)	0.0227 (14)	0.0283 (13)	0	0	−0.0011 (9)
Bi5	0.0300 (10)	0.0128 (6)	0.0408 (11)	−0.0002 (7)	0.0060 (6)	−0.0006 (7)
Pb5	0.0300 (10)	0.0128 (6)	0.0408 (11)	−0.0002 (7)	0.0060 (6)	−0.0006 (7)
Se1	0.0087 (16)	0.0137 (16)	0.0045 (14)	−0.0002 (12)	−0.0052 (12)	0.0030 (12)
Se2	0.033 (2)	0.0054 (15)	0.0203 (19)	−0.0021 (15)	−0.0042 (17)	0.0022 (13)
Se3	0.038 (2)	0.0120 (14)	0.0057 (17)	−0.0012 (17)	0.0059 (13)	−0.0012 (13)
Cl1	0.082 (16)	0.014 (5)	0.028 (9)	0	−0.010 (8)	0
Cl2	0.099 (18)	0.025 (6)	0.012 (7)	−0.023 (9)	0	0
Cl3	0.12 (3)	0.018 (10)	0.080 (17)	0.009 (11)	0.051 (16)	−0.001 (13)
Cl4	0.083 (17)	0.021 (9)	0.027 (9)	−0.003 (12)	0	0

Table S 84. Selected interatomic distances (Å) in $PbBi_{10}(SeO_3)_{12}Cl_8$

atom1	atom2	d, Å	atom1	atom2	d, Å
Bi1	4xO6	2.372(27)	Se1	1xO2	1.650(27)
	4xO3	2.440(30)		1xO3	1.670(31)
Bi2 Pb2	2xO4	2.490(28)	Se2	1xO8	1.720(31)
	2xO2	2.520(26)		1xO4	1.700(28)
	2xO9	2.560(29)		1xO6	1.730(28)
	2xO1	2.600(28)	Se3	1xO1	1.750(29)
	2xO8	2.720(28)		1xO7	1.690(27)
Bi3 Pb3	2xO4	2.480(28)		1xO5	1.720(31)
	2xO7	2.520(33)	Bi5 Pb5	1xO9	1.750(23)
	2xO8	2.650(28)		1xO2	2.980(28)
	2xO3	2.670(30)		1xO4	3.000(28)
	2xO9	2.700(29)		1xCl1	2.962(6)
Bi4 Pb4	2xO5	2.490(34)		1xCl4	3.002(2)
	2xO2	2.520(26)		1xCl2	3.094(9)
	2xO6	2.530(27)		1xCl3	3.099(2)
	2xO1	2.540(28)			
	2xO9	2.750(29)			
Bi5 Pb5	1xO7	2.400(30)			
	1xO5	2.400(33)			
	1xO8	2.450(30)			
	1xO1	2.530(29)			

13) Bi₂MnO(SeO₃)₂Cl₃**Table S 85. Crystal data, measurement and structural refinement parameters for Bi₂MnO(SeO₃)₂Cl₃**

Bi ₂ MnO(SeO ₃) ₂ Cl ₃	
Crystal data	
Crystal symmetry	Monoclinic
space group	<i>P</i> 12 ₁ / <i>m</i> 1
a (Å)	8.5875 (6)
b (Å)	7.1448 (5)
c (Å)	8.6194 (6)
β (°)	107.015 (4)
V (Å ³)	505.70 (6)
Z	2
D _x (g/cm ³)	5.575
μ(mm ⁻¹)(0.7107Å)	43.94
Appearance	Brown needle
Crystal size (mm)	0.32 × 0.03 × 0.03
Data collection	
λ(Mo Kα)(Å)	0.71073
Scan mode	ω and φ
θ(min–max)(°)	2.5 – 37.9
R(int) (%)	4.7
Reciprocal recording	–14 ≤ h ≤ 14
	–11 ≤ k ≤ 10
	–14 ≤ l ≤ 14
Refinement	
Meas., obs., / indep.all (obs=I>3σ(I))	18853, 2021/2639
No. of Refined parameters	83
Refinement method	F
R1(F ²)(obs)/R1(F ²)(all) (%)	2.41/ 4.08
wR2(F ²)(obs) /wR2(F ²)(all) (%)	2.34/2.52
GOF(obs) / GOF(all)	1.15/1.07
Δρ _{max} / Δρ _{min} (e Å ⁻³)	1.86 /–2.08
Extinction coefficient	0.0089(11)

Table S 86. Fractional atomic coordinates and isotropic or equivalent isotropic displacement parameters (\AA^2) of $\text{Bi}_2\text{MnO}(\text{SeO}_3)_2\text{Cl}_3$

	<i>x</i>	<i>y</i>	<i>z</i>	$U_{\text{iso}}^*/U_{\text{eq}}$
Bi1	0.20230 (3)	0.25	0.24192 (2)	0.01275 (6)
Bi2	0.27516 (3)	0.25	0.73356 (2)	0.01265 (6)
Se1	0.26359 (6)	0.75	0.17875 (6)	0.00809 (14)
Se2	0.60738 (6)	0.25	0.21511 (6)	0.00786 (14)
Mn1	0.5	0.5	0.5	0.0052 (2)
Cl1	0.02540 (18)	0.25	0.47771 (18)	0.0224 (5)
Cl2	0.11746 (12)	0.48480 (13)	0.88025 (11)	0.0160 (3)
O1	0.4033 (5)	0.25	0.1255 (4)	0.0135 (12)
O2	0.4346 (5)	0.75	0.1266 (5)	0.0153 (13)
O3	0.2972 (3)	0.9365 (3)	0.3149 (3)	0.0102 (8)
O4	0.6292 (3)	0.0620 (3)	0.3447 (3)	0.0102 (8)
O5	0.3967 (4)	0.25	0.4777 (4)	0.0079 (10)

Table S 87. Atomic displacement parameters (\AA^2) of $\text{Bi}_2\text{MnO}(\text{SeO}_3)_2\text{Cl}_3$

	U^{11}	U^{22}	U^{33}	U^{12}	U^{13}	U^{23}
Bi1	0.01091 (10)	0.01143 (10)	0.01418 (9)	0	0.00097 (7)	0
Bi2	0.01372 (10)	0.00921 (10)	0.01626 (10)	0	0.00632 (7)	0
Se1	0.0099 (2)	0.0059 (2)	0.0073 (2)	0	0.00078 (17)	0
Se2	0.0104 (2)	0.0061 (2)	0.0081 (2)	0	0.00429 (17)	0
Mn1	0.0070 (3)	0.0028 (3)	0.0063 (3)	−0.0009 (2)	0.0027 (2)	−0.0001 (2)
Cl1	0.0146 (7)	0.0350 (9)	0.0173 (6)	0	0.0043 (5)	0
Cl2	0.0173 (4)	0.0139 (5)	0.0186 (4)	0.0022 (3)	0.0080 (4)	−0.0029 (3)
O1	0.0100 (18)	0.016 (2)	0.0148 (18)	0	0.0037 (15)	0
O2	0.016 (2)	0.017 (2)	0.0154 (18)	0	0.0097 (16)	0
O3	0.0119 (12)	0.0081 (13)	0.0098 (11)	0.0010 (9)	0.0019 (9)	−0.0010 (8)
O4	0.0130 (13)	0.0075 (13)	0.0130 (12)	0.0021 (9)	0.0084 (10)	0.0032 (9)
O5	0.0095 (16)	0.0052 (17)	0.0086 (15)	0	0.0019 (13)	0

Table S 88. Selected bond distances (\AA) $\text{Bi}_2\text{MnO}(\text{SeO}_3)_2\text{Cl}_3$

Atom 1	Atom 2	d
Bi1	1xO5	2.2207(29)
	1xO1	2.2361(45)
	2xO3	2.4035(22)
	1xCl1	2.8714(18)
	2xCl2	3.2476(10)
	2xCl2	3.4255(10)
Bi2	1xO2	2.4304(39)
	2xO4	2.5344(24)
	1xCl1	2.5875(13)
	2xCl2	2.6924(11)
Se1	1xO5	2.7019(39)
	1xO2	1.6568(48)
Se2	2xO3	1.7429(23)
	1xO1	1.6958(39)
Mn1	2xO4	1.7218(23)
	2xO5	1.9785(15)
	2xO4	2.0219(29)
	2xO3	2.0392(22)

Abstract

One of the primary challenges concerns the discovery of novel inorganic compounds using a rational “design” in order to predict crystal structures and possible structure/properties relationships. In the absence of unified protocol for such a task, it remains a hot topic in the solid state chemistry community. At the UCCS, our group has a long experience and a strong “savoir-faire” related to the elaboration and characterization on new bismuth based compounds. Recently, a strategy to Design novel innovative compounds and/or establish bases for related mega-series of related compounds have been developed for these broad series compounds by our group. Results are such as a large family of compounds with related crystal structures have been understood in terms of building principles leading to the post prediction, preparation and characterization of novel members. In the chemical $\text{Bi}_2\text{O}_3 - \text{MO} - \text{P}_2\text{O}_5$ (M = various divalent metals) systems, at the origin of this work, these predictions have been feasible because versatile building units (BU) can be handled, modified and assembled in various manners. The key-description used for BUs relies on the anion-centered (here O^{2-}) polyhedra theory related to the bismuth atom. Thus, in the framework of ANR Multi-D InMaDe we have explored the Bi/M/X/O system, where M = Cu, Co, Mn etc. and X = P, V, As, Mo, Se and Cl. Several new compounds with new topologies have been obtained and their corresponding properties have been measured.

Key words: bismuth compounds, oxo-centered tetrahedra, design, transport properties, optical properties

Résumé

Un des enjeux majeurs en chimie du solide concerne la découverte de matériaux inorganiques à propriétés ciblées. En l’absence d’un protocole unique permettant d’y arriver, la situation des laboratoires français de « chimie du solide » en termes de prospection de nouveaux composés reste critique. A l’UCCS, notre groupe a une grande expérience et un savoir-faire reconnu liés à l’élaboration et la caractérisation de nouveaux matériaux à base de bismuth. Récemment, une stratégie de Design de composés innovants a été mise en place et développée pour cette série de composés. Il a ainsi été possible de décrire la majeure partie de nos composés en termes de briques élémentaires structurales permettant, à posteriori de prédire, préparer et caractériser de nouveaux membres. Dans les systèmes ternaires $\text{Bi}_2\text{O}_3 - \text{MO} - \text{P}_2\text{O}_5$ (M= métal de transition) à l’origine de ce travail, ces prédictions ont été rendues possibles parceque chacune de ces unités structurales peut être utilisée, modifiée et assemblée de différentes façons. Le point commun à ces briques élémentaires repose sur la description mettant en œuvre des tétraèdres centrés sur les anions (ici O^{2-}) et entourés par des atomes de bismuth. Ainsi, dans le cadre de l’ANR jeune chercheur Multi-D InMaDe, nous avons exploré les systèmes Bi/M/X/O avec M= Cu, Co, Mn... et X= P, V, As, Mo, Se et Cl-. De nouveaux composés présentant des topologies innovantes ont été obtenus et leurs propriétés mesurées dans certains cas.

Mots clés: bismuth composé, tétraèdres oxo-centrés, désign, propriétés de transport, propriétés optiques